A Study of the Pressure-Induced Mixed-Valence Transition in SmSe and SmS by X-Ray Absorption Spectroscopy

by

Karl Rudolf Bauchspieß

Diplom, Universität zu Köln, 1982

A THESIS SUBMITTED IN PARTIAL FULFILLMENT OF

THE REQUIREMENTS FOR THE DEGREE OF

DOCTOR OF PHILOSOPHY

in the Department

of

Physics

SIMON FRASER UNIVERSITY

August 1990

Approval

Name: Karl Rudolf Bauchspieß

Degree: Doctor of Philosophy

Title of Thesis: A Study of the Pressure-Induced Mixed-Valence Transition in SmSe and SmS by X-Ray Absorption Spectroscopy

Examining Committee:

Chairman: Dr. K.S. Viswanathan

Dr. E.D. Crozier

Senior Supervisor

Dr. A.E. Curzon

Dr. L.E. Ballentine

Dr. J.F. Cochran

University Examiner

Dr. T.M. Hayes

External Examiner

Department of Physics

Rensselaer Polytechnic Institute

Date approved: August 21, 1990

PARTIAL COPYRIGHT LICENSE

I hereby grant to Simon Fraser University the right to lend my thesis, project or extended essay (the title of which is shown below) to users of the Simon Fraser University Library, and to make partial or single copies only for such users or in response to a request from the library of any other university, or other educational institution, on its own behalf or for one of its users. I further agree that permission for multiple copying of this work for scholarly purposes may be granted by me or the Dean of Graduate Studies. It is understood that copying or publication of this work for financial gain shall not be allowed without my written permission.

Title of Thesis/Project/Extended Essay

A Study of the Pressure-Induced Mixed-Valence Transition in SmSe and SmS by X-Ray Absorption Spectroscopy

Author: _____
(Signature)

Karl Rudolf Bauchspiess
(Name)

September 24, 1990
(Date)

Abstract

SmSe and SmS undergo pressure-induced mixed-valence transitions. In the mixed-valence region the Sm ions fluctuate between the 2+ and 3+ valence state on the time scale of the Debye frequency. They are usually considered to be homogeneously mixed valent where the Sm-chalcogenide ion pairs take a single average separation rather than a dynamically distorted distribution with two different equilibrium positions corresponding to the two valence states of the rare earth ion. In this thesis x-ray absorption spectroscopy has been used to examine the transitions at pressures up to 75 kbar. The experiments were performed at the Sm L_{III}, L_{II} and Se K edges at room temperature on both compounds. In order to reduce the thermal contribution to the dynamical motion of the ions, the measurements were also made on SmSe at 77 K. These latter measurements represent the first low temperature x-ray absorption spectroscopy measurements to be made as a function of pressure.

Changes in the Sm valence with pressure were determined from the structure of the Sm L edges. Sm-chalcogenide pair distribution functions were obtained from the EXAFS spectra. In SmSe the EXAFS mean-square relative displacement between the Se and Sm ion pairs is observed to have a maximum in the mixed valence region. This maximum is discussed in view of the possible existence of two closely spaced Sm-coordination shells. From least-squares fitting in k- and in R-space and from a beating analysis of the EXAFS phase we conclude that if the lattice does respond to the fluctuation in the valence, then the two Sm-shells are separated by ~0.09 Å. To obtain this result it was first necessary to know the backscattering amplitudes and phase shifts for integer-valent Sm. In this thesis they were calculated from first principles according to curved-wave theory.

Acknowledgements

I would like to thank all those who have assisted me during my research through their comments and suggestions. I am indebted to Dr. Neil Alberding whose advice was always very helpful. I would like to thank Andrew Seary for his many suggestions regarding data analysis. Frequently he knew the answer to a computing problem before I even had finished my question. About data analysis I learned a lot from both of them.

Detong Jiang and Dr. Neil Alberding provided me with all the necessary information to run the word processor and use the drawing programs.

I would like to thank my advisor, Prof. Daryl Crozier, for his constant encouragement and interest in this work. I also thank him for his patience as the last parts of this thesis were being completed with delay because I was already working as a "postdoctoral" student.

Like Andrew Seary, Ken Urquhart was a profound source of information regarding computers. It makes work so much easier when one can depend on knowledgeable people.

During this work I appreciated many physics discussions with members of the "late-night" crowd at the physics department, in particular with Ross Walker, Don Hunter, and Steve Purcell.

The experiments were performed at the Stanford Synchrotron Radiation Laboratory in conjunction with the group of Prof. Robert Ingalls of the University of Washington in Seattle. I would like to thank him and his students for assistance and for many discussions: John Whitmore, John Tranquada, Brian Houser, and Jürgen Freund.

Thanks are due to Drs. A. Jayaraman, Fred Holtzberg, and Jim Allen for supplying SmSe samples. I am grateful to Dr. Grayson Via of EXXON Corp. who kindly let our group use his sample positioner, designed to move heavy loads.

I am grateful to Dr. Jorge E. Müller of the Kernforschungsanlage in Jülich / West Germany who took extra time to explain to me how to use his computer programs to calculate bandstructures in the linearized augmented plane-wave method. The knowledge and availability of his programs was the starting point for the calculation of scattering phases.

During my stay in Germany I also met with Prof. W.B. Holzapfel and Dr. J. Wittig who kindly provided me with information regarding the design of a high-pressure cell.

I thank Dr. Xiaohe Pan of IBM Corp. for lending me his laser printer to print drafts of this thesis.

I do express my thanks to my thesis examiners who took great care reading this thesis and in particular I wish to thank Prof. T.M. Hayes for his helpful suggestions.

My wish is that during my future career I will be encountering people who are equally helpful as those mentioned in these acknowledgements. This is a decisive contribution to the success of any project.

Table of Contents

		page
	Approval	ii
	Abstract	iii
	Acknowledgements	iv
	Table of Contents	vi
	List of Tables	x
	List of Figures	xii
1	**Introduction**	1
2	**The EXAFS Equation**	4
2.1	The EXAFS Formula	4
2.2	Obtaining g(R) from χ(k)	6
2.3	The Cumulant Expansion	9
2.4	The EXAFS Debye-Waller Factor	11
2.5	Many Body Effects	12
3	**Amplitudes and Phases**	19
3.1	Calculation of Atomic Charge Densities	19
3.2	Muffin-Tin Potentials	23
3.3	Logarithmic Derivatives	32

3.4 Calculation of Amplitudes and Phases 36
3.5 Central-Atom Phase Shifts 61
3.6 Pressure Dependence of Amplitude and Phase 64

4 **Mixed Valence** 73
4.1 Description of the Phenomenon 73
4.2 Sm Monochalcogenides 75
4.3 Valence Determination by L_{II}-/ L_{III}-Edge Spectroscopy 79

5 **Experiment** 82
5.1 Synchrotron Radiation 82
5.2 X-Ray Monochromator 84
5.3 Absorption Coefficients 94
5.4 Ionization Chambers 96
5.5 Optimum Sample Thickness 98
5.6 Signal-to-Noise Ratio 104
5.7 Absorption Coefficients Obtained from Experiment 106
5.8 Pressure Calibration 115
5.9 High-Pressure Cell 123
5.10 Liquid-Nitrogen Cryostat 136
5.11 Performing the Experiment 137

6 **Data Analysis** 140
6.1 Averaging Datasets 140
6.2 Step Number-to-Energy Conversion 143
6.3 Normalizing EXAFS Datasets 144
6.4 Monochromator Resolution 154
6.5 Fourier Transform 155

6.6 Window Functions 156
6.7 Fourier Filtering and the Determination of Amplitude and Phase . . . 159
6.8 Log-Ratio and Phase-Comparison Methods 162
6.9 Degrees of Freedom of a Signal 164
6.10 Least-Squares Fitting of EXAFS Spectra 166
6.11 Beating. 172
6.12 Valence Determination 176
6.13 Valence Interpolation Formula 180
6.14 Determination of Compression from the Scaling Relation k·R = const. . . 183

7 **Results for SmSe** 187
7.1 Pressure Determination 188
7.2 Analysis of the Se K Edge EXAFS of SmSe 210
7.3 Analysis of the Sm L_{III} Edge EXAFS of SmSe 236
7.4 Valence Determination 249

8 **Results for SmS** 265
8.1 Pressure Determination 265
8.2 Analysis of the Sm L_{III} Edge EXAFS of SmS 267
8.3 Valence Determination 275

9 **Discussion** 282
9.1 Two-Shell Analysis for the Se K Edge EXAFS 282
9.2 Grüneisen Parameter Derived from the Se K Edge EXAFS 289
9.3 Pressure Determination 291
9.4 EXAFS of the Sm L_{III} Edge 294
9.5 Future Work 295

10 **Summary** 298
10.1 Lattice Relaxation in SmSe 298
10.2 Valence of SmSe 300
10.3 Amplitudes and Phase Shifts 301
10.4 Additional Results 302

Appendix 304
A Rydberg Atomic Units 304
B Operating Range of the Monochromator 305
C Grüneisen Relation and Grüneisen Parameter 307
D Smoothing Function 310
E Least-Squares Fitting of EXAFS Spectra 314
F Formula for Valence Estimation 316

Bibliography 318

List of Tables

page

4.1 Properties of Sm monochalcogenides 78

5.1 Properties of Principal Reflections and their Harmonics for Si Single Crystals . 91
5.2 Properties of Principal Reflections for Si Single Crystals 92
5.3 Pressure vs. reduced volume for Cu at 300K and at 77K 119
5.4 Pressure vs. reduced volume for RbCl at 300K and at 77K 121

6.1 Properties of window functions 159

7.1 Pressure calibration from Cu K edge EXAFS at 300K (LOG.CU1.B) . . 199
7.2 Pressure calibration from Cu K edge EXAFS at 300K (LOG.CU1.C) . . 201
7.3 Pressure calibration from Rb K edge EXAFS in RbCl at 77K (LOG.RB6.F) . 203
7.4 Pressure calibration from Cu K edge EXAFS at 77K (LOG.CU1.G) . . . 207
7.5 Se K edge EXAFS at 300K (LOG.SE10.B) 213
7.6 Se K edge EXAFS at 77K (LOG.SEN13.F2) 217
7.7 Se K edge EXAFS at 77K (LOG.SEN14.F2) 218
7.8 Se K edge EXAFS at 77K (LOG.SEN19.F2) 222
7.9 Se K edge EXAFS at 77K (LOG.SEN24.F2) 225
7.10 Se K edge EXAFS at 77K (LOG.SEN8.F2) 227
7.11 Se K edge EXAFS at 77K (LOG.SE10.G) 229
7.12 Se K edge EXAFS at 77K (LOG.SE13.G) 233
7.13 Sm L_{III} edge EXAFS at 300K (LOG.SM4.B) 237
7.14 Sm L_{III} edge EXAFS at 77K (LOG.SM7.G) 242
7.15 Valence determination from the Sm L_{III} edge of EXAFS datasets at 300K (VAL.SMSEXF.B) 250
7.16 Valence determination from the Sm L_{III} edge at 300K (VAL.SMSEED.C) . 252
7.17 Valence determination from the Sm L_{III} edge of EXAFS datasets at 300K (VAL.SMSEXF.C) 253

7.18 Valence determination from the Sm L_{II} edge at 77K (VAL.SMSEE2.G) . . 254
7.19 Valence determination from the Sm L_{III} edge of EXAFS datasets at 77K (VAL.SMSEX3.G) 255

8.1 Pressure calibration from Cu K edge EXAFS at 300K (LOG.CU1.A) . . 266
8.2 Sm L_{III} edge EXAFS at 300K (LOG.SM2.A) 269
8.3 Valence determination from the Sm L_{III} edge at 300K (VAL.SMSX.A) . . 276
8.4 Valence determination from the Sm L_{III} edge of EXAFS datasets at 300K (VAL.SMSXAF.A) 278

9.1 Se K edge EXAFS at 77K (LOG.SEN25.F2) 284
9.2 Grüneisen parameter at 77K according to Eq. (9.3) 290
9.3 Pressure calibration from Cu K edge EXAFS by the scaling method . . 293

List of Figures

page

2.1 Inelastic mean free path λ as a function of k. 15

3.1 Muffin-tin potential along the [110]-direction in the fcc structure. . . . 24
3.2 Backscattering amplitude for copper metal in plane-wave approximation. . . 39
3.3 Backscattering phase for copper metal in plane-wave approximation. . . 40
3.4 Backscattering amplitude for copper metal in curved-wave theory for R = 2.5 Å and K- or L_I-edge absorption. 46
3.5 Backscattering phase for copper metal in curved-wave theory for R = 2.5 Å and K- or L_I-edge absorption. 47
3.6 Backscattering amplitude for Sm in SmSe in curved-wave theory for K- or L_I-edge absorption. 48
3.7 Backscattering phase for Sm in SmSe in curved-wave theory for K- or L_I-edge absorption. 49
3.8 Backscattering amplitude for Sm in SmSe in curved-wave theory for K- or L_I-edge absorption. 50
3.9 Backscattering phase for Sm in SmSe in curved-wave theory for K- or L_I-edge absorption. 51
3.10 Backscattering amplitude for Sm in SmSe in curved-wave theory for R = 2.5 Å and K- or L_I-edge absorption. 52
3.11 Backscattering phase for Sm in SmSe in curved-wave theory for R = 2.5 Å and K- or L_I-edge absorption. 53
3.12 Backscattering amplitude for Se in SmSe in curved-wave theory for R = 2.5 Å and L_{II}- or L_{III}-edge absorption. 54
3.13 Backscattering phase for Se in SmSe in curved-wave theory for R = 2.5 Å and L_{II}- or L_{III}-edge absorption. 55
3.14 Backscattering amplitude for Sm in SmSe in curved-wave theory for K- or L_I-edge absorption. 56

3.15 Backscattering phase for Sm in SmSe in curved-wave theory for K- or L_I-edge absorption. 57
3.16 Backscattering amplitude for Se in SmSe in curved-wave theory for L_{II}- or L_{III}-edge absorption. 58
3.17 Backscattering phase for Se in SmSe in curved-wave theory for L_{II}- or L_{III}-edge absorption. 59
3.18 Backscattering amplitude for Se in SmSe in curved-wave theory (R = 3.1 Å) for L_{II}- or L_{III}-edge absorption and for K- or L_I-edge absorption. . . . 60
3.19 Backscattering phase for Se in SmSe in curved-wave theory (R = 3.1 Å) for L_{II}- or L_{III}-edge absorption and for K- or L_I-edge absorption. . . . 61
3.20 Central-atom phase shift for Se (K or L_I edge). 63
3.21 Central-atom phase shift for Sm (L_{II} or L_{III} edge). 64

4.1 Pressure-volume relations for SmSe and SmS at room temperature. . . 76
4.2 Isothermal compressibility of SmSe at room temperature. 77
4.3 Sm L_{II} absorption edge in SmSe at 77K. 80
4.4 Se K absorption edge in SmSe at 77K. 81

5.1 $2/\mu_{SmSe}$ vs. photon energy. 104
5.2 Measured absorption-thickness product $\ln N_0/N_1$ vs. $\mu(E)\,\bar{x}$. . . . 109
5.3 Derivative with respect to $\mu(E)\,\bar{x}$ of the curve shown in Fig. 5.2. . . . 113
5.4 Pressure vs. reduced volume for Cu at 300K and at 77K. 120
5.5 Pressure vs. reduced volume for RbCl at 300K and at 77K. 122
5.6 High-pressure cell. 126
5.7 Geometry and force diagram for the pressure cell. 127
5.8 Distance between the flats as a function of the amount of gasket compression. . 132
5.9 Torque T necessary to generate the force $p_{ext}\,A$. 133
5.10 Schematic setup for an x-ray absorption experiment in transmission mode. . 137

6.1 Cu K edge in Cu metal at 48.4 kbar and at 77K. 145
6.2 Cu K edge in Cu metal at 48.4 kbar and at 77K after background subtraction. . 146

6.3 Energy derivative of the spectrum shown in Fig. 6.2. 147
6.4 Straight-line fit to estimate the stepsize at the absorption edge, i.e. at k = 0. . 148
6.5 Full spectrum of Cu after conversion to k-space. 149
6.6 Data of Fig. 6.5 with background overlayed. 151
6.7 $k^2 \chi(k)$ for Cu 153
6.8 Normalized absorption spectrum of the Sm L_{II} edge in SmSe at 58.6 kbar and at 77K. 178

7.1 Backscattering amplitude for copper metal calculated in curved-wave theory for R = 2.553 Å and K- or L_I-edge absorption. 190
7.2 Sum of backscattering phase for copper, calculated in curved-wave theory for R = 2.553 Å and K- or L_I-edge absorption, and Teo and Lee's central phase. . 191
7.3 Representative two-shell fit to RbCl in R-space at 42.9 kbar and 77K. The magnitude of the Fourier transform of $k^3 \chi(k)$ is shown. 192
7.4 Backscattering amplitude for Cl calculated in curved-wave theory for R = 3.366 Å and K- or L_I-edge absorption. 193
7.5 Sum of backscattering phase for Cl, calculated in curved-wave theory for R = 3.366 Å and K- or L_I-edge absorption, and Teo and Lee's central phase for Rb. 194
7.6 Backscattering amplitude for Rb calculated in curved-wave theory for R = 3.887 Å and K- or L_I-edge absorption. 195
7.7 Sum of backscattering phase for Rb, calculated in curved-wave theory for R = 3.887 Å and K- or L_I-edge absorption, and Teo and Lee's central phase for Rb. 196
7.8 Pressure of a copper calibrant vs. applied oil pressure according to Table 7.1. . 200
7.9 Pressure of a copper calibrant vs. applied oil pressure according to Table 7.2. . 202
7.10 Fourier transform magnitude of $k^3 \chi(k)$ for RbCl at 77K and for 42.9 kbar and 77.0 kbar. The central atom is Rb. 204
7.11 $k^3 \chi(k)$ for RbCl at 77K and for 42.9 kbar and 77.0 kbar. The central atom is Rb. 205

7.12 Pressure of a RbCl calibrant vs. applied number of turns according to Table 7.3. 206

7.13 Fourier transform magnitude of $k^3 \chi(k)$ for Cu at 77K and for 1 bar and 72.2 kbar. 208

7.14 $k^3 \chi(k)$ for Cu at 77K and for 1 bar and 72.2 kbar. 209

7.15 Pressure of a Cu calibrant vs. applied number of turns according to Table 7.4. . 210

7.16 Fourier transform magnitude of $k^2 \chi(k)$ for SmSe at 300K and for 1 bar and 68.3 kbar. The central atom is Se. 214

7.17 $k^2 \chi(k)$ for SmSe at 300K and for 1 bar and 68.3 kbar. The central atom is Se. . 215

7.18 σ_1^2 vs. R_1 at 300K according to Table 7.5. 216

7.19 Representative one-shell fit to SmSe in R-space at 52.0 kbar and 77K. The imaginary part of the Fourier transform of $k^2 \chi(k)$ is shown. . . . 219

7.20 Representative one-shell fit to SmSe in R-space at 52.0 kbar and 77K. The magnitude of the Fourier transform of $k^2 \chi(k)$ is shown. 220

7.21 σ_1^2 vs. R_1 at 77K according to Tables 7.6 and 7.7. 221

7.22 σ_2^2 vs. R_2 at 77K according to Table 7.8. 223

7.23 Sm radial distribution functions g(R) with respect to Se at 77K and at various pressures. 224

7.24 σ_1^2 vs. R_1 at 77K according to Table 7.9. 226

7.25 $\Delta\sigma_1^2$ vs. R_1 at 77K according to Table 7.10. 228

7.26 Fourier transform magnitude of $k^2 \chi(k)$ for SmSe at 77K and for 32.6 kbar and 72.2 kbar. The central atom is Se. 230

7.27 $k^2 \chi(k)$ for SmSe at 77K and for 32.6 kbar and 72.2 kbar. The central atom is Se. 231

7.28 σ_1^2 vs. R_1 at 77K according to Table 7.11. 232

7.29 $\Delta\sigma_1^2$ vs. R_1 at 77K according to Table 7.12. 234

7.30 Nearest-neighbour distance in SmSe with respect to the Se atoms as a function of pressure according to Table 7.12. 235

7.31 $\Delta\sigma_1^2$ vs. pressure at 77K according to Table 7.12. 236

7.32 Fourier transform magnitude of $k^2 \chi(k)$ for SmSe at 300K and for 1 bar and 68.3 kbar. The central atom is Sm. 239

7.33 $k^2 \chi(k)$ for SmSe at 300K and for 1 bar and 68.3 kbar. The central atom is Sm. . 240
7.34 σ_1^2 vs. R_1 at 300K according to Table 7.13. 241
7.35 Fourier transform magnitude of $k^0 \chi(k)$ for SmSe at 77K and for 1 bar and 72.2 kbar. The central atom is Sm. 243
7.36 $k^0 \chi(k)$ for SmSe at 77K and for 1 bar and 72.2 kbar. The central atom is Sm. . 244
7.37 σ_1^2 vs. R_1 at 77K according to Table 7.14. 245
7.38 Nearest-neighbour distance in SmSe with respect to the Sm atoms as a function of pressure according to Tables 7.14 and 7.13. 246
7.39 Next-nearest neighbour distance in SmSe with respect to the Sm atoms as a function of pressure according to Tables 7.14 and 7.13. . . . 247
7.40 Second-nearest neighbour distance R_2 (Sm-Sm) vs. nearest-neighbour distance R_1 (Sm-Se) according to Tables 7.14 and 7.13. 248
7.41 Valence vs. pressure according to Tables 7.15 (300K) and 7.19 (77K). . . 257
7.42 Valence vs. pressure at 300K according to Tables 7.15, 7.16, and 7.17. . . 258
7.43 Valence vs. pressure at 77K according to Tables 7.18 (L_{II}) and 7.19 (L_{III}). . 259
7.44 Power law, fitted to valence vs. pressure at 77K (Table 7.19). . . . 261
7.45 ΔE vs. valence according to Tables 7.15 (300K) and 7.19 (77K). . . . 262
7.46 ΔE vs. valence at 300K according to Tables 7.15, 7.16, and 7.17. . . . 263
7.47 ΔE vs. valence at 77K according to Table 7.18 (L_{II}) and 7.19 (L_{III}). . . 264

8.1 Pressure of a copper calibrant vs. applied oil pressure according to Table 8.1. . 267
8.2 Fourier transform magnitude of $k^2 \chi(k)$ for SmS at 300K and for 1 bar and 45.2 kbar. The central atom is Sm. 270
8.3 $k^2 \chi(k)$ for SmS at 300K and for 1 bar and 45.2 kbar. The central atom is Sm. . 271
8.4 σ_1^2 vs. R_1 at 300K according to Table 8.2. 272
8.5 Nearest-neighbour distance in SmS with respect to the Sm atoms as a function of pressure according to Table 8.2. 273
8.6 Next-nearest neighbour distance in SmS with respect to the Sm atoms as a function of pressure according to Table 8.2. 274
8.7 Second-nearest neighbour distance R_2 (Sm-Sm) vs. nearest-neighbour distance R_1 (Sm-S) according to Table 8.2. 275

8.8 Valence vs. pressure at 300K according to Table 8.3. 279
8.9 Valence vs. pressure at 300K according to Table 8.4. 280
8.10 ΔE vs. valence at 300K according to Table 8.3. 281

9.1 Sm radial distribution functions g(R) with respect to Se at 77K and at various pressures. 285
9.2 Two-shell fit in k-space to $k^2 \chi(k)$ for SmSe at 52.0 kbar and 77K. . . . 286
9.3 Phase derivative at 52.0 kbar and 77K for the first coordination shell of SmSe with respect to the Se atoms. 287
9.4 Breathing motion of teh Se atoms with respect to the central mixed-valent Sm atom. 288
9.5 $g(\varepsilon)$ vs. ε calculated according to Eq. (6.92) of Section 6.14. 292
9.6 Pressure $\tilde{p}$ obtained by scaling versus p obtained by fitting. . . . 294

B.1 Limiting rays for a double-crystal monochromator. 305

Chapter 1: **Introduction**

In this thesis the x-ray absorption spectra of SmSe and SmS are investigated. Under ambient conditions these compounds have two electrons in the conduction band and are therefore divalent. By applying pressure both compounds become mixed-valent. In SmS this transition is sudden and occurs at ~6.5 kbar[1] whereas in SmSe the valence changes gradually while the pressure increases from zero to ~100 kbar. By applying pressure the average occupation of the 4f level of the Sm atoms is reduced from $4f^6$ to $4f^5$ by promoting a 4f-electron into an empty 5d-state. This process makes the Sm atoms trivalent. The screening of the nuclear charge and likewise the atomic volume of Sm is reduced. Therefore the application of pressure will favour the trivalent state. In x-ray absorption this can be studied quantitatively. The high density of empty Sm-5d states shows up in the L_{II}- or L_{III}-spectra of Sm in SmSe and SmS as a strong absorption peak ("White Line") at the edge. Because of the reduced screening by 4f-electrons the position of the trivalent Sm-White Line is shifted by ~7eV to higher binding energy. The height of the White Line contains information about the relative occurence of di- and trivalent Sm atoms. In addition to the results from the near-edge region of Sm, information about the relative positions of a Se atom and a Sm atom is provided by the pair distribution function which is obtained from the extended x-ray absorption fine structure (EXAFS). The EXAFS is the oscillatory part of the absorption coefficient after an absorption edge. The pair distribution function of for example the Sm atoms contains information about the mean-square relative displacement σ^2 of the Sm atoms with respect to the absorbing atoms.

The Se and Sm absorption spectra that were measured have the following edge energies:

E_K^{Se} = 12655 eV, $E_{L_{III}}^{Sm}$ = 6717 eV, $E_{L_{II}}^{Sm}$ = 7313 eV.

For the pressure calibration the K-absorption edges of Cu and Rb were recorded. Their energies are:

E_K^{Cu} = 8980 eV, E_K^{Rb} = 15202 eV.

---

[1] I hope that I can be forgiven for employing the old fashioned units kbar and Å. They are related to the proper units, Pa and m, by powers of 10: 1 kbar = 0.1 GPa 1 Å = 100 pm.

The contents of each chapter are described in the following.

Chapter 2 describes the EXAFS equation, emphasizing its connection with the radial distribution function. The most important section of this chapter is Section 2.5 which contains useful results involving the inelastic mean free path. Further information on EXAFS spectroscopy is provided by Refs. 1 to 6.

In this work we analyze the behaviour of the pair distribution function with respect to the possible existence of two different equilibrium positions for the di- and trivalent Sm atoms, i.e. the relaxation of the Sm atoms. This result depends on the availability of Sm-backscattering amplitudes corresponding to the integer-valent states of Sm. Therefore amplitudes and phases for EXAFS were calculated. These first-principles calculations were performed in order to find out whether the scattering amplitudes and phases depend on the valence state and/or on pressure. The calculations yield the partial-wave phase shifts and hence also allow us to check the validity of the curved-wave theory of Schaich [7] and McKale et al. [8-10] which takes into account the fact that the outgoing and scattered electron waves are spherical rather than planar. This theory does not include multiple-scattering effects though. Curved-wave theory introduces a slowly varying distance dependence of amplitude and phase which are now also dependent on the orbital symmetry of the photoelectron, i.e. the type of edge (e.g. K or L_{III}). Chapter 3 describes the calculations in detail. Sections 3.1 to 3.4 explain the calculational steps leading to the scattering amplitude and phase. Central-atom phase shifts are not calculated but Section 3.5 explains how they are extrapolated from Teo and Lee's results [11] in order to cover a bigger k-space range. In Section 3.6 the pressure dependence of amplitude and phase are investigated.

Chapter 4 is a brief introduction to the phenomenon of mixed valence and contains information on the Sm monochalcogenides in particular.

Details regarding the experiment are presented in Chapter 5. Most of the experiments were performed at liquid-nitrogen temperature in order to reduce the temperature contribution to the mean-square relative displacement σ^2. Another reason for performing the high-pressure experiments at low-temperature is to investigate whether the continuous valence transition in SmSe becomes first order [12, 13].

The easiest way to generate the pressure that drives the valence transition is to alloy SmSe or SmS with an element whose atoms are small. As the concentration of this element increases the lattice compresses and the alloy becomes mixed valent. It has to be noted, however, that this "chemical" pressure created by doping is not equivalent to pressure generated mechanically [14, 15] because the dopant introduces extra electrons in the valence and conduction bands. We prefer applying pressure mechanically because in this way we can study a "cleaner" system. Because the experiments are also carried out at low temperature a pressure cell that can operate at these temperatures had to be built. This is described in Section 5.9. An existing pressure cell that generated the pressure hydraulically could not be used because the oil would freeze at low temperature. Of the remaining sections in Chapter 5, the most important are 5.6 to 5.8. Section 5.6 discusses the signal-to-noise ratio and Section 5.7 analyzes in which way the measured absorption coefficients are distorted by the presence of harmonics in the x-ray beam and pinholes in the sample. Section 5.8 describes how the pressure-volume calibration curves for 77K are obtained from those at room temperature.

A fair amount of EXAFS data analysis has been covered in this work (see Chapter 6 in particular). This is so because EXAFS data analysis is still a topic of discussion as evidenced by a recent report [16]. The data analysis is not straightforward and if one is not careful one may obtain wrong results. A further reason for presenting the data-analysis procedure is to enable the reader to follow in detail how the measured data is modified until the final result is obtained (Sections 6.1 to 6.9). These sections can be omitted on a first reading. The remaining sections should not be skipped because they contain information not so readily known. Section 6.10 describes in k- and in R-space the fitting procedure and how χ^2 is evaluated. Section 6.11 treats the beating of two closely-spaced coordination shells by analyzing the behaviour of the derivative of the EXAFS phase shift with respect to the wave vector k, rather than by analyzing the phase shift itself. Sections 6.12 and 6.13 describe the determination of the valence of the Sm atoms. They refer to previous work on this subject [17]. Finally, Section 6.14 describes a fast new method for obtaining the pressure from normalized EXAFS datasets.

The remaining four chapters are the most important ones: Chapter 7 contains the results obtained for SmSe and Chapter 8 contains those obtained for SmS. Chapter 9 contains a discussion of these results while Chapter 10 is a summary of this work.

Chapter 2: **The EXAFS Equation**

2.1 The EXAFS Formula

The EXAFS spectrum for a system consisting of one species is given by the following expression [5, 18, 19]:

$$\chi(k) = 4\pi\nu \frac{1}{k} S_o^2(k) |f(k,\pi)| \cdot \int_0^\infty g(R)\, e^{-2R/\lambda(k)} \frac{1}{R^2} \sin(2kR+\delta_c(k)+\delta_b(k))\, R^2 dR \quad . \tag{2.1}$$

Here ν is the number density, which is defined as the average number of atoms per unit volume. $|f(k,\pi)|$ and $\delta_b(k)$ are the magnitude and phase of the plane-wave complex backscattering amplitude $f(k,\pi)$ of an atom located a distance R away from the central (absorbing) atom. In the plane-wave approximation the backscattering amplitude and the phase shift have no R-dependence. However, when curved-wave theory is included and expressed as an effective (complex) scattering amplitude then an R-dependence is introduced. This is discussed in Section 3.4 of the next chapter. Multiple scattering, which can modify amplitude and phase, is not considered in this thesis. $\delta_c(k)$ is the central-atom phase shift which for K- or L_I-edge EXAFS is given by $\delta_c(k) = 2\,\delta_1(k) - \pi$. $\delta_1(k)$ is the l=1 partial-wave phase shift (see Sections 3.4 and 3.5). For L_{II}- or L_{III}-edge EXAFS the central-atom phase shift is equal to $2\,\delta_0(k)$ or $2\,\delta_2(k)$ where $\delta_0(k)$ and $\delta_2(k)$ are the l=0 and l=2 partial-wave phase shifts, respectively. $e^{-2R/\lambda(k)}$ is a damping term resulting from the mean free path $\lambda(k)$ and $S_o^2(k)$ is a slowly-varying dimensionless function of k which describes the reduction of the EXAFS signal due to multielectron excitations [20, 21]. The values of $S_o^2(k)$ are 0.7, approximately. g(R) is the radial distribution function which describes the R-dependence of the number density, averaged over a long period of time. g(R) is normalized such that

$$N = 4\pi\nu \int_0^\infty g(R)\, R^2 dR \,, \tag{2.2}$$

where $N = \sum N_j$ is the total number of atoms in the system. In an ideal solid (no disorder) the atoms can be grouped in coordination shells around the central atom and the radial distribution function becomes:

$$g(R) = \sum_j \frac{N_j}{4\pi R^2 v} \cdot \delta(R-R_j) \ . \qquad (2.3)$$

N_j is the number of atoms in the jth coordination shell.

A more realistic description of a solid is obtained by assuming broadened peaks rather than δ-functions. With Gaussian peaks, located at R_j, we obtain for g(R):

$$g(R) = \sum_j \frac{N_j}{4\pi R^2 v} \ \frac{1}{\sigma_j\sqrt{2\pi}} e^{-(R-R_j)^2/2\sigma_j^2} \ . \qquad (2.4)$$

Inserting this expression into Eq. (2.1) and writing sin(x) as $\mathbf{Im}(e^{ix})$ produces:

$$\chi(k) = S_o^2(k) \ \frac{1}{k} \ |f(k,\pi)| \cdot \sum_j \frac{N_j}{\sigma_j\sqrt{2\pi}} \ \mathbf{Im}\, e^{i\delta_t(k)} \cdot \int_0^\infty \frac{1}{R^2} e^{-(R-R_j)^2/2\sigma_j^2} \, e^{-2R/\lambda(k)} \, e^{i2kR} \, dR \ . \qquad (2.5)$$

Here we have introduced the total phase $\delta_t(k) \equiv \delta_c(k)+\delta_b(k)$. Since the integration cannot be done analytically, we may expand $\frac{1}{R^2}$ in a Taylor's series around R_j. This, however, becomes rather laborious and instead we prefer to approximate $\frac{1}{R^2}$ by an exponential which is tangent to it at R_j:

$$\frac{1}{R^2} \ \approx \ \frac{1}{R_j^2} \, e^{-2(R-R_j)/R_j} \ . \qquad (2.6)$$

This approximation will lead to the same modification of the phase (see Eq. (2.8)) as found by others [22, 23]. Inserting (2.6) into Eq. (2.5) yields after some tedious algebra:

$$\chi(k) = S_o^2(k) \ \frac{1}{k} \ |f(k,\pi)| \cdot \sum_j \frac{N_j}{R_j^2\sigma_j\sqrt{2\pi}} \, e^{-2R_j/\lambda} \, \exp\left[-2\sigma_j^2 \left(k^2 - (1/R_j + 1/\lambda)^2\right)\right]$$

$$\times \ \mathbf{Im}\, e^{i\delta_t(k)} \exp\left[i2kR_j\left(1 - \frac{2\sigma_j^2}{R_j}(1/R_j + 1/\lambda)\right)\right] \cdot \int_{-R_j+2\sigma_j^2(1/R_j+1/\lambda)-2ik\sigma_j^2}^{\infty} \exp\left(-z^2/2\sigma_j^2\right) dz \qquad (2.7)$$

Values for σ_j are of the order of 0.1 Å. This is much less than a typical coordination-shell radius R_j and because R_j itself is much less than the mean free path λ, the lower limit of integration can be replaced by R_j in Eq. (2.7). Since the integrand becomes very small at $|z| \cong 3\,\sigma_j \cong 0.3$ Å $<< R_j$ we can set the lower limit to $-\infty$. Then the integral becomes $\sigma_j\sqrt{2\pi}$. After taking the imaginary part we have:

$$\chi(k) = S_o^2(k)\,\frac{1}{k}\,|f(k,\pi)| \cdot \sum_j \frac{N_j}{R_j^2}\,e^{-2R_j/\lambda}\,\exp\left[-2\sigma_j^2\left(k^2 - (1/R_j + 1/\lambda)^2\right)\right]$$

$$\times\ \sin\left(2kR_j + \delta_t(k) - 4k\sigma_j^2\,(1/R_j + 1/\lambda)\right)\ . \qquad (2.8)$$

If we assume $\sigma_j << R_j << \lambda$ then we get the standard EXAFS formula for a one-component system:

$$\chi(k) = S_o^2(k)\,\frac{1}{k}\,|f(k,\pi)| \cdot \sum_j \frac{N_j}{R_j^2}\,e^{-2\sigma_j^2 k^2}\,e^{-2R_j/\lambda}\,\sin\left(2kR_j + \delta_t(k)\right)\ . \qquad (2.9)$$

The new term, $e^{-2\sigma_j^2 k^2}$, that we now have obtained is the EXAFS Debye-Waller factor which is a measure of static and dynamic disorder (see Section 2.4).

From the condition $R_j << \lambda$ we conclude that Eq. (2.9) will not be reliable near the minimum of the mean free path.

2.2 Obtaining g(R) from χ(k)

Eq. (2.1) suggests that we could obtain g(R) by inversion of the integral with the help of the Fourier transform. Practically the integration will be performed only over a finite interval of positive k-values and possibly some form of apodization will be used. We therefore include here a window function $w(k-k_0)$, which is centered at k_0, and obtain a broadening in R-space:

$$FT\left(w(k-k_0)\,\frac{k\,\chi(k)}{S_o^2(k)\,|f(k,\pi)|}\,e^{i\delta_t(k)}\right) = \frac{1}{\sqrt{\pi}} \cdot \int_{-\infty}^{\infty} w(k-k_0)\,\frac{k\,\chi(k)}{S_o^2(k)\,|f(k,\pi)|}\,e^{i\delta_t(k)}\,e^{+i2kR'}\,dk$$

$$= \frac{1}{\sqrt{\pi}} \cdot \int_{-\infty}^{\infty} dR'\,\tilde{W}(R-R')\,e^{i2k_0(R-R')} \int_{-\infty}^{\infty} dk\,\frac{k\,\chi(k)}{S_o^2(k)\,|f(k,\pi)|}\,e^{i\delta_t(k)}\,e^{i2kR'}\ . \qquad (2.10)$$

Here W(R) is the Fourier transform of w(k). w(k) and W(R) are both real and even. We now write sin(x) in Eq. (2.1) as $\frac{e^{ix} - e^{-ix}}{2i}$ and assume for simplicity that the mean free path is independent of k, i.e. $\lambda(k) \rightarrow \lambda_0$. This yields:

$$FT\left(w(k-k_0)\ \frac{k\,\chi(k)}{S_o^2(k)\,|f(k,\pi)|}\,e^{i\delta_t(k)}\right) = i\,2\sqrt{\pi}\ \nu \int_{-\infty}^{\infty} dR'\ W(R-R')\ e^{i2k_0(R-R')} \int_{0}^{\infty} dR''\ g(R'')\ e^{-2R''/\lambda_0}$$

$$\times \int_{-\infty}^{\infty} dk\ \left(e^{i2k(R'-R'')} - e^{i2\delta_t(k)}\ e^{i2k(R'+R'')}\right) . \qquad (2.11)$$

For analytical simplicity we make the assumption that the total phase $\delta_t(k)$ can be approximated by a straight line. This is a reasonable approximation over limited ranges of k if $k > 6\ \text{Å}^{-1}$. Hence we write:

$$\delta_t(k) \cong p_0 + p_1\,k\,, \qquad p_1 < 0\,. \qquad (2.12)$$

Using

$$\int_{-\infty}^{\infty} e^{i2kR}\,dk = \pi\,\delta(R) \qquad (2.13)$$

we thus obtain:

$$FT\left(w(k-k_0)\ \frac{k\,\chi(k)}{S_o^2(k)\,|f(k,\pi)|}\,e^{i\delta_t(k)}\right) = i\,2\sqrt{\pi}\ \nu \int_{-\infty}^{\infty} dR'\ W(R-R')\ e^{i2k_0(R-R')} \int_{0}^{\infty} dR''\ g(R'')\ e^{-2R''/\lambda_0}$$

$$\times \int_{-\infty}^{\infty} dk\ \left(e^{i2k(R'-R'')} - e^{i2p_0}\ e^{i2k(R'+R''+p_1)}\right)$$

$$= i\,2\pi\sqrt{\pi}\ \nu \int_{-\infty}^{\infty} dR'\ W(R-R')\ e^{i2k_0(R-R')} \int_{0}^{\infty} dR''\ g(R'')\ e^{-2R''/\lambda_0}$$

$$\times \left(\delta(R''-R') - e^{i2p_0}\,\delta(R''+R'+p_1)\right) .$$

The second δ-function peaks at a negative distance where g(R) is zero. Therefore this term vanishes. (The negative value of p_1 is insufficient to make this δ-function peak at a positive value.) We then have:

$$FT\left(w(k-k_0)\ \frac{k\,\chi(k)}{S_o^2(k)\,|f(k,\pi)|}\,e^{i\delta_t(k)}\right) = i\,2\,\pi\,\sqrt{\pi}\ \nu\ \int_{-\infty}^{\infty} dR'\ W(R-R')\,e^{i2k_0(R-R')}\,g(R')\,e^{-2R'/\lambda_0}\ . \tag{2.14}$$

We see that the pair distribution function g(R), together with the mean free path term, is convolved with the Fourier transform of the k-space window function. Since deconvolution methods are unreliable no attempt will be made at deconvolution.

If we employ the rectangular window of width $\Delta k \equiv k_{max} - k_{min}$ for maximum resolution we obtain with

$$W(R) = \frac{\Delta k}{\sqrt{\pi}}\,\frac{\sin(R\Delta k)}{R\Delta k}\ :$$

$$FT\left(w(k-k_0)\ \frac{k\,\chi(k)}{S_o^2(k)\,|f(k,\pi)|}\,e^{i\delta_t(k)}\right) = \pi\,\nu\cdot\int_{-\infty}^{\infty} dR'\ g(R')\,e^{-2R'/\lambda_0}\ \frac{1}{R-R'}\left(e^{i2k_{max}(R-R')} - e^{i2k_{min}(R-R')}\right)\ . \tag{2.15}$$

The imaginary part of Eq. (2.15) is given by:

$$\mathbf{Im}\ FT\left(w(k-k_0)\ \frac{k\,\chi(k)}{S_o^2(k)\,|f(k,\pi)|}\,e^{i\delta_t(k)}\right) =$$

$$\pi\,\nu\cdot\int_{-\infty}^{\infty} dR'\ g(R')\,e^{-2R'/\lambda_0}\ \frac{1}{R-R'}\left(\sin(2k_{max}(R-R')) - \sin(2k_{min}(R-R'))\right)\ .$$

If $k_{min} = 0$, we obtain:

$$\mathbf{Im}\ FT\left(w(k-k_0)\ \frac{k\,\chi(k)}{S_o^2(k)\,|f(k,\pi)|}\,e^{i\delta_t(k)}\right) = \pi\,\nu\cdot\int_{-\infty}^{\infty} dR'\ g(R')\,e^{-2R'/\lambda_0}\ \frac{\sin(2k_{max}(R-R'))}{R-R'}\ . \tag{2.16}$$

As $k_{max} \to \infty$, the function $\sin(2k_{max}(R-R'))/(R-R')$ approaches $\pi\,\delta(R'-R)$ and the integral becomes equal to $\pi\,g(R)\,e^{-2R/\lambda_0}$. It is therefore essential that $k_{min} = 0$ and k_{max} become as large as possible. For this calculation a rectangular window function was assumed which, however, has the disadvantage that large sidelobes are produced when a Fourier transform is performed. It was also assumed here that the mean free path is independent of k.

2.3 The Cumulant Expansion

A mathematical model for the radial distribution function is the expansion in cumulants [22]. This method yields the moments of $g(R)\, e^{-2R/\lambda(k)}$ and provides the correction terms to the amplitude and phase due to disorder.

Using Eq. (2.1) we can write:

$$\chi(k) = 4\pi\nu \frac{1}{k} S_o^2(k) |f(k,\pi)| \, \mathbf{Im} \langle e^{i\delta_t(k)} e^{i2kR} \rangle \ , \tag{2.17}$$

where the brackets signify the following average:

$$\langle f(R) \rangle \equiv B(k) \cdot \int_0^\infty f(R)\, g(R)\, e^{-2R/\lambda(k)}\, dR \ . \tag{2.18}$$

The normalization constant B(k) is calculated from:

$$B(k)^{-1} = \int_0^\infty g(R)\, e^{-2R/\lambda(k)}\, dR \ . \tag{2.19}$$

Eqs. (2.2) and (2.18) can be employed to obtain an expression for the number density ν:

$$4\pi\nu = \frac{N}{B(k)^{-1} \langle R^2 e^{2R/\lambda(k)} \rangle} \ . \tag{2.20}$$

Following Ref. 24 we can express $\chi(k)$ either in terms of the moments or of the cumulants of this distribution:

$$\mathbf{Im} \langle e^{i\delta_t(k)} e^{i2kR} \rangle = \mathbf{Im}\, e^{i\delta_t(k)} \sum_{n=0}^{\infty} \frac{1}{n!} (i2k)^n \langle R^n \rangle$$

$$= \mathbf{Im} \exp\left[i\delta_t(k) + \sum_{n=1}^{\infty} \frac{1}{n!} (i2k)^n C_n \right]$$

$$= \exp\left[\sum_{n=1}^{\infty} \frac{(-1)^n}{(2n)!} (2k)^{2n} C_{2n}\right]$$

$$\times \ \mathrm{Im} \exp\left[i\delta_t(k) + i \cdot \sum_{n=1}^{\infty} \frac{(-1)^{n-1}}{(2n-1)!} (2k)^{2n-1} C_{2n-1}\right]$$

$$= \exp\left[\sum_{n=1}^{\infty} \frac{(-1)^n}{(2n)!} (2k)^{2n} C_{2n}\right] \sin\left[\delta_t(k) + \sum_{n=1}^{\infty} \frac{(-1)^{n-1}}{(2n-1)!} (2k)^{2n-1} C_{2n-1}\right]$$

The cumulants can be expressed in terms of the moments of the distribution:

$$C_1 = \langle R \rangle$$

$$C_2 = \langle R^2 \rangle - \langle R \rangle^2$$

$$C_3 = \langle R^3 \rangle - 3 \langle R \rangle \langle R^2 \rangle + 2 \langle R \rangle^3$$

$$C_4 = \langle R^4 \rangle - 3 \langle R^2 \rangle^2 - 4 \langle R \rangle \langle R^3 \rangle + 12 \langle R \rangle^2 \langle R^2 \rangle - 6 \langle R \rangle^4 \qquad (2.21)$$

etc.

These equations can be inverted:

$$\langle R \rangle = C_1$$

$$\langle R^2 \rangle = C_2 + C_1^2$$

$$\langle R^3 \rangle = C_3 + 3 C_1 C_2 + C_1^3$$

$$\langle R^4 \rangle = C_4 + 4 C_1 C_3 + 6 C_1^2 C_2 + 3 C_2^2 + C_1^4 \qquad (2.22)$$

etc.

For $\chi(k)$ we obtain:

$$\chi(k) = 4 \pi \nu \frac{1}{k} S_o^2(k) |f(k,\pi)| \exp\left[\sum_{n=1}^{\infty} \frac{(-1)^n}{(2n)!} (2k)^{2n} C_{2n}\right]$$

$$\times \sin\left[\delta_t(k) + \sum_{n=1}^{\infty} \frac{(-1)^{n-1}}{(2n-1)!} (2k)^{2n-1} C_{2n-1}\right] .$$

Employing Eq. (2.20) we get:

$$\chi(k) = \frac{N\, S_o^2(k)\, |f(k,\pi)|}{k\, B(k)^{-1} \langle R^2\, e^{2R/\lambda(k)} \rangle} \exp\left(-2k^2C_2 + \frac{2}{3}k^4C_4 + \ldots\right)$$

$$\times \sin\left(\delta_1(k) + 2kC_1 - \frac{4}{3}k^3C_3 + \ldots\right) . \qquad (2.23)$$

Thus the even cumulants modify the amplitude and the odd ones modify the phase.

According to the above, $C_1 = \langle R \rangle$. In the limit of small disorder the pair distribution function can be approximated by a Gaussian and $C_2 = \sigma^2$ and all higher-order cumulants vanish. In this case, if $\langle R^2\, e^{2R/\lambda(k)} \rangle$ can be approximated by $R^2\, e^{2R/\lambda(k)}$, Eq. (2.23) reduces to Eq. (2.9) for one single shell. (B(k) is a slowly varying parameter.)

The cumulant expansion is an expansion about $k = 0$. The cumulant coefficients C_n are obtained by fitting $\chi(k)$ over a finite interval $k_{min} < k < k_{max}$. According to Section 2.2, it is desirable that $k_{min} = 0$ in order to determine g(R). Practically, however, k_{min} will always have a finite value. The determined cumulant coefficients will therefore depend on the fitting interval. Thus the C_n are not unique. The cumulant expansion, however, provides a convenient functional form to extrapolate to $k_{min} = 0$. One can then use the Splice Method [19, 23] to obtain g(R). The method will work if multiple scattering does not occur.

2.4 The EXAFS Debye-Waller Factor

The EXAFS Debye-Waller factor is given by $e^{-2\sigma_j^2 k^2}$ where σ_j^2 is the mean-square relative displacement which is defined as:

$$\sigma_j^2 = \langle (R_j - \langle R_j \rangle)^2 \rangle . \qquad (2.24)$$

Here the distances are referred to the central atom which is considered as being at rest. According to

Refs. 23 and 25 one can express σ_j^2 in terms of the phonon spectrum as:

$$\sigma_j^2 = \frac{h}{4\pi\mu} \int_0^\infty \frac{d\omega}{\omega} \rho_j(\omega) \coth\left(\frac{h\omega}{4\pi k_B T}\right) . \qquad (2.25)$$

Here μ is the reduced mass of the absorber backscatterer pair and $\rho_j(\omega)$ is the projected density of phonon modes, i.e. the density of modes assuming the central atom is at rest. In many cases this density can be approximated by a single δ-function, $\delta(\omega-\omega_{Ej})$, where ω_{Ei} is the Einstein frequency for coordination shell j. Then σ_j^2 is given by:

$$\sigma_j^2 = \frac{h}{4\pi\mu} \frac{1}{\omega_{Ej}} \coth\left(\frac{h\omega_{Ej}}{4\pi k_B T}\right) . \qquad (2.26)$$

For temperatures above approximately the Einstein temperature σ_j^2 increases linearly with T. For lower temperatures the behaviour is parabolic with a limiting value $\sigma_j^2|_{T=0} = \frac{h}{4\pi\mu} \frac{1}{\omega_{Ej}}$. In some cases the Einstein frequency ω_{Ej} (or Einstein temperature Θ_{Ej}) can be estimated from force constants but it is usually determined from a fit to $\sigma_j^2(T)$. A comparison with results of Raman measurements showed close agreement of the Einstein frequencies as obtained from EXAFS with the average of the symmetrical stretching mode frequencies [26]. The force constant of an absorber backscatterer pair, linked by a bond, can then be estimated from $f_E \equiv \mu \omega_E^2$.

Values for σ_j^2 generally increase with distance from the central atom.

Frequently the Einstein model is employed (e.g., for tetrahedrally coordinated semiconductors), but for metals the Debye model may be a better approximation.

2.5 Many Body Effects

Many body effects cause the decay of the excited state of the absorbing atom. They are manifest in the finite mean free path $\lambda(k)$ which results from the excitation of plasmons, electron-electron and electron-phonon interactions, and from the creation of electron-hole pairs. Multielectron excitations also play a role in filling up the core hole and they produce a k-independent overall reduction of the EXAFS signal. Of these effects the EXAFS equation only contains the one

due to the mean free path. The mean free path was investigated as a function of energy by Lindau and Spicer [27] and found to follow a "universal" curve for many elements and compounds. A more thorough analysis was presented by Seah and Dench [28]. They investigated elements and inorganic compounds and found curves for the two classes when they express λ as a multiple of the number of monolayers. Converting monolayers into lengths involves the density. Therefore their result becomes density dependent. Besides, an extra factor of 2 is included because Seah and Dench's values refer to intensities whereas the EXAFS function contains amplitudes [29]. The result is then:

$$\lambda = 2 \left(\frac{\alpha}{\nu^{1/3} E^2} + \frac{\beta}{\sqrt{10}} \sqrt{\frac{E}{\nu}} \right) . \qquad (2.27)$$

Here α and β have the following values:

$\alpha = 538\ (\text{eV})^2$ and $\beta = 0.41\ (\text{eV Å})^{-1/2}$ for elements and

$\alpha = 2170\ (\text{eV})^2$ and $\beta = 0.72\ (\text{eV Å})^{-1/2}$ for inorganic compounds.

ν is the number density, i.e. the number of atoms per unit volume, and E is the energy of the photoelectron.

For inorganic compounds we found from preliminary curve fits that the mean free path according to Eq. (2.27) leads to coordination numbers that are too small, implying that S_o^2 equals 0.5. Seah and Dench [28] investigated only ten inorganic compounds and stated regarding the validity of their results that "The experiments to determine inelastic mean free paths are very difficult and it is usually not possible to assess the experimental errors since the most important information, the adsorbate morphology, cannot usually be monitored independently." and that "Measurements for compounds by several different laboratories would enable the general differences in inelastic mean free path magnitude between elements and inorganic compounds to be clarified.". We therefore decided to employ for compounds the values $\alpha = 538\ (\text{eV})^2$ and $\beta = 0.41\ (\text{eV Å})^{-1/2}$, corresponding to elements.[1]

[1] After completion of the thesis, the program FEFF by Rehr et al. became available. The mean free path calculated for SmSe using FEFF was close to the value for copper shown in Fig. 2.1.

Defining

$$\gamma \equiv \frac{1}{2m_e}\left(\frac{h}{2\pi}\right)^2 = 3.80998\ldots \text{ eV Å}^2 \cong 3.81 \text{ eV Å}^2 \tag{2.28}$$

and

$$\eta \equiv \frac{1}{2\beta}\sqrt{10/\gamma}\,\sqrt{\nu} \tag{2.29}$$

we obtain using $E = \gamma k^2$:

$$\lambda = \frac{k}{\eta}\left(1 + \frac{\alpha}{\beta}\sqrt{10/\gamma^5}\,\frac{\nu^{1/6}}{k^5}\right) . \tag{2.30}$$

λ as a function of k (or E) exhibits a minimum at some $k = k_0$. Differentiating with respect to k we arrive at the following relation for η:

$$\eta = \frac{5}{4}\frac{k_0}{\lambda_{min}} \qquad \text{where } \lambda_{min} \equiv \lambda(k_0) . \tag{2.31}$$

The term k/η dominates λ for $k > 6$ Å^{-1} ($\cong$ 150 eV). For η we obtain:

η_{Cu} = 0.576 Å^{-2}

η_{RbCl} = 0.365 Å^{-2}

η_{SmSe} = 0.362 Å^{-2}

η_{SmS} = 0.383 Å^{-2} .

For RbCl we have used for the calculation of η its number density of $34.063 \cdot 10^{-3}$ Å^{-3} just after the NaCl-to-CsCl phase transition occuring at 5.2 kbar.

The following figure shows the mean free path λ for some materials that are of interest in this work. The curves are calculated using Eq. (2.27) or (2.30). They are similar for all substances.

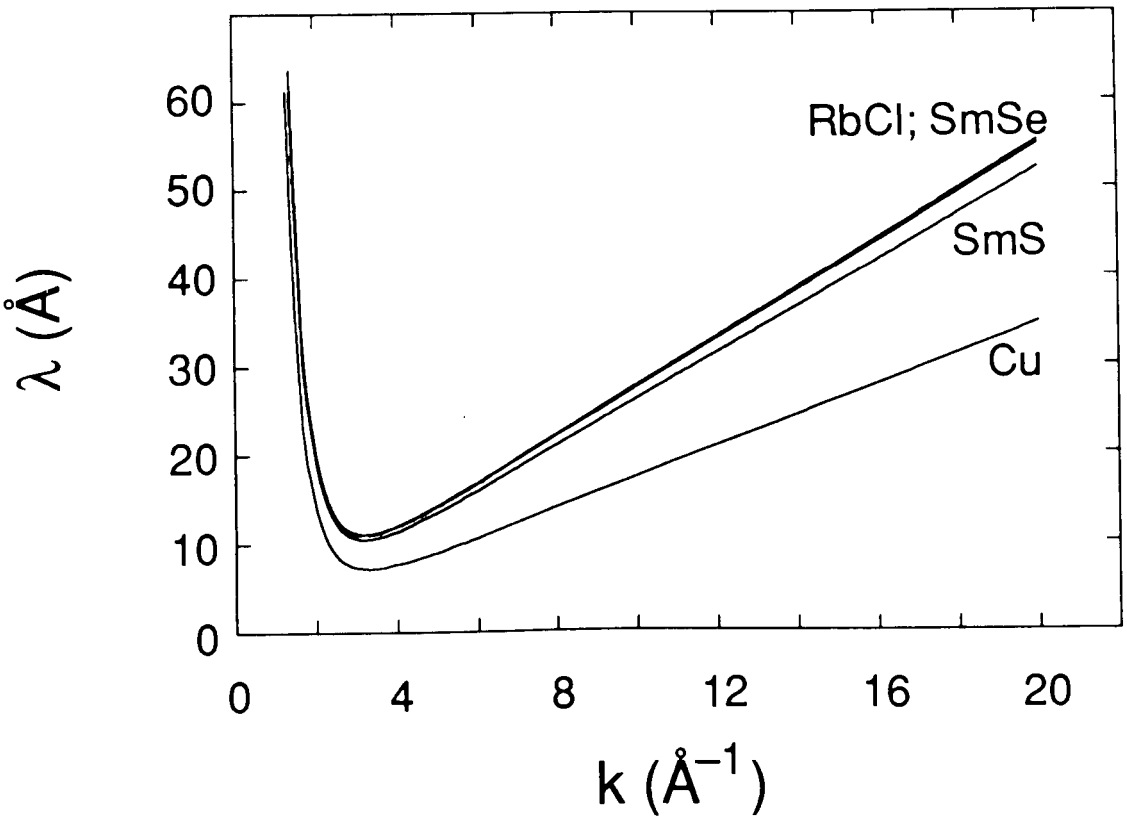

Fig. 2.1: Inelastic mean free path λ as a function of k according to Seah and Dench [28] and including a factor of 2 to convert from intensities to amplitudes. The parameters α and β were chosen as $\alpha = 538\ (eV)^2$ and $\beta = 0.41\ (eV\ Å)^{-1/2}$.

The finite mean free path corresponds to a lifetime τ_e of the photoelectron:

$$\tau_e = \frac{\lambda(k)}{v} = \frac{2\pi\, m_e}{h}\,\frac{\lambda(k)}{k} \quad . \tag{2.32}$$

For $k > 6\ Å^{-1}$ we have $\lambda(k) = \frac{k}{\eta}$ and τ_e becomes independent of k:

$$\tau_e = \frac{2\pi\, m_e}{h\ \eta} \quad . \tag{2.33}$$

As a consequence the finite lifetime τ_e resulting from many body effects can be incorporated into

the single-particle EXAFS formula by a Lorentzian broadening with a width Γ_e according to Heisenberg's uncertainty principle:

$$\tau_e \, \Gamma_e = \hbar/2\pi \ . \tag{2.34}$$

$$\Gamma_e = \frac{\hbar/2\pi}{\tau_e} = 2\,\gamma\,\eta \ \cong \ \eta\, 7.62\ \text{eV}\,\text{Å}^2 \ . \tag{2.35}$$

We obtain for Γ_e:

$$\begin{aligned} \Gamma_{e,Cu} &= 4.39\ \text{eV} \\ \Gamma_{e,RbCl} &= 2.78\ \text{eV} \\ \Gamma_{e,SmSe} &= 2.76\ \text{eV} \\ \Gamma_{e,SmS} &= 2.92\ \text{eV} \ . \end{aligned}$$

It is instructive to relate the mean free path in the form $\lambda(k) = k/\eta$ to an imaginary component $-V_{Im}$ of the scattering potential [30]. This gives rise to an imaginary component k_{Im} of the wave vector. We have:

$$E + i\,V_{Im} = \gamma\,(k + i\,k_{Im})^2 = \gamma\,(k^2 - k_{Im}^2) + i\,2\,\gamma\,k\,k_{Im} \ .$$

We will assume that $V_{Im} << E$ and therefore $k_{Im} << k$. Then we get:

$$E = \gamma\,k^2 \text{ and } V_{Im} = 2\,\gamma\,k\,k_{Im}, \text{ or } k_{Im} = \frac{V_{Im}}{2\ \gamma\ k} \ . \tag{2.36}$$

Combining e^{i2kR} and $e^{-2R/\lambda(k)}$ yields $e^{i2R(k\,+\,i/\lambda)}$. Thus $1/\lambda$ can be interpreted as the imaginary part of the wave vector:

$$k_{Im} \equiv \frac{1}{\lambda(k)} \ . \tag{2.37}$$

Using Eq. (2.36) we obtain:

$$\lambda(k) = \frac{2\ \gamma\ k}{V_{Im}} \quad \Rightarrow \quad \eta = \frac{V_{Im}}{2\ \gamma} \ . \tag{2.38}$$

Now we can rewrite Eq. (2.35) as $\Gamma_e = V_{Im}$ in accordance with the assumption $V_{Im} << E$.

The Lorentzian broadening, which is described by

$$w_e(E) = \frac{1}{\pi} \frac{\Gamma_e/2}{E^2+(\Gamma_e/2)^2} \tag{2.39}$$

produces in the time domain a multiplication with the Fourier transform of $w_e(E)$:

$$FT(w_e(E)) = \int_{-\infty}^{\infty} w_e(E)\, e^{iEt2\pi/h}\, dE = \exp\left(-\frac{\Gamma_e}{2\ h/2\pi}\ |\ t\ |\right) = e^{-|t|/(2\tau_e)} = e^{-t/(2\tau_e)}\ ; \qquad t > 0\ . \tag{2.40}$$

We can relate time with distance by noting that the photoelectron travels the distance $2R$ in time $t = 2R/v$. For τ_e we can write: $\tau_e = \frac{1}{2}\ \lambda(k)/v$. The factor $1/2$ is necessary because $\lambda(k)$ is the EXAFS mean free path, which refers to amplitudes. We thus obtain for the factor that multiplies the radial distribution function: $e^{-2R/\lambda(k)}$.

For very small values of k the k^{-4}-term in Eq. (2.30) becomes important and the width Γ_e becomes a function of k (or E). Thus $w_e(E)$ is not Lorentzian anymore. We will not consider the Fourier transform of this function. At low k we will use instead the above expression $e^{-2R/\lambda(k)}$ with $\lambda(k)$ as given by Eq. (2.30).

The lifetime of the core hole is finite because the hole is filled through radiative and Auger transitions. If the core hole is not in the K-shell then Coster-Kronig transitions, which shorten the lifetime considerably, also come into play. The finite core-hole lifetime results in a Lorentzian broadening of the absorption spectrum with a width Γ_c:

$$w_c(E) = \frac{1}{\pi} \frac{\Gamma_c/2}{E^2+(\Gamma_c/2)^2}\ . \tag{2.41}$$

Values for Γ_c can be found in Refs. 31 to 33. From Ref. 31 we obtain:

$\Gamma_{c,Cu}^{K}$ = 1.6 eV

$\Gamma_{c,Rb}^{K}$ = 3.3 eV

$\Gamma_{c,Se}^{K}$ = 2.5 eV

$\Gamma_{c,Sm}^{L_I}$ = 5.5 eV

$\Gamma_{c,Sm}^{L_{II}}$ = 4.4 eV

$\Gamma_{c,Sm}^{L_{III}}$ = 3.6 eV .

We see that the core-hole width increases with binding energy, thus corresponding to a decrease of core-hole lifetime. We also note that the core-hole widths Γ_c are comparable to the widths Γ_e describing the finite lifetime of the photoelectron.

For the sake of completeness, although not needed here, the following formula to calculate the width of a core hole in the K-shell of elements with $Z > 40$ is mentioned [34]:

$$\Gamma_{c,Z>40}^{K} = 1.73\ Z^{3.93}\ 10^{-6}\ \text{eV} \quad . \tag{2.42}$$

The twofold convolution of the EXAFS spectrum with the Lorentzians Eqs. (2.39) and (2.41) is equivalent to the convolution with a single Lorentzian of width $\Gamma_e + \Gamma_c$. The core-hole width Γ_c is obviously independent of k as is the case for Γ_e above ~6 $Å^{-1}$. Therefore we can absorb the core-hole width in the mean free path constant η using Eq. (2.35)

$$2\gamma\ \tilde{\eta} \equiv \Gamma_e + \Gamma_c \quad , \tag{2.43}$$

where γ is the constant defined in Eq. (2.28).

Thus, for $k > 6\ Å^{-1}$ the contributions from the finite mean free path as well as from the finite core-hole lifetime can both be accommodated in the modified mean free path constant $\tilde{\eta}$ of Eq. (2.43). If this is done the EXAFS equation, Eq. (2.1), takes these important many body effects into account.

Chapter 3: **Amplitudes and Phases**

In this chapter the calculation of scattering amplitudes and phases will be presented. It is convenient for this purpose to use atomic units. This will be done with the exception of Section 3.1 where relativistic units are employed. For a description of units see Appendix A. EXAFS amplitudes and phases have already been calculated by Teo and Lee [11] in the plane-wave approximation. The present calculation was motivated for three reasons:

i) Application of the curved-wave formalism of Schaich [7] and McKale [8-10].
This requires knowledge of the partial-wave phase shifts $\delta_l(k)$ which are not listed in Teo and Lee's work.

ii) Extension of the k-space interval for amplitudes and phases.
Teo and Lee's tabulations of amplitudes and phases extend from $k_{min} = 3.78$ Å^{-1} to $k_{max} = 15.12$ Å^{-1} while in the present work the scattering amplitudes and phases are calculated for an interval of $k_{min} \cong 1.5$ Å^{-1} to $k_{max} \cong 21$ Å^{-1}.

iii) Inclusion of crystal potentials.
It is desirable to include in the calculation crystal potentials to describe a solid, elemental or compound, rather than employing potentials for single atoms. We will employ the muffin-tin approximation for the crystal potential.

The procedure for calculating amplitudes and phases is briefly as follows: First atomic charge densities are calculated, then a muffin-tin potential is formed, for which the wave equation is solved. From the wave function the logarithmic derivative is calculated which immediately leads to the phase shifts. An alternative approach, to be tried in the future, is that of calculating the phase shifts directly from the potential, i.e. without logarithmic derivatives, according to the variable-phase method [35, 36].

3.1 Calculation of Atomic Charge Densities

Atomic charge densities are calculated from the time-independent Dirac equation:

$$H\psi = (\alpha\cdot\mathbf{p} + \beta + V(\mathbf{r}))\,\psi = W\psi \ . \qquad (3.1)$$

Here W is the energy including the rest energy. β and the three components of α are 4×4 matrices [37] and ψ is a four-component column vector. The polar form of the Dirac equation is:

$$\left\{-i\,\alpha_r\left(\frac{\partial}{\partial r} + \frac{1}{r} - \frac{\beta^2}{r}K\right) + \beta + V(r)\right\}\psi = W\psi \ . \qquad (3.2)$$

Here $\alpha_r \equiv \frac{1}{r}(\alpha\cdot\mathbf{r})$ and $K \equiv (\sigma\cdot\mathbf{l} + 1)$ and the wavefunction is [38]:

$$\psi_\kappa^\mu = \frac{1}{\sqrt{2l+1}}\begin{Bmatrix} g_\kappa(r)\,(1+\mu+1/2)^{1/2}\chi_{+1/2}Y_l^{\mu-1/2} \\ g_\kappa(r)\,(1-\mu+1/2)^{1/2}\chi_{-1/2}Y_l^{\mu+1/2} \\ -i\,f_\kappa(r)\,(1-\mu+1/2)^{1/2}\chi_{+1/2}Y_l^{\mu-1/2} \\ i\,f_\kappa(r)\,(1+\mu+1/2)^{1/2}\chi_{-1/2}Y_l^{\mu+1/2} \end{Bmatrix} . \qquad (3.3)$$

ψ_κ^μ is an eigenfunction of the Hamiltonian and also an eigenfunction of the operators j^2, j_z, and K with eigenvalues $j(j+1)$, μ, and $-\kappa$, respectively. μ runs from $-j$ to $+j$. κ is a non-zero integer and is given by:

$$\kappa = l(l+1) - (j+1/2)^2 \ . \qquad (3.4)$$

For electrons the two upper components of ψ_κ^μ are much larger than the lower ones. (The opposite is true for positrons.) Thus $g_\kappa(r)$ is called the "large component" while $f_\kappa(r)$ is dubbed the "small component". Inserting Eq. (3.3) into Eq. (3.2) produces the following two coupled differential equations for the radial functions $g \equiv g_\kappa(r)$ and $f \equiv f_\kappa(r)$:

$$\frac{dg}{dr} = (W - V + 1)\,f - \frac{\kappa+1}{r}\,g \ ,$$

$$\frac{df}{dr} = \frac{\kappa-1}{r}\,f - (W - V - 1)\,g \ . \qquad (3.5)$$

These radial wave functions are normalized such that

$$\int_0^\infty r^2 \, (g^2 + f^2) \, dr \; = 1 \tag{3.6}$$

and the local charge density is calculated by adding the contributions of each electron:

$$\rho(r) = \frac{1}{4\pi \, r^2} \cdot \sum_{i=1}^{N} \left[g_i^2(r) + f_i^2(r) \right] . \tag{3.7}$$

In order to calculate the wave functions of a system of more than one electron we have to solve the Hartree-Fock equations:

$$H_1 \, \psi_j(\mathbf{r}_1) + \left[\sum_{k=1}^{N} \int \psi_k^+(\mathbf{r}_2) \, \psi_k(\mathbf{r}_2) \, \frac{2}{r_{12}} \, d^3\mathbf{r}_2 \right] \psi_j(\mathbf{r}_1)$$

$$- \sum_{k=1}^{N} \left[\int \psi_k^+(\mathbf{r}_2) \, \psi_j(\mathbf{r}_2) \, \frac{2}{r_{12}} \, d^3\mathbf{r}_2 \right] \psi_k(\mathbf{r}_1) \; = E_j \, \psi_j(\mathbf{r}_1) \; ; \qquad j = 1,...N \; . \tag{3.8}$$

The integrations include summing over the spins. H_1 is the Hamiltonian of Eq. (3.1) for an electron at position $\mathbf{r}_1$. r_{12} is its distance to another electron at $\mathbf{r}_2$. The first summation on the left-hand side of Eq. (3.8) is the average Hartree potential, which is the Coulomb energy of an electron at $\mathbf{r}_1$ caused by <u>all</u> electrons. This means that the electron at $\mathbf{r}_1$ is acting on itself too. The second summation, the exchange term, corrects this deficiency by keeping electrons of like spins apart.This summation results from the use of antisymmetrized wave functions and it leads to a reduction of electrons of like spin in the vicinity of a given electron, called the "exchange-correlation hole". Besides this exchange correlation, all electrons are subject to their mutual Coulomb repulsion giving rise to a "Coulomb-correlation hole". The Hartree-Fock equations, however, do not include this latter effect. For electrons of like spin, which are already kept apart, Coulomb correlation is not very important but the

effect is larger for electrons of unlike spin. Eqs. (3.8) hold only for filled shells. Open shells, which exhibit a multiplicity of energy levels greater than one, are much more complicated to calculate.

The exchange term constitutes the main difficulty in solving the Hartree-Fock equations (3.8) because the number of exchange integrals that must be computed increases rapidly with the number of occupied orbitals. Slater [39] found that the exchange potential can be simplified by proper averaging. Furthermore, he applied the result to a free-electron gas and then obtained the following approximation for the exchange potential (see Ref. 40 for a discussion):

$$V_{exch.}(\mathbf{r}_1)\,\psi_j(\mathbf{r}_1) \equiv -\sum_{k=1}^{N}\left[\int \psi_k^{+}(\mathbf{r}_2)\,\psi_j(\mathbf{r}_2)\,\frac{2}{r_{12}}\,d^3\mathbf{r}_2\right]\psi_k(\mathbf{r}_1) = -6\left(\frac{3}{8\pi}\rho(\mathbf{r}_1)\right)^{1/3}\psi_j(\mathbf{r}_1)\,. \tag{3.9}$$

$\rho(\mathbf{r}_1)$ is the local charge density given by Eq. (3.7). This means that the exchange potential due to Slater replaces the non-local exchange appearing in the Hartree-Fock equations by a local exchange. This is not without problems because one cannot always expect a local potential to correctly model the true exchange [41]. The exchange potential should also be energy dependent in order to produce good scattering phases [42, 43]. Nevertheless Slater's exchange potential has been found quite useful. It is a good approximation for low photoelectron energies [3] as confirmed by many bandstructure calculations. Note that this exchange potential is attractive. Slater's exchange potential formed the basis of the Xα method [44] where the exchange appears as $\alpha\, V_{exch.}$ with $\alpha = 2/3$ and $\alpha_{optimized} \cong 0.7$. Values of α have been calculated for a number of elements [45]. The results do not differ much from $\alpha_{optimized}$. Eqs. (3.8) employing (3.9) are also referred to as the "Hartree-Fock-Slater" equations [40].

In this work only spherically-symmetric potentials will be considered. Therefore $\mathbf{r}_1$ can be replaced by r. Slater's form of the exchange energy vanishes for large values of r. Consequently, an electron far away from the nucleus would experience no force acting on it whereas it should be subjected to the attractive force of the nucleus minus the charge of $N - 1$ electrons, i.e. one elementary charge. In order to remedy this discrepancy we modify the exchange potential of Eq. (3.9) according to Latter [40, 46]:

$$\tilde{V}_{exch.}(r) \equiv \begin{cases} V_{exch.}(r) & ; \quad r < r_o \\ -\frac{2}{r} & ; \quad r \geq r_o \end{cases} . \tag{3.10}$$

r_o is the position where the function $-\frac{2}{r}$ intersects $V_{exch.}(r)$: $-\frac{2}{r_o} \equiv V_{exch.}(r_o)$. (3.11)

The modified potential $\tilde{V}_{exch.}(r)$ has a discontinuous slope at r_o but this does not result in discontinuities of the radial wave functions or their first and second derivatives at r_o.

The calculations were performed using a FORTRAN program, written by J.P. Desclaux (see also Ref. 47) and obtained from J.E. Müller. It performs self-consistent Dirac-Hartree-Fock-Slater calculations. Initial energy eigenvalues are obtained from Ref. 40. Although later on we will confine ourselves to non-relativistic results, it is still advisable to calculate atomic charge densities relativistically, particularly those for the heavier atoms.

For descriptions of multi-configuration Hartree-Fock codes see Refs. 48 to 51.

3.2 Muffin-Tin Potentials

We model the crystal potential by placing non-intersecting spheres around each atom. Inside these spheres the potential is assumed to be spherically symmetric. In the interstitial region between the spheres the potential is constant. This is the well-known muffin-tin model of a crystal potential. It becomes a better approximation as the spheres fill up the space. Therefore crystals of fcc, hcp, bcc, or sc type are good candidates, whereas open structures, like diamond, cannot be described well by muffin-tin models. The maximum filling factors for these crystal structures are: 0.74 (fcc, ideal hcp), 0.68 (bcc), 0.52 (sc), but only 0.34 for diamond. The NaCl structure, in which the Sm-monochalcogenides crystallize, has the same filling factor as the sc structure if equal spheres are assumed. Even in a dense structure, like fcc, the muffin-tin potential is not a good approximation to the real potential along those directions in the crystal lattice where the (linear) density of muffin-tin spheres is low, for example the [111]-direction in the fcc structure. It is convenient to set the constant interstitial

potential equal to zero. The energy scale is then referred to the so called "muffin-tin zero". A typical muffin-tin potential is sketched in Fig. 3.1.

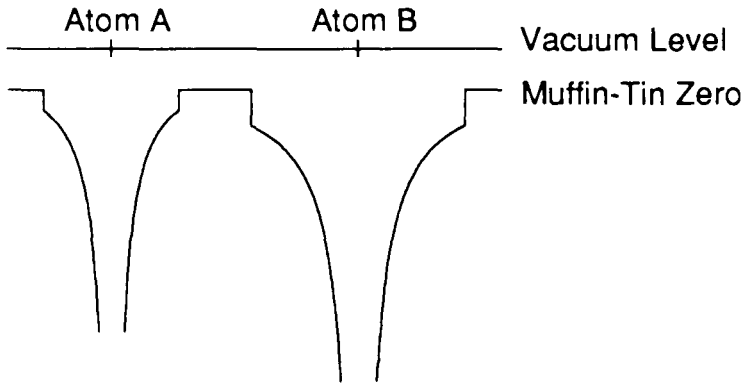

Fig. 3.1: Muffin-tin potential along the [110]-direction in the fcc structure. The distance between the two atoms is $(R_{MT,A} + R_{MT,B})\sqrt{2}$. Inside each atomic sphere the potential is shifted by a constant amount. The muffin-tin radii have been chosen such that the unshifted atomic potentials would intersect along the [100]-direction. Other choices of the radii are possible [52].

It is desirable to calculate the potential self-consistently. Satisfactory results can also be obtained if one constructs the muffin-tin potential in one of several non-self-consistent ways. One procedure is called the Mattheiss prescription [53], in which the potential is constructed in the following way [54]. First the atomic charge densities are calculated self-consistently and, preferably, relativistically. Then Poisson's equation is solved to determine the atomic potentials. There can be different types of atoms present and we call the one whose muffin-tin contribution we are calculating the central atom. To the potential of the central atom we now have to add the contributions from the neighbouring atoms. This is done by spherically averaging the atomic potentials of the neighbours with respect to the central atom and then adding the result to the central-atom potential:

$$V_{Coul.}(r) = V_{centre}(r) + \sum_{n} V_n(r) \quad . \tag{3.12}$$

Here the sum is over the potential tails of the neighbouring atoms, spherically averaged with respect to the central atom. In a crystalline solid the neighbouring atoms can be grouped in coordination shells around the central atom. For solids consisting of different types of atoms it is possible for a

coordination shell to contain atoms of different types. For the NaCl structure, however, it turns out that this is not the case. All shells are "pure". The same applies to the CsCl structure [55, 56]. The radii and coordination numbers have been tabulated for various crystal structures [54, 57-59].

In the present work only the first 15 coordination shells are considered in the calculation. (Loucks [54] employs 14 shells and Rehr et al. [60] use 34 coordination shells in a calculation for Cu.) The effect of higher coordination shells is to flatten the crystal potential between the atoms, an effect which to some extent the muffin-tin potential already takes care of due to its construction.

Eq. (3.12) constitutes the Coulombic part of the potential. The other part comes from the exchange potential:

$$V_{exch.}(r) = -6\left(\frac{3}{8\pi}\rho(r)\right)^{1/3} , \tag{3.13}$$

$$\rho(r) = \rho_{centre}(r) + \sum_{n} \rho_n(r) . \tag{3.14}$$

We have again employed Slater's exchange potential. This is necessary for consistency. The effect of the exchange potential is sizeable in comparison with the cohesive energy and using different formulae for exchange for the calculation of charge density and muffin-tin potential would produce the wrong result. The sum in Eq. (3.14) is again over the contributions of the neighbours. We have not modified the exchange potential as we did in Eq. (3.10) because now we calculate an r-dependent exchange potential only for $r \leq R_{MT} << \infty$. Note that unlike our procedure for the Coulombic part we now spherically average the charge density instead of the atomic potential. This, by the way, constitutes an approximation to Slater's exchange because only the spherically-symmetric part of the charge density is involved.

The final result for the potential with respect to the central atom is then:

$$V_{total}(r) = V_{Coul.}(r) + V_{exch.}(r) . \tag{3.15}$$

Now we have to determine the value of the constant potential in the interstitial region. This can be done in two ways: One consists of averaging the spherically-symmetric potential at a given site in the region from $r = R_{MT}$ to $r = R_{WS}$, where R_{MT} is the muffin-tin radius and R_{WS} the Wigner-Seitz radius [54]. The other, more precise, way consists of calculating the average potential by three-dimensional integration over the interstitial region. In the present work both methods are employed. For elemental solids the potential is calculated by the first method whereas for compounds, like SmSe, we employ the second method which allows us to calculate better the value of the interior potential with respect to the muffin-tin constant, i.e. the jump discontinuity of the potential at R_{MT}. This discontinuity is adjusted such that the averaged interstitial potential becomes zero. Then the potential inside a muffin-tin sphere corresponds to the electronic charge density contained within the sphere. The value ΔV_i of the discontinuity for an atom of type i at $R_{MT,i}$ is calculated as indicated in Ref. 61:

$$\Delta V_i \equiv \left\langle V^{ext.}_{Coul.}(r) \right\rangle \Big|_{Surface,i} - \left\langle V^{ext.}_{Coul.}(r) \right\rangle \Big|_{ext.\ Volume} \quad . \tag{3.16}$$

The first term is the average of the interstitial, or external, Coulomb potential over the surface of muffin-tin sphere i and the second term is the average of the external Coulomb potential over the volume of the interstitial region.

The calculation of the average external Coulomb potential can be performed by reducing the present problem to the so called "Ewald problem" [62]. Ewald calculated the potential of point charges embedded in a constant charge density of opposite polarity such that the net charge was zero. We can express the present case as an Ewald problem by calculating the average interstitial charge density and continuing it into the muffin-tin spheres. We will consider here only the NaCl crystal structure. The charge contained inside a given muffin-tin sphere is, in units of the elementary charge:

$$Q_{MT,i} = Z_i - \int_0^{R_{MT,i}} 4\pi\, r^2\, \rho(r)\, dr \qquad ; \qquad i = 1, 2 \ . \tag{3.17}$$

i labels the the two different types of atoms in the NaCl unit cell. The interstitial charge density $\bar{\rho}$ for this structure is:

$$\bar{\rho} \equiv \langle \rho^{ext.}(r) \rangle \Big|_{Volume} = \frac{Q_{MT,1} + Q_{MT,2}}{\frac{a^3}{4} - \frac{4\pi}{3}\left(R^3_{MT,1} + R^3_{MT,2}\right)} \quad . \tag{3.18}$$

a is the lattice constant. We now write for the charge inside the muffin-tin spheres:

$$Q_{MT,i} = \left(Q_{MT,i} + \frac{4\pi}{3} R^3_{MT,i}\,\bar{\rho}\right) - \frac{4\pi}{3} R^3_{MT,i}\,\bar{\rho} \quad . \tag{3.19}$$

The term outside the brackets is the uniform background of electronic charge extended into the muffin tin. Note that $\bar{\rho}$ was defined positive. The term in brackets will be called here the Ewald charge $Q_{Ewald,i}$. It is the value of the point charge located at the position of an atom of type i.

$$Q_{Ewald,i} \equiv Q_{MT,i} + \frac{4\pi}{3} R^3_{MT,i}\,\bar{\rho} \quad . \tag{3.20}$$

The Ewald problem for the case of the fcc structure has been described in Ref. 63 (see also Ref. 64). The result for the NaCl structure can be obtained by superposition of two fcc results, shifted by a/2 with respect to each other along the y-axis, say. The Coulomb potential of these charges is given by Ref. 63, p. 310:

$$V_{Coul.}(r) = 2\,Q_{Ewald,1}\left(\phi_1(r) + \phi_2(r)\right)\Big|_{(0,0,0)} + 2\,Q_{Ewald,2}\left(\phi_1(r) + \phi_2(r)\right)\Big|_{(0,a/2,0)} \tag{3.21}$$

with

$$a\,\phi_1(r) = \frac{a}{r} + \frac{8\pi}{3}\left(\frac{r}{a}\right)^2 + A_0 \tag{3.22}$$

and

$$a\,\phi_2(r) = A_4 \left(\frac{r}{a}\right)^4 \left(l^4 + m^4 + n^4 - \frac{3}{5}\right)$$

$$+ A_6 \left(\frac{r}{a}\right)^6 \left(l^6 + m^6 + n^6 - \frac{15}{11}\left(l^4 + m^4 + n^4\right) + \frac{30}{77}\right)$$

$$+ A_8 \left(\frac{r}{a}\right)^8 \left(l^8 + m^8 + n^8 - \frac{28}{15}\left(l^6 + m^6 + n^6\right) + \frac{14}{13}\left(l^4 + m^4 + n^4\right) - \frac{7}{39}\right) . \quad (3.23)$$

a is the lattice constant and l, m, n are the direction cosines: $l \equiv \frac{x}{r}$, $m \equiv \frac{y}{r}$, $n \equiv \frac{z}{r}$. (3.24)

The constants are: $A_0 = -4.584850$, $A_4 = -18.687$, $A_6 = -1002.05$, $A_8 = 2326.1$. (3.25)

The first term in Eq. (3.21) is the Coulomb potential of a charge $Q_{Ewald,1}$ located at (0,0,0) and the second term is the potential of a charge $Q_{Ewald,2}$ at $(0,a/2,0)$. The factor two results from the fact that we are using atomic units rather than cgs units as in Ref. 63. Now that the Coulomb potentials are known the surface and volume averages for Eq. (3.16) can be calculated. These averages need only be performed over 1/48 of an fcc Wigner-Seitz cell centered at (0,0,0). The calculation is complicated by the fact that the second term in Eq. (3.21) is not centered with respect to the sphere over which the surface average is to be performed. Therefore the integration is carried out numerically. The discontinuity ΔV_i at the muffin-tin radius of atom i can be expressed as:

$$\Delta V_i = Q_{Ewald,1}\, 2\Big[\big\langle \big(\phi_1(r) + \phi_2(r)\big)\big|_{(0,0,0)} \big\rangle \Big|_{Surface,i}$$

$$- \big\langle \big(\phi_1(r) + \phi_2(r)\big)\big|_{(0,0,0)} \big\rangle \Big|_{ext.\ Volume} \Big]$$

$$+ Q_{Ewald,2}\, 2\Big[\big\langle \big(\phi_1(r) + \phi_2(r)\big)\big|_{(0,a/2,0)} \big\rangle \Big|_{Surface,i}$$

$$- \big\langle \big(\phi_1(r) + \phi_2(r)\big)\big|_{(0,a/2,0)} \big\rangle \Big|_{ext.\ Volume} \Big] \quad . \tag{3.26}$$

Now we have to consider the exchange potential. In the interstitial region we calculate it as:

$$V_{exch.}^{ext.} = -6 \left(\frac{3}{8\pi} \bar{\rho} \right)^{1/3} \tag{3.27}$$

where $\bar{\rho}$ is given by Eq. (3.18). Since the exterior exchange potential is taken to be constant one can simply subtract it from the total potential inside and outside the spheres. It does not contribute to the jump discontinuity at the muffin-tin radius.

The result for the average interstitial potential is, taking into account Coulomb- and exchange-contributions:

$$\bar{V}_{ext.} = V(R_{MT,i}) - \Delta V_i + V_{exch.}^{ext.} \quad . \tag{3.28}$$

If $\bar{V}_{ext.}$ is subtracted from the muffin-tin potential then the potential in the interstitial, or external, region vanishes. Within the i-type spheres the shifted potential is:

$$V_{MT,i}(r) = V_{total,i}(r) - \bar{V}_{ext.} = V_{total,i}(r) - V(R_{MT,i}) + \Delta V_i - V_{exch.}^{ext.} \quad . \tag{3.29}$$

$V_{total,i}(r)$ is simply the sum of Coulomb- and exchange-potentials, Eq. (3.15). This result should be compared to Ref. 65, which differs in some respects.

Although this discussion focussed on a compound solid like NaCl it is of course also valid for an elemental solid like Cu. For Cu, however, one may use the simplified method mentioned before where one averages the potential in a shell with inner radius R_{MT} and outer radius R_{WS}. For Cu the results of both methods were similar.

Now we must choose the muffin-tin radius. There is no difficulty in selecting the value of the muffin-tin radius for an elemental solid because all muffin-tin spheres have the same radius. For touching spheres their radius simply becomes proportional to the lattice constant a. For the fcc structure $R_{MT} = \frac{a}{4}\sqrt{2}$. If the solid consists, however, of different types of atoms then one has to decide on the respective values of their muffin-tin radii. This will be explained for the NaCl structure. Essentially, we will determine the radii from the intersection of two potentials centered at the respective atom sites. These potentials depend, however, on the muffin-tin radius which is not yet known. Thus we start out with equal spheres and construct muffin-tin potentials for each atom type according to Eq. (3.29). These potentials are then simply extended beyond their muffin-tin radii in order to find their point of intersection. This gives a new set of radii. Then we repeat the above procedure until convergence is achieved. For touching spheres in the NaCl structure we always have:

$$R_{MT,1} + R_{MT,2} = \frac{a}{2} \quad . \tag{3.30}$$

In this case the minimum filling factor of $\frac{\pi}{6} = 0.524$ (compare sc) occurs when the two radii are equal to $\frac{a}{4}$. The maximum filling factor of $\frac{\pi}{3}\left(5 - 3\sqrt{2}\right) = 0.793$ occurs when one of the two radii has its maximum value of $\frac{a}{4}\sqrt{2}$.

As an alternative to the procedure of determining the muffin-tin radii from the intersection point of the potentials, which is applied here, it is frequently suggested that the radii be chosen such that the jump discontinuities ΔV_i become minimal. For SmSe it was found that this leads to one species having a much larger muffin-tin radius than the other, thus approaching the situation where the filling factor is maximum. If one chooses the muffin-tin radii of Sm and Se according to Norman [52] such that their ratio is equal to the ratio of the atomic numbers of Sm and Se then one also obtains a much larger radius for the Sm atoms. It would be interesting to compare scattering amplitudes and phase shifts for SmSe calculated for different choices of the muffin-tin radii of the Sm and Se atoms.

Finally we have to take into account that the atomic charge densities and the muffin-tin potentials are only given for a set of discrete r-values. These are chosen to lie on a grid suggested by Loucks [54]:

$$R_j = e^{-8.8 + 0.05\,(j-1)} \quad ; \qquad j = 1, 2, \ldots 250 \ . \tag{3.31}$$

Loucks' logarithmic grid puts more points in the region near the origin where the potentials are rapidly varying. The j-scale is thus expanded in that region. To convert to SI units simply multiply R_j by a_{Bohr}. In this work we only choose muffin-tin radii that lie on Loucks' mesh. This results in cases where the spheres do not touch, or, conversely, are allowed to overlap slightly. The muffin-tin radii were selected such as to minimize this discrepancy in a least-squares sense. Obviously, one can improve on this through interpolation procedures, allowing for r-values that are not on Loucks' grid. On the other hand, the precise value of the muffin-tin radius for a given lattice constant is not too critical [66].

With this constraint and according to the method described above, the muffin-tin radii for SmSe and for Cu were chosen as:

$Sm^{2+}Se$:	a = 6.200 Å	$R_{MT,Sm^{2+}}$ = 1.590 Å (j = 199)	$R_{MT,Se}$ = 1.512 Å (j = 198)	(slight overlap)
$Sm^{3+}Se$:	a = 5.7 Å	$R_{MT,Sm^{3+}}$ = 1.438 Å (j = 197)	$R_{MT,Se}$ = 1.368 Å (j = 196)	
Cu:	a = 3.61 Å	$R_{MT,Cu}$ = 1.238 Å (j = 194)		

Indicated in brackets is the corresponding index j of Loucks' mesh, Eq. (3.31).

3.3 Logarithmic Derivatives

In order to match interior and exterior wave functions at the muffin-tin radius one has to require that the two wave functions have the same value and slope at R_{MT}. This must be true independent of the normalization constant. Therefore one can merely require that for interior and exterior wave functions the ratio of slope to value, i.e. $\frac{1}{\Psi}\frac{d\Psi}{dr}$, be the same at $r = R_{MT}$. Since this expression resembles the derivative of log Ψ, it is called the logarithmic derivative. This, however, does not imply that Ψ be always positive. Some of the properties of the logarithmic derivative have been described in Ref. 61.

At the muffin-tin radius there can be a jump discontinuity of the potential. In this case the Schrödinger equation is not defined at R_{MT} and the requirement that value and slope of the wave function be continuous does not follow directly. Nevertheless it can be shown that these continuity conditions hold [67].

In this work the logarithmic derivative will always be expressed in the dimensionless form $D_l(E,R_{MT}) \equiv \frac{R_{MT}}{\Psi}\frac{d\Psi}{dr}\Big|_{R_{MT}}$. At the muffin-tin radius the logarithmic derivative will be matched to the logarithmic derivative for a free electron given by:

$$D_l^{f.e.}(E,R_{MT}) \equiv \left(\frac{x}{j_l(x)}\frac{dj_l(x)}{dx}\right)\Big|_{x=kR_{MT}} \quad ; \quad x \equiv kr \,. \tag{3.32}$$

$k = 0$ corresponds to the constant value of the interstitial potential. $j_l(x)$ is a spherical Bessel function as defined in Ref. 37.

In order to calculate the logarithmic derivative inside the muffin-tin spheres one has to solve the radial Schrödinger equation numerically, starting near $r = 0$. Loucks' mesh begins at $r = R_1 \equiv 1.5\cdot10^{-4}\, a_{Bohr}$ where the potential has a value comparable to or bigger than the electronic rest energy. Hence it becomes necessary to take relativistic effects into account. This is done by solving the radial Dirac equation instead. As explained in Section 3.1 this means solving the coupled equations (3.5). These two equations are converted to atomic units by multiplying energies by $2/c^2$

and lengths by c/2. At the same time one has to keep in mind that W contains the rest energy, that is $W = E + 1$. The result is then [54]:

$$\frac{dg}{dr} = \left(\frac{E - V}{c^2} + 1\right) c f - \frac{\kappa + 1}{r} g , \tag{3.33}$$

$$c\frac{df}{dr} = \frac{\kappa - 1}{r} c f - (E - V) g . \tag{3.34}$$

$V \equiv V(r)$ is the potential inside a muffin-tin sphere and E is the energy of the electron, which now does not include the rest energy. Like Eqs. (3.33) and (3.34) the radial Schrödinger equation, too, can be written as a system of two first-order differential equations. When this is done it can be shown that Eqs. (3.33) and (3.34) reduce to the non-relativistic case if, besides $c \to \infty$, the following relations hold:

$$j = l + 1/2 \text{ and } \kappa = -l - 1 . \tag{3.35}$$

In the non-relativistic limit g, the large component, approaches the solution of the radial Schrödinger equation and f goes to zero. The dimensionless logarithmic derivative is therefore calculated from Eq. (3.33) as:

$$\frac{r}{g}\frac{dg}{dr} = r\left(\frac{E - V}{c^2} + 1\right)\frac{c f}{g} + l . \tag{3.36}$$

This equation has to be evaluated at the muffin-tin radius R_{MT}. It is convenient to introduce the two new variables [54]:

$$P \equiv r g ; \quad Q \equiv r c f . \tag{3.37}$$

Furthermore, we put the abscissa on a logarithmic scale:

$$x \equiv \ln r ; \qquad r\,dx = dr \tag{3.38}$$

and obtain in place of Eqs. (3.33) and (3.34) by using Eq. (3.35):

$$\frac{dP}{dx} = e^x \left(\frac{E - V}{c^2} + 1 \right) Q + (l + 1)\, P \tag{3.39}$$

$$\frac{dQ}{dx} = -(l + 1)\, Q - e^x (E - V)\, P \ . \tag{3.40}$$

In terms of the new variables P and Q one obtains for the logarithmic derivative from Eq. (3.36):

$$D_l(E,r) \equiv \frac{r}{g}\frac{dg}{dr} = e^x \left(\frac{E - V}{c^2} + 1 \right) \frac{Q}{P} + l \ . \tag{3.41}$$

(The left-hand side can be written as $\frac{1}{P}\frac{dP}{dx} - 1$ but this is not needed here.)

Since we are not interested in effects of the spin we remove the spin-orbit term that automatically arises from the Dirac equation. In atomic units the spin-orbit interaction has the form:

$$V_{s.o.} = 2\, \mathbf{L}\cdot\mathbf{S}\ \frac{1}{r}\frac{dV}{dr}\frac{1}{4\, m^2\, c^2} \ . \tag{3.42}$$

With the choice (3.35) of j and κ one obtains $2\,\mathbf{L}\cdot\mathbf{S} = l$. Using $2\,m = 2\,(E - V)/c^2 + 1$, which is derived from $mc^2 = m_e c^2 + E - V$, one obtains for $V_{s.o.}$ expressed as a function of x:

$$V_{s.o.} = l\, e^{-2x}\, \frac{dV}{dx}\frac{1}{c^2} \left(\frac{2\,(E - V)}{c^2} + 1 \right)^{-2} \ . \tag{3.43}$$

The spin-orbit term will be significant only near the nucleus. $V_{s.o.}$ is suppressed by subtracting it

from V in Eqs. (3.39) and (3.40). Since the correction is much less appreciable for Eq. (3.39) it is applied only to Eq. (3.40). The set of coupled differential equations, that is to be solved, is then:

$$\frac{dP}{dx} = e^x \left(\frac{E - V}{c^2} + 1 \right) Q + (l+1)\, P \ , \tag{3.39}$$

$$\frac{dQ}{dx} = -(l+1)\, Q - e^x (E - V + V_{s.o.})\, P \ . \tag{3.44}$$

The logarithmic derivative, Eqs. (3.36) and (3.41), remains unchanged.

Note that one can readily obtain a first-order differential equation for the quantity $\frac{Q}{P}$ which is directly related to the logarithmic derivative. Combining Eqs. (3.39) and (3.44) one obtains:

$$\frac{d}{dx}\left(\frac{Q}{P}\right) = -e^x (E - V + V_{s.o.}) - 2(l+1)\frac{Q}{P} - e^x \left(\frac{E - V}{c^2} + 1 \right) \left(\frac{Q}{P}\right)^2 \ . \tag{3.45}$$

This Ricatti differential equation for $\frac{Q}{P}$ is not suitable for numerical integration because $\frac{Q}{P}$ can develop singularities at certain values of the radial coordinate. We therefore solve the two coupled first-order equations (3.39) and (3.44) which constitute an initial-value problem. In order to start the integration it is necessary to have starting values P_1, Q_1 for P and Q. Since the system is homogeneous one can choose one starting value, P_1 say, to be arbitrary and determine Q_1 from $Q_1 = \left(\frac{Q}{P}\right)_1 P_1$. Therefore one needs to know an initial value for $\frac{Q}{P} = \frac{c\,f}{g}$. The r-integration begins very close to the nucleus where the potential is Coulomb like:

$$\lim_{r \to 0} \ r\,V(r) = -2\,Z \ . \tag{3.46}$$

In this case the spin-orbit term, Eq. (3.42), becomes:

$$V_{s.o.}(r\to 0) = l\,\frac{2Z}{r^3}\,\frac{1}{c^2}\left(\frac{2}{c^2}\left(E + \frac{2Z}{r}\right) + 1\right)^{-2} . \qquad (3.47)$$

For $l \neq 0$ the spin-orbit term dominates for small r over the Coulomb potential. One determines then $\left(\frac{Q}{P}\right)_1$ by assuming solutions of Eqs. (3.39) and (3.44) in the form of power series in r (similar to Ref. 37, p. 485). The result is a complicated expression that is omitted here.

However, for the case $l = 0$, or generally for a mere Coulomb potential, one obtains for the initial value of the logarithmic derivative to lowest order (Ref. 68, Eq. (5.71)):

$$\left(\frac{Q}{P}\right)_1 = \frac{2Z}{\kappa - \sqrt{\kappa^2 - \left(\frac{2Z}{c}\right)^2}} = \frac{-2Z}{l + 1 + \sqrt{(l+1)^2 - \left(\frac{2Z}{c}\right)^2}} . \qquad (3.48)$$

The energy dependence of the initial value $\left(\frac{Q}{P}\right)_1$ is weak and therefore not taken into account. The final result does not depend sensitively on the starting values.

Once P_1 and Q_1 have been given the integration is started using the fourth-order Runge-Kutta method [69, 70] for the first six points and then calculating the result for the remaining 244 points of Loucks' mesh by the Milne Predictor-Corrector method [54, 71].

3.4 Calculation of Amplitudes and Phases

The complex scattering amplitude f can be decomposed into magnitude A and phase ϕ. In this Section we follow EXAFS terminology and call the magnitude of the complex scattering amplitude simply "amplitude".

Amplitude and phase depend on the magnitude k of the photoelectron wave vector and on the scattering angle θ. They also depend on whether plane or spherical waves are assumed. In the latter case the scattering is a function of the distance R between emitter and scatterer. For $R \to \infty$ the results of the curved-wave case approach the plane-wave result. The curved-wave modifications can

all be incorporated into amplitude and scattering phase. The central-atom phase δ_c remains unaffected. However, the curved-wave modifications of amplitude and scattering phase depend on the symmetry of the central-atom phase shift, i.e. on the angular momentum l of the photoelectron. In the following the plane-wave and the curved-wave cases are discussed. The equations are written down for an arbitrary scattering angle θ. For backscattering one has $\theta = \pi$ and $P_l(\cos\pi) = (-1)^l$.

Amplitude and phase are calculated from the tangent of the phase shift which is given by Ref. 37:

$$\tan\delta_l(k) = \frac{k\,R_{MT}\,\left.\frac{dj_l(x)}{dx}\right|_{x=k\,R_{MT}} - D_l(E,R_{MT})\,j_l(k\,R_{MT})}{k\,R_{MT}\,\left.\frac{dn_l(x)}{dx}\right|_{x=k\,R_{MT}} - D_l(E,R_{MT})\,n_l(k\,R_{MT})} \quad ; \qquad x \equiv k\,r \; ; \qquad (E - \overline{V}_{MT}) = k^2 . \tag{3.49}$$

$\overline{V}_{MT}$ is the constant interstitial potential. The sums that appear in the remainder of this chapter are from $l = 0$ to $l = l_{max}$. Knowing the muffin-tin radius one can estimate the maximum value k_{max} of k for a given maximum value l_{max} of l according to Ref. 37, p. 121:

$$k_{max} = \frac{l_{max}}{R_{MT}} \; . \tag{3.50}$$

From this equation we can immediately deduce the additional k-space gain Δk for each increase of l_{max} by one:

$$\Delta k = \frac{1}{R_{MT}} \; . \tag{3.51}$$

Thus one can divide the k-scale into channels of width Δk, labeled by l.

There are other formulae to estimate k_{max}, for example [60]:

$$k_{max} = \frac{\sqrt{l_{max}\,(l_{max}+1)}}{R_{MT}} \qquad \text{or (see Section 3.6):} \qquad k_{max} = \frac{l_{max}+\frac{1}{2}}{R_{MT}} \; .$$

a) Plane-Waves

From elementary quantum mechanics the complex scattering amplitude $f(k,\theta)$ is calculated according to:

$$f(k,\theta) \equiv A(k,\theta)\, e^{i\phi(k,\theta)} = \frac{1}{k} \cdot \sum_l (2l + 1)\, P_l(\cos\theta)\, e^{i\delta_l(k)} \sin\delta_l(k)) \quad . \tag{3.52}$$

Here θ is the scattering angle and the $\delta_l(k)$ are partial-wave phase shifts. It is assumed that the $\delta_l(k)$ have been calculated using a real potential. Thus the $\delta_l(k)$ are real functions, too. Eq. (3.52) can be cast into a form that involves the partial-wave phase shifts only via $\tan\delta_l(k)$:

$$A(k,\theta)\, e^{i\phi(k,\theta)} = \frac{1}{k} \cdot \sum_l (2l + 1)\, P_l(\cos\theta)\, \frac{\tan\delta_l(k)}{1 + \tan^2\delta_l(k)}\, (1 + i\tan\delta_l(k)) \quad . \tag{3.53}$$

This form is very useful because according to Eq. (3.49) the phase shifts are calculated in the form $\tan\delta_l(k)$ from the logarithmic derivative. Eq. (3.53) shows that the complex scattering amplitude depends on $\delta_l(k)$ modulo π, not 2π.

The calculation of the partial-wave phase shifts was described in the previous sections. Now with $\delta_l(k)$ known we can employ Eq. (3.53) to calculate the backscattering amplitude $A(k,\pi)$ and the backscattering phase $\phi(k,\pi)$ in the plane-wave approximation. We will show these results for the case of copper. At the same time we compare them with the tabulated data of Teo and Lee [11], shown as dashed curves.

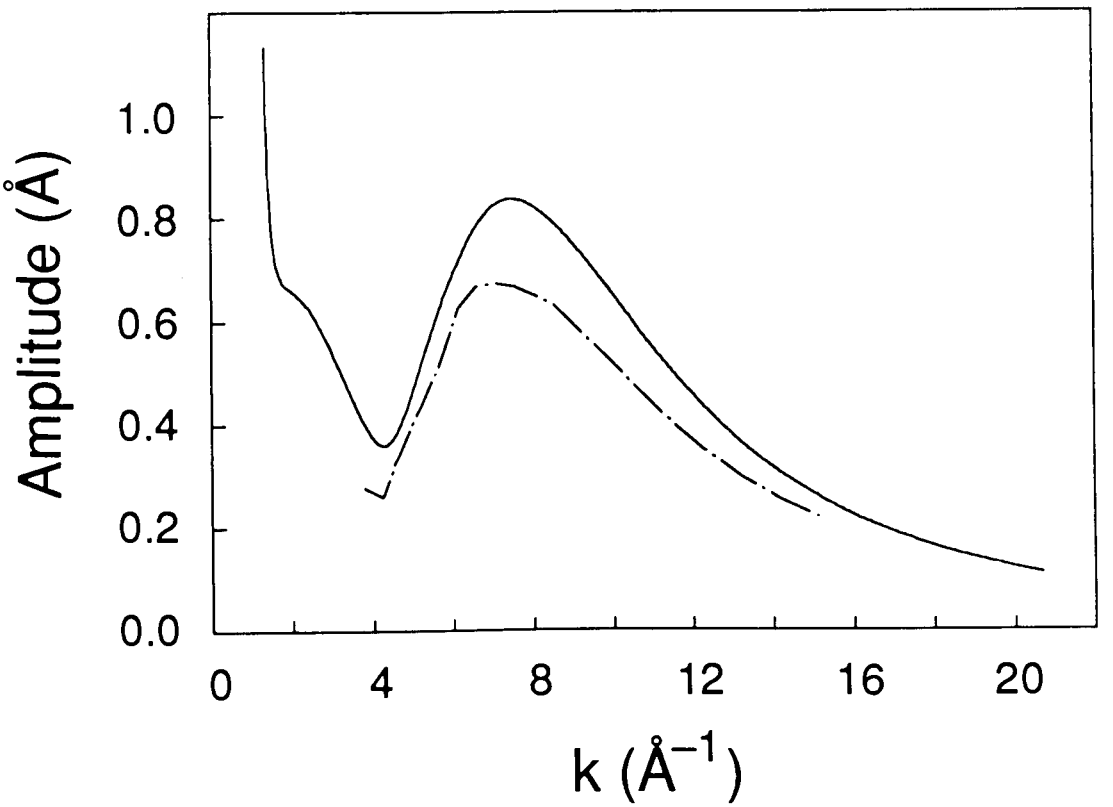

Fig. 3.2: Backscattering amplitude for copper metal calculated in the plane-wave approximation. The dashed line is the result of Teo and Lee [11]. Teo and Lee's amplitude is smaller because they include inelastic effects through a complex potential.

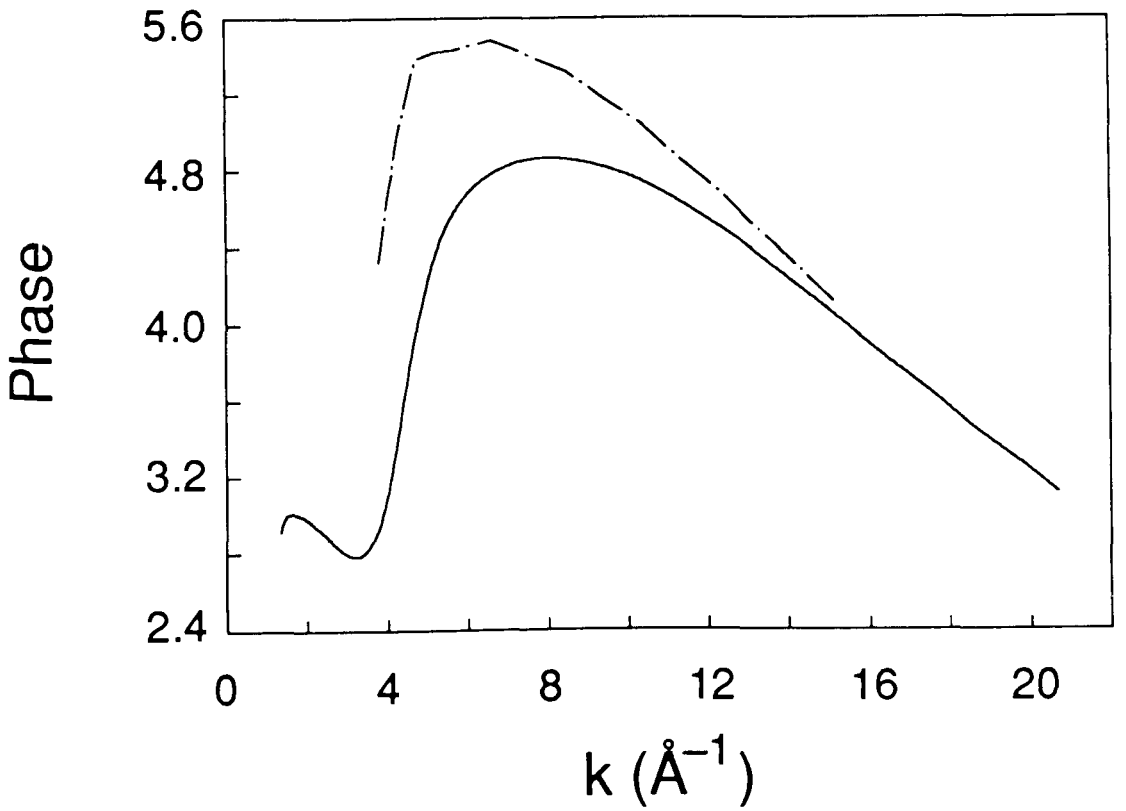

Fig. 3.3: Backscattering phase for copper metal calculated in the plane-wave approximation. The dashed line is the result of Teo and Lee [11]. There is a large discrepancy at low k-values which is most likely due to differences in the potentials. At larger k-values a small discrepancy in the slopes of the two phases occurs.

b) Curved-Waves

The curved-wave formalism of McKale et al. [8-10] is based on the work of Schaich [7] and Müller and Schaich [72]. It has the advantage that the form of the EXAFS equation remains unchanged because the curved-wave effects can all be put into amplitude and phase. This formalism does not include multiple-scattering contributions. It is argued that the EXAFS spectra can be explained by a single-scattering theory down to very low k-values [72]. This cannot always be taken for granted though [73]. An approach to curved-wave theory, that includes multiple scattering, is

given by Refs. 74 and 75. Also of interest in connection with curved-wave theory are three papers by Barton and Shirley [76-78].

The main effect of curved-wave theory is to introduce an R-dependence where R is the distance from the absorbing atom to the scattering atom. For this reason the complex scattering amplitude must now be written as $f(k,\theta,R)$. The plane-wave case would then correspond to $f(k,\theta,\infty)$. Note that no R-dependence was considered in the derivation of the standard EXAFS equation in Section 2.1. Amplitude and scattering phase also depend on the angular momentum of the photoelectron. For K- or L_I-shell absorption one has $l = 0$, whereas for L_{II}- or L_{III}-shell absorption one has $l = 0$ or $l = 2$. However, $l = 2$ is favoured 50:1 over the case $l = 0$ [11]. Therefore the latter is ignored.

i) K- or L_I-shell absorption:

The result for the complex scattering amplitude is [8]:

$$f(k,\theta,R) \equiv A(k,\theta,R)\, e^{i\phi(k,\theta,R)} = \frac{kR^2}{e^{i2kR}} \cdot \sum_l (2l+1)\, P_l(\cos\theta)\, e^{i\delta_l(k)} \sin\delta_l(k) \times \left[\frac{l+1}{2l+1}\, {h^+_{l+1}}^2(kR) + \frac{l}{2l+1}\, {h^+_{l-1}}^2(kR) \right] . \qquad (3.54)$$

$h^+_l(x)$ is an outgoing spherical Hankel function. Here it is defined as follows:

$$h^+_l(x) \equiv i^{l+1} \left(j_l(x) + i\, n_l(x) \right) . \qquad (3.55)$$

$j_l(x)$ and $n_l(x)$ are the spherical Bessel and Neumann functions, respectively. They are defined as in Ref. 37. With the definition (3.55) one has:

$$\lim_{x \to \infty} h^+_l(x) = \frac{1}{x}\, e^{ix} . \qquad (3.56)$$

Thus the term in square brackets on the right-hand side of Eq. (3.54) becomes in the limit of large R equal to $e^{i2kR}/(k^2R^2)$ and Eq. (3.54) correctly yields the plane-wave result of Eq. (3.52).

As in the plane-wave case it is useful to express Eq. (3.54) as a function of $\tan\delta_l(k)$. The result is:

$$A(k,\theta,R)\, e^{i\phi(k,\theta,R)} = \frac{kR^2}{e^{i2kr}} \cdot \sum_l (-1)^l \; P_l(\cos\theta) \; \frac{\tan\delta_l(k)}{1 + \tan^2\delta_l(k)}$$

$$\times \left(1 + i\,\tan\delta_l(k)\right) \left(A_l(kR) + i\,2B_l(kR)\right) . \qquad (3.57)$$

$A_l(kR)$ and $B_l(kR)$ are given by:

$$A_l(kR) \equiv (l+1)\left[j^2_{l+1}(kR) - n^2_{l+1}(kR)\right] + l\left[j^2_{l-1}(kR) - n^2_{l-1}(kR)\right] , \qquad (3.58)$$

$$B_l(kR) \equiv (l+1)\, j_{l+1}(kR)\, n_{l+1}(kR) + l\; j_{l-1}(kR)\; n_{l-1}(kR) \; . \qquad (3.59)$$

The curved-wave formalism has been programmed according to Eqs. (3.57) to (3.59). (For the spherical Bessel and Neumann functions a stable algorithm according to Ref. 79 was employed.)

It is instructive to compare curved-wave theory with the case of plane-waves. After some tedious algebra, which is omitted here, one arrives at the following result which is equivalent to that of Eqs. (3.54) or (3.57):

$$A(k,\theta)\, e^{i\phi(k,\theta)} = \frac{1}{k} \cdot \sum_l C_l(kR) \; P_l(\cos\theta) \; \frac{\tan\delta_l(k)}{1 + \tan^2\delta_l(k)} \; \left(1 + i\,\tan\delta_l(k)\right)$$

$$+ \frac{1}{k} \cdot \sum_l 2\, D_l(kR) \; \tan\delta_l(k)\; P_l(\cos\theta) \; \frac{\tan(\delta_l(k) - \pi/2)}{1 + \tan^2(\delta_l(k) - \pi/2)} \; \left(1 + i\,\tan(\delta_l(k) - \pi/2)\right) .$$

(3.60)

$C_l(kR)$ and $D_l(kR)$ are given by:

$$C_l(kR) \equiv (l+1)\left[p_{l+1}^2(kR) - q_{l+1}^2(kR)\right] + l\left[p_{l-1}^2(kR) - q_{l-1}^2(kR)\right] , \tag{3.61}$$

$$D_l(kR) \equiv (l+1)\, p_{l+1}(kR)\; q_{l+1}(kR) + l\; p_{l-1}(kR)\; q_{l-1}(kR) . \tag{3.62}$$

(There should be no confusion with the logarithmic derivative, labeled as $D_l(E,r)$.)

The p_l and q_l are polynomials:

$$p_l(x) \equiv \sum_{k=0}^{[l/2]} (-1)^k \frac{(l+2k)!}{(2k)!\,(l-2k)!} (2x)^{-2k} , \tag{3.63}$$

$$q_l(x) \equiv \sum_{k=0}^{[(l-1)/2]} (-1)^k \frac{(l+2k+1)!}{(2k+1)!\,(l-2k-1)!} (2x)^{-2k-1} . \tag{3.64}$$

The square brackets on the upper limits of the summation index signify the integer part of the term in brackets.

Evaluating the first two of the C_l's and D_l's yields:

$$C_0(kR) = \frac{1}{(kR)^2}\left((kR)^2 - 1\right) ; \qquad C_1(kR) = \frac{3}{(kR)^4}\left((kR)^4 - 10\,(kR)^2 + 6\right) ;$$

$$D_0(kR) = \frac{1}{kR} ; \qquad D_1(kR) = \frac{6}{(kR)^3}\left((kR)^2 - 3\right) .$$

The functions $C_l(kR)$ are even and the functions $D_l(kR)$ are odd. When the argument approaches zero $C_l(kR)$ diverges like $(kR)^{-2l-2}$ and $D_l(kR)$ diverges like $(kR)^{-2l-1}$. For $kR \to \infty$ we have $C_l \to 2l+1$ and $D_l \to 0$.

The two summations in Eq. (3.60) describe the addition of two sets of l-dependent phasors that are orthogonal to each other. The l-dependent amplitude ratio of the second set of phasors with respect to the first is given by $2\,D_l(kR)\,\tan\delta_l(k)/C_l(kR)$. From this one can immediately conclude that for $k \to 0$ the second sum in Eq. (3.60) can be neglected with respect to the first. (Only for $l = 0$ is it in principle possible that $\tan\delta_0(k)$ diverges as k approaches zero.) The behaviour of the complex scattering amplitude in curved-wave theory as $k \to 0$ is then determined by the term $\frac{1}{k}\,C_l(kR)\,\tan\delta_l(k)$. If k is small $\tan\delta_l(k)$ behaves like $-a_l\,k^{2l+1}$ [80]. Thus for $k \to 0$ the complex scattering amplitude behaves like k^{-2} . This is different from plane-wave theory where the amplitude tends to a constant.

ii) L_{II}- or L_{III}-shell absorption:

The result for the complex scattering amplitude is in this case [8]:

$$f(k,\theta,R) \equiv A(k,\theta,R)\,e^{i\phi(k,\theta,R)} = \frac{kR^2}{e^{i2kR}} \cdot \sum_l (2l+1)\,P_l(\cos\theta)\,e^{i\delta_l(k)}\,\sin\delta_l(k)$$

$$\times \left[\frac{3\,l\,(l-1)}{2\,(2l+1)\,(2l-1)}\,h^{+}_{l-2}{}^{2}(kR) + \frac{l\,(l+1)}{(2l+3)\,(2l-1)}\,h^{+}_{l}{}^{2}(kR) \right.$$

$$\left. + \frac{3\,(l+2)\,(l+1)}{2\,(2l+3)\,(2l+1)}\,h^{+}_{l+2}{}^{2}(kR) \right] . \qquad (3.65)$$

Again, it is useful to express this result as a function of $\tan\delta_l(k)$. One obtains:

$$A(k,\theta,R)\,e^{i\phi(k,\theta,R)} = \frac{kR^2}{e^{i2kr}} \cdot \sum_l (-1)^{l+1}\,P_l(\cos\theta)\,\frac{\tan\delta_l(k)}{1+\tan^2\delta_l(k)}$$

$$\times \left(1 + i\,\tan\delta_l(k)\right)\left(\tilde{A}_l(kR) + i\,2\tilde{B}_l(kR)\right) . \qquad (3.66)$$

Because of the term $(-1)^{l+1}$, instead of $(-1)^{l}$, there is now an extra minus sign compared to Eq. (3.57). $\tilde{A}_l(kR)$ and $\tilde{B}_l(kR)$ are given by:

$$\tilde{A}_l(kR) \equiv \frac{3\,l\,(l-1)}{2\,(2l-1)}\left[j^2_{l-2}(kR) - n^2_{l-2}(kR)\right]$$

$$+\frac{l\,(l+1)\,(2l+1)}{(2l-1)\,(2l+3)}\left[j^2_{l}(kR) - n^2_{l}(kR)\right] + \frac{3\,(l+1)\,(l+2)}{2\,(2l+3)}\left[j^2_{l+2}(kR) - n^2_{l+2}(kR)\right], \qquad (3.67)$$

$$\tilde{B}_l(kR) \equiv \frac{3\,l\,(l-1)}{2\,(2l-1)}\, j_{l-2}(kR)\, n_{l-2}(kR)$$

$$+\frac{l\,(l+1)\,(2l+1)}{(2l-1)\,(2l+3)}\, j_l(kR)\, n_l(kR) + \frac{3\,(l+1)\,(l+2)}{2\,(2l+3)}\, j_{l+2}(kR)\, n_{l+2}(kR)\ . \qquad (3.68)$$

The curved-wave formalism has been programmed according to Eqs. (3.66) to (3.68).

It is possible also in this case to derive a relation analogous to Eq. (3.60) but this is omitted.

We will now compare results of our calculations with those that have been published already by Teo and Lee [11] and McKale et al. [8-10]. This will give an impression about how much different calculations can deviate. It does not imply that Teo and Lee's or McKale's et al. values are correct. These values are frequently employed because no others are readily available. It is in fact rather difficult to claim that any calculation produces the "correct" amplitude and phase. If the correct backscattering (and central) phase were known, then one could obtain distances from EXAFS with absolute, rather than relative, precision.

The next figures show some of the results obtained for backscattering amplitude and phase from Eq. (3.57). Fig. 3.4 is a plot of the backscattering amplitude for copper metal, evaluated for a distance of $R = 2.5$ Å . This value was chosen in order to facilitate a comparison with the curved-wave calculation of McKale (dashed line) which is presented in Ref. 10 for $R = 2.5$ Å and $R = 4$ Å .

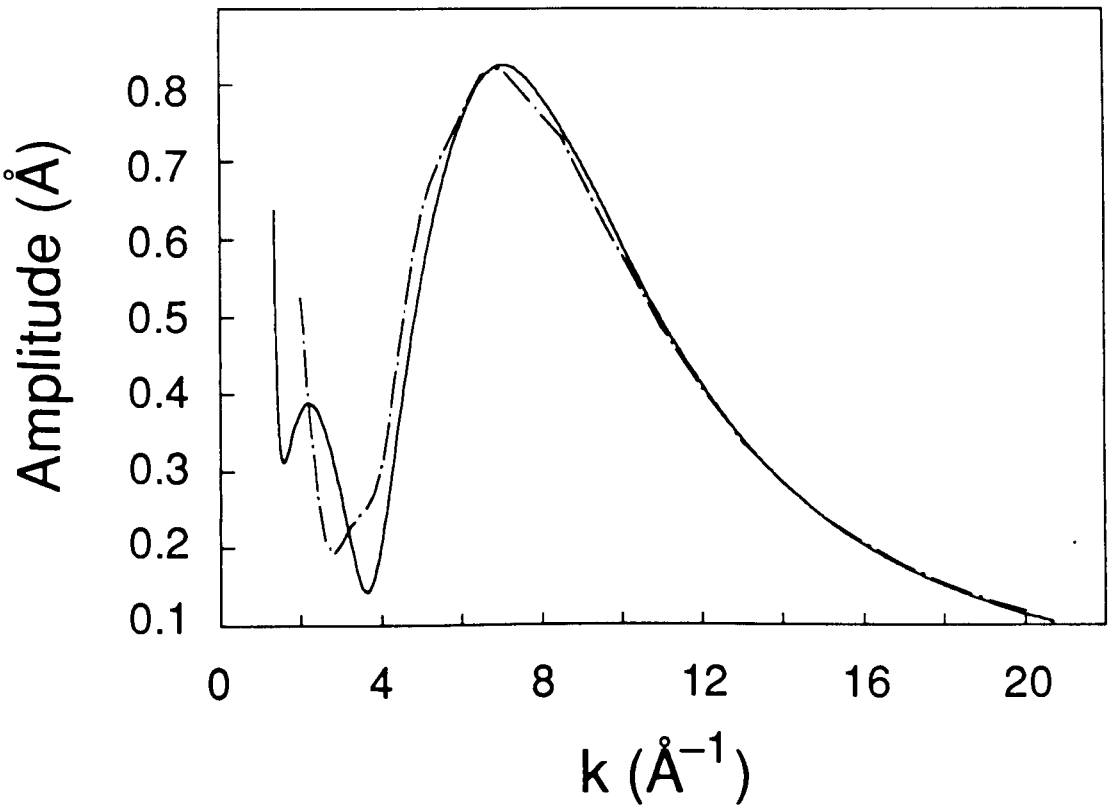

Fig. 3.4: Backscattering amplitude for copper metal calculated in curved-wave theory for R = 2.5 Å and K- or L_I-edge absorption. The dashed line is the result of McKale [10] who employed a real potential, as is done in this work. Therefore there is good agreement for the high k-values. The discrepancy below ~6 Å^{-1} is due to differences in the potential.

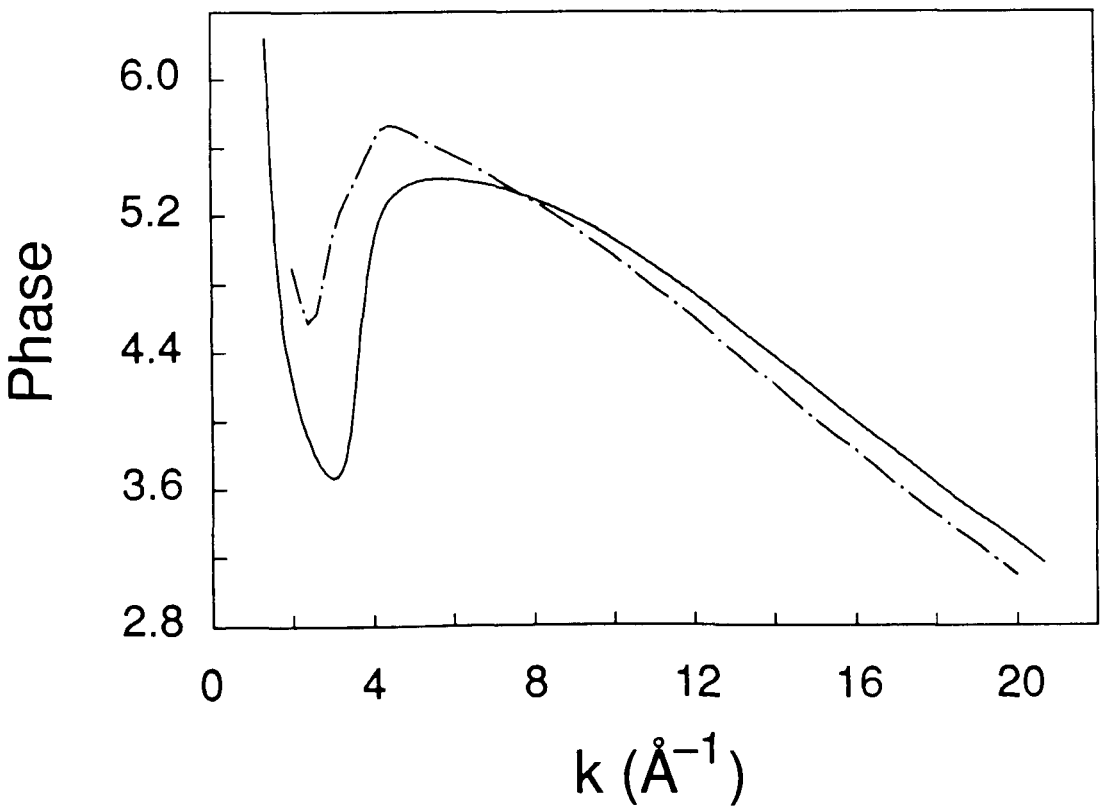

Fig. 3.5: Backscattering phase for copper metal calculated in curved-wave theory for R = 2.5 Å and K- or L_I-edge absorption. The dashed line is the result of McKale [10]. Since the phase is more sensitive to the choice of the potential (see Section 3.6), we obtain bigger discrepancies than in the previous figure. In particular, we notice that the phase calculated in this work (solid line) is shifted upwards by a small amount above k ~ 10 Å^{-1} . According to Section 3.6 below, this may be due to the fact that the Cu-potential used in this work may be shifted downwards compared to the potential employed by McKale et al., which is not published.

For SmSe the crystal potential was calculated for two cases. In the first case, ambient pressure was assumed. Thus the Sm atoms are divalent and the lattice constant is 6.2 Å. 30 partial-wave phase shifts (l = 0 - 29) were employed. In the second case, trivalent Sm atoms were assumed for the high-pressure phase where the lattice constant is 5.7 Å. This time 31 partial waves could be employed. For each of these cases the backscattering amplitude and phase were calculated.

Curved-wave theory was included with nearest-neighbour distances of 3.1 Å and 2.85 Å, respectively. The results are shown in the next two figures.

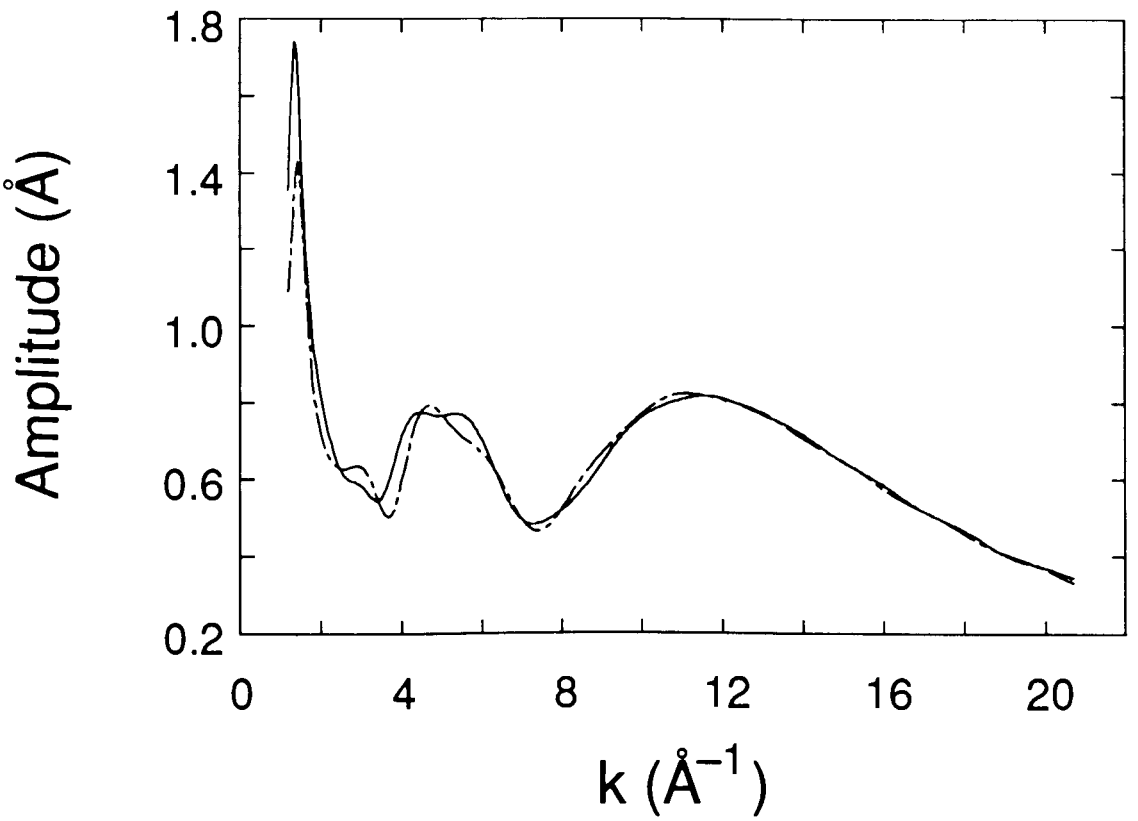

Fig. 3.6: Backscattering amplitude for Sm in SmSe in curved-wave theory and for K- or L_I-edge absorption. The solid line shows the result calculated for a crystal potential with Sm^{2+} atoms and a lattice constant of 6.2 Å. The absorber-backscatterer distance is R = 3.1 Å . The dashed line is the result calculated for a crystal potential with Sm^{3+} atoms and a lattice constant of 5.7 Å. The absorber-backscatterer distance is R = 2.85 Å . The two curves are practically identical.

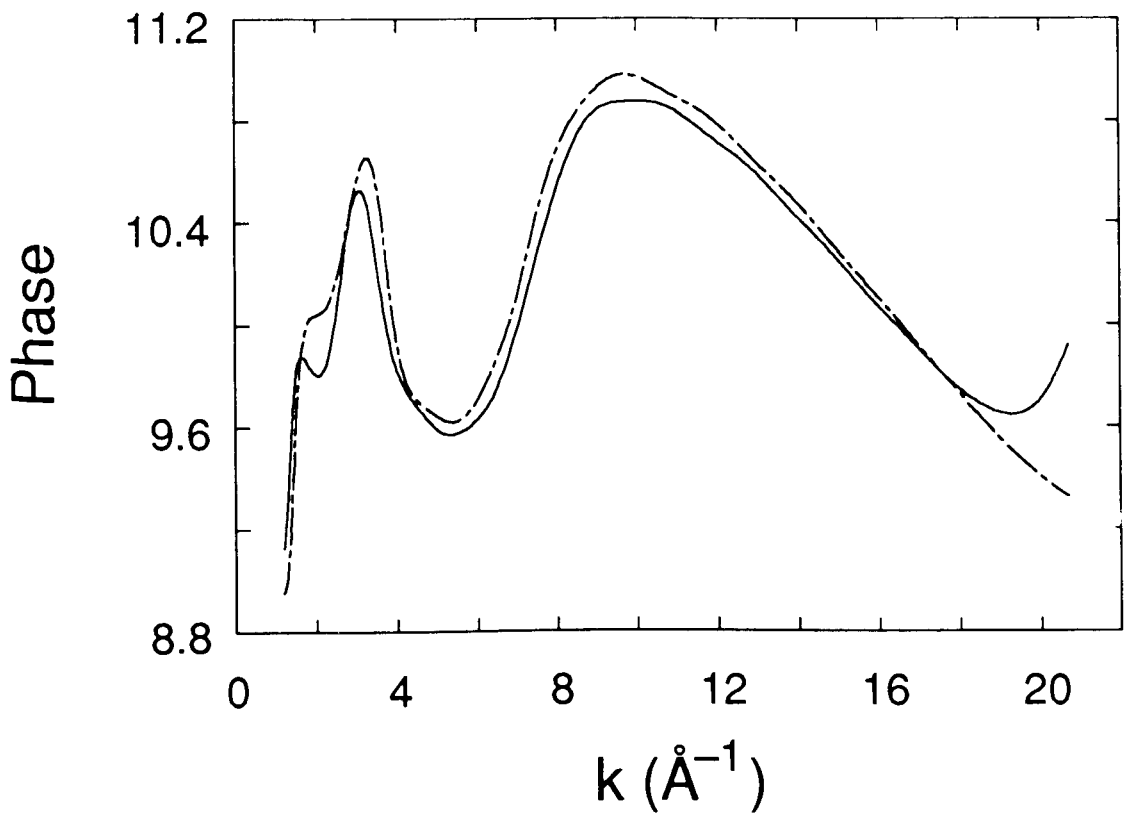

Fig. 3.7: Backscattering phase for Sm in SmSe in curved-wave theory and for K- or L_I-edge absorption. The solid line shows the result calculated for a crystal potential with Sm^{2+} atoms and a lattice constant of 6.2 Å. The absorber-backscatterer distance is R = 3.1 Å . The dashed line is the result calculated for a crystal potential with Sm^{3+} atoms and a lattice constant of 5.7 Å. The absorber-backscatterer distance is R = 2.85 Å . Above 18 $Å^{-1}$ the solid line curves up. This results from the fact that in the divalent case only 30 partial waves could be employed. With more partial waves numerical instability occurred.

We now see that the results calculated for a crystal potential with divalent Sm atoms are essentially equal to those for trivalent Sm atoms. Therefore only one and the same potential is employed. We choose the one corresponding to the high-pressure phase (dashed lines in the two previous figures) because in that case the backscattering phase can be calculated to higher k-values. The dashed lines, however, were calculated with R = 2.85 Å whereas in the low-pressure

phase the nearest-neighbour distance is 3.1 Å. In the following two figures we therefore compare the curved-wave results for R = 2.85 Å with those for R = 3.1 Å, both calculated for a crystal potential for trivalent Sm atoms. We see that the modifications due to curved-wave theory can be ignored for k-values above ~3 $Å^{-1}$.

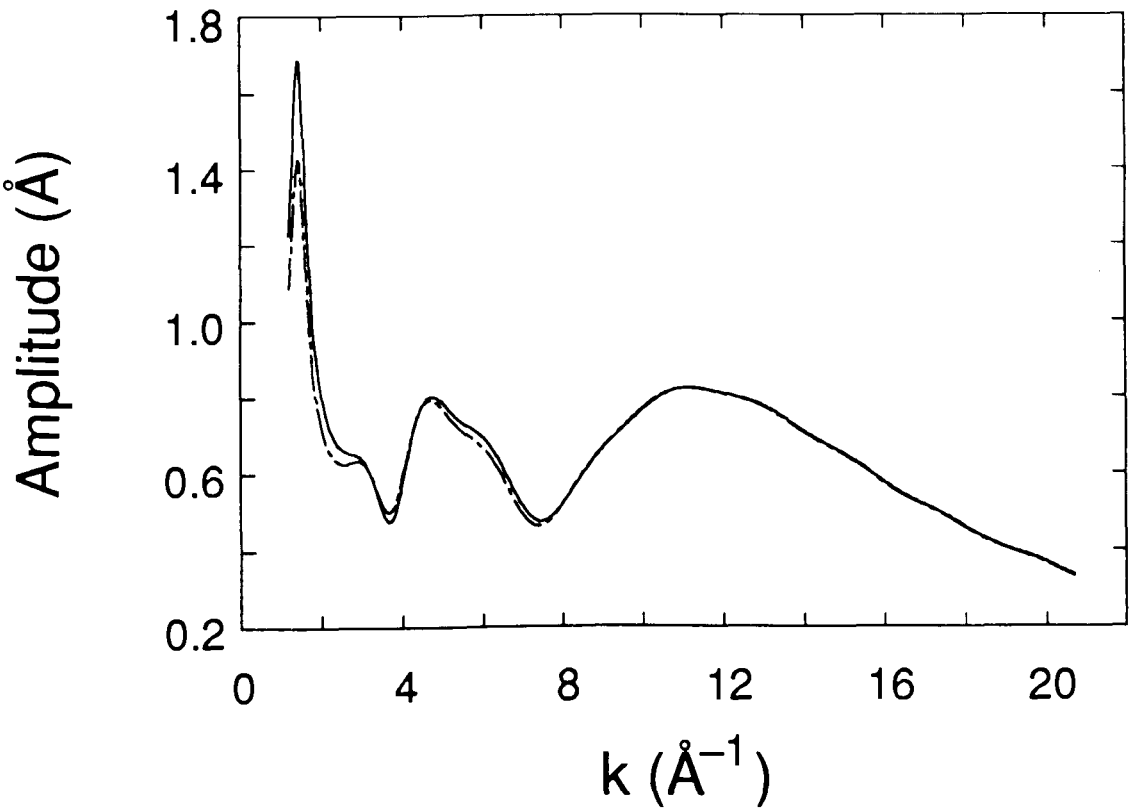

Fig. 3.8: Backscattering amplitude for Sm in SmSe in curved-wave theory and for K- or L_I-edge absorption. Results are calculated for a crystal potential with Sm^{2+} atoms and a lattice constant of 6.2 Å. The solid line refers to an absorber-backscatterer distance of R = 3.1 Å and the dashed line is the result for R = 2.85 Å.

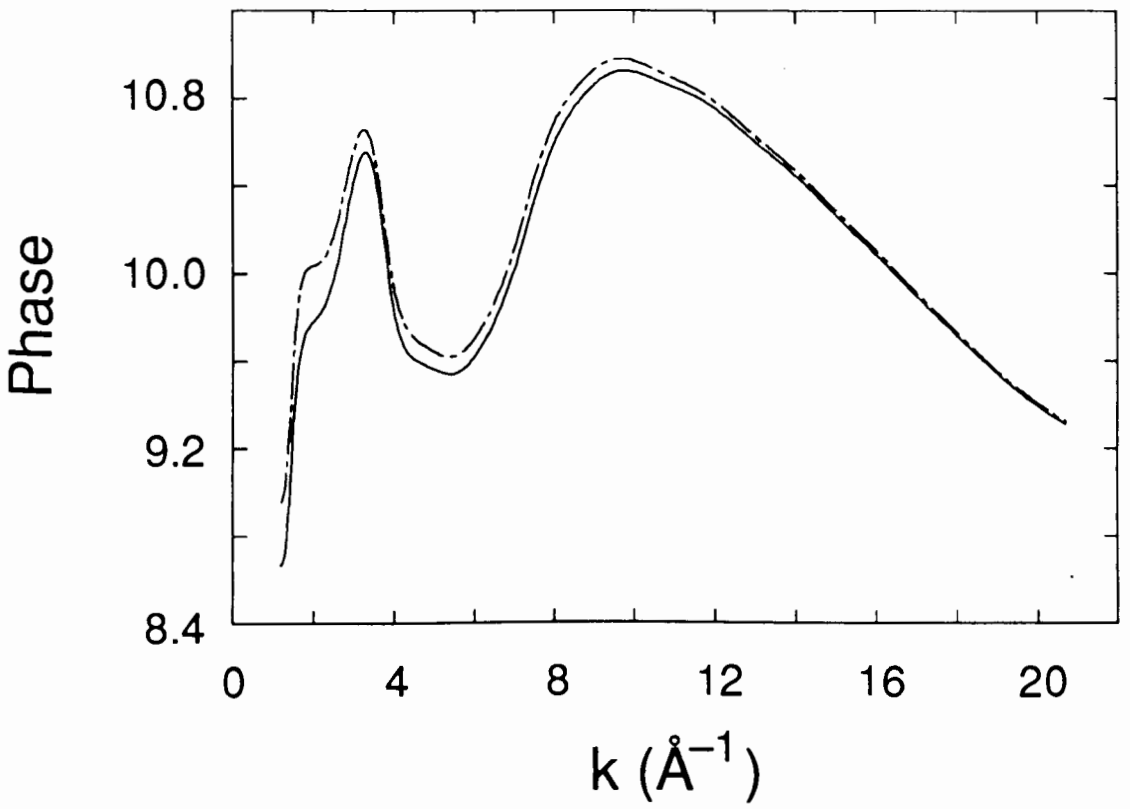

Fig. 3.9: Backscattering phase for Sm in SmSe in curved-wave theory and for K- or L_I-edge absorption. Results are calculated for a crystal potential with Sm^{2+} atoms and a lattice constant of 6.2 Å. The solid line refers to an absorber-backscatterer distance of R = 3.1 Å and the dashed line is the result for R = 2.85 Å .

The following figures show calculations of the Sm- and Se backscattering amplitude and phase for various values of the absorber-backscatterer distance R. Because there is no significant difference between Sm^{2+} and Sm^{3+} crystal potentials, we can employ in the calculations always the crystal potential for trivalent Sm atoms. Effects due to temperature are ignored.

In Figs. 3.10 to 3.13 we compare our results for SmSe with those available from McKale. In order to do this we calculated the backscattering curved-wave amplitude for R = 2.5 Å , although this

distance does not occur in SmSe. It is to be noted that McKale et al. do not list results for Sm, nor for Se, but for their neighbouring elements. Thus, for Sm and Se we have to perform an interpolation linear in the atomic number Z in order to obtain the proper amplitude and phase. If we had chosen to plot the result for the nearest-neighbour distance $R_1 = 3.1$ Å of SmSe, then a further interpolation (linear in 1/R) between McKale's et al. result for $R = 2.5$ Å and their result for $R = 4$ Å would have been necessary. Furthermore it is to be kept in mind that the (complex) scattering amplitude in curved-wave theory depends on the type of edge of the absorbing element. That is, for a Sm scatterer the absorber will be Se and we have to consider K- (or L_I-) shell absorption. For Se as the scatterer we have to consider an L_{II}- or L_{III}-absorption edge of Sm.

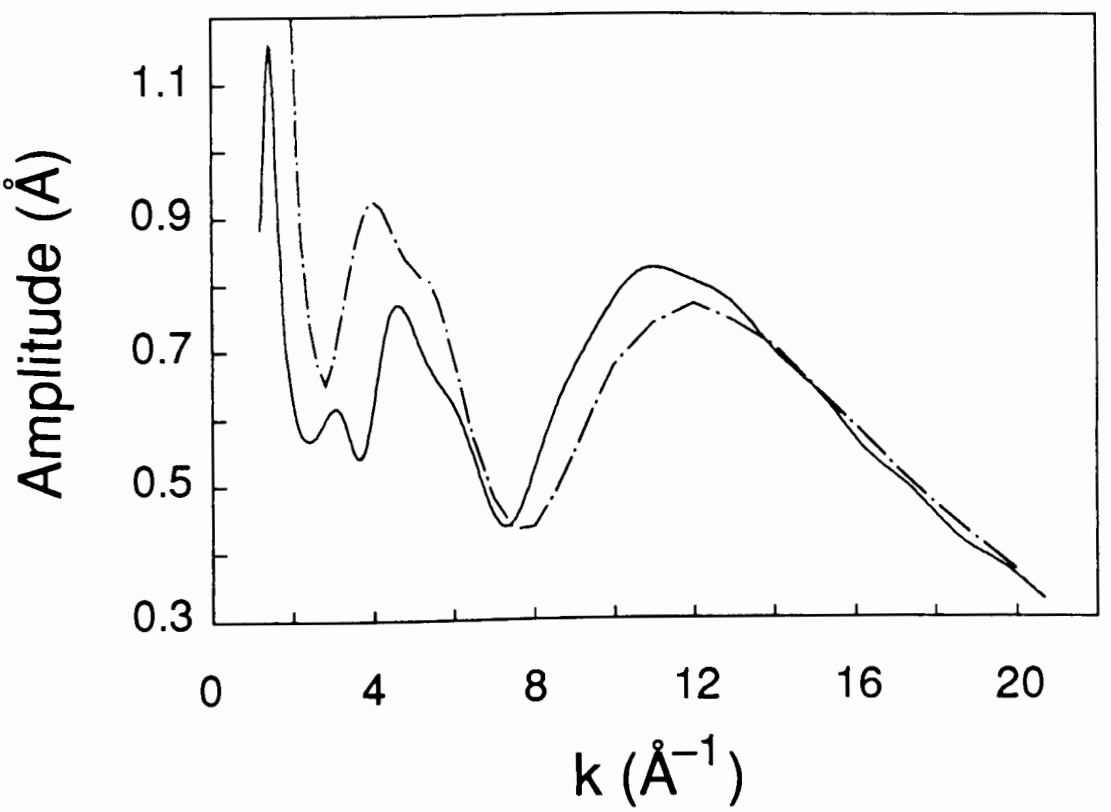

Fig. 3.10: Backscattering amplitude for Sm in SmSe calculated in curved-wave theory for $R = 2.5$ Å and K- or L_I-edge absorption. The dashed line is the result of McKale et al., obtained as in Ref. 10, who employed a real potential, as is done in this work. The discrepancy below ~12 Å^{-1} is due to different potentials.

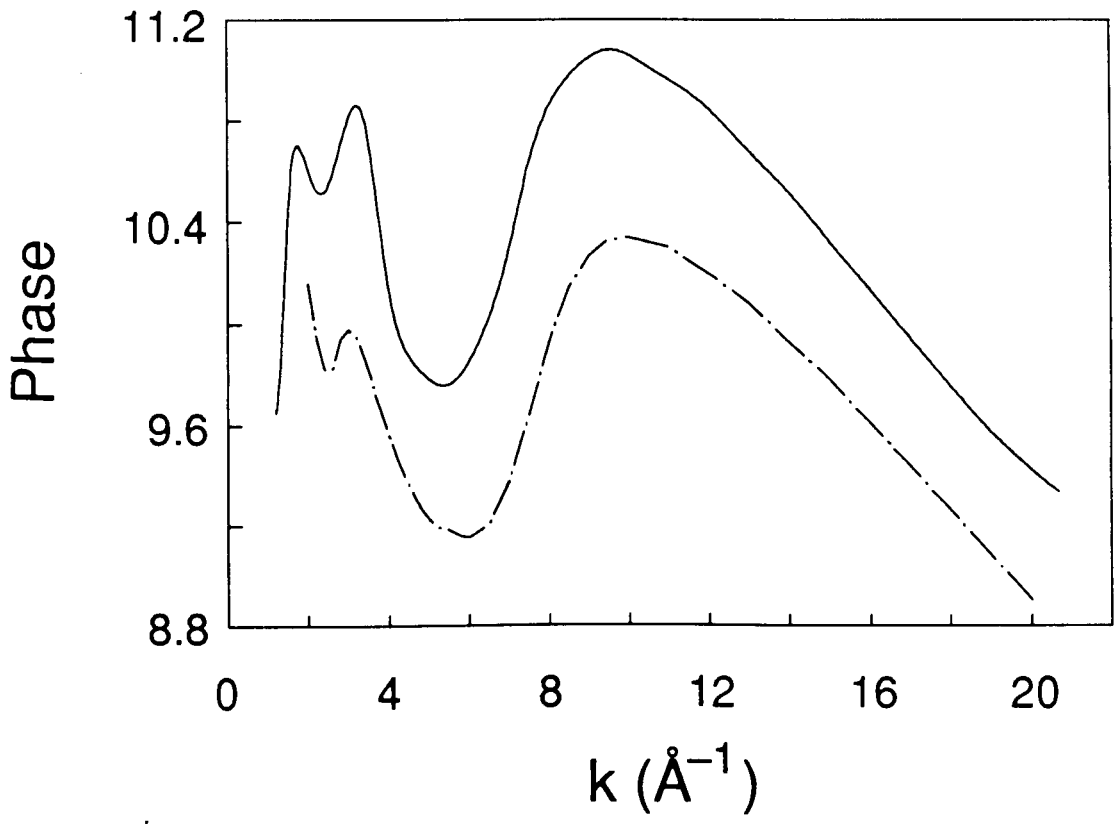

Fig. 3.11: Backscattering phase for Sm in SmSe calculated in curved-wave theory for R = 2.5 Å and K- or L_I-edge absorption. The dashed line is the result of McKale et al.. The backscattering phase calculated in this work is shifted upwards, probably stemming from the fact that our potential is a few eV lower than the one used by McKale et al..

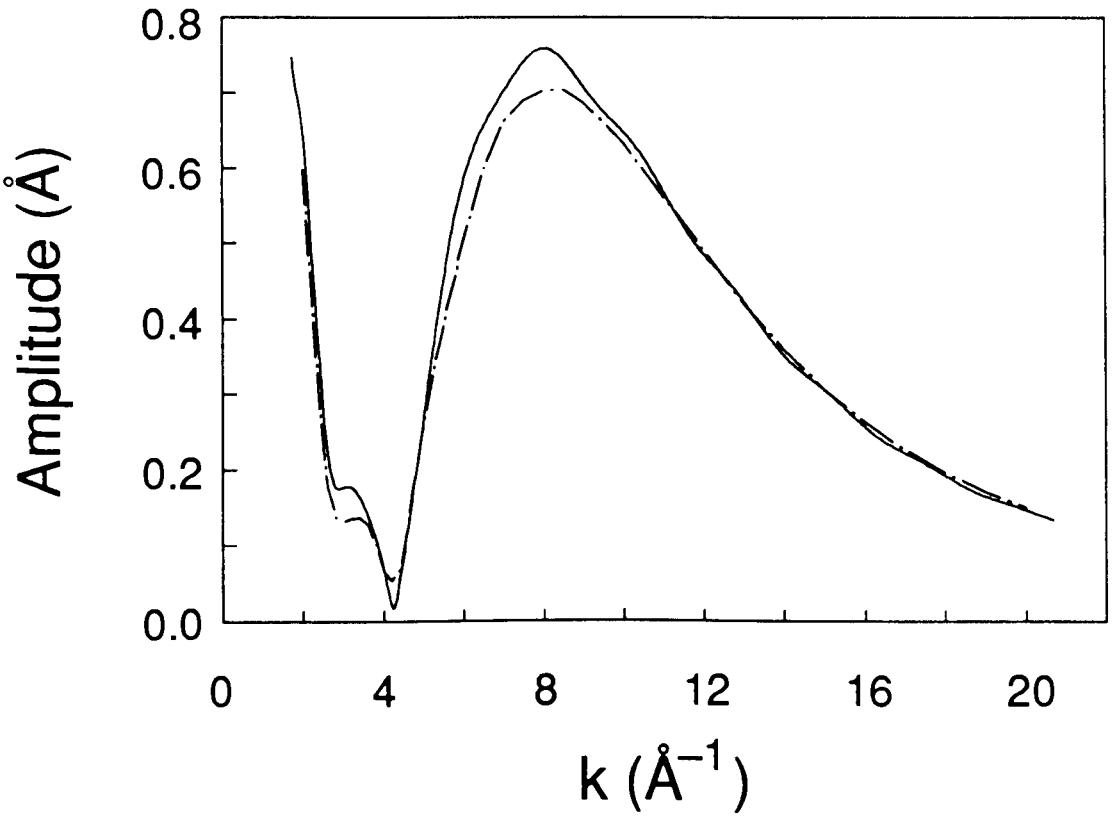

Fig. 3.12: Backscattering amplitude for Se in SmSe calculated in curved-wave theory for R = 2.5 Å and L_{II}- or L_{III}-edge absorption. The dashed line is the result of McKale et al.. The calculations agree.

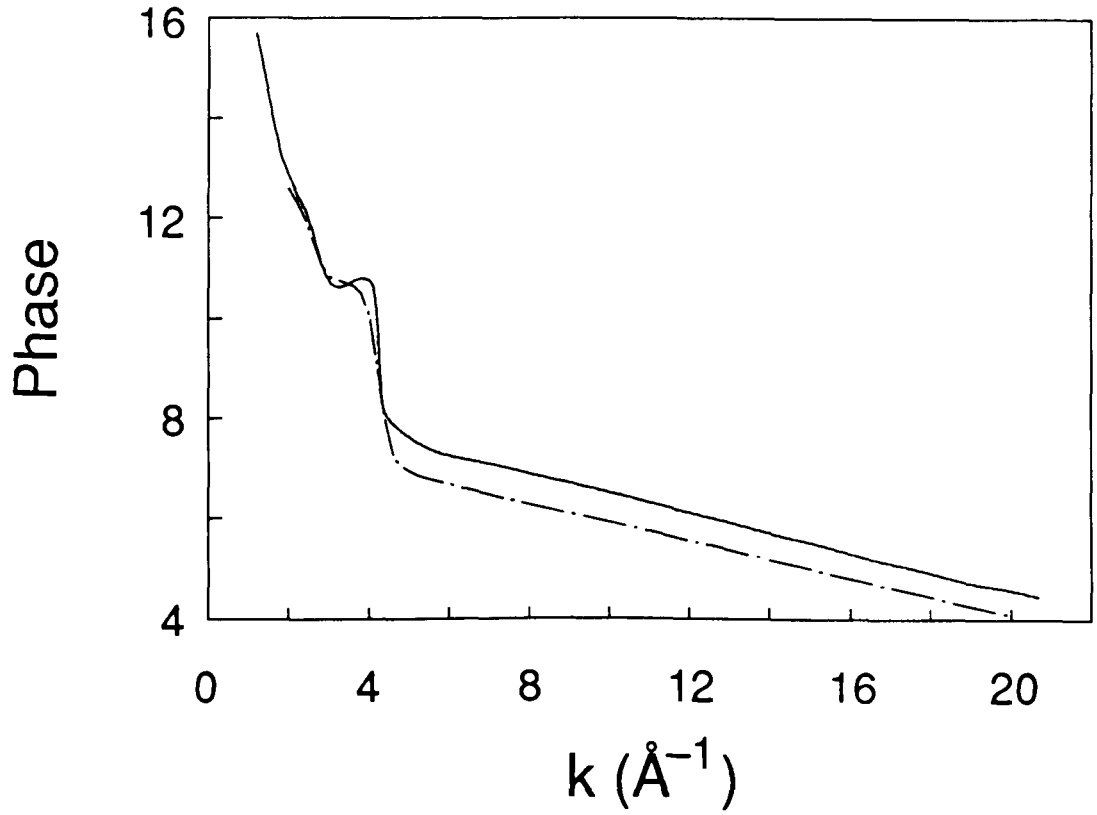

Fig. 3.13: Backscattering phase for Se in SmSe calculated in curved-wave theory for R = 2.5 Å and L_{II}- or L_{III}-edge absorption. The dashed line is the result of McKale et al.. As in Fig. 3.11, the backscattering phase calculated in this work is shifted upwards.

The next four figures are a comparison between the results of this work for R = 2.5 Å and for R = 3.1 Å . This difference in R is already larger than the change of the nearest-neighbour distance from R = 3.1 Å to R = 2.85 Å , achieved by pressurizing SmSe. The figures show that there is not much variation of the backscattering amplitudes and phases for the compressions occuring here.

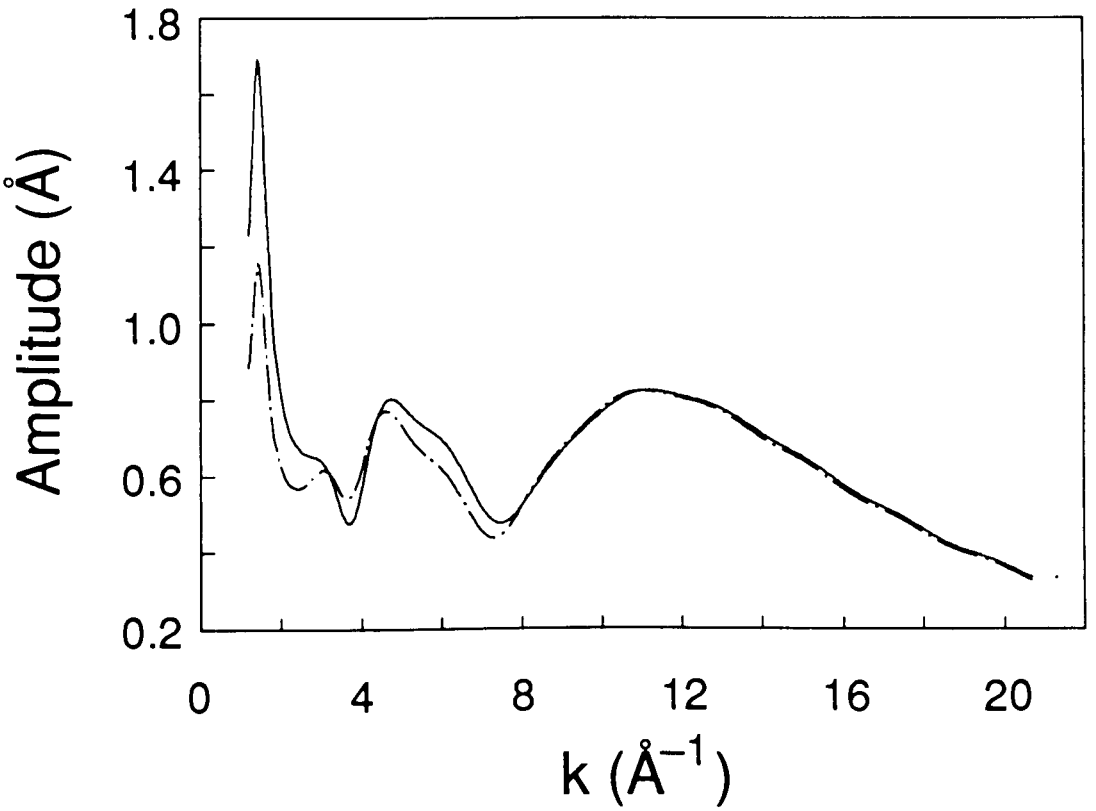

Fig. 3.14: Backscattering amplitude for Sm in SmSe calculated in curved-wave theory for K- or L_I-edge absorption. The solid line is the result for R = 3.1 Å and the dashed line corresponds to R = 2.5 Å.

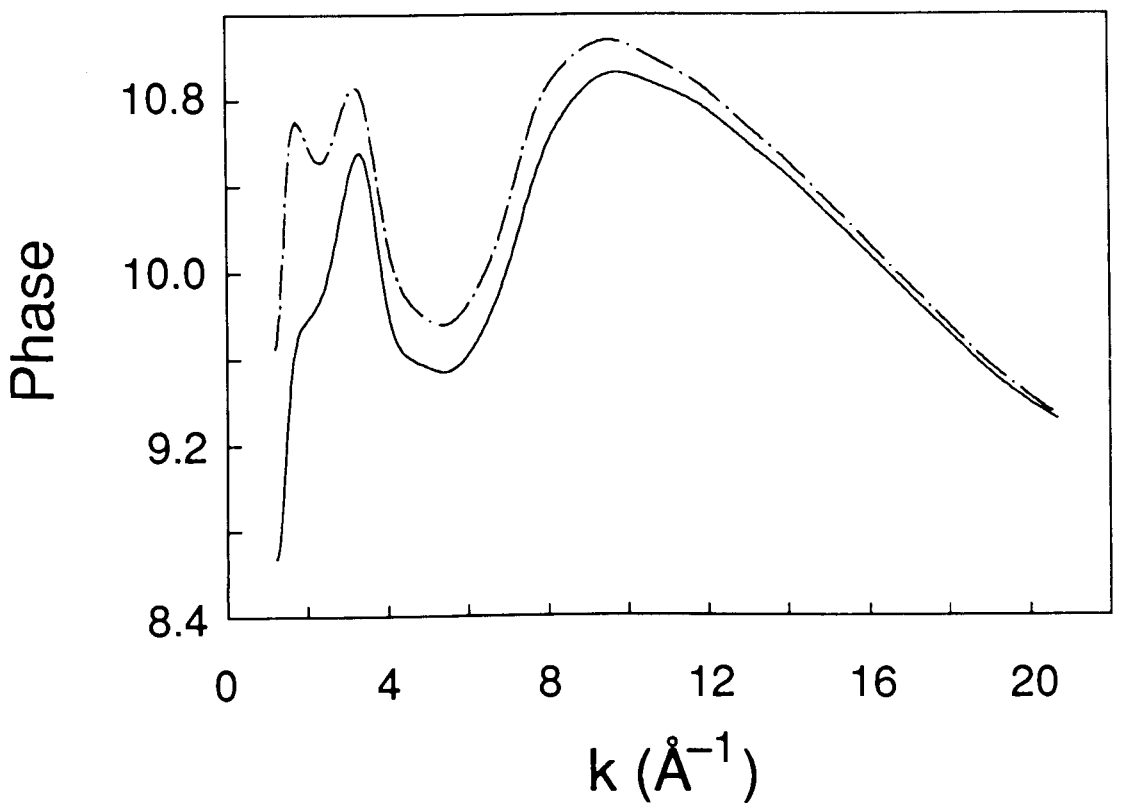

Fig. 3.15: Backscattering phase for Sm in SmSe calculated in curved-wave theory for K- or L_I-edge absorption. The solid line is the result for R = 3.1 Å and the dashed line corresponds to R = 2.5 Å .

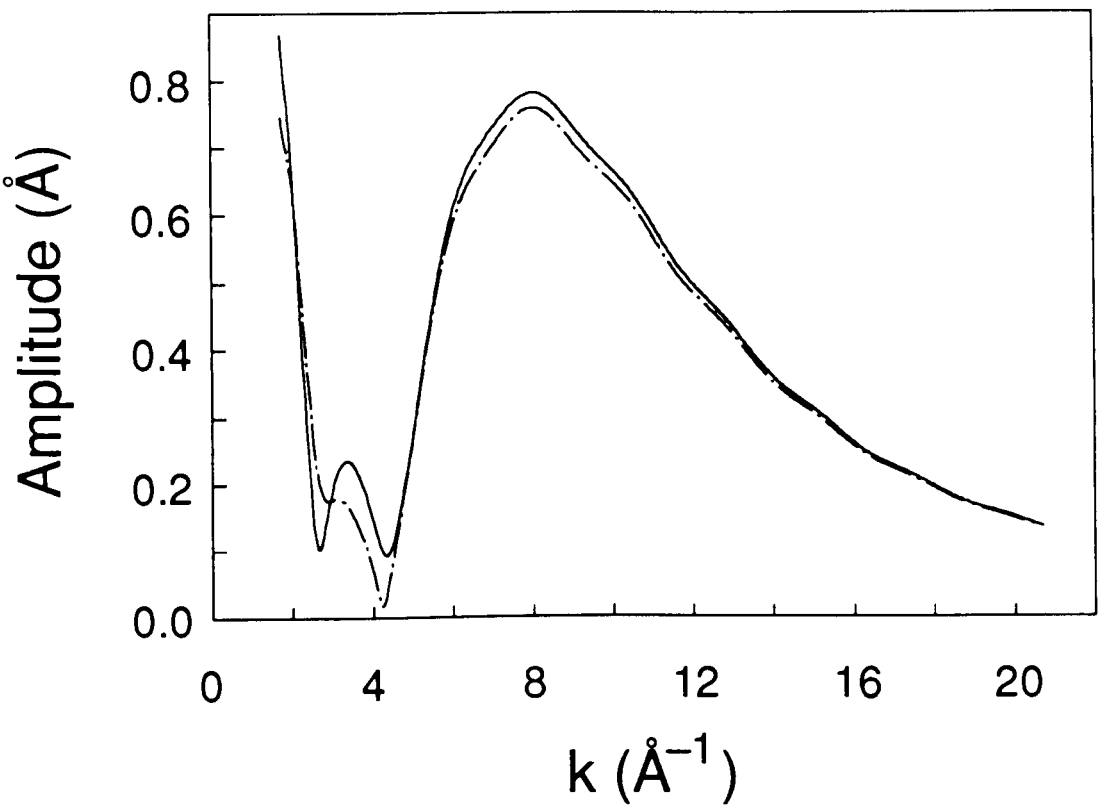

Fig. 3.16: Backscattering amplitude for Se in SmSe calculated in curved-wave theory for L_{II}- or L_{III}-edge absorption. The solid line is the result for R = 3.1 Å and the dashed line corresponds to R = 2.5 Å .

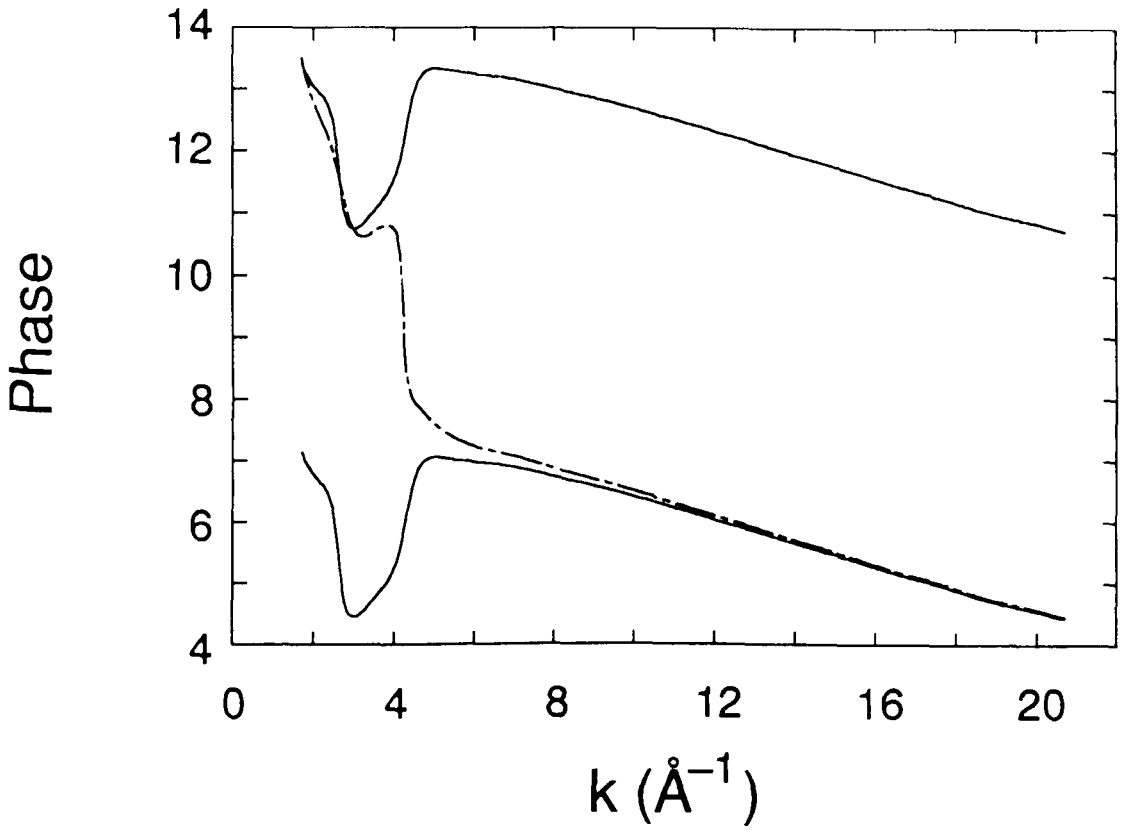

Fig. 3.17: Backscattering phase for Se in SmSe calculated in curved-wave theory for L_{II}- or L_{III}-edge absorption. The two solid lines, which differ by 2π, show the result for $R = 3.1$ Å and the dashed line corresponds to $R = 2.5$ Å. It is seen that there is a discrepancy for $4\ Å^{-1} < k < 6\ Å^{-1}$, which is entirely due to curved-wave theory. Similar effects have been observed in Ref. 10 when phases obtained from curved- and plane-wave theories are compared.

Finally, we study the effect of the different types of absorption edges of the absorbing atom on the curved-wave amplitude and phase. We choose Se with $R = 3.1$ Å and compare the results of L_{II}- or L_{III}-edge absorption with those of K- or L_I-edge absorption.

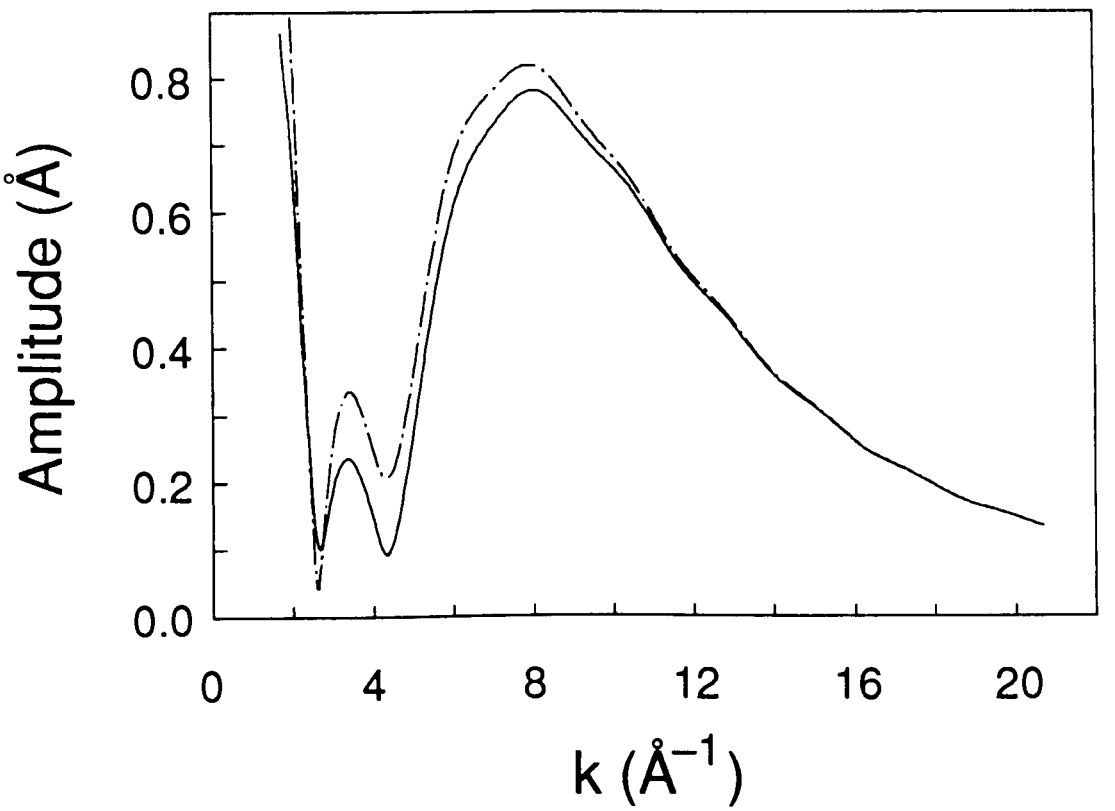

Fig. 3.18: Backscattering amplitude for Se in SmSe calculated in curved-wave theory (R = 3.1 Å) for L_{II}- or L_{III}-edge absorption (solid line) and for K- or L_I-edge absorption (dashed line).

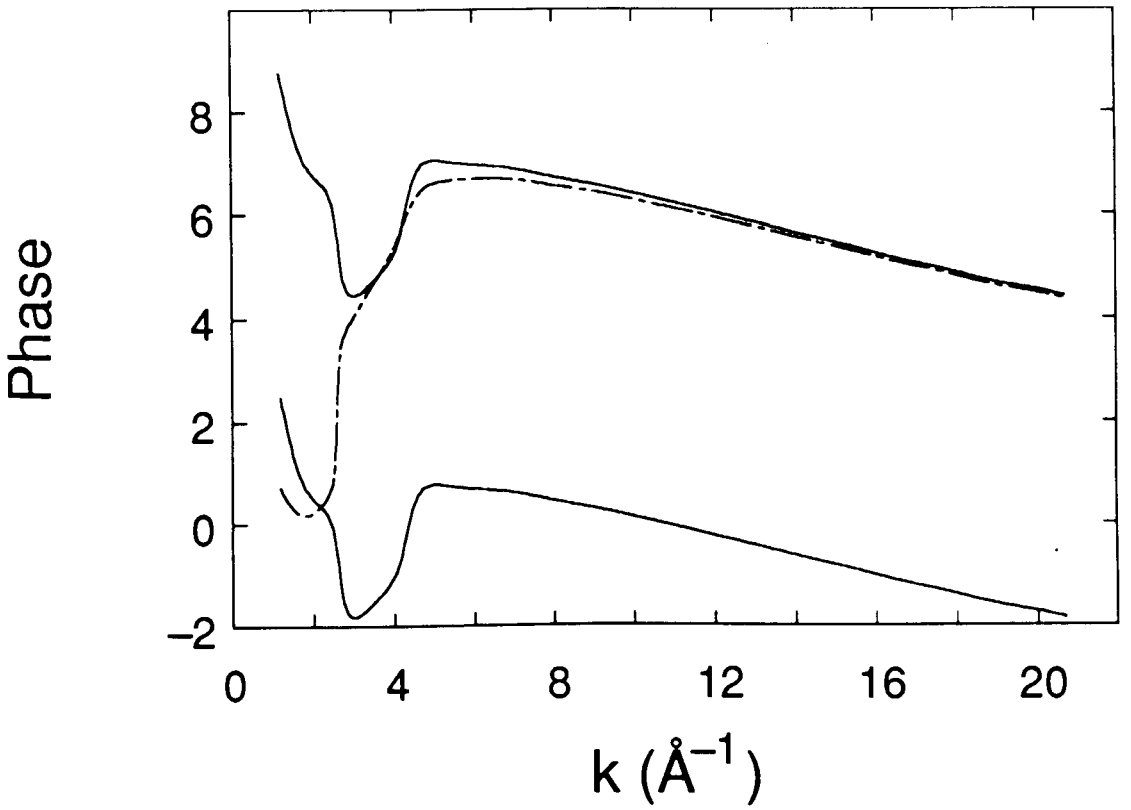

Fig. 3.19: Backscattering phase for Se in SmSe calculated in curved-wave theory (R = 3.1 Å) for L_{II}- or L_{III}-edge absorption (solid lines, differing by 2π) and for K- or L_I-edge absorption (dashed line).

3.5 Central-Atom Phase Shifts

For K- or L_I-shell absorption the phase shift of the central atom, i.e. of the absorbing atom, is given by Ref. 11:

$$\delta_c = 2\,\delta_1 - \pi \ . \tag{3.69}$$

For L_{II}- or L_{III}-shell absorption the $l = 2$ contribution dominates. Therefore the central phase involves only this angular-momentum value [11]:

$$\delta_c = 2\,\delta_2 \ . \qquad (3.70)$$

δ_c is obtained from the partial-wave phase shifts δ_1 or δ_2. However, one should take the effect of the core hole of the absorber into account. It results in the central-atom phase shift decaying more rapidly with k than the partial-wave phase shift calculated for a neutral atom.

No attempt is made to calculate central phases in this thesis. Instead the central phases calculated by Teo and Lee [11], which contain the effects of a core hole, are employed. As mentioned at the beginning of Section 3.4, these phases are tabulated only for a limited k-range. It is therefore necessary to extrapolate towards either side. In order to extrapolate to higher k-values one may make use of the Born approximation for the phase shift [37]:

$$\delta_{l,\mathrm{Born}}(k) = -k \cdot \int_0^\infty V(r)\, j_l^2(kr)\, r^2 dr \ . \qquad (3.71)$$

From the behaviour of $j_l(kr)$ it follows that for large values of k the behaviour of the phase shift can be described by a power series in 1/k omitting the constant term so that the phase shift properly goes to zero for $k \to \infty$. In order to extrapolate from 15.12 $Å^{-1}$ to 24 $Å^{-1}$ the first three terms of this power series are employed to fit Teo and Lee's central phases starting at ~5 $Å^{-1}$. The validity of this parametrization of the phase shifts at high k-values has been checked by fitting to partial-wave phase shifts, calculated for the case without the core hole, and found to be quite satisfactory.

For low k-values the central phase is extrapolated linearly to ~1.5 $Å^{-1}$. It cannot be extrapolated in this way all the way to $k = 0$ because the $l = 1$ or $l = 2$ phase shifts must have zero slope at $k = 0$. Furthermore, they have to approach an integer multiple of π in accordance with Levinson's theorem [37].

The following figures display the central-atom phase shifts for Se and Sm.

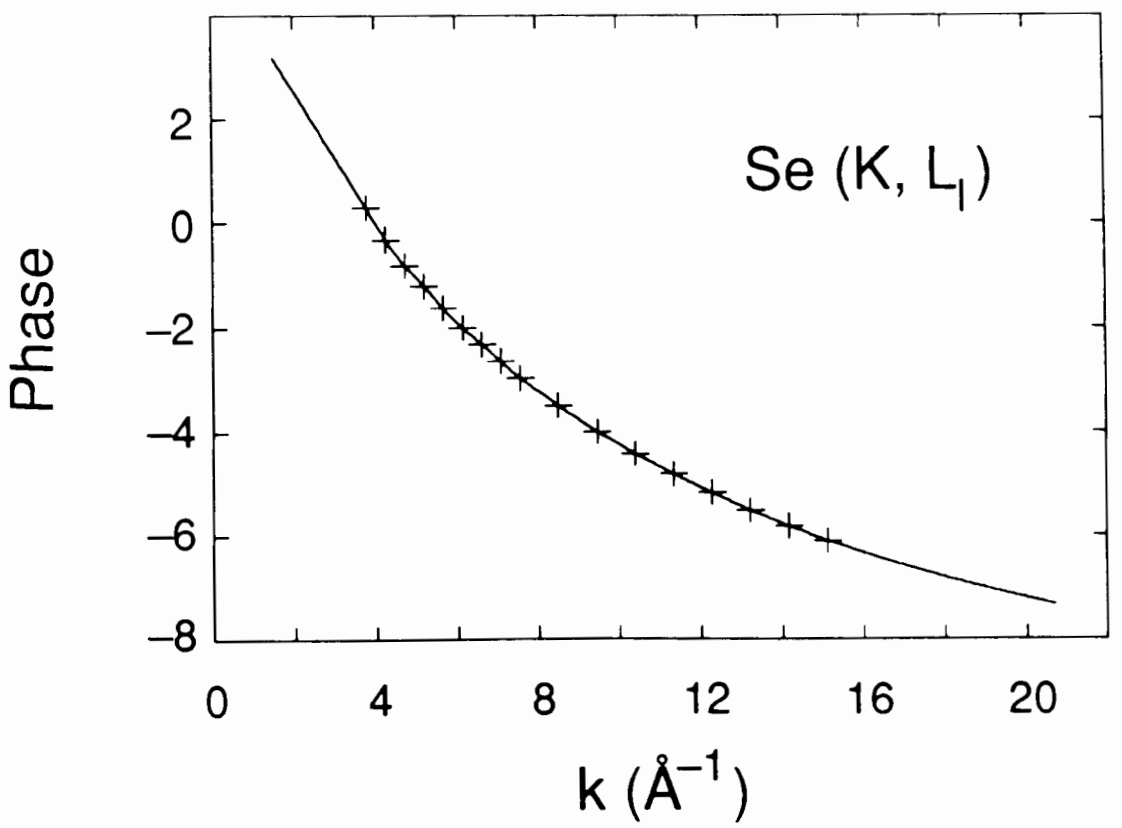

Fig. 3.20: Central-atom phase shift for Se (K or L_I edge). The solid line is the fit described in the text. The crosses show Teo and Lee's values [11].

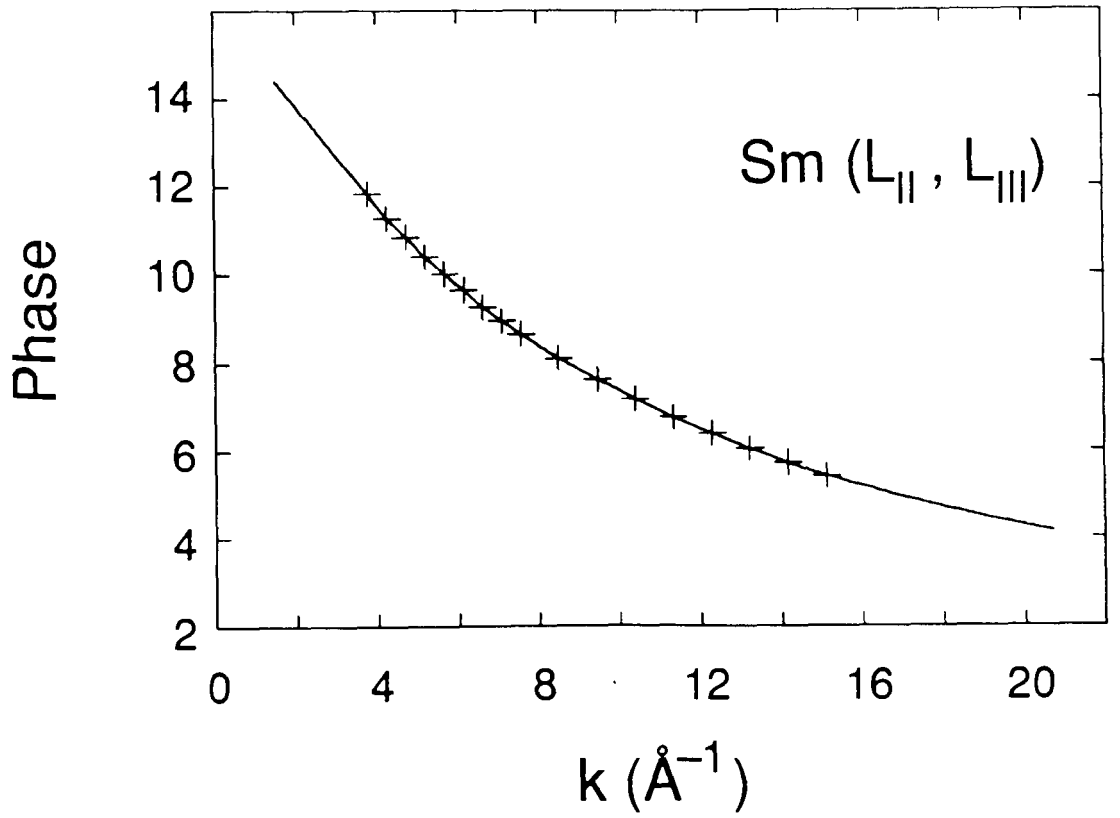

Fig. 3.21: Central-atom phase shift for Sm (L_{II} or L_{III} edge). The solid line is the fit and the crosses are Teo and Lee's values [11].

3.6 Pressure Dependence of Amplitude and Phase

In this section we will discuss a scaling relation between the energies and the lengths. Using this relation we can show that the scattering amplitude and phase are approximately pressure independent for small pressures, i.e. up to a few 100 kbar. For larger pressures the scattering phase will become pressure dependent and for pressures of several Mbar the scattering amplitude will do so too [81].

In a solid the effects of pressure, in the absence of a phase transition, are a broadening of the bands and a reduction of the density of electronic states with an associated increase of the Fermi level. When investigating the influence of pressure on the scattering amplitudes and phases one has to realize that the atomic unit of pressure is $1\ \mathrm{Ry}/a_{\mathrm{Bohr}}^3 = 147$ Mbar , where $1\ \mathrm{Ry} = 13.6$ eV . The pressures attained here are 1000 times smaller, namely of the order of 100 kbar. Thus the effect of this pressure on the atoms themselves is minute. We will show in this section that the logarithmic derivative, and therefore the complex scattering amplitude, are approximately independent of pressure, provided that a scaling relation between the energy scale and the length scale holds.

The scaling relation between energy and length scales had been suggested by Müller et al. [82] and Natoli [83] (see also Lytle [84]):

$$\left(E - \overline{V}\right) R^2 = \text{const.} \quad . \tag{3.72}$$

Here $\overline{V}$ is the inner potential. It is a constant like the muffin-tin zero, which in fact could coincide with it. $E - \overline{V}$ is the kinetic energy of a photoelectron and R is a characteristic length, for example the lattice constant. E refers to any feature in the spectrum but is not a variable. When the energy is scaled according to (3.72), absorption spectra of, say, Cu and Ni become very similar, with a scaling factor $\left(\frac{a_{Cu}}{a_{Ni}}\right)^2$.

Eq. (3.72) can also be used to relate spectra corresponding to two different pressures. In this case one has:

$$\left(E_1 - \overline{V}_1\right) a_1^2 = \left(E_2 - \overline{V}_2\right) a_2^2 \, . \tag{3.73}$$

We assume that $a_1 < a_2$. Thus the left-hand side of Eq. (3.73) corresponds to a higher pressure than the right-hand side. Applying pressure increases the crystal potential, i.e. makes it less attractive. In the core region this increase is very nearly constant. Therefore $\overline{V}_1 - \overline{V}_2$ is positive and constant, even if $\overline{V}_1$ and $\overline{V}_2$ were not. Hence we get:

$$\left(E_1 - (\overline{V}_1 - \overline{V}_2) - \overline{V}_2\right) a_1^2 = \left(E_2 - \overline{V}_2\right) a_2^2 \, . \tag{3.74}$$

Thus for higher pressure the zero of the kinetic energy is shifted to a higher value. The same applies to the bottom of the conduction band of metals (see Eq. (3.87) below).

This is important when estimating the position of the Fermi level as a function of pressure. This was studied for the case of Cu where an extensive bandstructure calculation for pressures up to several Mbar was available for comparison [81] (see also Ref. 85). In the calculations for this thesis the positive shift $\overline{V}_1 - \overline{V}_2$ was obtained as the difference of a muffin-tin potential $V_{MT,1}(r)$ at high pressure and a second one at atmospheric pressure, $V_{MT,2}(r)$. This difference was found to be constant in the core region. To this shift the free-electron Fermi energy was added and the agreement with the bandstructure result [81] for the Fermi energy was satisfactory. Changes in the position of the Fermi energy of Cu are very small though. The initial change is $\frac{\Delta E_F}{\Delta p} \cong 5.5$ eV/Mbar [81].

In order to estimate the influence of pressure on the scattering amplitude and phase we consider the logarithmic derivative at the muffin-tin radius. At $r = R_{MT}$ the potential is small and can be replaced by the inner potential or muffin-tin zero, $\overline{V}_{MT}$. At the muffin-tin radius the spin-orbit term can be neglected. Thus Eq. (3.45) can be written as

$$\frac{d}{dx}\left(\frac{Q}{P}\right) = -e^x (E - \overline{V}_{MT}) - 2(l+1)\frac{Q}{P} - e^x \left(\frac{Q}{P}\right)^2 \qquad (3.75)$$

where the term $(E - \overline{V}_{MT})/c^2$ has been neglected with respect to 1. Switching back to the variable $r \equiv e^x$ and introducing

$$u_l(E,r) \equiv u_l \equiv r\frac{Q}{P} \qquad (3.76)$$

one obtains:

$$-r\frac{d}{dr}\left(\frac{u_l}{r}\right) = r(E - \overline{V}_{MT}) + 2(l+1)\frac{u_l}{r} + \frac{u_l^2}{r}$$

or:

$$-r\frac{du_l}{dr} = r^2(E - \overline{V}_{MT}) + (2l+1)u_l + u_l^2 \,. \qquad (3.77)$$

With the approximation $(E - \overline{V}_{MT})/c^2 << 1$, the logarithmic derivative from Eq. (3.41) is then:

$$D_l = u_l + l \ . \tag{3.78}$$

Eq. (3.77) holds for a particular value of the muffin-tin radius R_{MT}. This equation can be cast into a more general form by employing Eq. (3.72):

$$\left(E - \overline{V}_{MT}\right) R_{MT}^2 = \text{const.} \equiv c_o^2 \ . \tag{3.79}$$

Equivalently one can express this relation as $$k_{MT} R_{MT} = c_o \tag{3.80}$$

where c_o is a positive constant. k_{MT} refers to any feature in the EXAFS spectrum and its subscript "MT" indicates that the inner potential, i.e. the origin of the k-scale, depends on R_{MT} as explained above in connection with Eq. (3.74). One obtains using (3.79):

$$-r \frac{du_l}{dr} = \left(\frac{r}{R_{MT}}\right)^2 c_o^2 + (2l + 1) u_l + u_l^2 \ .$$

Introducing the dimensionless variable $$\tau \equiv \frac{r}{R_{MT}} - 1 \tag{3.81}$$

which is small for $r \cong R_{MT}$, yields:

$$-(1 + \tau) \frac{du_l}{d\tau} = (1 + \tau)^2 c_o^2 + (2l + 1) u_l + u_l^2 \ . \tag{3.82}$$

This equation is independent of the muffin-tin radius. Consequently the resultant logarithmic derivative $D_l = u_l + l$ will not depend on R_{MT} either and therefore not depend on pressure. This, of course, is true only as long as the scaling relation (3.72) holds. While D_l is independent of pressure, or at least only weakly pressure dependent, the k-scale experiences a small pressure dependence because of the change of its origin with pressure. It turns out that the pressure-dependent shift of the potential is small so that this effect can be ignored.

The fact that the D_l, and D_0 in particular, are practically independent of pressure leads to an equation for E_o, the bottom of the conduction band, in accordance with Eq. (3.72). This can be seen

as follows. According to Ref. 86, p. 51, one can estimate the position E_o of the bottom of the conduction band with respect to the zero of the atomic potential as:

$$E_o = \frac{3\, a_s}{R_{MT}^3} \quad . \tag{3.83}$$

a_s is the scattering length which is obtained from the $l = 0$ phase shift as follows [37]:

$$\lim_{k \to 0} \; k \cot \delta_0(k) \; = \; - \frac{1}{a_s} \quad . \tag{3.84}$$

Using Eq. (3.49) one obtains:

$$a_s = R_{MT} \; \frac{D_0(\overline{V}_{MT}, R_{MT})}{1 \; + \; D_0(\overline{V}_{MT}, R_{MT})} \quad . \tag{3.85}$$

If we consider an fcc metal, like Cu, and touching muffin-tin spheres then we obtain from Eqs. (3.83) and (3.85):

$$E_o \, R_{MT}^2 = \frac{3 \; D_0(\overline{V}_{MT}, R_{MT})}{1 \; + \; D_0(\overline{V}_{MT}, R_{MT})} \quad . \tag{3.86}$$

If D_0 is indeed independent of pressure then we have a relation like Eq. (3.72), namely:

$$E_o \, R_{MT}^2 = \text{const.} \quad . \tag{3.87}$$

We can obtain an approximate solution to Eq. (3.82) by neglecting τ with respect to 1. This will result in an approximate equation for the logarithmic derivative. We get:

$$- \frac{du_l}{d\tau} = c_o^2 + (2\, l + 1)\, u_l + u_l^2 \qquad \Rightarrow \qquad -d\tau = \frac{du_l}{c_o^2 + (2\, l + 1)\, u_l + u_l^2} \quad . \tag{3.88}$$

Thus, by separation of variables this differential equation can be integrated readily. The result is, depending on the value of c_o^2 of Eq. (3.79):

i) $c_o^2 > (l + 1/2)^2$:

$$D_l = -\frac{1}{2} + \sqrt{c_o^2 - (l+1/2)^2}\ \cot\left[\frac{\pi}{2} + \left(\frac{r}{R_{MT}} - K_1\right)\sqrt{c_o^2 - (l+1/2)^2}\right] \qquad (3.89)$$

ii) $c_o^2 = (l + 1/2)^2$:

$$D_l = -\frac{1}{2} + \left(\frac{r}{R_{MT}} - K_2\right)^{-1} \qquad (3.90)$$

iii) $c_o^2 < (l + 1/2)^2$:

$$D_l = -\frac{1}{2} + \sqrt{(l+1/2)^2 - c_o^2}\ \coth\left[\left(\frac{r}{R_{MT}} - K_3\right)\sqrt{(l+1/2)^2 - c_o^2}\right] . \qquad (3.91)$$

In all three cases the logarithmic derivatives as a function of r have some resemblance to a cotangent. This is also true for their energy dependence [61]. K_1, K_2, K_3 are constants of integration determining the location of the singularities. In case i) D_l as a function of r has many poles. This will lead to strong variations of the complex scattering amplitude unless successive partial waves of higher angular momentum are included. Thus the complex scattering amplitude can be obtained satisfactorily as long as $k_{max} = (l_{max}+\frac{1}{2}) / R_{MT}$. In cases ii) and iii) D_l has at most one pole. We can now calculate $D_0(\overline{V}_{MT},R_{MT})$ appearing in Eq. (3.86). Since D_0 is to be evaluated at the muffin-tin zero, which is the zero of the energy scale, we have $c_o^2 = 0$ and therefore apply the result for case iii) with $l = 0$ and $r = R_{MT}$ obtaining instead of Eq. (3.86):

$$E_o R_{MT}^2 = e^{K_3 - 1} = \text{const.} > 0 . \qquad (3.92)$$

Thus E_o is positive. Since K_3 determines the location of the singularity, we can conclude:
If $E_o R_{MT}^2 > 1$, then $K_3 > 1$ and there are no poles inside the muffin tin.
If $E_o R_{MT}^2 = 1$, then $K_3 = 1$ and there is one pole at the muffin-tin radius.
If $E_o R_{MT}^2 < 1$, then $K_3 < 1$ and there is one pole inside the muffin tin if K_3 is positive.
If K_3 is negative there is no singularity. Notice that the constant in Eq. (3.92) is positive. This implies by comparison with Eq. (3.86) that the expression

$$\frac{D_0(\overline{V}_{MT},R_{MT})}{1 + D_0(\overline{V}_{MT},R_{MT})}$$

is positive and $D_0(\overline{V}_{MT},R_{MT})$ does therefore never fall within the interval [−1, 0]. Note also that the scattering length, Eq. (3.85), is positive.

It is of interest to check in how far Eqs. (3.89) to (3.91) approximate the logarithmic derivatives calculated as described in Section 3.6. This will be done in the future.

For pressures much higher than those occuring in this work the scattering phase does depend on pressure. Qualitatively, one can predict what will happen to the partial-wave phase shifts. When pressure is applied the atoms move closer together producing an increased overlap of their electronic charge densities. This in turn produces a positive change of the atomic potentials as the Coulomb attraction exerted by the nucleus is reduced. Employing the Born approximation for the phase shifts, Eq. (3.71), one concludes, at least for the larger k-values, that the positive change of the potential results in a negative change of all partial-wave phase shifts $\delta_l(k)$. In the Born approximation this can be investigated quantitatively if the potential V(r) changes by a constant amount ΔV. As in Eq. (3.71) the partial-wave phase shift is then:

$$\delta_{l,Born}(k) + \Delta\delta_l(k) = -k \int_0^{R_{MT}} (V(r) + \Delta V)\; j_l^2(kr)\; r^2\, dr$$

$$= -k \int_0^{R_{MT}} V(r)\, j_l^2(kr)\, r^2\, dr \;-\; k\,\Delta V \int_0^{R_{MT}} j_l^2(kr)\; r^2\, dr \qquad (3.93)$$

The first integral is the partial-wave phase shift corresponding to V(r). Switching to the integration variable k r yields:

$$\Delta\delta_l(k) = -\frac{\Delta V}{k^2} \cdot \int_0^{kR_{MT}} j_l^2(kr)\ (kr)^2\, d(kr) \quad . \tag{3.94}$$

For $l > 0$ the integral is given by an identity that holds for spherical Bessel (and Neumann) functions [37]:

$$\Delta\delta_l(k) = -\frac{\Delta V}{2\,k^2} \left(j_l^2(kR_{MT}) - j_{l-1}(kR_{MT})\, j_{l+1}(kR_{MT}) \right) (kR_{MT})^3 \quad . \tag{3.95}$$

For the Born approximation to hold k must be large. Thus kR_{MT} will be large too and the spherical Bessel functions can be replaced by their asymptotic formula [37]:

$$\lim_{kr \to \infty} j_l(kr) = \frac{1}{kr} \sin(kr - l\,\pi/2) \quad .$$

Inserting into Eq. (3.95) yields: $$\Delta\delta_l(k) = -\frac{R_{MT}\,\Delta V}{2\,k} \quad . \tag{3.96}$$

The importance of this result is that for large k the change of the partial-wave phase shift is independent of l. For $l = 0$ one obtains after inserting $j_0(kr) = \frac{\sin(kr)}{kr}$ into Eq. (3.94):

$$\Delta\delta_0(k) = -\frac{R_{MT}\,\Delta V}{2\,k} \left[1 - \frac{\sin(2kR_{MT})}{2kR_{MT}} \right] \cong -\frac{R_{MT}\,\Delta V}{2\,k} \quad .$$

Hence, Eq. (3.96) holds for $l = 0$ too.

We can now use these results to estimate the effect of the change ΔV in the potential on the (complex) plane-wave scattering amplitude, Eq. (3.52), which can be written as follows:

$$f'(k,\theta) \equiv \frac{1}{2\,i\,k} \sum_l (2l+1)\; P_l(\cos\theta)\left(e^{i2(\delta_l(k)+\Delta\delta(k))} - 1\right) = e^{i2\Delta\delta(k)}\, f(k,\theta) + f_\Delta(k,\theta)\ . \tag{3.97}$$

In this equation we have dropped the subscript on $\Delta\delta_l(k)$ because it does not depend on l. $f(k,\theta)$ is the scattering amplitude corresponding to the original potential $V(r)$ and $f_\Delta(k,\theta)$ is the scattering amplitude corresponding to the potential ΔV:

$$f_\Delta(k,\theta) \equiv \frac{1}{2\,i\,k} \sum_l (2l+1)\; P_l(\cos\theta)\left(e^{i2\Delta\delta(k)} - 1\right)\ . \tag{3.98}$$

Since the potential ΔV is small compared to $V(r)$ its scattering amplitude $f_\Delta(k,\theta)$ will have a small magnitude, too, when compared with $|f(k,\theta)|$. Therefore, like in the case of the $\delta_l(k)$, the effect of the extra potential ΔV will be a shift

$$2\,\Delta\delta(k) = -\frac{R_{MT}\,\Delta V}{k} \tag{3.99}$$

of the phase of $f(k,\theta)$. As an example, for $\Delta V = 0.5$ Ry $\cong 6.8$ eV, $R_{MT} = 4\,a_{Bohr} \cong 2.12$ Å, and $k = 8\,a_{Bohr}^{-1} \cong 15.12$ Å^{-1} we expect a change of the phase of $2\,\Delta\delta(k) = -0.25 \cong -14°$. (In order to transform Eq. (3.99) to the MKSA system, simply divide its right-hand side by $\gamma \cong 3.81$ eV Å^2, Eq. (2.28).)

The magnitude of $f(k,\theta)$ will be practically unchanged. This result is confirmed by calculations of the scattering amplitude, done during the course of this work. The backscattering amplitude and phase were calculated for Cu in the plane-wave approximation for various pressures, i.e. compressions, ranging from a lattice constant of $a = 3.61$ Å at 1 bar to $a = 2.5$ Å at 23 Mbar. It turned out that the pressure dependence of the amplitude was much less pronounced than the one for the scattering phase. Therefore changes in the potential are best detected by the scattering phase.

Chapter 4: **Mixed Valence**

This chapter constitutes a very brief introduction to mixed-valence materials, in particular the Sm monochalcogenides. For further reading the following list of articles of varying length is included in chronological order: [87, 88, 13, 89, 12, 90-99] .

4.1 Description of the Phenomenon

Mixed-valent compounds are those where one of the constituent atom types occurs in two or more valence states. Two cases are distinguished:

Inhomogeneous mixed valence is the case that occurs when the valence of a given atom remains constant in time. Another atom of the same type may have a different valence. This requires that the two atoms are located at inequivalent crystallographic positions. Otherwise their valence must be the same. It follows that inhomogeneous valence is a static phenomenon The value of the mixed valence is obtained by spatially averaging over the atoms under consideration.

Homogeneous mixed valence is the case that is of interest here. In this case one and the same mixed-valent atom assumes both valence states. This means that its valence has for a certain time a given value and then changes to another. In other words, its valence fluctuates. Thus homogeneous mixed valence describes a dynamic state of the mixed-valent atom. The value of the mixed valence is obtained by a temporal average over a mixed-valent atom. The valence fluctuations occur with a frequency of ~10^{13} Hz [100, 101] which is comparable to phonon frequencies. As a result, phonon anomalies are observed with mixed-valence transitions.

Measurements of the Mößbauer isomer shift [102] can be used to distinguish between inhomogeneous and homogeneous mixed valence because the time scale of Mößbauer experiments is much smaller than the time scale of the fluctuations of a homogeneously mixed-valent material. Therefore one average valence-dependent isomer shift is observed in the case of homogeneous mixed valence whereas for inhomogeneous mixed valence two isomer shifts, corresponding to the integer-valent 2+ and 3+ states, are seen.

In the following we will consider only homogeneous mixed valence. This phenomenon occurs in compounds containing 4f- and 5f-elements. Of these the lanthanides are of interest here, samarium in particular. Mixed-valence occurs with rare earth compounds that contain a rare earth element that is close to either end of the lanthanide series, like Ce, Pr, Tm, and Yb, or, like Sm and Eu, close to the middle of the series. The mixed-valence phenomenon may occur already under ambient conditions or it is brought about by variation of an external parameter such as temperature or pressure.

The reason why (homogeneous) mixed valence occurs stems from the fact that in the respective compounds the 4f-multiplet lies near the Fermi energy E_F. If the 4f-level is still below E_F then the valence of the rare earth is two. If by variation of an external parameter the 4f-multiplet moves up and empties one complete electron into the conduction band, which has 6s- and 5d-character, then the valence of the rare earth atom has increased by one. Symbolically we write this process as:

$$[\mathrm{Xe}]\ 4f^{n}\ (5d\ 6s)^{2} \quad \rightarrow \quad [\mathrm{Xe}]\ 4f^{n-1}\ (5d\ 6s)^{3}\ , \tag{4.1}$$

where [Xe] denotes the Xe-core. Referring to the charge of the rare earth core it is common to label the divalent state as 2+ and the trivalent state as 3+. Rare earth atoms and the electron sea together are, however, neutral. If $0 \le v \le 1$ is the fraction of trivalent atoms then the valence v is given by $v = 2 + v$. Note that more than two configurations of the rare earth atom are never present.

The extra valence electron is supplied by the 4f-level. In the trivalent state the occupation number of the 4f-level is reduced by one in comparison with the divalent case. As a result the electronic screening of the nuclear charge of the rare earth atom is reduced. Since with a radius of ~0.2 Å the orbit of the 4f-electrons is very close to the nucleus the reduction of screening affects all electron states appreciably. This gives rise to a reduction of the size of the rare earth atom in the 3+ state. This size reduction is appreciable. For the ionic radius of Sm we find [103]:

$$r^{2+} = 1.13\ \text{Å}\,; \quad r^{3+} = 0.964\ \text{Å} \quad \Rightarrow \quad r^{2+} - r^{3+} = 0.166\ \text{Å}\ . \tag{4.2}$$

The energetically lower electronic energy levels are affected more by the reduction in screening

than the levels at higher energy [104]. For the 2p levels of the rare earth atoms the energy difference for the two valence states is of the order of 7eV.

4.2 Sm Monochalcogenides

The Sm monochalcogenides, SmS, SmSe, and SmTe, are compounds that are integer valent (or almost integer valent) at atmospheric pressure but become mixed-valent at higher pressure. Higher pressure favours the 3+ state because trivalent 4f atoms are smaller than divalent ones. Nevertheless, full conversion to the trivalent state has not yet been observed in any of these compounds. In this context it is also interesting to note that according to L-edge spectroscopy (see next section) the valence at ambient pressure is not integral either. There seems to exist always a non-negligible admixture of the 3+ state.

The Sm monochalcogenides crystallize in the NaCl structure. Under pressure they undergo a phase transition without change in their crystal structure. At room temperature the transition is of first order in SmS and continuous in SmSe and SmTe. The volume reduction is entirely due to the change in size of the Sm atoms. Hence the transition is of electronic origin and since all Sm sites are equivalent the mixed valence is homogeneous. It has been argued [12, 13] that at sufficiently low temperature the pressure-induced valence transitions in SmSe and SmTe should become first order. From the results of the present work it can be said that at 77K SmSe still exhibits a continuous transition. This would be expected for SmTe also since its mixed-valence transition occurs more gradually than the one of SmSe which has been described as being weakly first order [105, 106].

The first to investigate such a pressure-induced valence transition was probably Rooymans [107] who investigated the continuous phase transition in SmTe. His work was repeated by Jayaraman et al. [108] who also discovered the transitions in SmSe and SmS [109].

The following figure shows the volume change that is brought about by applying pressure.

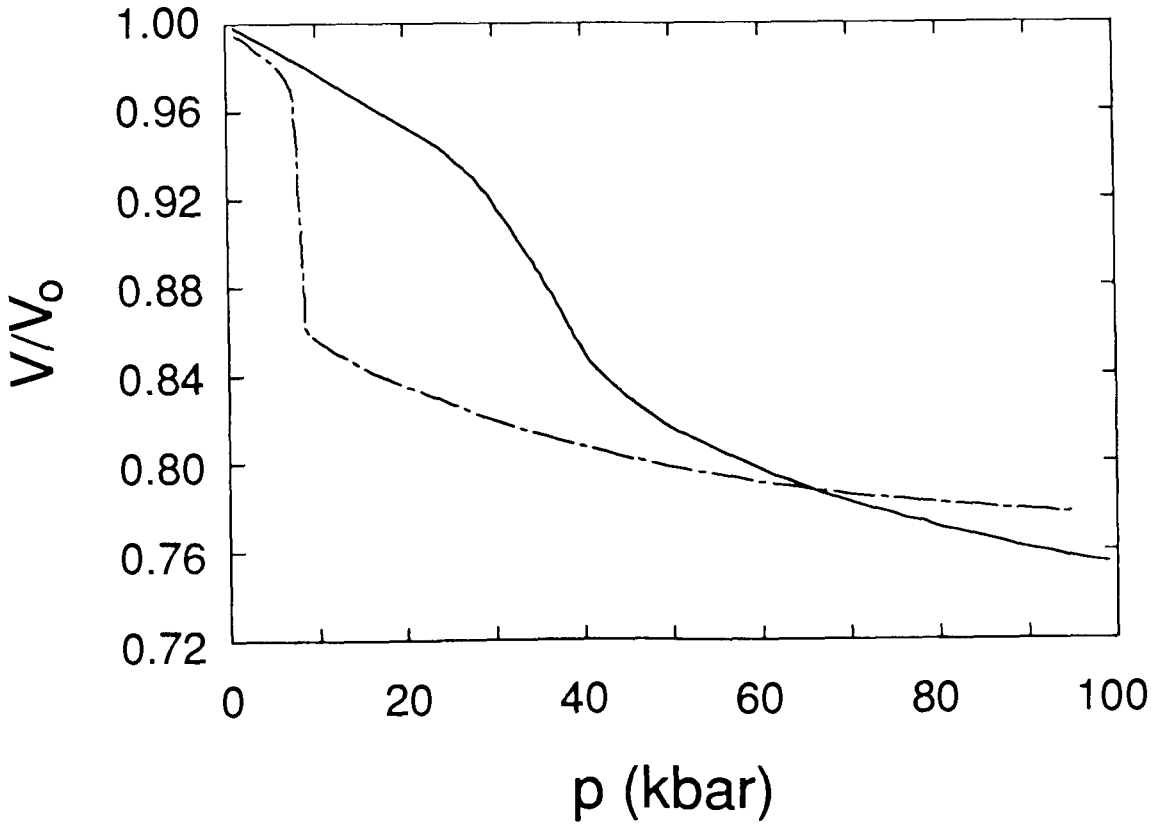

Fig. 4.1: Pressure-volume relations for SmSe (solid line) and SmS (dashed line) at room temperature according to Ref. 110. For SmSe the volume collapse is continuous whereas for SmS it is sudden.

Under ambient conditions SmS, SmSe, and SmTe, are relatively soft as manifested by their low Debye temperature of ~150K. In the transition region their volumes change such that with increasing pressure these substances become even more compressible (!). This is also described as volume collapse. Once the volume collapse is complete the Sm monochalcogenides behave normally, that is their compressibility decreases with increasing pressure.

The following figure shows the isothermal compressibility of SmSe. The transition region is characterized by a peak in the compressibility.

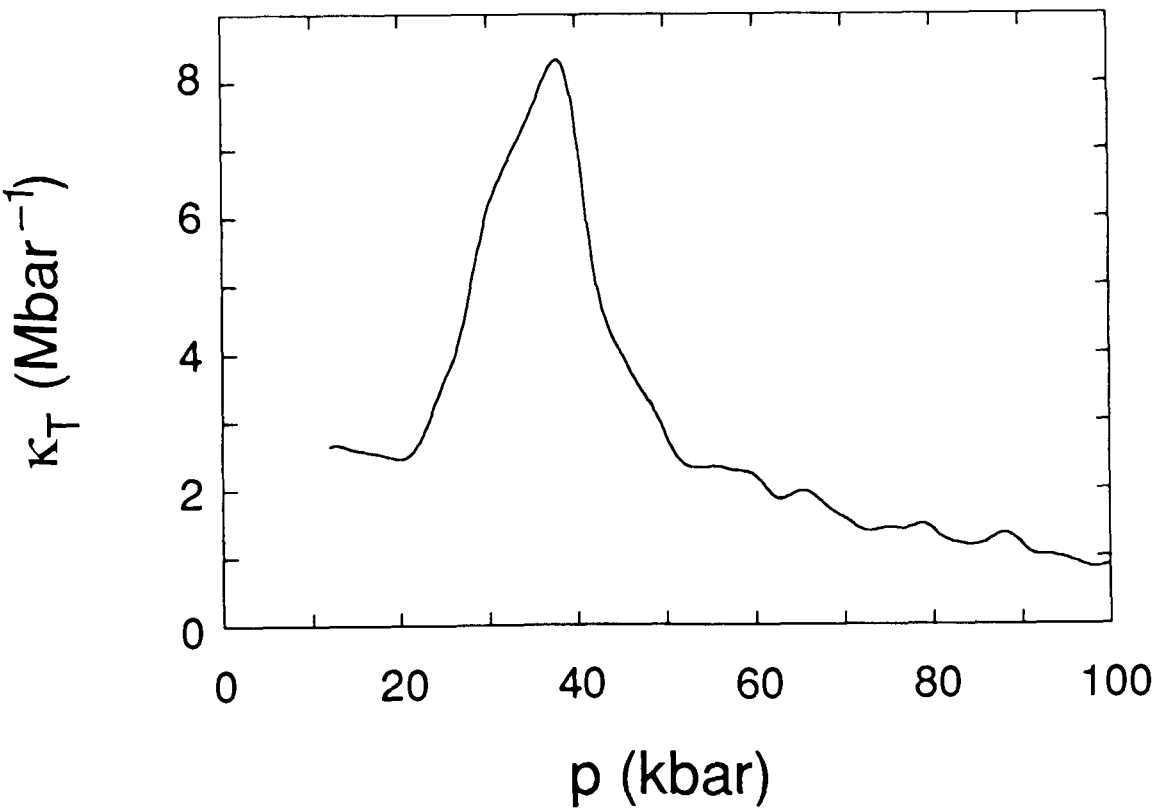

Fig. 4.2: Isothermal compressibility of SmSe at room temperature as derived from the previous figure. The data below 12 kbar has been omitted because it is distorted by end effects due to smoothing.

In the low-pressure phase the Sm monochalcogenides are semiconductors. The Sm atoms are divalent and have the configuration:

$$[Xe]\ 4f^6\ 5d^0\ 6s^2 \quad ; \quad {}^7F_0\ . \tag{4.3}$$

According to Hund's rules this state is non magnetic. In the high-pressure phase these compounds are metallic. The trivalent Sm atoms, that are present in this phase, have the magnetic configuration:

$$[Xe]\ 4f^5\ 5d^1\ 6s^2 \quad ; \quad {}^6H_{5/2}\ . \tag{4.4}$$

Contrary to Hund's rules, however, the compounds are not magnetic in the mixed-valent state [111]. Their semiconductor-to-metal transition is reflected in the pressure dependence of the resistivity [108, 109, 112-114]. At low pressure the resisitivity decreases exponentially with pressure, characteristic of a semiconductor. Above a certain critical pressure the resistivity becomes metallic and decreases at a much slower rate. For SmS the critical pressure is obviously the pressure where the first-order transition occurs. For SmSe and SmTe it can be extracted from a plot of log ρ vs. pressure , where ρ is the resistivity. The values can be found in the following table.

Table 4.1: Properties of Sm monochalcogenides:

	SmS		SmSe		SmTe	
Lattice Constant (Å) at 300K and 1 bar	5.970	[115] [109]	6.200	[115] [109]	6.594	[115] [109]
Density (g/cm^3) (from lattice constant)	5.694		6.390		6.438	
Bulk Modulus (kbar) at 300K and 1 bar	476	[116]	520	[110]	400	[110]
Critical Pressure (kbar) (from resistivity)	6.5	[99]	30	[99]	50	[99]
High-Pressure Valence	> 2.8	[95]	> 2.76	[98]	> 2.66	[98]
Debye Temp. (K)	155	[117]	153	[117]	151	[117]
Energy Gap (eV)	0.20	[112]	0.46	[112]	0.63	[112]
Susceptibility at T=0 (10^{-3} e.m.u./mol)	9.47	[112]	7.92	[112]	7.15	[112]

4.3 Valence Determination by L_{II}-/ L_{III}-Edge Spectroscopy

The size reduction that accompanies the valence change of rare earth atoms can be used to determine the valence. Methods involving the lattice constant, bulk modulus, magnetic susceptibility, and the Mößbauer isomer shift are in use. Here we will determine the valence by L-edge spectroscopy. This method involves the analysis of the near-edge structure at the L_{II} or L_{III} absorption edge of the rare earth atom (see Section 6.12). The method was introduced by Vainshtein et al. [118] who used it to determine the valence of SmB_6. It was later applied to a wide range of mixed-valent rare earth compounds [17, 119].

Since valence fluctuations are on a time scale that is much slower than the characteristic time for the x-ray absorption process (10^{-16} s) the x-ray absorption spectrum of a mixed-valent material is the sum of two absorption spectra, one corresponding to the divalent state and another one, shifted to higher energy by about 7 eV, from the trivalent atoms. Since the x-ray absorption process is much faster than the fluctuations we obtain a snapshot of the distribution of 2+ and 3+ atoms at any instant. However, this means also that it is not possible with x-ray absorption spectroscopy to distinguish between inhomogeneous (i.e. static) and homogeneous (i.e. dynamic) mixed valence (see also Ref. 120).

The shift of about 7 eV between the two states can be detected very easily because the Lanthanides have strong absorption peaks at their L_{II} / L_{III} absorption edges. These peaks, also called "White Lines", are due to the large density of unoccupied 5d states in the Lanthanides. The White Lines are not too broad and thus their shift due to the valence can be detected. The valence is determined from the relative weight of the two absorption profiles. The absorption edge for trivalent atoms occurs at higher energy than the one for divalent atoms because in trivalent rare earth atoms the screening is reduced leading to increased binding energies. The absolute value of the valence depends on the type of lineshape used to fit the data but valence changes can be determined very well. In other words, the precision of the method is excellent while its accuracy is not very good.

The following figure shows the measured Sm L_{II} edge for several pressures at 77K. The edge structure changes significantly under pressure. The 3+ structure at higher x-ray energy grows with pressure whereas the 2+ structure decreases.

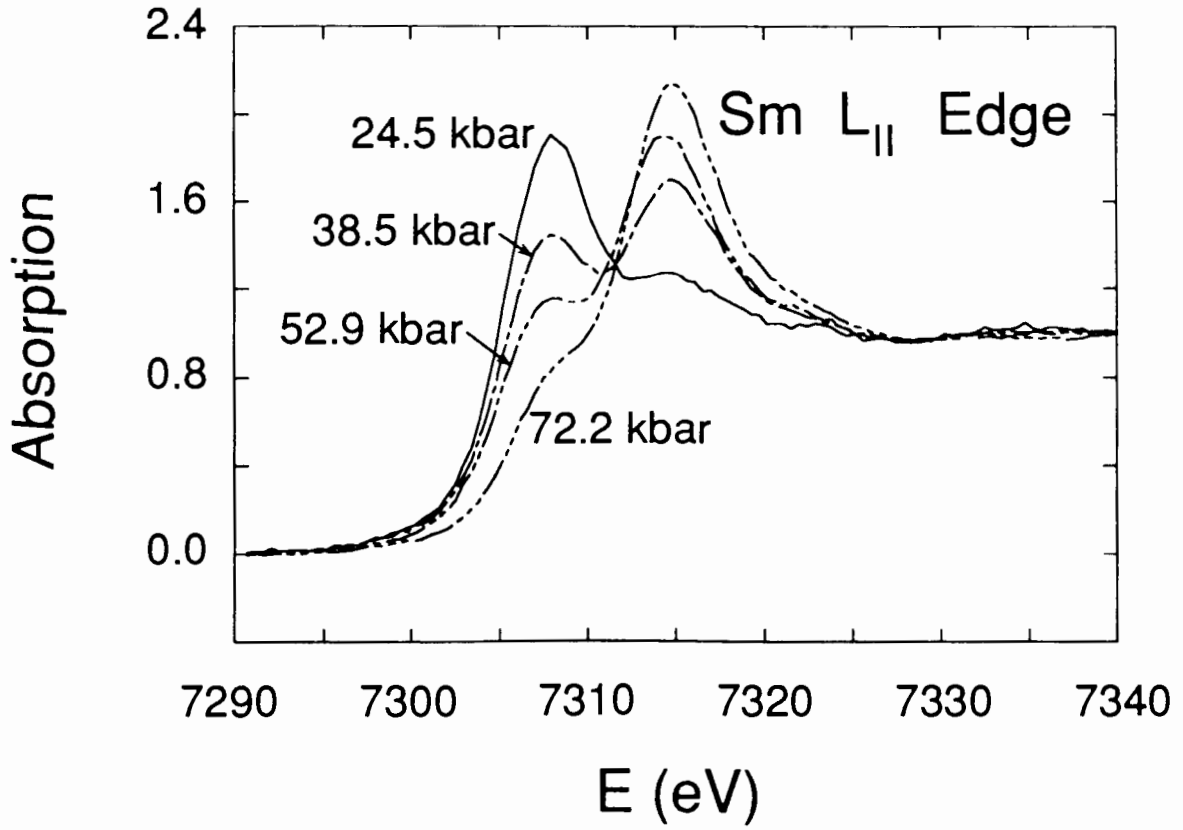

Fig. 4.3: Sm L_{II} absorption edge in SmSe at 77K for several pressures. The spectra are normalized to the edge jump.

In comparison the Se K edge in SmSe shows practically no pressure dependence as can be seen from the next figure.

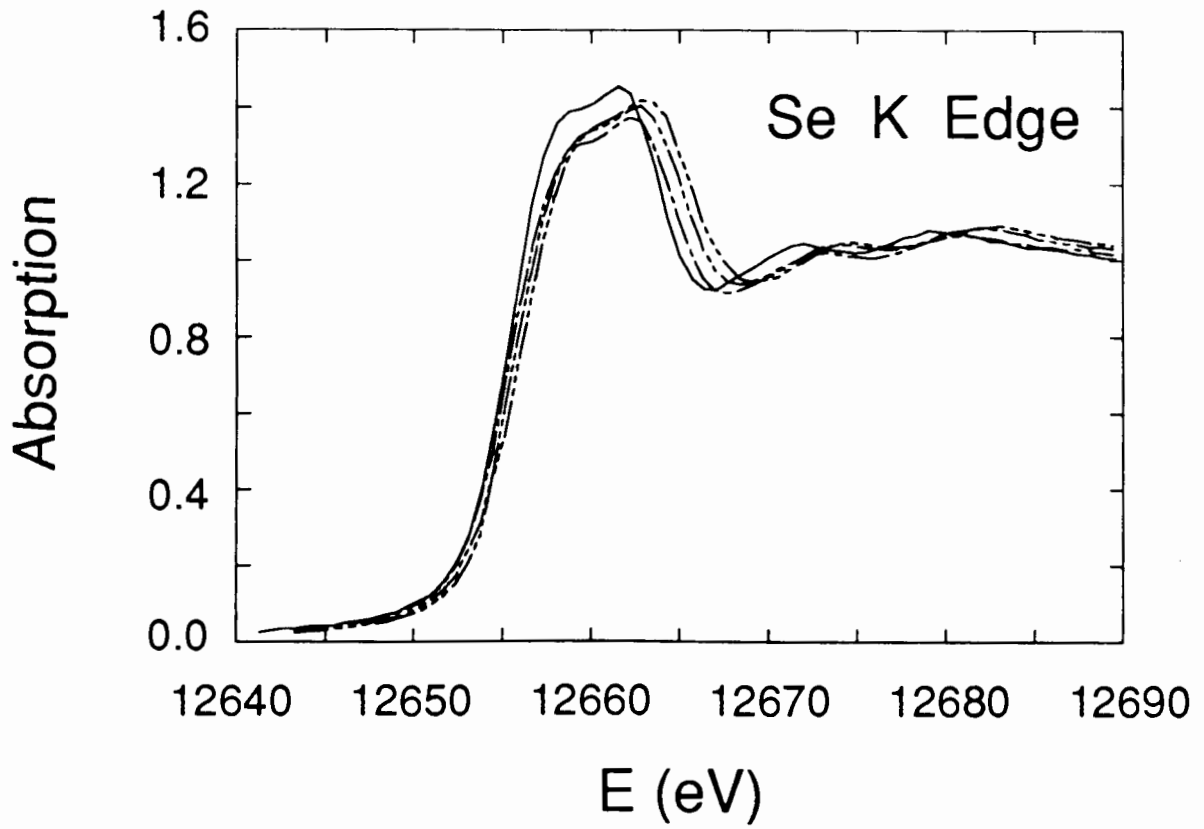

Fig. 4.4: Se K absorption edge in SmSe at 77K for the same pressures as in Fig. 4.3. A small pressure dependence of the absorption spectrum can be detected. The correspondence between line pattern and pressure is the same as in Fig. 4.3 and the spectra are normalized to the edge jump.

Chapter 5: **Experiment**

In this chapter we discuss experimental aspects of Bragg monochromators, ionization chambers, and high-pressure cells. We also derive equations for optimum sample thickness, signal-to-noise ratio, and discuss the effects of artifacts on the measured absorption spectrum.

5.1 Synchrotron Radiation

In this section some properties of synchrotron radiation are briefly reviewed. More information can be found in Ref. 121.

Synchrotron radiation has several desirable properties which are listed here:

a) The intensity is high.

b) It is highly collimated.

c) The spectrum is broad and continuous.

d) It has a high degree of linear polarisation. (In the plane of the accelerated electrons or positrons it is 100%.)

e) The time structure is well defined.

f) The radiation source is chemically clean.

g) The properties of synchrotron radiation can be calculated.

These properties make synchrotron radiation a superior tool in many fields of x-ray work. Since the EXAFS is a rather small signal, compared to the jump discontinuity of the absorption edge, synchrotron radiation with its high intensity provides an ideal x-ray source. The small sample volume present in high-pressure experiments demands even more a high intensity. High-pressure EXAFS experiments can, in fact, only be carried out at a synchrotron source. A further advantage of synchrotron radiation is its broad and continuous spectrum. This property, too, is desirable for EXAFS experiments. For the study of single crystals one can make use of the fact that synchrotron radiation is linearly polarized. In the present work, however, no single crystals are investigated and therefore this property is not exploited. Likewise, the time structure of the synchrotron-radiation

spectrum, resulting from the fact that the charged particles in the synchrotron move in bunches, is not exploited here but this property is used in experiments on biological specimens.

Synchrotron radiation is produced by any accelerated charged particle. In practice, charge particles are accelerated in a circular accelerator. More precisely, the accelerator consists of an evacuated tube passing through bending-magnet sections and being straight in between the magnets. The radiation is generated at the bending magnets and passes through beam tubes to the experimental stations. These evacuated tubes are sealed off by a Be-window. In vacuum ultra violet work the vacuum of the experimental apparatus becomes part of the vacuum system of accelerator because Be-windows would absorb too much intensity at these low energies.

In order to obtain a large x-ray intensity the charged particles are accumulated in a storage ring. A storage ring is a synchrotron that is able to store a relatively large particle current (~500 mA). When the current density is large the x-ray flux is high but beam instabilities can occur. At low current densities the particle (and thus the x-ray) beam is stable but its x-ray flux is low.

Recently wigglers and undulators have been developed and placed into the straight sections of the accelerator. They produce an approximately sinusoidally varying magnetic field which causes the charged particles to move transversally in a sinusoidal pass. Thus additional x-ray intensity is produced in the straight sections of the accelerator. Beam line IV at the Stanford Synchrotron Radiation Laboratory (SSRL) is a wiggler beam line employing 18 kG wiggler magnets.

The amount of energy radiated is inversely proportional to the fourth power of the particle's mass. Therefore electrons or positrons are accelerated in synchrotrons. Positrons have the advantage that they do not combine with the mainly positive ions of the residual gas atoms in the vacuum.

The energy that is radiated in form of x-ray photons is replenished by a microwave-cavity system inside the accelerator.

5.2 X-Ray Monochromator

In this section we will discuss properties of double-crystal Bragg monochromators. We will derive formulae for the minimum and maximum energies E^*_{min} and E^*_{max} for the transmitted x-rays resulting from the geometrical arrangement of the two crystals. After explaining monochromator resolution we will discuss harmonics and derive a maximum energy E^+_{max} based on resolution. The section concludes with a comparison of different Bragg planes used for diffraction and a brief discussion about multiple-diffraction effects in Bragg crystals.

The high-pressure experiments were done on beamline IV-1 at SSRL. The white x-ray beam is monochromatized by two Si-single crystals in a non-dispersive arrangement, which means that the monochromatic x-ray beam leaves the double-crystal monochromator parallel to the incoming beam. Using Bragg's law the energy of the monochromatic beam is given by:

$$E = \frac{h\,c}{2\,d_{hkl}\,\sin\theta_{hkl}} \quad . \tag{5.1}$$

h, *k*, and *l* are the Miller indices of the Bragg planes employed in the diffraction. The Miller indices denote the Bragg planes that are operative in the diffraction of the incident x-rays. In this work these planes are parallel to the crystal surface. For a given energy the Bragg-reflected x-ray occurs at a unique angle that depends on the d-spacing of the desired reflection. In the experiment only this reflected beam is tracked. θ_{hkl} is the Bragg angle and d_{hkl} is the spacing of the Bragg planes. In cubic crystals it is:

$$d_{hkl} = \frac{a}{\sqrt{h^2+k^2+l^2}} \quad , \tag{5.2}$$

where a is the lattice constant. The value for Si is: a_{Si} = 5.43102 Å [122, 123]
h c has the value of 12398.42 eVÅ [123].

Since $\sin\theta_{hkl} \leq 1$ we infer from Eq. (5.1) that there is a minimum energy E_{min} below which the monochromator cannot operate. E_{min} is given by:

$$E_{min} = \frac{h\,c}{2\,d_{hkl}} \quad . \tag{5.3}$$

Due to geometrical effects (see Appendix B) the actual minimum energy is larger than E_{min}. For a very small slit width s of the monochromator entrance slit we obtain using Eq. (B.4) of Appendix B:

$$E^*_{min} = \frac{h\,c}{2\,d_{hkl}\,\sin\theta_{max}} = \frac{h\,c}{2\,d_{hkl}}\sqrt{1+\left(\frac{h_o}{2d_s}\right)^2} = E_{min}\sqrt{1+\left(\frac{h_o}{2d_s}\right)^2}\,. \qquad (5.4)$$

Now there is also a maximum energy given by:

$$E^*_{max} = \frac{h\,c}{2\,d_{hkl}\,\sin\theta_{min}} = \frac{h\,c}{2\,d_{hkl}}\sqrt{1+\left(\frac{L_o}{d_s}\right)^2} = E_{min}\sqrt{1+\left(\frac{L_o}{d_s}\right)^2}\,. \qquad (5.5)$$

The monochromator crystals are dislocation-free nearly-perfect single crystals. They must therefore be described by the dynamical theory of x-ray diffraction. According to this theory, Bragg reflection will occur not only at the Bragg angle but in a narrow region around θ_{hkl} as well. Thus the diffraction profile is not a delta function but can be approximated by a rectangle of unit height and width $\delta\theta_1$ [124]:

$$\delta\theta_1 = \frac{2}{\pi}\,r_e\,\lambda^2\,\frac{|F_{hkl}|}{V}\,\frac{1}{\sin 2\,\theta_{hkl}}\,. \qquad (5.6)$$

$\lambda = \frac{h\,c}{E}$ is the wavelength of the radiation and F_{hkl} is the structure factor of the unit cell whose volume is V. r_e is the classical radius of the electron, defined by:

$$r_e \equiv \frac{1}{4\pi\varepsilon_o}\,\frac{e^2}{m_e c^2} = 2.818\cdot 10^{-5}\ \text{Å}\,. \qquad (5.7)$$

Applying Bragg's law and using Eq. (5.2) one obtains for $\delta\theta_1$:

$$\delta\theta_1 = \frac{4}{\pi}\,\frac{r_e}{a}\,\frac{|F_{hkl}|}{h^2+k^2+l^2}\,\tan\theta_{hkl}\,. \qquad (5.8)$$

Values for $\delta\theta_1$ at 10 keV are 1.31 eV and 0.57 eV for Si (111) and Si (220) crystals, respectively. The integrated intensity (integrated over θ) of the diffracted beam is proportional to $\delta\theta_1$, which is also

called the Darwin width. In the above approximation of a rectangular diffraction profile the result is simply $\delta\theta_1$. The correct result for the integrated intensity valid for negligible absorption is in dynamical theory [125]:

$$J_{hkl} = \frac{4}{3}\ \delta\theta_1 \ . \qquad (5.9)$$

Note that the proportionality to the Darwin width implies that the intensity is proportional to $|F_{hkl}|$, instead of $|F_{hkl}|^2$, as would be the case in kinematical theory [125]. Eqs. (5.6), (5.8), (5.9) are valid for σ-polarization (electric-field vector perpendicular to the plane of incidence) and for symmetrical Bragg reflection (crystal surface parallel to the *hkl* lattice planes).

Since there are two monochromator crystals the combined width is determined from the convolution of the diffraction profile with itself. In the approximation of rectangular profiles the FWHM remains unchanged at $\delta\theta_1$ with the full width at the base of the convolution being broadened to 2 · FWHM.

The finite angular range $\delta\theta_1$ gives rise to an intrinsic resolution of the monochromator. Hence resolution cannot be improved beyond $\delta\theta_1$. A much bigger contribution to the resolution of the monochromator stems from the divergence of the x-ray beam. If s is the width of the slit in front of the monochromator and L the distance to the x-ray source then the vertical angular divergence is simply:

$$\delta\theta_2 \equiv \frac{s}{L} \ . \qquad (5.10)$$

(Sometimes the vertical source dimension is added to s.) s is typically 1 or 2 mm. L is 18 m at SSRL. The final result for the monochromator resolution is determined from the relation:

$$\delta\theta = \sqrt{\delta\theta_1^2 + \delta\theta_2^2} \ . \qquad (5.11)$$

$\delta\theta$ corresponds to an energy width δE which is calculated by differentiating Bragg's law, Eq. (5.1), with respect to θ_{hkl}:

$$\frac{\delta E}{E} = \left|\frac{dE}{d\theta_{hkl}}\right| \delta\theta_{hkl} = (\delta\theta_{hkl}) \cot\theta_{hkl} = (\delta\theta_{hkl}) \sqrt{\left(\frac{E}{E_{min}}\right)^2 - 1} \quad . \tag{5.12}$$

(For convenience we have omitted a subscript *hkl* for E.)

If there were no geometrical broadening then $\delta\theta_2$ would vanish but because of $\delta\theta_1$ there would still be a finite resolution $(\delta E/E)_{min}$ which only depends on *hkl* and on the lattice constant and follows from Eqs. (5.8) and (5.12):

$$(\delta E/E)_{min} \equiv (\delta\theta_1) \cot\theta_{hkl} = \frac{4}{\pi} \frac{r_e}{a} \frac{|F_{hkl}|}{h^2+k^2+l^2} \quad . \tag{5.13}$$

This quantity is characteristic of the width of the diffraction profile and therefore of interest. For large values of *h*, *k*, and *l* the numerator of Eq. (5.13) decreases and the denominator increases and therefore $\delta\theta_1$ becomes very small. This in turn excludes the use of lattice planes belonging to high-order Miller indices because with a monochromator consisting of two independent crystals the two reflections would miss each other unless the crystals are perfectly parallel. Furthermore, mechanical vibrations would make it very difficult to operate the monochromator in a higher-order reflection.

The intensity of the reflections is directly related to $|F_{hkl}|$, the magnitude of the (complex) structure factor, which is defined by:

$$F_{hkl} \equiv \sum_{j=1}^{N} f_j \, e^{i2\pi(hu_j+kv_j+lw_j)} \quad . \tag{5.14}$$

The summation extends over all atoms in the unit cell. The atoms have positions u_j, v_j, and w_j, expressed as fractions of the lattice constant a. The f_j are atomic form factors. Since only one kind of atom is present, i.e. Si or Ge, we can replace f_j by f and take it outside the sum. Performing the summation over the 8 atoms in the cubic unit cell of the diamond structure yields the following result:

a) h, k, l all odd:

$$\mathbf{Re}\ \frac{1}{f} F_{hkl} = 4 \quad ; \qquad \mathbf{Im}\ \frac{1}{f} F_{hkl} = \begin{cases} -4; & h+k+l = 4n-1 \\ 4; & h+k+l = 4n+1 \end{cases}$$

$$\Rightarrow \quad |F_{hkl}| = f \cdot 4 \cdot \sqrt{2} \quad ; \qquad |F_{hkl}|^2 = f^2 \cdot 32 \tag{5.15}$$

b) h, k, l all even:

$$\mathbf{Re}\ \frac{1}{f} F_{hkl} = 8 \quad ; \qquad \mathbf{Im}\ \frac{1}{f} F_{hkl} = 0 \quad ; \qquad h+k+l = 4n$$

$$\Rightarrow \quad |F_{hkl}| = f \cdot 8 \ ; \qquad |F_{hkl}|^2 = f^2 \cdot 64$$

$$n = 1, 2, 3, \ldots$$

For the diamond structure for the permitted reflections all three indices are either odd or they are all even with their sum being an integer multiple of four.

Hence values for $|F_{hkl}|$ can quickly be calculated without having to analyze matters for a particular set of Miller indices. Note, however, that the atomic form factor f is different for different (hkl) due to its dependence on $(\sin\theta)/\lambda = 1/2d_{hkl} = \sqrt{h^2+k^2+l^2}/2a$. Values of the atomic form factor for Si and Ge can be found in Ref. 126. With this information a table of properties of Bragg reflections for Si crystals is set up (Table 5.2 below). The first three crystal types, (111), (220), and (400) are available at SSRL but only the first two were used.

Bragg monochromators do not only diffract x-rays by the desired set of hkl-planes but also by any set of planes that is parallel, i.e. those planes with Miller indices mh, mk, ml, $m = 2, 3, 4, \ldots$ provided the structure factor is non-zero. Since all planes are parallel the Bragg angle is the same for each. This gives rise to harmonics and as a consequence the Bragg-reflected beam is not perfectly monochromatic. Note that the problem of harmonics is aggravated for x-rays due to their linear dispersion but is far less a problem for neutrons, say.

We define the monochromaticity M_o [127], using Eq. (5.9), as:

$$M_o \equiv \frac{J_1}{\sum_{m=2}^{\infty} J_m} \quad . \tag{5.16}$$

Here the J_m are the intensities of the mth harmonic. m = 1 denotes the fundamental. If there were no harmonics M_o would be infinity. Harmonics can be reduced by detuning, i.e. rotating one monochromator crystal with respect to the other so that they are not parallel anymore. This procedure is based on the fact that the rocking curve of the harmonics is narrower than the one of the fundamental [128]. If this is done then the monochromaticity goes through a maximum, independent of the sign of the detuning angle, and then decreases because the intensity of the fundamental also decreases. Thus monochromaticity depends on the detuning angle. The subscript "o" in Eq. (5.16) indicates the case of tuned, i.e. parallel crystals. If we assume that the intensity of the incident x-ray beam is energy independent then we can write for the diffracted intensity, which is proportional to $\delta\theta_1$, Eq. (5.8):

$$M_o = \frac{|F_{hkl}|}{\sum_{m=2}^{\infty} \frac{|F_{mh;mk;ml}|}{m^2}} \quad . \tag{5.17}$$

We define the ratio p_m of the integrated intensity of the mth harmonic with respect to the intensity of the fundamental plus all harmonics and obtain:

$$p_m \equiv \frac{J_m}{\sum_{m=1}^{\infty} J_m} = \frac{J_m}{J_1} \frac{M_o}{1 + M_o} = \frac{1}{m^2} \frac{|F_{mh;mk;ml}|}{|F_{hkl}|} \frac{M_o}{1 + M_o} \quad . \tag{5.18}$$

Note that $\tan \theta_{hkl}$ from Eq. (5.8) cancels out in Eqs. (5.17) and (5.18) because the Bragg angle is the same for the lattice planes that produce harmonics.

The Bragg crystals of monochromators are not normally driven continuously but in steps of fixed size. Thus the increment in Bragg angle is also fixed. Due to Bragg's law increments in energy-space will therefore increase with energy. For a given number of steps per degree this will eventually lead to unacceptably large increments at small Bragg angles. The stepping motors employed at

beamline IV-1 at SSRL operate at 4000 steps per degree. A practical requirement is that the energy increment per monochromator step not exceed ~5 eV. This then defines a maximum energy E^{+}_{max} (see Eq. (5.22) below) above which the sampling in energy space, or k-space, becomes too coarse. We write the number of steps as ζ and obtain:

$$\frac{\Delta E}{\Delta \zeta} = \frac{\Delta E}{\Delta \theta} \left(\frac{\Delta \zeta}{\Delta \theta}\right)^{-1} . \tag{5.19}$$

Here $\Delta\theta$ is in radians. The number of steps per degree is given by:

$$\text{steps/degree} = \frac{\Delta \zeta}{\Delta \theta} \frac{\pi}{180^{\circ}} = 4000/\text{degree} . \tag{5.20}$$

We now make use of Eq. (5.12) to obtain $\Delta E/\Delta\theta$. We can expand the square root because $E_{min} << E$. This yields:

$$\frac{\Delta E}{\Delta \theta} = \left[\left(\frac{E}{E_{min}}\right)^{2} - \frac{1}{2}\right] E_{min} . \tag{5.21}$$

Inserting into (5.19) and writing E^{+}_{max} instead of E produces:

$$E^{+}_{max} = E_{min} \sqrt{\frac{1}{E_{min}} \frac{\Delta \zeta}{\Delta \theta} \frac{\Delta E}{\Delta \zeta} + \frac{1}{2}} . \tag{5.22}$$

Results for E^{+}_{max} , requiring $\frac{\Delta E}{\Delta \zeta} = 5$ eV/step and taking (5.20) into account, are presented in Table 5.2.

Table 5.1: Properties of Principal Reflections and their Harmonics for Si Single Crystals:

h k l	m	d_{hkl} (Å)	$f(\sin\theta/\lambda)$	$\lvert F_{hkl}\rvert$	$(\delta E/E)_{min}$ (10^{-6})	p_m %
1 1 1	1	3.13560	10.55	59.7	131	88
3 3 3	3	1.04520	6.4	36.2	8.86	6.7
4 4 4	4	0.78390	5.0	40.0	5.51	3.7
5 5 5	5	0.62712	3.75	21.2	1.87	1.3
7 7 7	7	0.44794	2.3	13.0	0.584	0.39
8 8 8	8	0.39195	1.9	15.2	0.523	0.35
9 9 9	9	0.34840	1.65	9.33	0.254	0.17
2 2 0	1	1.920155	8.7	69.6	57.5	80
4 4 0	2	0.96008	6.05	48.4	9.99	14
6 6 0	3	0.64005	3.9	31.2	2.86	4.0
8 8 0	4	0.48004	2.55	20.4	1.05	1.4
10 10 0	5	0.38403	1.85	14.8	0.489	0.68
12 12 0	6	0.32003	1.55	12.4	0.284	0.39
4 0 0	1	1.357755	7.5	60.0	24.8	84
8 0 0	2	0.67888	4.25	34.0	3.51	12
12 0 0	3	0.45259	2.35	18.8	0.863	2.9
16 0 0	4	0.33944	1.65	13.2	0.341	1.2
3 1 1	1	1.63751	8.1	45.8	27.5	93
9 3 3	3	0.54584	3.05	17.3	1.15	3.9
12 4 4	4	0.40938	2.05	16.4	0.616	2.1
15 5 5	5	0.32750	1.6	9.05	0.217	0.74
4 2 2	1	1.10860	6.7	53.6	14.8	87
8 4 4	2	0.55430	3.15	25.2	1.73	10
12 6 6	3	0.36953	1.8	14.4	0.440	2.6

Table 5.2: Properties of Principal Reflections for Si Single Crystals:

h k l	E_{min} (eV)	E^*_{min} (eV)	E^*_{max} (eV)	E^+_{max} (eV)	M_o
1 1 1	1977.0	2358.0	13197	47618	7.5
2 2 0	3228.5	3850.6	21551	60867	3.9
4 0 0	4565.8	5445.5	30478	72405	5.3
3 1 1	3785.7	4515.2	25271	65919	13.8
4 2 2	5591.9	6669.4	37328	80147	6.9

The minimum and maximum energies E^*_{min} and E^*_{max} are calculated according to Eqs. (5.4) and (5.5) using the following values: L_o =66 mm , h_o = 13 mm , and d_s = 10 mm . These energies are only correct if the x-ray beam is incident on the rotation axis as in Fig. B.1 of Appendix B. Otherwise E^*_{min} and E^*_{max} may be quite different. Indeed, we have used the Si (111) crystals to 17 keV and the Si (220) crystals to 33 keV in EXAFS experiments.

The index triple (111) constitutes the lowest-order reflection possible. It allows for the largest d-spacing which in turn reduces E_{min} to its smallest value. At the same time, however, the resolution is worst as can be inferred from Eq. (5.12). The biggest advantage of the (111) reflection is the absence of the harmonic at twice the energy of the regular beam. This is due to the fact that, according to the selection rule, Eq. (5.15), the (222) planes do not reflect x-rays. ("Umweganregung" (= detour excitation) which is the result of consecutive reflections and leads to for example a (222) reflection [129] is neglected here.) The first harmonic that can pass a (111) crystal is the m=3 harmonic due to the (333) reflection. For a (220) crystal, harmonics at any integer multiple of the fundamental energy can occur. This is a clear disadvantage of the (220) crystal but it is offset by the fact that its resolution is better and because of its greater structure factor. Even better resolution is offered by the (422) reflection. Reflections like the (440) cannot be used as principal reflections because they let the "subharmonic" resulting from the (220) planes pass. Besides, their Miller indices are high, resulting in a narrow diffraction width $\delta\theta_1$ as mentioned before. This width is an important parameter for the selection of crystals. The set of (311) planes may be a reasonable choice in this respect. Its resolution is slightly better than that of the (220) reflection and not all harmonics

can pass. Unfortunately $|F_{311}| = 45.8$ is a bit small. (311) crystals have not been employed on a large scale which perhaps may be also due to the fact that Si-single crystal rods are usually not available grown with (311) end faces but have to be cut from a larger piece of single crystal of (111) or (110) orientation, which may be too wasteful. At L.U.R.E., however, Si (311) crystals are used [130]. They are also employed in laboratory EXAFS facilities. See Ref. 131 for a review of these facilities.

The x-ray monochromator contains two independent single crystals so that they can be slightly detuned. This results, however, in the unwanted reduction of intensity of the regular beam as well. Employing simple float-glass mirrors is a superior way in comparison [132]. Mirrors act as low-pass filters for x-rays and can therefore suppress harmonics. Their x-ray reflectivities are as large as 95%. The advantage of glass mirrors is that the crystals can remain tuned and therefore the output intensity high. By detuning, in comparison, the x-ray intensity is reduced to approximately 50%. Another advantage of glass mirrors is that those crystal glitches (see below) that are associated with harmonics are eliminated.

Crystal glitches occur in monochromator crystals as a result of multiple diffraction of x-rays [133, 134]. They occur whenever the Bragg condition is fulfilled for one or more extra sets of Bragg planes simultaneously and at the same energy as the regular reflection. This can only occur at certain fixed energies. As a result the regular reflected beam loses intensity because suddenly more diffraction channels have become available. In principle this does not constitute a problem as the beam intensity is measured before and after the sample. The quantity of interest is the ratio of these two intensities and therefore any intensity variation should cancel out. It turns out, however, that the intensity variations due to multiple diffraction effects are drastic so that the ion-chamber detectors do not respond linearly. As a result the intensity variations will not cancel out upon forming the ratio. Feedback circuits have been developed in order to reduce these intensity variations [135]. The energy-, or Bragg-angle-, spectrum of the glitches depends on the crystallographic orientation of the rotation axis. The number of glitches increases with the ratio of wavelength to lattice constant. Thus there are many more glitches at higher energy but at the same time they become less severe. Conversely, at low energy there are fewer but more pronounced glitches. They can frequently be avoided by a proper choice of the rotation axis [133]. A grazing-incidence mirror placed after the monochromator will remove many glitches. Since such a mirror acts as a low-pass filter for x-rays this indicates that many glitches are due to harmonics.

In this work only Si-single crystals are used. It is also common to employ Ge crystals. Their main advantage is the increased structure factors due to the larger atomic number. They also reach to slightly lower energy because their lattice constant is bigger than the one of Si (5.66 Å as opposed to 5.43 Å). Their disadvantages are the lower resolution and, in particular, the Ge K absorption edge above which the reflectivity drops drastically. However, for energies below the Ge K edge, which occurs at ~11104 eV [136], Ge is a Bragg crystal with a high intensity and has the added advantage that those harmonics that are above the Ge K edge have a strongly reduced reflectivity [137].

5.3 Absorption Coefficients

This section defines the different types of absorption coefficients and how the absorption coefficient for a compound is obtained from the absorption coefficients of the constituent elements. Also their energy dependence is discussed.

Absorption of photons is described by an exponential decay of the incident intensity I_0:

$$I(x) = I_0 e^{-\mu x} . \qquad (5.23)$$

x is the sample thickness and μ is the linear absorption coefficient. The mass-absorption coefficient μ_m is equal to the linear absorption coefficient, normalized to the density ρ:

$$\mu_m \equiv \mu/\rho . \qquad (5.24)$$

In order to calculate the absorption of a compound it is useful to define the atomic absorption coefficient: $\mu_a \equiv \mu_m A/N_A$. (5.25)

N_A is Avogadro's number and A is the atomic weight. If v_i atoms of species i are present then we have:

$$\mu_a = \sum_i v_i \mu_{a,i} \quad \text{or} \quad \mu_m = \frac{1}{A} \cdot \sum_i v_i A_i \mu_{m,i} \quad ; \quad A \equiv \sum_i v_i A_i \quad . \qquad (5.26)$$

The atomic absorption coefficients μ_a for the elements are tabulated as a function of energy in Ref. 138, which also contains the following parametrization of the μ_a away from absorption edges:

$$\ln\left(\frac{\mu_a}{\text{barn}}\right) = \sum_{n=0}^{3} a_n \left[\ln\left(\frac{E}{\text{keV}}\right)\right]^n \quad . \tag{5.27}$$

It turns out that a two-parameter fit with a_0 and a_1 will describe most of the energy dependence of μ_a. We obtain then for the mass absorption coefficient:

$$\mu_m = \frac{N_A\,\text{bam}}{A}\, e^{a_0} \left(\frac{E}{\text{keV}}\right)^{a_1} \quad . \tag{5.28}$$

a_1 is roughly equal to -3 [139] which yields the first term of the Victoreen formula [140]:

$$\mu_m = C \cdot E^{-3} - D \cdot E^{-4} \quad . \tag{5.29}$$

At low Z the exponent a_1 is approximately -3.5 [139]. The fact that a_1 is approximately the same for each element implies that it is impossible to distinguish different elements or compounds on the basis of the energy dependence of their absorption coefficients unless absorption edges are present. Furthermore, the absorption coefficient $\mu_m(mE)$ at some multiple of the energy E is simply proportional to $\mu_m(E)$:

$$\mu_m(mE) = m^{a1}\,\mu_m(E) \cong \frac{\mu_m(E)}{m^3} \quad . \tag{5.30}$$

For harmonics (m = 2, 3, ...) this yields $\mu_m(2E) = \frac{1}{8}\,\mu_m(E)$ $\mu_m(3E) = \frac{1}{27}\,\mu_m(E)$, etc.,

with a transmission T_m, close to unity $T_m = \exp\left(-\rho\,\mu_m(E)\,x\,/m^3\right)$.

This means that for harmonics the thickness x appears to be reduced by a factor of $1/m^3$. Any absorber in the x-ray beam path will therefore preferentially transmit the harmonics rather than the fundamental. It does not matter whether the absorber is placed before or after the monochromator. Unnecessary absorbers, like for example Al filters, should therefore be avoided.

5.4 Ionization Chambers

The purpose of this section is to relate the measured signal from an ionization chamber to the intensity of the incident x-ray beam.

The x-ray flux, i.e. the number of photons crossing unit area per unit time, is monitored by ionization chambers before and after the sample. If the flux of the incident beam were sufficiently constant the first ion chamber would not be necessary. The signal detected by either one of the ion chambers is:

$$I_i = \tilde{\kappa}_i N_i = \tilde{\kappa}_i \frac{F_i}{A_i} \quad ; \quad i = 0, 1 \quad . \tag{5.31}$$

$i = 0$ refers to the first ionization chamber, i.e. the ion chamber before the sample and $i = 1$ refers to the second ionization chamber, that is the chamber after the sample. N_0 is the intensity of the incident x-ray beam and N_1 is the intensity of the beam after passage through the sample. The F_i are the x-ray fluxes and the A_i are the cross-sectional areas of the x-ray beam when passing through ion chamber i. Normally A_0 is equal to A_1 but when the pressure cell is placed into the beam the respective cross sections may differ. A_1 is then reduced because of the narrow collimator inserted in the pressure cell. The quantities $\tilde{\kappa}_i$ are proportional to the number of photons absorbed in ion chamber i. As a result the $\tilde{\kappa}_i$ are proportional to A_i and they depend on the species of counting gas used. Each ionization chamber is connected to a current-to-voltage converter whose output in turn is converted into a "count rate" by means of a voltage-to-frequency converter. The respective conversion factors are:

current-to-voltage converter: $S_{cv,i} = 10^{n_i}\ V/A$. (5.32)

voltage-to-frequency converter [141]: $S_{vf} = 100\ kHz/V$. (5.33)

For the Keithley picoammeters used in our experiments, $n_i \leq 11$ is an integer indicating the size of the selected scale factor. Usually $n_0 = 9$ and $n_1 = 11$ so that the output voltages are around 1 V.

The dimensionless gain factors g_i for the output signal are: $g_i \equiv e\, S_{vf}\, S_{cv,i}$. (5.34)

e is the (positive) elementary charge. For $\tilde{\kappa}_i$ we obtain: $$\tilde{\kappa}_i \equiv \kappa\, g_i\, A_i \left(1 - e^{-\mu_i x_i}\right) . \qquad (5.35)$$

κ is a dimensionless quantity, which is the same for both ion chambers. It is defined by:

$$\kappa \equiv E/E_{pair} . \qquad (5.36)$$

E is the photon energy. E_{pair} is the average energy required to generate an electron-ion pair. The signal detected by ionization chamber i is then:

$$I_i = N_i\, \kappa\, g_i\, A_i \left(1 - e^{-\mu_i x_i}\right) . \qquad (5.37)$$

We get:

$$\ln I_0/I_1 = \ln N_0/N_1 + \ln \left(\frac{g_0\, A_0 \left(1 - e^{-\mu_0 x_0}\right)}{g_1\, A_1 \left(1 - e^{-\mu_1 x_1}\right)} \right) . \qquad (5.38)$$

From the signal of the first ion chamber we can estimate the photon flux F_0 of the incident x-ray beam. F_0 is equal to the current $e\, I_0/g_0$ produced in the chamber (typically 1 nA), divided by the charge collected. Therefore we get:

$$F_0 = \frac{e\, I_0/g_0}{\left(1 - e^{-\mu_0 x_0}\right) e\, E/E_{pair}} = \frac{I_0\, E_{pair}}{g_0\, E \left(1 - e^{-\mu_0 x_0}\right)} . \qquad (5.39)$$

E_{pair} varies from 41 eV in He to 22 eV in Xe [142, 143]. Values around 30 eV are typical for many gases and for different types of radiation. For N_2 (or air) and Ar the values are 35 eV and 26 eV, respectively [142]. E_{pair} is much greater than the ionization energy because there are also excitation processes taking place which do not result in ionization and consequently increase the average energy required to produce an ion pair. The positive ions and the electrons can recombine and hence reduce the ionization-chamber current. If the operating voltage is increased to a sufficiently high value then the ion chamber operates in the saturation or plateau region where all charges produced by the x rays are collected before recombination. Under these conditions the output signal is truly proportional to the incident x-ray flux. The saturation current can be obtained from a plot

of $1/I$ versus $1/V^2$ according to the following equation [144], which holds when diffusion can be neglected:

$$\frac{1}{I} = \frac{1}{I_s} + \alpha \frac{d^3}{V^2} \quad . \tag{5.40}$$

I and I_s are the ion-chamber and saturation currents, respectively. d is the plate separation which here amounts to 10 mm. V is the applied voltage and α is a proportionality constant. Saturation sets in at voltages such that the strength of the electric field in the chamber exceeds 100V/cm.

Recombination of positive ions with negative ions instead of electrons also occurs. This type of recombination is very much faster than with electrons and it happens in gases, like for example oxygen, that readily form anions by attaching electrons. If a gas mixture is used in an ionization chamber then charge-transfer collisions become important. In such collisions a positive ion collides with a neutral atom and exchanges an electron. For gas mixtures the result is a net transfer of charge to the gas component with the lowest ionization energy.

The experiments were carried out using parallel-plate ionization chambers operated in current mode at a voltage of 300 V. The active region of the first ionization chamber was 119 mm long and that of the second had a length of 271.5 mm. The first chamber should be as short as possible so that not too much intensity is absorbed. The second ion chamber, on the other hand, should be very long so that all photons are counted. It is advisable to employ the same gases in both chambers in order to have the same diffusion times [145]. Each ionization chamber had two windows of Kapton foil, 1 mil (= 25.4 μm) thick. The gases were at atmospheric pressure.

5.5 Optimum Sample Thickness

In this section we derive a criterion for the optimum sample thickness for x-ray absorption experiments based on results from counting statistics [146] (see also Ref. 147).

Considering the counting time τ required for a given relative error p of the product μx, where μ is the linear absorption coefficient and x is the sample thickness, we have:

$$p^2 \equiv \left[\frac{\delta(\mu x)}{\mu x}\right]^2 = \left(\frac{\partial \mu x}{\partial T}\,\frac{\delta T}{\mu x}\right)^2 = \left(\frac{-\delta T}{\mu x\, T}\right)^2 = \left(\frac{\delta T}{T}\right)^2 \frac{1}{(\mu x)^2} \quad , \tag{5.41}$$

where $T \equiv e^{-\mu x}$ is the transmission. We can also express T as:

$$T = \frac{N_1}{N_0} = \frac{F_1}{F_0}\,\frac{A_0}{A_1} = \frac{c_1/\tau}{c_0/\tau}\,\frac{A_0}{A_1} = \frac{c_1}{c_0}\,\frac{A_0}{A_1} \quad . \tag{5.42}$$

$F_0 \equiv c_0/\tau$ and $F_1 \equiv c_1/\tau$ are the fluxes or count rates and c_0, c_1 are the number of counts of photons before and after the sample, respectively. For the relative error of the transmission we get:

$$\left(\frac{\delta T}{T}\right)^2 = \left(\frac{\partial T}{\partial c_0}\,\frac{\delta c_0}{T}\right)^2 + \left(\frac{\partial T}{\partial c_1}\,\frac{\delta c_1}{T}\right)^2 = \left(\frac{\delta c_0}{c_0}\right)^2 + \left(\frac{\delta c_1}{c_1}\right)^2 = \frac{1}{c_0} + \frac{1}{c_1} \quad . \tag{5.43}$$

In the last step we have employed a result from counting statistics: $(\delta c_i)^2 = c_i \quad (i = 0, 1)$. (5.44)
This yields:

$$p^2 = \frac{1}{(\mu x)^2}\left(\frac{1}{c_0} + \frac{1}{c_1}\right) = \frac{1}{(\mu x)^2}\,\frac{1}{c_0}\left(1 + \frac{1}{T}\right) \quad . \tag{5.45}$$

For a fixed count rate $F_0 \equiv c_0/\tau$ of the incident beam we obtain from Eq. (5.45):

$$\tau = \frac{1}{(\mu x)^2\, p^2}\,\frac{1}{F_0}\left(1 + e^{\mu x}\right) \quad . \tag{5.46}$$

τ, plotted versus μx, has a minimum determined by:

$$(\mu x)_{opt} - 2 = 2\, e^{-(\mu x)opt} \quad \Rightarrow \quad (\mu x)_{opt} \cong 2.22 \quad . \tag{5.47}$$

If we choose the sample thickness x such that (5.47) holds then we obtain the shortest counting time for a given precision p of the measured quantity μx . For the optimum, i.e. minimum, counting time we get using (5.47):

$$\tau_{opt} = \frac{1}{F_0\, p^2}\,\frac{1}{(\mu x)_{opt}}\,\frac{1}{(\mu x)_{opt} - 2} \cong \frac{2.05}{F_0\, p^2} \quad . \tag{5.48}$$

We can formulate the condition for an optimum also in terms of the number of photons c_0 by rewriting Eq. (5.46):

$$c_0 = \frac{1}{(\mu x)^2 p^2} \left(1 + e^{\mu x}\right) \Rightarrow \quad (c_0)_{opt} \cong \frac{2.05}{p^2} \quad . \tag{5.49}$$

We see that the counting time or the number of photons are inversely proportional to the square of the relative error in μx .

In order to get an idea of the sharpness of the optimum, it is useful to determine the points $(\mu x)_{min}$ and $(\mu x)_{max}$ where the function τ versus μx assumes twice its minimum value. The result is:

$$(\mu x)_{min} = 0.93 = (\mu x)_{opt} - 1.29 \quad ; \quad (\mu x)_{max} = 4.33 = (\mu x)_{opt} + 2.11 \quad . \tag{5.50}$$

Thus the minimum is rather wide and the optimum-thickness criterion not too stringent.

It turns out that the optimum condition depends also on the absorption in the ion chambers. The ion chamber before the sample produces a signal given by

$$I_0 = N_0 \kappa g_0 A_0 \left(1 - e^{-\mu_0 x_0}\right) = \frac{c_0}{\tau} \kappa g_0 \left(1 - e^{-\mu_0 x_0}\right) , \tag{5.51}$$

where I_0 is determined by c_0 incident photons during a time interval τ. Correspondingly, the second ion chamber measures the signal I_1:

$$I_1 = N_0 e^{-\mu_0 x_0} e^{-\mu x} \kappa g_1 A_1 \left(1 - e^{-\mu_1 x_1}\right)$$

$$= \frac{c_0}{\tau} e^{-\mu_0 x_0} e^{-\mu x} \kappa g_1 \frac{A_1}{A_0} \left(1 - e^{-\mu_1 x_1}\right) . \tag{5.52}$$

The first two exponentials in this equation are the transmissions of the first ion chamber and the sample, respectively. A_1 is the cross-sectional area of the beam after passage through the sample. A_1 can never exceed A_0: $A_1 \leq A_0$. (5.53)

Forming the ratio we obtain for the transmission of the sample:

$$T = e^{-\mu x} = \frac{I_1}{I_0}\,\frac{g_0}{g_1}\,\frac{A_0}{A_1}\,\frac{e^{\mu_0 x_0} - 1}{1 - e^{-\mu_1 x_1}} \tag{5.54}$$

$$\left(\frac{\delta T}{T}\right)^2 = \left(\frac{\partial T}{\partial I_0}\;\frac{\delta I_0}{T}\right)^2 + \left(\frac{\partial T}{\partial I_1}\;\frac{\delta I_1}{T}\right)^2 = \left(\frac{\delta I_0}{I_0}\right)^2 + \left(\frac{\delta I_1}{I_1}\right)^2$$

$$= \frac{1}{c_0\left(1 - e^{-\mu_0 x_0}\right)} + \frac{1}{c_0\, e^{-\mu_0 x_0}\, e^{-\mu x}\left(1 - e^{-\mu_1 x_1}\right) A_1/A_0} \,. \tag{5.55}$$

Similar to Eq. (5.44) we have used in the last step the following relations:

$$\left[\delta\, c_0\left(1 - e^{-\mu_0 x_0}\right)\right]^2 = c_0\left(1 - e^{-\mu_0 x_0}\right), \tag{5.56}$$

$$\left[\delta\, c_0\, e^{-\mu_0 x_0}\, e^{-\mu x}\left(1 - e^{-\mu_1 x_1}\right)\frac{A_1}{A_0}\right]^2 = c_0\, e^{-\mu_0 x_0}\, e^{-\mu x}\left(1 - e^{-\mu_1 x_1}\right)\frac{A_1}{A_0} \,. \tag{5.57}$$

Note that we have included here quantities like the number c_0 of incident photons, the absorber materials, and the cross-sectional areas of the x-ray beam, which all determine the number of counts. κ, g_0, and g_1, however, are merely gain factors which magnify the number of counts and their variation by the same factor. For p^2 we obtain:

$$p^2 = \frac{1}{(\mu x)^2}\left(\frac{\delta T}{T}\right)^2 = \frac{1}{(\mu x)^2}\,\frac{1}{c_0\left(1 - e^{-\mu_0 x_0}\right)}\left(1 + e^{\mu x}\,\frac{A_0}{A_1}\,\frac{e^{\mu_0 x_0} - 1}{1 - e^{-\mu_1 x_1}}\right) \,. \tag{5.58}$$

Writing $c_0 = F_0\,\tau$ yields an equation similar to Eq. (5.46):

$$\tau = \frac{1}{(\mu x)^2\, p^2}\,\frac{1}{F_0\left(1 - e^{-\mu_0 x_0}\right)}\left(1 + e^{\mu x}\,\frac{A_0}{A_1}\,\frac{e^{\mu_0 x_0} - 1}{1 - e^{-\mu_1 x_1}}\right) \,. \tag{5.59}$$

Because τ now depends on μx, $\mu_0 x_0$, and $\mu_1 x_1$ we have to set the partial derivatives of τ with respect to these quantities equal to zero in order to find the optimum. We see after a bit of thought that the derivative with respect to $\mu_1 x_1$ of the second ion chamber cannot be equal to zero but

approaches zero for: $\mu_1 x_1 \rightarrow \infty$. (5.60)

Setting the partial derivative with respect to $\mu_0 x_0$ equal to zero results in the equation:

$$\left(e^{\mu_0 x_0} - 1\right)^2 = \frac{A_1}{A_0} e^{-\mu x} \left(1 - e^{-\mu_1 x_1}\right) . \tag{5.61}$$

Similarly, setting the partial derivative with respect to μx equal to zero yields

$$\mu x - 2 = 2 e^{-\mu x} \frac{A_1}{A_0} \frac{1 - e^{-\mu_1 x_1}}{e^{\mu_0 x_0} - 1} = 2\left(e^{\mu_0 x_0} - 1\right) , \tag{5.62}$$

where the last step follows from Eq. (5.61). Solving for $\mu_0 x_0$ gives: $\mu_0 x_0 = \ln(\mu x/2)$. (5.63)

The optimum counting time is obtained by inserting Eqs. (5.61), (5.62), and (5.63) into Eq. (5.59):

$$\tau_{opt} = \frac{1}{p^2 F_0} \frac{1}{(\mu x - 2)^2} . \tag{5.64}$$

Applying Eq. (5.61) once again, produces an equation which can be iterated for a given value of $\mu_1 x_1$, the optimum being infinity, (5.60):

$$\mu x = 2\left(1 + \sqrt{\frac{A_1}{A_0} e^{-\mu x} \left(1 - e^{-\mu_1 x_1}\right)}\right) . \tag{5.65}$$

Once μx is known, $\mu_0 x_0$ is calculated from Eq. (5.63). For $\mu_1 x_1 \rightarrow \infty$ and $A_1 = A_0$ we obtain:

$$\mu x \cong 2.56 ; \qquad \mu_0 x_0 \cong 0.246 ;$$

$$\tau_{opt} = \frac{3.19}{p^2 F_0} = \frac{\kappa g_0}{p^2 I_0} \frac{1}{\mu x (\mu x - 2)} = 0.702 \frac{\kappa g_0}{p^2 I_0} . \tag{5.66}$$

In the second step we have used Eq. (5.64) together with $F_0 \equiv c_0/\tau$ and Eqs. (5.51) and (5.63).

These three conditions determine the optimum choice for the absorption-thickness product (subscript "opt" omitted) for the two ion chambers and the sample. The result $\mu x \cong 2.56$ is not too different from the previous one, (5.47), where the absorption of the ion chambers was ignored. Note that the result (5.66) is exactly the same as the one in Refs. 5 or 148 which had been obtained in a completely different way. The present criterion includes in addition the dependence on the ratio A_1/A_0 of the cross-sectional areas of the x-ray beam. For $\mu_1 x_1 \rightarrow \infty$ and $A_1 = 0.5\, A_0$ we get instead of (5.66):

$$\mu x \cong 2.42\,; \qquad \mu_0 x_0 \cong 0.191\,; \quad \tau_{opt} = \frac{5.63}{p^2\, F_0} = 0.980 \cdot \frac{\kappa\, g_0}{p^2\, I_0}\,. \tag{5.67}$$

Thus, if the cross section of the x-ray beam in the second ion chamber differs, i.e. is smaller than the first, then the sample thickness as well as the absorption in the first ion chamber are reduced for optimum conditions. This optimum-thickness criterion, which is based on counting statistics, always produces optimum sample thicknesses exceeding $\mu x = 2$. Otherwise Eq. (5.63) yields negative values for $\mu_0 x_0$.

Since μ depends on energy, whereas x does not, the product μx cannot remain constant. We will therefore choose the sample thickness such that the average value of μx in the EXAFS region is approximately equal to 2 or so. If a sample contains several edges of interest it may occur that the averages of μx at the corresponding edges cannot both be near 2. If that is the case then the thickness cannot be optimized for all edges. In order to check whether simultaneous optimization is possible it is useful to plot the quantity $2/\mu$. A plot of $2/\mu$ versus energy is shown in Fig. 5.1 for SmSe where the values of μ were obtained from the parametrizations in Ref. 138. We see that in this case it is possible to optimize for both edges simultaneously.

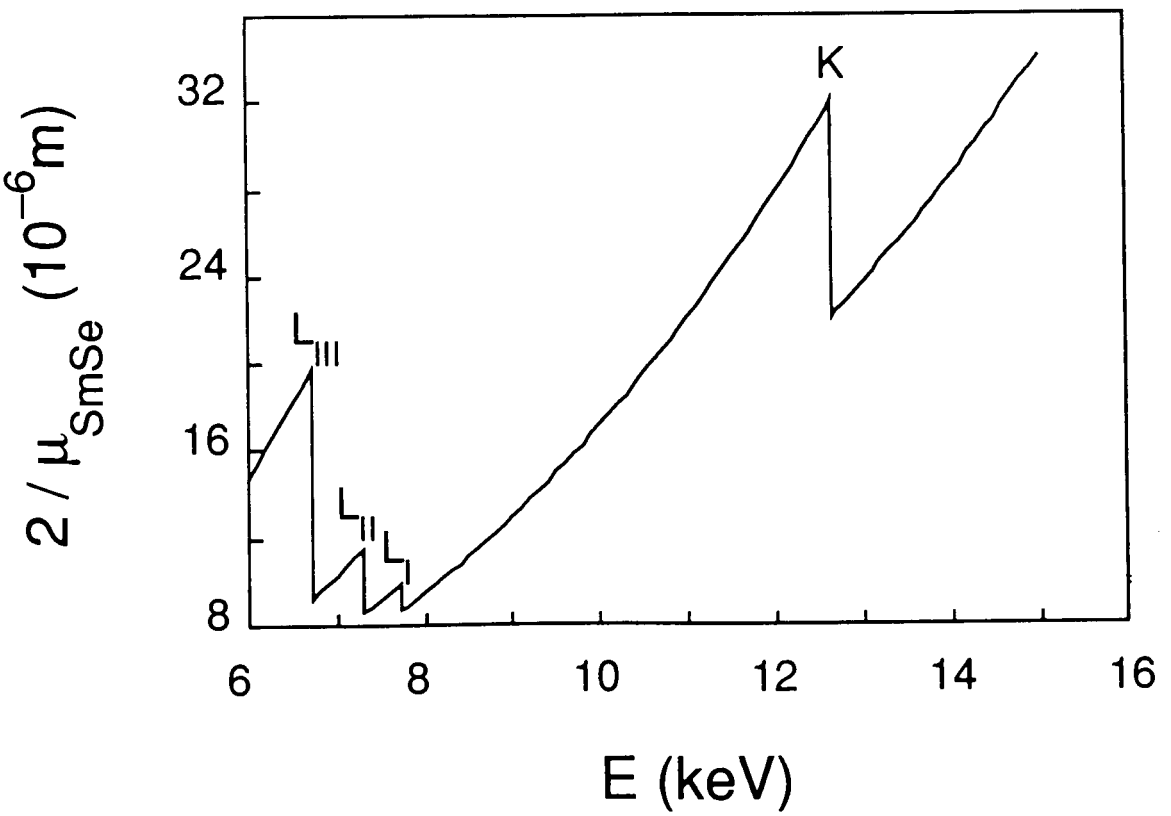

Fig. 5.1: $2/\mu_{SmSe}$ versus photon energy. The jumps occur at the absorption edges. We see that a sample thickness of $x \cong 16 \cdot 10^{-6}$ m would be a reasonable average thickness suited to measure the EXAFS of the Sm L edges as well as the Se K edge.

In Section 5.7 it will be shown that if harmonics are present then the sample thickness should be made as small as possible instead of being such that $\mu x \cong 2$.

5.6 Signal-to-Noise Ratio

This brief section describes how a quantitative measure of the signal-to-noise ratio in EXAFS is obtained.

As will be shown in Section 6.7 we can decompose the EXAFS function $\chi(k)$ into amplitude and phase which both depend on k. Therefore we get:

$$\chi(k) = A(k)\sin\Phi(k) = \frac{\mu - \mu_B}{\mu_B} \quad . \tag{5.68}$$

μ_B is the the background, i.e. the slowly varying part of the absorption coefficient. We define the signal-to-noise ratio as

$$S/N \equiv \frac{A_{eff}(k)}{|\delta(\mu x)|} = \frac{A_{eff}(k)}{p\,\mu x} \cong \frac{A_{eff}(k)}{p\,\mu_B x} \quad , \tag{5.69}$$

where the second step follows from Eq. (5.41). $A_{eff}(k)$ is the effective or rms value of the EXAFS signal. We obtain $A_{eff}(k)$ by assuming that A(k) is slowly varying with k. Hence we only consider the effective value of $\sin\Phi(k)$ which we assume is equal to $1/\sqrt{2}$, as it would be for a pure sine function. This is an approximation because in general there are several shells and $\Phi(k)$ is not proportional to k. We obtain:

$$A_{eff}(k) \equiv \frac{A(k)}{\sqrt{2}} \quad \Rightarrow \quad S/N = \frac{A(k)}{\sqrt{2}\,p\,\mu_B x} \quad . \tag{5.70}$$

As an example, if $\mu_B x = 2$ has been obtained with a precision of $p = 1\%$ and A(k) happens to be 0.1 then the signal-to-noise ratio is $S/N = 20\log_{10}\left(\frac{0.1}{\sqrt{2}\ 0.01\ \cdot\ 2}\right) = 11$ dB .

Thus far the equations have been general, but in the following we distinguish two cases. The first is that of not considering the ion chambers. Using Eq. (5.46) we obtain directly from Eq. (5.70):

$$S/N = \frac{A(k)\ \sqrt{F_0\,\tau}}{\sqrt{2\ \left(1+e^{\mu_B x}\right)}} = \frac{A(k)\ \sqrt{c_0}}{\sqrt{2\ \left(1+e^{\mu_B x}\right)}} \quad . \tag{5.71}$$

If we do take ion chambers into account then we obtain from Eq. (5.59) instead:

$$S/N = \frac{A(k)\sqrt{F_0\,\tau\left(1 - e^{-\mu_0 x_0}\right)}}{\sqrt{2\left(1 + e^{\mu_B x}\,\frac{A_0}{A_1}\,\frac{e^{\mu_0 x_0} - 1}{1 - e^{-\mu_1 x_1}}\right)}} \quad . \tag{5.72}$$

In this equation, too, we may replace $F_0\,\tau$ by c_0. We see that the signal-to-noise ratio is proportional to the square root of the total number c_0 of photons or, equivalently, to the square root of the incident x-ray flux F_0 multiplied by the counting time τ. Eq. (5.72) differs from the signal-to-noise ratio given in Ref. 148, the most important difference being the absence of the derivative of the absorption coefficient of the sample with respect to energy.

5.7 Absorption Coefficients Obtained from Experiment

In this section we investigate how harmonics, pinholes, and uneven sample thickness affect the measured absorption spectrum. In particular, we will investigate the effect of harmonics. We derive how a lower bound on h_1, the intensity fraction with the fundamental energy, can be calculated from the experimentally observed step size, Eq. (5.85). If the transmission of all other absorbers, besides the sample, is known then one can actually determine the minimum value of h_1, Eq. (5.90). After having discussed absorption coefficients we consider the EXAFS which can be treated as a small signal on top of the absorption coefficient. A small-signal gain is obtained from the derivative of $\ln N_0/N_1$ with respect to $\mu(E)\,\bar{x}$ and it describes the effects on the EXAFS envelope function due to artifacts (Eq. (5.93)). An example applying the results to a Cu foil is given at the end of this section.

Absorption coefficients determined from $\ln(N_0/N_1)$ are subjected to experimental artifacts such as the presence of harmonics in the beam, pinholes or bubbles in the sample, and an uneven thickness when making samples from powders. These effects lead always to an apparent reduction of the experimental absorption coefficient, i.e. $\ln(N_0/N_1) \leq \mu x$. Ideally, the equals sign would hold. In order to investigate these artifacts and to find out what can be done about them we first write down the transmitted intensity for a sample of uniform thickness with no pinholes.

We begin by considering the effect of harmonics. We may write:

$$N_1(E) = \int_0^\infty N_0(\tilde{E})\, h(E-\tilde{E})\, e^{-\mu(\tilde{E})\, x}\, d\tilde{E} \;; \qquad \int_0^\infty h(E-\tilde{E})\, d\tilde{E} = 1 \,. \tag{5.73}$$

Here $h(E-\tilde{E})$ is a normalized weighting function describing the variation in energy, which is due to harmonics and best described by a sum of δ-functions:

$$h(E-\tilde{E}) = \sum_{m=1}^{\infty} h_m\, \delta(mE-\tilde{E}) \;; \qquad \sum_{m=1}^{\infty} h_m = 1 \;; \qquad h_{m+1} < h_m \,. \tag{5.74}$$

Thus Eq. (5.73) becomes: $\quad N_1(E) = \sum_{m=1}^{\infty} N_0(mE)\, h_m\, e^{-\mu(mE)\cdot x}$.

We now put any energy dependence of the intensity N_0 of the incident beam into the coefficients h_m and can therefore assume that N_0 is constant. We can thus write:

$$N_1(E) = N_0 \cdot \sum_{m=1}^{\infty} h_m\, e^{-\mu(mE)\cdot x} \,. \tag{5.75}$$

For a powdered sample, such as SmSe, we have to take into account that the thickness x is not constant. Instead there is a thickness distribution characterized by a mean value $\bar{x}$ and moments M_k of higher order. Following Ref. 149 we replace Eq. (5.75) by:

$$N_1(E) = N_0 \cdot \sum_{m=1}^{\infty} h_m\, e^{-\mu(mE)\cdot\bar{x}}\; \frac{1}{S} \cdot \int_S e^{-\mu(mE)\cdot(x-\bar{x})}\, dS' \,. \tag{5.76}$$

The integration is over the illuminated cross-sectional area S of the sample. Writing the exponential underneath the integral as a series yields an expansion in terms of the central moments M_k [149]:

$$N_1(E) = N_0 \cdot \sum_{m=1}^{\infty} h_m\, e^{-\mu(mE)\cdot\bar{x}} \cdot \sum_{k=0}^{\infty} (-1)^k\, \frac{\mu^k(mE)}{k!}\, M_k \tag{5.77}$$

with $\quad M_k \equiv \frac{1}{S} \cdot \int_S (x-\bar{x})^k\, dS' \,. \tag{5.78}$

We have $M_0 = 1$ and $M_1 = 0$. The thickness distribution of $(x-\bar{x})$ can be assumed to be symmetric and therefore the odd central moments will vanish. Provided that moments higher than M_2 can be neglected we have:

$$N_1(E) = N_0 \cdot \sum_{m=1}^{\infty} h_m \, e^{-\mu(mE)\cdot\bar{x}} \left[1 + \frac{M_2}{2\,\bar{x}^2} \left(\mu(mE)\cdot\bar{x}\right)^2\right] . \qquad (5.79)$$

The absorption coefficient at the energies of the harmonics is much smaller than the absorption coefficient at the energy of the fundamental. We therefore neglect the former compared to the latter, that is $\mu(mE) \cong 0$ for $m = 2, 3, 4, \ldots$ and obtain:

$$N_1(E) = N_0 \left\{ h_1 \, e^{-\mu(E)\cdot\bar{x}} \left[1 + \frac{M_2}{2\,\bar{x}^2} \left(\mu(E)\cdot\bar{x}\right)^2\right] + \sum_{k=2}^{\infty} h_k \right\} . \qquad (5.80)$$

Using $\sum_{k=2}^{\infty} h_k = 1 - h_1$ from the normalization condition, (5.74), we get:

$$\ln \frac{N_0}{N_1(E)} = -\ln \left\{ 1 - h_1 + h_1 \, e^{-\mu(E)\cdot\bar{x}} \left[1 + \frac{M_2}{2\,\bar{x}^2} \left(\mu(E)\,\bar{x}\right)^2\right] \right\} . \qquad (5.81)$$

Having made the approximation of transparency of the sample for harmonics we can easily take the existence of pinholes into account because if there are pinholes then the sample is more transparent, just as it is for harmonics. Therefore we assume in the following that the effect of pinholes is contained in h_1 as well, besides the harmonics. h_1, the fraction of intensity at the energy of the fundamental, is of interest because it depends on the amount of harmonics and pinholes present during an experiment. In the remainder of this section we will therefore investigate in how far it is possible to determine h_1.

N_0 and N_1 are not the actually measured count rates. Instead $I_0 = \tilde{\kappa}_0 N_0$ and $I_1 = \tilde{\kappa}_1 N_1$ are measured according to Section 5.4 and we obtain $\ln N_0/N_1$ as follows:

$$\ln\left(\frac{N_0}{N_1}\right) = \ln\left(\frac{I_0}{I_1}\right) + \ln\left(\frac{\tilde{\kappa}_1}{\tilde{\kappa}_0}\right) . \qquad (5.82)$$

The absorption spectrum is therefore obtained by a constant shift of the measured quantity $\ln I_0/I_1$. Therefore differences of $\ln I_0/I_1$ will be equal to differences of $\ln N_0/N_1$. If the shift is known then $\ln N_0/N_1$ can be calculated directly.

The next figure is based on Eq. (5.81). For results from different treatments of the effects of harmonics and pinholes see for example Refs. 150 and 151.

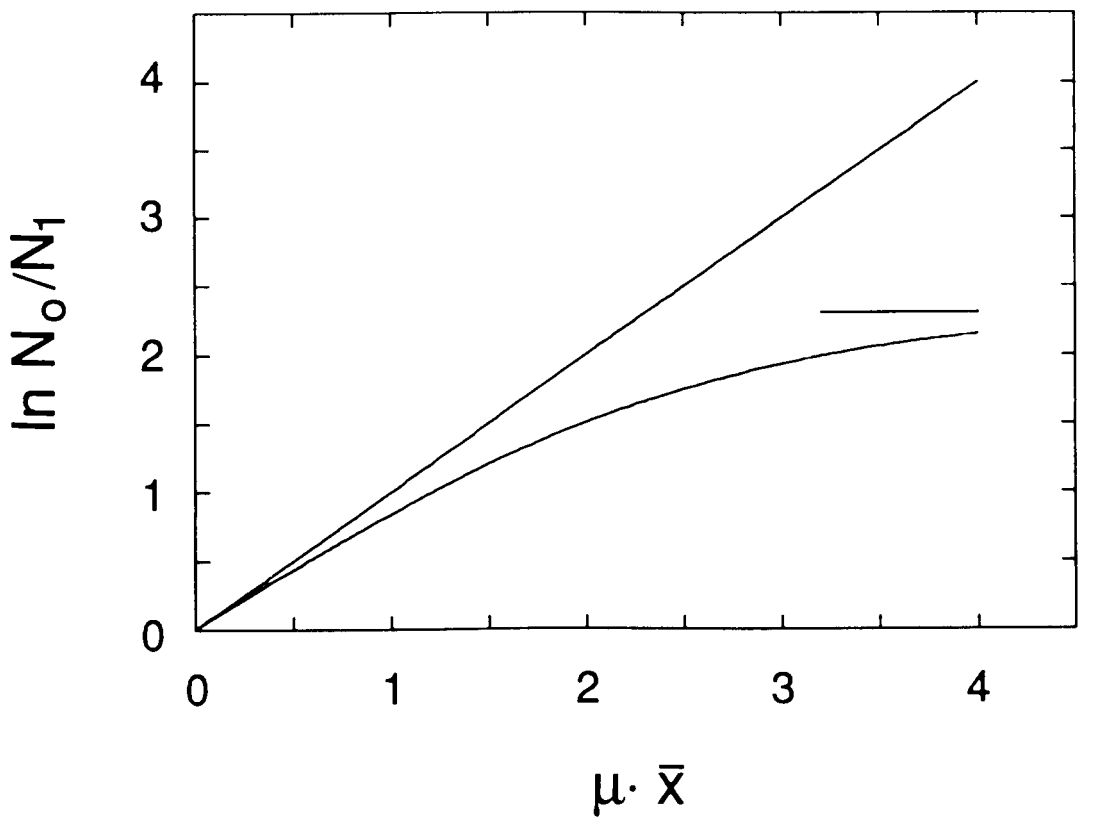

Fig. 5.2: Measured absorption-thickness product $\ln N_0/N_1$ versus the true value $\mu(E)\,\bar{x}$ according to Eq. (5.81) and for $h_1 = 0.9$ and $M_2 = 0$. The straight line corresponds to the ideal case. The limiting value $-\ln(1 - h_1) = 2.30$ is indicated by the horizontal line.

In Fig. 5.2 $\ln N_0/N_1$ is plotted versus $\mu(E)\,\bar{x}$ for $h_1 = 0.9$ and $M_2 = 0$. We see from the figure that $\ln N_0/N_1$ is always smaller than the true value $\mu(E)\,\bar{x}$. Regarding harmonics and pinholes it is therefore desirable to make the sample as thin as possible in order to minimize this discrepancy. For large values of $\mu(E)\,\bar{x}$ the function approaches its limiting value of $-\ln(1-h_1)$ if $h_1 < 1$. The existence of a limiting value for $h_1 < 1$ means that $\Delta(\ln N_0/N_1) = \Delta(\ln I_0/I_1)$ cannot exceed $-\ln(1-h_1)$. This implies a lower bound on h_1:

$$h_1 \geq 1 - e^{-D_{max}} \quad \text{with} \quad D_{max} \equiv \Delta\left(\ln N_0/N_1\right)\Big|_{max} = \Delta\left(\ln I_0/I_1\right)\Big|_{max} . \tag{5.83}$$

As was pointed out in connection with Eq. (5.82), differences of $\ln I_0/I_1$, like D_{max}, are useful quantities. If there are no other energy-dependent terms then the difference D_{max} can be evaluated at any two energies. Often, however, there are other absorbers, like for example B_4C anvil tips or simply air, present whose absorption changes with energy. Therefore it is best to evaluate quantities like D_{max} at two closely-spaced energy values. At an absorption edge the energy is practically unchanged, i.e. $E_\alpha \cong E_\beta$. Therefore it will be of advantage to use the size D_o of the measured edge step in a calculation. D_o is given by:

$$D_o \equiv \ln I_0/I_1\Big|_\beta - \ln I_0/I_1\Big|_\alpha = \ln N_0/N_1\Big|_\beta - \ln N_0/N_1\Big|_\alpha . \tag{5.84}$$

The lower estimate for h_1 can now be extended: $h_1 \geq 1 - e^{-D_{max}} \geq 1 - e^{-D_o}$. (5.85)

Eq. (5.85) is important because it allows one to calculate a lower bound on h_1, the intensity fraction with the fundamental energy, from the experimentally observed step size.

We now proceed to determine h_1. Using Eq. (5.81) we can calculate h_1 for a thickness $\bar{x}$ with D_o and M_2 as parameters. Rewriting Eq. (5.81) we have:

$$\frac{N_1}{N_0} = 1 - h_1 + h_1\, e^{-\mu(E)\cdot\bar{x}} \cdot T\left(1 + \frac{1}{2} M_2\, \mu(E)^2\right) . \tag{5.86}$$

Note that Eq. (5.86) now includes the quantity T which stands for the combined transmission of all other absorbers besides the sample, like for example B_4C, air, etc.. Writing this equation down for

the energy E_β above the edge and for E_α below it and forming the ratio yields

$$\frac{1}{h_1} = 1 + T \cdot \frac{e^{-\mu_\alpha \bar{x}} \left(1 + \frac{1}{2} M_2 \mu_\alpha{}^2\right) - e^{D_o} e^{-\mu_\beta \bar{x}} \left(1 + \frac{1}{2} M_2 \mu_\beta{}^2\right)}{e^{D_o} - 1} , \qquad (5.87)$$

where D_o is given by Eq. (5.84). Under ideal conditions we have $h_1 = 1$ and $M_2 = 0$. In this case the sample thickness has the smallest possible value:

$$x_{min} \equiv \frac{D_o}{\mu_\beta - \mu_\alpha} . \qquad (5.88)$$

According to Eq. (5.87) h_1 as a function of the sample thickness $\bar{x}$ possesses a minimum. This is so because $h_1 = 1$ occurs at the minimum thickness and it must also occur at infinite thickness. The minimum of $h_1(\bar{x})$ occurs at:

$$x_o \equiv x_{min} + \frac{\ln\left(r \mu_\beta/\mu_\alpha\right)}{\mu_\beta - \mu_\alpha} \quad ; \qquad r \equiv \frac{1 + \frac{1}{2} M_2 \mu_\beta{}^2}{1 + \frac{1}{2} M_2 \mu_\alpha{}^2} \geq 1 . \qquad (5.89)$$

x_{min} is given by Eq. (5.88). (For $r = 1$ the second term happens to be the optimum sample thickness determined from contrast maximization of the transmitted intensity at an absorption edge [152].) Thus the minimum of h_1 occurs close to some optimum thickness which in turn will be close to the actual sample thickness. Inserting this result into Eq. (5.87) yields:

$$\frac{1}{h_{1min}} = 1 + \frac{T\left(1 + \frac{1}{2} M_2 \mu_\alpha{}^2\right)}{e^{D_o} - 1} \left(1 - \frac{\mu_\alpha}{\mu_\beta}\right) \exp\left[\frac{-\mu_\alpha \left(D_o + \ln r \mu_\beta/\mu_\alpha\right)}{\mu_\beta - \mu_\alpha}\right] . \qquad (5.90)$$

Thus, if the sample thickness is unknown we can still estimate the minimum value h_{1min} of h_1.

If we again consider Eq. (5.86) just above and just below the absorption edge and subtract the two equations, instead of dividing, then we obtain an equation which can be combined with

Eq. (5.87) to eliminate the transmission T due to other absorbers. The result is an equation for h_1, independent of T, but containing now gain factors and cross-sectional areas:

$$h_1 = 1 - \frac{g_0 A_0 \left(1 - e^{-\mu_0 x_0}\right)}{g_1 A_1 \left(1 - e^{-\mu_1 x_1}\right)} \cdot \frac{I_1/I_0\big|_\beta \, e^{-\mu_\alpha \bar{x}} - I_1/I_0\big|_\alpha \, r\, e^{-\mu_\beta \bar{x}}}{e^{-\mu_\alpha \bar{x}} - r\, e^{-\mu_\beta \bar{x}}} , \qquad (5.91)$$

where r has been defined in Eq. (5.89). Because this equation is independent of T, i.e. of all the other absorbers, it should be more reliable for determining h_1. Eq. (5.91) contains three unknowns: The first fraction, evaluated at the edge, the sample thickness $\bar{x}$, and r, which frequently will be close to unity. If we assume that in a series of high-pressure scans only $\bar{x}$ in Eq. (5.91) changes, then the second fraction is invariant under pressure. If the second fraction were exactly zero this would indicate that there are no harmonics or pinholes. Practically, however, it will be non-zero and as long as the prefactor containing the gain factors is unknown h_1 cannot be determined.

The EXAFS is a small variation of the absorption coefficient and we can therefore consider it as a small signal. The small-signal gain g is obtained from the derivative of $\ln N_0/N_1$ with respect to $\mu(E)\,\bar{x}$ according to Eq. (5.81):

$$g \equiv \frac{d \ln N_0/N_1}{d\,(\mu(E)\,\bar{x})} = \frac{d \ln I_0/I_1}{d\,(\mu(E)\,\bar{x})}$$

$$= \left[1 - (1 - h_1)\,\frac{N_0}{N_1}\right] \cdot \left[1 - \frac{2\,\frac{M_2}{2\,\bar{x}^2}\,\mu(E)\,\bar{x}}{1 + \frac{M_2}{2\,\bar{x}^2}\left(\mu(E)\,\bar{x}\right)^2}\right] . \qquad (5.92)$$

Obtaining N_0/N_1 from Eq. (5.81) one can write equivalently:

$$g = \frac{d \ln N_0/N_1}{d\,(\mu(E)\,\bar{x})} = \frac{d \ln I_0/I_1}{d\,(\mu(E)\,\bar{x})} = \frac{1 + \frac{M_2}{2\,\bar{x}^2}\,\mu(E)\,\bar{x}\left(\mu(E)\,\bar{x} - 2\right)}{\frac{1-h_1}{h_1}\,e^{\mu(E)\,\bar{x}} + 1 + \frac{M_2}{2\,\bar{x}^2}\left(\mu(E)\,\bar{x}\right)^2} . \qquad (5.93)$$

For values of $M_2/2\bar{x}^2$ that are not too large, the right-hand side is positive and for $\mu(E)\,\bar{x} \to \infty$ it

tends to zero. This confirms the known fact that in the presence of harmonics and/or pinholes the EXAFS signal decreases with increasing sample thickness. Conversely, if one observes an EXAFS signal with the correct amplitude from a thick sample then this implies the absence of harmonics or pinholes (see (5.83)).

The result of the above equations is shown in Fig. 5.3. It is simply the derivative of the curve shown in Fig. 5.2.

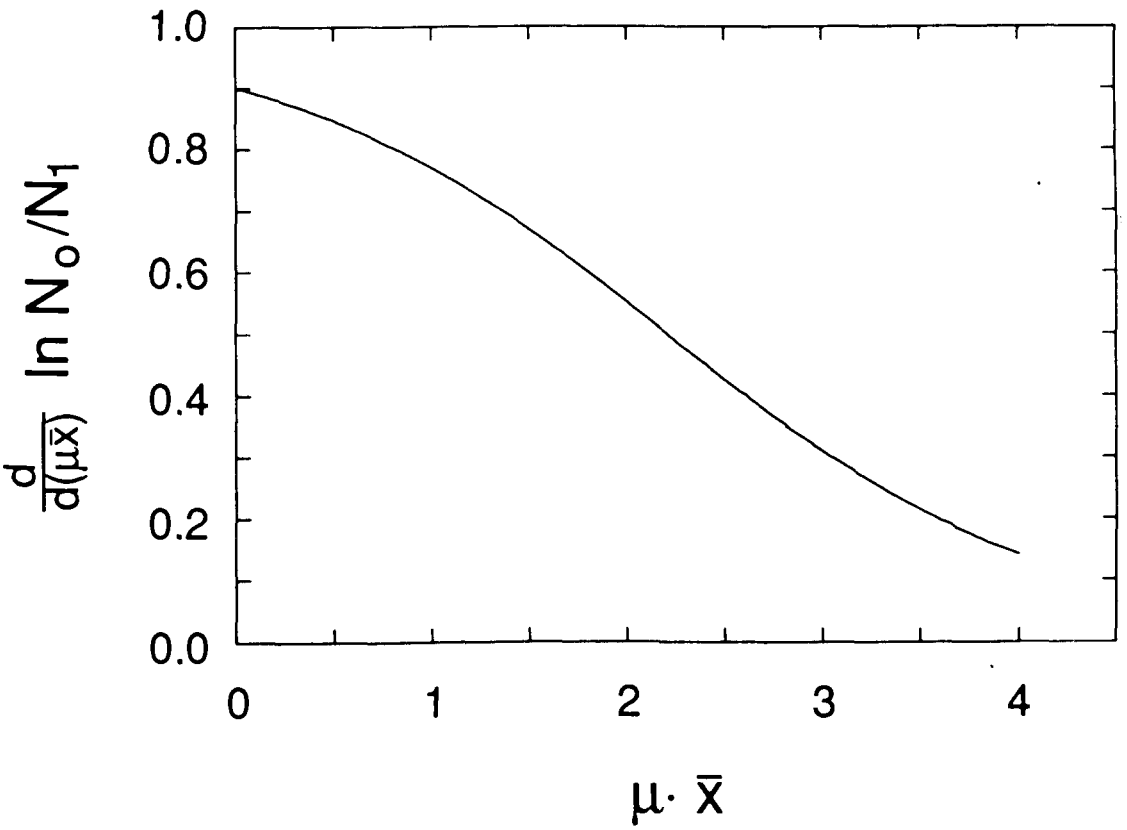

Fig. 5.3: Derivative with respect to $\mu(E)\,\bar{x}$ of the curve shown in Fig. 5.2.

The gain g resembles the amplitude reduction obtained in Ref. 150 by a different method. It achieves its maximum value h_1, independent of M_2, at $\mu(E)\,\bar{x} = 0$. Thus in order to maximize the amplitude of the EXAFS interference function the sample should be very thin. Since the absorption coefficient decreases during an EXAFS scan, the gain will increase approximately linearly with $\mu(E)\,\bar{x}$.

Let us now apply these results to calculate the gain of a Cu foil of known thickness x ($M_2 = 0$; $T = 1$). Using Eq. (5.81) we calculate h_1 from the measured jump D_o at the Cu K edge:

$$h_1 = \frac{e^{D_o} - 1}{e^{D_o}\left(1 - e^{-\mu_\beta x}\right) - \left(1 - e^{-\mu_\alpha x}\right)} \quad . \tag{5.94}$$

The subscripts α and β refer to the low- and high-energy side of the absorption edge, respectively. With $D_o = 1$, $\mu_\alpha = \rho\,\mu_{m\alpha} = 339.46\ cm^{-1}$, $\mu_\beta = \rho\,\mu_{m\beta} = 2589.3\ cm^{-1}$, and $x = 5{\cdot}10^{-4}$ cm we get $h_1 = 0.95$. The gain for the EXAFS signal right above the K edge is obtained from Eq. (5.93). The value is $g_\beta = 0.83$. Using Eq. (5.92) we can follow how the small-signal gain increases during a scan. We obtain:

$$\ln \frac{N_0}{N_1} = \ln\left(\frac{1 - g}{1 - h_1}\right) . \tag{5.95}$$

Writing Eq. (5.95) once again for the particular gain g_β at energy E_β just above the edge, subtracting, and solving for g yields:

$$g = 1 - (1 - g_\beta)\, e^{D} \qquad \text{with} \qquad D \equiv \ln I_0/I_1 - \ln I_0/I_1\Big|_\beta \quad . \tag{5.96}$$

This equation means that at least for the case of a foil of known thickness we can determine the increase of the gain as a function of energy E or wave vector k. This enhancement of the envelope of the measured EXAFS must be removed. If $g_\beta = 1$, as in the ideal case, then it is evident from Eq. (5.96) that $g = g_\beta = 1$. If M_2 is significant then the above analysis is not so simple.

In the high-pressure experiments on SmSe the thickness x is not known accurately but it could be measured by recording I_1 with and without the sample being present.

Looking at Fig. 5.2 again, one might suspect the generation of integer multiples of the EXAFS frequencies due to the curvature, in analogy to harmonic generation in an electronic amplifier. It turns out that moderately large values of M_2 straighten the curves shown in Fig. 5.2. For $M_2 = 0$ a comparison of the second derivative of $\ln N_0/N_1$ with the first derivative shows that the generation

of integer multiples is typically less than 10% but can increase for rather thick samples. Therefore the signal at twice the EXAFS spatial frequencies, which occur at $2\,(R_j + 0.5\,p_1)$, is about 10% of the signal at $R_j + 0.5\,p_1$.

The assumption made so far that the sample is transparent for the harmonics leads to an overestimate of the transmitted intensity N. Hence we write Eq. (5.81) as an inequality:

$$\mu(E)\,\bar{x} \;\geq\; \ln\frac{N_0}{N_1} \;\geq\; -\ln\left[1 - h_1 + h_1\, e^{-\mu(E)\,\bar{x}}\left(1 + \frac{1}{2}M_2\,\mu(E)^2\right)\right]. \qquad (5.97)$$

5.8 Pressure Calibration

The pressure is determined from the EXAFS of a calibration material that is placed in the gasket together with the sample. The contact of the calibrant with the sample requires that the two substances do not react chemically. Analyzing the EXAFS of the calibrant yields the nearest-neighbour distance. In order to convert this distance into a pressure the equation of state of the calibrant must be known. To this end it is of advantage to employ isotropic (cubic) calibrant materials. It is desirable that the EXAFS extend as far as possible. This requires that the Debye-Waller factor be small and that there be no intervening absorption edges from the sample. In order to facilitate the data analysis it is desirable for a calibrant to have a well separated first coordination shell and a Debye temperature equal to or bigger than the temperature at which the experiment is performed so that corrections due to asymmetry are not necessary. Furthermore, a calibrant should be highly compressible in order to reduce the error in the pressure determination. For minimizing the effects of non-hydrostaticity the calibrant should possess a low shear strength. Finally, its absorption edge must be in an accessible energy range and the absorption of the calibrant should be small in order to reduce the overall absorption.

In this work two pressure calibrants are employed: Cu and RbCl. RbCl has one unwanted property, namely a phase transition from the NaCl crystal structure to the CsCl structure. The transition occurs at 5.2 kbar [153] which is below the pressures that interest us here. Note that the error in pressure determination for RbCl is smaller due to its larger compressibility. The error in the

EXAFS pressure calibration employed here is still far greater than the error from the ruby fluorescence scale which is about 0.5 kbar to 0.1 kbar [154]. This method is not employed here as it requires that at least one of the anvil tips be made from diamond. However, in the axial geometry used in our experiments, this will introduce Bragg peaks in the EXAFS spectra preventing analysis [155].

At room temperature the p-V relation for Cu is taken from Ref. 156. The same reference contains also data for RbCl but these are discarded because they were obtained from shock experiments which are not corrected for the presence of the NaCl-CsCl phase transition. Instead we employ the data of Vaidya and Kennedy [153]. Their results, however, only extend up to 45 kbar and it becomes necessary to extrapolate to approximately 100 kbar. This is done by fitting the data of Ref. 153 in the interval from 5.2 kbar to 45 kbar to a theoretical p-V relation. As suggested in Ref. 157 we employ a modified form of Jamieson's equation of state [158] which reads:

$$\frac{p}{B_o} = \frac{\eta}{(1 - S\,\eta)^2} \quad ; \quad \eta \equiv 1 - \frac{V/V_o}{\alpha} \quad . \tag{5.98}$$

B_o, S, and α are parameters which are determined from a fit to Vaidya and Kennedy's data [153]. Their respective values are:

$$B_o = 184 \text{ kbar} \; ; \qquad S = 1.53 \; ; \qquad \alpha = 0.8458 \quad . \tag{5.99}$$

With the room-temperature p-V relations known we now have to determine the corresponding relations at liquid-nitrogen temperature. In doing this we will assume that the pressure for the NaCl-to-CsCl phase transition of RbCl is approximately temperature independent. For a relation like an equation of state which involves the three variables p, V, and T we can immediately write down the following:

$$\left.\frac{\partial p}{\partial T}\right|_V \left.\frac{\partial T}{\partial V}\right|_p \left.\frac{\partial V}{\partial p}\right|_T = -1 \qquad \text{or:} \qquad \left.\frac{\partial p}{\partial T}\right|_V = -V \left.\frac{\partial p}{\partial V}\right|_T \frac{1}{V} \left.\frac{\partial V}{\partial T}\right|_p = B_T \beta \; . \tag{5.100}$$

B_T is the isothermal bulk modulus and β is the coefficient of volume expansion. If these two quantities were known the change of pressure with temperature could be calculated.

When $B_T \beta$ is not known the Grüneisen relation (see Appendix C) is useful. It is given by:

$$B_T \beta = \gamma_G \frac{C_V}{V} \quad . \tag{5.101}$$

γ_G is the Grüneisen parameter. It depends on volume and temperature. For most substances the temperature dependence is weak in the range from 300K to 77K [159-164] (see Ref. 159 for RbCl in particular). We will therefore ignore it and consider γ_G as only volume dependent. Any temperature dependence of γ_G would be a direct consequence of increased anharmonicity.

C_V in Eq. (5.101) is the heat capacity at constant volume. In the Debye model it is given by:

$$\frac{C_V}{V} = \rho \frac{3R}{\bar{A}} f_D(\Theta_D/T) = \rho_o \frac{V_o}{V} \frac{3R}{\bar{A}} f_D(\Theta_D/T) \quad . \tag{5.102}$$

Θ_D is the Debye temperature which is here assumed to be temperature independent. However, Θ_D, like γ_G, does depend on volume. For Cu these volume dependencies can be found in Ref. 165. They are linear in the pressure range that is of interest here. For RbCl the volume dependence of the Debye temperature up to 20 kbar is given in Ref. 166. Values for higher pressures are obtained by linear extrapolation. The volume dependence of the Grüneisen parameter of RbCl is obtained from the Debye temperature using the relation (see Appendix C):

$$\gamma_G = -\frac{\partial \ln \Theta_D}{\partial \ln V} \quad . \tag{5.103}$$

The quantity $\bar{A}$ in Eq. (5.102) is the average atomic weight, i.e. $\bar{A} \equiv \frac{1}{n} \sum_{i=1}^{n} A_i$, where n is the number of atoms per formula unit. R is the gas constant, ρ the density, and $f_D(\Theta_D/T)$ is the Debye function defined by:

$$f_D(y) \equiv \frac{3}{y^3} \int_0^y \frac{e^x}{(e^x - 1)^2} x^4 \, dx \quad . \tag{5.104}$$

Using Eq. (5.101) we can rewrite Eq. (5.100) as follows: $\left.\frac{\partial p}{\partial T}\right|_V = \gamma_G \frac{C_V}{V}$. (5.105)

Integrating, using Eq. (5.102), yields the (negative) change Δp in pressure when the temperature is reduced,

$$\Delta p \equiv \int_{300K}^{77K} \left.\frac{\partial p}{\partial T}\right|_V dT = \gamma_G \cdot \int_{300K}^{77K} \frac{C_V}{V}\, dT = -\rho_o \frac{V_o}{V}\, \gamma_G(V)\, \frac{3R}{\bar{A}} \cdot \int_{77K}^{300K} f_D(\Theta_D(V)/T)\, dT \quad , \tag{5.106}$$

where in the last step we have emphasized the volume dependence of γ_G and Θ_D.

The pressure at liquid-nitrogen temperature is now:

$$p(77K) = p(300K) + \Delta p \quad . \tag{5.107}$$

The results for the calibration are:

Table 5.3: Pressure versus reduced volume for Cu at 300K and at 77K:

T = 300K		T = 77K	
V/V_o	p (kbar)	V/V_o	p (kbar)
0.896	200.0	0.904	188.12
0.904	180.0	0.912	168.05
0.912	160.0	0.920	147.98
0.921	140.0	0.929	127.90
0.930	120.0	0.938	107.825
0.940	100.0	0.948	87.74
0.945	90.0	0.953	77.69
0.951	80.0	0.959	67.64
0.956	70.0	0.964	57.60
0.962	60.0	0.970	47.54
0.968	50.0	0.976	37.49
0.971	45.0	0.979	32.46
0.974	40.0	0.982	27.44
0.977	35.0	0.986	22.41
0.980	30.0	0.989	17.38
0.983	25.0	0.992	12.355
0.986	20.0	0.995	7.33
0.990	15.0	0.999	2.29
0.993	10.0	1.000	0.0
0.996	5.0		
1.000	0.0		

The results contained in this table are plotted in the next figure.

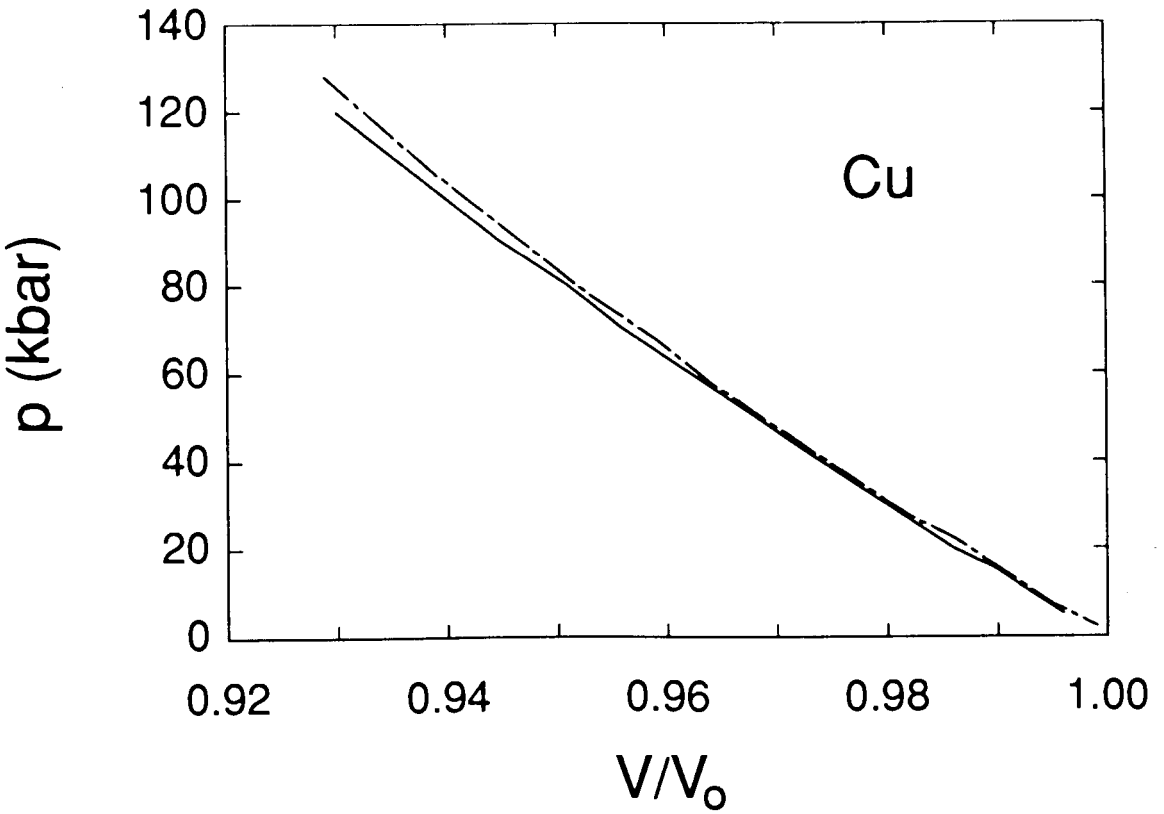

Fig. 5.4: Pressure versus reduced volume for Cu. The solid line refers to room temperature and the dashed line shows the result for liquid-nitrogen temperature.

Table 5.4: Pressure versus reduced volume for RbCl at 300K and at 77K:

T = 300K		T = 77K	
V/V_o	p (kbar)	V/V_o	p (kbar)
0.716	194.14	0.726	184.38
0.728	174.54	0.738	165.15
0.740	157.00	0.750	147.98
0.752	141.25	0.762	132.60
0.765	127.07	0.776	118.80
0.777	114.27	0.788	106.38
0.789	102.695	0.800	95.165
0.801	92.19	0.812	85.02
0.813	82.65	0.824	75.83
0.825	73.96	0.836	67.48
0.837	66.03	0.849	59.88
0.8495	58.78	0.862	52.95
0.862	52.15	0.874	46.62
0.874	46.07	0.886	40.83
0.876	45.20	0.888	40.00
0.887	39.84	0.899	34.915
0.899	34.81	0.9115	30.14
0.912	29.94	0.925	25.54
0.926	25.10	0.939	20.97
0.941	20.15	0.954	16.31
0.959	15.08	0.972	11.535
0.979	9.92	0.993	6.70
1.	5.16	1.	5.16

The results are shown in the following figure. It was assumed in the calculations that the pressure at which the first-order phase transition occurs in RbCl is independent of temperature.

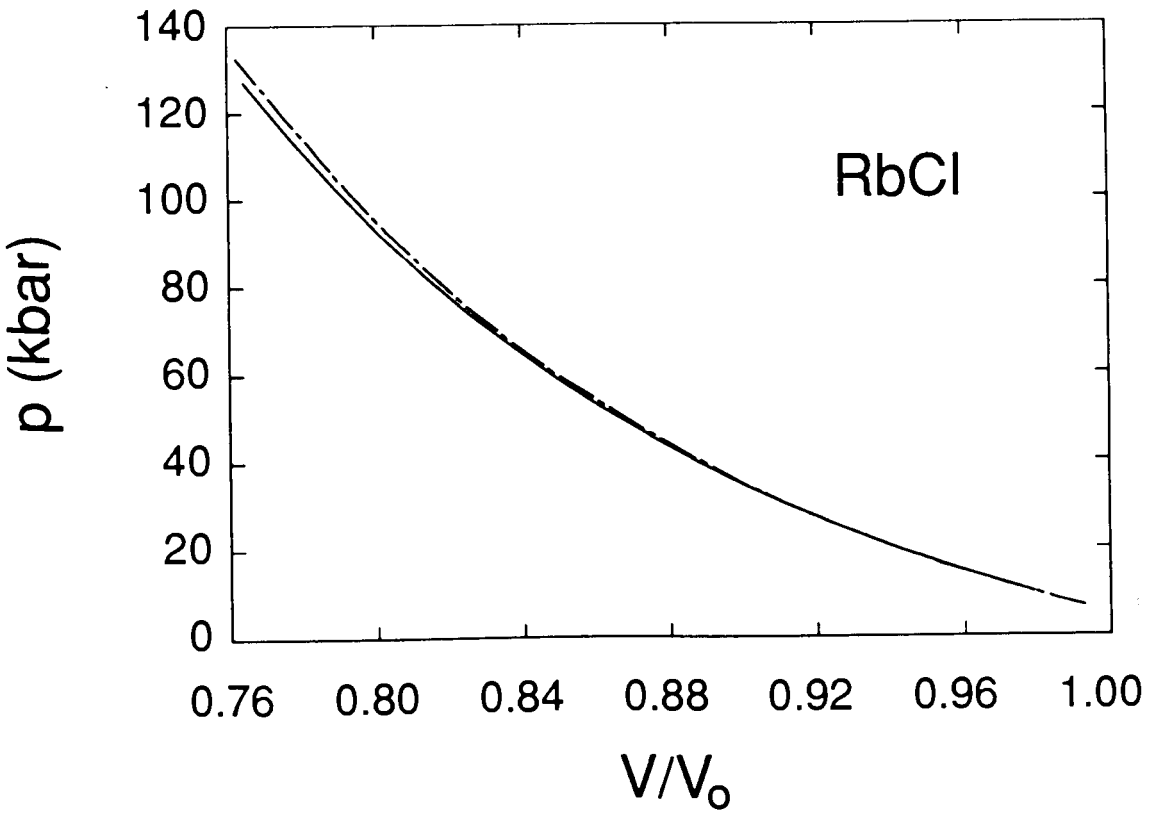

Fig. 5.5: Pressure versus reduced volume for RbCl. The solid line is the room-temperature result and the dashed line refers to liquid-nitrogen temperature.

We observe that the slope of the pressure-vs.-volume curves at 77K is more negative than the ones at 300K:

$$\left.\frac{\partial p}{\partial V}\right|_{77K} < \left.\frac{\partial p}{\partial V}\right|_{300K} \quad \text{or:} \quad \left.\frac{\partial V}{\partial p}\right|_{77K} > \left.\frac{\partial V}{\partial p}\right|_{300K} \tag{5.108}$$

or: $$\left.\frac{\partial}{\partial T}\right|_p \left.\frac{\partial V}{\partial p}\right|_T < 0 \qquad \text{or:} \quad \left.\frac{\partial}{\partial p}\right|_T \left.\frac{\partial V}{\partial T}\right|_p < 0 \ .$$

It turns out that this is always so. Following an argument of Bridgman [167, p. 175] we write for the

entropy content of a body:

$$S_o = \int_0^T \frac{C_p}{T} dT \geq -\int_0^\infty \left.\frac{\partial S}{\partial p}\right|_T dp = \int_0^\infty \left.\frac{\partial V}{\partial T}\right|_p dp \quad . \tag{5.109}$$

The last integral on the right-hand side of this equation thus has an upper bound S_o. This means that $\left.\frac{\partial V}{\partial T}\right|_p$ must decrease with increasing pressure such that the limit S_o is not exceeded. If $\left.\frac{\partial V}{\partial T}\right|_p$ is monotonic then this implies indeed $\left.\frac{\partial}{\partial p}\right|_T \left.\frac{\partial V}{\partial T}\right|_p < 0$ as in Eq. (5.108). Note that because of $\left.\frac{\partial S}{\partial p}\right|_T = -\left.\frac{\partial V}{\partial T}\right|_p < 0$ the entropy decreases with pressure. The argument presented here stems from the simple fact that the application of arbitrarily high pressure cannot reduce the entropy by more than its initial value S_o.

If we plot the reduced volume at 77K then it will always be larger than the corresponding one at 300K:

$$\left.\frac{V}{V_o}\right|_{p,\,77K} > \left.\frac{V}{V_o}\right|_{p,\,300K} \quad . \tag{5.110}$$

5.9 High-Pressure Cell

In this section a high-pressure cell for use at low temperatures is described and its design criteria are explained. The force gain is calculated and Eq. (5.125) is derived which specifies the angle at which to set the pressure cell before compressing the sample. A formula relating the compression to the applied pressure, Eq. (5.133), is derived also.

In order to carry out high-pressure work a pressure cell was designed for pressures up to 100 kbar. This cell is shown in Fig. 5.6. The pressure is generated mechanically by compressing a gasket placed between two opposing anvils. The gasket is an Inconel disk of ~10 mm diameter which contains the sample in a small central hole of ~0.7 mm diameter. The anvil flats have a diameter of about 3 mm. The axial geometry is employed, where the x-ray beam passes through anvils and sample, rather than horizontally through gasket and sample. In the transverse geometry the gasket has to be transparent to x-rays but at the same time strong. This makes Be the material of choice but there are possible health hazards (see below). In the axial geometry the cross-sectional area of the sample that is exposed to x-rays is unaffected by pressure and the sample thickness changes in a controlled way. The fact that the x-ray beam has to traverse the anvils has a distinct disadvantage though: it is not possible to employ anvil tips that are crystalline because Bragg diffraction would produce peaks in the measured absorption spectrum that would contaminate the EXAFS so that data analysis would become very difficult or impossible. Hence the anvils are made out of polycrystalline boron carbide, B_4C. Due to the lower hardness of this material, compared to diamond, the anvil tips have to be 2 to 3 mm in diameter. This in turn requires larger forces in order to produce a given pressure. In the future one may consider using sintered diamonds. They are hard and will not cause Bragg peaks.

The pressure cell is intended for low-temperature work. Therefore the anvils are driven mechanically rather than hydraulically as in earlier work at room temperature [155]. This will enable one to change the pressure while at low temperature. The entire apparatus is made out of one material in order to avoid problems with differential thermal contraction. The pressure cell is made from a maraging steel (VascoMax T-250) which can be easily machined in the soft condition and can be hardened by simple heat treatment without any significant distortion. Maraging (martensite age hardening) steels [168] are carbon-free alloy steels that acquire their high strength through precipitation of intermetallic compounds at ~480°C. Although of lower hardness than BeCu (1.8 wt. % Be), a maraging steel was preferred because the heat treatment of BeCu and the necessary subsequent grinding to final dimensions require the safety measures of a special Beryllium machine shop [169]. A disadvantage of maraging steels, not of concern here, is that they rapidly lose strength at temperatures above ~480°C. Since almost all materials embrittle with decreasing temperature the pressure cell has been designed with large safety margins applied to the room-temperature material specifications.

In the experiments performed for this thesis the thickness of the uncompressed gasket was selected to be in the range from 0.381 to 0.508 mm (15 to 20 mil). The displacement of the anvils cannot exceed this value. Therefore the cell is designed only for these small displacements. At the same time a large force multiplication is desired. A special constraint at beamline IV-1 at SSRL is that the x-ray beam is only 50 mm away from a wall so that the pressure cell has to be narrow along one cross-sectional dimension. The pressure cell was modeled after one designed by Syassen and Holzapfel [170, 171] for use with diamond anvils. The present cell, which is shown in Fig. 5.6, is bigger due to the larger force required. It has very good alignment stability because the force advancing the piston acts strictly axially and the piston is also sufficiently guided in the bore.

Fig. 5.7 shows a sketch of the pressure cell. Indicated are the lengths L_1 and L_2 of bracket and strut, their respective angles α_1 and α_2 with the centre line, and various forces. F is the magnitude of the force applied on one side and G is the magnitude of the resulting force that advances the anvil.

We will first investigate the kinematics. We introduce the quantity η, defined by:

$$\eta \equiv \frac{L_2}{L_1} < 1 \ . \tag{5.111}$$

From the figure we see:

$$L_1 \sin\alpha_1 = L_2 \sin\alpha_2 \qquad \Rightarrow \quad \eta = \frac{\sin\alpha_1}{\sin\alpha_2} \ , \tag{5.112}$$

$$L_1 \cos\alpha_1 = a - \xi + L_2 \cos\alpha_2 \qquad \Rightarrow \quad \frac{\xi}{L_1} = \frac{a}{L_1} + \sqrt{\eta^2 - \sin^2\alpha_1} - \cos\alpha_1 \ . \tag{5.113}$$

The angle α_1 can vary from $0°$ to $\arcsin\eta$. This corresponds to a maximum possible displacement d_{max} of:

$$d_{max}/L_1 \equiv \sqrt{1-\eta^2} - (1-\eta) \ . \tag{5.114}$$

d_{max}/L_1, plotted versus η has a maximum at $\eta = 1/\sqrt{2}$ with value $\sqrt{2} - 1 = 0.414$. The value chosen for η is $40/63 \equiv 0.635$ with $d_{max}/L_1 = 0.407$, close enough to the optimum.

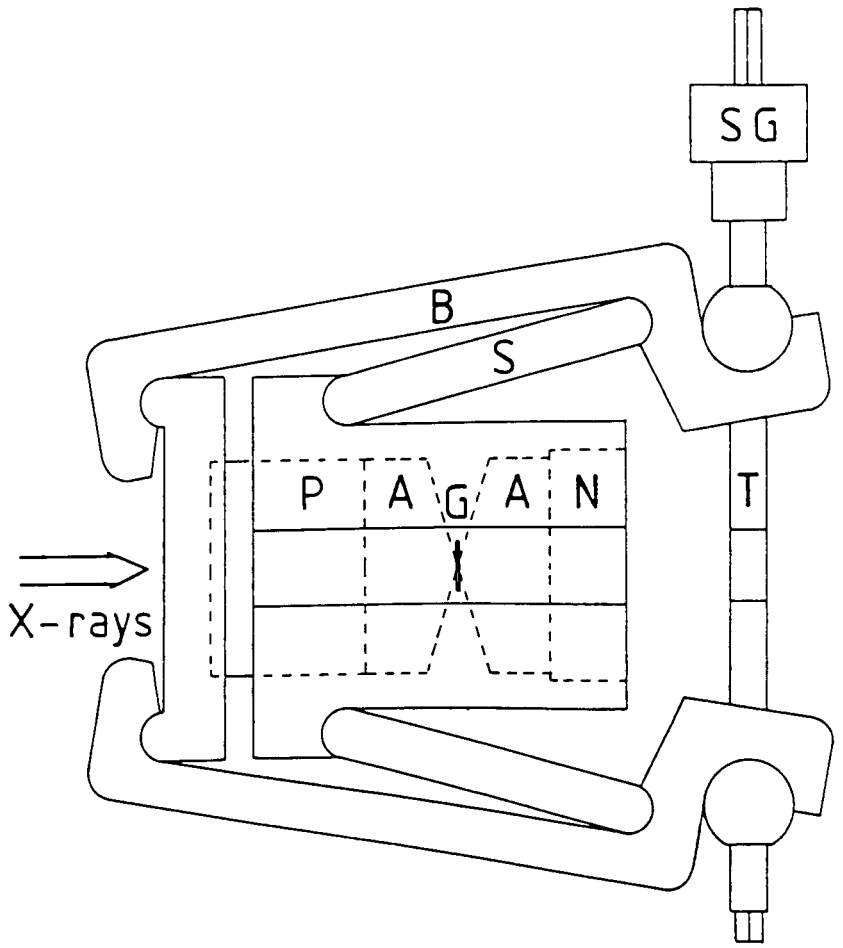

Fig. 5.6: High-pressure cell (from Ref. 172). The pressure is generated by turning two gear-set threaded spindles (T). The two spindles are driven by a spur gear (SG) and through brackets (B) and struts (S) move the two anvils (A) towards each other via the piston (P). The anvils compress the sample which is contained within the gasket (G). The end nut (N) is used to set the initial angle of the brackets with the cell body.

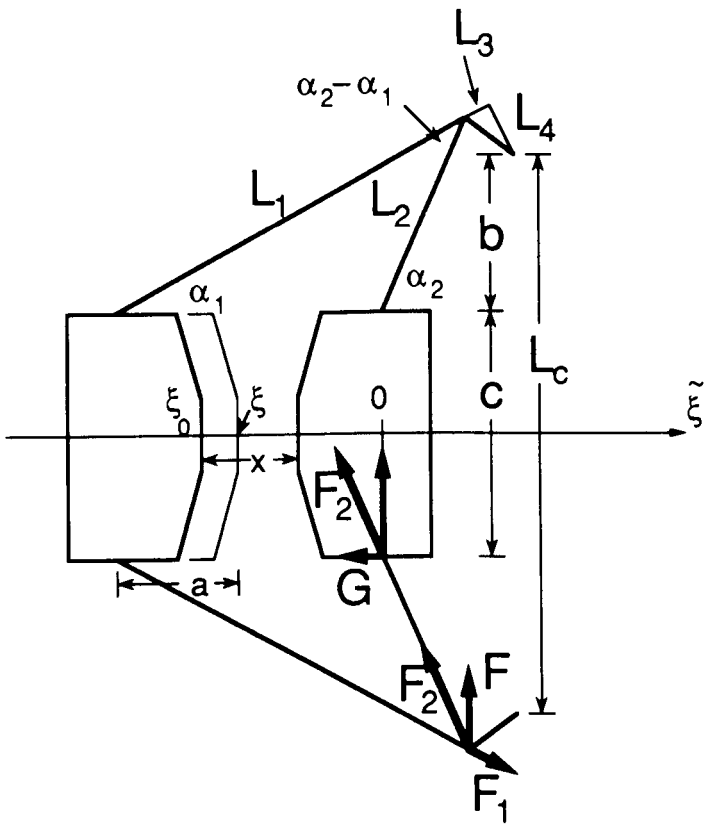

Fig. 5.7: Geometry and force diagram for the pressure cell, shown in Fig. 5.6. Turning the spindles reduces the distance L_c, which then moves the two anvils together. Assuming that the right-hand anvil is at rest, the left-hand anvil advances from its initial position ξ_o to the position ξ. The initial thickness of the gasket is x.

Analyzing now the forces we obtain from the law of sines:

$$\frac{F_2}{F} = \frac{\sin (90° + \alpha_1)}{\sin (\alpha_2 - \alpha_1)} = \frac{\cos \alpha_1}{\sin (\alpha_2 - \alpha_1)} \quad . \tag{5.115}$$

Using $G = F_2 \cos \alpha_2$ we get:

$$\frac{G}{F} = \frac{\cos\alpha_2 \cos\alpha_1}{\sin(\alpha_2 - \alpha_1)} = \frac{1}{\tan\alpha_2 - \tan\alpha_1} = \left(\frac{\sin\alpha_1}{\sqrt{\eta^2 - \sin^2\alpha_1}} - \tan\alpha_1\right)^{-1} . \qquad (5.116)$$

This equation describes the "force gain" G/F of the pressure cell. We have ignored the small lever action due to L_3 and L_4. This gain only depends on α_1 and η. G/F should always be greater than one which gives rise to a maximum angle $\alpha_{1,max}$ beyond which the gain is less than one. For $\eta = 40/63$ we obtain $\alpha_{1,max} = 32.9°$.

The force gain G/F increases with the ratio η. However, with increasing η the maximum possible displacement becomes smaller. Also, for a given length of the cell body the bracket and strut will have to become rather long for a bigger η-value. $\eta = 40/63$ is a compromise in this respect. It can be seen from Eq. (5.116) that for $\alpha_1 \to 0$ the force gain increases to a very large number (∞, theoretically).

The diameter of the piston is 45 mm. The pressure cell is designed to produce 100 kbar when the anvil-tip diameter is 4 mm. From this we can calculate the total force 2 G on the piston as:

$$2\,G = 100\,\text{kbar} \cdot (2\,\text{mm})^2 \cdot \pi = 126\,\text{kN} \quad \Rightarrow \quad G = 63\,\text{kN} . \qquad (5.117)$$

To be safe the pressure cell is designed for G = 100 kN . Using $G = \sigma A$ we could calculate the cross-sectional area A of brackets and struts required for a given tensile stress σ. This, however, does not yield an actual design criterion because the effects due to bending are much more pronounced than those due to tensile or compressive stress. The top plate as well as the two brackets are the members of the pressure cell that bend most easily. As an example we mention here an equation that approximately describes the bending of the bracket. From Fig. 5.7 we see that the force F_1 acts parallel to the bracket but displaced by a distance s giving rise to a torque that flexes the brackets slightly outward when the cell is pressurized. Following for example Ref. 173 we obtain for the deflection δ in the middle of the bracket (at $L_1/2$) with respect to either end:

$$\delta = \frac{3}{2} \cdot \frac{L_1^2 F_1 s}{E w t^3} . \qquad (5.118)$$

Here E, w, and t are Young's modulus, the width and the thickness of the bracket. F_1, the force

acting on the bracket, is obtained from $F_1 = F \cos \alpha_2 / \sin (\alpha_2 - \alpha_1)$. The displacement s will be equal to the thickness, hence $s = t$. Young's modulus for the maraging steel used here is $E_{ms} = 1.86$ Mbar ($27.0 \cdot 10^6$ psi) [168]. Specifying δ then yields values for the product $w\, t^2$. We chose $w = 57.15$ mm (2.25") and $t = 9.525$ mm (3/8") . With these specifications the brackets still visibly bend but this is necessary to provide a "spring action" so that a given pressure is maintained. This will also ensure that the pressure changes smoothly. Like the brackets the top plate, too, acts in this way.

The two brackets are pulled together by the action of two gear-set spindles turning in opposite directions, which requires right- and left-hand threads. In the design of this mechanism several points had to be considered. First the spindle diameter had to be decided upon. Using a modulus of rigidity for maraging steel of 0.71 Mbar ($10.3 \cdot 10^6$ psi) [168], it was estimated that a 5/16" UNF fine thread with 24 threads per inch would result in a tolerable torsion of approximately 0.014°/mm. Next the spindle length engaged in the threads of the two bolts was determined. Following an example in Ref. 174, p. 298, it was found that a bolt diameter of 3/4" would be safe. The cell is designed such that in the case of a thread seizure the two spindles can be cut apart and removed easily together with the bolts. For a screw thread with only one thread start one can show that the torque T corresponding to an axial force F_a is given by:

$$T = \frac{F_a}{2\,\pi\,n\,\varepsilon} \quad ; \qquad 0 < \varepsilon < 1 \ . \tag{5.119}$$

$n = 24/25.4$ mm is the number of threads per unit length and ε is the efficiency of the screw thread. ε takes care of friction in the thread and a practical value is $\varepsilon \cong 0.5$.

We can use Eq.(5.119) to calculate the necessary torque T for an applied pressure p_{ext}. Referring to Fig. 5.7, the axial force on the spindles is $F_a = 2\,F$, where the factor of two results because there are two threads per spindle. The fact that there are two spindles does not matter because we only calculate the torque required for one spindle driving the other. Using $p_{ext} = 2\,G/A$ for the external pressure we get:

$$T = \frac{F_a}{2\,\pi\,n\,\varepsilon} = \frac{2\,F}{2\,\pi\,n\,\varepsilon} = \frac{1}{2\,\pi\,n\,\varepsilon}\,\frac{2\,F}{2\,G}\,\frac{2\,G}{A}\,A = \frac{p_{ext}\,A}{2\,\pi\,n\,\varepsilon}\,\frac{F}{G} \ . \tag{5.120}$$

Using F/G from Eq. (5.116) we obtain:

$$T = \frac{p_{ext}\, A}{2\,\pi\, n\, \varepsilon}\left(\tan\alpha_2 - \tan\alpha_1\right) = \frac{p_{ext}\, A}{2\,\pi\, n\, \varepsilon}\left(\frac{\sin\alpha_1}{\sqrt{\eta^2 - \sin^2\alpha_1}} - \tan\alpha_1\right) . \qquad (5.121)$$

We see that the torque is proportional to the force applied to the area A of the anvil tips and inversely proportional to the number n of threads per unit length. The torque increases with the angle α_1.

In order to operate the pressure cell efficiently it is recommended that we make use of the maximum force gain. This will make compression easiest. The maximum force gain is achieved by starting out with the pressure cell opened by the correct amount. Then, after the two brackets are fully closed the gasket is just fully compressed.

To derive the necessary equations we begin with Eq. (5.113), which determines the position of the left-hand anvil tip as a function of angle α_1. We start compressing the gasket and sample at the angle $\alpha_{1,o}$. After complete compression the final angle is α_1. This can be achieved by properly positioning the right-hand anvil tip by means of the backing screw on the very right. We will briefly discuss the case in which the final angle becomes zero. Assuming now $\alpha_1 = 0°$ at the end we calculate the final position ξ of the left-hand anvil tip from Eq. (5.113). We get:

$$\frac{\xi}{L_1} = \frac{a}{L_1} + \eta - 1 . \qquad (5.122)$$

The angle at the beginning of the compression, when the left-hand anvil tip is at ξ_o, is $\alpha_{1,o}$ according to Eq. (5.113). Assuming that we intend to compress a fraction $0 \le f < 1$ of the initial thickness x of sample and gasket, we write:

$$\xi - \xi_o = f \cdot x \qquad \Rightarrow \qquad \frac{f\, x}{L_1} = \cos\alpha_{1,o} - \sqrt{\eta^2 - \sin^2\alpha_{1,o}} + \eta - 1 . \qquad (5.123)$$

From Fig. 5.7 we see that the distance L_c between the centres of the two bolts is given by:

$$L_c = 2b + c = 2\left(L_1 + L_3 + L_4 \tan\alpha_1\right)\sin\alpha_1 - \frac{2\, L_4}{\cos\alpha_1} + c$$

$$L_c = 2\left(L_1 + L_3\right)\sin\alpha_1 - 2\, L_4 \cos\alpha_1 + c . \qquad (5.124)$$

At the beginning of the compression we have $\alpha_1 = \alpha_{1,o}$ and $L_c = L_{c,o}$. Solving Eq. (5.123) for $\cos \alpha_{1,o}$ and inserting the result into Eq. (5.124) yields the length $L_{c,o}$ which has to be preset such that when $\alpha_1 = 0°$ the fraction f of the initial thickness x of sample and gasket is compressed. The initial centre-to-centre distance $L_{c,o}$ of the bolts is set by means of the end nut. $L_{c,o}$, expressed as a function of $f \cdot x$, is then:

$$L_{c,o} = c + 2\,(L_1 + L_3)\sqrt{1 - \frac{(1 - 2\,\eta\,\gamma + \gamma^2)^2}{4\,(\gamma - \eta)^2}} - 2\,L_4\,\frac{1 - 2\,\eta\,\gamma + \gamma^2}{2\,(\gamma - \eta)}\ ; \tag{5.125}$$

$$\gamma \equiv 1 + \frac{f\,x}{L_1}\ .$$

It is impractical though to measure $L_{c,o}$. Since the two bolts are not completely round but have flats one can easily measure the distance between the two flats with a vernier caliper. The distance $L_{F,o}$ between the flats is simply:

$$L_{F,o} = L_{c,o} + 16.51\ \text{mm}\ . \tag{5.126}$$

Fig. 5.8 is a plot of $L_{F,o}$ versus $f \cdot x$ according to Eqs. (5.125) and (5.126). For the lengths the following values were employed:

$L_1 = 63/16"$; $L_2 = 5/2"$; $L_3 = 15/16"$; $L_4 = 3/16"$; $c = 11/4"$.

$\eta \equiv L_2/L_1$ has the value 40/63. Values for $L_{F,o}$ read from the curve of Fig. 5.8 should be increased by some amount for safety. This insures that the arms of the pressure cell are not already closed before all the compression has taken place. In this context it is also worthwhile noting that, because there are 24 threads to the inch, each full turn of the gears changes L_c by $2 \cdot (1/24)" = (1/12)" =$ 2.1 mm .

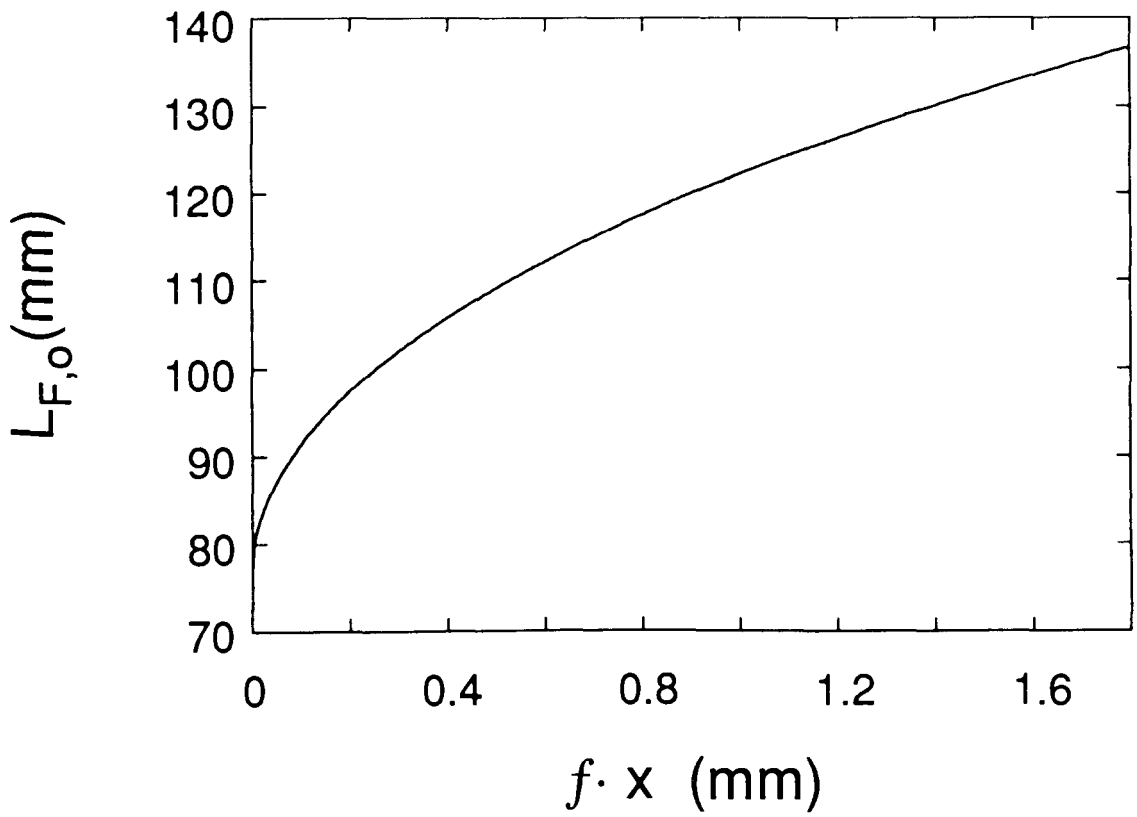

Fig. 5.8: Distance $L_{F,o}$ between the two flats that has to be set so that when the arms of the pressure cell are fully closed the amount $f \cdot x$ of the gasket is compressed.

Fig. 5.9 shows the quantity $T/(p_{ext} A)$, as obtained from Eq. (5.121), plotted versus L_F. The number of threads per inch was $n = 24/25.4$ mm and the efficiency of the thread was taken to be $\varepsilon \approx 0.5$. We see that the torque actually decreases with increasing pressure (decreasing length L_F). Contrary to Fig. 5.8 the curve shown here does not require that the cell is closed after the desired compression is obtained. In other words, the graph in Fig. 5.9 is independent of the particular starting value for L_c. This is because the thickness x of sample and gasket does not enter here.

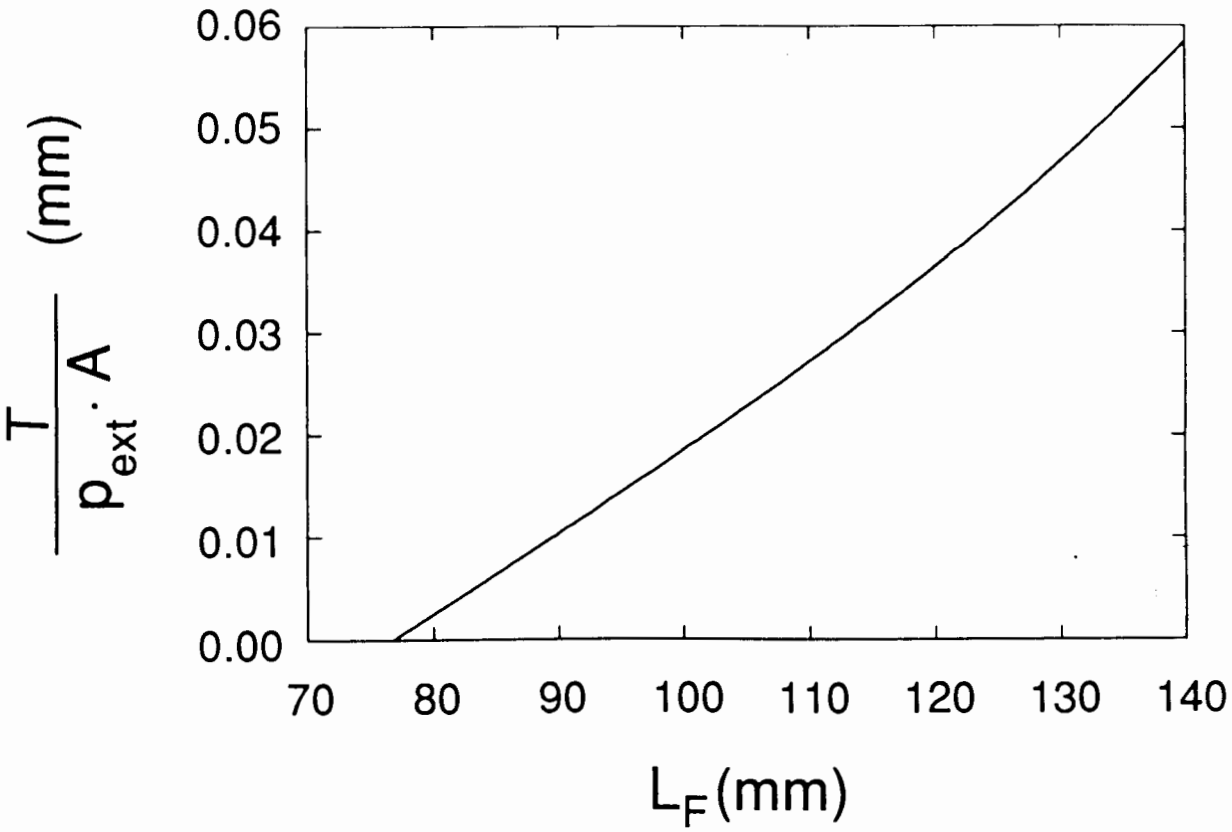

Fig. 5.9: Torque T necessary to generate the force p_{ext} A , plotted as a function of the distance L_F between the flats.

Applying torques on the spindles produces friction in the threads which should be reduced by lubrication with graphite powder or with MoS_2. This applies to the hinges as well.

We now develop a formula relating compression and pressure. Starting out from the defining equation for the (isothermal) bulk modulus we obtain for constant B_T:

$$B_T = -V \left.\frac{\partial p}{\partial V}\right|_T \quad \text{or, simplified:} \qquad B = -V\frac{dp}{dV} \ . \tag{5.127}$$

The volume contained between the two anvil tips is:

$$V = A\left(x - (\xi - \xi_o)\right) = A(x + \xi_o - \xi) \quad \Rightarrow \quad dV = -A\,d\xi \ . \tag{5.128}$$

A is the cross sectional area of the anvil tips. ξ_o is the initial position of the left-hand anvil tip in Fig. 5.7 and ξ is its position after compression. Combining the last two equations yields:

$$dp = \frac{B\,d\xi}{x + \xi_o - \xi} \quad \Rightarrow \quad \int_0^p dp' = \int_{\xi_o}^{\xi} \frac{B\,d\xi'}{x + \xi_o - \xi'}$$

$$\Rightarrow \quad p = -B \cdot \ln\left(1 - \frac{\xi - \xi_o}{x}\right) \ . \tag{5.129}$$

In the last step we have assumed that the bulk modulus is independent of volume. Considering a volume dependence, like for example $B = B_o \exp(\alpha\,\Delta V/V_o)$ with $\alpha \cong 4$ and $\Delta V > 0$ [175], one can show that the volume dependence of the bulk modulus constitutes only a second-order effect. We ignore here any volume dependence.

We can employ Eq. (5.129) to establish the relation between compression and externally applied pressure p_{ext}. To this end we consider the balance of the forces acting on sample and gasket:

$$p_{ext}\,A = p_s\,A_s + p_g\,A_g \ . \tag{5.130}$$

A_s is the cross-sectional area of the sample and A_g is the cross-sectional area of the gasket, excluding the sample and the uncompressed outer areas. p_s and p_g are sample and gasket pressures, respectively.

Introducing $$\rho \equiv \frac{A_s}{A} \tag{5.131}$$

yields: $$p_{ext} = p_s\,\rho + p_g\,(1-\rho) \ . \tag{5.132}$$

Applying Eq. (5.129) for p_s and p_g yields eventually:

$$\frac{V_o - V}{V_o} = \frac{\xi - \xi_o}{x} = \frac{f\,x}{x} = f = 1 - \exp\left(\frac{-p_{ext}}{B_s\,\rho + B_g\,(1-\rho)}\right) . \qquad (5.133)$$

f is the (positive) relative compression (see Eq. (5.123)). B_s and B_g are the (isothermal) bulk moduli of sample and gasket, respectively. Because B_s and B_g may differ p_{ext} will not be constant across the area A. We mention here that one could insert the result for f into Eq. (5.125) in order to get the corresponding length $L_{c,o}$ (or $L_{F,o}$).

We obtain further:

$$\frac{p_s}{p_{ext}} = \frac{1}{\rho + \frac{B_g}{B_s}(1-\rho)} \cong \frac{B_s}{B_g} . \qquad (5.134)$$

The second step follows from the fact that $\rho << 1$ and that usually $B_g \gtrsim B_s$. Thus, if the bulk modulus of the gasket is much bigger than that of the sample the sample will only experience a small pressure. Conversely, if B_g were much smaller than B_s then the gasket would not contain the sample. Ideally, one would like to have B_g a little bit larger than B_s.

When performing the experiment it is difficult to ascertain by how much the pressure has increased after turning the spindle by, say, a quarter turn. It has been attempted recently to monitor the force acting on the piston by using electrical-resistance strain gauges. In this way it may be possible to get an idea of the approximate pressure. Ideally, one would obtain something like a calibration curve to estimate the pressure. This work is not yet completed. One strain gauge each is attached to the two struts. The 120 Ω single-element strain gauges are attached to the struts because the struts do not bend as much as the brackets thus producing a more reliable measurement. Under strain the resistance of the strain gauges changes by a very small amount, typically a few mΩ. These small changes can be measured conveniently with a Wheatstone-bridge. Following a recommendation in Ref. 176, p. 232, the circuit is designed with a resistance ratio in either arm of the bridge of approximately 9:1. This yields a reasonable circuit sensitivity. A reference gauge, attached to the same material and at the same temperature as the active gauges, must be included in order to balance temperature effects. Since only small voltage changes (~mV) are measured it is also necessary to use a regulated voltage source (~20 V).

The Wheatstone bridge will be balanced only in the strain-free state. The small nonlinearity, produced when the gauges are under strain, is ignored here. In careful work one will take this nonlinearity into account or re-balance the bridge each time.

It may perhaps be possible to estimate quickly the pressure through the relative volume change determined from one measured dataset according to the method presented in Section 6.14.

5.10 Liquid-Nitrogen Cryostat

The cryostat designed to cool the pressure cell to liquid-nitrogen temperature is made out of brass and consists of two chambers: One chamber houses the pressure cell and the other is the reservoir for the liquid nitrogen. It would be ideal if the reservoir would connect to both sides of the pressure-cell chamber. However, since beamline IV-1 is a side station, the centre of the x-ray beam is only 50 mm away from the hutch wall. Hence the chamber housing the cell can only be cooled from one side. For liquid-nitrogen temperatures this does not pose a severe problem though. This cryostat is not evacuated. It therefore boils off quite a bit of liquid nitrogen (~5 l/hr). Because of the large thermal mass of cryostat and pressure cell it takes about two hours to achieve liquid-nitrogen temperature. This implies that the temperature, which was monitored by thermocouples, will only rise very slowly.

To prevent icing up of the whole device the cryostat was covered with a few layers of aluminized Mylar and it was enclosed in highly insulating "blue" styrofoam. The cryostat has a feedthrough for a wrench in order to adjust the pressure. When not in use the wrench is partly retracted in order to reduce heat losses.

5.11 Performing the Experiment

The setup for an x-ray absorption experiment in transmission mode is shown in the following figure.

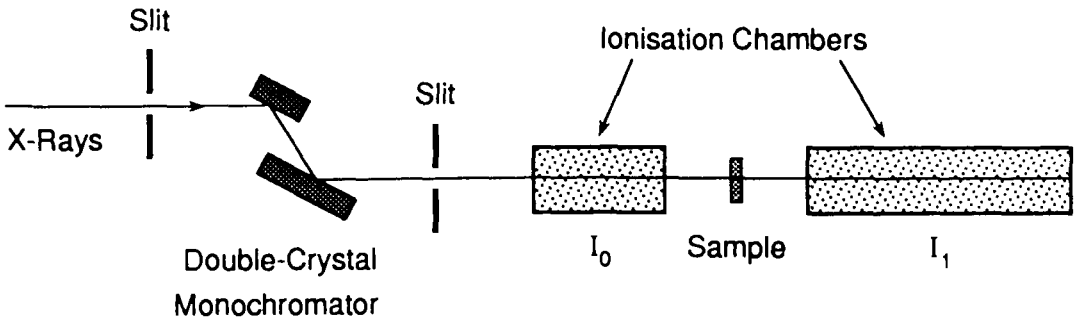

Fig. 5.10: Schematic setup for an x-ray absorption experiment in transmission mode.

In the figure an x-ray beam from the synchrotron source is incident onto a double-crystal monochromator. A narrow entrance slit is placed in front of the monochromator in order to reduce the angular spread of the incident x-ray beam. The x-ray optics is completed with the exit slit in front of the first ionization chamber which can be used to match the cross section of the beam to that of the sample. The monochromatic x-ray beam enters the first ionization chamber, passes through the sample, and enters the second ionization chamber. The ionization chambers measure the intensities I_0 and I_1 from which the absorption is obtained through $\ln I_0/I_1$ (Section 5.4).

As explained in Section 5.2 the monochromator is positioned by means of a stepping motor. The number ζ of monchromator steps depends linearly on the Bragg angle θ (in degrees):

$$\zeta = (\text{steps/degree}) \cdot \theta + \zeta_o \ . \qquad (5.135)$$

ζ_o is an offset which is frequently set to zero. Usually the Cu K edge is used for calibration. We set the energy of the minimum, that occurs halfway up the edge, to $E_{Cu} = 8982.7$ eV . At the Cu K edge we have:

$$\zeta_{Cu} = (\text{steps/degree}) \cdot \theta_{Cu} + \zeta_o \quad ; \qquad \theta_{Cu} = \arcsin\frac{E_{min}}{E_{Cu}} \quad . \tag{5.136}$$

For a Si (220) monochromator with 4000 steps per degree we get $\theta_{Cu} = 21.064°$. If we set $\zeta_{Cu} = 200000$ we obtain $\zeta_o = 115744$. If we set $\zeta_o = 0$ we obtain $\zeta_{Cu} = 84256$.

If it happens that the monochromator is miscalibrated by a number $\Delta\zeta$ of steps then a change ΔE in the energy calibration results. The amount ΔE of this miscalibration increases with energy. It is obtained by combining Eqs. (5.19), (5.20), and (5.21) of Section 5.2:

$$\Delta E = \frac{\pi}{180} \cdot \frac{E_{min}}{4000} \cdot \left[\left(\frac{E}{E_{min}}\right)^2 - \frac{1}{2}\right] \Delta\zeta \; . \tag{5.137}$$

If at the Cu K edge a Si (220) monochromator is miscalibrated by 1 step (= 1/4000 of a degree) then the energy shift at the Cu K edge is 0.102 eV. At the K edge of Y (17038 eV), say, the energy shift already amounts to 0.385 eV. The effects of miscalibration are worse for Bragg reflections with small Miller indices.

After the monochromator is calibrated the table carrying the experimental setup is positioned so that the centre of the x-ray beam passes through the two ionization chambers. Then table and monochromator are linked by computer so that they move jointly when a new x-ray energy is selected. This linkage is necessary because the output beam of the two-crystal monochromator moves vertically when another energy (or Bragg angle) is selected.

Finally, the two ion chambers have to be flushed with counting gases. Frequently the same gases are used in both chambers in order that they have the same characteristics. This reduces nonlinear behaviour.

After this setup has been done the sample is placed between the two ion chambers and the actual experiment can begin. Usually three EXAFS scans are taken for later averaging. Then another sample is put in the beam or, in pressure experiments, another pressure is selected. The software controlling the experiment was written by Andrew Seary and it allows one to perform some on-line data analysis in order to determine whether the quality of the data is good enough for EXAFS analysis. In pressure scans it is necessary to perform some EXAFS data analysis, for example plotting

the magnitude of the Fourier transform, in order to find out whether and by how much the pressure has been increased by turning the wrench. In the experiments on the mixed-valence compounds, SmS and SmSe, pressure changes are confirmed by the change in the valence, readily visible from the Sm L_{III} or Sm L_{II} absorption edge. It is planned to monitor changes in pressure by strain gauges attached to the pressure cell. It is also possible to estimate the pressure quickly by applying the method explained in Section 6.14 of the next chapter.

Chapter 6: **Data Analysis**

6.1 Averaging Datasets

In EXAFS spectroscopy it is common to measure a sample three or more times and then average the resulting datasets. Compared to a procedure where one would measure just one dataset for a correspondingly longer time, this method has the advantage that if the x-ray beam is suddenly switched off one has at least some complete datasets. Also, all experimental parameters, like for example beam current, have to be stable for only the approximately 20 minutes that it takes to complete one scan.

The question then arises as to how the datasets are to be averaged. Let us assume that three scans of one sample had been taken and let F_0, G_0, and H_0 be their respective signals of the I_0 chamber and F_1, G_1, and H_1 the signals of the I_1 chamber. We will average only datasets that are on exactly the same x-axis grid with the same number N of data points. Only those data sets will be averaged that were taken with the same type of monochromator crystals, i.e. (111) or (220). This is because different monochromator crystals have a different spectrum of harmonics (see Section 5.2). There are then two possibilities to obtain the averaged I_0/I_1 spectrum for any data point i:

a) Adding the individual signals:

In this case I_0/I_1 is obtained by dividing the sum of all I_0 signals by the sum of all I_1 signals:

$$\left.\frac{I_0}{I_1}\right|_i = \frac{F_{0,i} + G_{0,i} + H_{0,i}}{F_{1,i} + G_{1,i} + H_{1,i}} \qquad (6.1)$$

with $$I_{0,i} \equiv \frac{1}{3}\left(F_{0,i} + G_{0,i} + H_{0,i}\right)$$

and $$I_{1,i} \equiv \frac{1}{3}\left(F_{1,i} + G_{1,i} + H_{1,i}\right) .$$

b) Averaging the ratios:

Here I_0/I_1 is obtained by averaging the individual I_0/I_1 signals:

$$\left.\frac{I_0}{I_1}\right|_i = \frac{1}{3}\left(\frac{F_{0,i}}{F_{1,i}} + \frac{G_{0,i}}{G_{1,i}} + \frac{H_{0,i}}{H_{1,i}}\right) . \qquad (6.2)$$

Eqs. (6.1) and (6.2) are not quite correct yet because the gain settings on the current-to-voltage converters have not yet been taken into account. The gain settings may differ from scan to scan. Similarly, the entrance slit, or some other aperture, may have been changed in between scans. Thus the data of various scans may appear scaled with respect to the first scan, say, and this scaling has to be accounted for when the averaging is done. The dataset containing G_0 and G_1 and the one containing H_0 and H_1 are referenced to the first, which contains F_0 and F_1. We therefore define scaling factors as follows:

$$g_0 \equiv \frac{1}{N} \cdot \sum_{i=1}^{N} \frac{G_{0,i}}{F_{0,i}} \; ; \qquad g_1 \equiv \frac{1}{N} \cdot \sum_{i=1}^{N} \frac{G_{1,i}}{F_{1,i}} \; ; \qquad g_{01} \equiv \frac{1}{N} \cdot \sum_{i=1}^{N} \frac{G_{0,i}}{G_{1,i}} \Big/ \frac{F_{0,i}}{F_{1,i}}$$

and similarly: (6.3)

$$h_0 \equiv \frac{1}{N} \cdot \sum_{i=1}^{N} \frac{H_{0,i}}{F_{0,i}} \; ; \qquad h_1 \equiv \frac{1}{N} \cdot \sum_{i=1}^{N} \frac{H_{1,i}}{F_{1,i}} \; ; \qquad h_{01} \equiv \frac{1}{N} \cdot \sum_{i=1}^{N} \frac{H_{0,i}}{H_{1,i}} \Big/ \frac{F_{0,i}}{F_{1,i}} \; .$$

Hence Eqs. (6.1) and (6.2) will be rewritten as:

a) $$\left.\frac{I_0}{I_1}\right|_i = \frac{F_{0,i} + \frac{1}{g_0} G_{0,i} + \frac{1}{h_0} H_{0,i}}{F_{1,i} + \frac{1}{g_1} G_{1,i} + \frac{1}{h_1} H_{1,i}} \qquad (6.4)$$

with $$I_{0,i} \equiv \frac{1}{3}\left(F_{0,i} + \frac{1}{g_0} G_{0,i} + \frac{1}{h_0} H_{0,i}\right) \qquad (6.5)$$

and $$I_{1,i} \equiv \frac{1}{3}\left(F_{1,i} + \frac{1}{g_1} G_{1,i} + \frac{1}{h_1} H_{1,i}\right) \; ; \qquad (6.6)$$

b) $$\left.\frac{I_0}{I_1}\right|_i = \frac{1}{3}\left(\frac{F_{0,i}}{F_{1,i}} + \frac{1}{g_{01}} \frac{G_{0,i}}{G_{1,i}} + \frac{1}{h_{01}} \frac{H_{0,i}}{H_{1,i}}\right) \; . \qquad (6.7)$$

If there were only one scan or if all measurements were exactly the same then, of course, there would not be any difference between the two methods. But there are differences from scan to scan and accordingly one may determine standard deviations $\delta I_{0,i}$, $\delta I_{1,i}$, and $\delta(I_0/I_1)_i$:

a)

$$\delta I_{0,i} \equiv \sqrt{\frac{1}{3}\left[\left(F_{0,i} - I_{0,i}\right)^2 + \left(\frac{1}{g_0} G_{0,i} - I_{0,i}\right)^2 + \left(\frac{1}{h_0} H_{0,i} - I_{0,i}\right)^2\right]} \quad , \tag{6.8}$$

$$\delta I_{1,i} \equiv \sqrt{\frac{1}{3}\left[\left(F_{1,i} - I_{1,i}\right)^2 + \left(\frac{1}{g_1} G_{1,i} - I_{1,i}\right)^2 + \left(\frac{1}{h_1} H_{1,i} - I_{1,i}\right)^2\right]} \tag{6.9}$$

where $I_{0,i}$ and $I_{1,i}$ are given by Eqs. (6.5) and (6.6).

b)

$$\delta(I_0/I_1)_i \equiv \sqrt{\frac{1}{3}\left[\left(\frac{F_{0,i}}{F_{1,i}} - \left.\frac{I_0}{I_1}\right|_i\right)^2 + \left(\frac{1}{g_{01}} \frac{G_{0,i}}{G_{1,i}} - \left.\frac{I_0}{I_1}\right|_i\right)^2 + \left(\frac{1}{h_{01}} \frac{H_{0,i}}{H_{1,i}} - \left.\frac{I_0}{I_1}\right|_i\right)^2\right]} \tag{6.10}$$

where $\left.\frac{I_0}{I_1}\right|_i$ is given by Eq. (6.7).

a) With the first method the relative error of the signal is:

$$\frac{\delta(I_0/I_1)_i}{(I_0/I_1)_i} = \frac{\delta I_{0,i}}{I_{0,i}} + \frac{\delta I_{1,i}}{I_{1,i}} \tag{6.11}$$

where $I_{0,i}$, $I_{1,i}$ and $\delta I_{0,i}$ and $\delta I_{1,i}$ are given by Eqs. (6.5), (6.6) and Eqs. (6.8), (6.9).

b) In the second case the relative error $\frac{\delta(I_0/I_1)_i}{(I_0/I_1)_i}$ is directly given by Eqs. (6.7) and (6.10).

If all errors are statistical in nature then both methods will yield the same relative error for each data point. It turned out, however, that relative errors are always smaller in case b). This is so because

fluctuations of the I_0 and I_1 signals correlate and cancel out to some extent when ratios are formed, as in case b). As a result, all datasets are averaged according to procedure b), Eqs. (6.7) and (6.10).

6.2 Step Number-to-Energy Conversion

So far the abscissa of the data is in step numbers, ζ, that is the number of stepping motor steps needed for positioning the monochromator. As already explained in Section 5.11, this scale is proportional to the Bragg angle θ:

$$\zeta = (\text{steps/degree}) \cdot \theta + \zeta_o \ .$$

ζ_o is an arbitrary offset. Writing this equation down for the Cu K edge we get:

$$\zeta_{Cu} = (\text{steps/degree}) \cdot \theta_{Cu} + \zeta_o \ .$$

Taking differences we obtain:

$$\theta - \theta_{Cu} = \frac{\zeta - \zeta_{Cu}}{(\text{steps/degree})} \equiv \beta \ . \qquad (6.12)$$

After a bit of algebra we obtain:

$$E = \left[\frac{\cos \beta}{E_{Cu}} + (\sin \beta) \sqrt{E_{min}^{-2} - E_{Cu}^{-2}} \right]^{-1} \ . \qquad (6.13)$$

Here we have used the following relations:

$$E_{min} \equiv \frac{h\ c}{2\ d_{hkl}} \ ; \qquad E_{Cu} \equiv \frac{E_{min}}{\sin \theta_{Cu}} \equiv 8982.7 \text{ eV} \ ; \qquad E = \frac{E_{min}}{\sin \theta} \ . \qquad (6.14)$$

The calibration value of 8982.7 eV for E_{Cu} refers to the small dip that occurs in the absorption spectrum halfway up the edge jump. In order to determine β, the number of steps per degree must be known as well as the (arbitrary) step number ζ_{Cu} at the Cu K edge. (Of course, ζ_{Cu} must be chosen such that ζ never becomes negative.)

Eq. (6.13) thus describes how the x-ray energy E is obtained from the number of steps, ζ.

6.3 Normalizing EXAFS Datasets

This section describes how $\chi(k)$ is obtained from the averaged datasets.

The first step is the subtraction of a pre-edge background. This means that we fit a function to that part of the absorption spectrum which is at a lower energy than the energy of the absorption edge. The fitting function of the fit to the pre-edge part of the absorption spectrum is then extended over the complete spectrum and then subtracted from the spectrum. Now the pre-edge region hovers around zero. The fitting function is a slightly modified Victoreen fit [140]:

$$\ln\left(\frac{I_0}{I_1}\right) = A_0 + \frac{A_3}{E^3} + \frac{A_4}{E^4} \quad . \tag{6.15}$$

A_0 vanishes for a Victoreen fit. Here, however, it is necessary to include this parameter in order to take care of the fact that due to scaling factors contained in I_0 and/or I_1 the measured spectrum may be shifted by a constant value. It is possible, actually, that $\ln(I_0/I_1)$ is negative. This fact can only be accounted for by the extra fit parameter A_0.

Including the remaining parameters A_3 and A_4 would produce a three-parameter fit. The pre-edge background is, however, rather featureless and resembles more or less a straight line. Thus one can only afford two fit parameters. Consequently A_4 is set to zero in the present work. If A_4 were to vary then there would be strong correlations among the three parameters. The fitting function for the pre-edge background is therefore:

$$\ln\left(\frac{I_0}{I_1}\right) = A_0 + \frac{A_3}{E^3} \quad . \tag{6.16}$$

The following two figures illustrate the pre-edge fitting.

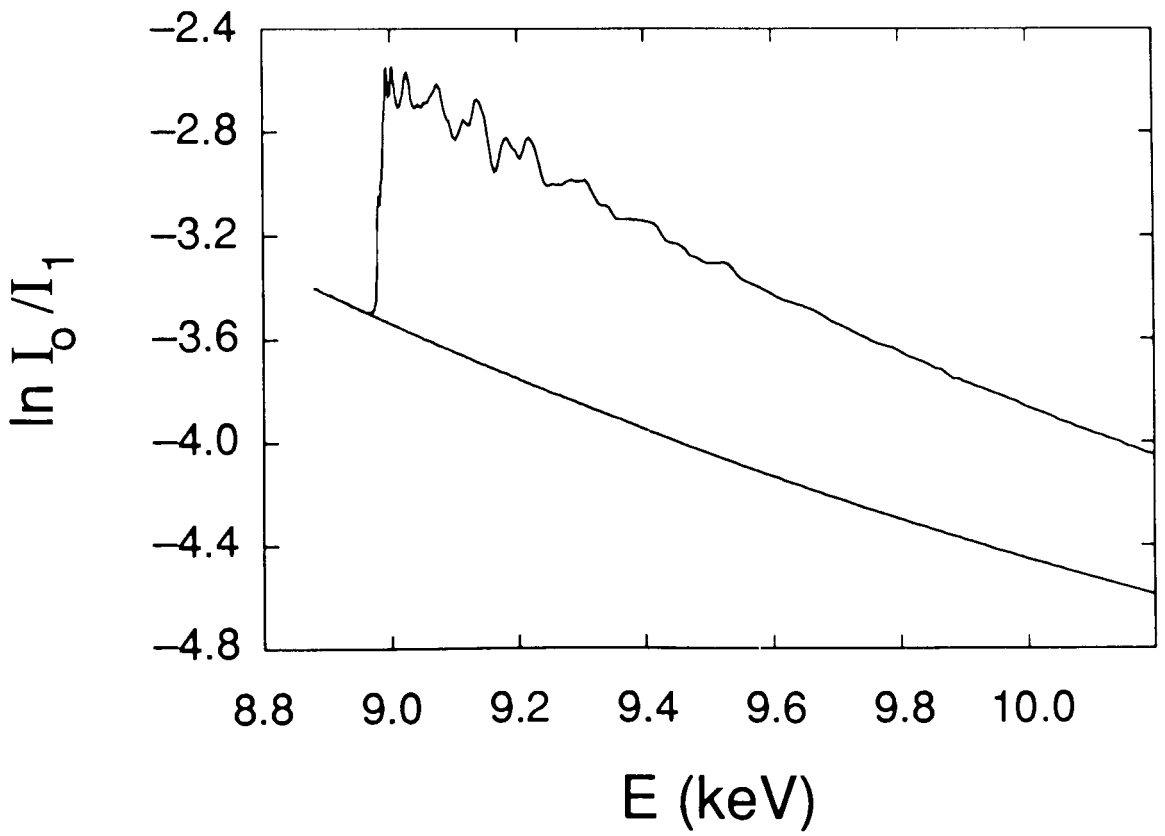

Fig. 6.1: Absorption spectrum of the Cu K edge in Cu metal at 48.4 kbar and at 77K. The data, which is an average of two scans, and the pre-edge Victoreen fit according to Eq. (6.16) are shown. $\ln(I_0/I_1)$ is negative due to scaling of I_0 and/or I_1. The pre-edge fit is over the interval from 8890.4 eV to 8961.73 eV.

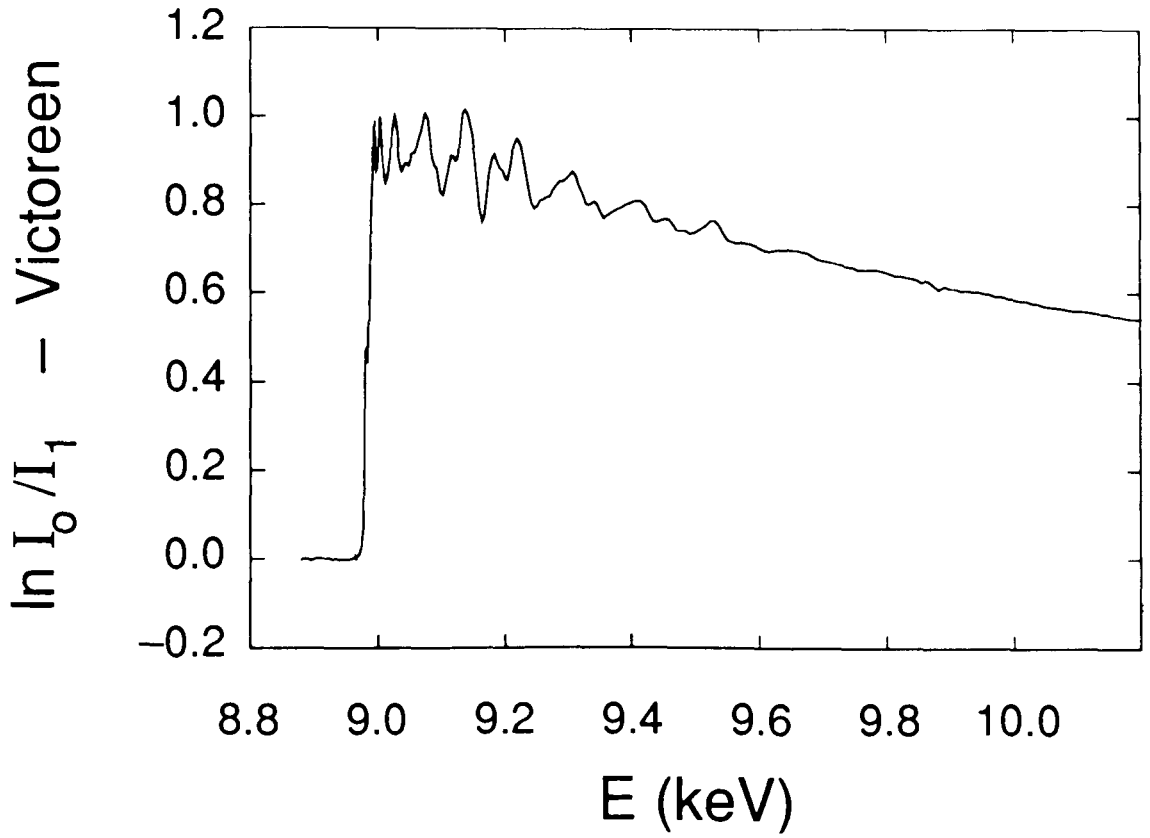

Fig. 6.2: Absorption spectrum of the Cu K edge in Cu metal at 48.4 kbar and at 77K after subtraction of the Victoreen fit shown in the previous figure.

After the Victoreen fit is subtracted from the spectrum the energy scale must be converted to a k-scale. This applies only to that part of the spectrum that is above the absorption edge. Therefore the absorption edge has to be located first. This is done conventionally by chosing the first inflection point of the edge jump. This *inflection point* is easily identified as the position of the first maximum of the derivative of the edge jump. This is illustrated in the following figure:

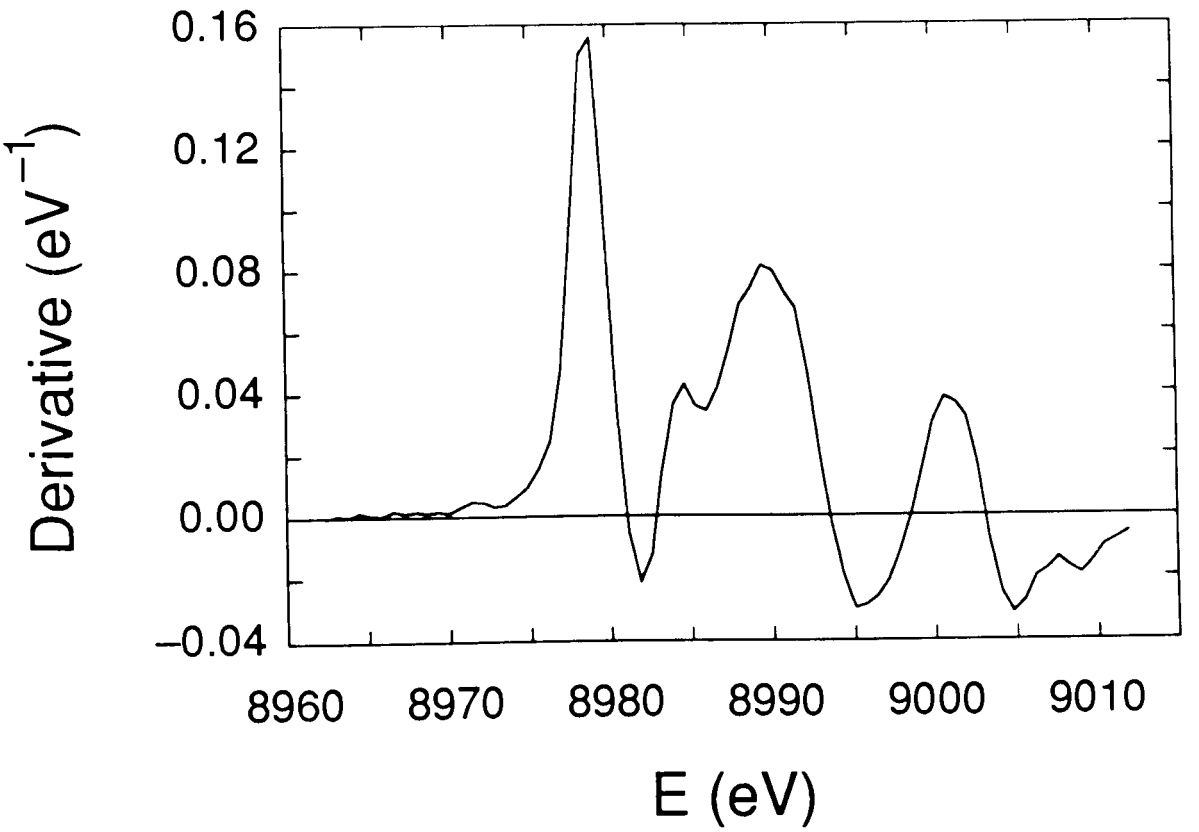

Fig. 6.3: Energy derivative of the spectrum shown in Fig. 6.2. The first peak defines the position of the absorption edge. Here it is located at 8979.05 eV, according to the monochromator calibration employed.

The conversion to the k-scale is then performed according to:

$$k = \sqrt{\frac{E - E_{Edge}}{\gamma}} \quad . \tag{6.17}$$

$\gamma = \frac{1}{2m_e}\left(\frac{h}{2\pi}\right)^2 \cong 3.81$ eV Å^2 is the constant introduced in Eq. (2.28).

Now we have to estimate the size of the absorption jump. This jump is simply a number that we need to know in order to obtain a $\chi(k)$ that is properly normalized. The EXAFS signal is proportional to the size of this edge jump. We can obtain the step size by fitting a straight line to the spectrum from $k \cong 2$ Å^{-1} to $k \cong 7$ Å^{-1} . (The fit may also be performed in energy space.) The value of this straight line at $k = 0$ (or $E = E_{Edge}$) yields the step size, which will be used later on. Fig. 6.4 illustrates this.

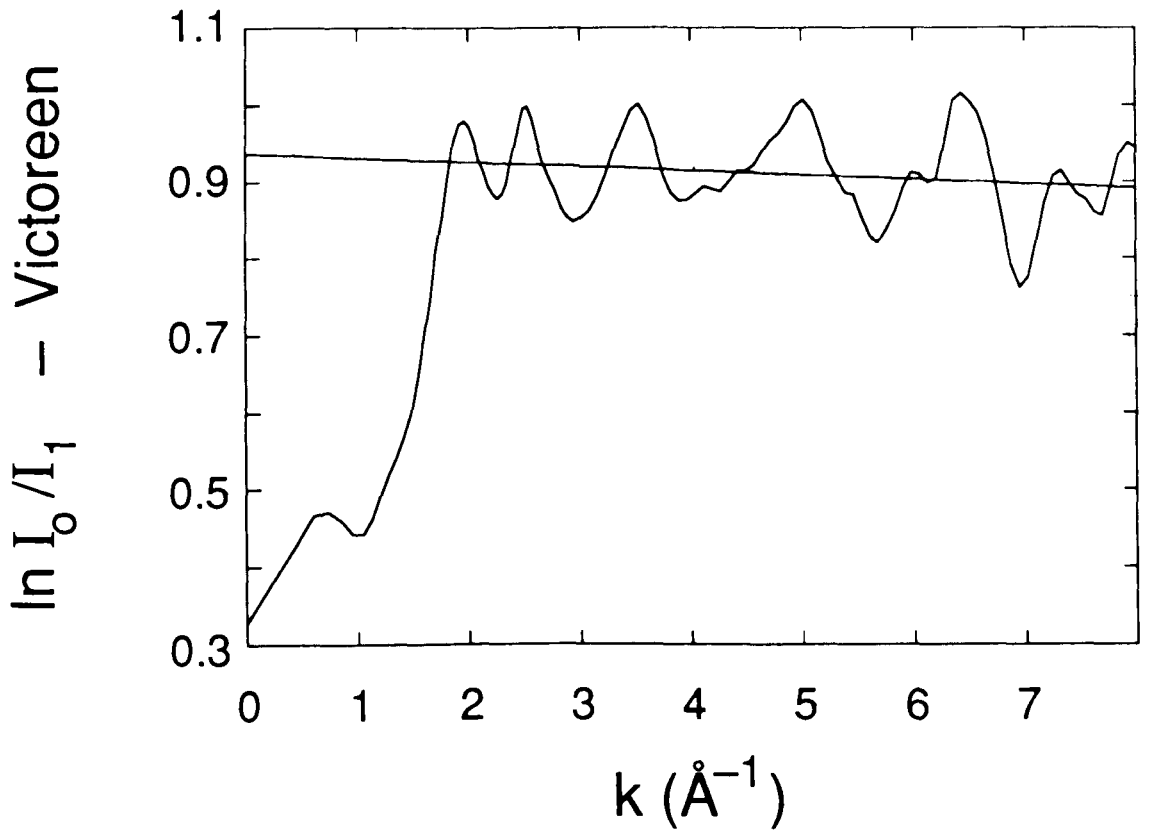

Fig. 6.4: Straight-line fit to estimate the stepsize at the absorption edge, i.e. at $k = 0$. Shown is part of the data of Fig. 6.2 after conversion to k-space. In this example the step size is 0.937.

Eventually we want to compute the Fourier transform of $\chi(k)$. This will be done using the FFT which requires a uniform grid in k-space. We therefore linearly interpolate the data in its present form onto a grid consisting of uniformly-spaced k-values. The number of points for this new grid is equal to the number of points of the old, non-uniform, grid. (Andrew Seary's data-aquisition software takes the E-to-k conversion into account by positioning the monochromator such that the data points are

as close as possible to being on a uniform grid. In this way when the energy scale is converted to a k-scale the interpolation error is minimized.) Fig. 6.5 shows the k-space data.

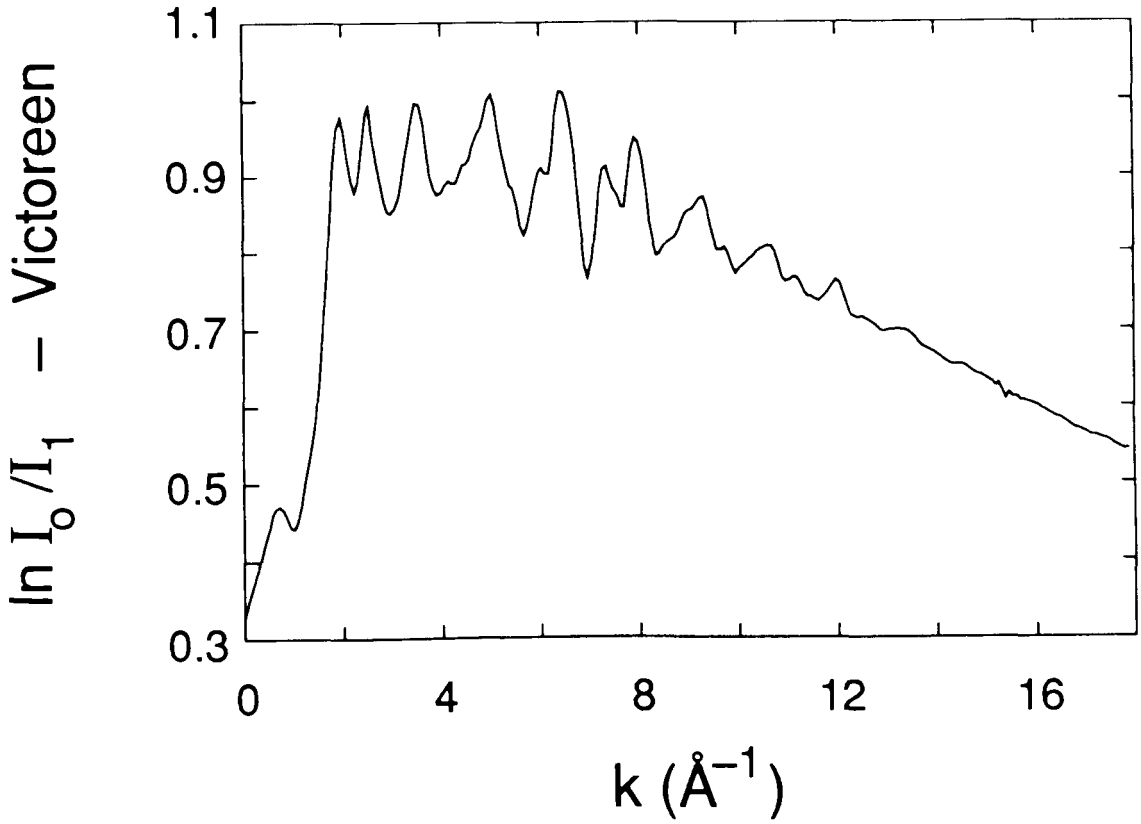

Fig. 6.5: Full spectrum of Cu after conversion to k-space. At ~15 Å^{-1} we notice a glitch due to multiple-diffraction effects in the Si (111) single crystals of the Bragg monochromator (Section 5.2).

The next step is the fitting of a background to the data. The fit will not start immediately at E_{Edge} because of edge features. Instead it will begin at $k \sim 2$ Å^{-1}. The fit interval frequently extends to the last data point. Due to various effects the background frequently exhibits slow variations that do not result from the actual absorption coefficient. It is therefore difficult to prescribe a certain functional form for this type of background. Various methods are in use, like for example polynomial or spline fits [177], and each method has its advantages and drawbacks. In the present work we will use a background that results from the sequential smoothing of the data. This type of background has the advantage of being rather flexible but still easy to apply. The data is smoothed anywhere from 100 to

600 times depending on how complicated the background is. Each smoothing pass is calculated according to the three-point formula [178]:

$$y_{new,i} \equiv \frac{1}{4}\left(y_{old,i-1} + 2\, y_{old,i} + y_{old,i+1}\right) . \qquad (6.18)$$

The normalization factor of 1/4 is necessary so that a constant function would remain unchanged after smoothing. Although not explicitly stated, smoothing assumes a uniform grid. Then Eq. (6.18) could be called a "triangular" smoothing function because the midpoint is weighted twice as high as the neighbours.

With the above formula there are problems with the endpoints. This means that $y_{new,1}$ is not defined because $y_{old,0}$ does not exist and $y_{new,N}$ is not defined because there is no $y_{old,N+1}$ to apply Eq. (6.18). These end-effect problems are common with smoothing functions. According to Ref. 178 the first and last points are therefore defined as

$$y_{new,1} \equiv \frac{1}{4}\left(3\, y_{old,1} + y_{old,2}\right) \quad \text{and} \quad y_{new,N} \equiv \frac{1}{4}\left(y_{old,N-1} + 3\, y_{old,N}\right) .$$

This prescription leaves the endpoints variable. This, however, is not useful for background subtraction because of the application of very many smoothing passes which cause this end effect to migrate inwards from the ends. Thus, after several smoothing passes the background may become "disconnected" from the actual data. One way of fixing this problem is by setting $y_{new,1} \equiv y_{old,1}$ and $y_{new,N} \equiv y_{old,N}$ after each smoothing pass. This procedure, however, produces a $\chi(k)$ whose endpoints are tied to zero.

In order to avoid all of these difficulties, we make the endpoints variables in a two-parameter least-squares fit that fits the background to the data for a given number of passes. Because the endpoint values do not affect the inner part of the background, only 20%, say, of the data range at either end have to be considered in this fit. (This also increases the sensitivity of the fit.) We may also apply a weighting function of the form k^p, where p is some number, for example $p=1$. Thus we have solved our problem by optimizing the endpoint values of the background by fitting to the data.

There is so far no way of precisely determining the number of smoothing passes that is required. One may, however, judge whether the background is correct by checking whether the area of $k\chi(k)$ above the zero line is approximately equal to the area below. In addition, a formula is given in Appendix D to estimate the required number of passes. Also by examining the magnitude of the Fourier transform in the small-R region, it is possible to observe the extent to which the background subtraction affects the Fourier components that contribute to the nearest-neighbour coordination shell.

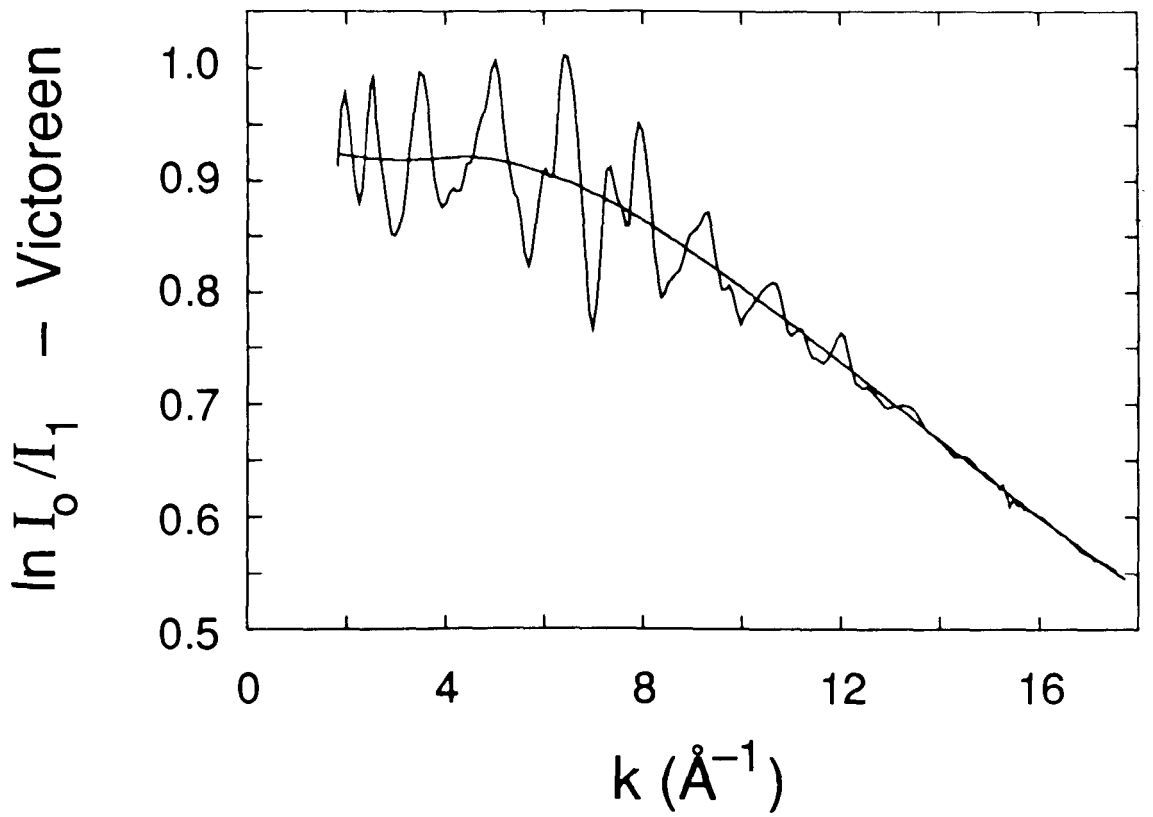

Fig. 6.6: Same data as in Fig. 6.5 but with a background extending from 1.82 Å^{-1} to 17.73 Å^{-1} overlayed. The background was determined by smoothing with 300 passes as described above.

The background-subtraction method described here has been employed for all datasets. There are still some flaws with it which have not yet been solved. It occurs frequently that the number of smoothing passes that are required for the high-k part of the background is much smaller than the

number of passes needed for the low-k part. This can presently not be taken care of since the smoothing passes are always calculated for the entire spectrum. However, this is only a minor problem. The k χ(k) and their Fourier transforms obtained by polynomial background removal were practically identical to those obtained by the smoothing procedure.

It is important to keep in mind that the background extends over all of R-space. If this were not the case then there would be coordination shells that could simply be filtered out without previous background removal because there is no background component for this shell. Unfortunately, it is not possible to circumvent a proper background-subtraction procedure.

Finally we have obtained a χ(k) given by:

$$\chi(k) = \frac{y - y_{bkg}}{step} \quad , \tag{6.19}$$

where y, y_{bkg}, and step are data, background, and step size, respectively. In the following graph we show $k^2 \chi(k)$, where χ(k) is obtained according to Eq. (6.19).

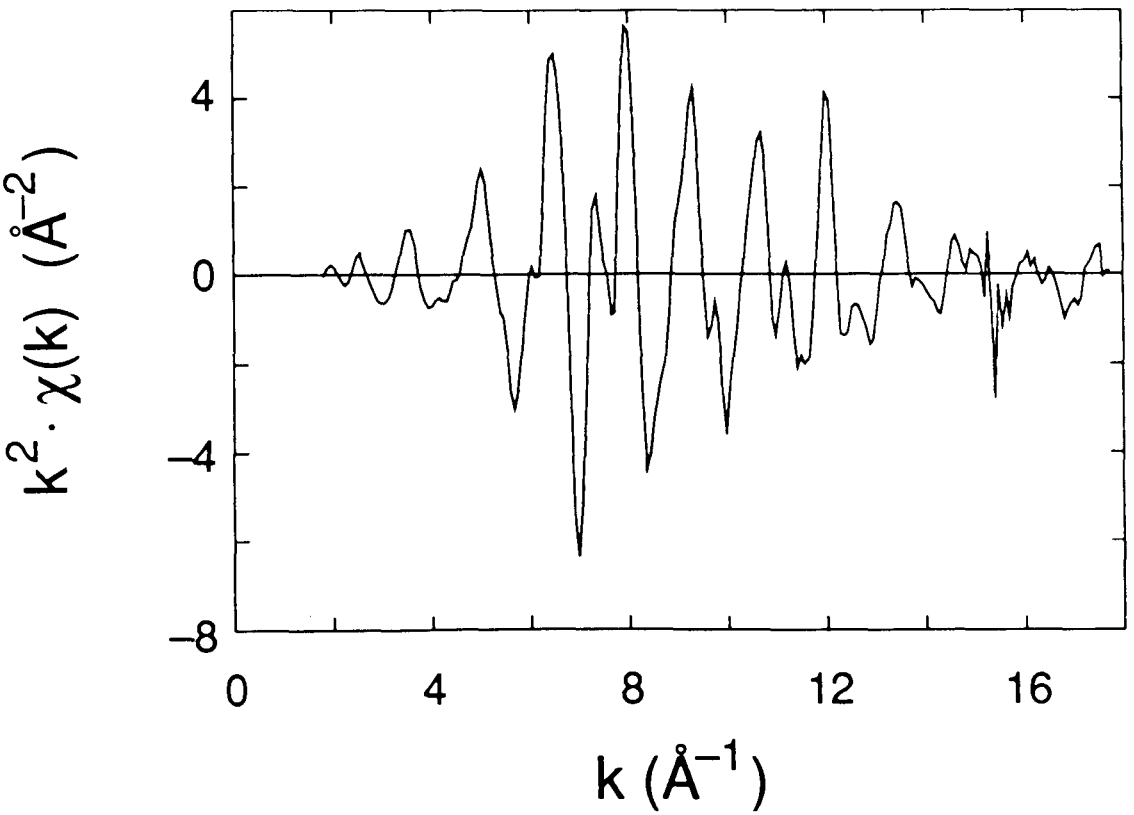

Fig. 6.7: The function $k^2 \chi(k)$ for Cu extending from 1.82 Å^{-1} to 17.73 Å^{-1}, as in the previous figure. The positive area of $k^2 \chi(k)$ is 51.3% and the negative area is 48.7%. The Si (111) glitch at ~15 Å^{-1} either has to be removed by some method or be excluded by limiting k_{max} to 15 Å^{-1}, thus sacrificing resolution in R-space.

We have now obtained a normalized $\chi(k)$ but we will nevertheless apply a small correction which takes the physical variation of the x-ray absorption coefficient with energy into account. This correction becomes important above $k \equiv 10$ Å^{-1} . It is applied as follows:

According to Ref. 138 the mass absorption coefficient $\mu_m(E)$ above the absorption edge is computed as a function of energy for the element whose edge is being studied. A corrected $\chi(k)$ is then obtained through:

$$\chi_c(k) \equiv \chi(k) \frac{\mu_m(E_{Edge})}{\mu_m(E(k))} \quad ; \quad E(k) = \gamma k^2 \ . \tag{6.20}$$

$\mu_m(E_{Edge})$ is the mass absorption coefficient just above the absorption edge. $\chi(k)$ is thus being multiplied by a slowly increasing function whose value at E_{Edge} is unity. This correction is applied to all datasets.

6.4 Monochromator Resolution

The broadening of the spectra due to the finite resolution of the monochromator is small for the Sm L_{II}, L_{III} edges but it becomes appreciable at higher energy. Luckily its effect on the EXAFS is not severe and can be easily taken care of. The effect of the monochromator resolution is taken into account as described in Ref. 179 where a Gaussian was assumed for the spectrometer function. τ denotes the width of this Gaussian and it is related to the FWHM according to:

$$\tau = \frac{FWHM}{2\sqrt{2\ ln2}} \ . \tag{6.21}$$

The width of the spectrometer function as a function of energy is given by Eq. (5.12):

$$FWHM \equiv \delta E = \delta\theta \cdot (E_o+\gamma k^2) \cdot \sqrt{\left(\frac{E_o+\gamma k^2}{E_{min}}\right)^2 - 1} \ . \tag{6.22}$$

In this equation we have expressed the photoelectron energy in terms of its wave vector k: $E \equiv E_o + \gamma k^2$, where E_o is the edge energy and γ is 3.81 eV Å^2 (see Eq. (2.28)). E_{min} is the energy corresponding to $\theta = 90^\circ$, Eq. (5.3).

$\delta\theta$ is obtained from Eq. (5.11) of Section 5.2 but may be approximated by

$$\delta\theta \equiv \frac{s}{L} \ , \tag{6.23}$$

where s is the width of the slit in front of the monochromator and L is the distance between the monochromator and the x-ray source.

According to Ref. 179 the finite monochromator resolution is taken into account by multiplying each shell with the following function:

$$\rho_\tau(k) \equiv \exp\left[\frac{-(2\ R_j + p_{1j})^2\ \tau^2}{8\ \gamma^2\ k^2}\right] \quad . \tag{6.24}$$

τ is obtained from the resolution $\delta\theta$ using Eqs. (6.21) and (6.22). $\rho_\tau(k)$ depends on the coordination-shell radii R_j and on the average slope p_{1j} of the total phase of shell j.

The above approach has the advantage that a convolution of the data, which always slows down the computation, is avoided.

6.5 Fourier Transform

The Fourier transform is calculated using the Fast Fourier Transform (FFT) [180]. For the FFT to produce correct results it is necessary that the data be on a uniform grid in k-space. The FFT uses only ordinate values. For the k-to-R and, symmetrically, for the R-to-k transform the ordinate is multiplied by $1/\sqrt{\pi}$. Thus the Fourier transform H(R) of a function h(k) is calculated as:

$$H(R) = \frac{1}{\sqrt{\pi}} \cdot \int_{-\infty}^{\infty} h(k)\ e^{+2ikR}\ dk \quad . \tag{6.25}$$

The abscissa in R-space is calculated as follows:

$$R_m = \frac{\pi\ m}{n_{FFT}\ \delta k} \quad ; \qquad m = 0, 1, 2, \ldots, \frac{n_{FFT}}{2} \quad . \tag{6.26}$$

n_{FFT} is the number of points used for the FFT. It has to be a power of 2. Here n_{FFT} is usually 2048. δk is the distance between two adjacent points in k-space. $\delta R \equiv \pi/(n_{FFT}\delta k)$, the point separation in R-space, contains a factor of π which combines with $1/\sqrt{\pi}$ to a resultant factor of $\sqrt{\pi}$ for the inverse transform. Because the FFT employs only ordinate values its result must be multiplied by δk for the k-to-R transform and by δR for the inverse transform in order to obtain a result equivalent to the analytical transform. Note that there are $1+ n_{FFT}/2$ points in R-space for an n_{FFT} -point transform and that the R-space signal begins at $R = 0$ and extends to $R_{max} = \pi/(2\delta k)$. The plus sign has been

chosen in the exponent of Eq. (6.25) so that the imaginary part of the Fourier transform exhibits a peak, rather than a minimum, at the abscissa value corresponding to a particular coordination shell. Thus one can easily compare peak positions of imaginary part and transform magnitude.

It may happen that the EXAFS data $\chi(k)$ is rather noisy. In this case the interpolation onto a uniform grid, needed for the FFT, is questionable because it may add even more noise. One then has to employ the conventional Fourier transform.

The inverse transform is given by:

$$h(k) = \frac{1}{\sqrt{\pi}} \cdot \int_{-\infty}^{\infty} H(R)\, e^{-2ikR}\, dR \quad . \tag{6.27}$$

6.6 Window Functions

Window functions, also called apodization functions, are employed in order to reduce interference effects that result from the finite range of the data. They are functions which multiply the data that is to be Fourier transformed. Window functions are usually symmetric with respect to the midpoint of the data interval and normally tend towards zero at the endpoints. They are non-negative and their maximum value is one. Although a window function will broaden a given peak it does suppress sidelobes that arise after Fourier transformation. In this work window functions are only applied when going from k- into R-space. If the inverse Fourier transform, i.e. the R-to-k transform, is to be performed then the window function must be removed in k-space after the transformation. This is simply done by dividing by the same window function that had been used initially. Therefore we require that the window function be nowhere equal to zero. Furthermore, we will only consider symmetric window functions.

The simplest window function is a rectangle of unit height. This is equivalent to not applying any window function at all. Sometimes this is permissible when the data is already tapered at the ends of the data range. The rectangular window yields the highest possible resolution because it is broad in k-space and therefore its Fourier transform will be rather narrow. In order to discuss Fourier

transforms of window functions it is sufficient to assume that the k-space data is centered at k=0 . Thus $-\Delta k/2 \le k \le \Delta k/2$, where $\Delta k \equiv k_{max} - k_{min}$, and the Fourier transform is a real function. For the Fourier transform of a rectangular window function centered at k=0 we obtain a function of the form (sin x)/x, also called a "sinc function":

$$W_o(R) \equiv \frac{1}{\sqrt{\pi}} \cdot \int_{-\Delta k/2}^{\Delta k/2} e^{+2ikR}\, dk = \frac{\Delta k}{\sqrt{\pi}} \frac{\sin(R\,\Delta k)}{R\,\Delta k} \quad . \tag{6.28}$$

The suppression of the biggest sidelobe is calculated from:

$$\text{Sidelobe suppression} \equiv 20 \cdot \log_{10} \left(\frac{|W(R=0)|}{|W(R^*)|} \right) \text{ dB} \quad . \tag{6.29}$$

R^* is the position where the biggest sidelobe occurs. For the rectangular window the sidelobe suppression is only 13dB.

According to the convolution theorem the multiplication of the k-space data with a window function leads to a convolution of the Fourier transform of the data with the Fourier transform of the window function. We see from Eq. (6.28) that the sidelobes extend rather far and thus there will be a strong admixture of information from adjacent peaks which cannot always be tolerated. A window function which achieves a better apodization, i.e. reduces the overlap of the peaks in R-space can be constructed by refining the Fourier transform of the rectangular window function. Since we want to reduce the spread of the sidelobes one can simply add to $W_o(R)$ two other sinc functions shifted by a half period $\pi/\Delta k$ in either direction so that these functions interfere destructively with the central sinc function. The result is then [181]:

$$W_M(R) \equiv \alpha\, W_o(R) + \frac{1-\alpha}{2} \left[W_o(R-\pi/\Delta k) + W_o(R+\pi/\Delta k) \right] \quad . \tag{6.30}$$

The central sinc function is weighted by α and the two shifted sinc functions are both weighted by $(1-\alpha)/2$. For the Hamming window α is chosen such that the first sidelobe of $W_o(R)$, i.e. the second sidelobe of $|W_o(R)|$, perfectly cancels. This is the case for $\alpha = 25/46 = 0.543...$. For the Hamming window α is set to 0.54. In order to determine the form of Eq. (6.30) in k-space we write:

$$W_M(R) \equiv (\alpha - (1 - \alpha))\, W_o(R) + 2\,(1-\alpha)\, W_N(R) \quad , \tag{6.31}$$

$$W_N(R) \equiv \frac{1}{4}\, W_o(R-\pi/\Delta k) + \frac{1}{2}\, W_o(R) + \frac{1}{4}\, W_o(R+\pi/\Delta k) \ . \qquad (6.32)$$

$W_N(R)$ has a simple Fourier transform [180]: $\quad w_N(k) = 0.5 + 0.5 \cos(\pi\, 2k/\Delta k) \ . \qquad (6.33)$

Thus we obtain for the Hamming window:

$$w_M(k) \ = \ 2\alpha - 1 + 2\,(1-\alpha)\, w_N(k) \ = \ \alpha + (1-\alpha) \cos(\pi\, 2k/\Delta k) \ = \ 0.54 + 0.46 \cos(\pi\, 2k/\Delta k) \ . \qquad (6.34)$$

Note that this function does not go to zero anywhere. In fact, the Hamming window is a special case of the so called "Hanning" window (Don't confuse the two similar names!). The Hanning window is obtained when $\alpha = 0.5$. Thus $W_N(R)$, Eq. (6.32), and $w_N(k)$, Eq. (6.33), describe the Hanning window.

The Hamming window $w_M(k)$, Eq. (6.34), will be used in this work most of the time. Very closely related is the 10% Gaussian window function which consists of a Gaussian with endpoint values of 10% of its maximum value, i.e. endpoint values of 0.1. The Gaussian window functions are defined by:

$$w_G(k) \equiv \exp\left[\left(\frac{2k}{\Delta k}\right)^2 \cdot \ln w_G(\Delta k/2) \right] \ . \qquad (6.35)$$

$w_G(\Delta k/2) \equiv w_G(-\Delta k/2)$ is the value of $w_G(k)$ at the endpoints. For a 10% Gaussian we have $w_G(\Delta k/2) = 0.1$. The Fourier transform of the Gaussian cannot be calculated analytically over a finite k-space interval and is therefore omitted.

Note that the k-space interval and the type of window function determine the minimum peak width in R-space. A measure for this width is $2\, R_o$, where R_o is the zero crossing of W(R) closest to $R = 0$. Some results for the window functions discussed here are summarized in the following table:

Table 6.1: Properties of window functions:

Type	$2 R_0 \Delta k$	Sidelobe suppression
Rectangle	2π	13 dB
Hamming	4π	43 dB
Hanning	4π	32 dB
10% Gaussian	12.147	34 dB

For a systematic review of the plethora of window functions that exist see Ref. 181. Choosing a window function means finding the best compromise between resolution and sidelobe suppression. The Hamming window is a good choice in this respect.

If $k_{min} \le k \le k_{max}$ instead of $-\Delta k/2 \le k \le \Delta k/2$, then the window functions must be shifted by $k_0 \equiv (k_{min} + k_{max})/2$ which means replacing k by $k - k_0$.

6.7 Fourier Filtering and the Determination of Amplitude and Phase

Fourier filtering, or filtering in R-space, is effected by selecting an R-space interval for the region of interest and setting all the rest of the Fourier transform to zero. A subsequent transform to k-space yields the filtered $\chi(k)$.

In more detail, what one does is the following: First the EXAFS function $\chi(k)$ is multiplied by some power of k, p_F, say, such that the resulting function $k^{pF}\chi(k)$ has very roughly the same amplitude everywhere. Then a window function $w(k-k_0)$ is applied in order to suppress sidelobes in the Fourier transform. The window function is even with respect to the midpoint k_0 of the k-space interval. For illustrative purposes we will consider the simple case where the distribution of atoms is adequately described by a Gaussian and both $|f_j(k,\pi)|$ and $\delta_{ij}(k)$ are assumed to be independent of R. Hence we have in k-space:

$$w(k-k_0)\,k^{pF}\,\chi(k) \;=\; w(k-k_0)\,k^{pF}\cdot\sum_j A_j(k)\,\sin\!\left(2kR_j+\delta_{tj}(k)\right) \qquad (6.36)$$

where $A_j(k)$ is given by:

$$A_j(k) \equiv \frac{N_j}{k\,R_j^{\,2}}\;|f_j(k,\pi)|\;e^{-2\sigma_j^2 k^2}\;e^{-2R_j/\lambda}\quad . \qquad (6.37)$$

Now the Fourier transform is computed. Each coordination shell that is sufficiently resolved will appear as a separate peak in a plot of the transform magnitude versus the coordination-shell radius R. (The modulation of the backscattering amplitude of the heavier elements due to the Ramsauer-Townsend effect may introduce a small sidelobe peak besides a major peak.) For the coordination shell of interest an interval is now selected that encloses the peak. At the interval limits, R_{min} and R_{max}, of a well-resolved peak the magnitude of the Fourier transform vanishes (or almost vanishes). If we assume that in R-space we have isolated the jth coordination shell then we are left only with the Fourier transform of EXAFS of the jth coordination shell, namely:

$$H_j(R) \equiv \frac{1}{\sqrt{\pi}}\cdot\int_{-\infty}^{\infty} w(k-k_0)\,k^{pF}\,A_j(k)\,\sin\!\left(2kR_j+\delta_{tj}(k)\right)\,e^{+2ikR}\,dk \qquad \text{for} \quad R_{min}\le R\le R_{max}$$

$$H_j(R) = 0 \qquad \text{otherwise}\quad .$$

(6.38)

According to this equation the Fourier transform outside the interval $R_{min}\le R\le R_{max}$ is set to zero. R_{min} and R_{max} are never negative. Therefore $H_j(R)$ always vanishes for negative R-values. This fact can be exploited by using the identity $\sin x = (e^{+ix}-e^{-ix})/(2i)$ and writing $H_j(R)$ in the interval $R_{min}\le R\le R_{max}$ as:

$$H_j(R) = \frac{1}{2i}\frac{1}{\sqrt{\pi}}\cdot\int_{-\infty}^{\infty} w(k-k_0)\,k^{pF}\,A_j(k)\,e^{+i\delta_{tj}(k)}\,e^{+2ik(R+R_j)}\,dk$$

$$-\frac{1}{2i}\frac{1}{\sqrt{\pi}}\cdot\int_{-\infty}^{\infty} w(k-k_0)\,k^{pF}\,A_j(k)\,e^{-i\delta_{tj}(k)}\,e^{+2ik(R-R_j)}\,dk\quad .$$

The first integral in the above equation will peak at $R=-R_j$ (actually slightly shifted due to the presence of the total phase $\delta_{tj}(k)$ which is approximately linear in k). Because of the application of a window function and because of the $1/R_j^{\,2}$ dependence of $A_j(k)$, the peak centered at negative R

will hardly extend into the the region of positive R-values. Since the first term peaks at a negative R-value and because according to Eq. (6.38) the Fourier transform is set to zero for negative R-values we are left only with the second integral which peaks at a positive R-value:

$$H_j(R) = \frac{1}{\sqrt{\pi}} \cdot \int_{-\infty}^{\infty} \left[\left(-\frac{1}{2i} \right) w(k-k_0)\, k^{PF}\, A_j(k)\, e^{-i\delta_{tj}(k)}\, e^{-2ikR_j} \right] e^{+2ikR}\, dk \quad \text{for} \quad R_{min} \le R \le R_{max}$$

$$H_j(R) = 0 \qquad \text{otherwise} \; .$$

(6.39)

Taking the inverse Fourier transform according to Eq. (6.27) yields in k-space a modified EXAFS function $\tilde{\chi}_j(k)$ corresponding to the jth shell. This function is now complex because $H_j(R)$ does not contain anymore contributions from negative R-values. $\tilde{\chi}_j(k)$ is obtained from the term in square brackets in Eq. (6.39) after division by the window function and k^{PF}:

$$\tilde{\chi}_j(k) \equiv \left(-\frac{1}{2i} \right) A_j(k)\, e^{-i\delta_{tj}(k)}\, e^{-2ikR_j} \; . \tag{6.40}$$

The desired unmodified EXAFS function $\chi_j(k)$ of the jth coordination shell is then obtained as:

$$\chi_j(k) \equiv 2\, \mathbf{Re}\, \tilde{\chi}_j(k) = A_j(k) \sin\left(2kR_j + \delta_{tj}(k)\right) \; . \tag{6.41}$$

Because it is necessary in the process to remove the effect of the window function by dividing it out in k-space, the window function must never be zero anywhere. Hence those window functions that taper off to zero at the ends cannot be employed for EXAFS analysis.

We can also obtain the amplitude $A_j(k)$ and the phase $2kR_j+\delta_{tj}(k)$ by employing the following relations:

$$A_j(k) = 2\left|\tilde{\chi}_j(k)\right| \; , \tag{6.42}$$

$$2kR_j + \delta_{tj}(k) = \arctan\left(\frac{\mathbf{Re}\ \tilde{\chi}_j(k)}{\mathbf{Im}\ \tilde{\chi}_j(k)} \right) . \tag{6.43}$$

The last equation can also be written in a form similar to the one given in Ref. 4:

$$2kR_j + \delta_{tj}(k) = -\arctan\left(\frac{\mathbf{Im}\ \tilde{\chi}_j(k)}{\mathbf{Re}\ \tilde{\chi}_j(k)}\right) + \frac{\pi}{2} \quad . \tag{6.44}$$

Because the tangent has a period of π rather than 2π there is an ambiguity with respect to multiples of π. This ambiguity is removed by considering the signs of real and imaginary part individually. For example the phase $2kR_j + \delta_{tj}(k)$ should be between 0 and $\pi/2$ when $\mathbf{Re}\ \tilde{\chi}_j(k)$ and $\mathbf{Im}\ \tilde{\chi}_j(k)$ are both positive. Similar conclusions hold for the other quadrants of the unit circle in the complex plane. Thus the formulae must be as presented in Eqs. (6.43) and (6.44) above, with no π added or subtracted. The phase is, of course, only determined modulo 2π.

It is important to note that the modified EXAFS function $\tilde{\chi}_j(k)$ may also be defined to refer to several coordination shells instead of only one. This occurs for example with beating when two (or more) shells are too close together to be resolved. Then the beating effect can be studied by employing Eq. (6.41) or by investigating the amplitude or phase according to Eqs. (6.42) or (6.43).

It must be kept in mind that Eqs. (6.41) to (6.43) can only be obtained by employing an integral transform like for example the Fourier transform. This results in transform artifacts that will always appear as end effects. Therefore the filtered EXAFS function, the extracted amplitude or phase will not be reliable at the ends. These artifacts may extend up to 10% of the available k-space interval on each side.

6.8 Log-Ratio and Phase-Difference Methods

In EXAFS data analysis one needs a reference backscattering amplitude $|f_j(k,\pi)|$ and a reference total phase $\delta_{tj}(k)$ for each coordination shell j that is to be analyzed. These functions can be taken from the plane-wave calculations of Teo and Lee [11], the curved-wave calculations of McKale et al. [8-10], or they may be calculated as in Chapter 3. Alternatively, one may employ empirical amplitudes and phases. Hereby one assumes that the amplitude $|f_{ref}(k,\pi)|$ and phase $\delta_{t,ref}(k)$ are the same for reference compound and for sample. One may for example analyze GeO_2 by employing amplitude and phase obtained from pure Ge, say. This approach assumes that the amplitudes and phases

depend mainly on the elements themselves and remain unchanged in a compound or alloy. This, however, cannot always be taken for granted. On the other hand it is to be kept in mind that Teo and Lee [11] also computed their amplitudes and phases only for elements, not for compounds (for practical reasons, of course). Assuming now that the amplitudes and phases do not depend significantly on the chemical environment we can employ the method described in the previous chapter and obtain $A_{ref}(k)$ and the phase $\Phi_{ref}(k) \equiv \left(2kR_{ref} + \delta_{t,ref}(k)\right)$. Assuming that the distance R_{ref} of the reference material is known we can obtain the reference phase simply by subtraction:

$$\delta_{t,ref}(k) = \Phi_{ref}(k) - 2\,k\,R_{ref} \quad . \tag{6.45}$$

For the sample under investigation we obtain $\Phi_x(k) \equiv \left(2kR_x + \delta_{t,x}(k)\right)$. Using $\delta_{t,x}(k) \equiv \delta_{t,ref}(k)$ we can write for the unknown distance R_x of the sample:

$$\Phi_x(k) - \Phi_{ref}(k) = 2\,k\left(R_x - R_{ref}\right) \quad . \tag{6.46}$$

According to this equation R_x is best determined by fitting $\Phi_x(k) - \Phi_{ref}(k)$ to a straight line that passes through the origin. It may be necessary to adjust the k-scale of the sample by shifting ΔE_o such that the straight line indeed passes through the origin [4]. From the slope we immediately obtain R_x. This is the Phase-Difference Method. It can be applied for pressure-dependent studies because the phase $\delta_{t,x}(k)$ remains practically unchanged under pressure. However, the method is not employed in this work because the pressure-induced distance changes are simply too small that R_x could be determined reliably from a straight-line fit according to Eq. (6.46). The result becomes dependent on the choice of the fitting interval. Instead the EXAFS function $\chi_x(k)$ is fitted by least squares (Section 6.10) because it is believed that in this way the results for R_x are much less dependent on the choice of the fitting interval.

The empirical amplitudes $A_{ref}(k)$ and $A_x(k)$ are obtained by employing Eq. (6.42) and we can write:

$$A_{ref}(k) \equiv \frac{N_{ref}}{k\,R_{ref}^2}\,|f_{ref}(k,\pi)|\,e^{-2\sigma_{ref}^2 k^2}\,e^{-2R_{ref}/\lambda} \quad ,$$

$$A_x(k) \equiv \frac{N_x}{k\,R_x^2}\;|f_x(k,\pi)|\;e^{-2\sigma_x^2 k^2}\;e^{-2R_x/\lambda}\;.$$

These two relations can be combined to yield:

$$\ln\left(\frac{A_x(k)}{A_{ref}(k)}\right) = \ln\left(\frac{N_x}{N_{ref}}\right) - 2k^2\left(\sigma_x^2 - \sigma_{ref}^2\right) + 2\ln\left(\frac{R_{ref}}{R_x}\right) - \frac{2}{\lambda}\;(R_x - R_{ref})\;. \qquad (6.47)$$

Here we have used $|f_x(k,\pi)| \equiv |f_{ref}(k,\pi)|$. The last two terms on the right-hand side of this equation can be neglected compared to the first terms. Then we get:

$$\ln\left(\frac{A_x(k)}{A_{ref}(k)}\right) \equiv \ln\left(\frac{N_x}{N_{ref}}\right) - 2k^2\left(\sigma_x^2 - \sigma_{ref}^2\right). \qquad (6.48)$$

We see now that a plot of the left-hand side of this equation versus k^2 will yield a straight line. A fit will then provide the ratio $\frac{N_x}{N_{ref}}$ of the coordination numbers as well as the difference $\sigma_x^2 - \sigma_{ref}^2$ of the EXAFS Debye-Waller factors. Eq. (6.48) is the basis for the Log-Ratio Method [182]. It is assumed that the k-scales of sample and reference were adjusted by a ΔE_o shift with respect to each other such that their phase difference, Eq. (6.46), passes through the origin. Again, this method is hardly applied in this work because Eq. (6.48) is not a very reliable way for determining the EXAFS Debye-Waller factor since the result depends on the choice of the fit interval when σ_x^2 differs very little from σ_{ref}^2 . Again, the fit to $\chi_x(k)$ is preferred because it gives more consistent results. To make the Log-Ratio Method work well it is necessary to weight the straight-line fit to Eq. (6.48) properly [183].

Note that the Phase-Difference and Log-Ratio methods are valid only in the case that a single shell can be isolated.

6.9 Degrees of Freedom of a Signal

According to the sampling theorem a signal that is bandlimited in Fourier-space need only be sampled at a certain rate. The *minimum* number of points that is needed to describe the signal is called the number of degrees of freedom, n_{free}. Since the original signal can be in k- or R-space we discuss both these cases.

In k-space, n_{free} is given by:

$$n_{free} = 1 + \frac{\Delta k}{\rho_k} \quad . \tag{6.49}$$

Here ρ_k is the Nyquist sampling rate. If Fourier filtering is applied then the filtered data is bandlimited in R-space and we have for ρ_k (see Ref. 180, p. 87):

$$\rho_k = \frac{\pi}{2\, R_{max}} \left[\frac{R_{max}}{\Delta R} \right] . \tag{6.50}$$

$\Delta k \equiv k_{max} - k_{min}$ is the k-space fit interval and $\Delta R \equiv R_{max} - R_{min}$ is the interval employed for Fourier filtering. The square brackets denote the integer part of the argument. For n_{free} we then obtain:

$$\text{k-space:} \qquad n_{free} = 1 + \frac{2\, \Delta k\, \Delta R}{\pi} \frac{\frac{R_{max}}{\Delta R}}{\left[\frac{R_{max}}{\Delta R} \right]} \quad . \tag{6.51}$$

We see that n_{free} increases linearly with Δk. If no filtering is applied then $R_{min} = 0$ and $R_{max} = \Delta R = \pi/(2\delta k)$, Eq. (6.26), and we obtain:

$$n_{free} = 1 + \frac{\Delta k}{\delta k} = M_k = 1 + \frac{2\, \Delta k\, \Delta R}{\pi} \quad .$$

In this case the number of degrees of freedom is equal to M_k, the number of data points.

In R-space, n_{free} is given by:

$$n_{free} = 1 + \frac{\Delta R}{\rho_R} \quad . \tag{6.52}$$

Since the R-space data is bandlimited in k-space, ρ_R, the Nyquist sampling rate for R-space, is:

$$\rho_R = \frac{\pi}{2\, k_{max}} \left[\frac{k_{max}}{\Delta k} \right] . \tag{6.53}$$

$\Delta R \equiv R_{max} - R_{min}$ is the R-space fit interval, $\Delta k \equiv k_{max} - k_{min}$ is the interval used for the Fourier

transform and we have for n_{free}:

R-space: $$n_{free} = 1 + \frac{2\,\Delta k\,\Delta R}{\pi}\,\frac{\frac{k_{max}}{\Delta k}}{\left[\frac{k_{max}}{\Delta k}\right]} \quad . \tag{6.54}$$

6.10 Least-Squares Fitting of EXAFS Spectra

An EXAFS dataset contains contributions from the backscattering of various coordination shells. The distances of these shells enter the EXAFS formula in amplitude and phase, where the effect on the phase is much more pronounced. In k-space this corresponds to the summation of sine functions of different spatial frequencies. In R-space this is seen as an assembly of peaks in the Fourier-transform magnitude. Ideally, these peaks are well separated so that each one can be Fourier filtered. Thus, in the ideal case, after filtering one would merely have to analyze single shells. This analysis can be performed by employing the Log-Ratio Method. Obviously, one can also perform a least-squares fit to a single shell. In order to approach the ideal case it is necessary that the EXAFS signal extends far enough in k-space.

Frequently, however, it is not possible that k_{max} be very large because the signal has already decayed. Closely-spaced coordination shells, in particular, require a prohibitively large k-space interval in order to be resolved. Therefore in practice one normally cannot separate individual coordination shells but groups of shells instead. Typically 2 to 4 shells together can be Fourier filtered thus producing a k-space EXAFS signal with a reduced number of coordination shells. When there is more than one atomic species present this signal has to be analyzed by least-squares fitting. If one wants to avoid the Fourier transform required for filtering, and thus all the artifacts that come with it, one can perform a least-squares fit in R-space instead. If the measured EXAFS spectrum contains contributions of only a few coordination shells, for example because of large Debye-Waller factors, then this spectrum can be fitted directly without having to perform any Fourier transform at all.

In this work we fit EXAFS spectra to the following expression:

$$\chi(k) = \sum_j e^{-(2R_j+s_j)^2\tau^2/8\gamma^2 k_j^2}\, e^{-2R_j/\lambda}\, e^{(2/3)C_{4j}k_j^4}\quad \frac{N_j}{k_j R_j^2}$$

$$\times\ \left|f_j(k_j,\pi)\right|\ e^{-2\sigma_j^2 k_j^2} \sin\left(2k_jR_j+\delta_{tj}(k_j)+a_j - (4/3)C_{3j}k_j^3\right)\ . \qquad (6.55)$$

The first three terms of this sum over the coordination shells j are frequently not included in EXAFS analysis. They are, respectively, the monochromator resolution function according to Eq. (6.24), the mean-free path term, and the amplitude correction due to a non-zero fourth-order cumulant. The next terms in Eq. (6.55) involve the radii R_j of shell j having coordination number N_j, the magnitude of the backscattering amplitude, the EXAFS Debye-Waller factor, and the sine of the phase which here includes a correction term due to a non-vanishing third-order cumulant. Besides, we allow for an adjustment of the reference phase $\delta_{tj}(k_j)$ by the parameter a_j. If a_j is variable then one need not necessarily vary the correction ΔE_j of the inner potential for amplitude and phase of shell j. This is so because a_j acts approximately like ΔE_j. ΔE_j does not appear explicitly in Eq. (6.55) but it is contained in the definition of k_j:

$$k_j = \sqrt{k^2 - \Delta E_j/\gamma}\ , \qquad (6.56)$$

with $\gamma \equiv \dfrac{h^2}{8\pi^2 m_e} \cong 3.81$ eV Å^2 according to Eq. (2.28).

k is the magnitude of the wave vector of the photoelectron. This is the k-scale of the measured EXAFS function and it is never modified for fitting. The ΔE_j are shell-dependent modifications of the reference amplitudes and phases. Their effect is most pronounced at low k-values. a_j instead is a k-independent phase correction. Since ΔE_j and a_j are correlated only one of them should be varied in a fit.

As mentioned before, one can perform a fit either in k-space or in R-space. In k-space one would fit directly to the EXAFS equation (6.55) which may correspond to the full EXAFS data or to Fourier-filtered data. In R-space no Fourier filtering is necessary and one fits the Fourier transform of the model to the Fourier transform of the data. Both transforms are calculated in the same way using the FFT. Thus transform artifacts will be equally present in both the data and the model. In order to compensate for the decrease of the backscattering amplitude with k the data and the model $\chi(k)$ are multiplied by k^p. The power p of k is chosen to be 1, 2, or 3, depending on the type of backscattering

atom (p could also be fractional.). Thus, in k-space we fit $k^p \chi(k)$ to $k^p y$ where y is the full EXAFS data or the filtered data. In R-space we fit **Re**(FT($k^p \chi(k)$)) to **Re**(FT($k^p y$)) and simultaneously **Im**(FT($k^p \chi(k)$)) to **Im**(FT($k^p y$)) , where FT denotes the Fourier transform and **Re** and **Im** stand for the real and imaginary part, respectively. It is also possible to fit the envelope and phase extracted from the data. If one fits them separately then one suppresses any possible correlation among the parameters used to fit these two datasets. Therefore it is recommended to fit to the full data, i.e. simultaneously to the extracted amplitude and phase. This, however, poses problems as amplitude and phase have quite a different k-dependence and one cannot decide how to weight the two so that they become equally important in the fit. Fitting to the real and imaginary part of the data, however, does not present this difficulty because they are both oscillatory functions possessing the same envelope. Real and imaginary part are therefore weighted equally. A different method of weighting, involving derivatives, is described in Ref. 5.

In order to perform the fit we have to calculate χ^2, which is a measure of the deviations of the model from the data, at each iteration step. χ^2 is evaluated depending on whether k-space or R-space is selected. In k-space the expression is:

$$\chi^2 = \frac{n_{free}}{n_{free}-n} \frac{1}{M_k} \cdot \sum_{i=1}^{M_k} \left[(y_i - \chi(k_i))\, k_i^p\right]^2 w_k(k_i) \quad . \tag{6.57}$$

In R-space the formula becomes:

$$\chi^2 = \frac{n_{free}}{n_{free}-n} \frac{1}{2M_R} \cdot \sum_{i=1}^{M_R} \Big(\left[\mathbf{Re}(FT(k^p y)) - \mathbf{Re}(FT(k^p \chi(k)))\right]_i^2 + \left[\mathbf{Im}(FT(k^p y)) - \mathbf{Im}(FT(k^p \chi(k)))\right]_i^2 \Big) \; w_R(R_i) \quad . \tag{6.58}$$

M_k is the number of points in k-space. If the data is Fourier filtered then y_i is the filtered data. $w_k(k)$ is a weighting function which is the reciprocal of the square of the envelope of $k^p y$. (In order to avoid a possible division by zero the minimum value of the envelope is never less than 10% of its maximum value.) If this weighting is applied the effect of k^p is practically removed.

In R-space there are M_R points and $w_R(R)$ is an R-space weighting function which is the reciprocal of the the square of the magnitude of the Fourier transform. (For the weighting function the magnitude never goes below 10% of its maximum value, as before.)

If the error $\sigma_i^2 \equiv \sigma_i^2|_{statistical} + \sigma_i^2|_{systematic}$ of each data point [16] is known then the weighting functions $w_k(k_i)$ and $w_R(R_i)$ can be replaced by $1/\sigma_i^2$. In this case $\chi^2 = 1$ will indicate a good fit. In this work no weighting is employed. Therefore $w_k(k)$ and $w_R(R)$ are equal to one.

n which occurs in Eqs. (6.57) and (6.58) is the number of variable parameters. n_{free} is the maximum number of variable parameters and is always $\geq n$.

If one fits to M_R points of the real and imaginary parts of a Fourier transform, which had been obtained from M_k k-space points, then the number of points that are used has changed by a factor $\mu \equiv 2M_R/M_k$. This change is artificial because in R-space there is now neither more nor less information available than before in k-space. Therefore n_{free} and n have to be weighted by the same factor μ. Thus the term in front of the summation of Eq. (6.58) is

$$\frac{\mu\, n_{free}}{\mu\, n_{free} - \mu\, n}\,\frac{1}{2\,M_R} \quad .$$

If we are fitting the Fourier transform from $R_{min} = 0$ to $R_{max} = \frac{\pi}{2\,\delta k}$ and if $\frac{k_{max}}{\Delta k} = \left[\frac{k_{max}}{\Delta k}\right]$, then

$n_{free} = M_k$ as before and the factor in Eq. (6.58) becomes

$$\frac{2\,M_R}{2\,M_R - \mu\, n}\,\frac{1}{2\,M_R} \quad \text{instead of} \quad \frac{2\,M_R}{2\,M_R - n}\,\frac{1}{2\cdot M_R} \quad .$$

If we approximate n_{free} as $n_{free} = 1 + 2\,\Delta k\,\Delta R/\pi$ then we can derive the following relation using $\delta R\,\delta k = \pi/n_{FFT}$, where n_{FFT} is the number of points used for the k-to-R Fast Fourier transform:

$$n_{free} - 1 = \frac{2}{n_{FFT}}\,(M_R - 1)\cdot(M_k - 1) \quad . \qquad (6.59)$$

If χ^2 is defined as here then one can compare fits with different number of parameters and therefore one can decide whether an added fit parameter actually has any significance. For this to be so we require that χ^2 involving the extra parameter must be reduced by a factor of two.

In order to perform the fit we employ Marquardt's algorithm [184] as programmed in Ref. 178. This algorithm works very well unless the starting values are extremely far off. The algorithm proceeds towards the minimum in parameter space by making use of the following approximation for the curvature matrix α, which in k-space is given by Ref. 178:

$$(\alpha)_{mn} \equiv \frac{1}{2} \frac{\partial^2 \chi^2}{\partial p_m \partial p_n}\Big|_{\vec{p}_o} \cong \sum_i \frac{\partial\, k_i p\ \chi(k_i)}{\partial p_m}\Big|_{\vec{p}_o} \cdot \frac{\partial\, k_i p\ \chi(k_i)}{\partial p_n}\Big|_{\vec{p}_o} \cdot w_k(k_i) \quad . \tag{6.60}$$

An analogous relation holds in R-space. $\vec{p}_o \equiv (p_{1,o}, p_{2,o}, \ldots)$ is the vector indicating the position in parameter space where the derivatives are evaluated. We see that α has been approximated by employing products of first order derivatives to avoid the second order derivatives. Note that the curvature matrix is 1/2 times the Hessian. The fitting procedure terminates when $\chi^2_{previous} - \chi^2_{current} < 10^{-4} \cdot \chi^2_{previous}$.

One can use the curvature matrix to calculate the error Δp_κ of a particular fit parameter p_κ. This can be done as follows [185, 186]:

$$\Delta p_\kappa = \pm \sqrt{\chi^2 \cdot (\alpha^{-1})_{\kappa\kappa}} \quad . \tag{6.61}$$

Eq. (6.61) is frequently employed but in this work we will use a different approach [187, 188]. In order to determine the error of a particular parameter p_κ of an n-parameter fit we will vary the parameter in steps near its optimum value and perform an (n–1)-parameter fit at each step. This will produce χ^2 as a function of the incremented parameter p_κ. The error bars for p_κ are determined from the intersection points of the χ^2 vs. p_κ curve with a horizontal line at $2\,\chi^2_{min}$. The factor of two results because for a reduced χ^2, which ideally is equal to one at its minimum, the error is determined by going from the minimum to a value of $\chi^2_{min}+1$, that is to 2. Here, however, we do not obtain a reduced χ^2 and therefore go to $2\,\chi^2_{min}$ instead. Error bars determined in this way can be

asymmetric because χ^2 is not always parabolic. They contain all effects of parameter correlations and are therefore a reliable measure of the quality of the fit.

This method has another advantage because it allows to search for other possible minima of the χ^2-surface. By stepping one parameter (and keeping it fixed at each step) while the other $n-1$ are adjusted by least-squares fitting we immediately see whether there are other minima of χ^2 and if any one of these is deeper than the one that we have found already. Investigating R_j will in general produce several minima when more than one shell is present.

While the error Δp_κ determined according to the above description takes all correlations into account we do not know which parameters correlate with which ones. This information can be obtained from the correlation matrix **c** which is calculated from the inverse of the curvature matrix α:

$$(\mathbf{c})_{ij} = \frac{(\alpha^{-1})_{ij}}{\sqrt{(\alpha^{-1})_{ii} \cdot (\alpha^{-1})_{jj}}} \; ; \qquad -1 \le (\mathbf{c})_{ij} \le 1 \quad . \tag{6.62}$$

The elements of the correlation matrix provide information about the sign and degree of the correlation of any two of the variable parameters. Values of $(\mathbf{c})_{ij}$ with absolute values close to unity signify strong correlation whereas $(\mathbf{c})_{ij} = 0$ indicates no correlation between parameters i and j. According to Eq. (6.62) the diagonal elements of the correlation matrix are equal to one.

A measure of the overall correlation are the global correlation coefficients g_k [189]:

$$g_k = \sqrt{1 - \frac{1}{(\mathbf{a})_{kk} \cdot (\mathbf{a}^{-1})_{kk}}} \quad . \tag{6.63}$$

The least-squares fitting program, which has been written, is too big (more than 5000 lines of FORTRAN code) to be listed here. A brief introduction is presented in Appendix E and a detailed description is given in Ref. 187.

6.11 Beating

Beating has been investigated before [190, 191], but we will consider the effect here in more detail.

We determine the resulting amplitude A(k) and phase $\Psi(k)$ when several coordination shells m of amplitudes $a_m(k)$ and phases $\psi_m(k)$ are added. All amplitudes and phases depend only on one continuous parameter k. The amplitudes are generalized to contain all terms in front of the sine function in the EXAFS formula and the phase is the argument of the sine function, including the 2kR-term. Beating will occur when two or more coordination shells are close together.

For simplicity we write each shell as a phasor. Adding the shells then gives:

$$A(k)\, e^{i\Psi(k)} = \sum_m a_m(k)\, e^{i\psi_m(k)} \quad . \tag{6.64}$$

Beating phenomena are manifest in the amplitude as well as the phase. When beating occurs, the amplitude exhibits a local minimum and the phase shows a step. We prefer to investigate the behaviour of the phase rather than that of the amplitude because it is analytically easier and because jumps in the phase are easier to detect than minima in the amplitude. Strictly, both effects need not occur at the same k-value. It must be kept in mind that minima in the amplitude and steps in the phase can also result from the k-dependence of the backscattering amplitudes and phases.

Writing the real and imaginary parts of Eq. (6.64) yields:

$$A(k) \cos \Psi(k) = \sum_m a_m(k) \cos \psi_m(k) \quad , \tag{6.65}$$

$$A(k) \sin \Psi(k) = \sum_m a_m(k) \sin \psi_m(k) \quad . \tag{6.66}$$

For the phase we therefore obtain the relation:

$$\tan \Psi(k) = \sum_m a_m(k) \sin \psi_m(k) \Big/ \sum_m a_m(k) \cos \psi_m(k) \quad . \tag{6.67}$$

For the amplitude we have:

$$A^2(k) = \left(\sum_m a_m(k) \cos \psi_m(k)\right)^2 + \left(\sum_m a_m(k) \sin \psi_m(k)\right)^2 \quad . \tag{6.68}$$

or:

$$A^2(k) = \left(\sum_m a_m(k)\, e^{i\psi_m(k)}\right) \cdot \left(\sum_n a_n(k)\, e^{i\psi_n(k)}\right) = \sum_{m,n} a_m(k)\, a_n(k)\, e^{i(\psi_m(k)-\psi_n(k))}$$

$$A^2(k) = \sum_{m,n} a_m(k)\, a_n(k) \cos\left(\psi_m(k) - \psi_n(k)\right) \quad . \tag{6.69}$$

We now determine the derivative of $\Psi(k)$ with respect to k:

$$\Psi'(k) = (\tan \Psi(k))' \cos^2\Psi(k) = \frac{(\tan \Psi(k))'}{1 + \tan^2\Psi(k)} \quad . \tag{6.70}$$

Here the prime indicates a derivative with respect to k. Inserting Eq. (6.67) yields:

$$\Psi'(k) = \frac{1}{A^2(k)} \cdot \sum_{m,n} a_m(k)\, a_n'(k) \sin\left(\psi_n(k) - \psi_m(k)\right) + a_m(k)\, a_n(k))\, \psi_n'(k) \cos\left(\psi_n(k) - \psi_m(k)\right) \quad .$$

(6.71)

This equation forms the basis for our analysis of the beating effect. $A^2(k)$ is given by Eqs. (6.68) or (6.69). For three or more coordination shells Eq. (6.71) becomes too complicated because all possible differences of distances appear. The equation is therefore evaluated only for the beating of two shells. To this end we introduce the abbreviations:

$$C(k) \equiv \frac{a_2(k)}{a_1(k)} \qquad \text{and} \qquad \phi(k) \equiv \psi_2(k) - \psi_1(k) - \pi \quad . \tag{6.72}$$

Using Eq. (6.71) we get after some tedious algebra the following formula describing the beating of two shells:

$$\Psi' = \frac{\psi_1'(k) + \psi_2'(k)}{2} + \frac{\frac{1}{2}\phi'(k)\,(C(k) - 1/C(k)) - (\ln C(k))' \sin \phi(k)}{C(k) + 1/C(k) - 2 \cos \phi(k)} \quad . \tag{6.73}$$

We will use this equation to determine the beating condition. A beat will occur at k-values where the two phasors $\psi_1(k)$ and $\psi_2(k)$ are antiparallel. In this case $\phi(k)$ is equal to an integer multiple of 2π: $\phi(k_\nu) = 2\pi\nu$, $\nu = 0, 1, 2, \ldots$

Note that Eq. (6.73) is invariant under the interchange of the two shells, i.e. for $C(k) \rightarrow 1/C(k)$ and $\phi(k) \rightarrow \phi(k) = \psi_1(k) - \psi_2(k) - \pi$. A closer inspection of Eq. (6.73) reveals that a divergence will occur if $C(k_\nu) \rightarrow 1$ for $k \rightarrow k_\nu$.

The case of $C(k) \equiv 1$ deserves special attention because then the second term on the right-hand side of Eq. (6.73) is undefined at a beating node. Analyzing Eqs. (6.65) and (6.66) for the case of equal amplitudes yields the result:

$$\Psi' = \frac{\psi_1'(k) + \psi_2'(k)}{2} \quad . \tag{6.74}$$

which is just the first term on the right-hand side of Eq. (6.73). Now, however, there will not be any structure in the phase derivative at a beating node. In other words, there is no beating effect in the phase when the two amplitudes are equal. This can be understood also in the following way. The two coordination shells, which have the same amplitude a(k), add up to:

$$A(k) \sin \Psi(k) = a(k) \left(\sin \psi_1(k) + \sin \psi_2(k)\right) \qquad \text{or}$$

$$A(k) \sin \Psi(k) = 2\, a(k) \cos\left(\frac{\psi_1(k) - \psi_2(k)}{2}\right) \sin\left(\frac{\psi_1(k) + \psi_2(k)}{2}\right) . \tag{6.75}$$

This result is well known. The rapidly varying sine term is modulated by a slowly varying cosine term. Therefore the term of the right-hand side is also of the form amplitude x sin(phase) and hence looks like a single shell with amplitude and phase given by:

$$A(k) = 2\, a(k) \cos\left(\frac{\psi_1(k) - \psi_2(k)}{2}\right) \qquad \text{and} \qquad \Psi(k) = \frac{\psi_1(k) + \psi_2(k)}{2} \quad . \tag{6.76}$$

The beating is contained only in the amplitude, not in the phase. The phase is simply the arithmetic

average of the two individual phases. Therefore, if we have two coordination shells of equal amplitude that cannot be resolved in R-space we can still extract their combined phase (Section 6.7). If the two shells consist of the same type of atoms (which is almost implied by the condition that their amplitudes are identical) then we obtain the average distance $R = (R_1 + R_2)/2$. Since the two amplitudes are never exactly equal, be it only for reasons of numerical precision, there may still be peaks, or dips, ocurring in the phase derivative. The important point here is that the two shells with equal (or almost equal) amplitudes can be analyzed as one single shell.

We will analyze beating by fitting to Eq. (6.73). The advantage of employing Eq. (6.73) is that if a beat extends only over a small k-range, the amplitude ratio C(k), as well as the phasors $\psi_1(k)$ and $\psi_2(k)$, can be assumed to be constant. This means then that no reference amplitudes or phases are necessary. However, since the generation of $\Psi(k)$ involves an integral transform there will be artifacts and thus a beating node near the high-k end cannot be analyzed. (Beating nodes near the low-k end need not be analyzed because they correspond to fairly large distance differences and because they are repeated at higher k-values.) Thus the situation here is the same as with the Log-Ratio Method.

For EXAFS the phases $\psi_j(k)$, j = 1, 2, are given as $\psi_j(k) = 2kR_j + \delta_{tj}(k)$ where $\delta_{tj}(k)$ is the sum of the central and the backscattering phases. With $\phi(k_v) = 2\pi v$ we get:

$$2\pi v = \psi_2(k_v) - \psi_1(k_v) - \pi = 2k_v\Delta R + \delta_{t2}(k_v) - \delta_{t1}(k_v) - \pi\,, \qquad \Delta R \equiv R_2 - R_1\ . \qquad (6.77)$$

We can sometimes approximate $\delta_{t2}(k) - \delta_{t1}(k)$ as a straight line (Chapter 2):
$\delta_{t2}(k) - \delta_{t1}(k) \equiv (p_{02} - p_{01}) + (p_{12} - p_{11})\,k$. Then we obtain for k_v:

$$k_v = \frac{(2v+1)\,\pi - (p_{02} - p_{01})}{2\Delta R + p_{12} - p_{11}}\ . \qquad (6.78)$$

If ΔR is rather small then the first beating node may lie outside the data range. It is thus difficult to confirm the existence of beating. If the presence of beating is not realized then wrong bondlengths may be obtained [192].

The beating nodes k_ν are evenly spaced with separation $\Delta k_\nu = \frac{2\pi}{2\Delta R + p_{12} - p_{11}}$.

If both shells consist of the same type of atoms then we get exactly $k_\nu = \frac{(2\nu+1)\pi}{2\Delta R}$.

Here we see another advantage of investigating the phase rather than the amplitude: The position of the minimum of the amplitude would involve the Debye-Waller factor and the mean free path whereas in Eq. (6.77) only the phase shift $\delta_1(k)$ appears.

We have not considered here the phase change associated with a local maximum of the amplitude because it is less pronounced. We also have not taken into account a broadening of the phase derivative of the data due to the finite transform range of the k-to-R Fourier transform employed in extracting the phase.

6.12 Valence Determination

As explained in Chapter 4, the mixed valence of rare earth compounds can be determined from the L_{II}- or L_{III}-absorption edges by fitting two integer-valent edge profiles of the same shape but with different weighting to the normalized spectrum. We employ here the same lineshape as was used before [17]. Other lineshapes [84, 193-196] involve a Lorentzian peak superposed onto an arctan-shaped background, a lineshape that is based on an early paper by Richtmyer et al. [197] who assumed a constant density of final states. The lineshape employed here consists of a Lorentzian convolved with a Gaussian, also called a Voigt line profile, with the edge jump built in afterwards according to Ref. 17, p. 75:

$$Y(E) \equiv \frac{Y_{max}}{K} \cdot \int_{-\infty}^{\infty} \frac{1}{(\tilde{E}-E_o)^2 + \Gamma^2}\, e^{-(\tilde{E}-E)^2/2\sigma^2}\, d\tilde{E} \qquad ; \quad E \le E_o$$

$$Y(E) \equiv 1 + \frac{Y_{max}-1}{K} \cdot \int_{-\infty}^{\infty} \frac{1}{(\tilde{E}-E_o)^2 + \Gamma^2}\, e^{-(\tilde{E}-E)^2/2\sigma^2}\, d\tilde{E} \qquad ; \quad E \ge E_o \tag{6.79}$$

where K is given by:

$$K \equiv \int_{-\infty}^{\infty} \frac{1}{\tilde{E}^2 + \Gamma^2} \, e^{-\tilde{E}^2/2\sigma^2} \, d\tilde{E} \quad . \tag{6.80}$$

The lineshape peaks at the energy E_o with peak height $Y_{max} \geq 1$. Γ is the Lorentzian half width at half maximum (HWHM) and σ describes the width of the Gaussian contribution. Thus the lineshape is characterized by four parameters: E_o, Y_{max}, Γ, and σ . In order to fit the white line of a mixed-valence material a second equal line profile, shifted in energy by ΔE, is added. If we write the valence v as

$$v \equiv 2 + \nu \; ; \qquad 0 \leq \nu \leq 1 \quad . \tag{6.81}$$

and assume that the first peak of the white line corresponds to the divalent state then its weight is $1-\nu$ and the weight of the trivalent state is ν. Thus in the case of mixed valence we need six fit parameters.

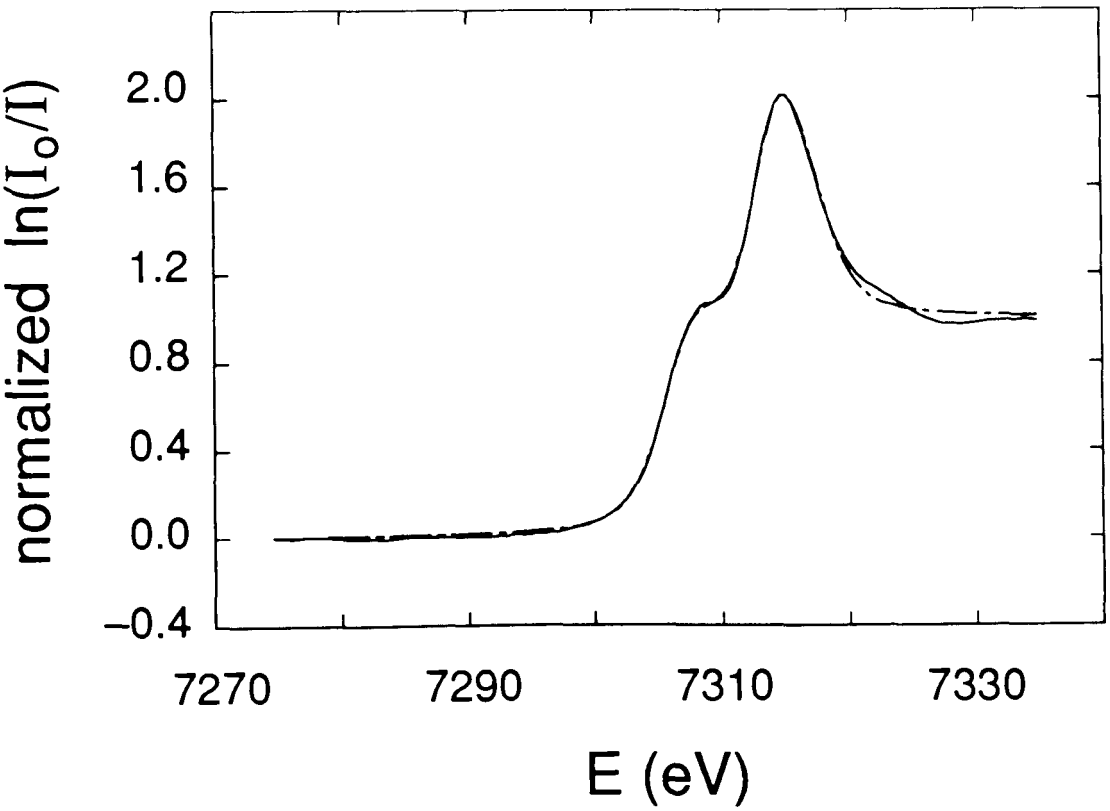

Fig. 6.8: Normalized absorption spectrum of the Sm L_{II} edge in SmSe at 58.6 kbar and at 77K. The solid line is the data, an average of two scans, and the dashed line is the fit.

These near-edge fits are excellent as one can see from Fig. 6.8. (Deviations on the high-energy side are due to the onset of EXAFS and not of concern in valence determination.) This may be due to the fact that the lineprofile employed here is constructed such that it resembles the normalization procedure. Normalization for edges, as opposed to EXAFS, consists of subtracting straight lines in energy space from the left- and right-hand sides of the absorption maximum. Subsequently the spectrum is normalized to the absorption step. The good fits insure that the results for the valence are sensitive to small changes in the height of the white line. A table of the correlation coefficients for the fit of Fig. 6.8 is shown below:

ΔE	−0.81				
2Γ	+0.21	−0.39			
σ	−0.20	+0.43	−0.91		
Y_{max}	−0.01	+0.05	−0.26	−0.06	
ν	−0.33	+0.09	+0.38	−0.24	−0.32
	E^{2+}	ΔE	2Γ	σ	Y_{max}

(E^{2+} and ΔE specify the energies of the 2+ and 3+ states.)

With this empirical approach we cannot claim to obtain the valence in an absolute sense, though. Other methods will yield different values but should produce the same trends. There is a certain amount of correlation between the two width parameters Γ and σ. It is, however, not possible to do without either one of them because the white lines of the rare earths are fairly broad both at the top and at the bottom. This is not solely due to finite instrumental resolution which at the Sm L_{II} or L_{III} edge is rather small. In this work the resolution is normally neglected. Otherwise it is taken into account by convolving the quantity I/I_0 as a function of energy with a Gaussian of full width equal to the given instrumental resolution. I/I_0 is obtained by adding to the model the previously subtracted background. This procedure is exact if I_0 is constant. Ideally, one would convolve the individual counting rates I and I_0 but they cannot be obtained from the model. No attempt is made at deconvolution of the absorption spectrum because, besides noise, it yields results that are not uniquely defined. Note that the actual HWHM of the Voigt line profile has to be determined numerically from Γ and σ [17, 198].

Frequently the second derivatives of the absorption spectra are fitted [199-201] in order to determine better the positions of certain features in the spectrum. For valence determination this is not a good method because the valence is contained in the amplitude and the second derivative (or even the first derivative) has lost sensitivity to the amplitude. A fit result obtained by fitting to derivatives is clearly in error when viewing it in the underived form. Besides, derivatives always add noise to the signal so that smoothing may become necessary. In Chapters 7 and 8 we see that there exists a linear dependence of the valence obtained from fits and the energy difference $\Delta E \equiv E^{3+} - E^{2+}$ between the positions of the two absorption profiles. This dependence is not an

artifact since ΔE and the valence are hardly correlated in the fits. Therefore one should be able to determine the valence from ΔE alone.

Since the same lineshapes are employed for the two valence states it is not necessary to integrate the area underneath the peaks in order to determine the valence. However, when comparing different spectra, knowledge of the peak area may be useful. To this end, we provide the area A underneath a single peak, Eq. (6.79), excluding the step:

$$A = \frac{\pi\sqrt{2\pi}}{2\,K}\,\frac{\sigma}{\Gamma}\,\left(2\,Y_{max} - 1\right) . \qquad (6.82)$$

6.13 Valence Interpolation Formula

Fractional valences are frequently determined according to Vegard's law [202] by linear interpolation between the two lattice constants a^{2+} and a^{3+} corresponding to integer-valent states. Based on Ref. 203 it has been suggested to interpolate intermediate valences between the integer-valent bulk moduli instead [204].

One may, however, also treat $\left(Sm^{2+}_{1-v}Sm^{3+}_{v}\right)Se$ as a mixture and then employ volumes instead of lattice constants. This has been done for some alloys [205, 206] and we will adopt this latter ansatz and write:

$$V = (1-v)\,V^{2+} + v\,V^{3+} \qquad (6.83)$$

where V^{2+} is the volume of a unit cell if only Sm^{2+} atoms are present and V^{3+} is its volume if there are only Sm^{3+} atoms. Eq. (6.83) states that the volume of an intermediate-valent state is obtained by linear interpolation.

This model will now be used to examine the limiting behaviour of the pressure dependence of the valence, to introduce a valence compressibility κ_v, and to examine the relationship between the inflection point in the valence-vs.-pressure curve and in the volume-vs.-pressure curve.

Taking the derivative with respect to pressure we get:

$$\frac{dV}{dp} = \frac{dv}{dp}\left(V^{3+} - V^{2+}\right) + (1-v)\frac{dV^{2+}}{dp} + v\frac{dV^{3+}}{dp} \quad . \tag{6.84}$$

This equation tells us that if dv/dp is positive then dV/dp must be negative (because dV^{2+}/dp, dV^{3+}/dp, and $V^{3+} - V^{2+}$ are all negative). The reverse conclusion does not follow. If dv/dp is positive then Eq. (6.84) also shows that a transition that has a more rapid change in volume will produce a more rapid change in the valence too provided that the pressure dependence of V^{2+} and V^{3+} remains the same. These conclusions only confirm what we intuitively expected.

For the compressibility κ we obtain from Eq. (6.84):

$$\kappa \equiv -\frac{1}{V}\frac{dV}{dp} = \frac{dv}{dp}\left(\frac{V^{2+} - V^{3+}}{V}\right) + (1-v)\frac{V^{2+}}{V}\kappa^{2+} + v\frac{V^{3+}}{V}\kappa^{3+} \quad . \tag{6.85}$$

The compressibilities κ^{2+} and κ^{3+} are defined as:

$$\kappa^{2+} \equiv -\frac{1}{V^{2+}}\frac{dV^{2+}}{dp} \quad ; \quad \kappa^{3+} \equiv -\frac{1}{V^{3+}}\frac{dV^{3+}}{dp} \quad . \tag{6.86}$$

For $v = 0$ we have $V = V^{2+}$ and κ must become equal to κ^{2+}. Therefore we require:

$$v = 0: \qquad \frac{dv}{dp} = 0 \quad . \tag{6.87}$$

For $v = 1$ we have $V = V^{3+}$ and for κ to be equal to κ^{3+} we must require:

$$v = 1: \qquad \frac{dv}{dp} = 0 \quad . \tag{6.88}$$

Hence, in this simple model the valence as a function of pressure must approach its limiting values with zero slope.

Eq. (6.85) furnishes the definition of a compressibility κ_v stemming from the variation of v with pressure:

$$\kappa_\nu \equiv \frac{d\nu}{dp}\left(\frac{V^{2+} - V^{3+}}{V}\right). \tag{6.89}$$

In accordance with Eqs. (6.87) and (6.88) we have:

$$\nu = 0 \text{ or } 1: \qquad \kappa_\nu = 0\ . \tag{6.90}$$

We can eliminate V^{3+} by employing Eq. (6.83). This yields:

$$\kappa_\nu = \frac{1}{\nu}\frac{d\nu}{dp}\left(\frac{V^{2+}}{V} - 1\right). \tag{6.91}$$

This equation is undefined at $\nu = 0$ but according to Eq. (6.90) κ_ν assumes its limiting value of zero as $\nu \to 0$.

By taking the second derivative of the volume V with respect to pressure we realize that the position of the inflection point of the volume-vs.-pressure curve need not coincide with the inflection point of the valence-vs.-pressure curve:

$$\frac{d^2V}{dp^2} = \frac{d^2\nu}{dp^2}\left(V^{3+} - V^{2+}\right) + 2\frac{d\nu}{dp}\frac{d}{dp}\left(V^{3+} - V^{2+}\right) + \nu\frac{d^2}{dp^2}\left(V^{3+} - V^{2+}\right) + \frac{d^2V^{2+}}{dp^2}\ .$$

Inspecting this equation, we see that $\frac{d^2V}{dp^2} = 0$ does not imply $\frac{d^2\nu}{dp^2} = 0$ and vice versa. This will be shown in Chapter 9.

By investigating the above equations it was not possible to obtain a useful relation that applies to either the inflection point of the volume-vs.-pressure curve or the inflection point of the valence-vs.-pressure curve. Neither could a practical equation involving the position of the maximum of the compressibility κ be obtained.

6.14 Determination of Compression from the Scaling Relation k·R = const.

If the application of pressure leads to a uniform compression of the solid, i.e. a scaling of the lattice constant, then the k-scale of the EXAFS of the compressed solid is expanded. Therefore one may expect that by compressing the k-scale again one can reproduce the original EXAFS spectrum, at least as far as its phase is concerned. We now suggest a method in which this idea can be used to determine the pressure.

We define the function $g(\varepsilon)$, with ε being a small positive quantity:

$$g(\varepsilon) \equiv \frac{2}{k_{max}-k_{min}} \cdot \int_{k_{min}}^{k_{max}} dk\; k^{n+\tilde{n}}\; \chi(k)\;\; \tilde{\chi}(k\,(1+\varepsilon)) \quad . \tag{6.92}$$

Here $\chi(k)$ is the EXAFS of the sample at a reference pressure. $\tilde{\chi}(k)$ is the EXAFS of the same sample at a different pressure which we assume, without loss of generality, is higher. The application of pressure leads to an expansion of the k-scale. If the compression is uniform then according to the scaling relation, Eqs. (3.72), (3.79), and (3.80), the low-pressure EXAFS measurement $\chi(k)$ and the high-pressure result $\tilde{\chi}(k)$ should coincide after a proper compression of the k-scale of the latter. This compression is indicated in Eq. (6.92) by $k\cdot(1+\varepsilon)$, which means that for a finite positive ε the magnitude k of the wave vector has to be smaller. n and $\tilde{n}$ are powers of k chosen such that $\chi(k)$ and $\tilde{\chi}(k)$, respectively, have overall amplitudes that are almost independent of k. It should now be apparent that if $\chi(k)$ and the compressed $\tilde{\chi}(k)$ do coincide, then $g(\varepsilon)$ will have a maximum and the compression can be determined.

We introduce $$k_o \equiv \frac{1}{2}\;(k_{min} + k_{max}) \quad \text{and} \quad \Delta k \equiv k_{max} - k_{min} \tag{6.93}$$

and substitute the EXAFS expressions:

$$g(\varepsilon) = \frac{2}{\Delta k} \cdot \int_{k_o-\Delta k/2}^{k_o+\Delta k/2} dk \sum_{i\;j} \left| f_i(k) \right| \left| \tilde{f}_j(k) \right| \frac{k^{n+\tilde{n}-2}}{R_i^2\;\tilde{R}_j^2}\; e^{-2(\sigma_i^2+\tilde{\sigma}_j^2)\,k^2}$$

$$\times\; \sin\!\left(2\,k\,R_i + \delta_{ti}(k)\right)\; \sin\!\left((2\,k\,(1+\varepsilon)\,\tilde{R}_j + \tilde{\delta}_{tj}(k)\right) \quad . \tag{6.94}$$

The tilde refers to the high-pressure EXAFS, $\tilde{\chi}(k)$, and the indices i and j label the coordination shells for χ (k) and $\tilde{\chi}$, respectively. Note that we have modified k only in the phase of $\tilde{\chi}(k)$. The changes of the coordination-shell radii are so small that they can be neglected in the amplitude terms as well. Besides, since the compression is so small, it is evident that the integral in Eq. (6.94) will only relate coordination shells of the same order, which means i = j . According to Chapter 3 we will assume that the backscattering amplitudes and the total phases are independent of pressure, i.e. $\left|\tilde{f}_i(k)\right| \cong \left|f_i(k)\right|$ and $\tilde{\delta}_{ti}(k) \cong \delta_{ti}(k)$. By proper choice of the powers n and $\tilde{n}$ one can minimize the k-dependence of the overall amplitudes. We thus assume that these terms are slowly varying functions of k and put them in front of the integral:

$$g(\varepsilon) = \sum_i \left| f_i(k) \right|^2 \frac{k^{n+\tilde{n}-2}}{R_i^4} \, e^{-2(\sigma_i^2+\tilde{\sigma}_i^2)\,k^2} \cdot I(\varepsilon) \ . \tag{6.95}$$

where $I(\varepsilon)$ is defined by:

$$I(\varepsilon) \equiv \frac{2}{\Delta k} \cdot \int_{k_o-\Delta k/2}^{k_o+\Delta k/2} dk \ \sin\left(2\,k\,R_i + \delta_{ti}(k)\right) \ \sin\left((2\,k\,(1+\varepsilon)\,\tilde{R}_i + \delta_{ti}(k)\right) \ . \tag{6.96}$$

We approximate the total phases by straight lines, Eq. (2.12):

$$\delta_{ti}(k) \cong p_{0i} + p_{1i}\,k \ ; \qquad p_{1i} < 0 \ . \tag{6.97}$$

We introduce the abbreviations:

$$a \equiv 2\,R_i + p_{1i} \ ; \quad \tilde{a} \equiv 2\,(1+\varepsilon)\,\tilde{R}_i + p_{1i} \ ; \quad b \equiv p_{0i} \ . \tag{6.98}$$

This yields for the integrand of $I(\varepsilon)$:

$$\sin\left(2\,k\,R_i + \delta_{ti}(k)\right) \ \sin\left((2\,k\,(1+\varepsilon)\,\tilde{R}_i + \delta_{ti}(k)\right) = \sin(a\,k+b) \ \sin(\tilde{a}\,k+b)$$

$$= \sin(a\,k) \ \sin(\tilde{a}\,k) \ + \ \sin^2(b) \ \cos((a+\tilde{a})\,k) \ + \ \sin(b) \ \cos(b) \ \sin((a+\tilde{a})\,k) \ .$$

We now integrate. For this purpose we need the following integral:

$$\frac{2}{\Delta x} \int_{x_o-\Delta x/2}^{x_o+\Delta x/2} \sin(px)\, \sin(qx)\, dx = \cos\Big((p-q)\, x_o\Big)\, \frac{\sin\Big((p-q)\, \Delta x/2\Big)}{(p-q)\, \Delta x/2}$$

$$- \cos\Big((p+q)\, x_o\Big)\, \frac{\sin\Big((p+q)\, \Delta x/2\Big)}{(p+q)\, \Delta x/2} \quad . \qquad (6.99)$$

We obtain for $I(\varepsilon)$ after some algebra:

$$I(\varepsilon) = \cos\Big((a-\tilde{a})\, k_o\Big)\, \frac{\sin\Big((a-\tilde{a})\, \Delta k/2\Big)}{(a-\tilde{a})\, \Delta k/2} - \cos\Big((a+\tilde{a})\, k_o+2\, b\Big)\, \frac{\sin\Big((a+\tilde{a})\, \Delta k/2\Big)}{(a+\tilde{a})\, \Delta k/2} \quad . \qquad (6.100)$$

Resubstituting the original quantities, (6.98), yields:

$$I(\varepsilon) = \cos\Big((R_i-(1+\varepsilon)\, \tilde{R}_i)\, 2\, k_o\Big)\, \frac{\sin\Big((R_i-(1+\varepsilon)\, \tilde{R}_i)\, \Delta k\Big)}{(R_i-(1+\varepsilon)\, \tilde{R}_i)\, \Delta k}$$

$$- \cos\Big((R_i+(1+\varepsilon)\, \tilde{R}_i+p_{1i})\, 2\, k_o+2\, p_{0i}\Big)\, \frac{\sin\Big((R_i+(1+\varepsilon)\, \tilde{R}_i+p_{1i})\, \Delta k\Big)}{(R_i+(1+\varepsilon)\, \tilde{R}_i+p_{1i})\, \Delta k} \quad . \qquad (6.101)$$

The first term of this integral contains a sinc function, defined as $\mathrm{sinc}(x) \equiv (\sin x)/x$. It is centered at $\varepsilon = \varepsilon_o$ where ε_o is given by:

$$\varepsilon_o \equiv \frac{R_i - \tilde{R}_i}{\tilde{R}_i} \quad . \qquad (6.102)$$

The sinc function is thus centered at a (positive) value equal to the relative compression, referred to the high-pressure state ($\tilde{R}_i$ in the denominator.). For uniform compression of the lattice the relative changes of each coordination-shell radius will be all equal and therefore ε_o is independent of the index i. If we ignore the cosine term, which is close to unity, then the FWHM is:

$$\left|R_i-(1+\varepsilon)\,\tilde{R}_i\right|\,\Delta k = \left|\varepsilon_o - \varepsilon_{1/2}\right|\,\tilde{R}_i\,\Delta k = 1.8955$$

$$\Rightarrow \qquad FWHM = 2\left|\varepsilon_o - \varepsilon_{1/2}\right| = \frac{2\cdot 1.8955}{\tilde{R}_i\,\Delta k} \quad . \tag{6.103}$$

$\varepsilon_{1/2}$ is the argument where the sinc function assumes half the value it has at ε_o. Note that the width, as opposed to ε_o, depends on the coordination shell radii $\tilde{R}_i$. Hence each coordination shell produces a peak (or valley, depending on the cos prefactor) at the same position but with a shell-dependent width. The broadest peak results from the first coordination shell.

The second sinc function has the same width as the first and is centered at:

$$\varepsilon_o^* \equiv -\,\frac{R_i+\tilde{R}_i+p_{1i}}{\tilde{R}_i} < 0 \quad . \tag{6.104}$$

Thus the peak position depends on the order i of the coordination shell. The separation of the two sinc functions is approximately equal to 2, independent of i:

$$\varepsilon_o - \varepsilon_o^* = 2\,(1+\varepsilon_o) + \frac{p_{1i}}{\tilde{R}_1} \cong 2 \quad .$$

Their widths are approximately $2/\Delta k$, assuming $\tilde{R}_i \rightarrow \tilde{R}_1 \cong 2$ Å in Eq. (6.103). Since normally $2/\Delta k << 2$, it will therefore be possible to distinguish the two sinc functions.

Thus the function $g(\varepsilon)$ according to Eq. (6.95) together with $I(\varepsilon)$ as given in Eq. (6.101) constitutes a model-independent method of determining the compression. The widths are less useful because $g(\varepsilon)$ is a superposition of peaks (or valleys) of varying width and because the selected powers of k, n and $\tilde{n}$, cannot completely remove the k-dependence of the amplitude. If the compression is known and $g(\varepsilon)$ peaks (or dips) at $\varepsilon_o \equiv (R_i - \tilde{R}_i)/\tilde{R}_i$ then this is a confirmation that the scaling relation mentioned above actually exists.

Chapter 7: **Results for SmSe**

We begin the data analysis with the determination of the pressures from the EXAFS of a calibrant. Then we investigate the Se K edge EXAFS which provides good R-space resolution. Afterwards the EXAFS of the Sm L_{III} edge in SmSe is analyzed and finally the valence is determined from the Sm L_{II} and L_{III} edges.

The EXAFS data are always fitted to the following expression [187], which is a detailed form of Eq. (2.9):

$$\chi(k) = \sum_j \frac{N_j}{k_j R_j^2} \rho_\tau(k_j)\, e^{-2R_j/\lambda} \exp\left(\frac{2}{3} C_{4j}\, k_j^4\right) \times f_j(k_j,\pi)\, e^{-2\sigma_j^2 k_j^2} \sin\left(2\, k_j\, R_j + \delta_{t,j}(k_j) + a_j - \frac{4}{3} C_{3j}\, k_j^3\right) . \qquad (7.1)$$

The index j labels the coordination shells which are located at R_j. Each shell j has its individual k-scale which is calculated from the k-scale of the data as follows:

$$k_j \equiv \sqrt{k^2 - \Delta E_j/\gamma} \quad . \qquad (7.2)$$

The function $\rho_\tau(k_j)$ results from the finite resolution of the monochromator and is defined in Section 6.4. For theoretical amplitudes $f_j(k_j,\pi)$ the mean free path is incorporated as $e^{-2R_j/\lambda}$, where $\lambda(k) = k/\tilde{\eta}$ (Section 2.5). σ_j^2 is the mean-square relative displacement and $\delta_{t,j}(k_j)$ the total phase of shell j. a_j is an offset that can be used to correct the phase if necessary. The terms involving C_{3j} and C_{4j} are cumulants, taking effects due to asymmetry into account (Section 2.3). Seven parameters may thus be allowed to vary for coordination shell j:

$$a_j,\ \Delta E_j,\ R_j,\ C_{3j},\ C_{4j},\ \sigma_j^2,\ N_j\ .$$

Of course, not all parameters are being varied simultaneously. Furthermore there are the two parameters $\tilde{\eta}$ (Eq. (2.43)) and the pre-monochromator slit width s which apply to all coordination shells jointly. Here they are always kept fixed.

For R-space fits the Fourier transform of Eq. (7.1) is fitted to the Fourier transform of the data.

The data analysis is done separately for each run and in chronological order. The results are given in tabular form and important graphs are presented. In all cases where the finite resolution of the x-ray monochromator is considered the pre-monochromator slit width is assumed to be 1 mm.

In all cases a Hamming window (Section 6.6) was employed for the k-to-R Fourier transform. No window function was employed for the R-to-k back transform.

While it is common practice when applying the phase-difference method to have the identical k-space range for the unknown and the reference datasets, we have found with the R-space fitting procedure (using empirical amplitudes and phases) that small changes of the k-space range have an insignificant effect on the fit interval in R-space.

The tables with the EXAFS results contain also the R-space fit interval, the transform interval in k-space, the edge energy, and the value χ^2_{min} at the optimum according to Eq. (6.58). The numerical results presented in the tables have more significant figures than warranted by our error analysis. However, the numbers were entered in this manner in order to permit one to repeat the fit results if necessary and also to enable one to see the trends in the results with pressure.

7.1 Pressure Determination

The pressure for the SmSe datasets is determined from the EXAFS of a calibrant. Here this calibrant is either Cu or RbCl and it is pressurized together with the sample. The EXAFS datasets for the calibrant are measured for several applied pressures and the interatomic distances are determined. With this knowledge the reduced volume V/V_o is calculated. Using known calibration curves of V/V_o vs. pressure one can then interpolate the pressure. In Cu we measure the nearest-neighbour distance and in RbCl we determine both the nearest and next-nearest-neighbour distances because it was not possible to separate a single shell satisfactorily. For temperatures other than room temperature the pressure calibration curves have to be modified as detailed in Section 5.8. This modification is more pronounced for RbCl than it is for Cu.

In all cases the EXAFS analyses for the pressure calibrants are performed in R-space only. In this way the data and the fitting function are both Fourier transformed and thus artifacts are present in both cases. If we fitted in k-space the data would have to be Fourier filtered and thus possibly exhibiting some artifacts while the fitting function would not have undergone any Fourier transformation.

We can analyze the EXAFS of Cu by, for example, extracting the EXAFS phase shift and then applying the phase-comparison method (Section 6.8). However, because the compressibility of Cu is not very high the pressure-induced changes in the nearest-neighbour distance are rather small. Fitting the phase difference has subjective difficulties because the difference is not a nice straight line when changes of the nearest-neighbour distance are minute. The pressure-induced change in R that is obtained by using different fit intervals varies and the error bars for the change in R can be obtained from approximate error analysis.

We, however, prefer least-squares fitting. It has the added advantage that the data range is not reduced due to Fourier-filtering artifacts as is the case with the phase comparison where experimental phases have to be extracted. Also if one fits in R-space rather than k-space the artifacts due to fitting to the inverse transform do not exist. The disadvantage with least-squares fitting is that the scattering amplitude and phase must be known. It turned out that they hardly change under the pressures involved here (see Ref. 81 for Cu). Hence we employ one and the same backscattering amplitude and phase for all pressures.

We also employ the curved-wave theory of Schaich [7] and McKale [8-10]. Since the changes of the interatomic distances are too small to produce any significant variations in the curved-wave effects on the backscattering amplitudes and phases we will calculate amplitudes and phases only for atmospheric pressure. This calculation has been described in detail in Chapter 3. The central phases are those of Teo and Lee [11] and no curved-wave effects need to be considered for them.

For Cu it turned out that one has to subtract $\pi/2$ from Teo and Lee's central phase because otherwise it is not possible to obtain a reasonable fit. Besides, the nearest-neighbour distance would deviate too much from the crystallographic value of 2.553 Å. The Cu-backscattering amplitude and the total phase are shown in Figs. 7.1 and 7.2 as a function of k. The amplitude is practically identical

to the one of Fig. 3.4 of Chapter 3 (2.553 Å as compared to 2.5 Å). The phase displayed in Fig. 7.2 is the total phase, that is the sum of the backscattering and the central phase.

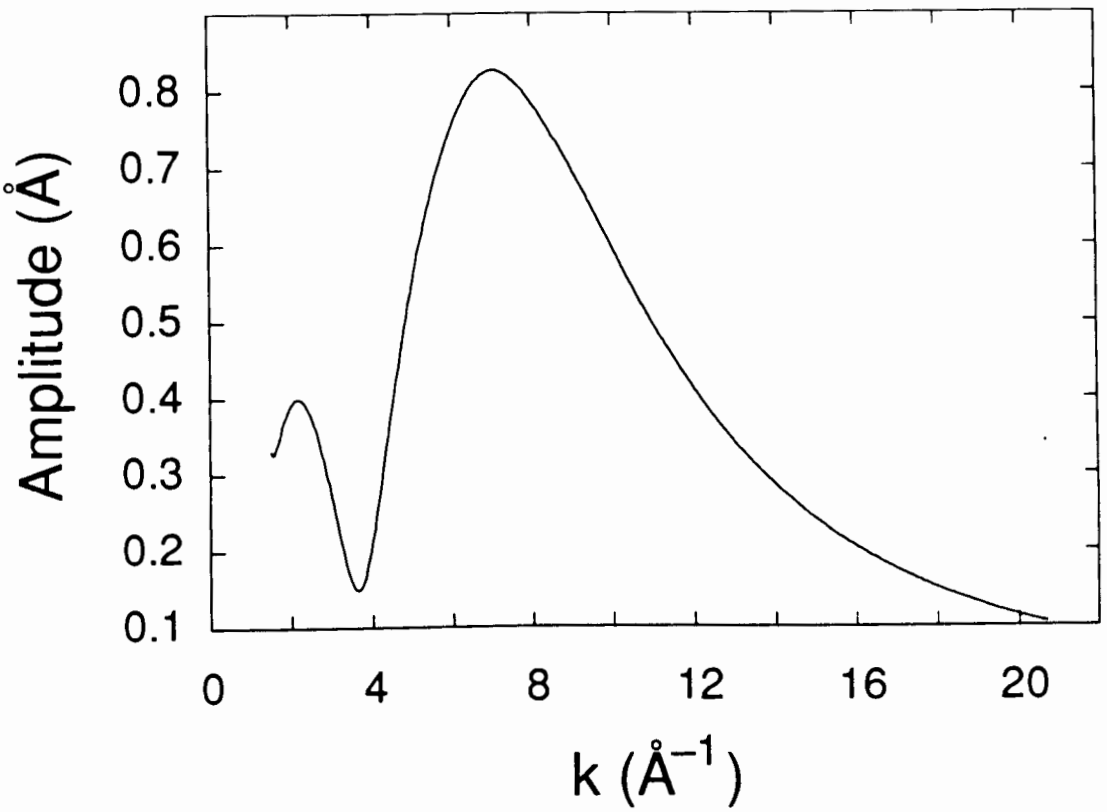

Fig. 7.1: Backscattering amplitude for copper metal calculated in curved-wave theory for R = 2.553 Å and K- or L_I-edge absorption.

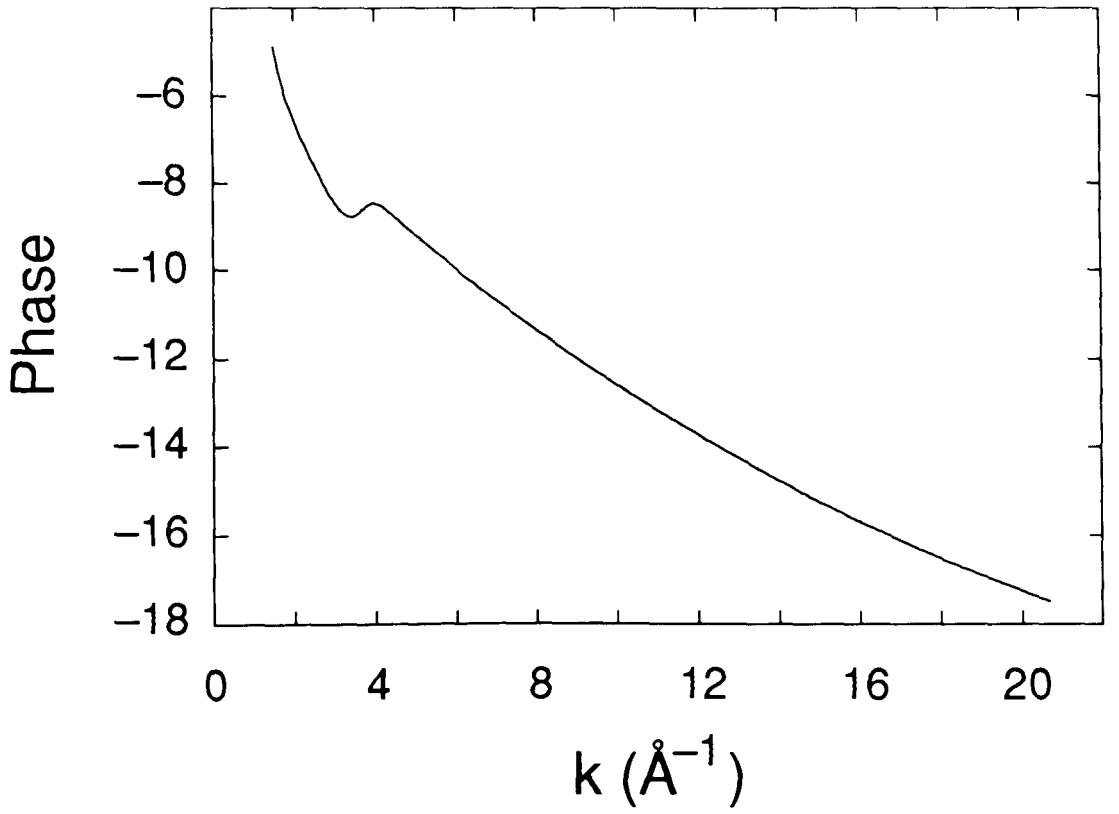

Fig. 7.2: Sum of backscattering phase for copper metal, calculated in curved-wave theory for R = 2.553 Å and K- or L_I-edge absorption, and Teo and Lee's [11] central phase extrapolated as described in Section 3.5.

It was not necessary to include asymmetry terms in the EXAFS analysis of copper.

In the case of RbCl we calculate the Cl- and Rb-backscattering amplitudes and phases somewhat crudely by using simply the atomic potentials. It would have been better to do a more extensive calculation like the one for SmSe but under pressure RbCl transforms very soon (at 5.2 kbar) from the NaCl structure into the CsCl structure. Because of this different crystal structure it would thus be necessary to go through the whole formalism again. It is assumed that we can also get reasonable results for interatomic distances with backscattering amplitudes and phases calculated from atomic potentials rather than from muffin-tin potentials. Besides, we are only interested in

changes of interatomic distances. For Rb it was not necessary to subtract $\pi/2$ from Teo and Lee's central phase.

The Fourier transform magnitude of a typical RbCl dataset is shown below. From this figure it is clear that the pressure determination for RbCl involves the EXAFS analysis of two coordination shells.

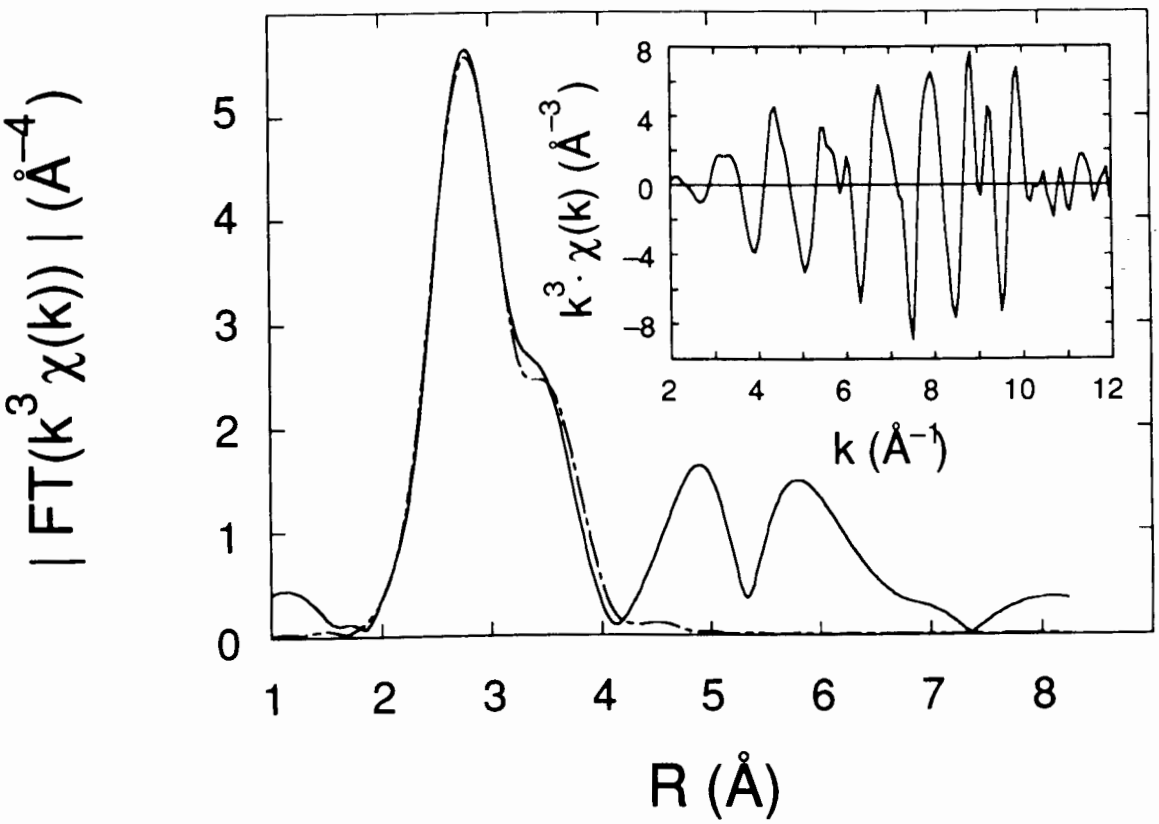

Fig. 7.3: Magnitude of the Fourier transform of $k^3\,\chi(k)$ of RbCl at 42.9 kbar (CsCl structure) and at 77K. The solid line is the data and the dashed line is the fit. The abscissa is not corrected for the EXAFS phase shift. The insert shows the unfiltered data as $k^3\,\chi(k)$.

In RbCl the first coordination shell with respect to a Rb atom consists of Cl atoms, located at the nearest-neighbour distance of R = 3.366 Å . Its backscattering amplitude and total phase are shown

in Figs. 7.4 and 7.5. Figs. 7.6 and 7.7 correspond to the next-nearest-neighbour shell of Rb atoms located at R = 3.887 Å .

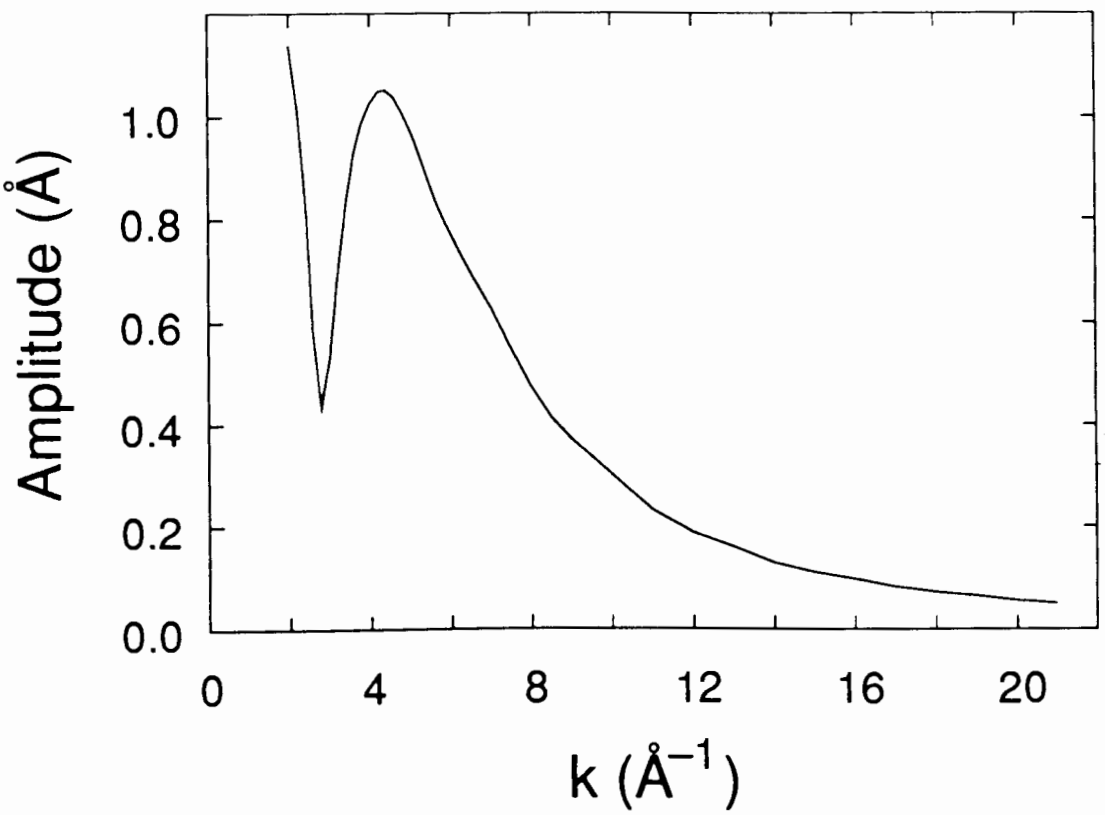

Fig. 7.4: Backscattering amplitude for Cl calculated in curved-wave theory for R = 3.366 Å and K- or L_I-edge absorption.

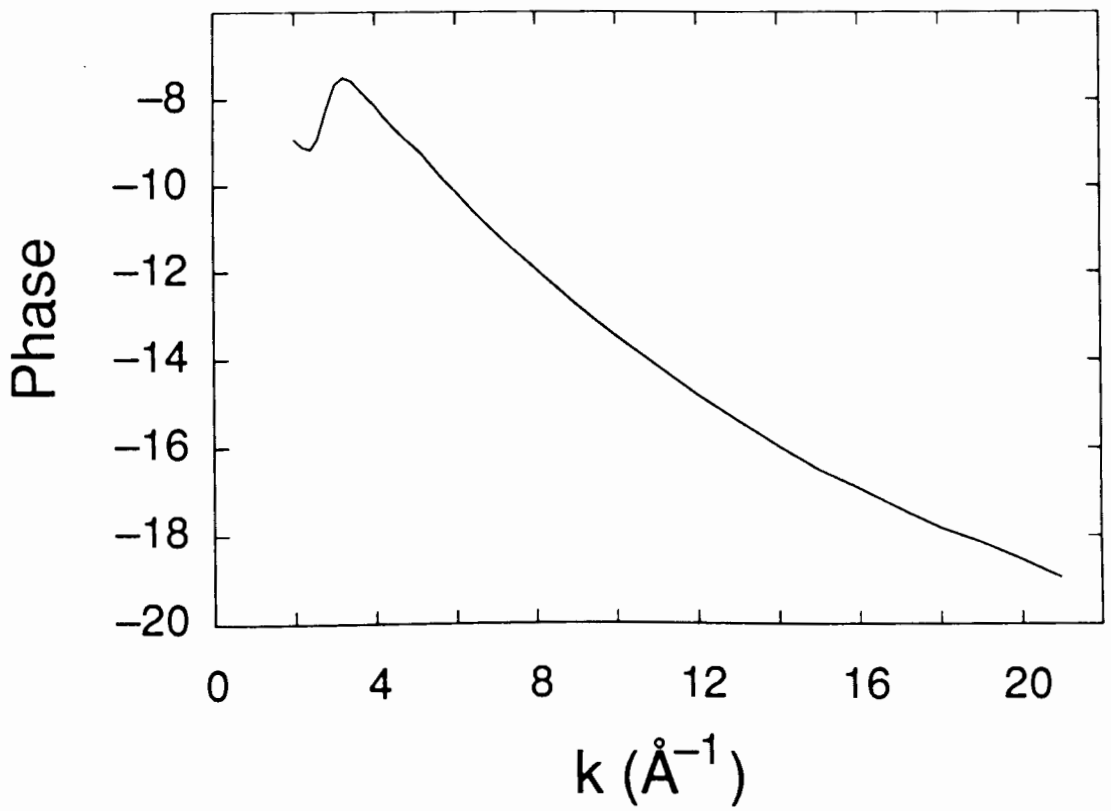

Fig. 7.5: Sum of backscattering phase for Cl, calculated in curved-wave theory for R = 3.366 Å and K- or L_I-edge absorption, and Teo and Lee's [11] central phase for Rb extrapolated as described in Section 3.5.

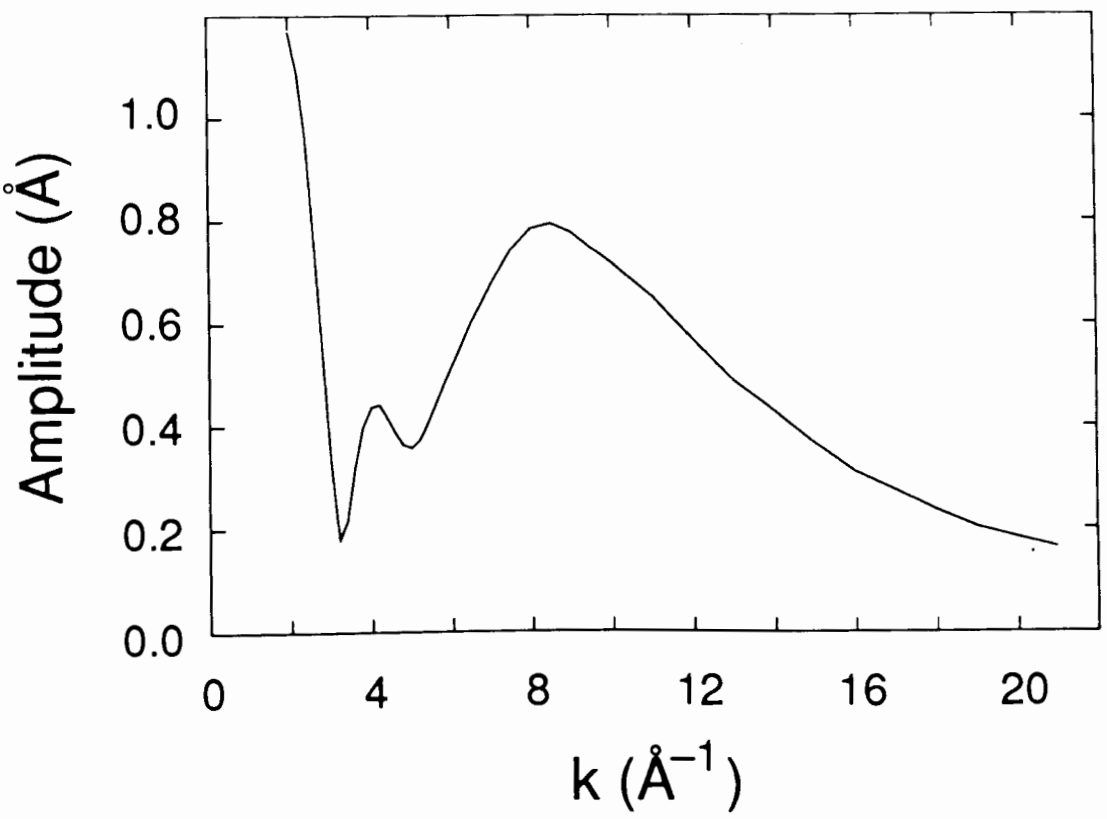

Fig. 7.6: Backscattering amplitude for Rb calculated in curved-wave theory for R = 3.887 Å and K- or L_I-edge absorption.

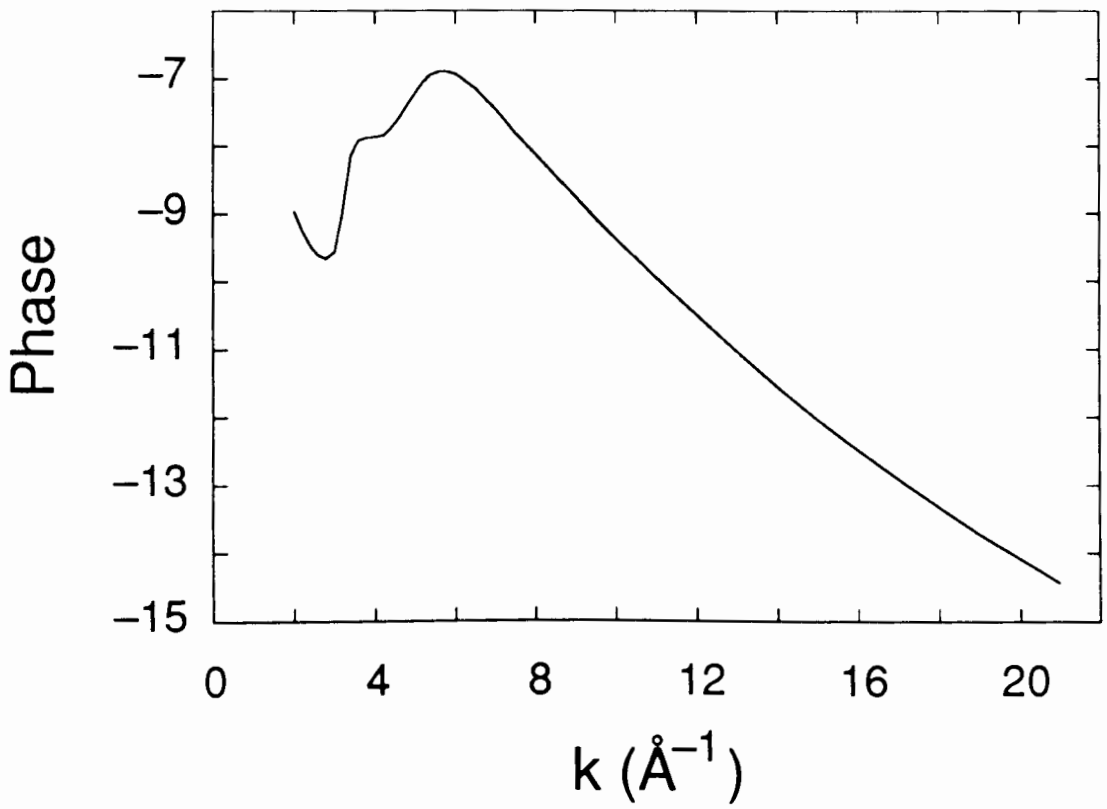

Fig. 7.7: Sum of backscattering phase for Rb, calculated in curved-wave theory for R = 3.887 Å and K- or L_I-edge absorption, and Teo and Lee's [11] central phase for Rb extrapolated as described in Section 3.5.

In these two-shell fits to RbCl we fix the ratio N_2/N_1 of the number of atoms in the second and first coordination shells at its crystallographic value of 0.75. When R_2/R_1 is fixed at a value of 1.17 the parameter of interest, R_1, becomes uncorrelated with any other and good fits are obtained. $R_2/R_1 = 1.17$ is sufficiently close to the value of $2/\sqrt{3} = 1.1547$, known from crystallography.

In order to obtain reliably the changes of interatomic distances with pressure it is important that we suppress any correlation of the fitted distance R_1 with other fit parameters, especially with ΔE_j. We first performed fits where ΔE_j was variable. There was no evident pressure dependence in ΔE_j.

The fluctuation in ΔE_j was 1 to 1.5 eV, approximately. Thus it was sufficient to perform a second series of fits in which ΔE_j was fixed at its average value.

The correlation between σ_1^2 and N_1 is strong, too. However, neither of these parameters is correlated with R_1 and they can therefore be allowed to vary simultaneously, thus improving the fit. Since σ_1^2 (and σ_2^2, in the case of RbCl) and N_1 are varied simultaneously in the EXAFS fits, their individual values do not have much meaning and are therefore omitted from the following tables.

We do not consider any asymmetry effects in RbCl at 77K because they do not improve the fits. Asymmetry is important at room temperature in the NaCl phase [157]. However, in the high-pressure CsCl-phase Tranquada [157] found it sufficient to do two-shell fits without including asymmetry effects. Besides, it is expected that asymmetry terms will decrease with increasing pressure and with decreasing temperature. Thus $C_{3j} \equiv 0$ and $C_{4j} \equiv 0$.

Before we can analyze the data we have to calculate $\tilde{\eta}$. According to Section 2.5, this quantity contains the effects of a mean free path but also those stemming from the finite core-hole lifetime. The results are:

Cu: $$\tilde{\eta} = \frac{\Gamma_e + \Gamma_c}{2\,\gamma} = \frac{4.39\text{eV} + 1.6\text{eV}}{2\,\gamma} = 0.786\ \text{Å}^{-2}\ ,$$

RbCl: $$\tilde{\eta} = \frac{\Gamma_e + \Gamma_c}{2\,\gamma} = \frac{2.78\text{eV} + 3.3\text{eV}}{2\,\gamma} = 0.798\ \text{Å}^{-2}\ ,$$

(absorbing element underlined).

The following tables contain the results of the pressure calibrations. All fits to the calibrants were performed in R-space to the Fourier transform ("FT") of $k^3\,\chi(k)$. One-shell fits were employed for Cu and two-shell fits for RbCl. From the nearest-neighbour distance R_1 and a reference nearest-neighbour distance R_o, indicated in boldface in the tables, one obtains the reduced volume for cubic crystals simply through:

$$V/V_o = (R_1/R_o)^3\ . \qquad (7.3)$$

Using known curves of V/V_o versus pressure (Section 5.8) one can then determine the pressure. At room temperature a hydraulically driven pressure cell is employed and the applied oil pressure P_{Oil} is listed. At liquid-nitrogen temperature the mechanically driven cell, described in Section 5.9, is used and the number of turns, N_T, is listed in the tables. In this way it is possible to estimate pressures based on P_{Oil} or N_T so that the EXAFS of the pressure calibrant need not be measured for every pressure point. A plot of the calibrant pressure as a function of either P_{Oil} or N_T follows each table.

The error in extracting R_1 is determined according to the method outlined in Section 6.10 and in Refs. 187 and 188. The error bars are determined by the change of R_1 when χ^2 increases to $2 \cdot \chi^2_{min}$ while the other fit parameters are allowed to vary. Error bars obtained in this way are rather conservative. From the error for R_1 we obtain the error in the pressure by using the known calibration curves. It turns out that the uncertainty in the pressure obtained from a copper calibration is approximately 2.5 times greater than the pressure uncertainty resulting from a calibration using RbCl. This is due to the smaller compressibility of copper as compared to RbCl.

Table 7.1: Pressure calibration from Cu K edge EXAFS (LOG.CU1.B):
(Dec. '83; Si (111); T = 300K)

One-shell fits in R-space to $FT(k^3 \chi(k))$ using theoretical amplitude and phase

fixed: $a_1 \equiv -1.5708$; $\Delta E_1 \equiv 1.036$ eV; $C_{31} \equiv 0.0$; $C_{41} \equiv 0.0$

variable: R_1; σ_1^2; N_1

					Fit interval (Å)		Transform interval ($Å^{-1}$)	
Dataset	R_1 (Å)	V/V_o	P_{Oil}(psi)	p (kbar)	R_{min}	R_{max}	k_{min}	k_{max}
E_{Edge}(eV)						χ^2_{min} ($Å^{-6}$)		
CUSE00.N00.B	**2.555**	**1**	**0**	**0**	**1.083**	**2.953**	**1.812**	**12.159**
8978.19	**± 0.004**			**±6.1**		**0.12**		
CSSE07.N07.B	2.551	0.995	700	6.4	1.129	2.909	1.850	12.096
8978.53	±0.006			±11.0		0.26		
CSSC13.N10.B	2.542	0.984	1300	22.7	1.214	2.876	1.850	12.506
8981.14	±0.004			±7.0		0.20		
CSSE19.N13.B	2.533	0.974	1900	39.6	1.127	2.850	1.813	13.571
8981.66	±0.005			±9.6		0.42		
CSSE20.N27.B	2.531	0.9715	2000	44.1	1.131	2.849	1.812	12.605
8978.53	±0.004			±7.7		0.22		
CSSE23.N30.B	2.525	0.965	2300	55.1	1.120	2.844	1.850	12.529
8979.57	±0.004			±7.6		0.22		
CSSE27.N33.B	2.518	0.957	2700	68.3	1.077	2.909	1.850	12.529
8979.57	±0.004			±8.2		0.20		

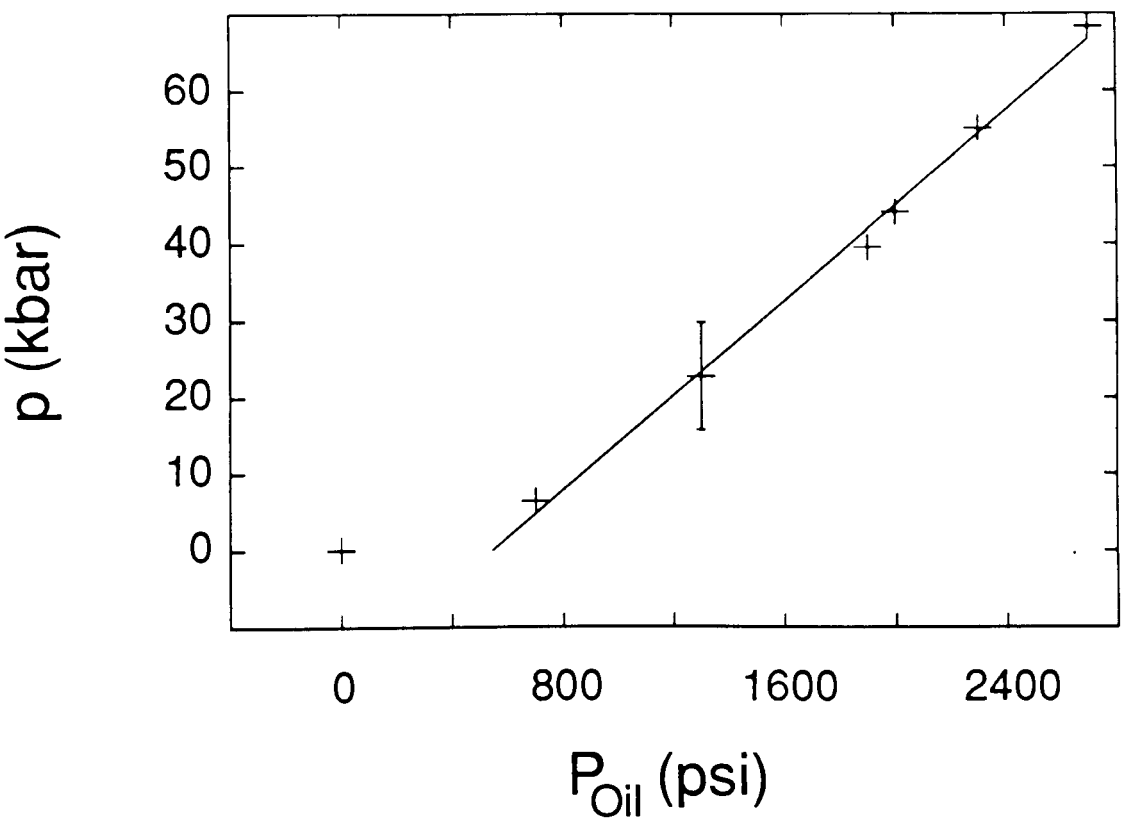

Fig. 7.8: Pressure p of a copper calibrant versus the oil pressure P_{Oil} applied by a hydraulic pump. The data are those of the previous table. A straight line was fitted excluding the origin. Its slope is 3.1 ± 0.1 kbar/(100 psi) and the intercept is -17 ± 2 kbar .

Table 7.2: Pressure calibration from Cu K edge EXAFS (LOG.CU1.C):
(April '84; Si (111); T = 300K)

One-shell fits in R-space to $FT(k^3 \chi(k))$ using theoretical amplitude and phase

fixed: $a_1 \equiv -1.5708$; $\Delta E_1 \equiv -0.924$ eV; $C_{31} \equiv 0.0$; $C_{41} \equiv 0.0$

variable: R_1; σ_1^2; N_1

					Fit interval (Å)		Transform interval ($Å^{-1}$)	
Dataset	R_1 (Å)	V/V_o	P_{Oil}(psi)	p (kbar)	R_{min}	R_{max}	k_{min}	k_{max}
E_{Edge}(eV)						χ^2_{min} ($Å^{-6}$)		
Reference at 300K: R_o = 2.542 Å (estimated)								
CUCA10.N20.C	2.538	0.996	1000	5.6	1.342	2.925	1.812	12.946
8978.71	±0.004			±7.8		0.24		
CUCA17.N31.C	2.5325	0.989	1700	16.4	1.271	2.901	1.812	13.074
8978.71	±0.006			±10.9		0.49		
CUCA20.N59.C	2.521	0.975	2050	38.1	1.271	2.901	1.812	12.882
8978.71	±0.005			±9.7		0.41		
CUCA22.N78.C	2.519	0.973	2250	41.6	1.313	2.912	1.862	12.787
8978.71	±0.008			±15.5		1.08		

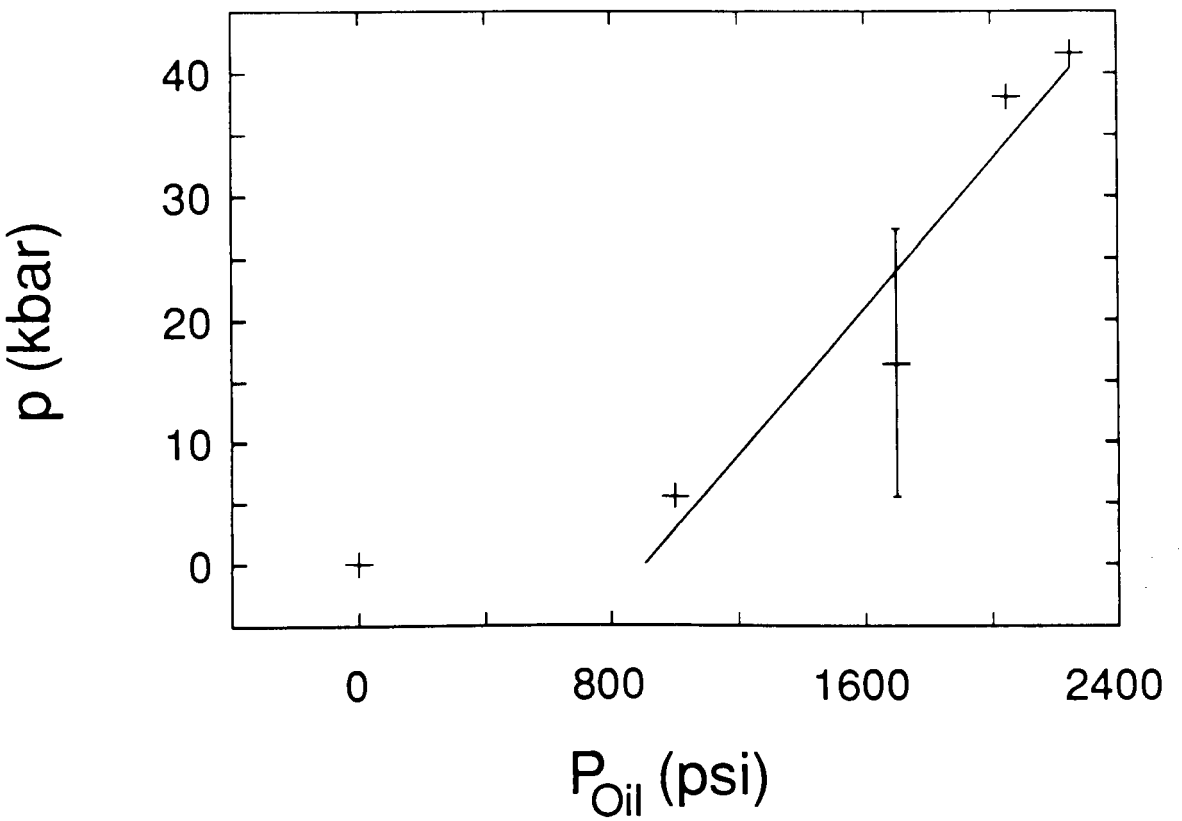

Fig. 7.9: Pressure p of a copper calibrant versus the oil pressure P_{Oil} applied by a hydraulic pump for the data of Table 7.2. The straight-line fit excluded the origin. The slope is 3.0 ± 0.7 kbar/(100 psi) and the intercept is -27 ± 12 kbar .

The following table contains the results for the pressure calibration with RbCl. The reference nearest-neighbour distance is the distance just above the pressure of the NaCl-to-CsCl phase transition at 77K. According to the discussion in Section 5.8 this value is $R_o = 3.3504$ Å at a pressure of 5.2 kbar.

Table 7.3: Pressure calibration from Rb K edge EXAFS in RbCl (LOG.RB6.F):
(June '86; Si (220); T = 77K)

Two-shell fits in R-space to $FT(k^3 \chi(k))$ using theoretical amplitudes and phases:

1st shell: Cl; 2nd shell: Rb

fixed: $a_1 \equiv 0.0$; $\Delta E_1 \equiv -2.3$ eV; $C_{31} \equiv 0.0$; $C_{41} \equiv 0.0$;
$a_2 \equiv 0.0$; $\Delta E_2 \equiv -2.3$ eV; $R_2/R_1 \equiv 1.17$; $C_{32} \equiv 0.0$; $C_{42} \equiv 0.0$; $N_2/N_1 \equiv 0.75$

variable: R_1; σ_1^2; N_1; σ_2^2

					Fit interval (Å)		Transform interval ($Å^{-1}$)	
Dataset	R_1 (Å)	V/V_o	N_T	p (kbar)	R_{min}	R_{max}	k_{min}	k_{max}
E_{Edge}(eV)						χ^2_{min} ($Å^{-6}$)		
Reference at 77K: R_o = 3.3504 Å								
RBCLN2.N30.F	3.209	0.879	1.75	44.2	1.700	4.167	1.850	11.913
15199.36	±0.005			±2.0		0.028		
RBCLN3.N35.F	3.213	0.882	3	42.9	1.693	4.170	1.858	11.963
15200.27	±0.006			±2.3		0.041		
RBCLN5.N40.F	3.191	0.864	5	52.0	1.700	4.167	1.850	12.061
15199.36	±0.006			±2.5		0.046		
RBCLN8.N45.F	3.172	0.848	8	60.1	1.734	4.026	1.858	11.963
15200.27	±0.007			±3.2		0.084		
RBCLN9.N51.F	3.146	0.828	9	73.2	1.741	4.022	1.850	11.987
15199.36	±0.007			±3.9		0.090		
RBCLNF.N57.F	3.1395	0.823	15	77.0	1.672	4.046	1.858	11.963
15200.27	±0.006			±3.5		0.078		

The next two figures show in one graph data for low and for high pressure. Fig. 7.10 shows Fourier transform magnitudes and Fig. 7.11 shows the same data in k-space.

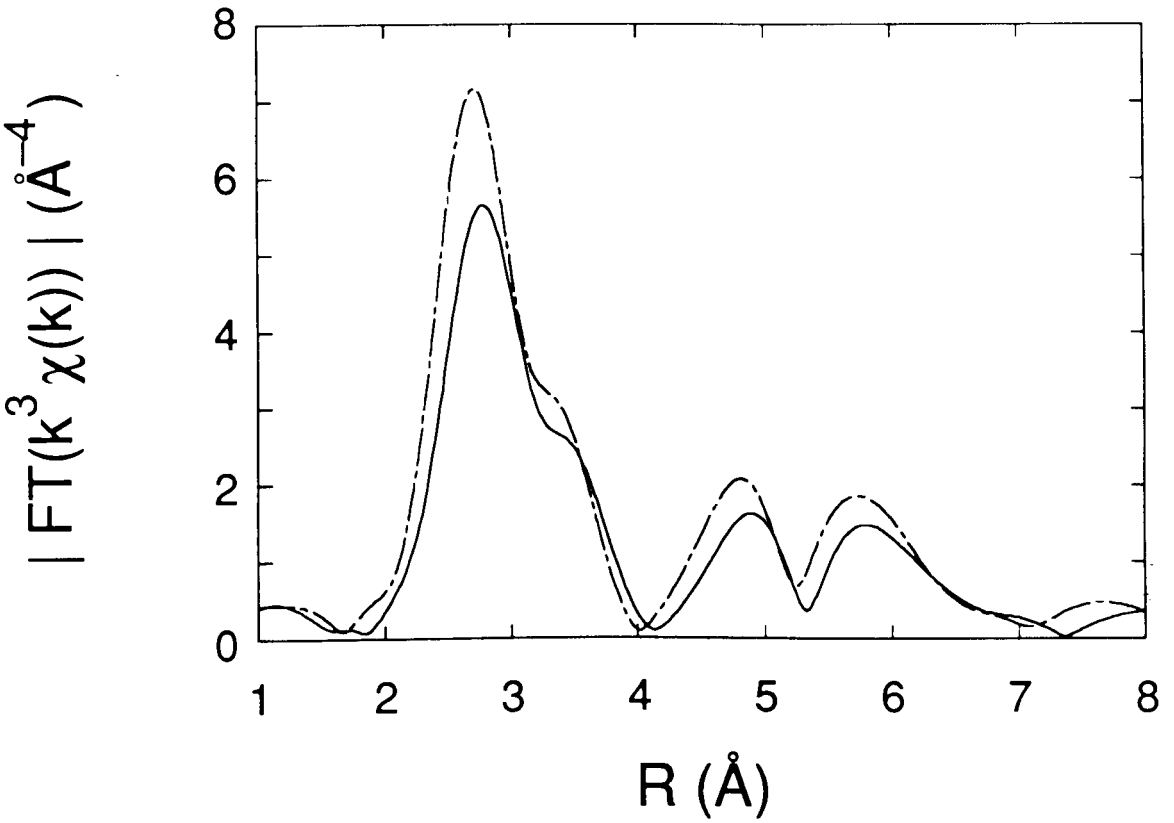

Fig. 7.10: Fourier transform magnitude of $k^3 \chi(k)$ for RbCl at 77K. The central atom is Rb. The solid line corresponds to 42.9 kbar and the dashed line to 77.0 kbar.

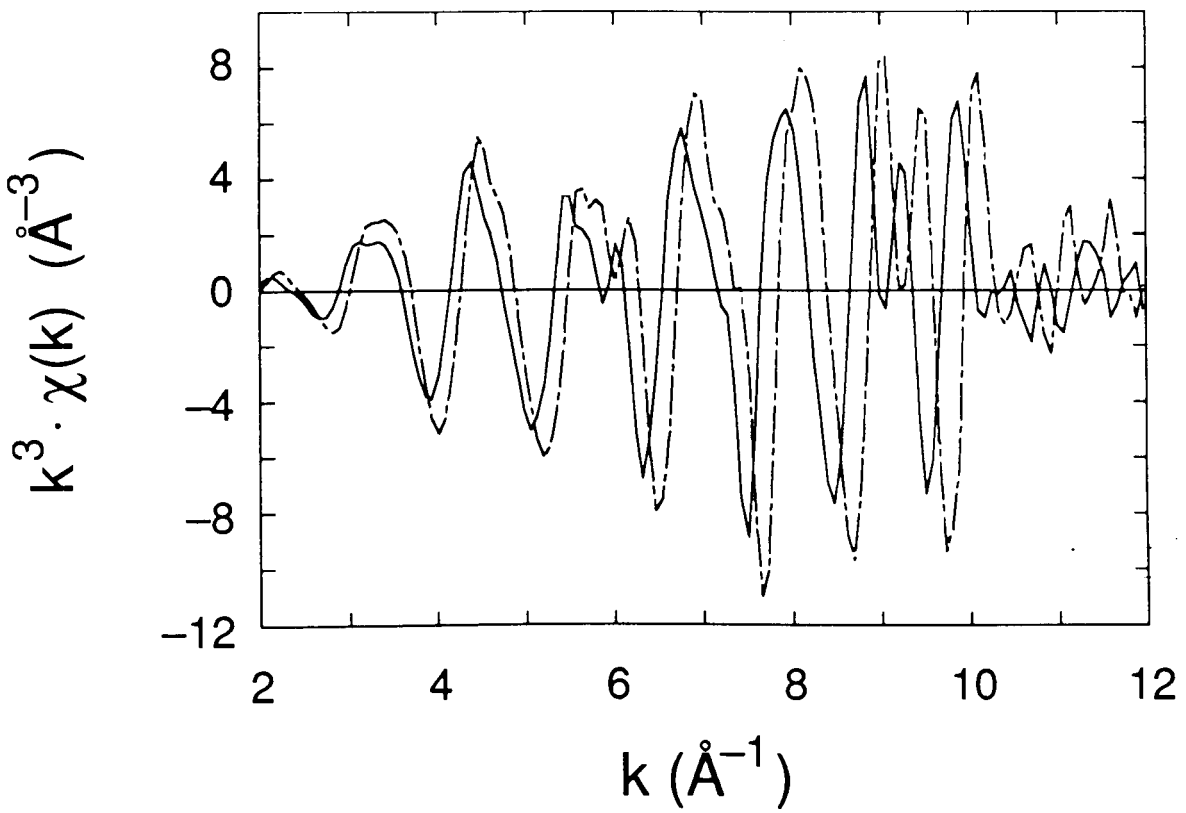

Fig. 7.11: $k^3\,\chi(k)$ for RbCl at 77K for the same data as in the previous figure. The central atom is Rb. The solid line corresponds to 42.9 kbar and the dashed line to 77.0 kbar.

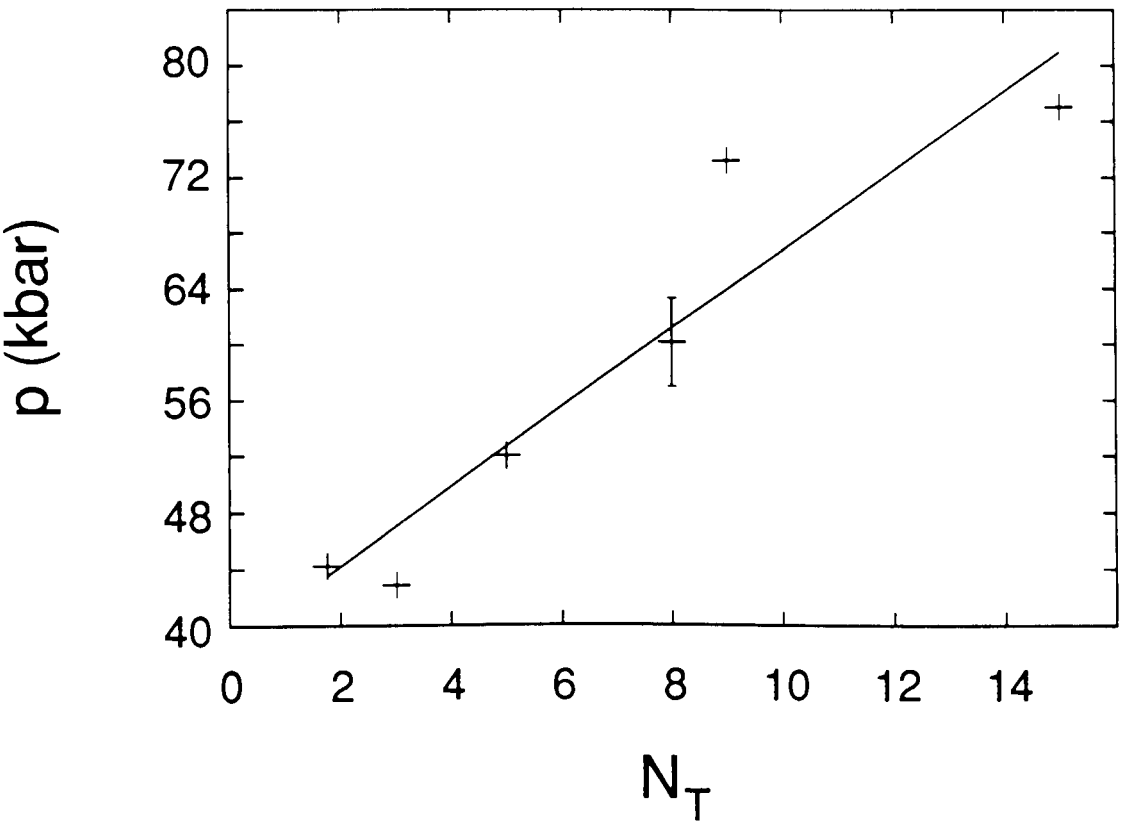

Fig. 7.12: Pressure p of a RbCl calibrant versus the number of turns N_T that were applied according to the data of Table 7.3. The slope of the straight-line fit, which excluded the origin, is 2.8 ± 0.5 kbar/turn and the intercept is 39 ± 4 kbar . The straight line is outside the error bars of the data points corresponding to 3 and to 9 turns, respectively.

Table 7.4: Pressure calibration from Cu K edge EXAFS (LOG.CU1.G):
(Dec. '86; Si (111); T = 77K)

One-shell fits in R-space to $FT(k^3 \chi(k))$ using theoretical amplitude and phase

fixed: $a_1 \equiv -1.5708$; $\Delta E_1 \equiv 0.846$ eV; $C_{31} \equiv 0.0$; $C_{41} \equiv 0.0$

variable: R_1; σ_1^2; N_1

					Fit interval (Å)		Transform interval ($Å^{-1}$)	
Dataset	R_1 (Å)	V/V_o	N_T	p (kbar)	R_{min}	R_{max}	k_{min}	k_{max}
E_{Edge}(eV)						χ^2_{min} ($Å^{-6}$)		
CU00.N86.G	**2.559**	**1**	**0**	**0**	**1.431**	**2.883**	**1.822**	**14.944**
8979.05	**±0.004**			**±6.9**		**0.73**		
CU01.N88.G	2.554	0.994	1	9.40	1.435	2.870	1.817	15.045
8979.05	±0.003			±5.3		0.55		
CU03.N03.G	2.546	0.9845	3	24.3	1.640	2.902	1.824	14.955
8979.75	±0.004			±6.9		1.35		
CU04.N08.G	2.5455	0.984	4	24.5	1.514	2.923	1.824	15.101
8979.75	±0.004			±6.9		0.85		
CUSM4T.N30.G	2.541	0.980	4.75	31.4	1.440	2.880	1.764	15.216
8981.14	±0.003			±5.7		0.56		
CUSM05.N38.G	2.541	0.979	5	32.6	1.266	2.892	1.890	15.117
8979.05	±0.003			±5.7		0.28		
CUSM5Q.N57.G	2.540	0.978	5.25	33.55	1.435	2.870	1.817	15.117
8979.05	±0.003			±5.8		0.51		
CUSM06.N89.G	2.533	0.9695	6	48.4	1.266	2.892	1.817	14.827
8979.05	±0.003			±5.8		0.55		
CUS11Q.N39.G	2.521	0.956	11.25	72.2	1.435	2.870	1.817	15.190
8979.05	±0.003			±5.9		0.56		

Fig. 7.13 shows the Fourier transform magnitudes of the data for low and for high pressure and Fig. 7.14 shows the same data in k-space.

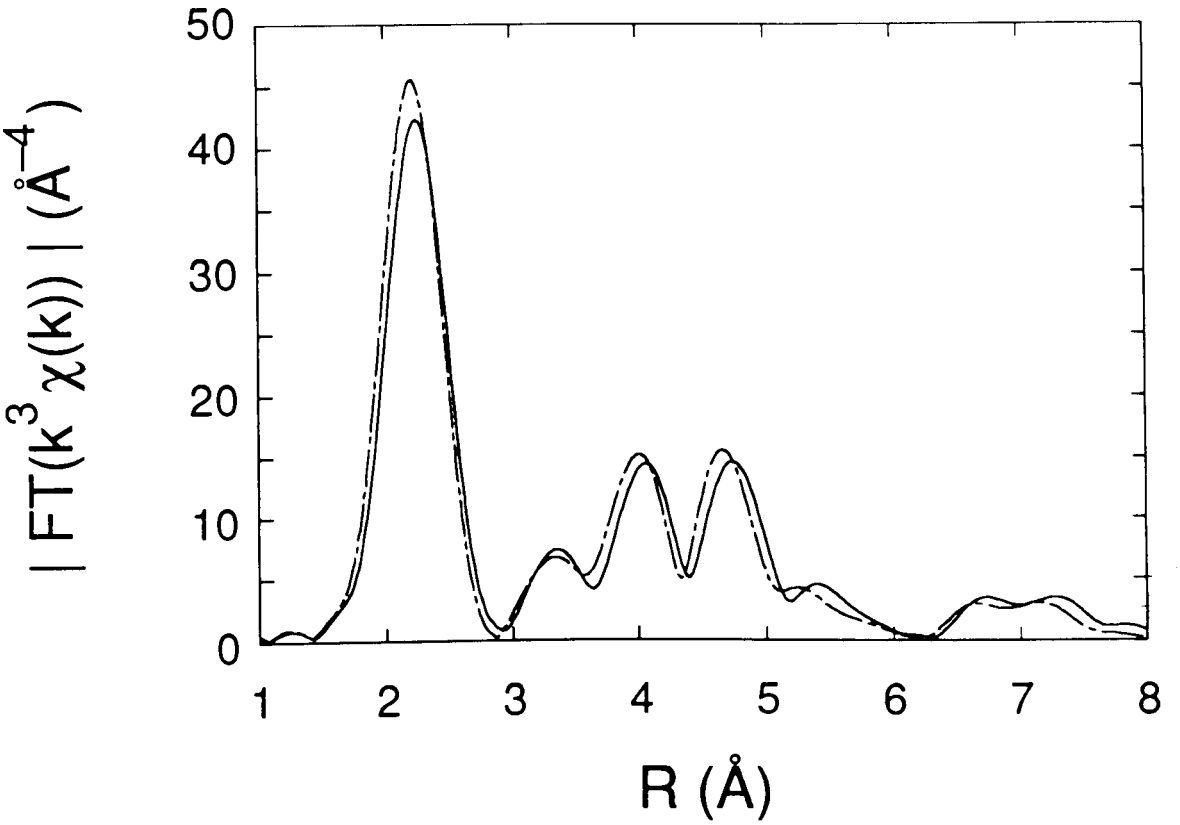

Fig. 7.13: Fourier transform magnitude of $k^3 \chi(k)$ for Cu at 77K. The solid line corresponds to 1 bar and the dashed line to 72.2 kbar.

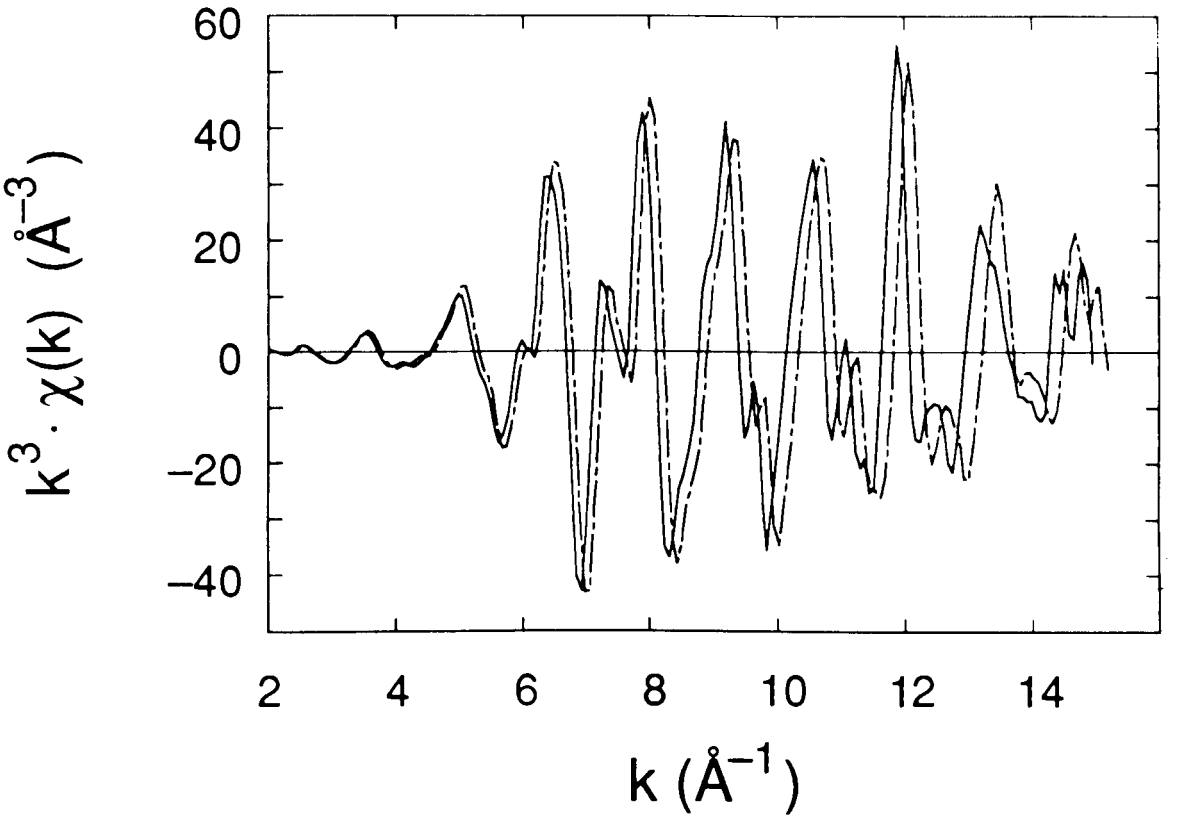

Fig. 7.14: $k^3 \chi(k)$ for Cu at 77K for the same data as in the previous figure. The solid line corresponds to 1 bar and the dashed line to 72.2 kbar.

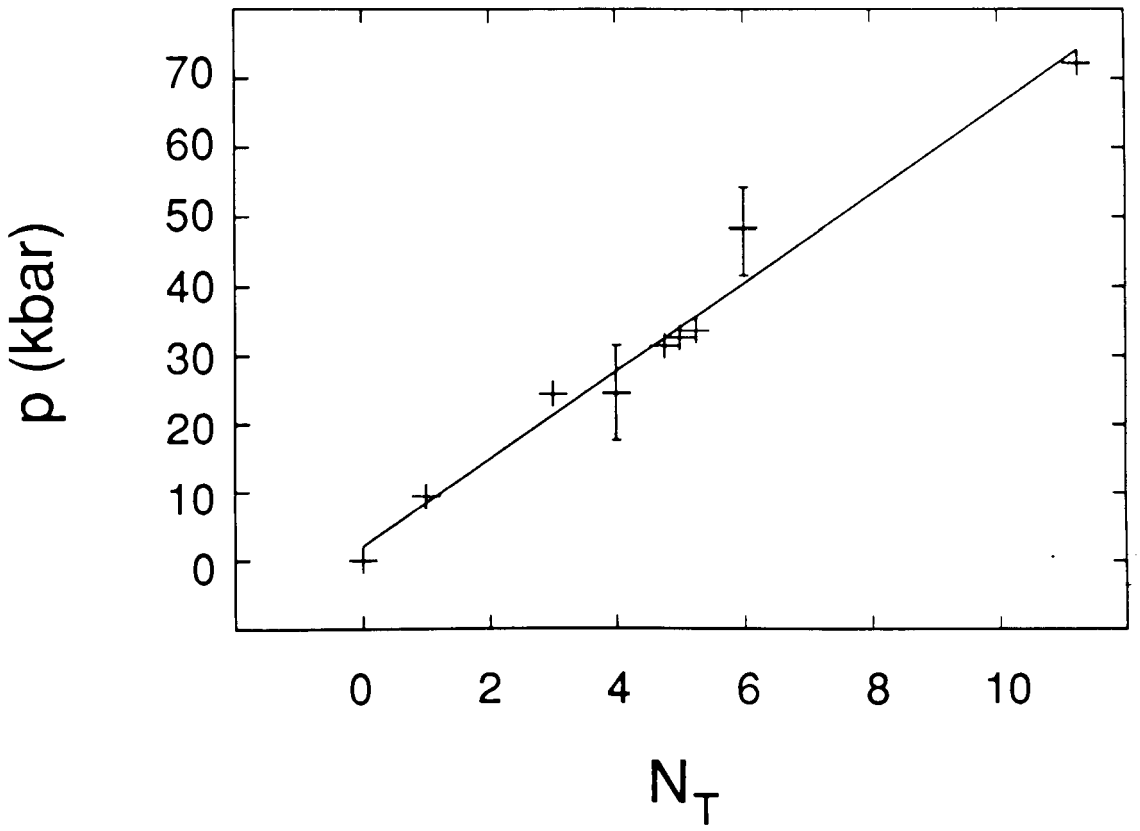

Fig. 7.15: Pressure p of a copper calibrant versus the number of turns N_T that were applied. The data are those of Table 7.4. The slope of the straight-line fit, including the origin, is 6.4 ± 0.4 kbar/turn and the intercept is 2 ± 2 kbar .

7.2 Analysis of the Se K Edge EXAFS of SmSe

In this section we analyze the EXAFS data of the Se K edge, measured at 77K as a function of pressure. Most of the data analysis is done by performing one-shell fits with two variable parameters to the nearest-neighbour coordination shell, which consists of Sm atoms. Table 7.8, however, shows the results obtained by fitting two closely-spaced Sm shells to the nearest-neighbour shell. Another series of two-shell fits will be discussed in Chapter 9. Table 7.9 contains the results of a one shell fit to the nearest Se shell.

All data are fitted to the Fourier transform of $k^2 \chi(k)$. Most of the data are fitted using theoretical amplitudes and phases. Tables 7.10 and 7.12 contain results obtained with empirical amplitudes and phases. For the analysis with theoretical amplitudes and phases curved-wave theory is employed and it was found that better fits could be obtained by subtracting $\pi/2$ from the central phase of Se, as was also done for Cu.

The one-shell fits using theoretical amplitudes and phases are arrived at as follows: The phase offset a_1 is set to $-\pi/2$. The remaining six parameters ΔE_1, R_1, C_{31}, C_{41}, σ_1^2, and N_1 are all varied in an initial fit to the datasets considered. Then the values of each parameter are plotted versus the values of any other parameter obtained from the datasets under investigation. This is done in order to make sure that no possible physical relationship among them is overlooked. Then the one parameter which varies the least for all datasets is fixed at its average value and new fits are performed with only five variable parameters. The procedure is repeated until it is not physically reasonable to reduce the number of parameters further. In this process it is important to observe how χ^2, which takes the number of parameters into account (Eqs. (6.57) and (6.58)), changes when this number is reduced. If χ^2 increases drastically upon fixing one parameter then this parameter must be released again.

The end result is a two-parameter fit. The nearest-neighbour distance R_1 and the mean-square relative displacement σ_1^2 are varied. Their correlation in each fit is almost zero which implies that the fit results for these two parameters are physically meaningful. Note that for N_1, the number of nearest neighbours, we frequently find a value smaller than the correct value of 6. This is not unexpected because many body effects reduce the actual coordination number to approximately 70%.

For the fits employing theoretical amplitudes and phases we take the finite monochromator resolution into account and consider the mean free path and core-hole lifetime effects by defining $\tilde{\eta}$ as:

$$\text{Sm}\underline{\text{Se}}: \qquad \tilde{\eta} = \frac{\Gamma_e + \Gamma_c}{2\gamma} = \frac{2.76\text{eV} + 2.5\text{eV}}{2\gamma} = 0.690\ \text{Å}^{-2} ,$$

(absorbing element underlined) .

For the fits employing empirical amplitudes and phases, resolution, mean free path, and core-hole lifetime need not be considered for fitting because they are already contained in the reference amplitude. This reference amplitude is obtained from one of the datasets (indicated in boldface) in the form $f_1(k_1,\pi)\, N_1\, e^{-2\sigma_1{}^2 k_1{}^2}$ after multiplication by R_1^2/k_1 . k_1 is the k-scale, adjusted with ΔE_1 according to Eq. (7.2). The empirical phase is obtained after subtraction of $2\, k_1\, R_1$, where R_1 is obtained from fitting. The method of extracting amplitude and phase is described in Section 6.7. Since ΔE_1 and N_1 are already contained in the reference amplitude and phase, all datasets are fitted with $\Delta E_1 \equiv 0$ and $N_1 \equiv 1$ when empirical amplitudes and phases are employed. It is not necessary, of course, to subtract $\pi/2$ from the phase. Hence the phase offset a_1 is equal to zero. The mean-square relative displacement is obtained as a difference with respect to the reference dataset, namely $\Delta\sigma s_1^2 \equiv \sigma_1^2 - \sigma_1^2\Big|_{\text{ref.}}$.

For Table 7.5 the pressure is found from the oil pressure of a hydraulic pump, given in psi, by interpolation using Table 7.1. For Tables 7.6 to 7.10 the pressure is found with the help of Table 7.3 and for Tables 7.11 and 7.12 it is determined using Table 7.4.

For the fits in this section the error bars are determined according to the method presented in Section 6.10. The error bars for σ^2 are asymmetric, the positive error bars being the larger ones. The listed error bars for σ^2 are averages of the positive and negative error bars.

The following table contains the results for R_1 and σ_1^2 at room temperature. In order to improve the fits asymmetry was taken into account for the amplitude.

Table 7.5: Se K edge EXAFS (LOG.SE10.B):
(Dec. '83; Si (111); T = 300K)

One-shell fits in R-space to $FT(k^2 \chi(k))$ using theoretical amplitude and phase

fixed: $a_1 \equiv -1.5708$; $\Delta E_1 \equiv -4.0$; $C_{31} \equiv 0.0$; $C_{41} \equiv 0.107 \cdot 10^{-3}$ Å^4; $N_1 \equiv 8.4$

variable: R_1; σ_1^2

Dataset	P_{Oil}(psi)	p (kbar)	R_1(Å)	σ_1^2 (10^{-3} Å^2)	
E_{Edge}(eV)	k_{min}(Å^{-1})	k_{max}(Å^{-1})	R_{min}(Å)	R_{max}(Å)	χ^2_{min} (10^{-3} Å^{-6})
SESM00.N00.B	0	0	3.109 ± 0.007	18.0 ± 0.8	
12658.27	3.680	15.157	2.080	3.497	0.36
SESM13.N08.B	1300	22.7	3.059 ± 0.007	15.75 ± 0.7	
12661.07	3.734	14.829	1.848	3.470	0.65
SESM19.N10.B	1900	39.6	2.969 ± 0.007	14.5 ± 0.7	
12661.07	3.918	14.751	1.734	3.377	1.31
SESM20.N30.B	2000	44.1	2.955 ± 0.006	14.4 ± 0.6	
12656.87	3.862	14.711	1.693	3.316	0.93
SESM20.N32.B	2050	45.9	2.946 ± 0.005	14.8 ± 0.6	
12656.87	3.891	14.711	1.895	3.235	0.87
SESM23.N32.B	2300	55.1	2.915 ± 0.005	13.3 ± 0.5	
12656.87	3.921	15.194	1.909	3.250	1.81
SESM27.N34.B	2700	68.3	2.8945 ± 0.005	12.7 ± 0.5	
12656.87	3.921	13.574	1.613	3.250	1.02

Fig. 7.16 shows the Fourier transform magnitudes of the data for low and for high pressure and Fig. 7.17 shows the same data in k-space.

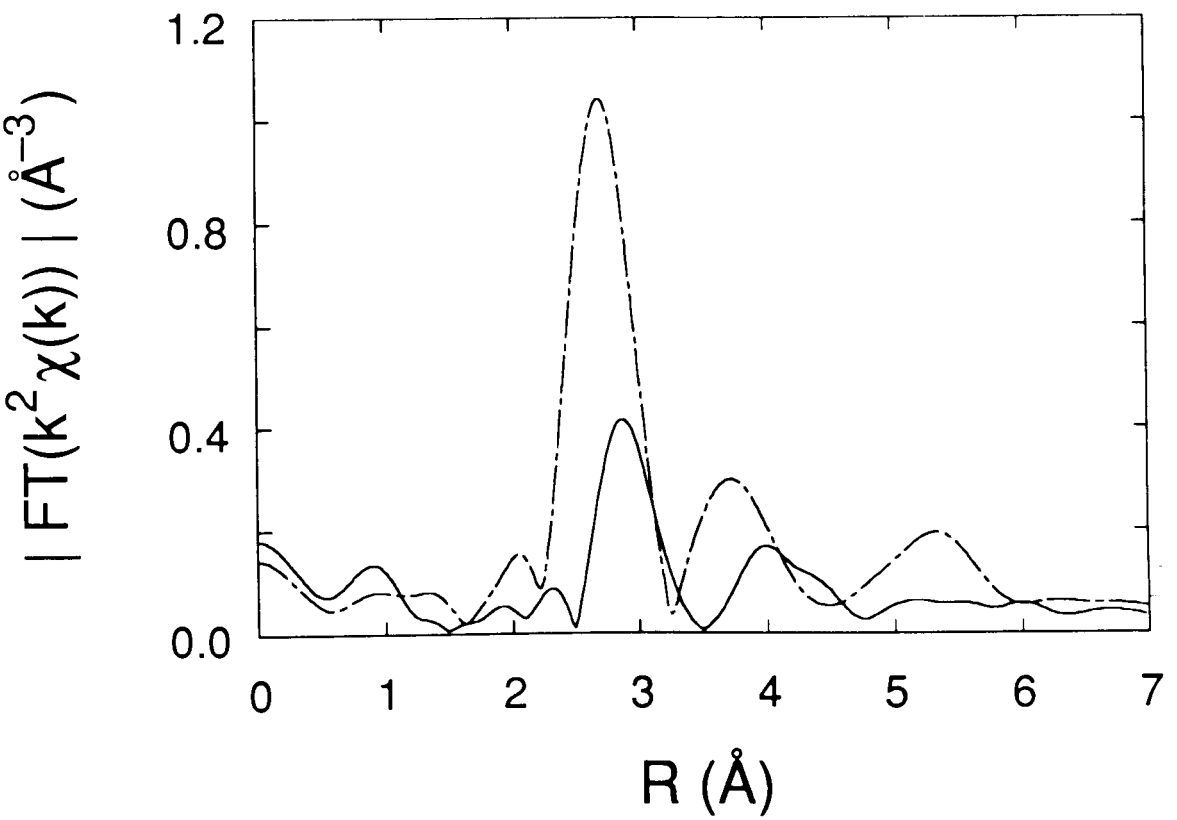

Fig. 7.16: Fourier transform magnitude of $k^2 \chi(k)$ for SmSe at 300K. The central atom is Se. The solid line corresponds to 1 bar and the dashed line to 68.3 kbar.

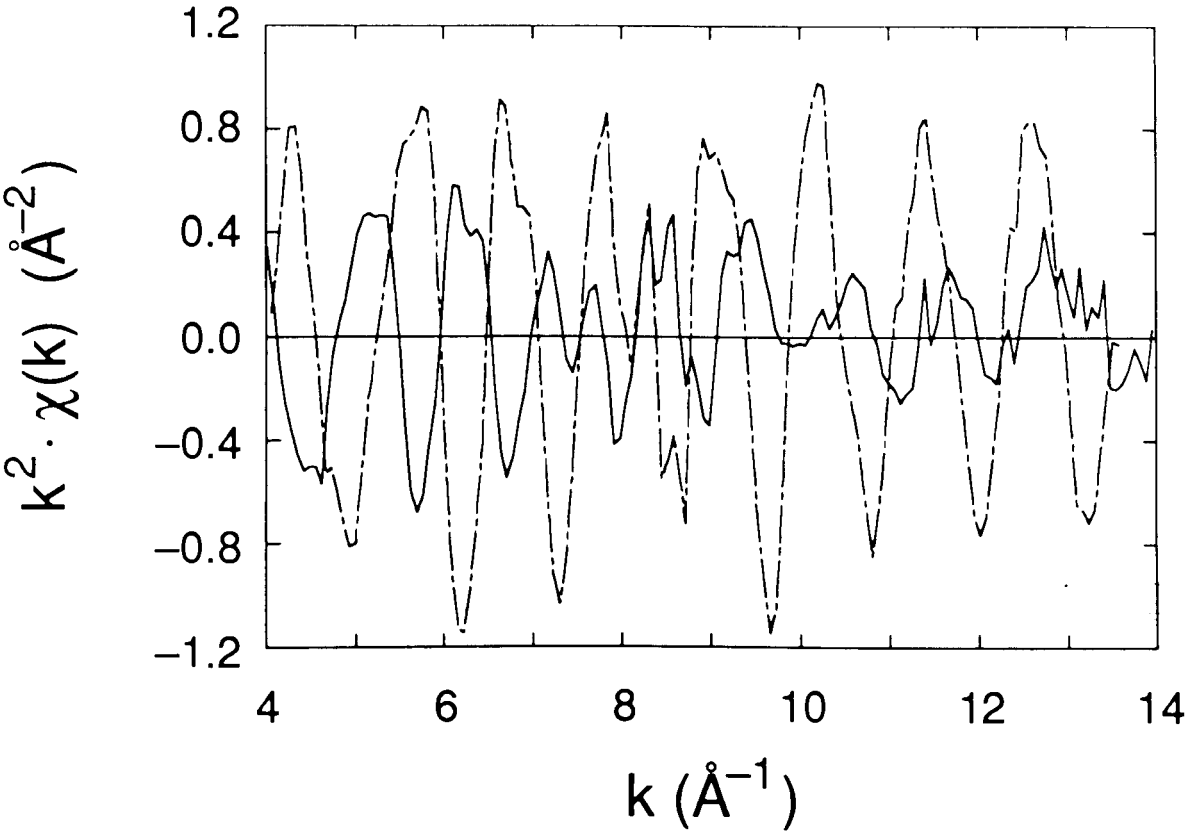

Fig. 7.17: $k^2\chi(k)$ for SmSe at 300K for the same data as in the previous figure. The central atom is Se. The solid line corresponds to 1 bar and the dashed line to 68.3 kbar.

Fig. 7.18 shows the fit result. At 300K we see the reduction of σ_1^2 with increasing pressure (decreasing R_1) as expected. There may be a small shoulder near 2.95 Å but there is no peak as in the corresponding graphs for 77K.

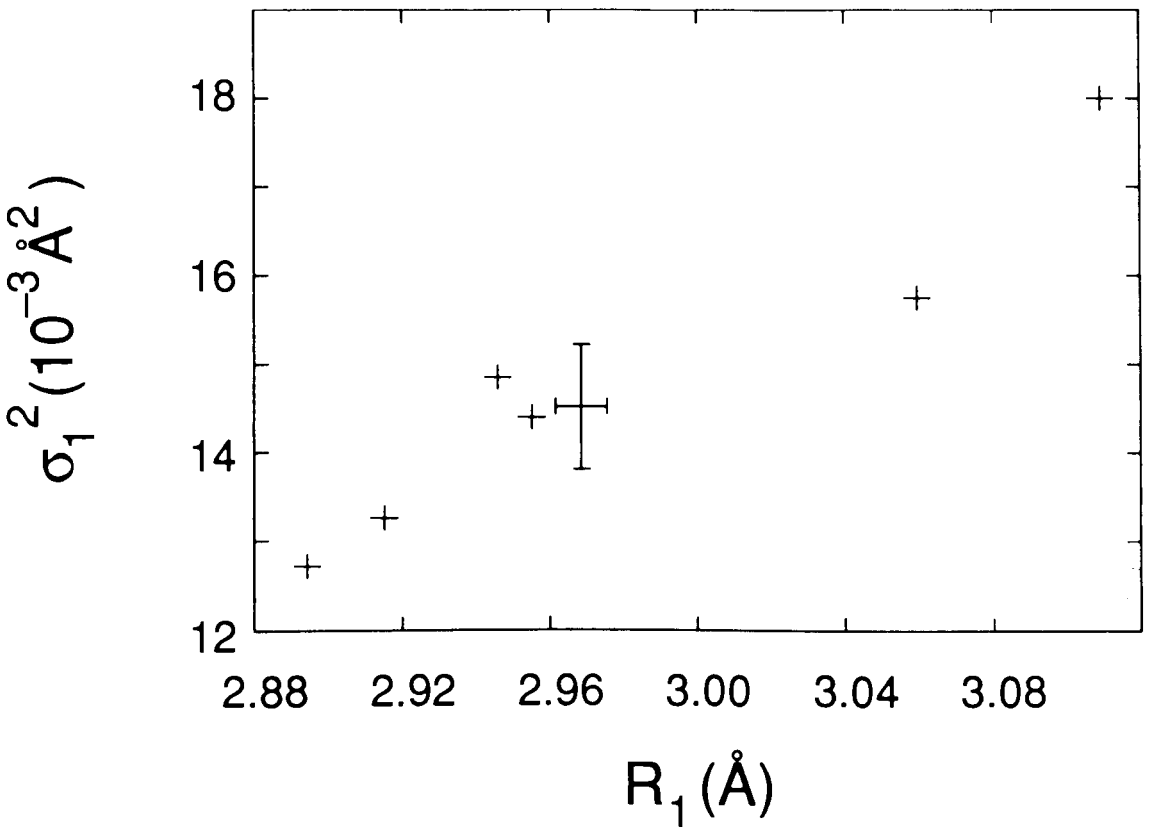

Fig. 7.18: σ_1^2 versus R_1 at 300K according to Table 7.5. N_1 was set to 8.4.

The following five tables all contain the same datasets and refer to 77K. They contain results of different ways of fitting the data.

Table 7.6 lists the results when asymmetry is included for the amplitude.

Table 7.6: Se K edge EXAFS (LOG.SEN13.F2):
(June '86; Si (220); T = 77K)

One-shell fits in R-space to $FT(k^2 \chi(k))$ using theoretical amplitude and phase

fixed: $a_1 \equiv -1.5708$; $\Delta E_1 \equiv 0.0$; $C_{31} \equiv 0.0$; $C_{41} \equiv 0.16 \cdot 10^{-4}$ Å^4; $N_1 \equiv 4.2$

variable: R_1; σ_1^2

Dataset	N_T	p (kbar)	R_1(Å)	σ_1^2 (10^{-3} Å^2)	
E_{Edge}(eV)	k_{min}(Å^{-1})	k_{max}(Å^{-1})	R_{min}(Å)	R_{max}(Å)	χ^2_{min} (10^{-3} Å^{-6})
SESMN2.N32.F	2.25	43.7	3.046 ± 0.004	4.4 ± 0.3	
12654.04	3.718	17.728	2.033	3.350	2.91
SESMN3.N33.F	3	42.9	3.043 ± 0.005	4.4 ± 0.4	
12654.04	3.851	18.126	2.056	3.373	4.91
SESMN5.N38.F	5	52.0	3.001 ± 0.005	5.0 ± 0.5	
12654.04	3.851	15.736	1.918	3.396	3.14
SESMN6.N42.F	6	54.7	2.971 ± 0.005	4.4 ± 0.4	
12654.04	3.917	16.732	1.894	3.327	4.39
SESMN8.N44.F	8	60.1	2.944 ± 0.004	3.9 ± 0.3	
12653.41	3.905	17.938	1.784	3.291	4.24
SESMN9.N47.F	9	73.2	2.918 ± 0.004	3.6 ± 0.3	
12654.04	3.917	20.052	2.125	3.258	12.64
SESMNT.N53.F	10.5	74.15	2.915 ± 0.003	3.5 ± 0.3	
12654.04	3.984	18.458	1.964	3.234	5.66
SESMNW.N54.F	12	75.1	2.912 ± 0.003	3.4 ± 0.2	
12653.41	3.971	17.210	1.877	3.221	2.96
SESMNH.N55.F	13.5	76.05	2.914 ± 0.003	3.6 ± 0.2	
12654.66	3.930	17.916	1.889	3.201	2.82
SESMNF.N56.F	15	77.0	2.911 ± 0.003	3.4 ± 0.2	
12654.04	3.984	18.591	1.918	3.211	3.34

Including asymmetry for the amplitude and not for the phase may be artificial. Besides, at low temperature asymmetry is not expected to be significant. Therefore it is useful to fit the same data without asymmetry, accepting increased values of χ^2_{min}. These results are shown in the next table.

Table 7.7: Se K edge EXAFS (LOG.SEN14.F2):
(June '86; Si (220); T = 77K)

One-shell fits in R-space to $FT(k^2 \chi(k))$ using theoretical amplitude and phase

fixed: $a_1 \equiv -1.5708$; $\Delta E_1 \equiv 0.0$ eV; $C_{31} \equiv 0.0$; $C_{41} \equiv 0.0$; $N_1 \equiv 3.4$

variable: R_1; σ_1^2

Dataset	N_T	p (kbar)	R_1(Å)	σ_1^2 (10^{-3} Å^2)	
E_{Edge}(eV)	k_{min}(Å^{-1})	k_{max}(Å^{-1})	R_{min}(Å)	R_{max}(Å)	χ^2_{min} (10^{-3} Å^{-6})
SESMN2.N32.F	2.25	43.7	3.046 ± 0.005	2.9 ± 0.5	
12654.04	3.718	17.728	2.033	3.350	3.42
SESMN3.N33.F	3	42.9	3.043 ± 0.005	2.8 ± 0.4	
12654.04	3.851	18.126	2.056	3.373	4.46
SESMN5.N38.F	5	52.0	3.001 ± 0.005	3.5 ± 0.5	
12654.04	3.851	15.736	1.918	3.396	3.87
SESMN6.N42.F	6	54.7	2.971 ± 0.006	2.8 ± 0.6	
12654.04	3.917	16.732	1.894	3.327	4.80
SESMN8.N44.F	8	60.1	2.944 ± 0.005	2.4 ± 0.5	
12653.41	3.905	17.938	1.784	3.291	4.83
SESMN9.N47.F	9	73.2	2.918 ± 0.005	2.0 ± 0.4	
12654.04	3.917	20.052	2.125	3.258	10.93
SESMNT.N53.F	10.5	74.15	2.915 ± 0.002	2.0 ± 0.2	
12654.04	3.984	18.458	1.964	3.234	4.36
SESMNW.N54.F	12	75.1	2.912 ± 0.004	1.8 ± 0.4	
12653.41	3.971	17.210	1.877	3.221	3.61
SESMNH.N55.F	13.5	76.05	2.914 ± 0.004	2.0 ± 0.4	
12654.66	3.930	17.916	1.889	3.201	3.26
SESMNF.N56.F	15	77.0	2.911 ± 0.003	1.9 ± 0.2	
12654.04	3.984	18.591	1.918	3.211	3.09

The following two figures are shown to illustrate the fit quality.

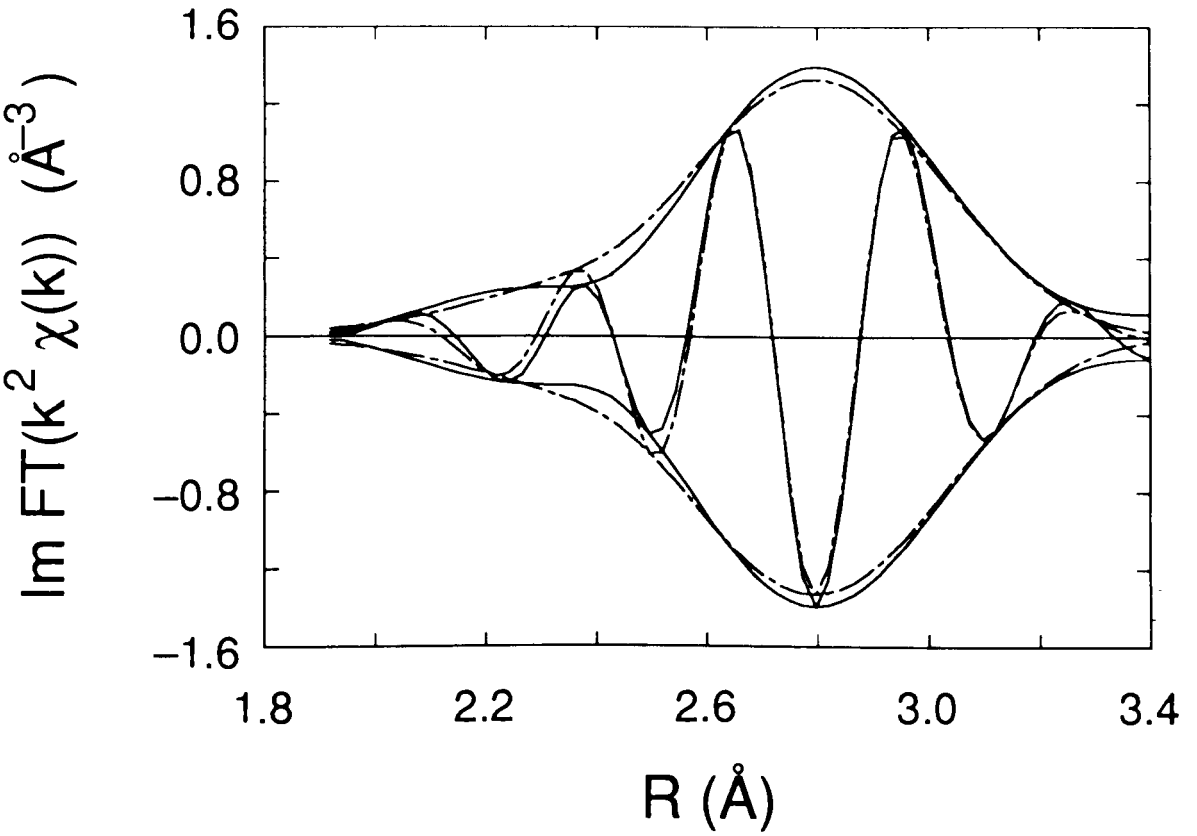

Fig. 7.19: Dataset SESMN5.N38.F (solid line) and R-space fit according to Table 7.7 (dashed line). The imaginary part and the magnitude of the Fourier transform of $k^2 \chi(k)$ are shown.

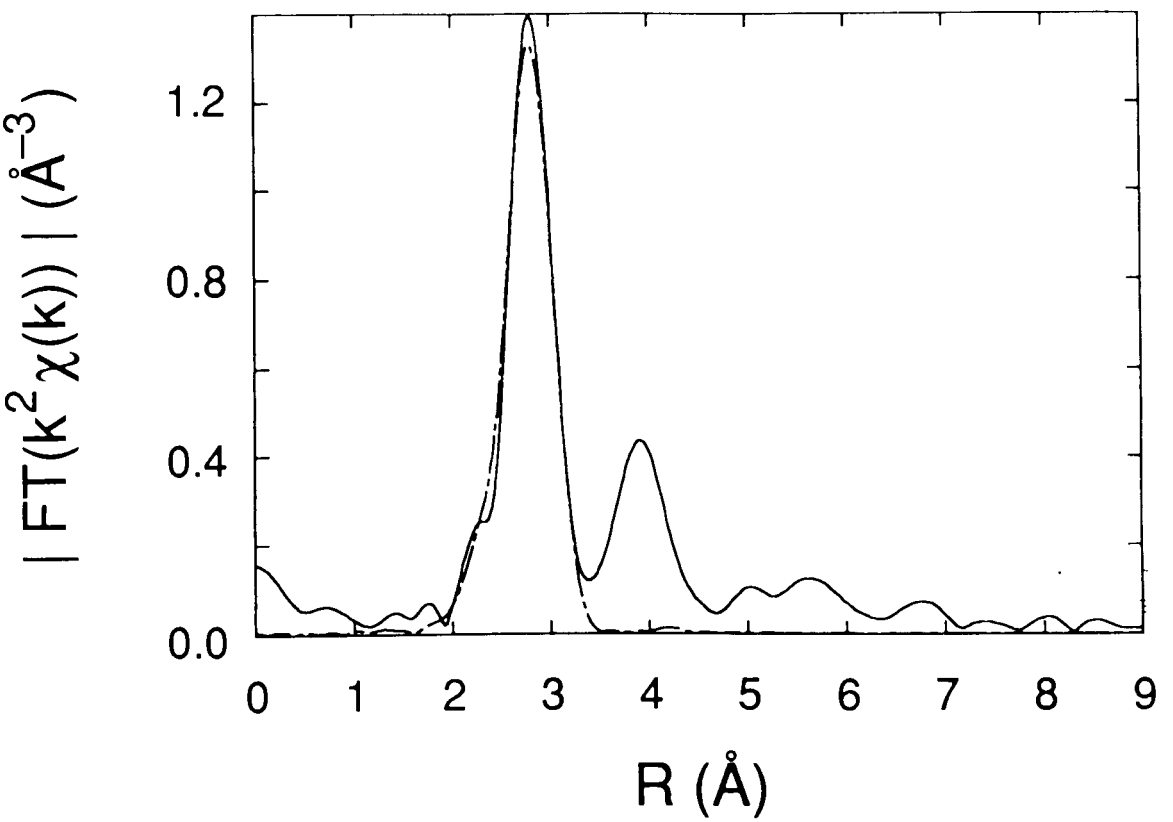

Fig. 7.20: Same data and fit as in the previous figure but the magnitude of the Fourier transform of $k^2 \chi(k)$ is shown.

The results of the two previous tables are summarized in the following graph. When no asymmetry is included N_1 is smaller and σ_1^2 can become smaller, too. With no asymmetry the values for σ_1^2 are simply shifted downwards. The relative changes in σ_1^2 remain the same.

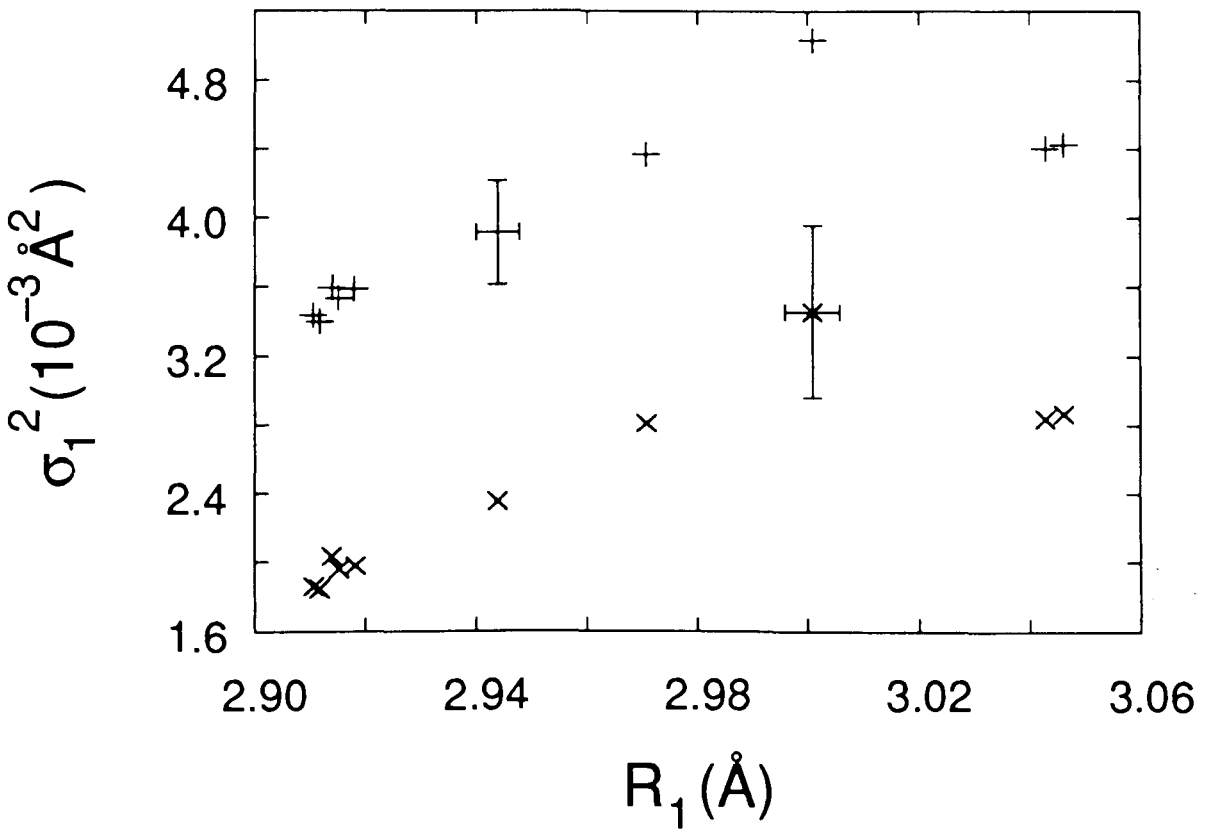

Fig. 7.21: σ_1^2 versus R_1 at 77K. The '+' symbols refer to the results of Table 7.6, where asymmetry for the amplitude was included and N_1 was equal to 4.2. The 'x' symbols refer to Table 7.7, where no asymmetry was considered and N_1 was equal to 3.4.

The next table contains the results of fitting the first coordination shell with two closely-spaced Sm shells instead of one. The R-space intervals as well as the k-space intervals employed for the Fourier transform are the same as for the one-shell fits. The parameters describing asymmetry are never varied because otherwise the correlation among the parameters would increase too much. The ΔE and σ^2 values for the two Sm shells are always forced to be equal. We thus start out with initial fits with six variable parameters: ΔE_1, R_1, σ_1^2, N_1, R_2, and N_2. Reducing the number of variables one by one we arrive at the three-parameter two-shell fits presented in Table 7.8, where R_1, σ_1^2, and R_2 are varied. The sum of the coordination numbers turned out to be $N_1 + N_2 = 5.5$ and N_1 was equal to 0.8.

Table 7.8: Se K edge EXAFS (LOG.SEN19.F2):
(June '86; Si (220); T = 77K)

Two-shell fits in R-space to $FT(k^2 \chi(k))$ using theoretical amplitudes and phases:

1st shell: Sm; 2nd shell: Sm

fixed: $a_1 \equiv -1.5708$; $\Delta E_1 \equiv -1.9$ eV; $C_{31} \equiv 0.0$; $C_{41} \equiv 0.0$; $N_1 \equiv 0.8$;
$a_2 \equiv -1.5708$; $\Delta E_2 \equiv -1.9$ eV; $C_{32} \equiv 0.0$; $C_{42} \equiv 0.0$; $\sigma_2^2 \equiv \sigma_1^2$; $N_2 \equiv 4.7$

variable: R_1; σ_1^2; R_2

Dataset	N_T	p (kbar)	R_1(Å)	R_2(Å)	σ_1^2 (10^{-3} Å^2)
E_{Edge}(eV)	k_{min}(Å^{-1})	k_{max}(Å^{-1})	R_{min}(Å)	R_{max}(Å)	χ^2_{min} (10^{-3} Å^{-6})
SESMN2.N32.F	2.25	43.7	2.863 ± 0.066	3.035 ± 0.007	3.7 ± 0.4
12654.04	3.718	17.728	2.033	3.350	2.43
SESMN3.N33.F	3	42.9	2.86 ± 0.16	3.032 ± 0.008	3.6 ± 0.6
12654.04	3.851	18.126	2.056	3.373	3.61
SESMN5.N38.F	5	52.0	2.85 ± 0.16	2.995 ± 0.008	4.0 ± 0.9
12654.04	3.851	15.736	1.918	3.396	2.41
SESMN6.N42.F	6	54.7	2.792 ± 0.056	2.960 ± 0.006	3.5 ± 0.4
12654.04	3.917	16.732	1.894	3.327	2.68
SESMN8.N44.F	8	60.1	2.767 ± 0.048	2.934 ± 0.005	3.1 ± 0.4
12653.41	3.905	17.938	1.784	3.291	3.18
SESMN9.N47.F	9	73.2	2.734 ± 0.029	2.908 ± 0.003	2.85 ± 0.3
12654.04	3.917	20.052	2.125	3.258	3.85
SESMNT.N53.F	10.5	74.15	2.73 ± 0.12	2.904 ± 0.005	2.8 ± 0.5
12654.04	3.984	18.458	1.964	3.234	8.12
SESMNW.N54.F	12	75.1	2.735 ± 0.041	2.901 ± 0.005	2.6 ± 0.3
12653.41	3.971	17.210	1.877	3.221	3.28
SESMNH.N55.F	13.5	76.05	2.737 ± 0.049	2.904 ± 0.005	2.8 ± 0.3
12654.66	3.930	17.916	1.889	3.201	4.45
SESMNF.N56.F	15	77.0	2.752 ± 0.039	2.902 ± 0.004	2.4 ± 0.2
12654.04	3.984	18.591	1.918	3.211	3.25

Because N_2 is much larger than N_1, the second shell dominates. It exhibits the peak in the mean-square relative displacement as a function of R_2, known from the one-shell fits. This is shown in the next figure:

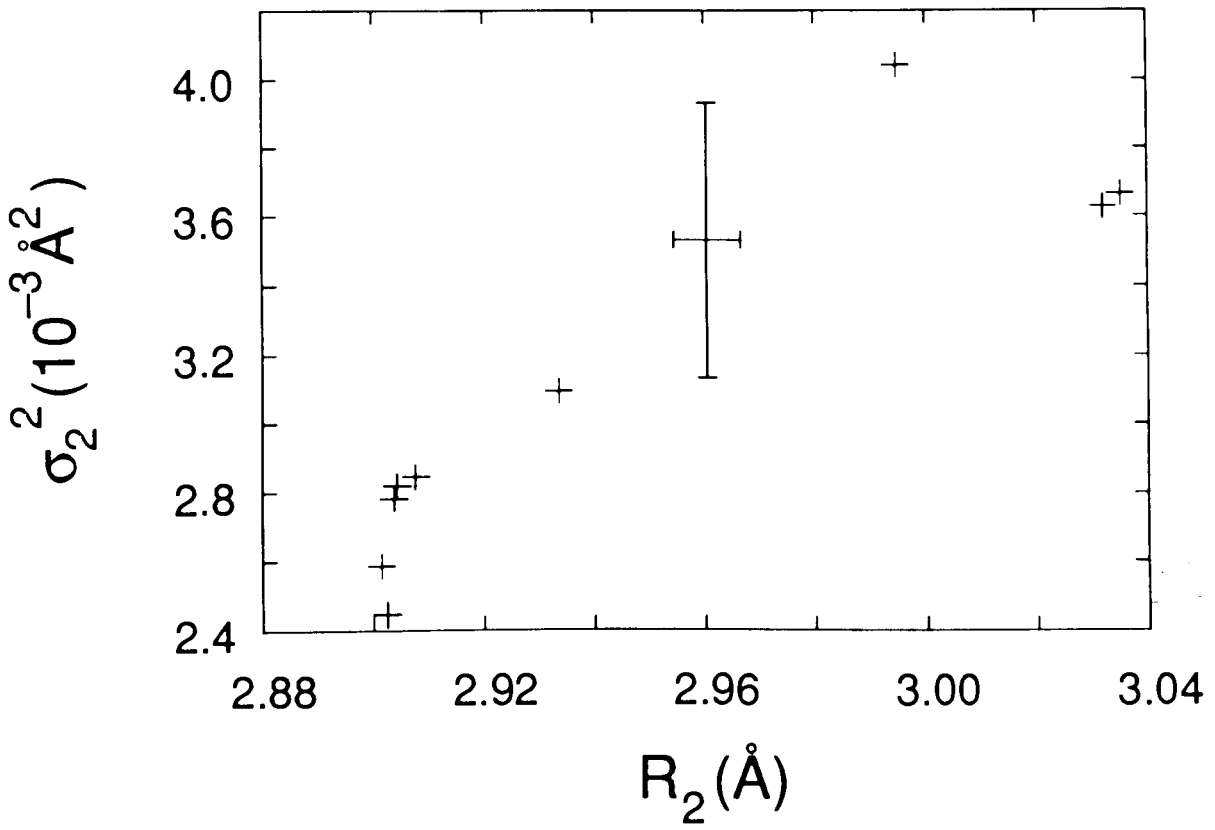

Fig. 7.22: σ_2^2 versus R_2 at 77K according to Table 7.8. $N_1 + N_2$ was set to 5.5 and N_1 was equal to 0.8.

The first shell constitutes only a small modification of the results of the one-shell fits by creating a tail in the radial distribution function on the low-R side. This is expected from the large error bars for R_1, which signify that R_1 is not well defined. Nevertheless, the radial distribution functions obtained from these two-shell fits are of interest because even if the fit parameters are not well defined the resulting distribution functions may still be correct because they are the combined result of these fit parameters. Because of this integral property we draw the following figure:

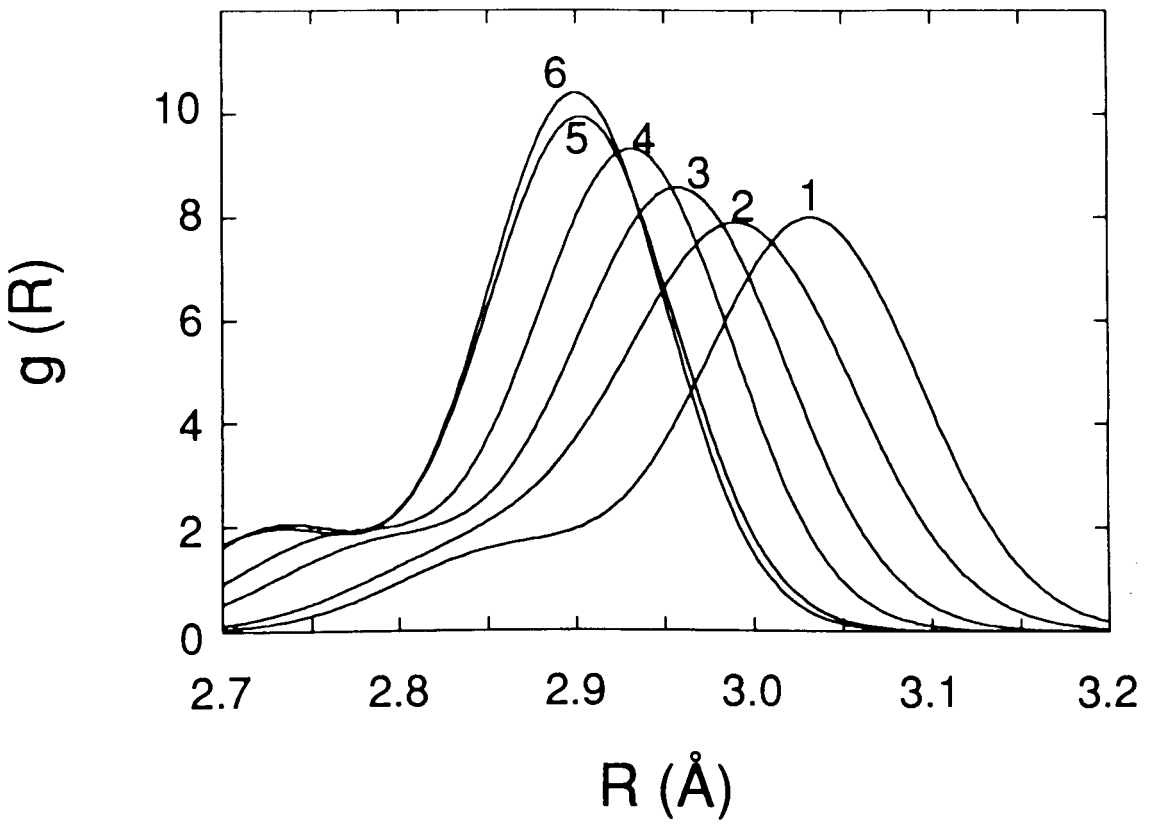

Fig. 7.23: Sm radial distribution functions g(R) with respect to Se at 77K obtained from the two-shell fits of Table 7.8. The numbers on the curves indicate the following pressures:
#1: 43.7 kbar; #2: 52.0 kbar; #3: 54.7 kbar; #4: 60.1 kbar; #5: 74.15 kbar; #6: 75.1 kbar

Comparing the values of χ^2_{min} from Tables 7.6, 7.7, and 7.8 we notice that in Table 7.7, which contains the results of simple one-shell fits, they are usually highest. On the other hand, the fits of Table 7.6 (asymmetry for the amplitude included) or Table 7.8 (two shells) produce significantly lower values for χ^2_{min} . This indicates that either the theoretical amplitude and/or phase are not quite correct or that the radial distribution function is not Gaussian.

It is worthwhile investigating the behaviour of the nearest Se coordination shell around a Se atom. Table 7.9 shows the results of one-shell fits in R-space to the Se shell. The R-space fit interval begins with the endpoint of the R-space fit interval of the previous one-shell fits. The k-space interval

used for the Fourier transform is the same as before. N_1 turns out to be 7.1, which is 59% of the correct value of 12.

Table 7.9: Se K edge EXAFS (LOG.SEN24.F2):
(June '86; Si (220); T = 77K)

Se - Se; k_{min}, k_{max} same as before;
R_{min}(this table) = R_{max}(previous one-shell fits, Se-Sm)

One-shell fits in R-space to $FT(k^2 \chi(k))$ using theoretical amplitude and phase

fixed: $a_1 \equiv -1.5708$; $\Delta E_1 \equiv -0.8$ eV; $C_{31} \equiv 0.0$; $C_{41} \equiv 0.0$; $N_1 \equiv 7.1$

variable: R_1; σ_1^2

Dataset	N_T	p (kbar)	R_1(Å)	σ_1^2 (10^{-3} Å^2)	
E_{Edge}(eV)	k_{min}(Å^{-1})	k_{max}(Å^{-1})	R_{min}(Å)	R_{max}(Å)	χ^2_{min} (10^{-3} Å^{-6})
SESMN2.N32.F	2.25	43.7	4.305 ± 0.010	6.0 ± 1.0	
12654.04	3.718	17.728	3.350	4.782	1.99
SESMN3.N33.F	3	42.9	4.299 ± 0.008	6.0 ± 0.8	
12654.04	3.851	18.126	3.373	4.782	1.31
SESMN5.N38.F	5	52.0	4.240 ± 0.006	8.1 ± 0.6	
12654.04	3.851	15.736	3.396	4.667	0.39
SESMN6.N42.F	6	54.7	4.1875 ± 0.006	7.2 ± 0.7	
12654.04	3.917	16.732	3.327	4.528	0.69
SESMN8.N44.F	8	60.1	4.151 ± 0.005	5.8 ± 0.5	
12653.41	3.905	17.938	3.291	4.450	0.78
SESMN9.N47.F	9	73.2	4.116 ± 0.006	5.4 ± 0.6	
12654.04	3.917	20.052	3.258	4.459	1.34
SESMNT.N53.F	10.5	74.15	4.114 ± 0.010	5.2 ± 1.0	
12654.04	3.984	18.458	3.234	4.482	3.93
SESMNW.N54.F	12	75.1	4.102 ± 0.005	5.0 ± 0.5	
12653.41	3.971	17.210	3.221	4.519	1.16
SESMNH.N55.F	13.5	76.05	4.112 ± 0.008	5.4 ± 0.8	
12654.66	3.930	17.916	3.201	4.468	2.35
SESMNF.N56.F	15	77.0	4.103 ± 0.007	5.7 ± 0.7	
12654.04	3.984	18.591	3.211	4.390	1.77

Plotting the results yields the familiar behaviour, this time, however, for the Se coordination shell: $\sigma_1^2 \equiv \sigma_{Se\text{-}Se}^2$.

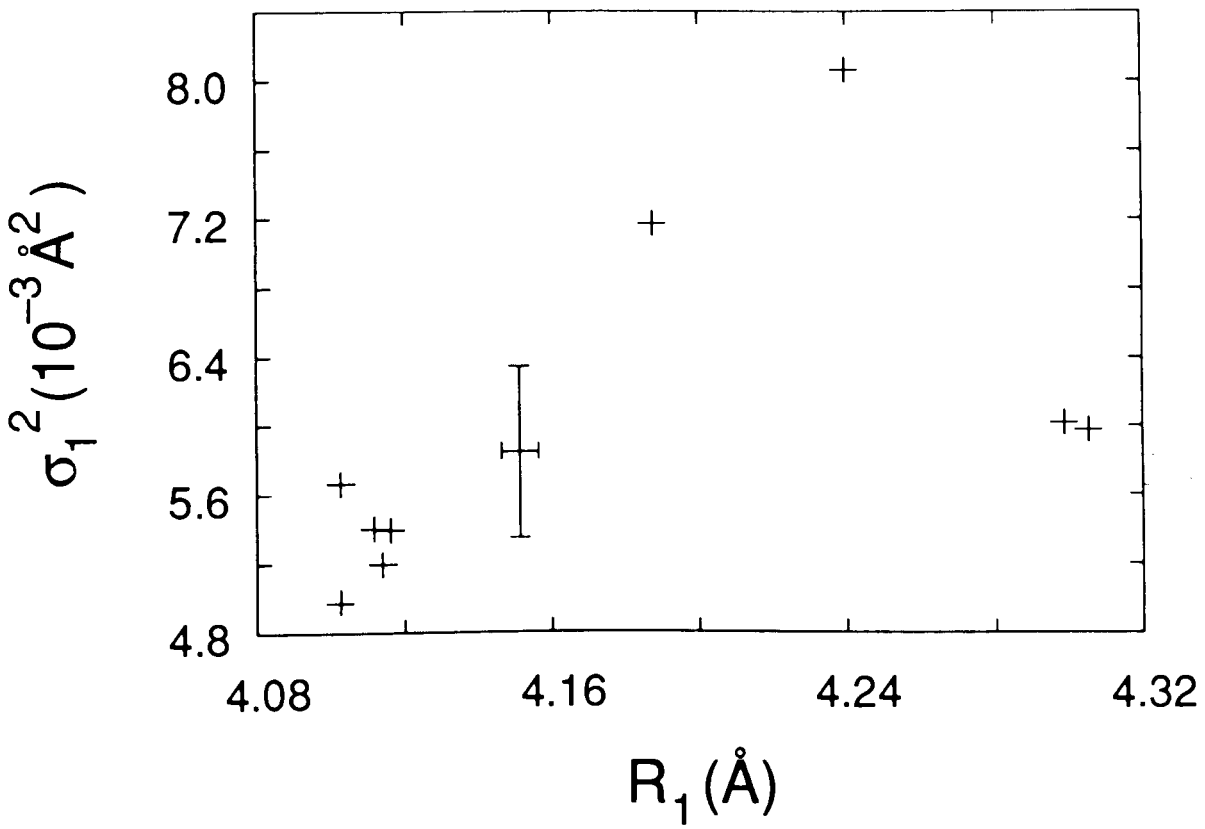

Fig. 7.24: σ_1^2 versus R_1 at 77K according to Table 7.9.

So far the analysis of the Se K edge EXAFS employed theoretical amplitude and phase. It is also of interest to apply empirical amplitude and phase. Table 7.10 shows these results. Amplitude and phase are extracted from the first dataset, which is indicated in boldface.

Table 7.10: Se K edge EXAFS (LOG.SEN8.F2):
(June '86; Si (220); T = 77K)

One-shell fits in R-space to $FT(k^2 \chi(k))$ using empirical amplitude and phase

fixed: $a_1 \equiv 0.0$; $\Delta E_1 \equiv 0.0$; $C_{31} \equiv 0.0$; $C_{41} \equiv 0.0$; $N_1 \equiv 1.0$

variable: R_1; $\Delta\sigma_1^2$

Dataset	N_T	p (kbar)	R_1(Å)	$\Delta\sigma_1^2$ (10^{-3} Å^2)	
E_{Edge}(eV)	k_{min}(Å^{-1})	k_{max}(Å^{-1})	R_{min}(Å)	R_{max}(Å)	χ^2_{min} (10^{-3} Å^{-6})
SESMN2.N32.F	**2.25**	**43.7**	**3.042 ± 0.000**	**0.03 ± 0.04**	
12654.04	**3.718**	**17.728**	**2.033**	**3.350**	**0.044**
SESMN3.N33.F	3	42.9	3.039 ± 0.003	0.00 ± 0.2	
12654.04	3.851	17.728	2.056	3.373	1.69
SESMN5.N38.F	5	52.0	2.997 ± 0.004	0.55 ± 0.3	
12654.04	3.851	15.736	1.918	3.396	1.36
SESMN6.N42.F	6	54.7	2.967 ± 0.002	–0.09 ± 0.2	
12654.04	3.917	16.732	1.894	3.327	1.18
SESMN7.N43.F	7	57.4	2.944 ± 0.004	–0.98 ± 0.5	
12653.41	3.971	13.238	1.599	3.291	1.72
SESMN8.N44.F	8	60.1	2.940 ± 0.003	–0.50 ± 0.3	
12653.41	3.905	17.673	1.784	3.291	2.92
SESMN9.N47.F	9	73.2	2.915 ± 0.002	–0.87 ± 0.2	
12654.04	3.917	17.728	2.125	3.258	2.53
SESMNT.N53.F	10.5	74.15	2.911 ± 0.004	–0.93 ± 0.3	
12654.04	3.984	17.728	1.964	3.234	5.75
SESMNW.N54.	12	75.1	2.908 ± 0.002	–1.04 ± 0.2	
12653.41	3.971	17.210	1.877	3.221	1.68
SESMNH.N55.F	13.5	76.05	2.910 ± 0.002	–0.83 ± 0.2	
12654.66	3.930	17.717	1.889	3.201	2.12
SESMNF.N56.F	15	77.0	2.906 ± 0.003	–1.015 ± 0.2	
12654.04	3.984	17.728	1.918	3.211	4.13

Because σ_1^2 is now defined with respect to a reference we obtain the mean-square relative displacement as a difference: $\Delta\sigma_1^2$. The curve shown below has the familiar shape.

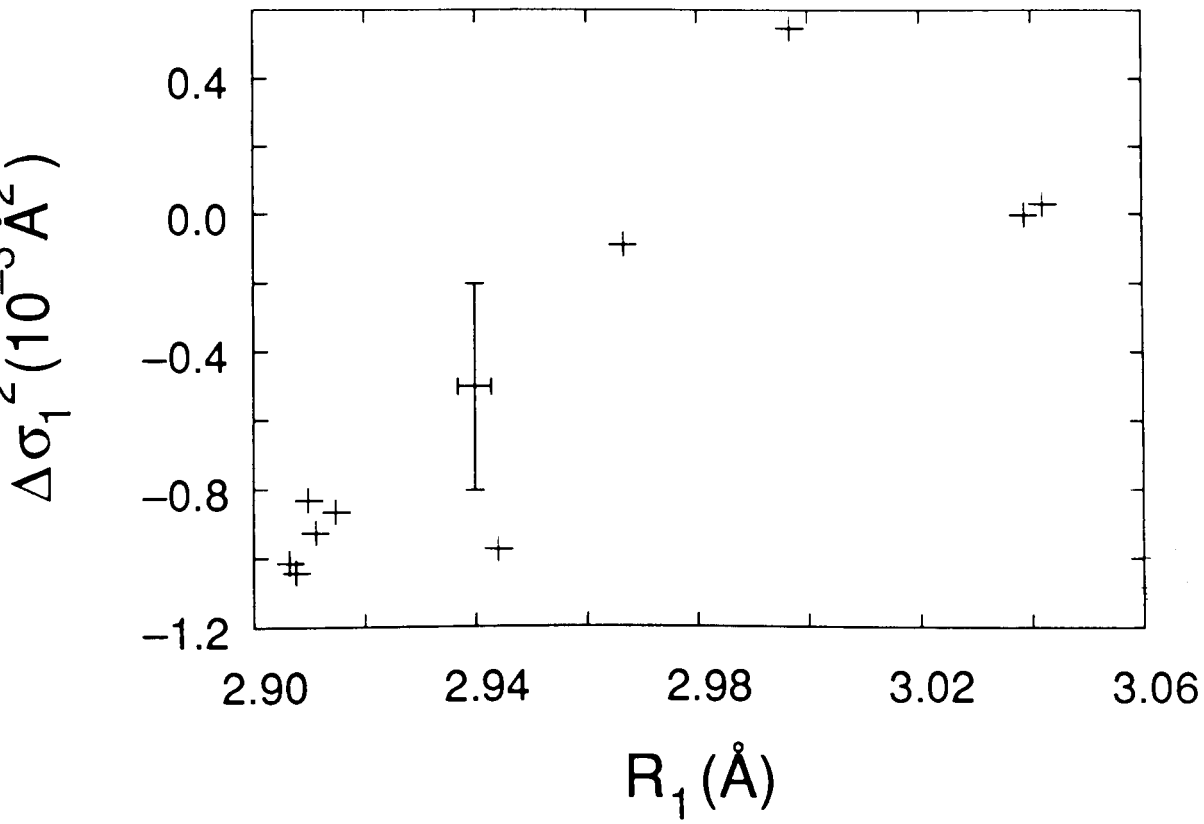

Fig. 7.25: $\Delta\sigma_1^2$ versus R_1 at 77K according to Table 7.10. Empirical amplitude and phase are employed.

Looking at values for χ^2_{min} we see that they are generally lower than those of Tables 7.6 or 7.8. This could mean that the empirical amplitude and phase are better than the theoretical ones. On the other hand, if the radial distribution function is indeed not Gaussian one would not be able to detect this because this effect is absorbed in the empirical amplitude and phase.

The previous graph completes the analysis for the run of June '86. The next two tables, which contain results of two-parameter one-shell fits to the nearest-neighbour Sm shell, refer to another run which also was taken at 77K. Its results are not as good as the ones from June '86 but its pressure calibration was more reliable. Table 7.11 contains the results found with theoretical amplitude and phase and Table 7.12 refers to empirical amplitude and phase. Each of these two

Table 7.11: Se K edge EXAFS (LOG.SE10.G):
(Dec. '86; Si (111); T = 77K)

One-shell fits in R-space to $FT(k^2 \chi(k))$ using theoretical amplitude and phase

fixed: $a_1 \equiv -1.5708$; $\Delta E_1 \equiv -1.73$ eV; $C_{31} \equiv 0.0$; $C_{41} \equiv 0.0$; $N_1 \equiv 5.2$

variable: R_1; σ_1^2

Dataset	N_T	p (kbar)	R_1(Å)	σ_1^2 (10^{-3} Å^2)	
E_{Edge}(eV)	k_{min}(Å^{-1})	k_{max}(Å^{-1})	R_{min}(Å)	R_{max}(Å)	χ^2_{min} (10^{-3} Å^{-6})
SESM04.D10.G	4	24.5	3.054 ± 0.011	5.2 ± 1.3	
12657.22	3.773	12.101	1.702	3.426	4.43
SESM05.D42.G	5	32.6	3.012 ± 0.007	5.9 ± 0.7	
12654.43	3.708	15.040	2.109	3.397	3.54
SESM05.D43.G	5	32.6	3.025 ± 0.007	5.5 ± 0.7	
12655.83	3.769	15.493	2.425	3.240	6.66
SESM5Q.D59.G	5.25	33.55	3.005 ± 0.014	5.1 ± 1.3	
12655.83	3.758	16.684	2.117	3.369	27.18
SESM5H.D70.G	5.5	38.5	2.979 ± 0.014	5.9 ± 1.7	
12655.13	3.758	11.500	1.857	3.283	6.18
SESM5H.D71.G	5.5	38.5	2.978 ± 0.014	6.7 ± 1.7	
12655.13	3.901	11.436	1.532	3.259	3.69
SESM5T.D72.G	5.75	43.45	2.929 ± 0.010	6.8 ± 1.2	
12655.13	3.689	11.370	1.337	3.149	1.81
SESM5T.D73.G	5.75	43.45	2.927 ± 0.007	5.4 ± 0.8	
12654.43	3.884	11.535	1.710	3.183	1.75
SESM06.D92.G	6	48.4	2.931 ± 0.006	3.4 ± 0.5	
12654.43	3.889	17.347	2.101	3.184	16.53
SESM07.D00.G	7	52.9	2.940 ± 0.010	4.0 ± 0.9	
12655.83	3.834	17.371	2.067	3.380	27.22
SESM7Q.N16.G	7.25	54.1	2.935 ± 0.007	3.5 ± 0.6	
12656.52	3.975	17.817	1.988	3.436	16.99
SESM7Q.N17.G	7.25	54.1	2.932 ± 0.005	4.0 ± 0.4	
12656.52	3.904	16.185	1.837	3.133	4.98
SESM8Q.D24.G	8.25	58.6	2.928 ± 0.009	3.9 ± 0.7	
12656.52	3.850	19.907	2.119	3.317	28.88
SES11Q.D41.G	11.25	72.2	2.900 ± 0.005	3.4 ± 0.4	
12655.83	3.900	17.689	1.770	3.065	9.80

tables has multiple entries for some pressure values. Figures 7.28 to 7.31, which show results of Tables 7.11 and 7.12, contain, however, only averaged data at these pressures.

Fig. 7.26 shows the Fourier transform magnitudes of the data for low and for high pressure and Fig. 7.27 shows the same data in k-space.

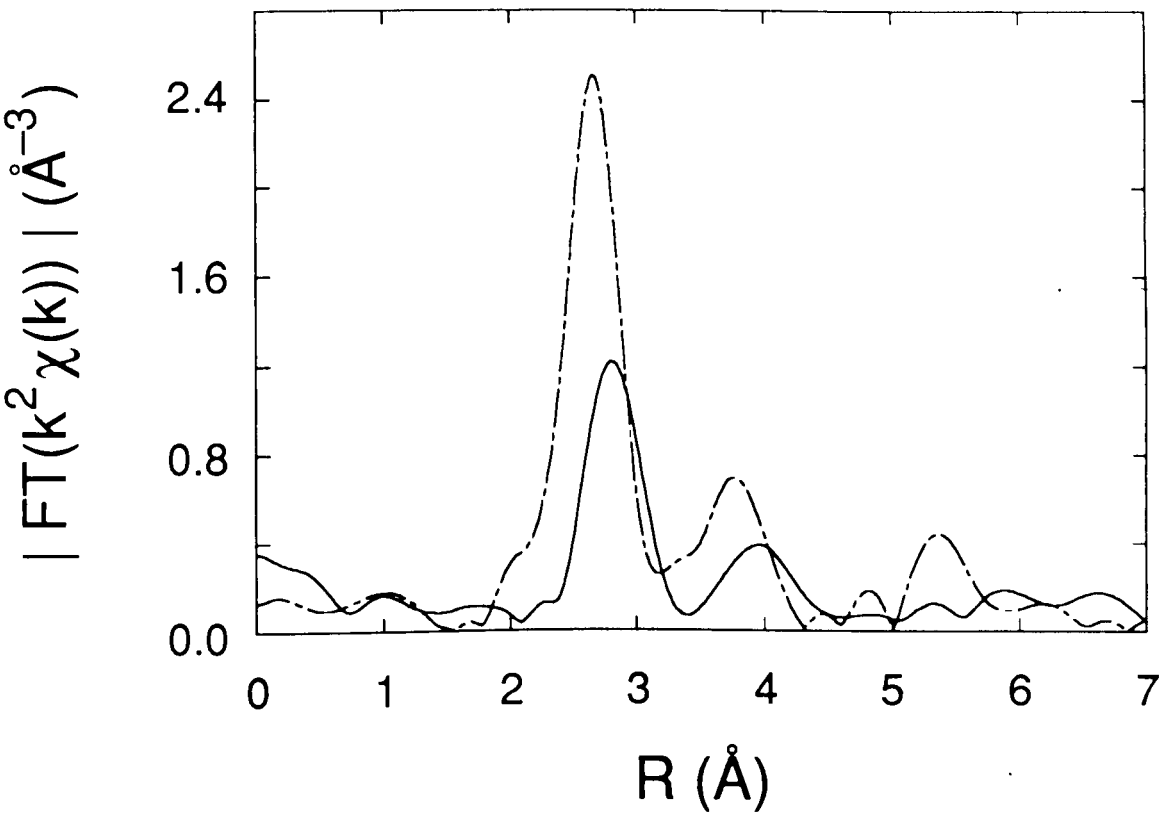

Fig. 7.26: Fourier transform magnitude of $k^2 \chi(k)$ for SmSe at 77K. The central atom is Se. The solid line corresponds to 32.6 kbar and the dashed line to 72.2 kbar.

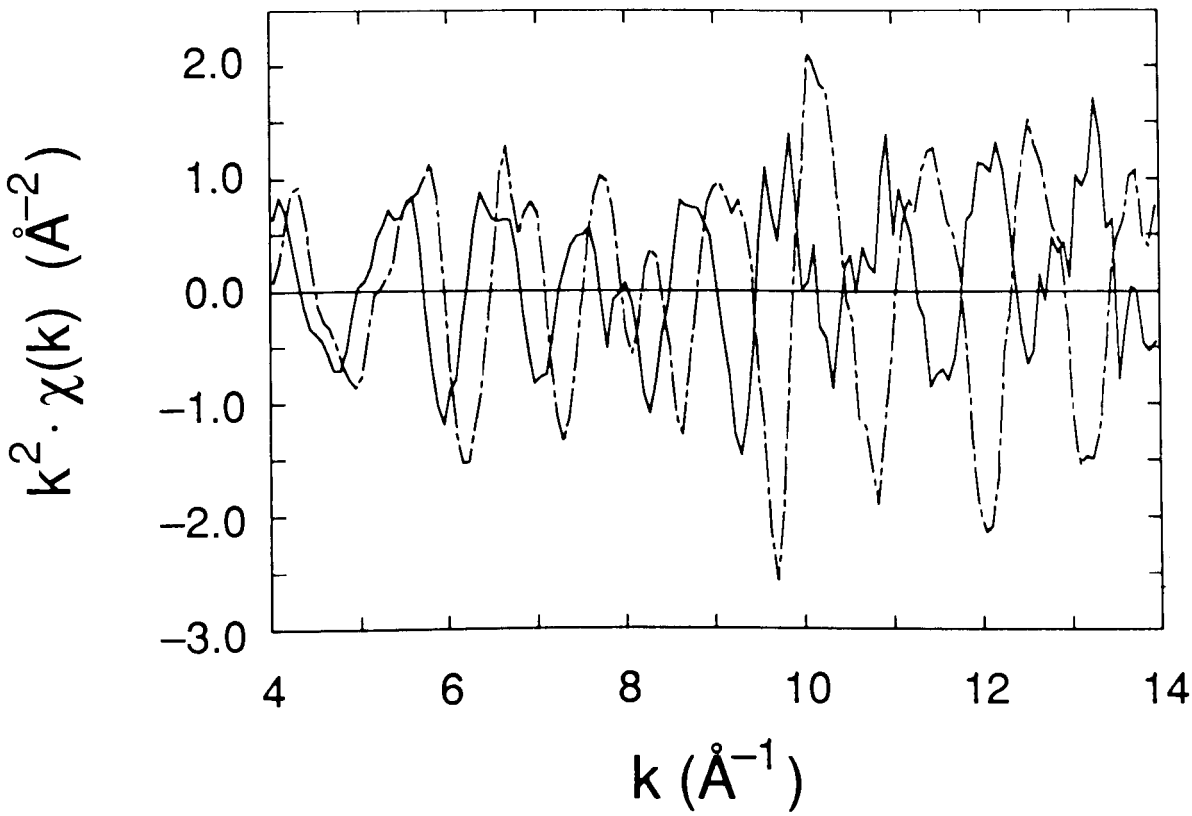

Fig. 7.27: $k^2\chi(k)$ for SmSe at 77K for the same data as in the previous figure. The central atom is Se. The solid line corresponds to 32.6 kbar and the dashed line to 72.2 kbar.

Fig. 7.28 shows the fit result:

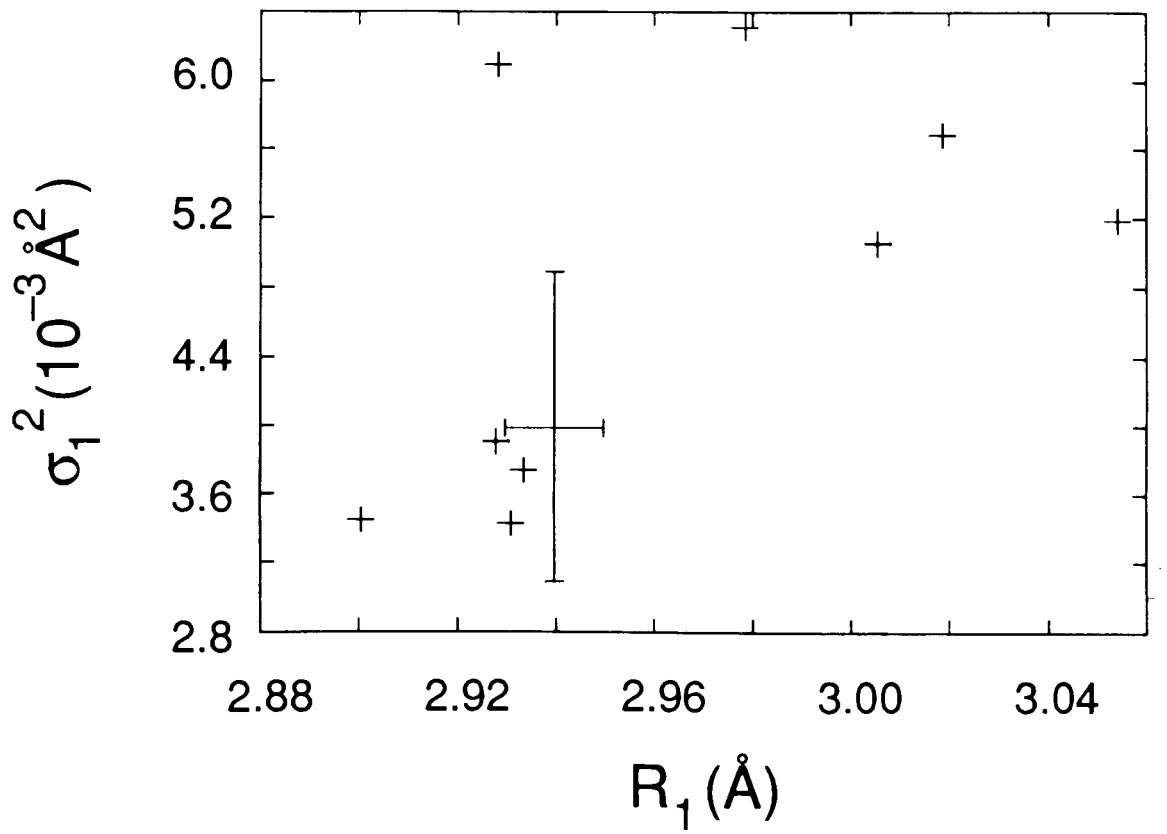

Fig. 7.28: σ_1^2 versus R_1 at 77K according to Table 7.11. N_1 was set to 5.2.

In the next table we see empirical amplitude and phase employed. They were extracted from the second dataset, which is indicated in boldface.

Table 7.12: Se K edge EXAFS (LOG.SE13.G):
(Dec. '86; Si (111); T = 77K)

One-shell fits in R-space to $FT(k^2 \chi(k))$ using empirical amplitude and phase

fixed: $a_1 \equiv 0.0$; $\Delta E_1 \equiv 0.0$; $C_{31} \equiv 0.0$; $C_{41} \equiv 0.0$; $N_1 \equiv 1.0$

variable: R_1; $\Delta\sigma_1^2$

Dataset	N_T	p (kbar)	R_1(Å)	$\Delta\sigma_1^2$ (10^{-3} Å^2)	
E_{Edge}(eV)	k_{min}(Å^{-1})	k_{max}(Å^{-1})	R_{min}(Å)	R_{max}(Å)	χ^2_{min} (10^{-3} Å^{-6})
SESM04.D10.G	4	24.5	3.056 ± 0.013	−0.63 ± 1.6	
12657.22	3.773	12.101	1.702	3.426	5.58
SESM05.D42.G	**5**	**32.6**	**3.013 ± 0.001**	**0.00 ± 0.1**	
12654.43	**3.708**	**15.040**	**2.109**	**3.397**	**0.0830**
SESM05.D43.G	5	32.6	3.027 ± 0.006	−0.25 ± 0.6	
12655.83	3.769	14.992	2.425	3.240	4.37
SESM5Q.D59.G	5.25	33.55	3.004 ± 0.006	−0.48 ± 0.6	
12655.83	3.758	14.979	2.117	3.369	3.64
SESM5H.D70.G	5.5	38.5	2.979 ± 0.010	0.04 ± 1.2	
12655.13	3.758	11.500	1.857	3.283	2.75
SESM5H.D71.G	5.5	38.5	2.978 ± 0.018	1.06 ± 2.2	
12655.13	3.901	11.436	1.532	3.259	5.68
SESM5T.D72.G	5.75	43.45	2.960 ± 0.012	0.94 ± 1.5	
12655.13	3.760	11.370	1.337	3.149	2.51
SESM5T.D73.G	5.75	43.45	2.957 ± 0.008	−0.54 ± 1.0	
12654.43	3.884	11.535	1.710	3.183	2.38
SESM06.D92.G	6	48.4	2.930 ± 0.008	−2.22 ± 0.7	
12654.43	3.889	15.009	2.101	3.184	17.87
SESM07.D00.G	7	52.9	2.939 ± 0.005	−1.45 ± 0.5	
12655.83	3.834	15.020	2.067	3.380	4.93
SESM7Q.N16.G	7.25	54.1	2.935 ± 0.007	−2.01 ± 0.7	
12656.52	3.975	14.978	1.988	3.436	10.13
SESM7Q.N17.G	7.25	54.1	2.932 ± 0.007	−1.76 ± 0.6	
12656.52	3.904	14.978	1.837	3.133	10.62
SESM8Q.D24.G	8.25	58.6	2.927 ± 0.005	−1.31 ± 0.5	
12656.52	3.850	15.033	2.119	3.317	4.89
SES11Q.D41.G	11.25	72.2	2.901 ± 0.008	−2.21 ± 0.8	
12655.83	3.900	14.988	1.770	3.065	16.06

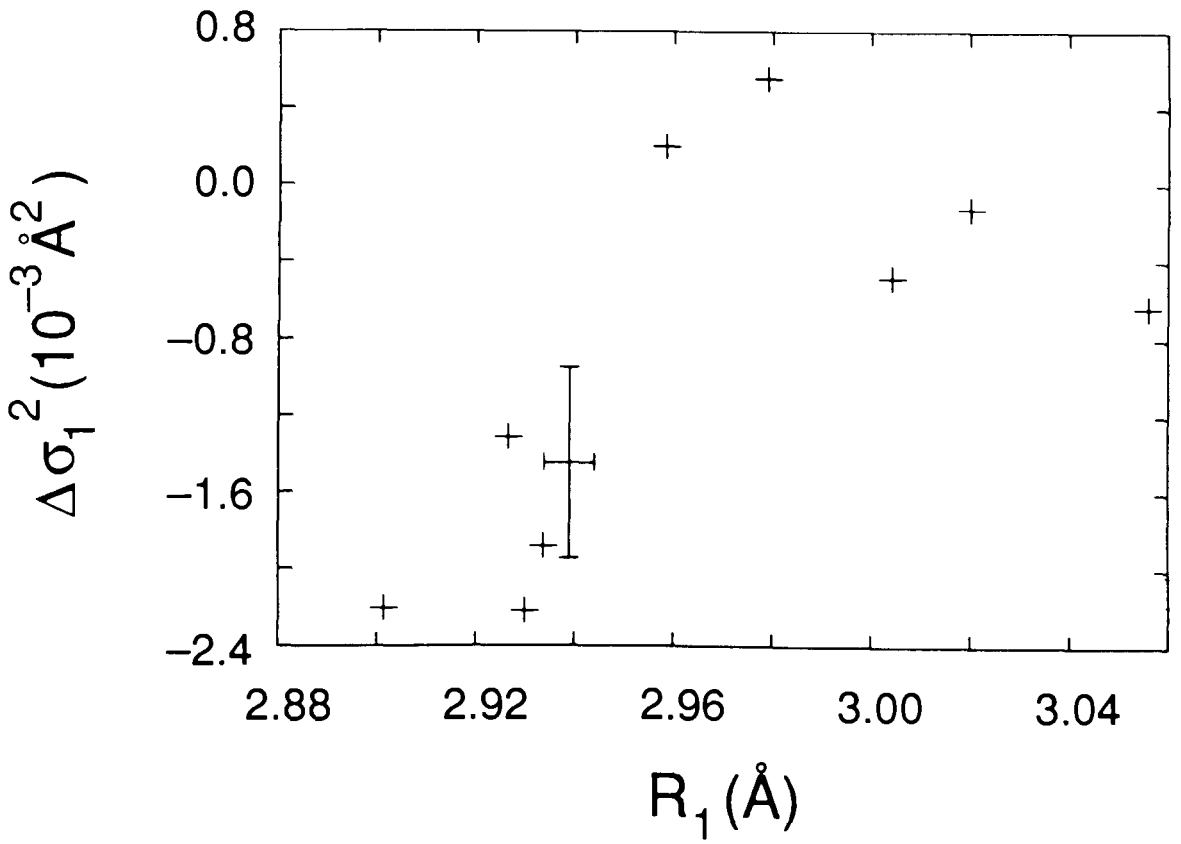

Fig. 7.29: $\Delta\sigma_1^2$ versus R_1 at 77K according to Table 7.12. Empirical amplitude and phase are employed.

Since for the run of Dec. '86 the pressure calibration was reliable we can compare the results for R_1 versus pressure from Table 7.12 with Jayaraman's data [110, 207]. However, no data point at room temperature and ambient pressure is available for absolute calibration of the nearest-neighbour distances R_1. We therefore have to use some of the information that will be presented in the next section. Table 7.14 of Section 7.3 contains values for R_1 as a function of pressure, measured at 77K with respect to the Sm atoms, rather than the Se atoms. The R_1 values of Table 7.14 can be calibrated absolutely by shifting them by −0.0085 Å, as discussed in connection with Fig. 7.38. By shifting the R_1 values of Table 7.12 according to $R_1 \rightarrow R_1 - 0.023$ Å they will agree, within experimental error, with the calibrated R_1 values of Table 7.14 shown in Fig. 7.38.

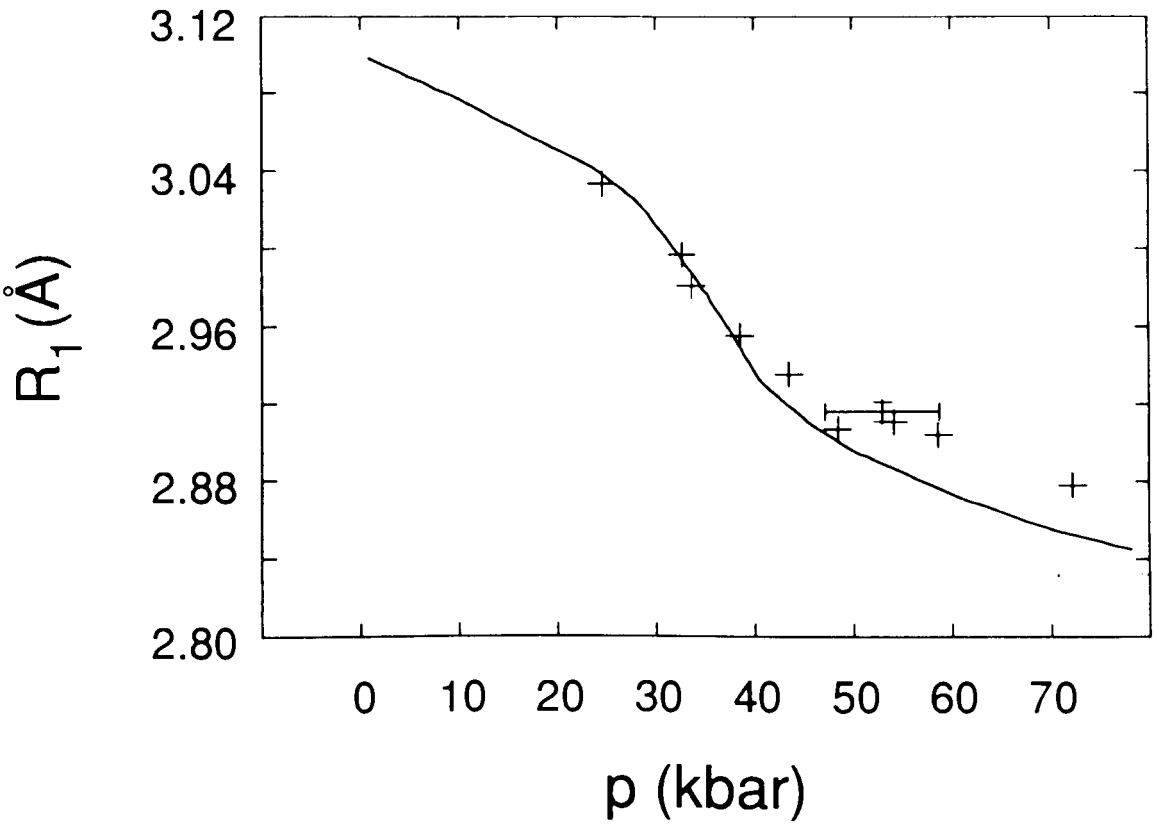

Fig. 7.30: Nearest-neighbour distance in SmSe with respect to the Se atoms as a function of pressure. The solid line refers to the x-ray diffraction data of Jayaraman et al. [110, 207] at room temperature. The crosses are the data of Table 7.12, obtained at 77K. They were shifted according to: $R_1 \rightarrow R_1 - 0.023$ Å .

The normal behaviour of σ_1^2 as a function of pressure (or R_1) is to decrease with increasing pressure (or decreasing R_1) because the atoms have less room to move away from their equilibrium positions. For SmSe we find instead that σ_1^2 exhibits a maximum. At large R_1-values the mean-square relative displacement decreases again. This behaviour could result from the fact that the first coordination shell of Sm atoms consists of two closely-spaced Sm shells in the region of the valence transition rather than one shell as assumed in our fit model. This point will be investigated in Chapter 9. Plotting for example the $\Delta\sigma_1^2$-values of Table 7.12 versus pressure shows that the peak occurs in

the region of the valence transition. It coincides with the peak in the isothermal compressibility derived from the data of Jayaraman et al. [110, 207] and shown in Fig. 4.2.

The final graph of this section shows $\Delta\sigma_1^2$ as a function of pressure, rather than R_1, at 77K.

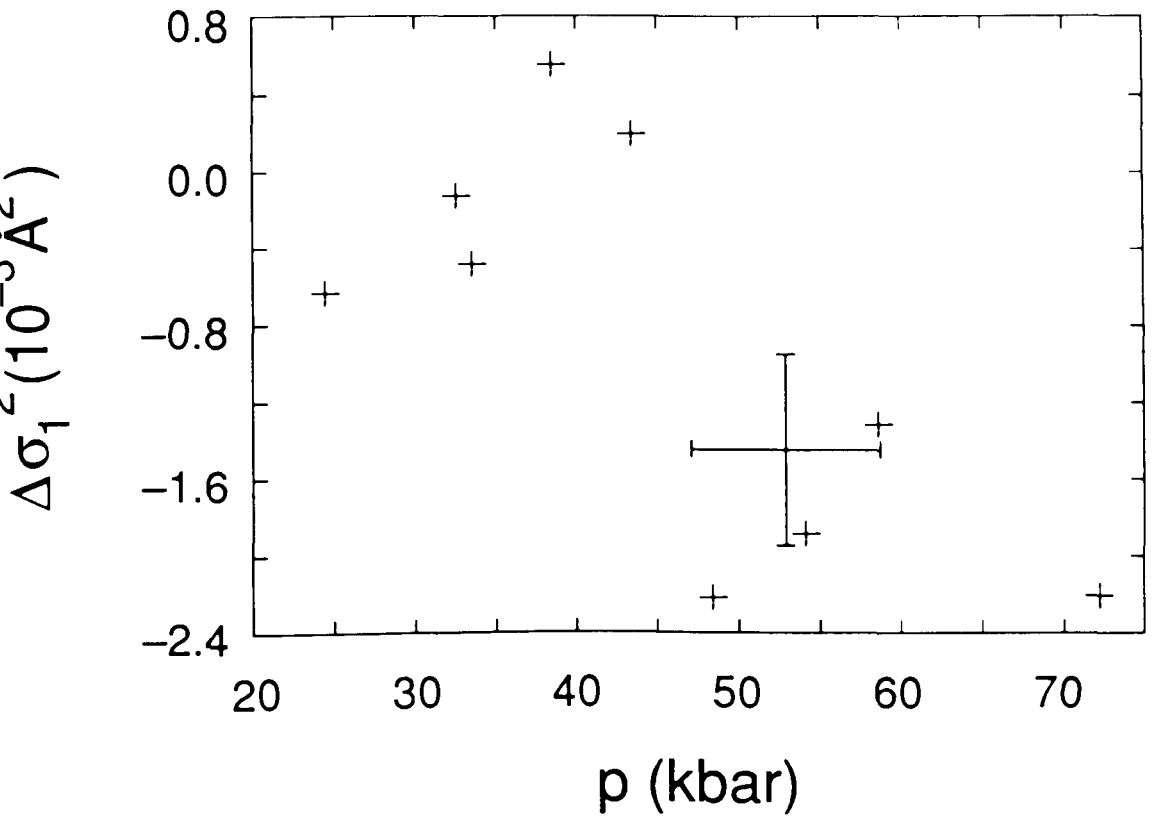

Fig. 7.31: $\Delta\sigma_1^2$ versus pressure (instead of R_1) at 77K according to Table 7.12. Empirical amplitude and phase are employed.

7.3 Analysis of the Sm L_{III} Edge EXAFS of SmSe

The EXAFS of the Sm L_{III} edge provides only limited R-space resolution because the Sm L_{II} edge intervenes at 7313 eV, thus limiting the k-scale to a maximum value of 12.5 $Å^{-1}$. However, there was some Fe contamination present in the anvil tips so the data were even further limited

because the Fe K edge occurs at 7111 eV. Thus the maximum of the k-scale was at ~10 $Å^{-1}$. No attempt was made to subtract the Fe K absorption edge. Because of this limited resolution in R-space it was not possible to filter the first coordination shell satisfactorily. Therefore two-shell fits were performed. Theoretical Sm and Se curved-wave backscattering amplitudes and phases were employed. A phase offset of $-\pi/2$ was again introduced and the ratio N_2/N_1 of the number of next-nearest neighbour atoms to nearest neighbour atoms was fixed at the value 2 according to the NaCl crystal structure. Furthermore, we assumed the ΔE values of both shells to be the same. Starting out by varying the six parameters ΔE_1, R_1, σ_1^2, N_1, and R_2 and σ_2^2 we obtained the value at which to fix N_1. ΔE_1 can be left variable in these fits because the precision in the determination of R_1 or R_2 is not as stringent as in a pressure calibration. The fits were performed in R-space to the Fourier transform of $k^2\,\chi(k)$ with five variable parameters: ΔE_1, R_1, σ_1^2, R_2/R_1, and σ_2^2. The finite monochromator resolution was included in the fits as well as the mean free path and core-hole lifetime effects. The latter effects are included via $\tilde{\eta}$ which for the Sm L_{III} edge amounts to:

$$\underline{\text{Sm}}\text{Se:} \qquad \tilde{\eta} = \frac{\Gamma_\theta + \Gamma_c}{2\,\gamma} = \frac{2.76\text{eV} + 3.6\text{eV}}{2\,\gamma} = 0.834\ Å^{-2}\ ,$$

(absorbing element underlined) .

The following two tables contain the results from fits to the Sm L_{III} edge EXAFS at 300K and at 77K. The k-space interval used for the Fourier transform is indicated by k_{min} and k_{max} and the fit interval by R_{min} and R_{max}. Again, multiple entries exist for some pressures but the graphs contain only averaged values at these pressures.

For Table 7.13 N_1 turned out to be 4.4. We obtained for the ratio R_2/R_1 of the radii of the second coordination shell to the first the following value: $R_2/R_1 = 1.4120 \pm 0.0047$. This is in excellent agreement with the expected result of $\sqrt{2}$.

Table 7.13: Sm L_{III} edge EXAFS (LOG.SM4.B):
(Dec. '83; Si (111); T = 300K)

Two-shell fits in R-space to $FT(k^2 \chi(k))$ using theoretical amplitudes and phases:

1st shell: Se; 2nd shell: Sm

fixed: $a_1 \equiv -1.5708$; $C_{31} \equiv 0.0$; $C_{41} \equiv 0.0$; $N_1 \equiv 4.4$;

$a_2 \equiv -1.5708$; $\Delta E_2 \equiv \Delta E_1$; $C_{32} \equiv 0.0$; $C_{42} \equiv 0.0$; $N_2/N_1 \equiv 2.0$

variable: ΔE_1; R_1; σ_1^2; R_2/R_1; σ_2^2

Dataset	P_{Oil}(psi)	p (kbar)	ΔE_1(eV)	R_1(Å)	R_2(Å)	σ_1^2 (10^{-3} Å^2)	σ_2^2 (10^{-3} Å^2)
E_{Edge}(eV)	k_{min}(Å^{-1})	k_{max}(Å^{-1})	R_{min}(Å)	R_{max}(Å)		χ^2_{min} (10^{-3} Å^{-6})	
SMSE00.N00.B	0	0	0.8	3.112	4.396	10.8	13.7
6711.40	4.281	10.370	1.552	5.354		0.12	
SMSE00.N01.B	0	0	–0.6	3.097	4.353	11.7	12.9
6701.44	4.252	9.993	1.755	5.028		0.24	
SMSE00.N05.B	0	0	0.3	3.104	4.367	12.0	14.5
6701.16	4.267	10.006	1.770	5.022		0.19	
SMSE00.N06.B	0	0	3.0	3.121	4.423	13.7	14.6
6702.86	4.288	10.084	1.753	5.013		0.40	
SMSE07.N11.B#	700	6.4	2.4	3.094	4.376	12.3	13.2
6711.40	4.355	9.597	1.408	5.174		0.20	
SMSE07.N13.B	700	6.4	2.3	3.083	4.388	13.7	16.4
6711.40	4.329	10.040	1.767	5.032		0.31	
SMSE13.N14.B	1300	22.7	1.3	3.066	4.332	11.0	13.4
6711.97	4.339	10.099	1.764	5.024		0.34	
SMSE18.N20.B	1800	36.8	2.1	2.974	4.208	8.7	16.1
6711.97	4.529	10.099	1.608	4.900		0.27	
SMSE19.N17.B	1900	39.6	0.9	2.961	4.185	8.8	15.3
6711.97	4.561	10.132	1.607	4.899		0.23	
SMSE20.N24.B	2000	44.1	1.2	2.935	4.145	7.4	15.7
6712.54	4.611	10.125	1.563	4.802		0.36	
SMSE20.N34.B	2050	45.9	1.4	2.931	4.129	6.8	14.6
6711.40	4.645	10.006	1.495	4.793		0.39	
SMSE21.N37.B	2125	48.7	–6.5	2.919	4.105	6.4	13.7
6718.82	4.448	10.043	1.469	4.739		0.265	
SMSE23.N39.B	2300	55.1	–5.2	2.902	4.094	5.6	14.8
6718.25	4.522	10.017	1.400	4.532		0.24	
SMSE27.N42.B	2700	68.3	–5.1	2.880	4.056	5.45	14.7
6718.25	4.559	10.051	1.401	4.609		0.25	

#: The energy calibration was adjusted for this and the following datasets.

Fig. 7.32 shows the Fourier transform magnitudes of the data for low and for high pressure and Fig. 7.33 shows the same data in k-space.

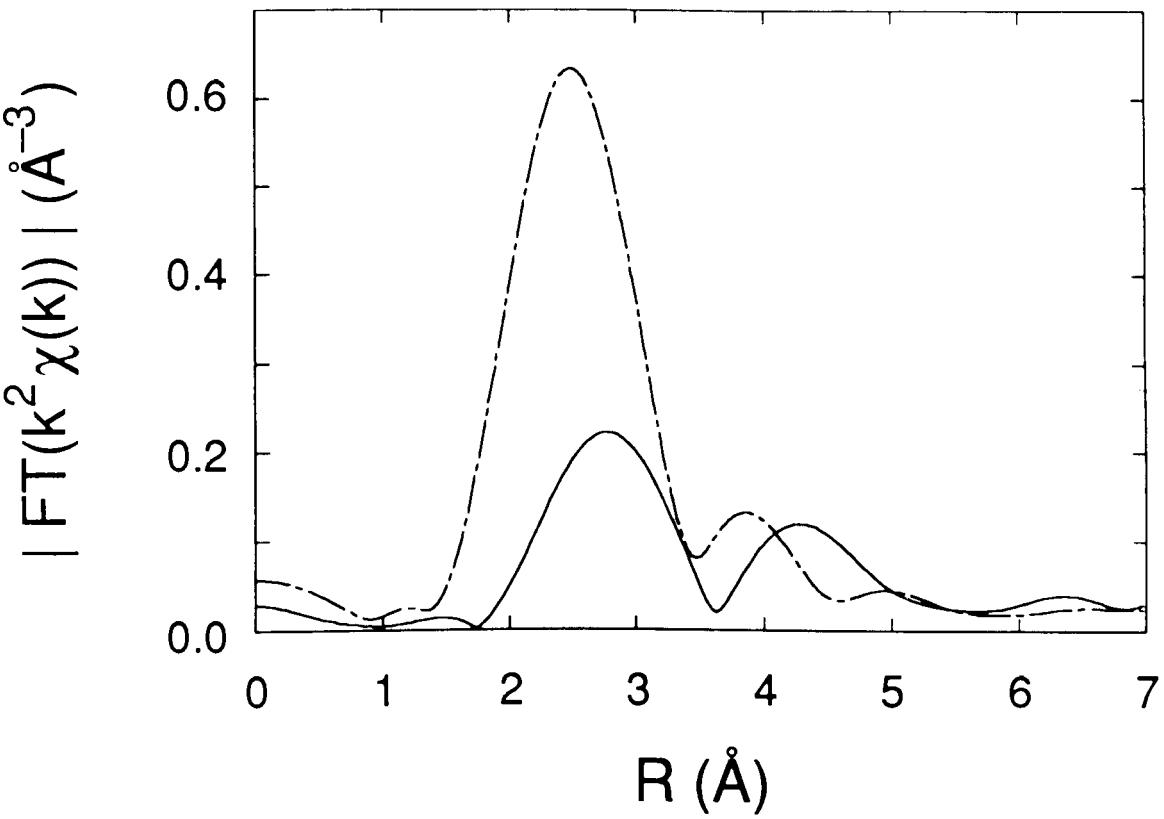

Fig. 7.32: Fourier transform magnitude of $k^2 \chi(k)$ for SmSe at 300K. The central atom is Sm. The solid line corresponds to 1 bar and the dashed line to 68.3 kbar.

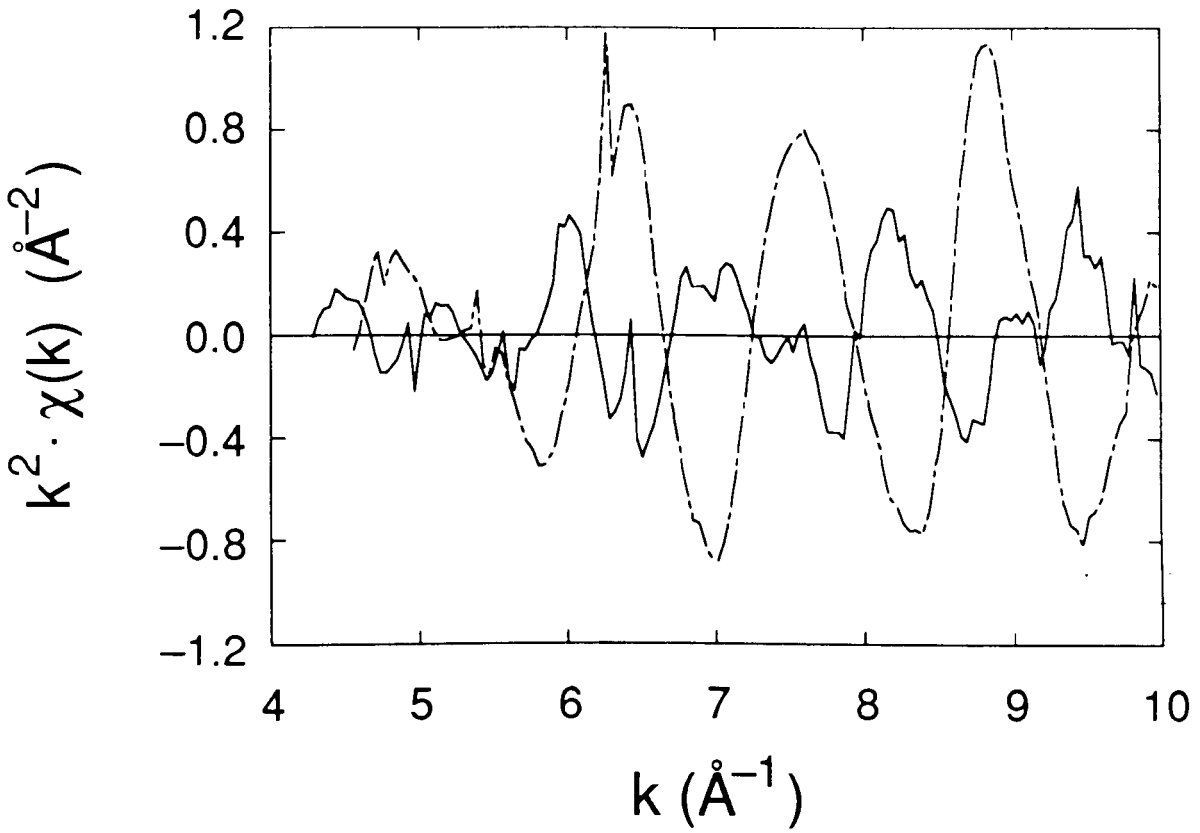

Fig. 7.33: $k^2 \chi(k)$ for SmSe at 300K for the same data as in the previous figure. The central atom is Sm. The solid line corresponds to 1 bar and the dashed line to 68.3 kbar.

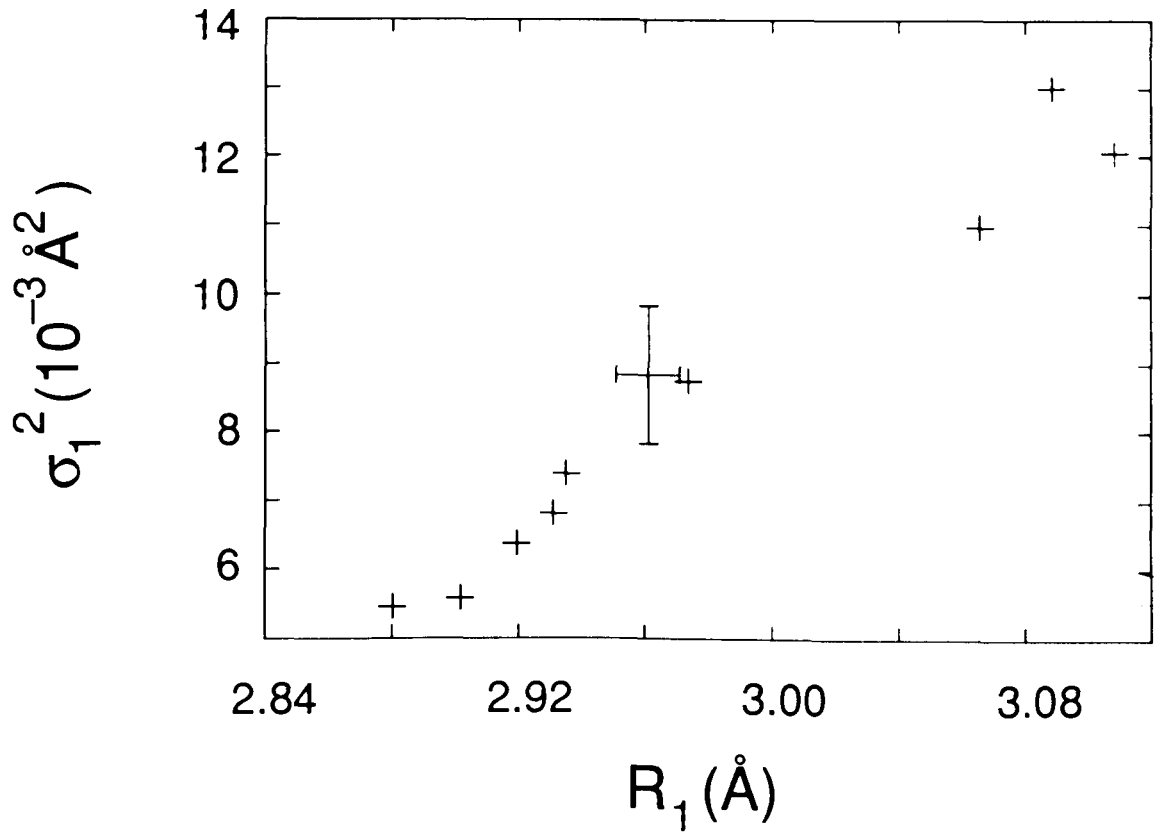

Fig. 7.34: σ_1^2 versus R_1 at 300K according to Table 7.13. N_1 was set to 4.4. Like in Fig. 7.18, which also refers to room temperature, no peak in the mean-square relative displacement is present.

Table 7.14 shows the results at 77K. N_1 was set to 4.55. For the ratio R_2/R_1 we obtained $R_2/R_1 = 1.4118 \pm 0.0040$, again close to $\sqrt{2}$.

Fig. 7.35 shows the Fourier transform magnitudes of the data for low and for high pressure and Fig. 7.36 shows the same data in k-space.

Table 7.14: Sm L_{III} edge EXAFS (LOG.SM7.G):
(Dec. '86; Si (111); T = 77K)

Two-shell fits in R-space to $FT(k^0 \chi(k))$ using theoretical amplitudes and phases:

1st shell: Se; 2nd shell: Sm

fixed: $a_1 \equiv -1.5708$; $C_{31} \equiv 0.0$; $C_{41} \equiv 0.0$; $N_1 \equiv 4.55$;
$a_2 \equiv -1.5708$; $\Delta E_2 \equiv \Delta E_1$; $C_{32} \equiv 0.0$; $C_{42} \equiv 0.0$; $N_2/N_1 \equiv 2.0$

variable: ΔE_1; R_1; σ_1^2; R_2/R_1; σ_2^2

Dataset	N_T	p (kbar)	ΔE_1(eV)	R_1(Å)	R_2(Å)	σ_1^2 (10^{-3} Å^2)	σ_2^2 (10^{-3} Å^2)
E_{Edge}(eV)	k_{min}(Å^{-1})	k_{max}(Å^{-1})	R_{min}(Å)	R_{max}(Å)		χ^2_{min} (10^{-6} Å^{-2})	
SMSE00.N81.G	0	0	0.6	3.094	4.350	4.4	6.4
6710.26	4.205	9.872	1.410	4.934		0.575	
SMSE00.N82.G	0	0	3.8	3.111	4.419	3.55	5.7
6710.74	4.285	9.794	1.729	4.887		0.92	
SMSE00.N83.G	0	0	1.5	3.100	4.368	4.1	3.7
6710.74	4.285	9.794	1.529	4.987		0.49	
SMSE00.N85.G	0	0	–0.2	3.081	4.356	4.2	4.1
6710.74	4.346	9.794	1.704	4.837		0.88	
SMSE03.N99.G	3	24.3	1.5	3.056	4.313	2.95	6.4
6710.74	4.346	9.916	1.704	4.887		0.50	
SMSE04.N14.G	4	24.5	1.7	3.041	4.307	4.0	6.7
6710.26	4.388	9.933	1.712	4.883		0.48	
SMSE05.N33.G	5	32.6	2.8	3.013	4.276	5.2	8.5
6709.79	4.429	10.011	1.694	4.905		0.43	
SMSE05.N36.G	5	32.6	1.1	3.007	4.234	5.3	6.9
6709.79	4.490	10.071	1.694	4.905		0.34	
SMSE05.N45.G	5	32.6	3.7	3.014	4.272	4.5	9.1
6709.79	4.429	10.011	1.745	4.753		0.78	
SMSE06.N85.G	6	48.4	3.8	2.9305	4.133	3.45	12.5
6710.26	4.631	9.994	1.384	4.732		0.11	
SMSE07.N06.G	7	52.9	1.8	2.916	4.106	3.6	8.9
6710.74	4.652	10.222	1.529	4.736		0.23	
SMSE4T.N24.G	4.75	31.4	–0.1	3.018	4.262	4.4	6.6
6710.26	4.409	10.043	1.628	4.760		0.48	
SMSE5H.N64.G	5.5	38.5	1.3	2.956	4.172	3.9	8.5
6710.26	4.510	10.238	1.535	4.732		0.43	

Table 7.14, continued:

SMSE5H.N66.G	5.5	38.5	1.1	2.955	4.167	3.5	8.75
6710.26	4.534	10.261	1.543	4.783		0.21	
SMSE5Q.N51.G	5.25	33.55	1.5	2.987	4.220	3.8	8.2
6709.79	4.429	10.132	1.542	4.779		0.31	
SMSE5T.N76.G	5.75	43.45	1.4	2.933	4.138	3.9	9.3
6710.26	4.571	10.299	1.586	4.707		0.40	
SMSE7Q.N12.G	7.25	54.1	4.9	2.926	4.121	3.5	10.9
6710.26	4.692	10.238	1.485	4.682		0.19	
SMSE8Q.N28.G	8.25	58.6	3.2	2.916	4.107	3.4	10.95
6710.74	4.652	10.161	1.479	4.686		0.27	
SMS11Q.N36.G	11.25	72.2	3.5	2.883	4.062	3.0	10.1
6711.21	4.734	10.207	1.372	4.665		0.17	

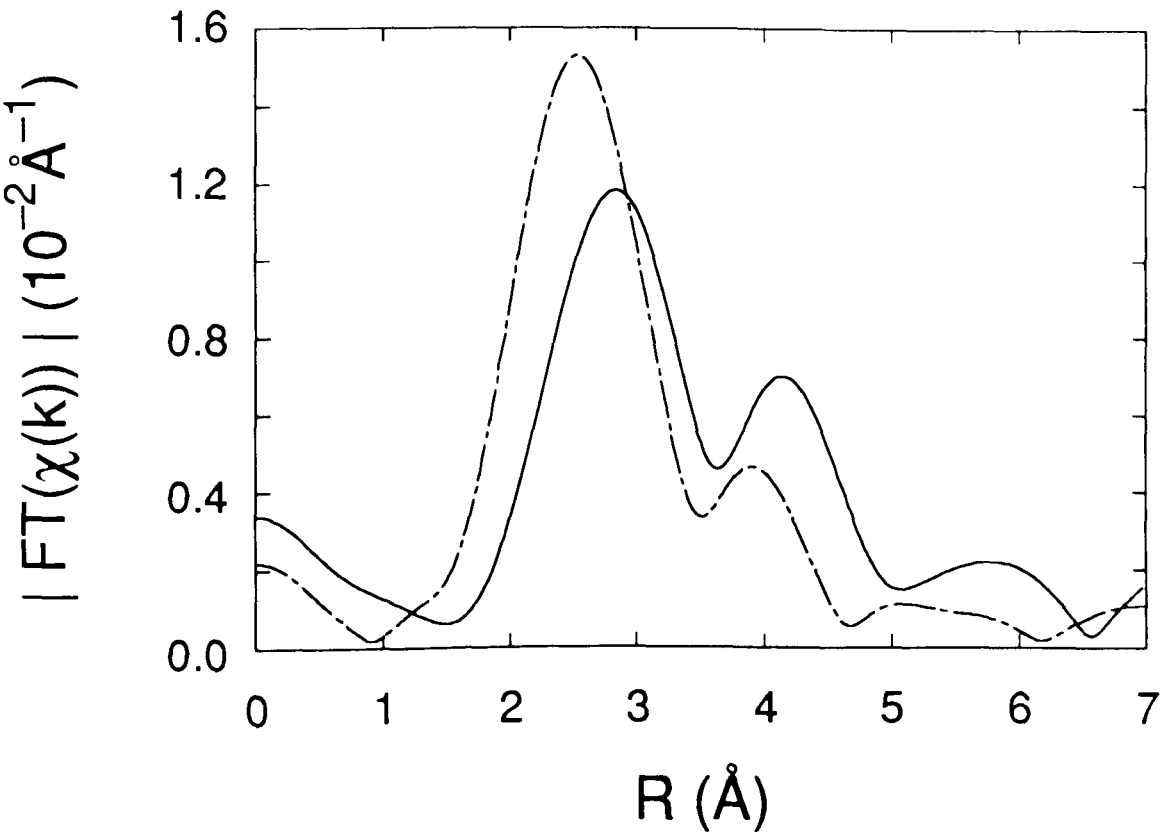

Fig. 7.35: Fourier transform magnitude of $k^0 \chi(k)$ for SmSe at 77K. The central atom is Sm. The solid line corresponds to 1 bar and the dashed line to 72.2 kbar.

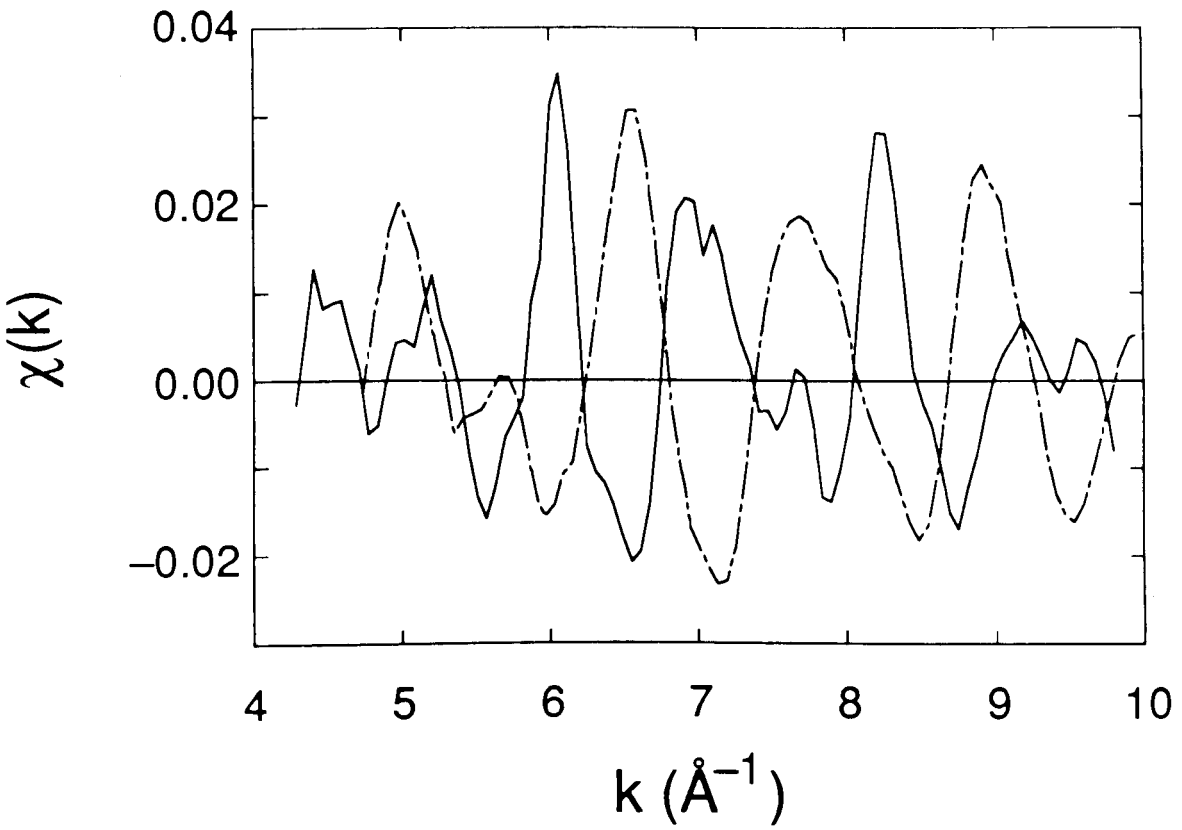

Fig. 7.36: $k^0 \chi(k)$ for SmSe at 77K for the same data as in the previous figure. The central atom is Sm. The solid line corresponds to 1 bar and the dashed line to 72.2 kbar.

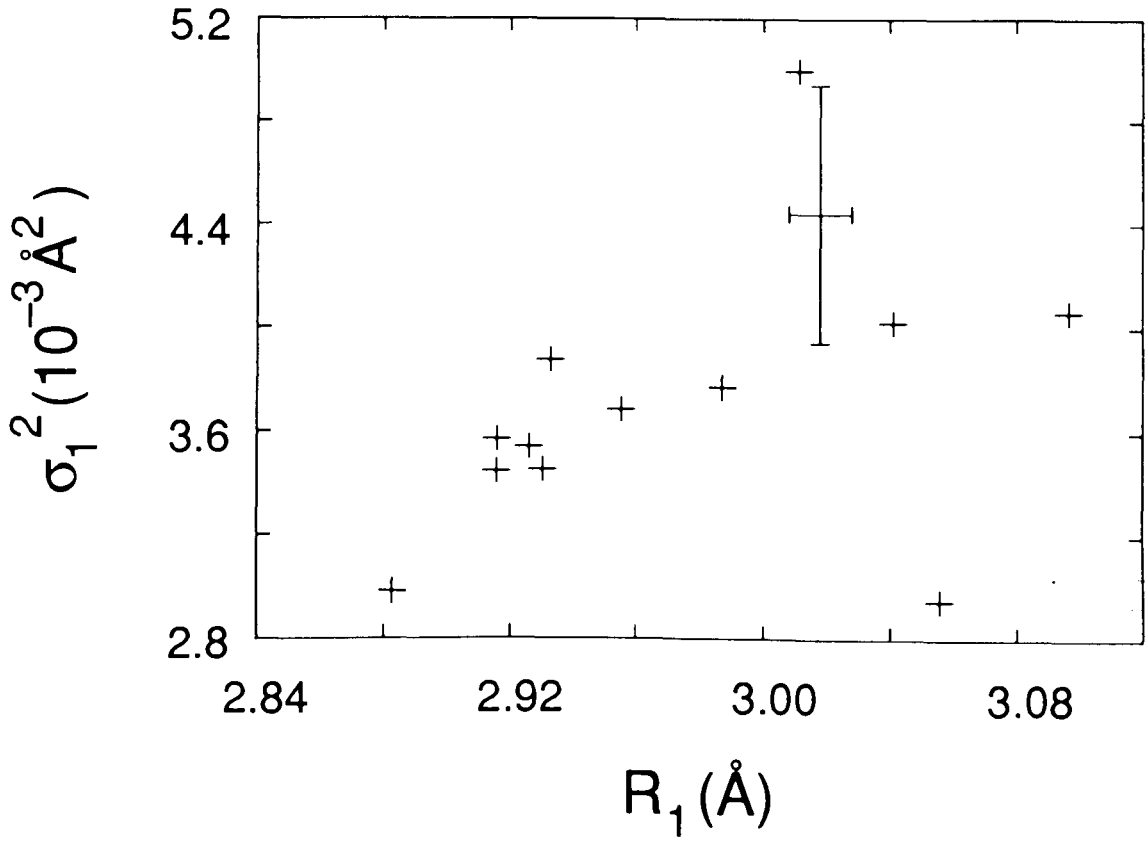

Fig. 7.37: σ_1^2 versus R_1 at 77K according to Table 7.14. N_1 was set to 4.55. We see that at 77K σ_1^2 exhibits a peak.

Figs. 7.38 and 7.39 are plots of R_1 and R_2 as functions of pressure. They are compared with the room-temperature x-ray diffraction result of Jayaraman et al. [110, 207]. Since distances obtained from EXAFS are not absolutely correct, we must shift the data at room temperature and at liquid-nitrogen temperature by the same amount such that the room temperature data at ambient pressure agree with the crystallographic value. For SmSe the nearest-neighbour distance at room temperature and ambient pressure is $R_1 = 3.100$ Å and the next-nearest neighbour distance has the value $R_2 = 3.100\ \text{Å}\ \sqrt{2} = 4.384$ Å.

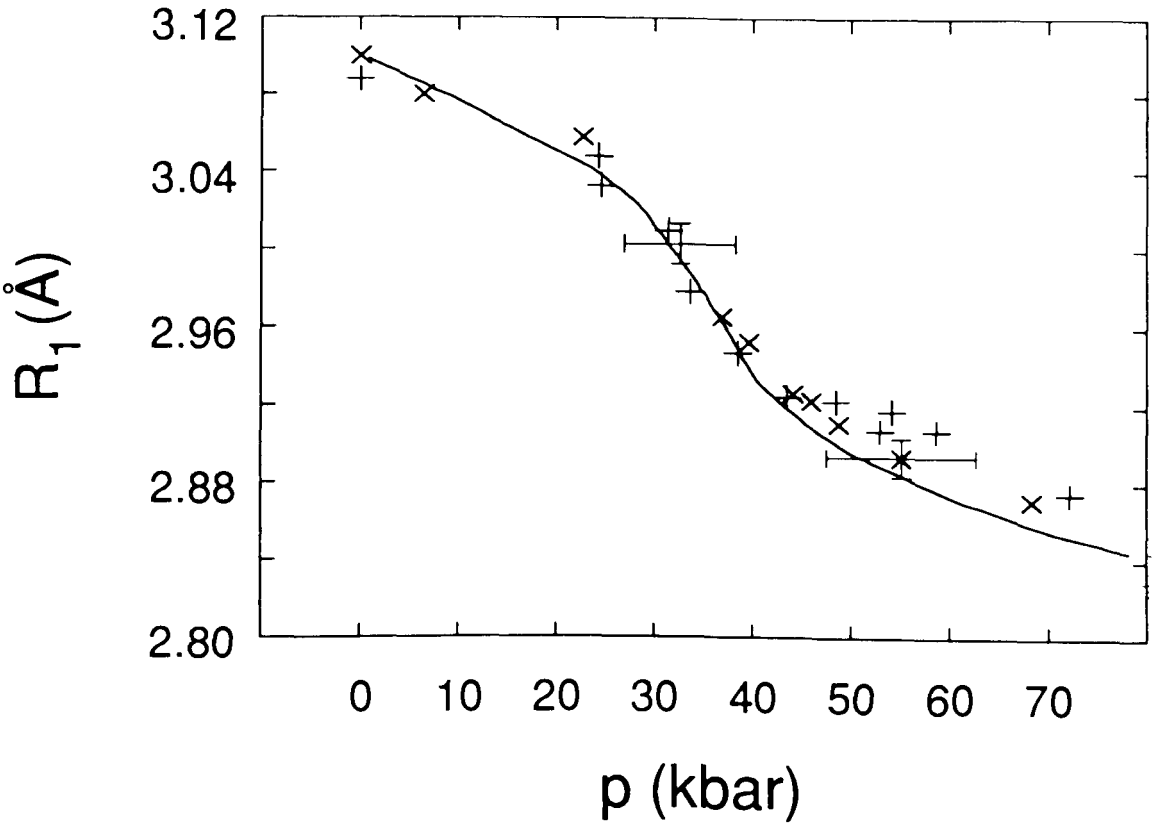

Fig. 7.38: Nearest-neighbour distance in SmSe with respect to the Sm atoms as a function of pressure. The solid line is obtained from the result of Jayaraman et al. [110, 207] at room temperature. The 'x' symbols refer to the data of Table 7.13 (300K) and the '+' symbols refer to the data of Table 7.14 (77K). Both data were shifted by the same amount: $R_1 \rightarrow R_1 - 0.0085$ Å . The error for R_1 was estimated to be ±0.01 Å.

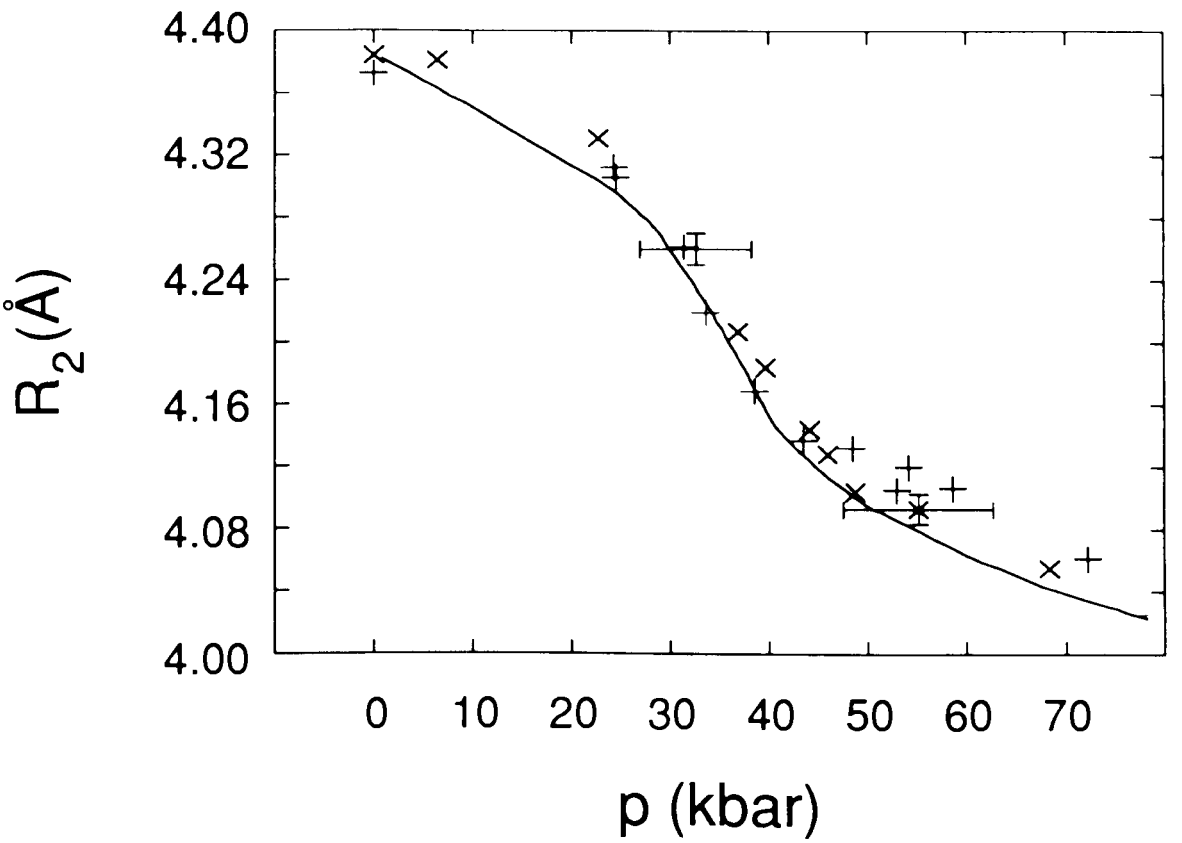

Fig. 7.39: Next-nearest-neighbour distance in SmSe with respect to the Sm atoms as a function of pressure. The solid line is obtained from the result of Jayaraman et al. [110, 207] at room temperature. The 'x' symbols refer to the data of Table 7.13 (300K) and the '+' symbols refer to the data of Table 7.14 (77K). Both data were shifted by the same amount: $R_2 \rightarrow R_2 - 0.0007$ Å . The error for R_2 was estimated to be ±0.01 Å.

We see that after shifting R_1 and R_2 such that their room-temperature values at 1 bar become equal to the correct values, the data follow Jayaraman's curve rather well. As in Fig. 7.30, the low-temperature data points lie above the x-ray diffraction result at high pressures, possibly indicating a lower compressibility. It may be relevant that our calculations in Section 5.8 for Cu (Fig. 5.4) and RbCl (Fig. 5.5) indicated a lower compressibility at 77K.

Finally we plot R_2 as a function of R_1 with these values shifted as explained in the previous two figure captions. As is evident from the next figure they follow rather closely a straight line, which indicates that the fitting is internally consistent.

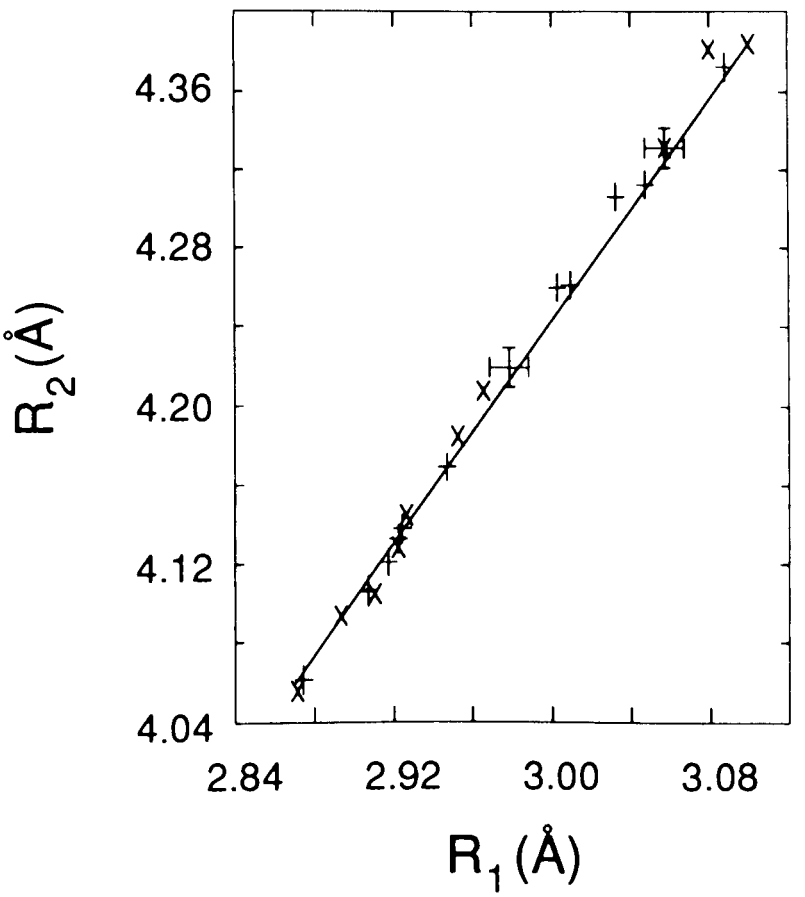

Fig. 7.40: Second-nearest neighbour distance R_2 (Sm-Sm) versus the nearest-neighbour distance R_1 (Sm-Se), with R_1 and R_2 adjusted as explained in connection with Figs. 7.38 and 7.39. The 'x' symbols refer to the data of Table 7.13 (300K) and the '+' symbols refer to the data of Table 7.14 (77K). Error bars are ±0.01 Å. The solid line is the result according to the NaCl crystal structure: $R_2 = R_1 \sqrt{2}$.

7.4 Valence Determination

The valence values are determined by fitting as explained in Section 6.12. The fit parameters are the position E^{2+} of the White Line of the divalent state, the difference $\Delta E \equiv E^{3+} - E^{2+}$ of the positions of tri- and divalent states, the HWHMs of the Lorentzian and Gaussian that are convolved, that is Γ and $\sigma\sqrt{2\cdot\ln 2}$, the amplitude Y_{max} of the White Line, and of course the valence v. With the exception of the two width parameters all other parameters are hardly correlated with each other. These six parameters are listed in the following tables as well as the derived quantities "$HWHM_{Voigt}$" and "Area", which are, respectively, the resulting HWHM of the fitted lineshape and the peak area according to Eq. (6.82). The pressure p is found by interpolation from the applied oil pressure P_{Oil} or from the number of turns N_T, depending on which pressure cell was used. All these quantities are presented here for completeness.

The results from edge scans are listed separately from those obtained from EXAFS scans. This is so because the density of data points in the edge region is higher for an edge scan than for an EXAFS scan. Hence it is possible that the peak amplitude Y_{max} comes out smaller when an absorption edge from an EXAFS dataset is analyzed (compare Tables 7.16 and 7.17).

The results are also listed separately for different temperatures and edge types (Sm L_{II} or Sm L_{III}).

At times the tables contain several entries for the same setting of the pressure cell. In such cases the graphs, that correspond to these tables, only contain the average value. Plotting several values for one setting of the pressure cell would emphasize certain data points too much. For the same reason only averaged values from one pressure point are included when a fit is performed to the data. These are fits to ΔE vs. valence and to the valence vs. pressure .

Table 7.15 contains the results of Sm L_{III} edge EXAFS scans at room temperature. The pressures were determined according to Table 7.1. By inspection of Table 7.15 one will notice that the energy calibration was adjusted after the data for zero pressure had been measured. However, this adjustment affects only E^{2+}, the peak position of the divalent absorption line.

Table 7.15: Valence determination from the Sm L_{III} edge of EXAFS datasets (VAL.SMSEXF.B):
(Dec. '83; Si (111); T = 300K)

Dataset	P_{Oil}(psi)	p (kbar)	v	ΔE (eV)	E^{2+} (eV)
	$HWHM_{Voigt}$ (eV)	Γ (eV)	$\sigma\sqrt{2\cdot\ln 2}$ (eV)	Y_{max}	Area (eV)
SMSE00.000.B	0	0	2.11	8.33	6705.68
	3.64	3.14	1.30	1.67	12.695
SMSE00.A01.B	0	0	2.12	8.11	6704.24
	3.58	2.525	1.895	1.685	11.97
SMSE00.004.B	0	0	2.12	8.22	6704.23
	3.62	2.43	2.02	1.65	11.60
SMSE00.005.B	0	0	2.12	8.12	6704.14
	3.60	2.38	2.04	1.68	11.74
SMSE00.A06.B	0	0	2.12	8.15	6705.67
	3.60	2.39	2.03	1.69	11.90
SMSE07.010.B#	700	6.4	2.12	8.19	6712.79
	3.64	2.44	2.035	1.64	11.57
SMSE07.011.B	700	6.4	2.12	8.12	6714.20
	3.58	2.455	1.95	1.66	11.62
SMSE07.013.B	700	6.4	2.105	7.97	6714.36
	3.63	2.72	1.77	1.61	11.55
SMSE13.A14.B	1300	22.7	2.14	7.87	6714.45
	3.33	2.25	1.85	1.86	12.62
SMSE19.A17.B	1900	39.6	2.43	7.32	6714.74
	3.24	2.01	1.96	2.155	14.645
SMSE18.A20.B	1800	36.8	2.41	7.36	6714.72
	3.25	2.02	1.955	2.12	14.43
SMSE20.023.B	2000	44.1	2.45	7.30	6714.87
	3.27	1.96	2.02	2.11	14.24
SMSE20.A24.B	2000	44.1	2.52	7.21	6714.96
	3.305	1.96	2.06	2.16	14.79
SMSE20.A34.B	2050	45.9	2.55	7.14	6714.03
	3.26	1.91	2.06	2.22	15.12
SMSE21.037.B	2125	48.7	2.58	7.10	6714.07
	3.28	1.86	2.12	2.22	15.09
SMSE21.038.B	2125	48.7	2.58	7.07	6714.11
	3.28	1.855	2.12	2.22	15.06

Table 7.15, continued:

SMSE23.A39.B	2300	55.1	2.65	6.98	6713.96
	3.31	1.905	2.11	2.25	15.51
SMSE27.A42.B	2700	68.3	2.73	6.82	6714.14
	3.38	1.915	2.18	2.25	15.80

#: The energy calibration was adjusted for this and the following datasets.

The next two tables contain results from the Sm L_{III} edge of another run, also at 300K. The pressures were determined according to Table 7.2. Table 7.16 contains the results from edge scans and Table 7.17 lists the results from EXAFS scans.

Table 7.16: Valence determination from the Sm L_{III} edge (VAL.SMSEED.C): (April '84; Si (111); T = 300K)

Dataset	P_{Oil}(psi)	p (kbar)	v	ΔE (eV)	E^{2+} (eV)
	$HWHM_{Voigt}$ (eV)	Γ (eV)	$\sigma\sqrt{2\cdot\ln 2}$ (eV)	Y_{max}	Area (eV)
SME05.007.C	500	2.8	2.19	8.08	6712.80
	3.32	1.24	2.59	2.39	15.52
SMED10.008.C	1000	5.6	2.19	8.19	6712.78
	3.365	1.23	2.65	2.42	15.98
SMSE12.020.C	1200	8.7	2.19	8.02	6713.31
	3.23	1.23	2.51	2.47	15.84
SMSE13.021.C	1300	10.2	2.19	8.01	6713.32
	3.27	1.38	2.45	2.44	16.01
SMSE14.022.C	1400	11.8	2.20	7.98	6713.30
	3.27	1.29	2.50	2.50	16.31
SMSE15.023.C	1500	13.3	2.20	7.90	6713.32
	3.29	1.38	2.465	2.45	16.19
SMSE16.024.C	1600	14.9	2.21	8.05	6713.34
	3.33	1.27	2.585	2.48	16.41
SMSE17.025.C	1700	16.4	2.22	7.94	6713.35
	3.31	1.375	2.49	2.48	16.46
SMSE18.040.C	1800	22.6	2.22	7.87	6713.36
	3.27	1.255	2.53	2.51	16.35
SMSE19.046.C	1900	28.8	2.24	7.79	6713.33
	3.24	1.29	2.485	2.55	16.65
SMSE19.047.C	1950	31.9	2.29	7.72	6713.36
	3.27	1.26	2.53	2.60	17.075
SMSE20.053.C	2050	38.1	2.40	7.60	6713.43
	3.31	1.34	2.515	2.64	17.70
SMSE21.063.C	2150	39.85	2.49	7.39	6713.49
	3.35	1.33	2.57	2.66	18.09
SMSE22.069.C	2250	41.6	2.55	7.24	6713.72
	3.35	1.45	2.48	2.68	18.51

Table 7.17: Valence determination from the Sm L_{III} edge of EXAFS datasets (VAL.SMSEXF.C):
(April '84; Si (111); T = 300K)

Dataset	P_{Oil}(psi)	p (kbar)	v	ΔE (eV)	E^{2+} (eV)
	$HWHM_{Voigt}$ (eV)	Γ (eV)	$\sigma\sqrt{2\cdot\ln 2}$ (eV)	Y_{max}	Area (eV)
SM000.000.C	0	0	2.11	8.07	6712.62
	3.23	2.49	1.51	1.90	13.11
SMSE00.A01.C	0	0	2.11	8.08	6712.49
	3.22	2.44	1.55	1.85	12.48
SMSE10.A09.C	1000	5.6	2.11	8.02	6712.53
	3.27	2.47	1.57	1.85	12.67
SMSE17.A26.C	1700	16.4	2.15	7.87	6713.08
	3.27	2.53	1.52	1.94	13.62
SMSE18.AAT.C	1800	22.6	2.16	7.81	6713.20
	3.22	2.51	1.47	1.98	13.83
SMSE19.A48.C	1950	25.7	2.26	7.61	6713.22
	3.24	2.48	1.53	2.05	14.48
SMSE20.A54.C	2050	38.1	2.37	7.45	6713.25
	3.25	2.43	1.60	2.10	14.92
SMSE21.A64.C	2150	39.85	2.47	7.31	6713.41
	3.27	2.28	1.75	2.15	15.18
SMSE22.A70.C	2250	41.6	2.53	7.22	6713.48
	3.32	2.24	1.84	2.16	15.35
SMSE22.073.C	2250	41.6	2.52	7.24	6713.45
	3.29	2.18	1.87	2.16	15.145

The following two tables correspond to a run at 77K. The pressures were determined according to Table 7.4. Table 7.18 contains results from edge scans of the Sm L_{II} edge and Table 7.19 lists the results from Sm L_{III} edge EXAFS scans.

Table 7.18: Valence determination from the Sm L_{II} edge (VAL.SMSEE2.G):
(Dec. '86; Si (111); T = 77K)

Dataset	N_T	p (kbar)	v	ΔE (eV)	E^{2+} (eV)
	$HWHM_{Voigt}$ (eV)	Γ (eV)	$\sigma\sqrt{2\cdot\ln 2}$ (eV)	Y_{max}	Area (eV)
SMSE04.218.G	4	24.5	2.16	7.50	7307.77
	2.99	1.24	2.255	2.20	12.80
SMSE4Q.219.G	4.25	26.8	2.17	7.56	7307.76
	2.98	1.23	2.25	2.28	13.33
SMSE4H.220.G	4.5	29.1	2.19	7.50	7307.70
	3.01	1.25	2.27	2.28	13.48
SMSE4T.221.G	4.75	31.4	2.21	7.47	7307.71
	3.00	1.30	2.22	2.25	13.33
SMSE4T.A22.G	4.75	31.4	2.21	7.52	7307.86
	3.03	1.20	2.32	2.28	13.48
SMSE05.231.G	5	32.6	2.28	7.45	7307.96
	3.03	0.94	2.49	2.49	14.54
SMSE05.A47.G	5	32.6	2.30	7.43	7307.53
	3.07	1.00	2.49	2.43	14.43
SMSE5Q.A49.G	5.25	33.55	2.34	7.38	7307.42
	3.05	1.11	2.41	2.41	14.39
SMSE5H.A61.G	5.5	38.5	2.44	7.27	7307.65
	3.11	1.23	2.38	2.42	14.94
SMSE5T.A74.G	5.75	43.45	2.54	7.14	7307.52
	3.14	1.31	2.37	2.37	14.765
SMSE06.283.G	6	48.4	2.58	7.11	7307.93
	3.16	1.09	2.52	2.49	15.38
SMSE06.284.G	6	48.4	2.58	7.08	7307.66
	3.19	1.10	2.55	2.49	15.55
SMSE6Q.296.G	6.25	49.5	2.57	7.13	7307.19
	3.15	1.26	2.40	2.42	15.10
SMSE6H.297.G	6.5	50.7	2.57	7.08	7307.14
	3.11	1.06	2.50	2.40	14.47
SMSE6T.298.G	6.75	51.8	2.58	7.07	7307.49
	3.13	1.19	2.43	2.46	15.18
SMSE07.299.G	7	52.9	2.59	7.06	7307.42
	3.15	1.13	2.49	2.45	15.11
SMSE7Q.A10.G	7.25	54.1	2.63	6.99	7308.07
	3.17	1.11	2.52	2.44	15.07

Table 7.18, continued:

SMSE08.321.G	8	57.5	2.64	6.99	7307.90
	3.17	1.16	2.49	2.48	15.48
SMSE8Q.322.G	8.25	58.6	2.64	6.99	7308.01
	3.19	1.25	2.46	2.43	15.31
SMSE8Q.A26.G	8.25	58.6	2.65	6.96	7308.07
	3.17	1.15	2.50	2.50	15.61
SMSE8T.A30.G	8.75	60.9	2.67	6.92	7307.95
	3.19	1.23	2.47	2.41	15.115
SMSE9Q.332.G	9.25	63.1	2.68	6.86	7307.90
	3.20	1.15	2.525	2.44	15.27
SMSE9H.333.G	9.5	64.3	2.68	6.84	7307.89
	3.18	1.23	2.46	2.41	15.08
SMS10Q.334.G	10.25	67.7	2.70	6.79	7307.89
	3.21	1.23	2.48	2.49	15.89
SMS11Q.335.G	11.25	72.2	2.74	6.73	7308.18
	3.215	1.31	2.44	2.49	16.02

Table 7.19: Valence determination from the Sm L_{III} edge of EXAFS datasets (VAL.SMSEX3.G):
(Dec. '86; Si (111); T = 77K)

Dataset	N_T	p (kbar)	v	ΔE (eV)	E^{2+} (eV)
	$HWHM_{Voigt}$ (eV)	Γ (eV)	$\sigma\sqrt{2\cdot\ln 2}$ (eV)	Y_{max}	Area (eV)
SMSE00.182.G	0	0	2.085	8.22	6713.28
	3.44	2.58	1.66	1.71	11.98
SMSE00.A83.G	0	0	2.09	8.21	6713.17
	3.42	2.27	1.94	1.77	12.04
SMSE00.185.G	0	0	2.09	8.21	6713.34
	3.44	2.175	2.04	1.76	11.86
SMSE03.A99.G	3	24.3	2.13	8.04	6713.38
	3.49	1.86	2.34	1.73	11.28
SMSE04.A14.G	4	24.5	2.14	8.00	6713.13
	3.47	2.06	2.165	1.80	12.18
SMSE4T.A24.G	4.75	31.4	2.18	7.72	6712.81
	3.30	2.12	1.93	1.89	12.62

Table 7.19, continued:

SMSE4T.228.G	4.75	31.4	2.17	7.38	6712.74
	2.87	2.23	1.32	2.10	13.33
SMSE05.232.G	5	32.6	2.23	7.75	6712.70
	3.42	2.16	2.03	1.82	12.34
SMSE05.A33.G	5	32.6	2.24	7.77	6712.63
	3.465	2.00	2.21	1.81	12.16
SMSE05.A36.G	5	32.6	2.26	7.82	6712.55
	3.44	1.67	2.43	1.91	12.55
SMSE05.A45.G	5	32.6	2.24	7.78	6712.64
	3.52	2.28	2.04	1.74	12.07
SMSE5Q.A51.G	5.25	33.55	2.29	7.79	6712.76
	3.52	2.03	2.25	1.79	12.16
SMSE5H.A64.G	5.5	38.5	2.39	7.61	6712.83
	3.45	2.03	2.17	1.89	12.92
SMSE5H.266.G	5.5	38.5	2.38	7.62	6712.61
	3.46	2.17	2.07	1.80	12.305
SMSE5T.A76.G	5.75	43.45	2.47	7.46	6712.87
	3.49	2.00	2.23	1.93	13.38
SMSE06.A85.G	6	48.4	2.52	7.42	6712.80
	3.53	1.85	2.39	1.94	13.40
SMSE07.A06.G	7	52.9	2.55	7.37	6713.33
	3.51	1.84	2.37	2.02	14.00
SMSE7Q.A12.G	7.25	54.1	2.57	7.30	6713.20
	3.47	1.79	2.375	2.01	13.73
SMSE8Q.A28.G	8.25	58.6	2.60	7.28	6713.26
	3.465	1.94	2.255	2.13	15.01
SMS11Q.A36.G	11.25	72.2	2.70	6.99	6713.52
	3.57	1.97	2.34	2.07	14.92
SMS11Q.338.G	11.25	72.2	2.70	6.98	6713.49
	3.555	1.87	2.40	2.10	14.975

By plotting all possible combinations of the parameters listed in these tables the most pronounced relations were found. These are the valence as a function of pressure (Figs. 7.41 to 7.43) and the difference ΔE of peak positions as a function of valence (Figs. 7.45 to 7.47).

In Figs. 7.41 to 7.43 we compare the pressure dependence of the valence as obtained from the L_{II} or L_{III} edge, at room temperature or at 77K, or as obtained from edge scans or EXAFS scans.

For EXAFS scans only a few data points are measured near the absorption edge and as a consequence some of the fit results may be affected. In Figs. 7.41 to 7.43 typical error bars are indicated. The uncertainty in the pressure was obtained from the error bars listed with the results of the pressure calibrations, Tables 7.1, 7.2, and 7.4. The fit error in the valence determination was assumed to be ±0.04, based on previous experience with valence determination [17].

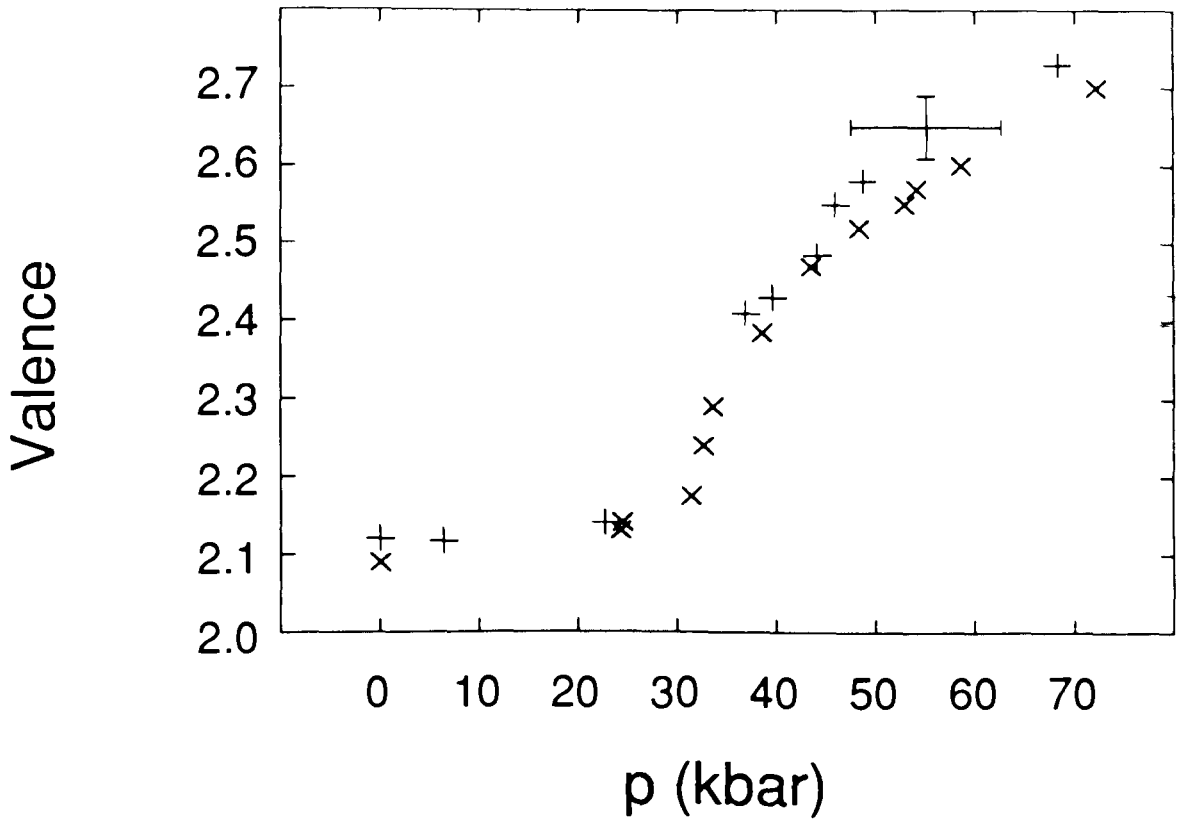

Fig. 7.41: Valence versus pressure as obtained from EXAFS scans of the Sm L_{III} edge. The '+' symbols refer to Table 7.15 (300K) and the 'x' symbols refer to Table 7.19 (77K). The valence at room temperature is slightly higher. There are not many room-temperature data points in the immediate transition region so it is difficult to judge whether the transition at room temperature is equally sharp as at 77K.

Fig. 7.42 shows the transition at room temperature with data from one edge and two EXAFS scans.

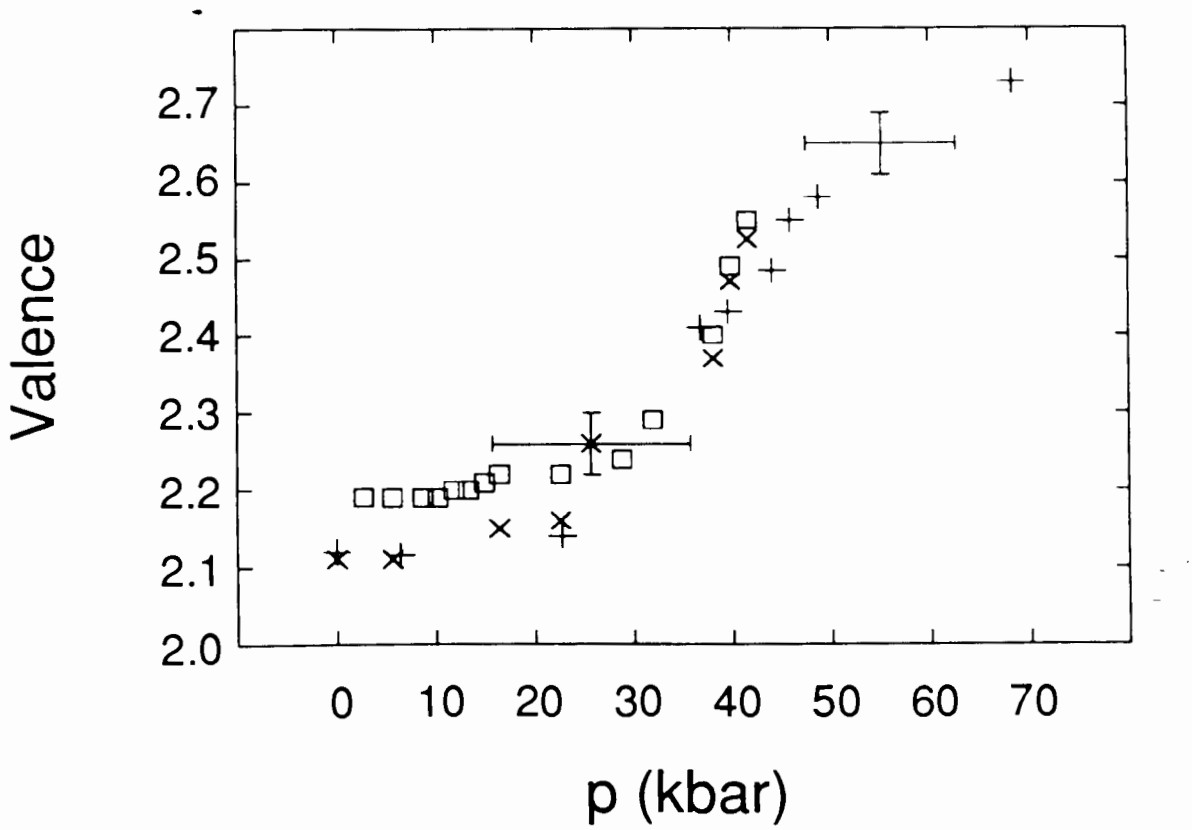

Fig. 7.42: Valence versus pressure at 300K as obtained from scans of the Sm L_{III} edge. The '+' symbols refer to Table 7.15, the 'x' symbols refer to Table 7.17, and the '□' symbols refer to Table 7.16.

The next figure shows results at liquid-nitrogen temperature. The valence obtained from Sm L_{II} edge scans is slightly larger than the valence obtained from Sm L_{III} EXAFS scans.

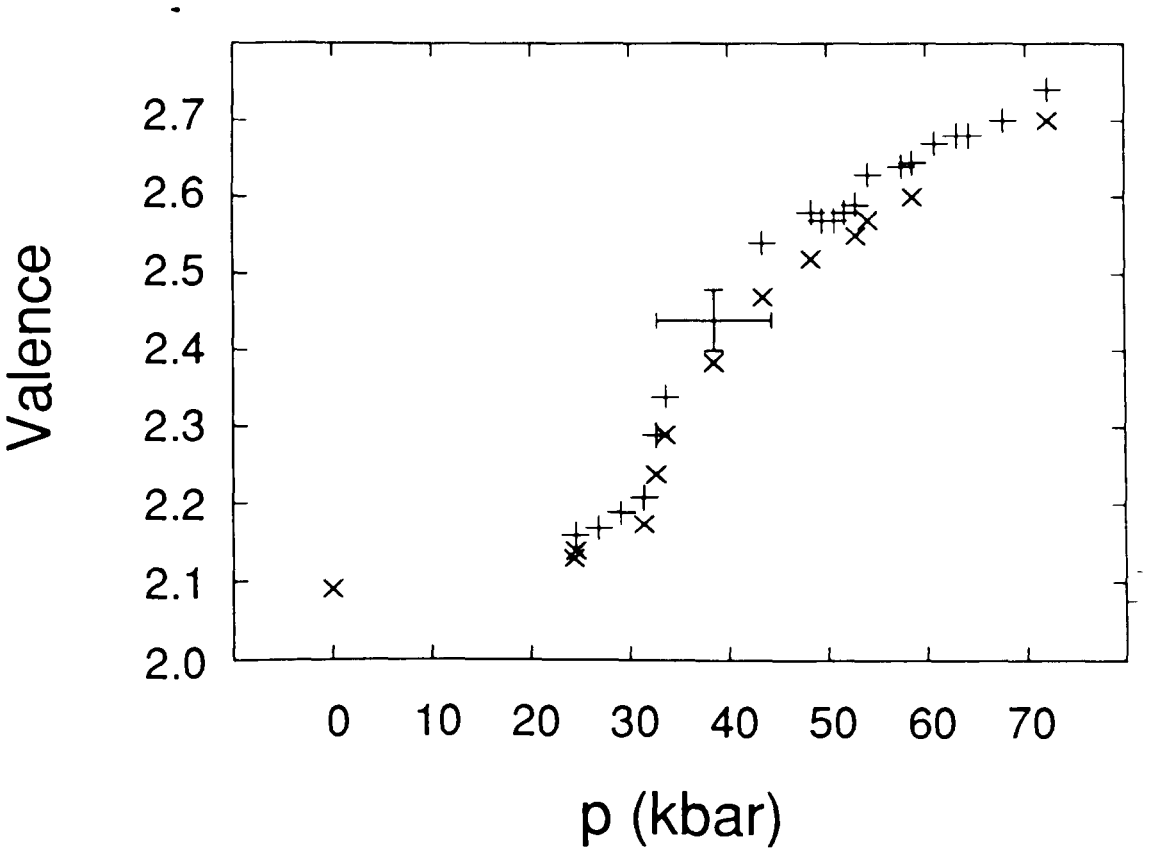

Fig. 7.43: Valence versus pressure at 77K as obtained from a Sm L_{II} edge scan and a Sm EXAFS scan of the L_{III} edge. The '+' symbols refer to Table 7.18 (L_{II}), and the 'x' symbols refer to Table 7.19 (L_{III}). The valence obtained from L_{II} edge scans is slightly larger than the valence obtained from Sm L_{III} EXAFS scans.

In the vicinity of a phase transition the properties of a physical system are described by power laws. Therefore the pressure dependence of the valence is fitted to the following equation:

$$v = B \qquad \text{for} \quad p \le p_c$$

$$v = B + A\left(\frac{p - p_c}{p_c}\right)^{\alpha} \qquad \text{for} \quad p \ge p_c \tag{7.4}$$

This equation contains four parameters: B is a constant background, which is practically equal to the

valence for $p \leq p_c$, where p_c is the critical pressure. A is an amplitude factor and α is a positive exponent.

With these four parameters being variables in a least-squares fit the following results are obtained:

Table 7.15:	B = 2.125;	A = 0.57;	p_c = 31.0 kbar;	α = 0.44 .
Table 7.18:	B = 2.18;	A = 0.50;	p_c = 31.9 kbar;	α = 0.40 .
Table 7.19:	B = 2.13;	A = 0.50;	p_c = 31.6 kbar;	α = 0.44 .

The errors associated with the fit parameters are estimated to be:

$\Delta B = \pm 0.04$; $\Delta A = \pm 0.05$; $\Delta p_c = \pm 1$ kbar; $\Delta \alpha = \pm 0.05$.

The pressure dependence of the valence as obtained from Tables 7.16 and 7.17 is not fitted because there are not enough data points above p_c.

The following figure shows as an example the fit to the data of Table 7.19.

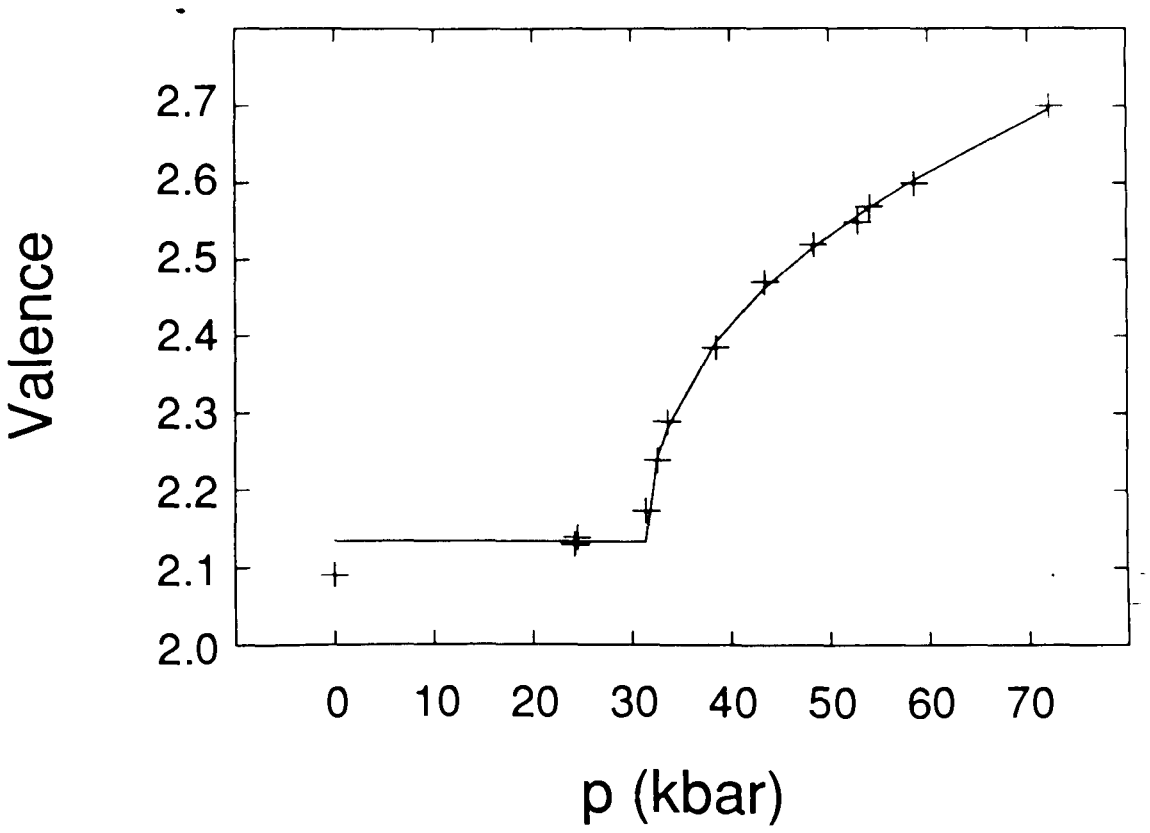

Fig. 7.44: Valence versus pressure at 77K. The '+' symbols refer to Table 7.19 (L_{III}). The solid line is a fit according to Eq. (7.4).

Apart from the pressure dependence of the valence the dependence of ΔE on the valence is of interest. This relation is established independently of the pressure calibration. ΔE versus the valence is approximately linear as can be seen from the following figures.

One may argue that this dependence of ΔE vs. the valence is an artifact of the fitting procedure. However, the fitting parameters are not very much correlated and the fitting correlation coefficient between ΔE and the valence is particularly small. Thus the almost linear relation between ΔE and the valence as obtained from different datasets is meaningful. It is probably due to differences in the screening of the Sm^{2+} and Sm^{3+} ions. This will be discussed in Section 10.4.

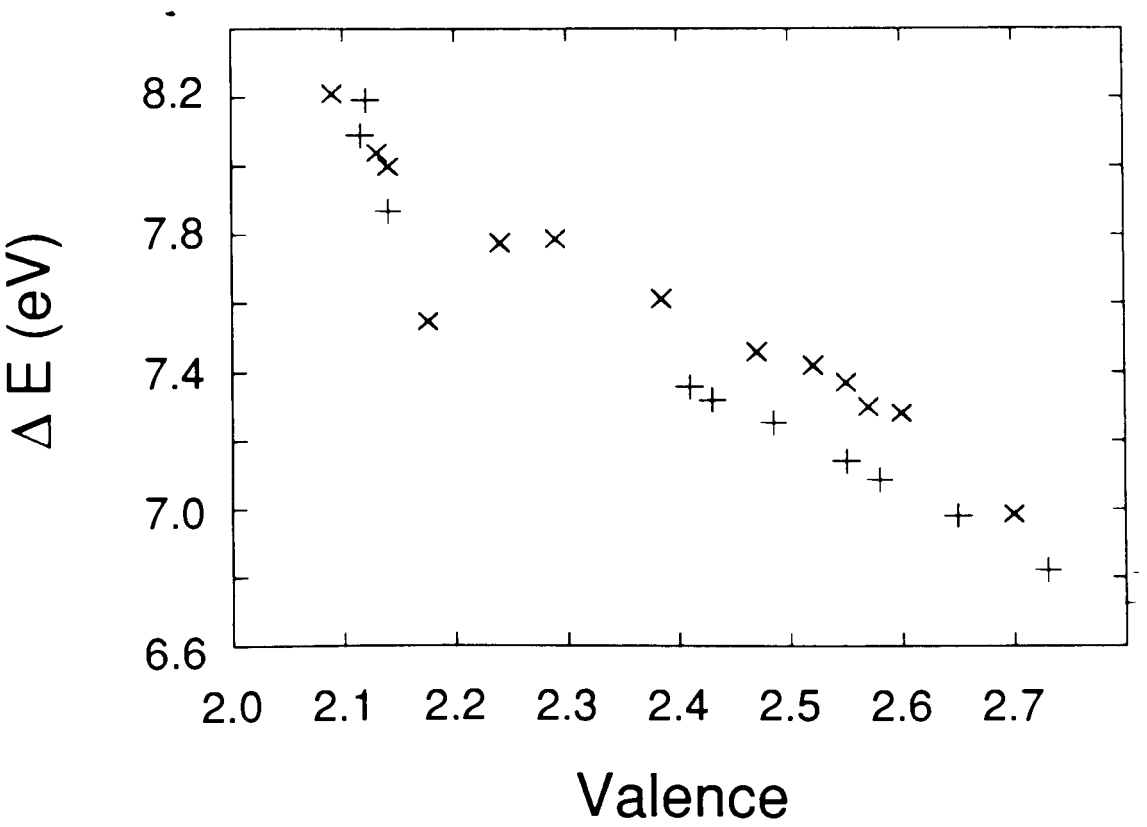

Fig. 7.45: ΔE versus valence. The '+' symbols refer to Table 7.15 (300K) and the 'x' symbols refer to Table 7.19 (77K).

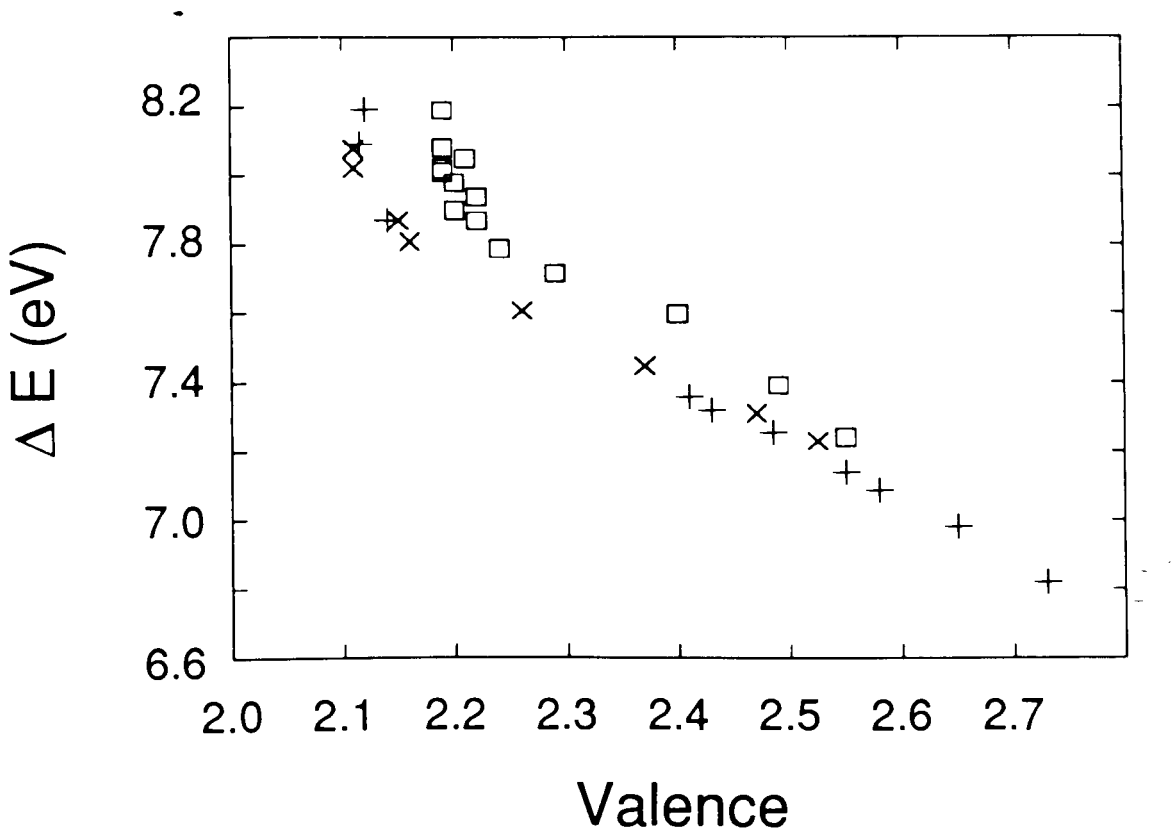

Fig. 7.46: ΔE versus valence at 300K. The '+' symbols refer to Table 7.15, the 'x' symbols refer to Table 7.17, and the '□' symbols refer to Table 7.16.

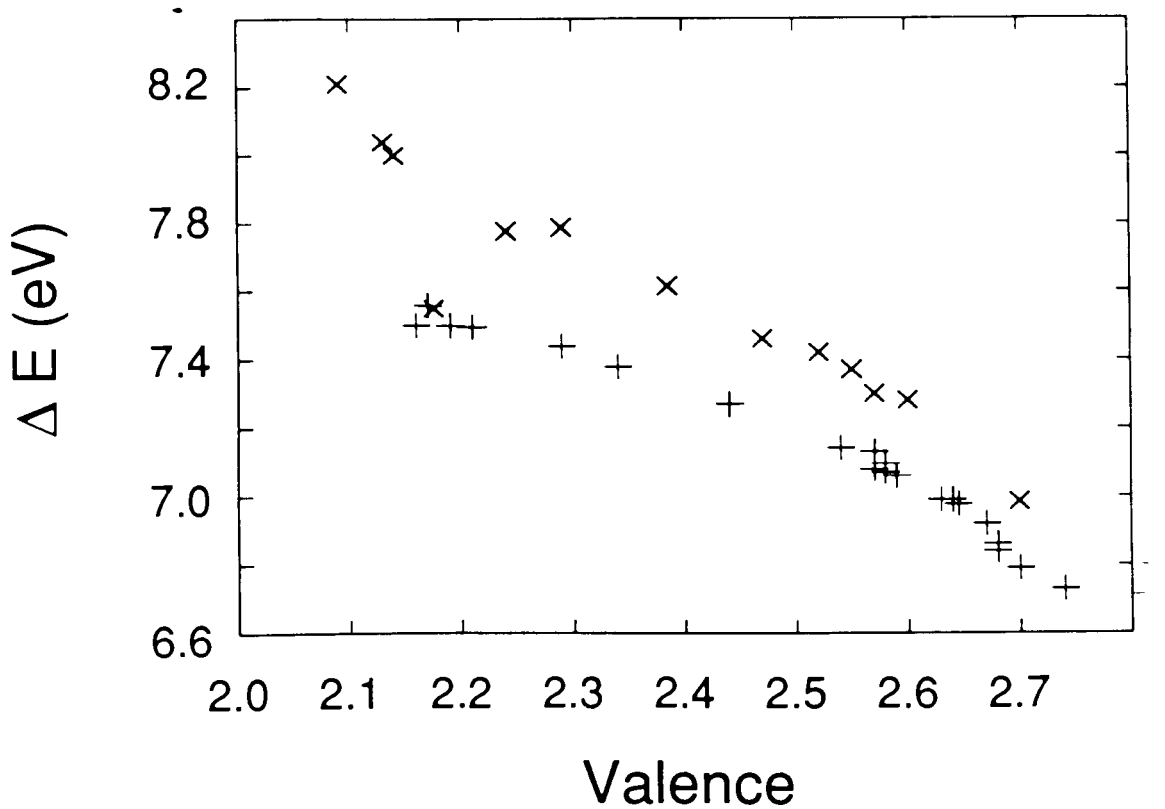

Fig. 7.47: ΔE versus valence at 77K. The '+' symbols refer to Table 7.18 (L_{II}), and the 'x' symbols refer to Table 7.19 (L_{III}).

Fitting straight lines to ΔE as a function of the valence v, excluding points with ΔE exceeding approximately 8 eV, yields:

Table 7.15:	$\Delta E = 11.6\ eV - v \cdot 1.75\ eV$	or	$v = 6.63 - 0.572\ eV^{-1} \cdot \Delta E$.
Table 7.16:	$\Delta E = 12.5\ eV - v \cdot 2.07\ eV$	or	$v = 6.05 - 0.483\ eV^{-1} \cdot \Delta E$.
Table 7.17:	$\Delta E = 11.4\ eV - v \cdot 1.65\ eV$	or	$v = 6.90 - 0.607\ eV^{-1} \cdot \Delta E$.
Table 7.18:	$\Delta E = 10.4\ eV - v \cdot 1.29\ eV$	or	$v = 8.03 - 0.774\ eV^{-1} \cdot \Delta E$.
Table 7.19:	$\Delta E = 11.8\ eV - v \cdot 1.74\ eV$	or	$v = 6.75 - 0.573\ eV^{-1} \cdot \Delta E$.

Chapter 8: **Results for SmS**

This chapter is structured like the previous one. After the pressure calibration the EXAFS of the Sm L_{III} edge in SmS is analyzed, and finally the valence is determined. As before, the EXAFS is analyzed in R-space.

The S K edge EXAFS could not be measured. The double-crystal monochromator used in our experiments can function at energies as low as the S K edge. However, to avoid absorption by air the exit beam must travel in helium. But even if this were done, the large absorption of the anvil tips in the pressure cell at these low energies would have made the measurement impossible.

8.1 Pressure Determination

For the SmS datasets the pressure is determined from the EXAFS of a Cu-calibrant. As in the previous chapter the nearest-neighbour distance is determined from one-shell fits in R-space to the Fourier transform of $k^3 \chi(k)$. Theoretical amplitude and phase in curved-wave theory are employed in the analysis. $\pi/2$ is subtracted from Teo and Lee's central phase, as before. In the fits we consider the finite resolution by assuming that the width of the entrance slit of the monochromator is 1 mm. Mean free path and core-hole lifetime effects are included with $\tilde{\eta}$ given by:

Cu: $$\tilde{\eta} = \frac{\Gamma_e + \Gamma_c}{2\ \gamma} = \frac{4.39eV + 1.6eV}{2\ \gamma} = 0.786\ \text{Å}^{-2}\ .$$

The following table contains the pressure calibration. First the pressure is increased, then completely released, and finally increased again.

Table 8.1: Pressure calibration from Cu K edge EXAFS (LOG.CU1.A):
(Jan. '83; Si (111); T = 300K)

One-shell fits in R-space to $FT(k^3 \chi(k))$ using theoretical amplitude and phase

fixed: $a_1 \equiv -1.5708$; $\Delta E_1 \equiv 1.531$ eV; $C_{31} \equiv 0.0$; $C_{41} \equiv 0.0$

variable: R_1; σ_1^2; N_1

					Fit interval (Å)		Transform interval ($Å^{-1}$)	
Dataset	R_1 (Å)	V/V_o	P_{Oil}(psi)	p (kbar)	R_{min}	R_{max}	k_{min}	k_{max}
E_{Edge}(eV)						χ^2_{min} ($Å^{-6}$)		
CUSM00.N00.A	**2.563**	**1**	**0**	**0**	**1.484**	**2.908**	**1.838**	**13.889**
8979.57	**±0.004**			**±6.1**		**0.25**		
CUSM11.N02.A	2.558	0.994	1100	8.6	1.242	2.908	1.838	13.737
8979.57	±0.004			±7.1		0.20		
CUSM30.N04.A	2.546	0.980	3000	30.1	1.236	2.893	1.862	13.111
8979.92	±0.004			±7.7		0.27		
CUSM36.N06.A	2.539	0.972	3600	43.5	1.222	2.882	1.838	13.639
8980.27	±0.005			±9.6		0.40		
CUSM36.N07.A	2.541	0.974	3600	39.5	1.363	2.878	1.838	14.041
8979.57	±0.004			±7.7		0.18		
CUSM36.N08.A	2.5415	0.975	3600	38.0	1.363	2.938	1.838	12.269
8979.57	±0.004			±7.7		0.27		
CUSM42.N10.A	2.538	0.971	4200	45.2	1.356	2.863	1.862	14.536
8979.92	±0.004			±7.7		0.31		
CUSM02.N13.A	2.551	0.986	250	19.7	1.475	2.919	1.838	12.288
8980.27	±0.004			±6.9		0.18		
CUSM14.N15.A#	2.559	0.995	1400	6.55	1.242	2.908	1.838	14.092
8979.57	±0.004			±6.9		0.16		

#: The externally applied pressure was completely released before pressure was applied for this dataset.

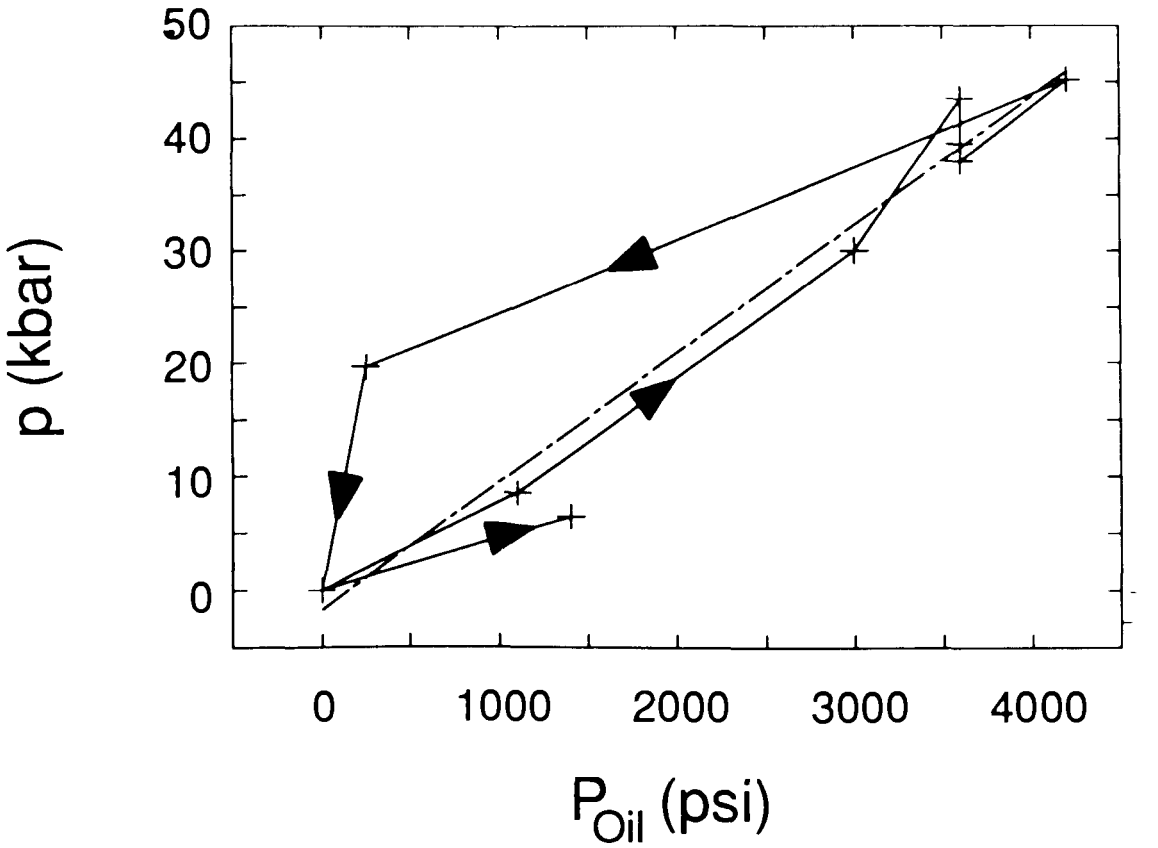

Fig. 8.1: Pressure p of a copper calibrant versus the oil pressure P_{Oil} applied by a hydraulic pump for the data of the previous table. The arrows indicate the sequence of pressure points. First the pressure is increased, then completely released, and finally increased again. A straight-line fit (dashed line) was performed for rising pressure only. The slope is 1.14 ± 0.07 kbar/(100 psi) and the intercept is -1.7 ± 2.1 kbar . Error bars are omitted for clarity. The data points for rising pressure follow the straight line within their error bars.

8.2 Analysis of the Sm L_{III} Edge EXAFS of SmS

As in the previous chapter the maximum k-value for the EXAFS of the Sm L_{III} edge is ~10 $Å^{-1}$ and two-shell fits are performed. Theoretical Sm and S curved-wave backscattering amplitude and phase are employed. The phase offset is $-\pi/2$ and the ratio N_2/N_1 is fixed at 2 according to the NaCl

structure. We assume that the values for ΔE are the same for both coordination shells. As discussed earlier in Section 7.3, by first varying the six parameters ΔE_1, R_1, σ_1^2, N_1, and, R_2 and σ_2^2 one obtains a value of 4.2 at which N_1 is fixed. Fits to the Fourier transform of $k^2 \chi(k)$ are performed with five variable parameters: ΔE_1, R_1, σ_1^2, R_2/R_1 , and σ_2^2 . The finite monochromator resolution is included in the fits together with the mean free path and core-hole lifetime effects. These latter effects are included through $\tilde{\eta}$ which for the Sm L_{III} edge in SmS amounts to:

$$\underline{\text{Sm}}\text{S:} \qquad \tilde{\eta} = \frac{\Gamma_e + \Gamma_c}{2\gamma} = \frac{2.92\text{eV} + 3.6\text{eV}}{2\gamma} = 0.855\ \text{Å}^{-2} ,$$

(absorbing element underlined) .

The following table contains the results from R-space fits to the Sm L_{III} edge EXAFS at 300K. The k-space interval used to take the Fourier transform is indicated by k_{min} and k_{max} and the fit - interval by R_{min} and R_{max}. We obtain for the ratio R_2/R_1 of the radii of the second coordination shell to the first the value $R_2/R_1 = 1.418 \pm 0.013$ deviating some amount from the correct value of $\sqrt{2}$. At 8.6 kbar Table 8.2 contains two entries. Figs. 8.4 to 8.7, which show the results, contain only averaged values at this pressure.

Table 8.2: Sm L_{III} edge EXAFS (LOG.SM2.A):
(Jan. '83; Si (111); T = 300K)

Two-shell fits in R-space to $FT(k^2 \chi(k))$ using theoretical amplitudes and phases:

1st shell: S; 2nd shell: Sm

fixed: $a_1 \equiv -1.5708$; $C_{31} \equiv 0.0$; $C_{41} \equiv 0.0$; $N_1 \equiv 4.2$;
$a_2 \equiv -1.5708$; $\Delta E_2 \equiv \Delta E_1$; $C_{32} \equiv 0.0$; $C_{42} \equiv 0.0$; $N_2/N_1 \equiv 2.0$

variable: ΔE_1; R_1; σ_1^2; R_2/R_1; σ_2^2

Dataset	P_{Oil}(psi)	p (kbar)	ΔE_1(eV)	R_1(Å)	R_2(Å)	σ_1^2 (10^{-3} Å^2)	σ_2^2 (10^{-3} Å^2)
E_{Edge}(eV)	k_{min}(Å^{-1})	k_{max}(Å^{-1})	R_{min}(Å)	R_{max}(Å)		χ^2_{min} (10^{-3} Å^{-6})	
SMS000.N13.A	0	0	3.1	2.975	4.265	14.6	11.7
6709.79	4.158	10.217	1.524	4.989		0.47	
SMS011.N17.A	1100	8.6	0.6	2.852	4.024	9.1	17.0
6717.39	4.339	10.119	1.299	4.764		0.225	
SMS011.N19.A	1100	8.6	3.6	2.872	4.046	7.9	14.2
6717.39	4.295	10.119	1.409	4.875		0.29	
SMS030.N23.A	3000	30.1	5.2	2.826	3.995	4.1	11.7
6716.63	4.443	10.129	1.388	4.816		0.31	
SMS036.N30.A	3600	40.3	7.5	2.841	4.009	4.8	10.7
6716.63	4.443	10.129	1.558	4.844		0.42	
SMS042.N40.A	4200	45.2	3.4	2.808	3.956	4.8	11.8
6717.01	4.459	10.124	1.408	4.787		0.45	
SMS002.N46.A	250	19.7	5.6	2.843	4.020	4.8	10.85
6717.01	4.404	10.124	1.464	4.872		0.31	
SMS11.N51.A	1100	5.1	6.0	2.960	4.270	16.6	14.3
6709.79	4.216	9.700	1.601	5.100		0.28	

Fig. 8.2 shows the Fourier transform magnitudes of the data for low and for high pressure and Fig. 8.3 shows the same data in k-space.

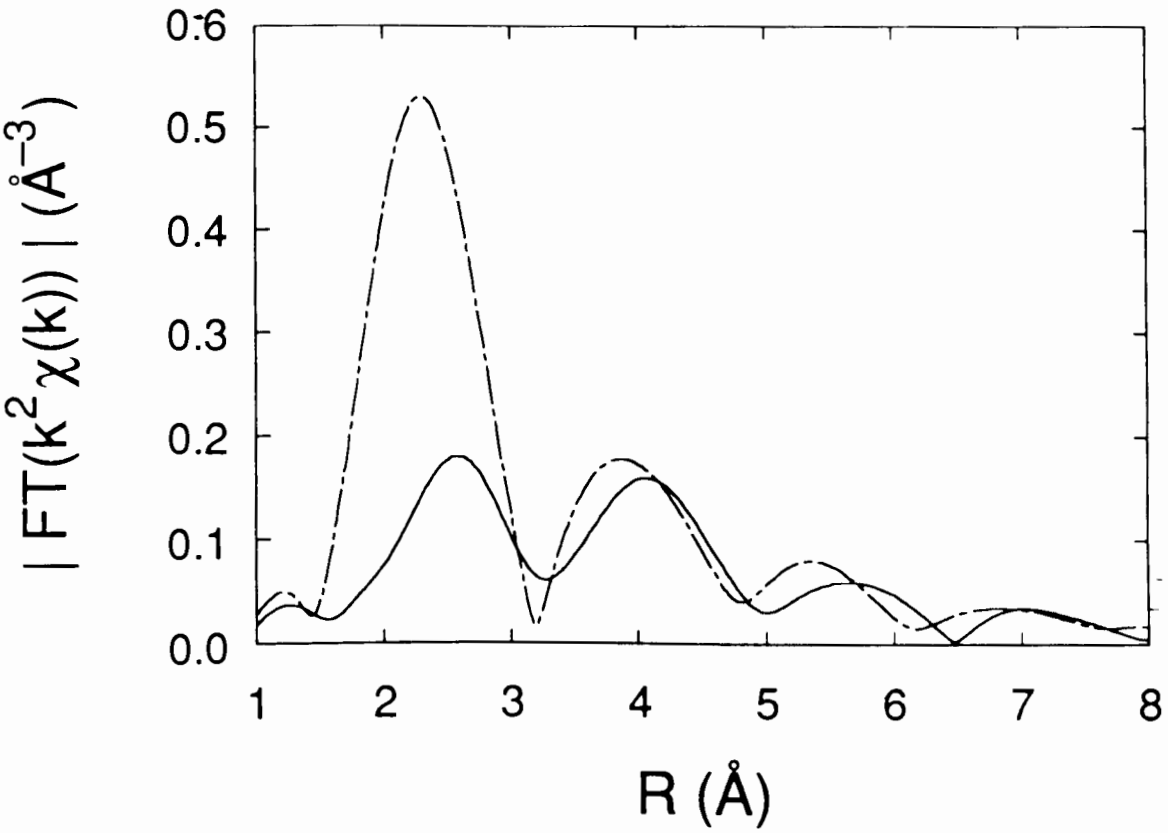

Fig. 8.2: Fourier transform magnitude of $k^2 \chi(k)$ for SmS at 300K. The central atom is Sm. The solid line corresponds to 1 bar and the dashed line to 45.2 kbar.

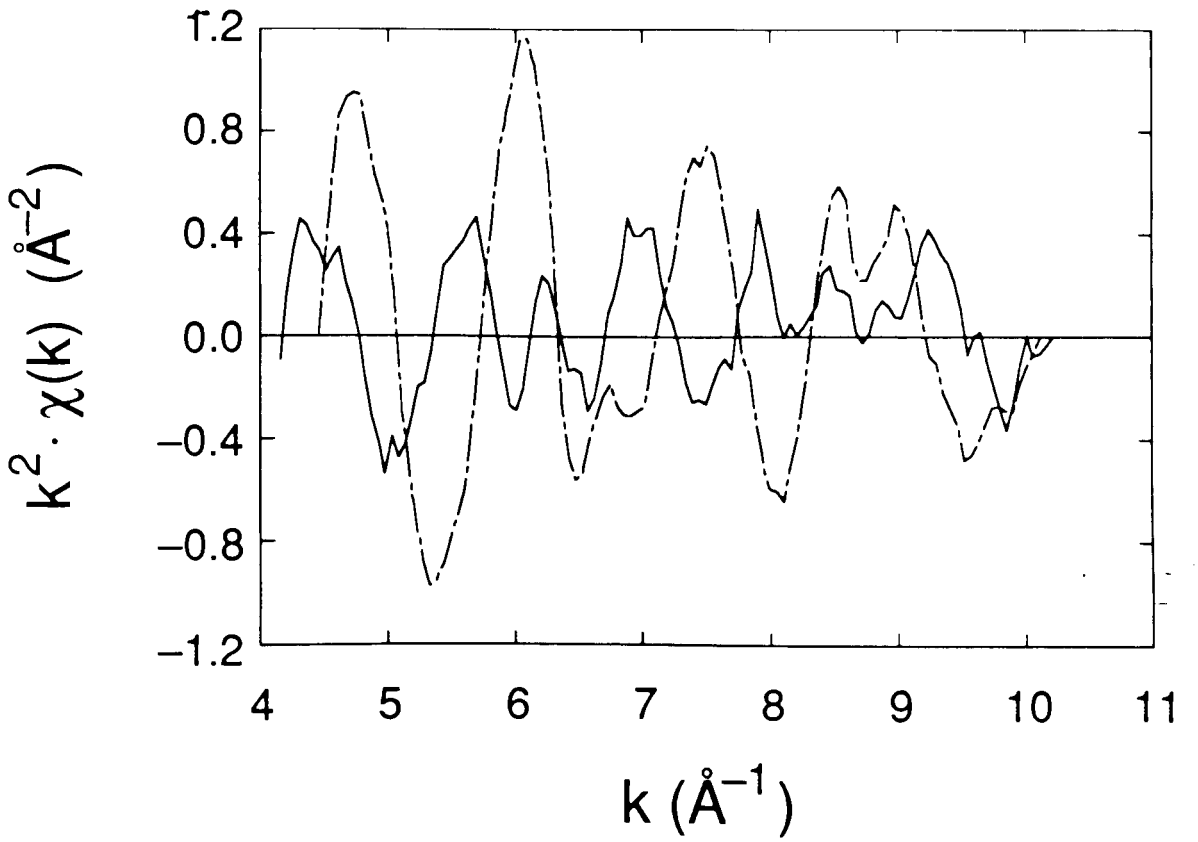

Fig. 8.3: $k^2\,\chi(k)$ for SmS at 300K for the same data as in the previous figure. The central atom is Sm. The solid line corresponds to 1 bar and the dashed line to 45.2 kbar.

The next figure shows σ_1^2 versus R_1 . As for SmSe at 300K, no peak is visible.

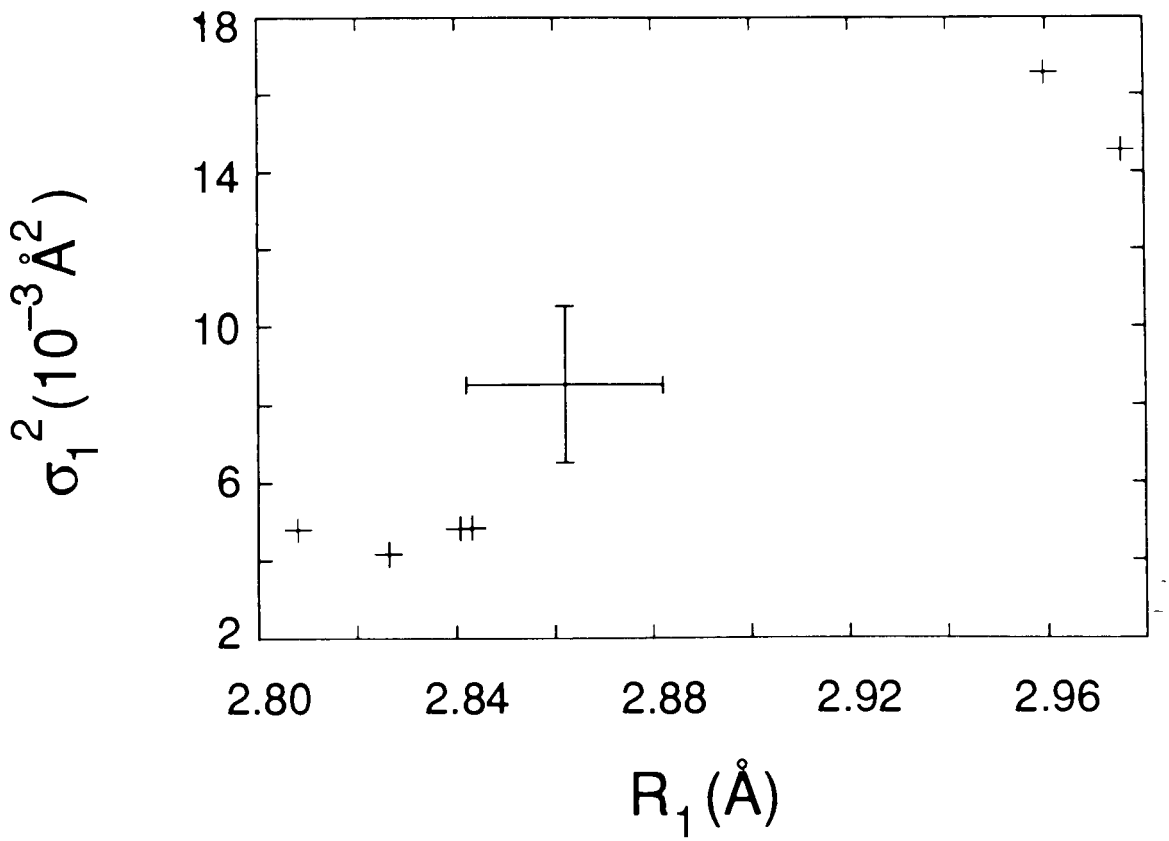

Fig. 8.4: σ_1^2 versus R_1 at 300K according to Table 8.2. N_1 was equal to 4.2.

The pressure dependence of the nearest-neighbour distance R_1 and next-nearest neighbour distance R_2 is shown in the next two figures. The data is compared to the x-ray diffraction result of Jayaraman et al. [110, 207]. The values for R_1 and R_2 from Table 8.2 are shifted such that their values at atmospheric pressure become equal to the crystallographic values. For SmS the nearest-neighbour distance at room temperature and ambient pressure is $R_1 = 2.985$ Å and the next-nearest neighbour distance is equal to $R_2 = 2.985$ Å $\sqrt{2} = 4.221$ Å.

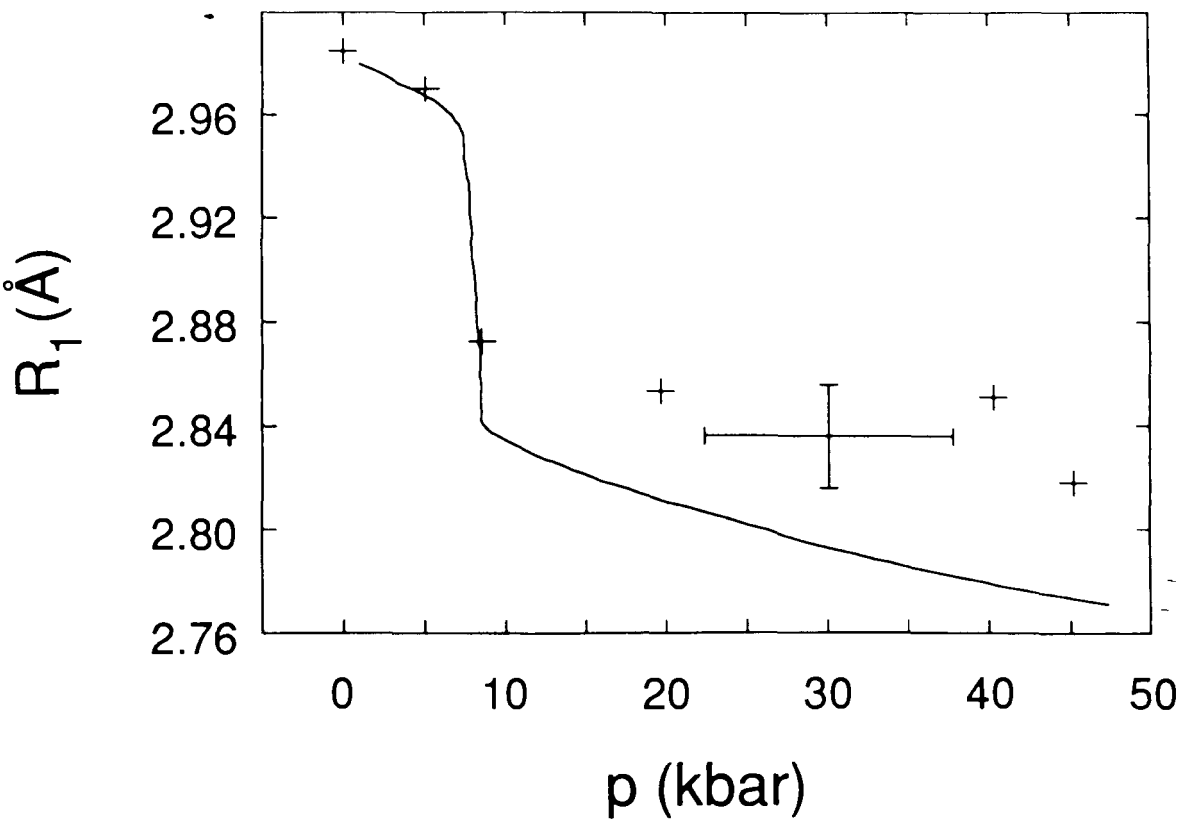

Fig. 8.5: Nearest-neighbour distance R_1 in SmS with respect to the Sm atoms as a function of pressure and at room temperature. The crosses are the data of Table 8.2 and the solid line is obtained from the result of Jayaraman et al. [110, 207]. The data were shifted according to: $R_1 \rightarrow R_1 + 0.01$ Å . The error for R_1 is estimated to be ±0.02 Å.

We notice that in Fig. 8.5 the values of R_1 above the mixed-valence transition deviate systematically from the x-ray diffraction result. The error bars cannot account for this discrepancy. However, the two data points below the phase transition agree with the x-ray diffraction result. Since the same phase shifts are employed at all pressures, the deviation is surprising. Furthermore, the values of R_2 (as shown in Fig. 8.6) do follow very well the x-ray diffraction data. We do not yet know why the values of R_1 above the phase transition exceed the x-ray diffraction result.

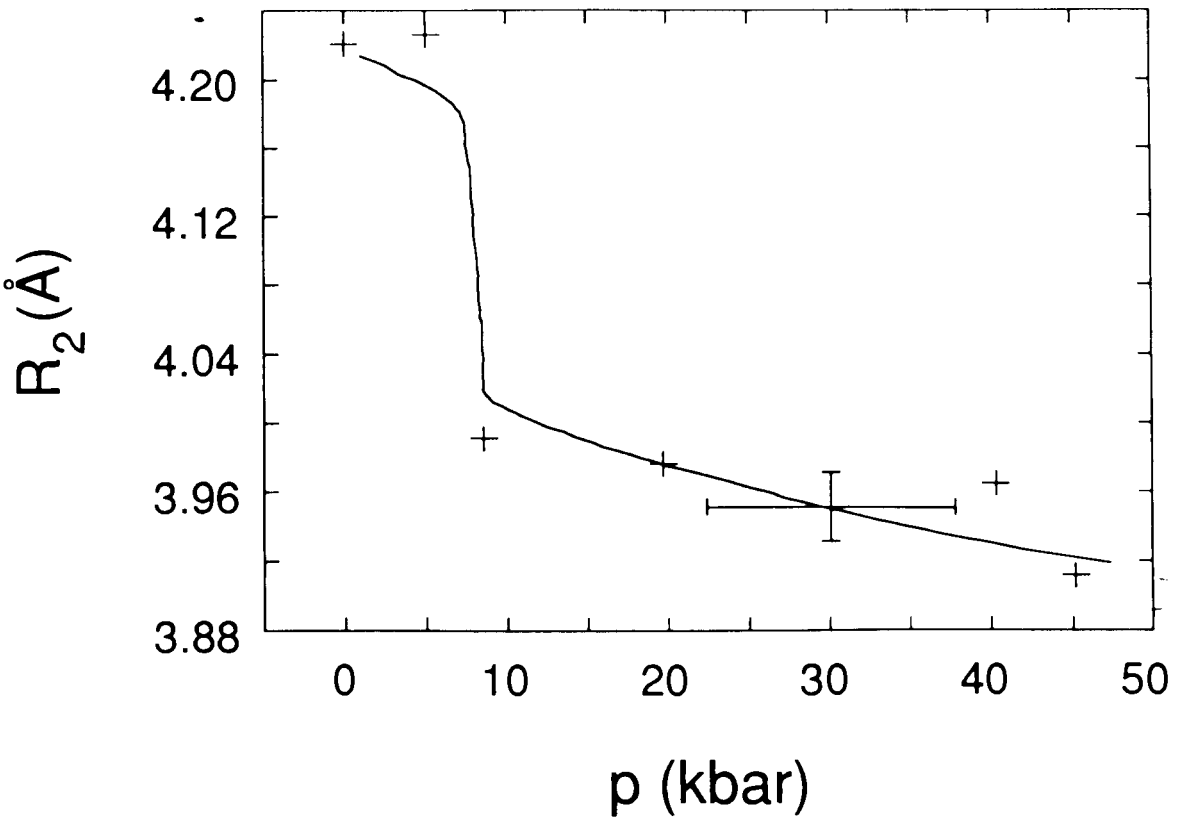

Fig. 8.6: Next-nearest neighbour distance R_2 in SmS with respect to the Sm atoms as a function of pressure and at room temperature. The crosses are the data of Table 8.2 and the solid line is obtained from the result of Jayaraman et al. [110, 207]. The data were shifted according to: $R_2 \rightarrow R_2 - 0.044$ Å . The error for R_2 is estimated to be ±0.02 Å.

In Fig. 8.7 we compare R_2 and R_1. This plot is independent of the pressure calibration and it should agree with the result for the NaCl structure: $R_2 = R_1 \sqrt{2}$. However, because R_1 is too large above the transition pressure (see Fig. 8.5) the agreement with the crystallographic result is not good.

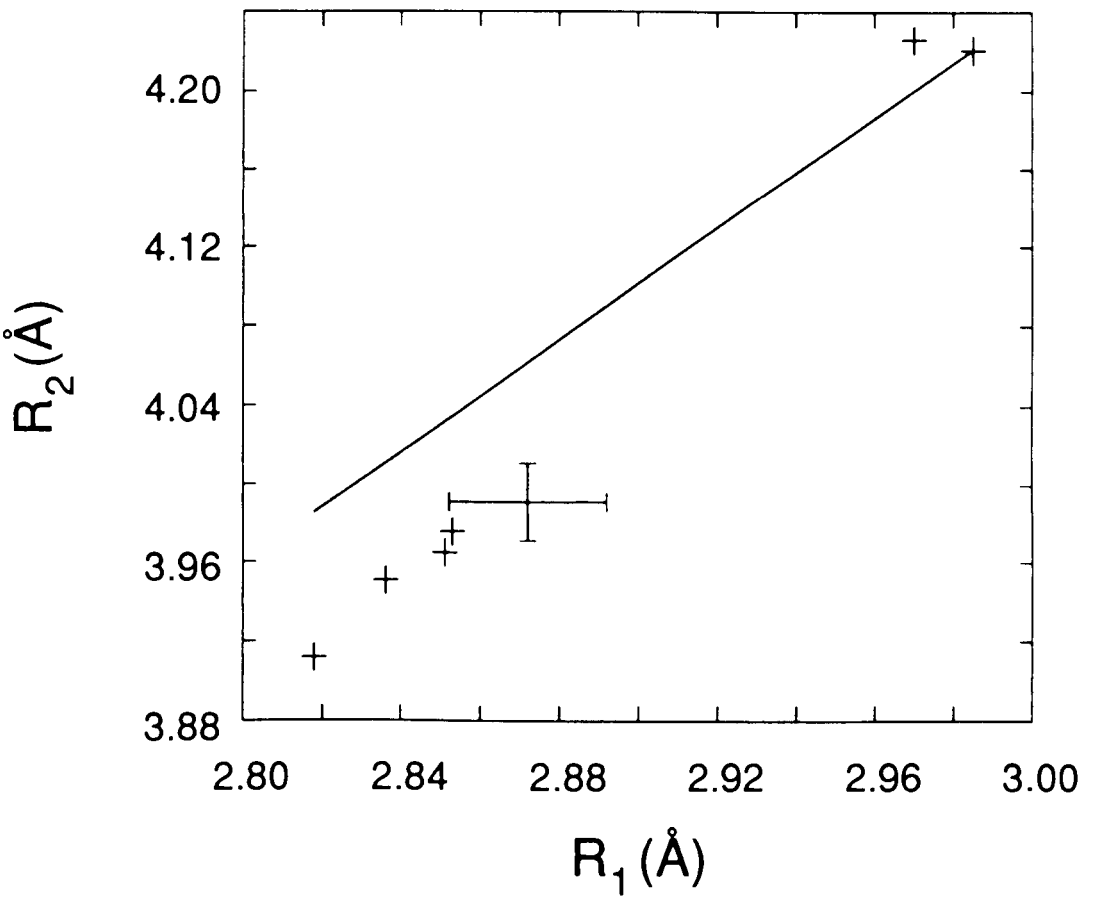

Fig. 8.7: Second-nearest neighbour distance R_2 (Sm-Sm) versus the nearest-neighbour distance R_1 (Sm-S), with R_1 and R_2 adjusted as explained in connection with Figs. 8.5 and 8.6. The crosses refer to the data of Table 8.2 and the solid line is $R_2 = R_1 \sqrt{2}$ according to the NaCl structure. Error bars are ±0.02 Å.

8.3 Valence Determination

The tables in this section are exactly analogous to the ones in Section 7.4 and therefore need not be described. The pressure is determined by interpolation from the applied oil pressure P_{Oil}. The first table contains the results from edge scans and the second lists those obtained from EXAFS

datasets.

Table 8.3: Valence determination from the Sm L_{III} edge (VAL.SMSX.A):
(Jan. '83; Si (111); T = 300K)

Dataset	P_{Oil}(psi)	p (kbar)	v	ΔE (eV)	E^{2+} (eV)
	$HWHM_{Voigt}$ (eV)	Γ (eV)	$\sigma\sqrt{2\cdot\ln 2}$ (eV)	Y_{max}	Area (eV)
SMSX05.101.A	500	3.9	2.29	7.81	6712.64
	3.54	1.27	2.80	2.17	14.53
SMSX07.102.A	700	5.5	2.29	7.90	6712.53
	3.545	1.44	2.69	2.02	13.56
SMSX09.103.A	900	7.0	2.32	7.81	6712.62
	3.61	1.42	2.77	2.01	13.63
SMSX11.104.A	1100	8.6	2.60	7.13	6713.50
	4.10	1.07	3.49	1.99	14.40
SMSX38.105.A	3800	40.4	2.85	6.66	6713.28
	4.35	1.29	3.605	2.15	17.20
SMSX40.106.A	4000	42.8	2.86	6.46	6713.52
	4.355	1.31	3.60	2.13	17.10
SMSX42.107.A	4200	45.2	2.86	6.35	6713.59
	4.31	1.62	3.365	2.15	17.58
SMSX30.108.A	3000	37.45	2.85	6.53	6713.68
	4.48	1.41	3.67	2.07	17.00
SMSX20.109.A	2000	31.0	2.85	6.55	6713.64
	4.31	1.43	3.48	2.13	17.135
SMSX10.110.A	1000	24.5	2.84	6.48	6713.70
	4.195	1.61	3.25	2.17	17.46
SMSX05.111.A	500	21.3	2.83	6.52	6713.69
	4.11	1.57	3.19	2.22	17.535
SMSX02.112.A	250	19.7	2.82	6.65	6713.54
	4.07	1.395	3.26	2.24	17.33
SMSX00.113.A	0	0	2.27	7.72	6712.50
	3.34	1.32	2.56	2.22	14.37
SMSX03.114.A	300	1.4	2.29	7.60	6712.57
	3.31	1.375	2.49	2.23	14.43
SMSX07.115.A	700	3.3	2.30	7.61	6712.58
	3.33	1.33	2.54	2.23	14.415
SMSX09.115.A	900	4.2	2.31	7.60	6712.61
	3.34	1.35	2.54	2.24	14.59

Table 8.3, continued:

SMSX11.116.A	1100	5.1	2.35	7.57	6712.61
	3.335	1.34	2.54	2.27	14.80
SMSX12.117.A	1200	5.6	2.36	7.615	6712.60
	3.375	1.31	2.61	2.28	14.97
SMSX13.118.A	1300	6.1	2.38	7.59	6712.66
	3.37	1.34	2.58	2.29	15.09
SMSX14.119.A	1400	6.55	2.44	7.55	6712.75
	3.42	1.285	2.67	2.31	15.335

In the next table there are multiple entries at some pressure points. For these pressures the graphs and fits will only take into account a single averaged value of valence or ΔE.

Table 8.4: Valence determination from the Sm L_{III} edge of EXAFS datasets (VAL.SMSXAF.A): (Jan. '83; Si (111); T = 300K)

Dataset	P_{Oil}(psi)	p (kbar)	v	ΔE (eV)	E^{2+} (eV)
	$HWHM_{Voigt}$ (eV)	Γ (eV)	$\sigma\sqrt{2\cdot\ln 2}$ (eV)	Y_{max}	Area (eV)
SMS000.A01.A	0	0	2.26	7.49	6712.77
	3.16	1.85	1.995	2.16	14.13
SMS000.A03.A	0	0	2.26	7.48	6713.04
	3.19	1.83	2.04	2.13	13.94
SMS000.A11.A	0	0	2.25	7.60	6712.50
	3.48	2.27	2.00	1.85	12.96
SMS000.A13.A	0	0	2.26	7.63	6712.49
	3.44	1.90	2.26	1.895	12.765
SMS011.A17.A	1100	8.6	2.59	7.11	6713.37
	3.965	1.535	3.06	1.81	12.97
SMS011.A19.A	1100	8.6	2.60	7.12	6713.22
	3.92	1.60	2.975	1.85	13.28
SMS030.A23.A	3000	30.1	2.80	6.91	6713.25
	4.11	1.39	3.31	1.925	14.305
SMS036.A30.A	3600	40.3	2.82	6.95	6713.02
	4.125	1.57	3.21	1.93	14.625
SMS042.A40.A	4200	45.2	2.84	6.87	6713.09
	4.12	1.55	3.21	1.95	14.81
SMS042.144.A	4200	45.2	2.84	6.98	6712.99
	4.155	1.55	3.245	1.94	14.78
SMS002.A46.A	250	19.7	2.80	6.82	6713.30
	3.78	1.57	2.85	2.095	15.17
SMS11.A51.A	1100	5.1	2.34	7.51	6712.66
	3.32	1.72	2.26	2.08	13.73
SMS014.A56.A	1400	6.55	2.47	7.405	6712.71
	3.39	1.56	2.445	2.14	14.23

In Figs. 8.8 and 8.9 the valence is plotted as a function of pressure. Fig. 8.8 contains the results from edge scans and Fig. 8.9 lists the results obtained from EXAFS datasets. The error bars for the pressure were obtained from Table 8.1 and the fit error for the determination of the valence was assumed to be ±0.04.

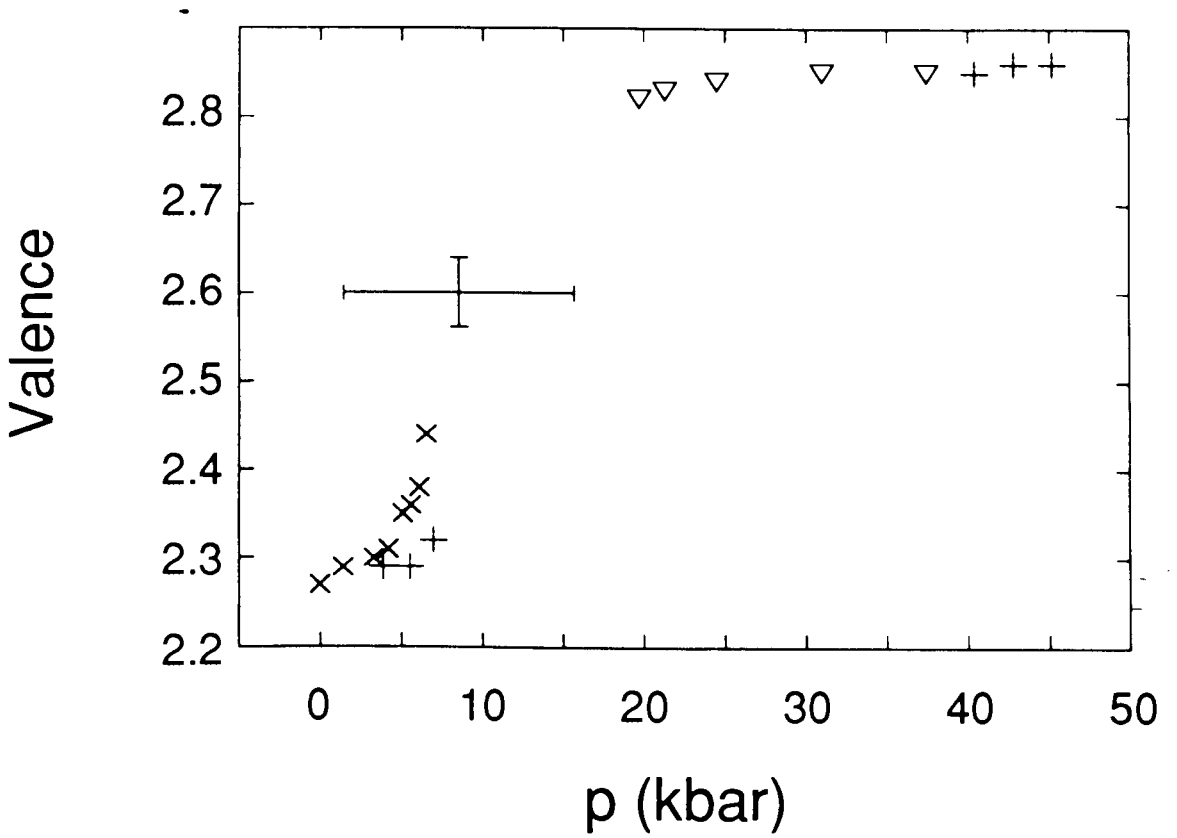

Fig. 8.8: Valence versus pressure at room temperature according to Table 8.3. The '+' symbols correspond to rising pressure. The '∇' symbols indicate the valence when the pressure is decreasing and the 'x' symbols refer to increasing pressure.

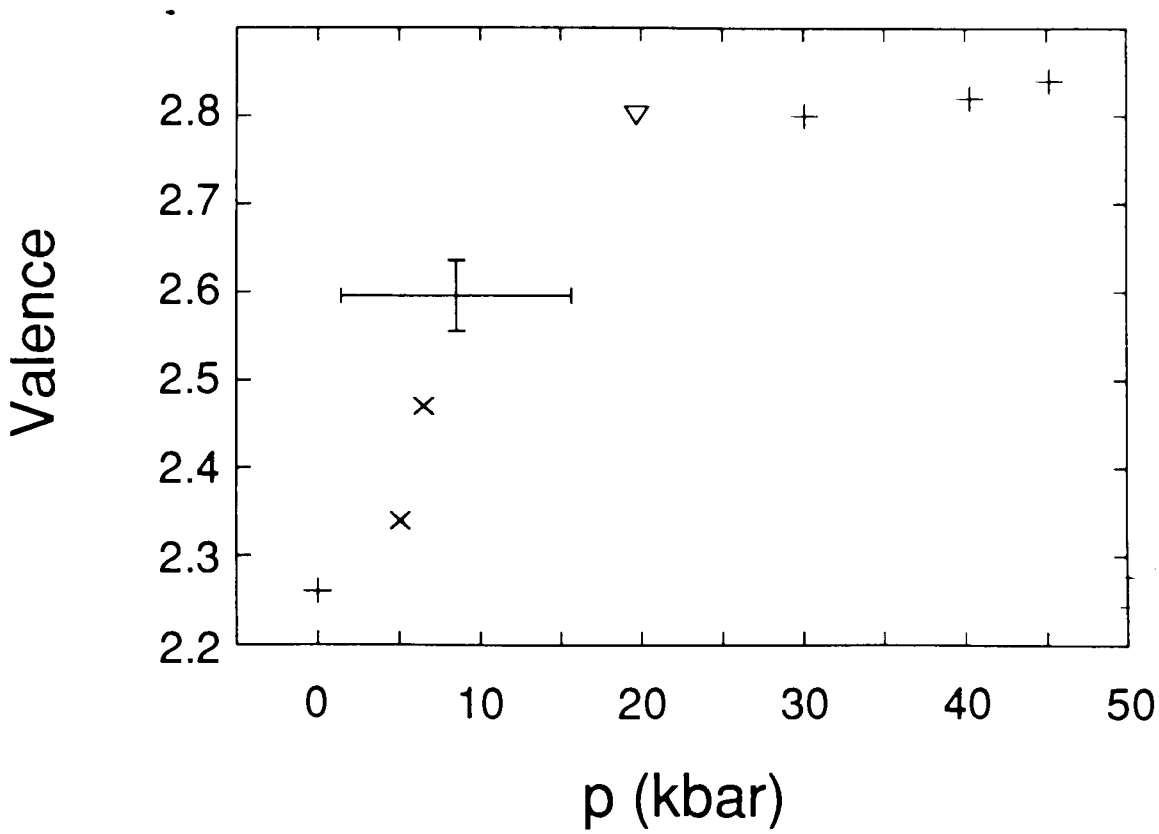

Fig. 8.9: Valence versus pressure at room temperature according to Table 8.4. The '+' symbols correspond to rising pressure. The '∇' symbols indicate the valence when the pressure is decreasing and the 'x' symbols refer to increasing pressure.

The dependence of ΔE on the valence is shown in the next figure.

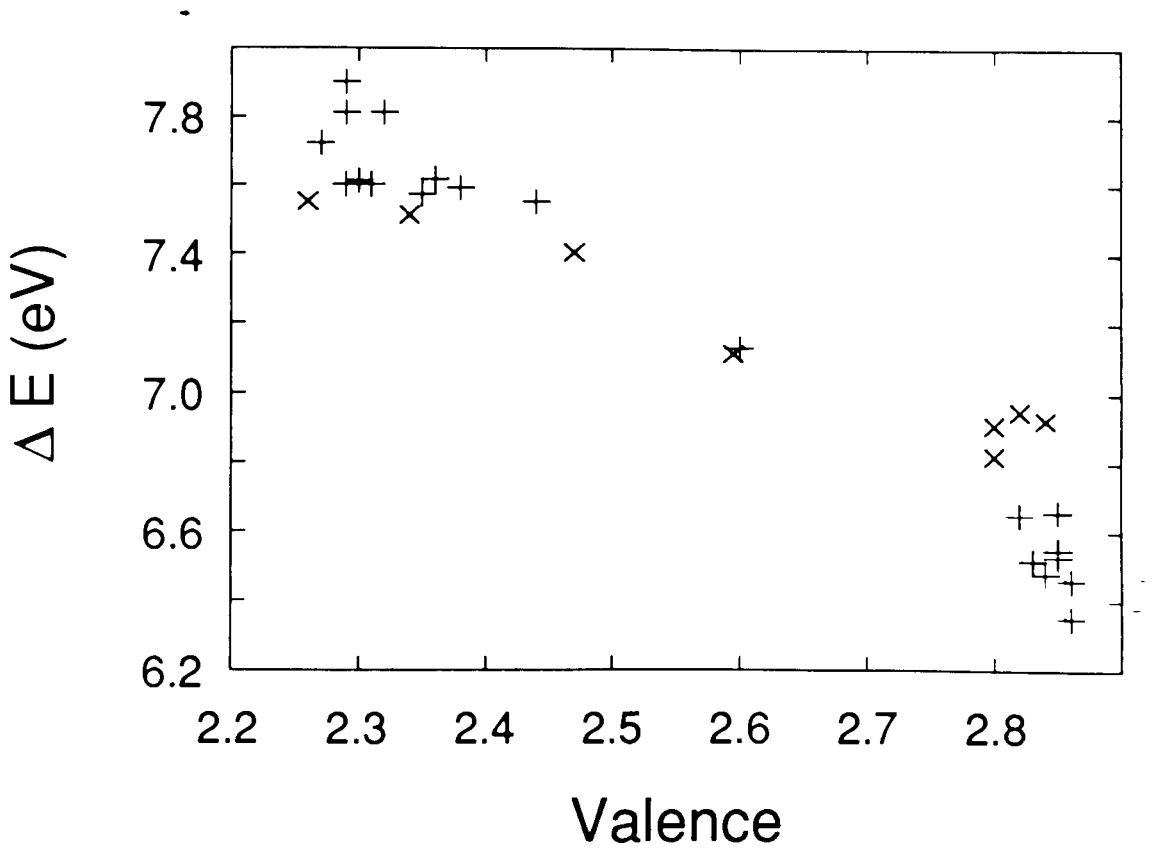

Fig. 8.10: ΔE versus valence. The '+' symbols refer to Table 8.3 and the 'x' symbols refer to Table 8.4.

Fitting straight lines to ΔE as a function of the valence v gives:

Table 8.3: $\Delta E = 12.8\ eV - v \cdot 2.19\ eV$ or $v = 5.82 - 0.456\ eV^{-1} \cdot \Delta E$.

Table 8.4: $\Delta E = 10.4\ eV - v \cdot 1.23\ eV$ or $v = 8.405 - 0.810\ eV^{-1} \cdot \Delta E$.

In Section 10.4 the linear dependence of ΔE on the valence is discussed in terms of the different screening of the Sm^{2+} and Sm^{3+} ions.

Chapter 9: **Discussion**

In this chapter we discuss the peak in the mean-square relative displacement as a function of pressure with respect to the possible existence of lattice relaxation in SmSe. We also calculate the Grüneisen parameter which is a measure of anharmonicity. Then we discuss the scaling method, introduced in Sections 3.6 and 6.14, with respect to pressure determination. A final section lists topics of future work.

9.1 Two-Shell Analysis for the Se K Edge EXAFS

We may wonder whether the maximum in σ^2 as a function of pressure (or coordination-shell radius) may be due to the presence of two closely spaced Sm coordination shells around a Se atom. This may be expected because valence fluctuations occur with phonon frequencies and the interaction between valence fluctuations and phonons may result in relaxation of the crystal lattice around a Sm atom. This means that the first coordination shell around a Sm atom will have a smaller radius when the central Sm atom is trivalent and small. However, the first shell will have a larger radius when the central Sm atom is divalent and 0.17 Å bigger. Since the x-ray absorption process is much faster than phonon or valence fluctuation frequencies, the information contained in an x-ray absorption spectrum corresponds to a "snapshot" picture of the atomic positions. For mixed-valent SmSe one would therefore expect two slightly different Sm-Se distances corresponding to the sampled distribution of di- and trivalent Sm atoms. Since the distance difference is expected to be small it is advisable to analyze the Se K edge EXAFS, which can yield higher resolution than the Sm L edge EXAFS. The Sm L_{III} EXAFS has limited resolution because of the intervening Sm L_{II} edge and the Sm L_{II} edge EXAFS is contaminated by the underlying remnants of the EXAFS of the Sm L_{III} edge. In the same way the Sm L_{I} edge is contaminated by the remnants of the EXAFS of the Sm L_{II} edge.

We now present the results of two-shell fits to the Se K edge EXAFS data. A larger k-space domain was used for the fits than was employed in Chapter 7, although the data at high k are not as good as at low k. The results are for weighted two-shell fits in k-space. The k-space weighting function was described in Section 6.10 and consists of the square of the envelope function, raised

to the power of –1. In this way regions of small amplitude, for example a beat node, have the same weight as regions with large amplitude. Trying two-shell fits in R-space does not help because the high-k end, where a possible beat node would occur, is not weighted sufficiently in a Fourier transform with an apodization window.

The results of these weighted two-shell fits in k-space are presented in Table 9.1 below. Although this table is similar to Table 7.8 it is not possible to compare readily the values of χ^2_{min} because this time the fits are performed in k-space. The R-space interval used for Fourier filtering is indicated by R_{min} and R_{max}. Mean free path and core-hole lifetime effects are taken into account by setting $\tilde{\eta}$ equal to 0.690 $Å^{-2}$, as in Section 7.2.

Table 9.1: Se K edge EXAFS (LOG.SEN25.F2):

(June '86; Si (220); T = 77K)

Weighted two-shell fits in k-space to $k^2 \chi(k)$ using theoretical amplitudes and phases:

1st shell: Sm; 2nd shell: Sm

fixed: $a_1 \equiv -1.5708$; $\Delta E_1 \equiv -1.9$ eV; $C_{31} \equiv 0.0$; $C_{41} \equiv 0.0$;

$a_2 \equiv -1.5708$; $\Delta E_2 \equiv -1.9$ eV; $C_{32} \equiv 0.0$; $C_{42} \equiv 0.0$; $\sigma_2^2 \equiv \sigma_1^2$; $N_1 + N_2 \equiv 4.6$

variable: R_1; σ_1^2; N_1; R_2

Dataset	N_T	p (kbar)	R_1(Å)	R_2(Å)	σ_1^2 (10^{-3} Å^2)	N_1
E_{Edge}(eV)	k_{min}(Å^{-1})	k_{max}(Å^{-1})	R_{min}(Å)	R_{max}(Å)	χ^2_{min} (10^{-2} Å^{-4})	
SESMN2.N32.F	2.25	43.7	2.948	3.046	2.7	0.7
12654.04	1.992	20.052	2.041	3.379	4.00	
SESMN3.N33.F	3	42.9	2.947	3.0465	2.5	1.0
12654.04	1.992	19.587	1.996	3.379	6.37	
SESMN5.N38.F	5	52.0	2.951	3.037	1.6	2.2
12654.04	1.992	19.985	2.041	3.274	8.10	
SESMN6.N42.F	6	54.7	2.755	2.956	3.3	0.5
12654.04	2.058	19.786	1.891	3.379	5.13	
SESMN8.N44.F	8	60.1	2.756	2.933	2.7	0.5
12653.41	2.052	20.056	1.861	3.274	4.28	
SESMN9.N47.F	9	73.2	2.906	3.004	1.7	3.7
12654.04	2.058	19.985	1.816	3.244	3.63	
SESMNT.N53.F	10.5	74.15	2.7615	2.909	2.7	0.25
12654.04	2.058	19.521	1.966	3.199	2.79	
SESMNW.N54.F	12	75.1	2.789	2.908	1.95	0.5
12653.41	2.118	19.990	1.891	3.168	3.92	
SESMNH.N55.F	13.5	76.05	2.912	2.912	2.8	0.0
12654.66	2.065	19.848	1.891	3.244	3.61	
SESMNF.N56.F	15	77.0	2.909	3.115	2.7	4.4
12654.04	2.125	19.786	1.936	3.199	5.08	

We see that no clear picture emerges regarding N_1. Nevertheless, the Sm radial distribution function with respect to a Se central atom is useful. In Fig. 9.1 a graph of g(R) is shown for some

datasets of the previous table. The figure corresponds to Fig. 7.23 of Chapter 7, except that now the k-space intervals are larger and the two-shell fits are in k-space.

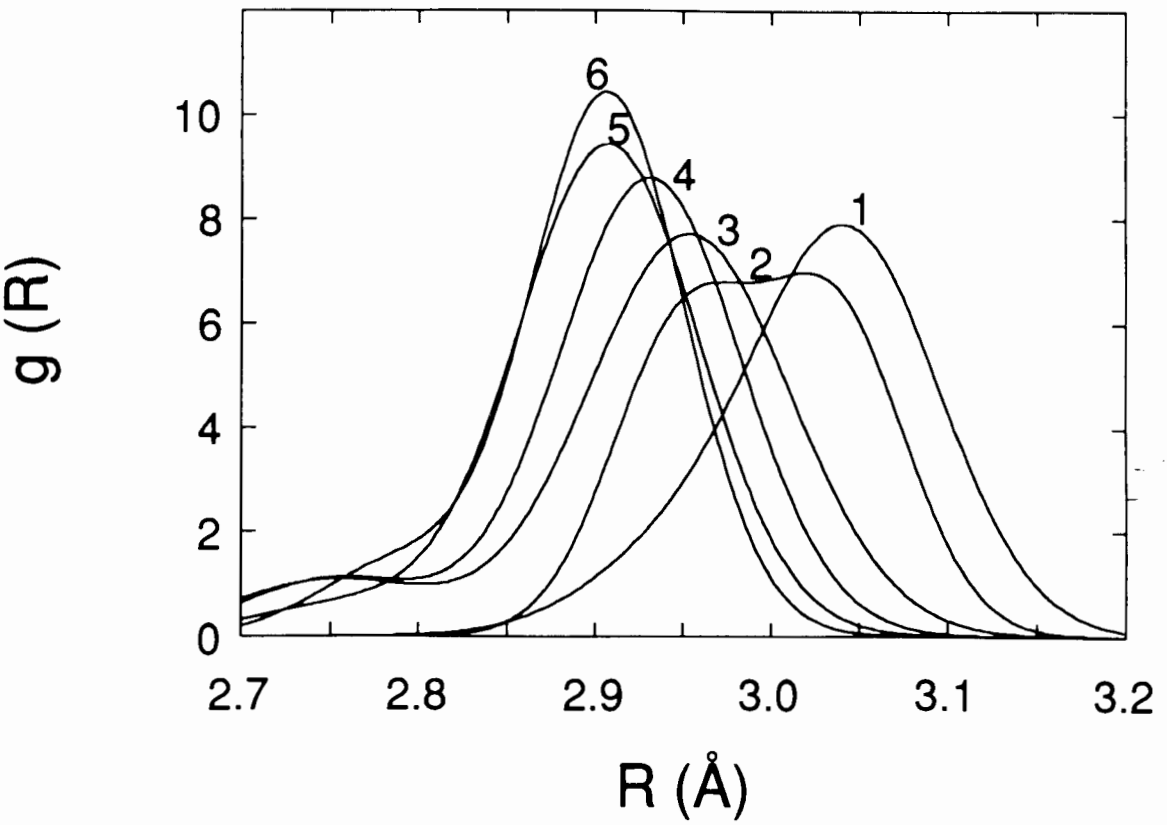

Fig. 9.1: Sm radial distribution functions g(R) with respect to Se at 77K obtained from the two-shell fits of Table 9.1. The numbers on the curves indicate the following pressures:
#1: 43.7 kbar; #2: 52.0 kbar; #3: 54.7 kbar; #4: 60.1 kbar; #5: 74.15 kbar; #6: 75.1 kbar .

We notice that for the dataset at 52.0 kbar (SESMN5.N38.F) the radial distribution function clearly shows two peaks. This was the only dataset that exhibited a radial distribution function with two peaks and this dataset also was the one which produced the largest value of σ^2 in the one-shell fits of Chapter 7. Fig. 9.2 shows the filtered k-space data at 52.0 kbar. At $k = 18$ Å^{-1} a beat can clearly be seen. At the expense of increasing the correlation between variables, the overall fit could be improved by changing more than the four variables R_1, σ_1^2, N_1, and R_2 used in the present fits.

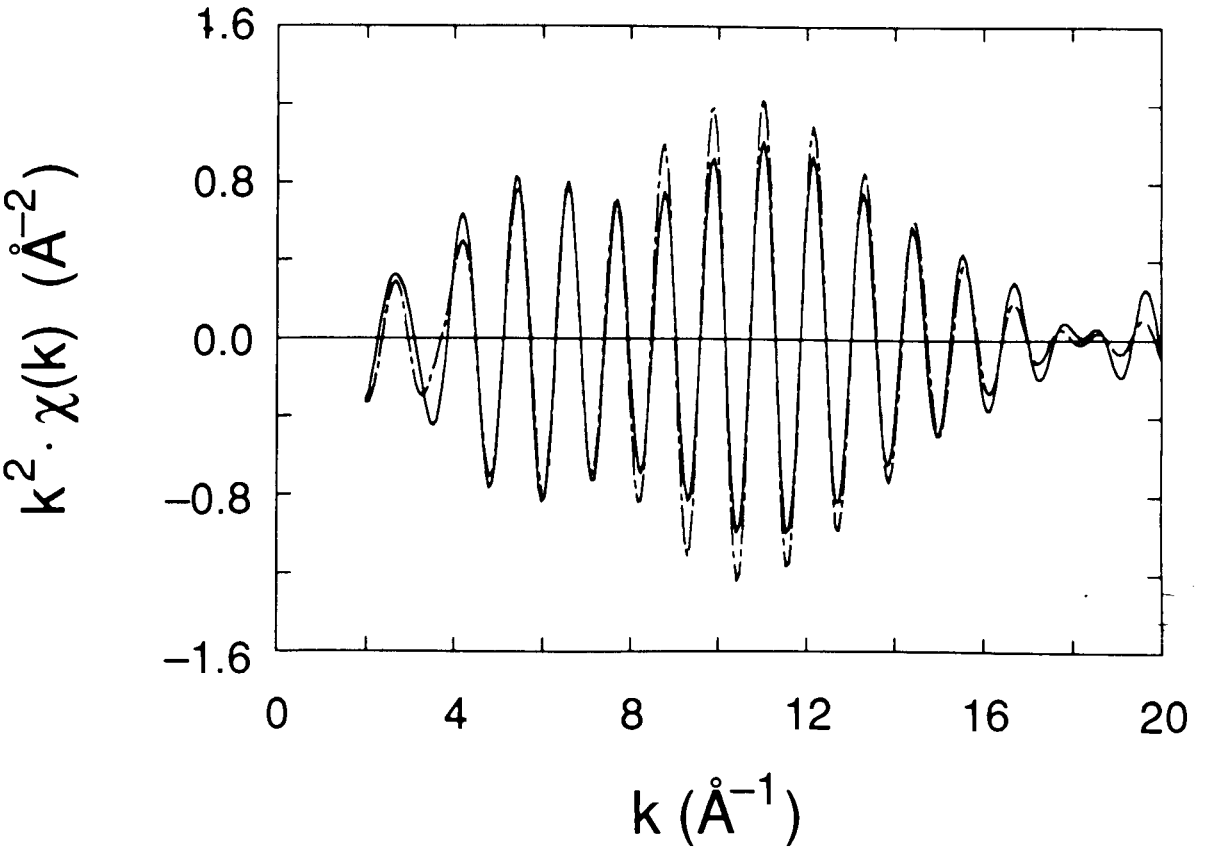

Fig. 9.2: $k^2\,\chi(k)$ for SmSe for the dataset SESMN5.N38.F at 52.0 kbar and 77K. The central atom is Se. The solid line is the data and the dashed line is the fit.

We notice that the envelope goes almost to zero at $k \cong 18.1$ Å^{-1}. Assuming that the two Sm shells have the same EXAFS Debye-Waller factor and scattering amplitude we can conclude that the two shells have approximately equal weight. This would correspond to the presence of equal amounts of 2+ and 3+ Sm atoms and hence a fractional valence of 2.5. The position of the beat node yields a distance difference of $\Delta R = \pi/(2 \cdot 18.1\ \text{Å}^{-1}) = 0.087$ Å (see Eq. (6.78)), confirmed by the least-squares fit result of Table 9.1.

In order to increase the confidence in the result a fit was also performed to the phase derivative of the first coordination shell. This function is shown in Fig. 9.3 together with a fit according to Eq. (6.73). Again the effect of the beat node at $k \cong 18.1$ Å^{-1} can be seen showing that the first

coordination shell is indeed split into two. The structure at around 8 $Å^{-1}$ stems from the Sm backscattering phase and has nothing to do with beating. This was not clear originally but could be traced back to the Sm phase that had been calculated in Chapter 3. The results from the k-space fit and the fit to the phase derivative agree as expected.

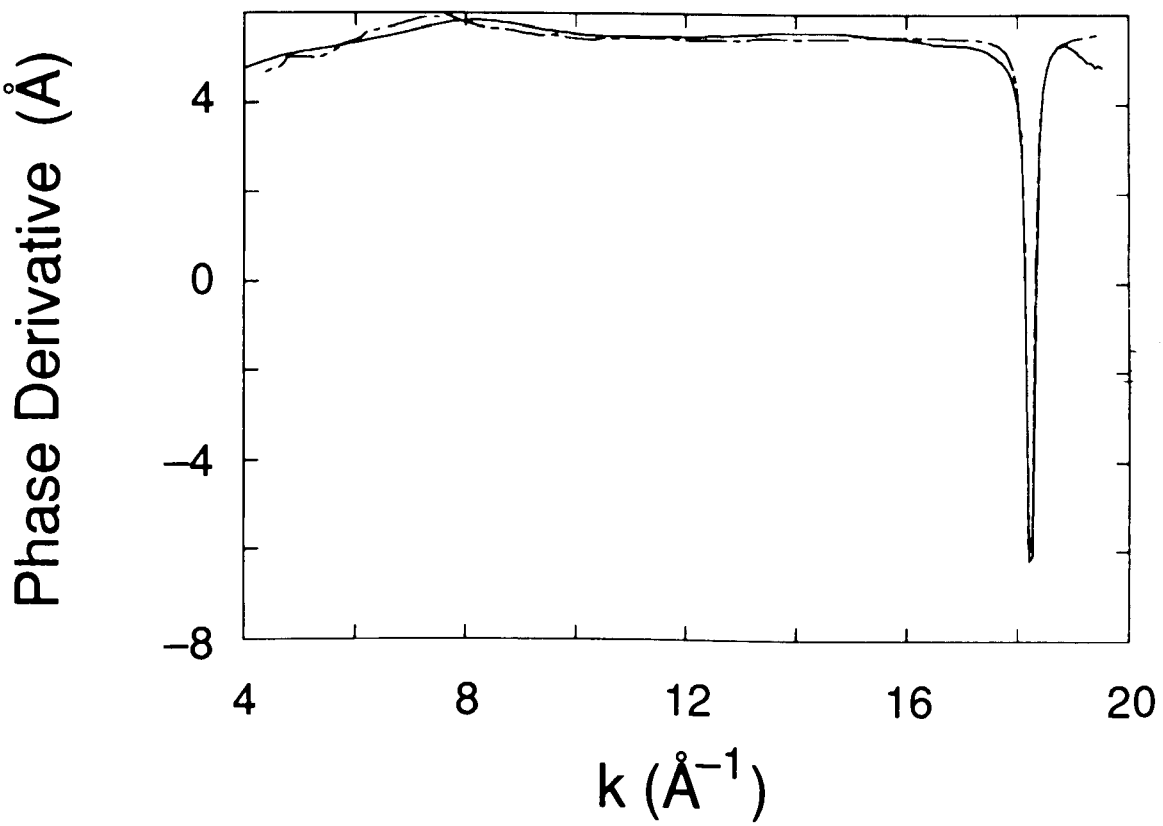

Fig. 9.3: Phase derivative at 52.0 kbar and 77K for the first coordination shell of SmSe with respect to the Se atoms. The solid line is the data (SESMN5.N38.F, Table 9.1) and the dashed line is the fit according to Eq. (6.73).

The results of this fit to the phase derivative are:

$R_1 = 2.932$ Å ; $\Delta R = 0.086$ Å ; $N_2/N_1 = 0.99$.

The fit interval extended from $k_{min} = 4.0$ Å^{-1} to $k_{max} = 19.5$ Å^{-1} and it was assumed that $\sigma_2^2 \equiv \sigma_1^2$. The value for ΔR_2 is the same as the one found from the fit of Table 9.1.

It seems then that in the middle of the valence transition two Se-Sm distances are present as claimed previously [208]. This can be understood by considering the breathing motion performed by the Se atoms around a mixed-valent Sm atom. As the Sm ion changes its valence from 2+ to 3+, say, its volume decreases and the nearest-neighbour Se atoms move towards the central Sm atom. This relaxation is indicated in the following figure.

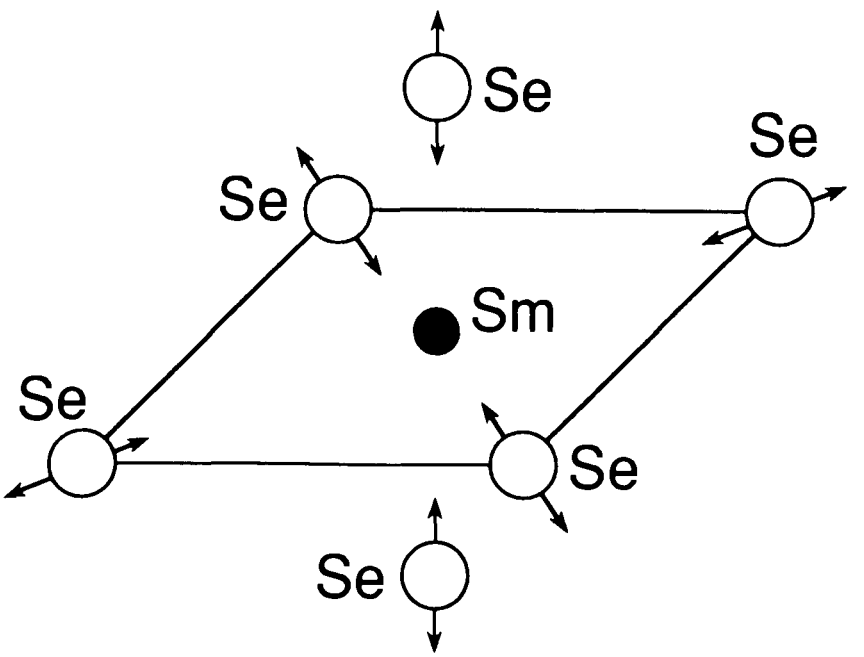

Fig. 9.4: Breathing motion of the Se atoms with respect to the central mixed-valent Sm atom.

9.2 Grüneisen Parameter Derived from the Se K Edge EXAFS

In this section we calculate the Grüneisen parameter γ_G, which appears in the quasi-harmonic approximation. In this approximation, anharmonicity of the pair potential is taken into account by introducing a volume (or pressure) dependence to the vibrational frequencies via the Grüneisen parameter and leaving the pair potential harmonic. γ_G is zero for a harmonic potential and positive when anharmonicity is present.

The one-shell fits of Chapter 7 showed that at 77K σ^2 as a function of R or pressure exhibited a maximum, which was not clearly present at room temperature. According to Tranquada [157] a change in σ^2 can be related to a change in R according to:

$$\frac{\delta\sigma^2}{\sigma^2} = 6\gamma_G \frac{\delta R}{R} \quad . \tag{9.1}$$

γ_G is the Grüneisen parameter. We can rewrite this equation as:

$$\frac{d \ln (\sigma^2/10^{-3}\ \text{Å}^2)}{d \ln (R/\text{Å})} = 6\gamma_G \quad . \tag{9.2}$$

Thus γ_G can be determined immediately from the slope of $\ln \sigma^2$ versus $\ln R$, which is very similar to σ^2 versus R. We denote the position of the maximum in σ^2 by R_c. Hence for $R < R_c$ we have normal behaviour, characterized by a positive value of the Grüneisen parameter. According to Appendix C a positive value of γ_G means that the vibrational frequencies increase with a reduction in volume, i.e. compression. For $R > R_c$ we find anomalous behaviour because γ_G is negative, indicating a decrease of phonon frequencies when the volume is reduced. This means that the solid becomes "softer" under compression. Unfortunately, there is only one data point above R_c. Therefore it is not clear whether softening sets in immediately under compression. Probably one will find that under compression the solid will initially behave normally and then become soft and then become normal again, similar to the behaviour of the bulk modulus or compressibility (see Chapter 4). In fact there is a relation involving the bulk modulus and the Grüneisen parameter (see Appendix C, Eq. (C.13)). This relation was also used to determine γ_G from Jayaraman's data [110] but it turned out that the derivative involved in determining the compressibility made the result too noisy. Thus

γ_G could not be obtained reliably with this method. Probably one should fit Jayaraman's data to a model and then determine γ_G from the model.

According to the Grüneisen relation (Appendix C, Eq. (C.8)),

$$B_T \beta = \gamma_G \frac{C_V}{V} = \left.\frac{\partial p}{\partial T}\right|_V .$$

A negative value of γ_G also implies a negative coefficient of thermal expansion as well as an increase of pressure with decreasing temperature. No thermal expansion or specific heat data for SmSe was available to compare to γ_G via the Grüneisen relation.

The results obtained for nearest-neighbour atom pairs from the slope of $\ln \sigma^2$ versus $\ln R$ are listed in the following table:

Table 9.2: Grüneisen parameter at 77K, obtained from the data of Tables 7.6 to 7.8 using Eq. (9.2):

		$R < R_c$	$R > R_c$	
Se – Sm	(LOG.SEN13.F2)	2.00 ± 0.09	−1.50	(Asymmetry included)
Se – Sm	(LOG.SEN14.F2)	3.28 ± 0.14	−2.22	
Se – (Sm, Sm)	(LOG.SEN19.F2)	2.26 ± 0.26	−1.32	(Two Sm shells)

The results vary depending on what type of fit was performed. The positive values for the Grüneisen parameter for the Se-Sm coordination vary from 2 to 3.3.

No error bars are listed for the results corresponding to $R > R_c$ because not enough data points were available for an error estimate. Note that determining γ_G according to Eq. (9.2) involves absolute values of σ^2. Since σ^2 is frequently overestimated in the fits, the values in the preceding table constitute upper bounds for γ_G where γ_G is positive and lower bounds where it is negative.

There are no data to compare these results to, except an investigation of samarium glasses [209] where at ambient pressure a Grüneisen parameter of -0.615 was found.

9.3 Pressure Determination

It may be argued that the pressure that we measure is not truly hydrostatic. However, the Sm monochalcogenides are rather soft materials so that any pressure inhomogeneity in these samples will be small. According to Ref. 210, at 50 kbar the pressure gradient across the sample is ~4 kbar.

The errors in the pressure calibration as obtained from least-squares fitting were found to be as large as ±8 kbar for Cu. As described in detail in Section 6.10, the error of a particular fit parameter was determined by incrementing this parameter in steps around its optimum value and performing least-squares fits at each step. In this way the effect of parameter correlations is taken into account and one obtains χ^2 as a function of the parameter in question. Its error bars are determined from the intersection points of the χ^2 curve with a horizontal line at twice the minimum value of χ^2. However, plots of the valence versus pressure indicate a much smaller error in the pressure determination, say ±4 kbar. If the error were really as large as ±8 kbar then it would be impossible to observe the rapid valence variation in the transition region. The fact that the error in the pressure is indeed smaller is also supported by the slope of the straight-line fit in Fig. 7.15 of Section 7.1. The slope is 6.4 kbar/turn and if we assume that we may be out by 1/2 turn then the error is ±3.2 kbar. We conclude then that our error bars are very conservative, overestimating the true error by approximately a factor of two.

We now illustrate an approximate method of pressure determination which does not require least-squares fitting and is therefore easy to apply. It is based on Section 3.6 where it was argued that a scaling relation exists between energies and lengths. In Section 6.14 the quantity $\varepsilon \equiv (R_o - R)/R_o$ was introduced. ε is the relative change of the length scale with respect to a reference length R_o, which is measured relative to the absorbing atom at a reference pressure, usually atmospheric pressure. A function $g(\varepsilon)$ was derived which peaks at a value $\varepsilon = \varepsilon^*$, with ε^* corresponding to R^*, the value of R at the applied pressure. With this information we immediately obtain the relative change in volume:

$$\varepsilon^* \equiv \frac{R_o - R^*}{R_o} \qquad \Rightarrow \qquad \frac{V}{V_o} = (1-\varepsilon^*)^3 \quad . \tag{9.3}$$

Using calibration curves we can obtain the pressure from V/V_o as usual. This was done for the data in Table 7.4. Each dataset was multiplied by k^3 prior to calculating $g(\varepsilon)$ in order to make the amplitude of the EXAFS signals more even. The function $g(\varepsilon)$, referenced to atmospheric pressure, is shown in the next figure for two datasets at different pressures.

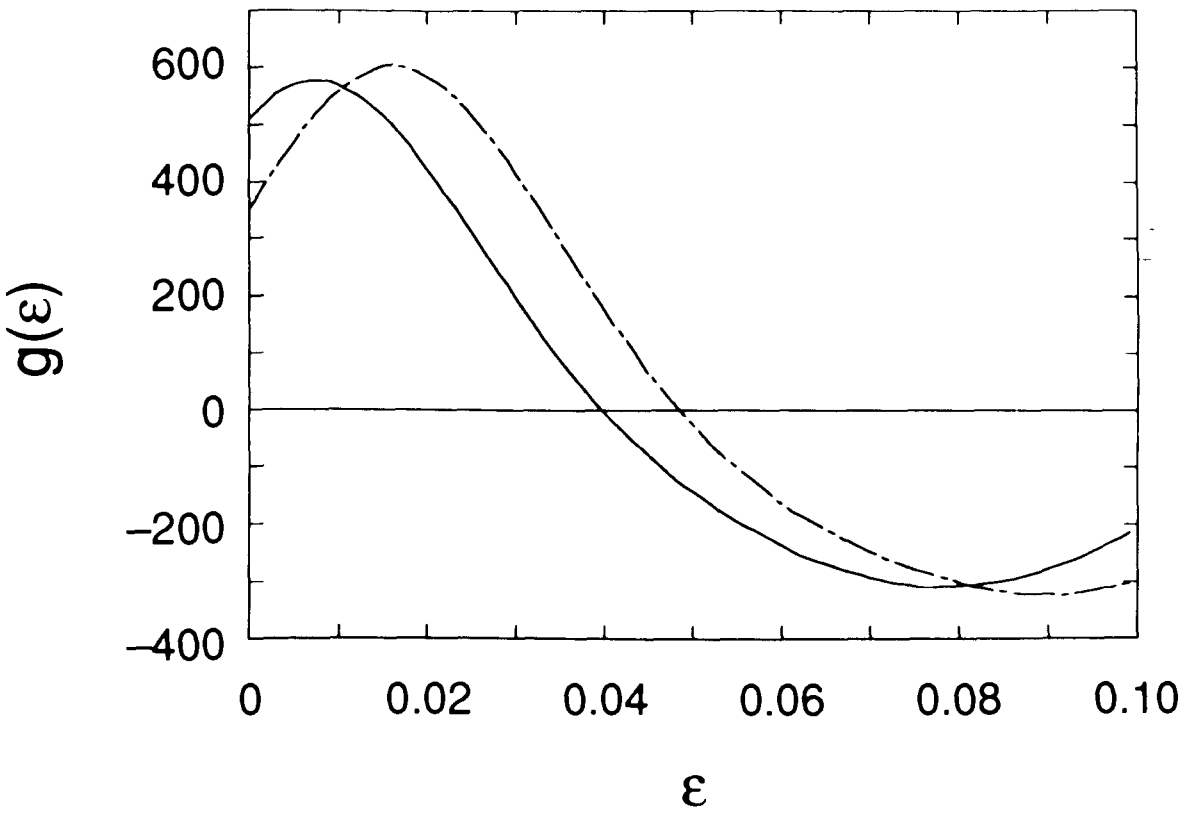

Fig. 9.5: Function $g(\varepsilon)$ versus ε calculated according to Eq. (6.92) of Section 6.14. The solid line corresponds to a pressure of $p = 32.6$ kbar as obtained from the fit (Table 7.4) or $\tilde{p} = 37.5$ kbar according to the scaling method (Table 9.3). The dashed line is the result for pressures $p = 72.2$ kbar and $\tilde{p} = 77.7$ kbar, respectively.

From this graph we see that the precision of locating the maximum and hence of estimating $\tilde{p}$ depends on the sharpness of the peak in $g(\varepsilon)$. The peak will be narrower the larger the k-space domain of the data is.

The next table shows the pressure $\tilde{p}$ obtained with the scaling method for the datasets of Table 7.4. The pressure p obtained by least-squares fitting and listed in Table 7.4 is shown for comparison. The domain of data is the same as in Table 7.4. To obtain $g(\varepsilon)$ each dataset was multiplied by k^3. $g(\varepsilon)$ is calculated using the first dataset, indicated in boldface, as the reference.

Table 9.3: Pressure calibration from Cu K edge EXAFS by the scaling method:
(compare Table 7.4 – Dec. '86; Si (111); T = 77K)

Dataset	$(R_o - R^*)/R_o$	V/V_o	N_T	Scaling $\tilde{p}$ (kbar)	Fit p (kbar)	Domain of data ($Å^{-1}$) k_{min}	k_{max}
CU00.N86.G	**0**	**1**	**0**	**0**	**0**	**1.822**	**14.944**
CU01.N88.G	0.003	0.991	1	14.0	9.40	1.817	15.045
CU03.N03.G	0.007	0.979	3	32.5	24.3	1.824	14.955
CU04.N08.G	0.007	0.979	4	32.5	24.5	1.824	15.101
CUSM4T.N30.G	0.008	0.976	4.75	37.5	31.4	1.764	15.216
CUSM05.N38.G	0.008	0.976	5	37.5	32.6	1.890	15.117
CUSM5Q.N57.G	0.008	0.976	5.25	37.5	33.55	1.817	15.117
CUSM06.N89.G	0.012	0.964	6	57.6	48.4	1.817	14.827
CUS11Q.N39.G	0.016	0.953	11.25	77.7	72.2	1.817	15.190

Fig. 9.6 compares the pressures $\tilde{p}$ obtained by scaling with p from least-squares fitting. There seems to be an offset of the $\tilde{p}$ values by about 6 kbar.

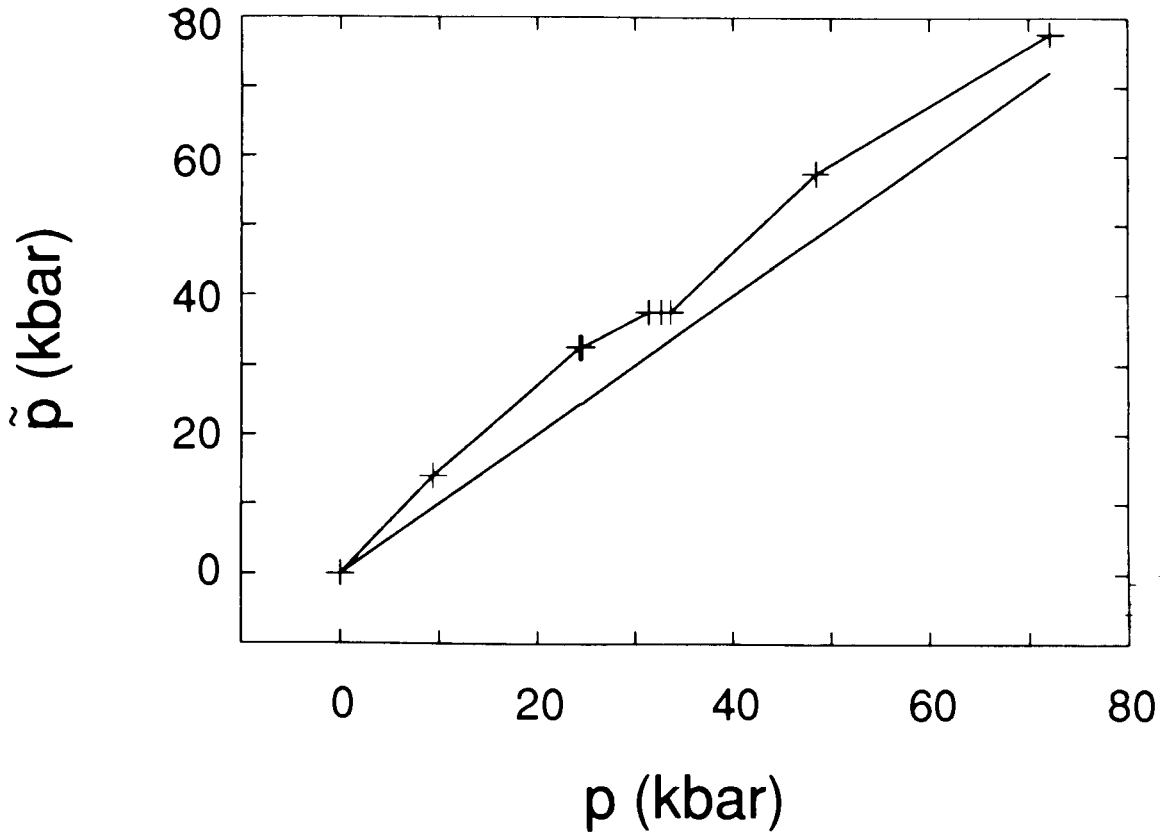

Fig. 9.6: Pressure $\tilde{p}$ obtained by scaling versus p obtained by fitting. The straight line corresponds to $\tilde{p} \equiv p$.

It seems then that this method of estimating the compression, and hence the pressure, is fairly reliable. Since the method is also very easy to apply, it could be employed to estimate the compression of the sample during the course of the experiment.

9.4 EXAFS of the Sm L_{III} Edge

As mentioned before, the x-ray absorption process is much faster than the valence fluctuations. Therefore, in the case of the Sm L_{II} or L_{III} edge one would expect that the EXAFS spectra each consist of a superposition of two spectra whose energy thresholds differ by ΔE, that is

by approximately 7 eV. This has been considered in the work of Krill et al. [211-213], Wetta [214], and Martin et al. [215]. In order to decide whether this is really the case the minimum k-value used in the data analysis must be very small. This in turn requires very good amplitudes and phases. At the same time one has to extend k_{max} to its maximum value of 12.5 $Å^{-1}$ determined by the energy of the intervening Sm L_{II} absorption edge. In the present data analysis k_{min} was approximately 4 $Å^{-1}$. At this k-value a shift of 7 eV in the origin of the k-scale will create a shift in k-space of ~0.2 $Å^{-1}$, which is rather small. k_{max} was limited to 10.2 $Å^{-1}$ due to the presence of an Fe contamination. Consequently, due to our restricted k-space range, we did not address the question of two energy thresholds in our data analysis.

9.5 Future Work

The results presented thus far suggest further experiments:

i) Measuring the valence transition below 77K

This experiment would decide whether the valence transition becomes indeed discontinuous at low enough temperature as predicted by theory [12, 13]. At 77K no significant sharpening could be observed. A cryostat for an experiment at temperatures below 77K has already been designed. In order to be able to observe a discontinuous phase transition one has to make certain that no significant pressure distribution exists in the sample.

ii) Measuring the valence at very high pressures

This experiment could determine whether the phase transition will be completed at a high enough pressure. Thus far it is not known whether in the Sm monochalcogenides the Sm atoms become fully trivalent. This experiment should be relatively easy to do since it suffices to perform it at room temperature.

In addition to these experiments, improvement in data analysis may be desirable. One problem is the determination of the correct EXAFS background. In this work the background was determined by smoothing, which yielded good results. Smoothing, however, is not without problems. Regions

with large signal amplitude require more smoothing passes than those with smaller amplitude. Alternatively one may fit a polynomial to the data and use it as the background. However, when the endpoints of the fit interval differ by too much, as is the case in k-space where $k_{min} \cong 3$ Å^{-1} and $k_{max} \cong 15$ Å^{-1}, then the polynomial develops too many inflection points. Furthermore, it will go to $\pm \infty$ at the endpoints. A way around this difficulty may be to fit to polynomials in ln E, instead of k. (Since the absorption coefficient varies approximately as E^{-3} one should fit the logarithm of the data to ln E.) Another functional form for the background may be a spline fit [177]. This was not investigated in the present work, but one problem with a spline fit is the dependence of the result on the choice of the location of the nodes.

In EXAFS data analysis it is customary to employ the Fast Fourier Transform (FFT). However, the FFT requires a uniform k-space grid. In our data collection procedures, the EXAFS portion of the absorption spectrum is collected with a k-space grid that is nearly uniform. Since the data is measured versus monochromator step numbers, which are nonlinearly related to the wavenumber k of the photoelectron, the conversion to k-space will not produce an exactly uniform grid. Hence interpolation onto a uniform k-space grid is always necessary. While this poses no difficulty with good quality data there may be distortion of the data when interpolating noisy data. Therefore one may consider using the conventional Fourier transform instead which does not require a uniform k-space grid. With present computing speeds the slowness of the conventional Fourier transform should be no problem.

The data analysis presented here may be augmented by simultaneous fits to the Se- and the Sm-EXAFS. In this way one could use constraints such as the nearest-neighbour distance as obtained from the Se-EXAFS must be equal to the nearest-neighbour distance as obtained from the Sm-EXAFS measured at the same pressure. One may even consider fitting the spectra of a whole pressure run by forcing the number of nearest-neighbours to be the same throughout. A possible problem with all these "grand fits", apart from computing effort, is the relative weighting of the various spectra. Nevertheless, it is worthwhile fitting several spectra at a time.

The scattering phases calculated in this work contain curved-wave effects. It turns out, however, that the scattering amplitude tends to diverge as k approaches zero. This results from the curved-wave modifications which contain spherical Neumann functions. These functions diverge at

$k = 0$ and apparently the partial-wave phase shifts $\delta_l(k)$ do not prevent this divergence. A divergence for $k \rightarrow 0$ is, however, unphysical. A measured absorption spectrum does not show signs of a divergence at $k = 0$.

In all fits to the Cu K, Se K, or Sm L_{III} edge EXAFS employing theoretical phase shifts we had to subtract $\pi/2$ from the central-atom phase shifts of Teo and Lee [11] in order to obtain correct distances. The origin of this artificial phase offset is not clear and should be investigated.

When fits to asymmetric pair distribution functions are performed it may be better to fit directly to the expansion coefficients of the pair potential rather than to the cumulants derived from it. These cumulants are related to the expansion coefficients of the pair potential by a set of equations rather than corresponding to the expansion coefficients one by one.

Chapter 10: **Summary**

For this thesis we carried out successfully x-ray absorption experiments at high pressure and liquid-nitrogen temperature for the first time. The two principal results are a lattice relaxation in SmSe and a power-law behaviour of the Sm valence of SmSe as a function of pressure. In this chapter we will first summarize these results. We will then briefly mention our first-principles calculations of EXAFS amplitude and phase shifts. Finally we will indicate some additional results.

10.1 Lattice Relaxation in SmSe

From a thorough analysis of the EXAFS of the Se K edge we obtained evidence of the existence of a split radial distribution function for the nearest-neighbour Sm atoms surrounding the Se atoms. This double-peak radial distribution function was not observed when we analyzed the Sm L_{III} edge EXAFS in SmSe or SmS. The split radial distribution function occurred at a pressure of 52.0 kbar ± 2.5 kbar, Fig. 9.1, with the peak separation being 0.09 Å ± 0.02 Å. At this pressure the valence has the value 2.50 ± 0.04, i.e. the average numbers of divalent and trivalent Sm ions are equal. Two different distances may also occur at other pressures but the associated pair distribution functions are not resolved. These facts suggest that lattice relaxation exists in the homogeneously mixed-valent compound SmSe.

The EXAFS of the Sm L_{III} edge is limited to a maximum k-value of 12.5 $Å^{-1}$ due to the intervening Sm L_{II} edge. This value of k_{max} is too small to detect a distance difference of 0.09 Å with its associated beat node at ~18 $Å^{-1}$ but it would be sufficient if the lattice relaxation had its maximum possible value of 0.17 Å given by the difference of the ionic radii of divalent and trivalent Sm ions [103].

In previous EXAFS experiments on mixed-valence compounds only the rare earth L_{III} edge EXAFS was measured. Martin et al. [215] and Boyce et al. [216] investigated the $Sm_xY_{1-x}S$ system and Krill et al. [211] measured the Sm L_{III} edge EXAFS of the $SmS_{1-x}O_x$ system. In the first system the smaller yttrium atoms replace the larger samarium atoms thereby compressing the lattice. Similarly, in the $SmS_{1-x}O_x$ system the smaller oxygen atoms replace the bigger sulfur atoms. This

way of chemically generating pressure has the disadvantage that foreign atoms are introduced into the crystal structure. This could result in properties that are not quite like those of SmS. It is therefore desirable to measure the EXAFS of SmS by applying pressure externally. This has been done by Krill et al. [217] and they find again that only one average nearest-neighbour distance is present in SmS. These negative results do not mean that there is no lattice relaxation in SmS but rather that it is too small to be detected from the Sm L_{III} edge EXAFS. Note also that for TmSe, which is mixed valent at ambient pressure, the results from the EXAFS of the Tm L_{III} edge do not show any lattice relaxation [218]. (The Se K edge EXAFS was not measured.)

The present findings of lattice relaxation in SmSe are in contrast to results of a theory by Kohn et al. [219] who investigated SmS. They considered the breathing motion of the six nearest-neighbour sulfur atoms, which surround each Sm atom, when they respond to the changing size of the Sm atom as it undergoes valence fluctuations. Taking into account that for a given valence there is a balance between the energy of the conduction electrons, the elastic energy of the lattice, and the energy of hybridization of the Sm-4f and conduction electrons they find that the displacement of the S ions is small when the hybridization energy is large. With their choice of input parameters Kohn et al. conclude that the difference between the Sm^{2+}-S and Sm^{3+}-S distances is less than 0.05 Å. However, their result depends sensitively on the magnitude of the hybridization matrix element, which is difficult to obtain reliably, and the calculated separation could be larger. It is of interest to see what the theory of Kohn et al. [219] would predict if it were applied to SmSe instead of SmS.

On the other hand, our result lends support to a theory by Baba and Kuroda [220] and Kuroda and Bennemann [221] who claim that relaxation always occurs, leading to two dynamically distorted positions of the anions. The amount of distortion depends strongly on the ratio of phonon frequencies to valence-fluctuation frequencies.

The present high-pressure experiments on SmSe had the advantage that the Se K edge EXAFS could be measured to much higher photon energies than the EXAFS of the Sm L_{III} edge. This meant that higher resolution could be obtained. In addition, we performed the experiments at liquid-nitrogen temperature. Thereby the thermal contribution to the EXAFS Debye-Waller factor due to dynamical motion of the lattice was reduced and the effect of the breathing motion became more evident. At 77K this breathing motion of Se atoms surrounding a pulsating Sm atom gives rise

to a peak in the pressure dependence of the mean-square relative displacement of the Sm-Se atom pairs when the data analysis assumes a single nearest-neighbour coordination shell. In SmSe this peak is seen either in the EXAFS of the Se K edge (Figs. 7.21, 7.22, 7.25, 7.28, 7.29, 7.31) or the Sm L_{III} edge (Fig. 7.37). In Chapter 9 we found that the maximum of σ^2, as obtained from the Se K edge EXAFS, led to a split radial distribution function of the surrounding Sm atoms at 52 kbar when we replaced the nearest-neighbour Sm coordination shell by two closely spaced Sm coordination shells. The peak in σ^2, obtained from one-shell fits, is also seen at liquid-nitrogen temperature for the second-nearest neighbour Se-Se atom pairs (Fig. 7.24).

One-shell fits to the data at room temperature do not yield a peak in σ^2, at most perhaps a weak shoulder (see Fig. 7.18, obtained from the Se K edge in SmSe, Fig. 7.34, obtained from the Sm L_{III} edge in SmSe, and Fig. 8.4, obtained from the Sm L_{III} edge in SmS). The mean-square relative displacement σ^2 decreases with increasing pressure.

10.2 Valence of SmSe

The near edge spectra were measured for the Sm L_{III} and Sm L_{II} edges which exhibit a double-peak structure in the intermediate-valent state. From this structure the valence was obtained by fitting two single-peak lineshapes, corresponding to integer-valent states. Since the behaviour of a system near a phase transition is frequently described by power laws with the exponent being characteristic of the system we fitted the pressure dependence of the valence of SmSe to Eq. (7.4):

$$v = B + A\left(\frac{p - p_c}{p_c}\right)^{\alpha} \qquad \text{for} \quad p \geq p_c \ .$$

The power-law behaviour of the valence as a function of pressure has not been observed before. The exponent α was found to have the value 0.43 ± 0.05 and hence is close to the one found in the Ising model. There may be a similarity of the mixed-valence problem to the Ising model because the Sm atoms can exist in one of two possible configurations: they can be either divalent or trivalent.

The power law also showed that at liquid-nitrogen temperature the mixed-valence transition in SmSe is not yet first order but still continuous. It has been suggested that the transition would become first order at a low enough temperature [12, 13].

Furthermore, the power law defines a critical pressure p_c at which the mixed-valence transition sets in. The value obtained for p_c was 31.5 ± 1 kbar . This result agrees remarkably well with the value of 32 kbar obtained from Raman experiments by Elmiger and Wachter [15] as the pressure at which the $^7F_0 \rightarrow {}^7F_1$ transition disappears. This transition vanishes because the 4f multiplet reaches the Fermi energy at p_c and the 4f electrons are promoted into the conduction band. Our value of p_c is in agreement with results from measurements of the resistivity as a function of pressure. Below the critical pressure the resisitivity decreases exponentially with increasing pressure as expected for a semiconductor. Above the critical pressure the resistivity becomes metallic and the decrease is much slower. From these measurements a critical pressure of 30 kbar was obtained [99]. Finally, in a bandstructure calculation by Farberovich [115] the onset of hybridization of the f band with the (5d, 6s) conduction band is predicted to occur in SmSe at a lattice constant of 6.0 Å. With 6.2 Å being the lattice parameter at ambient pressure this corresponds to a reduced volume of $V/V_o = 0.906$. Using the p-V relation for SmSe as measured by Jayaraman et al. [110, 207] at room temperature we arrive at a pressure of 31.9 kbar for the onset of hybridization.

We can thus summarize that at approximately 32 kbar hybridization sets in, the $^7F_0 \rightarrow {}^7F_1$ transition disappears, the valence begins to increase, and SmSe becomes metallic.

10.3 Amplitudes and Phase Shifts

The analysis of EXAFS data can proceed if there is a suitable reference material from which empirical amplitudes and phase shifts can be extracted. Normally the best reference material in a pressure-dependent study would be the material itself at atmospheric pressure. However, in our samples of SmSe and SmS there was always a small 3+ admixture at ambient pressure and a pure valence state for the extraction of amplitude and phase was not present. The small trivalent contribution may be due to the fact that the samples were not completely stoichiometric. It may also result from grinding the crystals to produce powdered samples.

Moreover, the size of the effect that we were studying in this thesis was expected to be small and could have been obscured if the amplitudes and phase shifts were pressure or valence dependent. Thus in this work we calculated backscattering amplitudes and phase shifts from first principles. These calculations, which are presented in detail in Chapter 3, were performed for the SmSe solid in the muffin-tin approximation rather than for isolated Sm and Se atoms. The atomic potentials were not calculated self consistently but the effects of the potentials of the neighbouring atoms were included. Furthermore, the potentials inside the muffin tin spheres, which at first are defined with the zero of energy at the vacuum level, were shifted such that the averaged interstitial potential became zero [61]. In this way the potential inside the muffin-tin spheres corresponded to the electronic charge density contained within the spheres. Our calculations showed that there is a small pressure dependence of amplitudes and phase shifts. Up to 100 kbar, however, this dependence is small. We also found that amplitudes and phases depend only weakly upon the valence of Sm.

10.4 Additional Results

The near-edge analysis of SmSe and SmS also indicated that ΔE, which is the energy separation of the absorption line shapes of the 3+ and 2+ states of the Sm ions, decreases linearly with increasing valence. This linearity has been observed before for other mixed-valence compounds [222] but has not been explained. We think that it may be due to a change in the screening by the conduction electrons. The Sm^{3+} ions are more screened by the conduction electrons than the Sm^{2+} ions. As the valence increases, more conduction electrons become available for screening. This leads to a bigger rise of the L-level of the Sm^{3+} ions than of the L-level of the Sm^{2+} ions. As a result, ΔE becomes smaller.

The one-shell fits to the Se K edge EXAFS yielded a maximum in the mean-square relative displacement. From σ^2, as a function of the nearest-neighbour Se-Sm distance, we can determine the Grüneisen parameter γ_G. At low pressure γ_G is negative meaning that the solid becomes soft. This, in turn, indicates a phase transition. Note also that according to Eq. (C.8) of the Appendix a negative value of the Grüneisen parameter leads to a negative coefficient of thermal expansion.

Because of the pronounced pressure dependence of the Sm valence, SmSe could be used as a pressure calibrant in x-ray absorption experiments. A possible disadvantage of SmSe may be its relatively large absorption coefficient for x-rays.

In order to determine the compression of a pressure calibrant like Cu (or perhaps SmSe) one may employ the scaling method described in Section 6.14 and discussed in Section 9.3. Without having to perform a complete EXAFS data analysis one can obtain the compression and then, as usual, determine the pressure from the known p-V relation of the calibrant. This scaling method is fast and could be used to approximate quickly the pressure of the calibrant in the course of the experiment.

Appendix

A Rydberg Atomic Units

Rydberg atomic units are obtained from SI units by the following substitutions:

$$\frac{e^2}{4\pi\varepsilon_o} \rightarrow 2 \; ; \qquad \frac{h}{2\pi} \rightarrow 1 \; ; \qquad a_B \rightarrow 1 \; . \tag{A.1}$$

This means that the Bohr radius, $a_B = 0.5291772$ Å , is the unit of length. In SI units a_B is given by:

$$a_B \equiv \left(\frac{h}{2\pi}\right)^2 \cdot \frac{4\pi\varepsilon_o}{e^2} \cdot \frac{1}{m_e} \; .$$

Making all three substitutions of (A.1) one obtains: $m_e = \frac{1}{2}$. (A.2)

The fine-structure constant is in SI units:

$$\alpha \equiv \frac{2\pi}{hc} \cdot \frac{e^2}{4\pi\varepsilon_o} \cdot \frac{1}{m_e} = 1/137.03599 \; .$$

Using Eq. (A.2) and the first two substitutions of (A.1) yields for the speed of light:

$$c = \frac{2}{\alpha} = 274.07198 \; . \tag{A.3}$$

For the Rydberg constant we obtain by substitution:

$$Ry = \left(\frac{2\pi}{h}\right)^2 \cdot \left(\frac{e^2}{4\pi\varepsilon_o}\right)^2 \cdot \frac{m_e}{2} = 1 \; . \tag{A.4}$$

Thus energy is measured in Rydbergs (1 Ry = 13.6057 eV).

Sometimes Hartree atomic units are employed. They differ in that the first substitution of (A.1) is $e^2/4\pi\varepsilon_o \rightarrow 1$, instead of 2. As a result energy is measured in Hartrees (1 Hartree ≡ 2 Ry).

The number values were taken from Ref. 123.

B Operating Range of the Monochromator

In this section we investigate the range of Bragg angles for which a double-crystal monochromator can operate. Outside the range given by the limiting angles θ_{min} and θ_{max} part of the x-ray beam is lost and the output decreases. Fig. B.1 illustrates the situation:

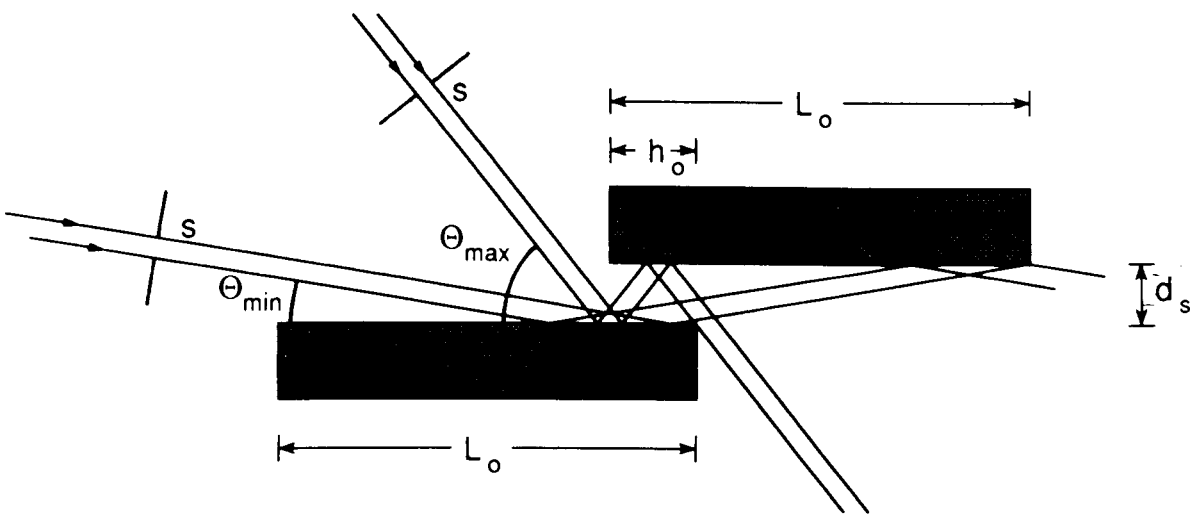

Fig. B.1: Limiting rays for a double-crystal monochromator. The x-rays are entering from the left. The central rays are directed towards the rotation axis, indicated by the circle.

For simplicity we assume that the monochromator is stationary and that a perfectly-collimated x-ray beam is incident at variable Bragg angles θ. The vertical width of the beam is equal to the pre-monochromator slit width s. We will consider only the case where the central ray intersects the rotation axis of the monochromator which in Fig. B.1 is at the origin. It is assumed that the two crystals are parallel and that each ray strikes each crystal once. Both crystals have length L_o and they overlap by the amount h_o. Without loss of generality we can assume that the overhang h_o does not exceed $L_o/2$. The projection of the vertical beam width onto the crystal surface is given by $s/\sin\theta$. In order that the full beam hits the first crystal it is necessary that this projection does not exceed the crystal dimensions. Since $h_o \le L_o - h_o$ we have that $s/(2\cdot\sin\theta) \le h_o$. Thus we obtain the following restriction on the Bragg angle:

$$\sin\theta \geq \frac{s}{2 \cdot h_o} \quad . \tag{B.1}$$

The two crystals are separated by the distance d_s. In Fig. B.1 the two limiting rays determining the minimum and maximum Bragg angles, θ_{min} and θ_{max}, have been indicated. From the geometry we can establish the following relations:

a) minimum Bragg angle:

$$\tan\theta \geq \frac{d_s}{L_o - s/(2 \cdot \sin\theta)} \qquad \text{or} \qquad \cot\theta \leq \frac{L_o}{d_s} - \frac{s}{2 \cdot d_s \cdot \sin\theta} \quad .$$

Multiplying through by $\sin\theta$, which is positive, yields:

$$\frac{L_o}{d_s} \cdot \sin\theta - \cos\theta - \frac{s}{2 \cdot d_s} \geq 0 \quad . \tag{B.2}$$

b) maximum Bragg angle:

$$\tan\theta \leq \frac{d_s}{\frac{1}{2} \cdot \left(h_o + s/(2 \cdot \sin\theta)\right)} \qquad \text{or} \qquad \cot\theta \geq \frac{h_o}{2 \cdot d_s} + \frac{s}{4 \cdot d_s \cdot \sin\theta} \quad .$$

Multiplying by $\sin\theta$ again gives:

$$\frac{h_o}{2 \cdot d_s} \cdot \sin\theta - \cos\theta + \frac{s}{4 \cdot d_s} \leq 0 \quad . \tag{B.3}$$

We see that all lengths scale with d_s, the separation of the two crystals. For zero slit width we get immediately:

$$\cot\theta_{min}\Big|_{s=0} = \frac{L_o}{d_s} \qquad \text{and} \qquad \cot\theta_{max}\Big|_{s=0} = \frac{h_o}{2 \cdot d_s} \quad . \tag{B.4}$$

We see that the minimum Bragg angle is determined by L_o/d_s and that θ_{max} is given by h_o/d_s. When the slit width s is finite θ_{min} becomes bigger and θ_{max} becomes smaller. Since Eqs. (B.2) and (B.3) have the same form we can write for both of them:

$$A \cdot \sin\theta - B \cdot \cos\theta - C = 0 \quad , \tag{B.5}$$

where we have written an equals sign instead of "≥". Eq. (B.5) can be solved readily for θ:

$$C = A \cdot \sin\theta - B \cdot \cos\theta \equiv \alpha \cdot \sin(\theta + \beta) \quad \Rightarrow \quad \alpha = \sqrt{A^2+B^2} \quad ; \quad \tan\beta = -B/A \tag{B.6}$$

$$\theta = \arctan\left(\frac{B}{A}\right) + \arcsin\left(\frac{C}{\sqrt{A^2+B^2}}\right) . \tag{B.7}$$

Making the corresponding substitutions we obtain:

$$\theta_{min} = \arctan\left(\frac{d_s}{L_o}\right) + \arcsin\left[\frac{s/2d_s}{\sqrt{1+L_o^2/d_s^2}}\right] ; \tag{B.8}$$

$$\theta_{max} = \arctan\left(\frac{2 \cdot d_s}{h_o}\right) - \arcsin\left[\frac{s/4d_s}{\sqrt{1+h_o^2/4d_s^2}}\right] . \tag{B.9}$$

The parameters L_o, h_o, and d_s for the crystals used at beamline IV-1 at SSRL are:

$$L_o = 66 \text{ mm} \; ; \quad h_o = 13 \text{ mm} \; ; \quad d_s = 10 \text{ mm} \; . \tag{B.10}$$

The pre-monochromator slit width s is typically 1 mm.

C Grüneisen Relation and Grüneisen Parameter

In order to establish an equation of state the pressure is calculated from the Helmholtz free energy as $p = -\left.\frac{\partial(U-T\cdot S)}{\partial V}\right|_T$, where the entropy is obtained from $S = \int_0^T \frac{dT'}{T'} \left.\frac{\partial U}{\partial T'}\right|_V$. Assuming small oscillations one can write the internal energy in the harmonic approximation as

$$U = U_o + \sum_{\mathbf{k}s} h\cdot\nu_s(\mathbf{k})\cdot n_s(\mathbf{k}) \quad ; \quad n_s(\mathbf{k}) \equiv \frac{1}{e^{h\cdot\nu_s(\mathbf{k})/k_B T} - 1} \; , \tag{C.1}$$

where **k** is the wave vector and s labels the phonon branches. The first term, which is independent of temperature, is the internal energy at equilibrium at $T = 0$ and includes the zero-point energy. The second term is the thermal energy due to the lattice vibrations. Inserting Eq. (C.1) into the expression for the entropy and integrating by parts finally gives for the pressure and its temperature derivative [223]:

$$p = -\left.\frac{\partial U_o}{\partial V}\right|_T - \sum_{\mathbf{ks}} h \cdot \frac{\partial \nu_s(\mathbf{k})}{\partial V} \cdot n_s(\mathbf{k}) \quad ; \tag{C.2}$$

$$\left.\frac{\partial p}{\partial T}\right|_V = -\sum_{\mathbf{ks}} h \cdot \frac{\partial \nu_s(\mathbf{k})}{\partial V} \cdot \left.\frac{\partial n_s(\mathbf{k})}{\partial T}\right|_V = \sum_{\mathbf{ks}} \gamma_{\mathbf{ks}} \cdot \frac{h \cdot \nu_s(\mathbf{k})}{V} \cdot \left.\frac{\partial n_s(\mathbf{k})}{\partial T}\right|_V \quad . \tag{C.3}$$

Here we have assumed that the $\nu_s(\mathbf{k})$, like U_o, depend only on volume. The quantities $\gamma_{\mathbf{ks}}$ are the so called "mode gammas" defined by:

$$\gamma_{\mathbf{ks}} \equiv -\frac{V}{\nu_s(\mathbf{k})} \cdot \frac{\partial \nu_s(\mathbf{k})}{\partial V} = -\frac{\partial \ln \nu_s(\mathbf{k})}{\partial \ln V} \quad . \tag{C.4}$$

The term following $\gamma_{\mathbf{ks}}$ in Eq. (C.3) is the specific heat per unit volume for the mode **ks**:

$$\frac{C_{Vs}(\mathbf{k})}{V} \equiv \frac{h \cdot \nu_s(\mathbf{k})}{V} \cdot \left.\frac{\partial n_s(\mathbf{k})}{\partial T}\right|_V \quad . \tag{C.5}$$

The Grüneisen parameter γ_G is now defined as:

$$\gamma_G \equiv \frac{\sum_{\mathbf{ks}} \gamma_{\mathbf{ks}} \cdot \frac{C_{Vs}(\mathbf{k})}{V}}{\sum_{\mathbf{ks}} \frac{C_{Vs}(\mathbf{k})}{V}} = \frac{1}{C_V} \cdot \sum_{\mathbf{ks}} \gamma_{\mathbf{ks}} \cdot C_{Vs}(\mathbf{k}) \quad . \tag{C.6}$$

Thus Eq. (C.3) can be written as $\left.\frac{\partial p}{\partial T}\right|_V = \gamma_G \cdot \frac{C_V}{V}$, (C.7)

which, when combined with Eq. (5.100), $\left.\frac{\partial p}{\partial T}\right|_V = B_T \cdot \beta$, yields the Grüneisen relation:

$$B_T \beta = \gamma_G \frac{C_V}{V} . \tag{C.8}$$

In the harmonic approximation the frequencies $\nu_s(\mathbf{k})$ will not depend on volume and thus the mode gammas $\gamma_{\mathbf{k}s}$, as well as γ_G, will be zero. According to Eq. (C.8) β will be zero as expected. A non-zero value of γ_G therefore is an approximate way of taking modest anharmonicity into account while at the same time retaining the harmonic approximation for the potential energy. This is referred to as the quasi-harmonic approximation. It is useful if the temperature is not too high. γ_G introduces a volume dependence for the vibrational frequencies as a compromise for neglecting anharmonic terms. If γ_G becomes actually temperature dependent then this means that there is strong anharmonicity.

One sees that γ_G can be calculated either microscopically, Eq. (C.6), or macroscopically by using Eq. (C.8). In the Debye approximation all frequencies are proportional to the Debye frequency:

$$\nu_D = c_s \cdot \left(\frac{3}{4\pi} \cdot \frac{\rho \cdot N_A}{A}\right)^{1/3} \equiv \frac{k_B}{h} \cdot \Theta_D . \tag{C.9}$$

Therefore all mode gammas are equal to γ_G which is given by:

$$\gamma_G = -\frac{\partial \ln \nu_D}{\partial \ln V} = -\frac{\partial \ln \Theta_D}{\partial \ln V} . \tag{C.10}$$

c_s is the sound velocity and the other parameters are the same as in Eq. (5.102). From the dependence of ν_D on c_s Slater [224] established that in the Debye model the Grüneisen parameter can be calculated as:

$$\gamma_{G,\text{Slater}} = -\frac{1}{6} - \frac{1}{2} \cdot \frac{d \ln B_T}{d \ln V} = -\frac{1}{6} + \frac{1}{2} \cdot \frac{dB_T}{dp} = -\frac{2}{3} - \frac{V}{2} \cdot \frac{\left.\frac{\partial^2 p}{\partial V^2}\right|_T}{\left.\frac{\partial p}{\partial V}\right|_T} . \tag{C.11}$$

This formula has a drawback though because $\gamma_{G,\text{Slater}}$ does not vanish for a harmonic solid. This can be seen as follows: The bulk modulus can be written as [225]:

$$B_T = V \cdot \left.\frac{\partial^2 U}{\partial V^2}\right|_T - \beta \cdot T \cdot V \cdot \left(\left.\frac{\partial B_T}{\partial V}\right|_T - \left.\frac{\partial B_T}{\partial V}\right|_p \right) . \qquad (C.12)$$

For a harmonic solid we have $\beta = 0$ and $U = K \cdot \left(V^{1/3} - V_o^{1/3}\right)^2$, [226], where K is a positive constant. This yields:

$$B_T = V \cdot \left.\frac{\partial^2 U}{\partial V^2}\right|_T \text{ and } \frac{d\ \ln B_T}{d\ \ln V} = -\frac{1}{3} - \frac{2}{3} \cdot \frac{1}{2 - (V/V_o)^{1/3}} .$$

Evaluating this expression for the case of no compression yields for $\gamma_{G,Slater}$ according to Eq. (C.11):

$$\gamma_{G,Slater} = \frac{1}{3} \neq 0 .$$

This deficiency was corrected by Dugdale and MacDonald [226], who derived the following expression for γ_G:

$$\gamma_G = -1 - \frac{V}{2} \cdot \frac{\left.\frac{\partial^2 p}{\partial V^2}\right|_T - \frac{10 \cdot p}{9 \cdot V^2}}{\left.\frac{\partial p}{\partial V}\right|_T + \frac{2 \cdot p}{3 \cdot V}} = -\frac{1}{3} - \frac{V}{2} \cdot \frac{\left.\frac{\partial^2 (pV^{2/3})}{\partial V^2}\right|_T}{\left.\frac{\partial (pV^{2/3})}{\partial V}\right|_T} . \qquad (C.13)$$

For $V = V_o$, i.e. $p = 0$, this expression is simply equal to $\gamma_{G,Slater} - \frac{1}{3}$ (Eq. (C.11)).

Since it correctly reduces to zero for a harmonic solid, Eq. (C.13) should be employed rather than Eq. (C.11).

D Smoothing Function

We will estimate the atomic background by smoothing the EXAFS spectrum until all the oscillations have disappeared. The procedure consists in the repeated application of the three-point smoothing formula [178] given in Section 6.3:

$$y_{new,i} \equiv \frac{1}{4} \cdot \left(y_{old,i-1} + 2 \cdot y_{old,i} + y_{old,i+1} \right) . \qquad (D.1)$$

It is assumed here that the data $y_i \equiv y(k_i)$ is given on a uniform grid of k-points extending from k_1 to k_N. The difference of two successive k-points is labeled by δk: $\delta k = k_{i+1} - k_i$, $i = 1, 2, ..., N-1$.

We now want to estimate how the smoothing in k-space affects the result in R-space. We will deal with the problem of endeffects, which was mentioned in Section 6.3, by assuming that the endpoints are unchanged under smoothing. Actually, the endpoint values of the smoothed function are found by fitting but this would be too difficult to take into account here. Since the endpoint values are fixed we simply have:

$$y_{new,1} \equiv y_{old,1} \quad \text{and} \quad y_{new,N} \equiv y_{old,N} \quad ; \quad i = 1, 2, ..., N \; . \tag{D.2}$$

The $\chi(k)$ that is obtained after subtracting this background will have its endpoints tied to zero.

The number of smoothing passes will be labeled by s and the ith data point after s passes will be denoted by $y_i^{(s)}$. Since the first and last points are fixed we can write:

$$y_1^{(s)} = y_1 \quad \text{and} \quad y_N^{(s)} = y_N \; . \tag{D.3}$$

To calculate the effects in R-space we compute the Fourier series:

$$y(k) = \frac{A_0}{2} + \sum_{n=1}^{\infty} \left(A_n \cdot \cos 2kR_n + B_n \cdot \sin 2kR_n \right) \; . \tag{D.4}$$

Here we have employed the following definitions:

$$R_n \equiv \frac{\pi \cdot n}{\Delta k} \quad \text{and} \quad \Delta k \equiv k_N - k_1 \; . \tag{D.5}$$

The coefficients A_n and B_n are determined by the well-known relations

$$A_n = \frac{2}{\Delta k} \int_0^{\Delta k} y(k) \cdot \cos 2kR_n \, dk \quad ; \quad n = 0, 1, 2, ...$$

$$B_n = \frac{2}{\Delta k} \int_0^{\Delta k} y(k) \cdot \sin 2kR_n \, dk \quad ; \quad n = 1, 2, ...$$

which are mentioned here for completeness. They are not needed to determine the change of A_n and B_n after a smoothing pass.

We now calculate the resulting Fourier series after one smoothing pass. In k-space we have after one pass:

$$y_i^{(1)} = \frac{1}{4} \cdot y_{i-1} + \frac{1}{2} \cdot y_i + \frac{1}{4} \cdot y_{i+1} \quad ; \quad i = 2, 3, ..., N-1 \ . \tag{D.6}$$

We can expand each of the three terms appearing on the right-hand side of this equation in a Fourier series according to Eq. (D.4). For y_{i-1} we obtain for example:

$$y_{i-1} = \frac{A_0}{2} + \sum_{n=1}^{\infty} \left(A_n \cdot \cos 2(k_i - \delta k) R_n + B_n \cdot \sin 2(k_i - \delta k) R_n \right) \quad ; \quad k_{i-1} \equiv k_i - \delta k \ .$$

Inserting this and the analogous relations for the other two terms into Eq. (D.6) yields:

$$y_i^{(1)} = \frac{A_0}{2} + \sum_{n=1}^{\infty} A_n \cdot \left(\frac{1}{4} \cdot \cos 2(k_i - \delta k) R_n + \frac{1}{2} \cdot \cos 2 k_i R_n + \frac{1}{4} \cdot \cos 2(k_i + \delta k) R_n \right)$$

$$+ \sum_{n=1}^{\infty} B_n \cdot \left(\frac{1}{4} \cdot \sin 2(k_i - \delta k) R_n + \frac{1}{2} \cdot \sin 2 k_i R_n + \frac{1}{4} \cdot \sin 2(k_i + \delta k) R_n \right) ,$$

$$i = 2, 3, ..., N-1$$

$$y_1^{(1)} = y_1 \quad ; \quad y_N^{(1)} = y_N \ .$$

(D.7)

After some algebra this formula is brought into the form:

$$y_i^{(1)} = \frac{1}{2} \cdot A_0^{(1)} + \sum_{n=1}^{\infty} A_n^{(1)} \cdot \cos 2 k_i R_n + B_n^{(1)} \cdot \sin 2 k_i R_n \quad ; \quad i = 2, 3, ..., N-1 \ ;$$

(D.8)

where

$$A_n^{(1)} \equiv A_n \cdot \cos^2\left(R_n \delta k\right) \quad ; \quad n = 0, 1, 2, \ldots$$

$$B_n^{(1)} \equiv B_n \cdot \sin^2\left(R_n \delta k\right) \quad ; \quad n = 1, 2, \ldots \quad .$$

Eq. (D.8) constitutes the Fourier series of y(k) after one smoothing pass. After s passes the Fourier coefficients will be:

$$A_n^{(s)} \equiv A_n \cdot \cos^{2s}\left(R_n \delta k\right) \quad ; \quad n = 0, 1, 2, \ldots$$

$$B_n^{(s)} \equiv B_n \cdot \sin^{2s}\left(R_n \delta k\right) \quad ; \quad n = 1, 2, \ldots \quad . \tag{D.9}$$

One can now calculate the change ρ_n of each frequency component R_n as follows:

$$\rho_n \equiv \sqrt{\frac{\left[A_n^{(s)}\right]^2 + \left[B_n^{(s)}\right]^2}{A_n^2 + B_n^2}} = \cos^{2s}\left(R_n \delta k\right) \quad . \tag{D.10}$$

δk appears here because the effect of the smoothing depends on the density of the data points in k-space. The first zero of ρ_n occurs at $R_n^{\bullet} \equiv \pi/(2\delta k)$. This is the Nyquist condition. There is no further information beyond $R_n^{\bullet}$.

From Eq. (D.10) we can calculate the required number of passes s for a desired reduction ρ_n at distance R_n:

$$s = \frac{\ln(\rho_n)}{2 \cdot \ln \cos\left(R_n \delta k\right)} \quad . \tag{D.11}$$

If it is required, for example, that ρ_n be 0.1 at $R_n = 1$ Å and if $\delta k = 0.15$ Å , then the number of passes has to be $s = 102$.

If we assume that R is a continuous variable then we can omit the subscript n in Eqs. (D.10) and (D.11). Since in practical cases $R \cdot \delta k \lesssim 0.3$ we can approximate Eq. (D.11) as:

$$s = \frac{\ln \rho}{2 \cdot \ln \cos(R \cdot \delta k)} \cong \frac{\ln \rho}{2 \cdot \ln \left(1 - \frac{1}{2} \cdot (R \cdot \delta k)^2\right)} \cong \frac{-\ln \rho}{(R \cdot \delta k)^2} \quad . \tag{D.12}$$

We see that $\ln s$ versus $\ln (R \cdot \delta k)$ is linear.

In practice the number of smoothing passes is determined by trials. Eq. (D.12) is useful nevertheless because it allows one to estimate the effect of the k-space smoothing in R-space.

E Least-Squares Fitting of EXAFS Spectra

In this appendix we present a brief introduction to some features of an interactive least-squares fitting program that has been written to fit EXAFS data in k- or R-space [187].

The program introduced here fits EXAFS data in k-space to the expression (6.55). In R-space the program fits the Fourier transform of the data to the Fourier transform of the model. The Fourier transform of the latter is calculated numerically rather than analytically so that artifacts are equally present in both Fourier transforms. Reference amplitudes and reference total phases can be read in irrespective of their particular k-space grid. Up to nine coordination shells can be fitted which is much more than normally needed but may be useful when creating model spectra. The fit parameters are as follows (6.55):

There are two parameters that apply to all shells: The pre-monochromator slit width s (Chapter 5) and the mean-free path constant η (Chapter 2). Each shell is characterized by seven parameters: The phase offset a_j, the adjustment ΔE_j for the inner potential, the radius R_j of the coordination shell, the third- and fourth-order cumulants C_{3j} and C_{4j}, the mean-square relative displacement σ_j^2, and the coordination number N_j. Nine shells correspond to a total of 65 parameters, 20 of which can be varied.

Least-squares fitting of EXAFS spectra frequently involves many parameters. It is therefore desirable to restrict this number to a minimum. This is achieved by taking any existing physical constraints on the parameters into account. Such constraints are, for example, a fixed ratio of coordination numbers known from the crystal structure or the same values of ΔE for coordination shells consisting of like atoms. The fitting routine provides for the following constraints:

Fixing the difference of phase offset, ΔE, R, σ^2, or N for any two shells.
Fixing the ratio of R, σ^2, or N for any two shells.

These constraints eliminate superfluous fit parameters. Nevertheless the number of parameters can remain quite large, say, eight or so. In order to obtain information about as to whether these parameters are meaningful one has to investigate their mutual correlation and estimate their errors. The correlation coefficients are obtained from Eq. (6.62) and provide information about which parameters interact with each other. The error estimates for each fit parameter are obtained by scanning the parameter in question, as explained in Chapter 6. The program does this automatically.

In order to be versatile the program offers several built-in window functions: rectangle, Gaussian of arbitrary percentage, Hamming, and Hanning window of arbitrary percentage and also with a central plateau region of arbitrary width specified. For k-space fits Fourier filtering is possible. Furthermore the interval over which Fourier transforms are taken can be set and a weighting function which is equal to the inverse of the envelope of the k- or R-space data can be applied. Furthermore limits can be specified for each parameter. A useful feature is the option to draw the EXAFS due to separate coordination shells or due to partial sums of coordination shells. This can be done in k- and in R-space. It is also possible to monitor selected parameters in the course of a fit. All parameters specifying a fit are written into a parameter file so that the program can easily be restarted without having to type them in again. This can also serve for archiving. There are several output files that the program generates. Everything that happened during a fitting session is written into a temporary file called –LOG. The output is written into the file –OUT. These files exist always. Amplitude and phase of the data (if one-shell fit) or the model (if multishell fit) can be extracted and written into the files –AMP and –PHASE. The model itself can be written into a file called –MODEL and Fourier-filtered data can be written into the file –DATAF. The Fourier transform of the data including the magnitude of the transform can be written into –DATAR.

F Formula for Valence Estimation

In order to derive a formula for the valence we write down the values of the fitting function at the positions E^{2+} and E^{3+} of the two lines. Using Eqs. (6.79) and (6.80) we get [17]:

$$Y(E^{2+}) = (1-\nu)\cdot Y_{max} + \nu\cdot Y_{max}\cdot \frac{1}{K}\cdot \int_{-\infty}^{\infty} \frac{1}{(\tilde{E}-E^{3+})^2 + \Gamma^2}\, e^{-(\tilde{E}-E^{2+})^2/2\sigma^2}\, d\tilde{E} \quad . \tag{F.1}$$

$$Y(E^{3+}) = (1-\nu)\cdot (Y_{max}-1)\cdot \frac{1}{K}\cdot \int_{-\infty}^{\infty} \frac{1}{(\tilde{E}-E^{2+})^2 + \Gamma^2}\, e^{-(\tilde{E}-E^{3+})^2/2\sigma^2}\, d\tilde{E} \quad + 1-\nu+\nu\cdot Y_{max} \quad . \tag{F.2}$$

The integrals appearing in the two equations are equivalent. Eliminating them, rather than Y_{max} as in Ref. 17, yields after some algebra the following formula for the fractional part ν of the valence v:

$$\nu = \left(1 + \frac{Y_{max}}{Y_{max}-1}\cdot \frac{Y_{max}-Y(E^{3+})}{Y_{max}-Y(E^{2+})}\right)^{-1} \quad ;$$

$$v \equiv 2 + \nu \text{ , except for Ce compounds where } v \equiv 3 + \nu \quad . \tag{F.3}$$

Unlike $Y(E^{2+})$ and $Y(E^{3+})$, the peak height Y_{max} of an individual line profile cannot be read from the measured spectrum. Usually, however, $Y_{max} \cong 2$. In this case we get for ν:

$$Y_{max} = 2 \quad \Rightarrow \quad \nu = \frac{2 - Y(E^{2+})}{6 - Y(E^{2+}) - 2\cdot Y(E^{3+})} \quad . \tag{F.4}$$

In principle it is possible to introduce another function value of the normalized spectrum, like, for example, $Y((E^{2+}+E^{3+})/2)$, in order to eliminate Y_{max}. This will not be pursued here.

Application of Eq. (F.3) is not limited to estimate rapidly the valence from an absorption edge of a mixed-valent compound. It can also be used to analyze the error of the determined valence v.

In this derivation the effects due to the finite resolution of the monochromator have been ignored because even at the highest L edge of a mixed-valent material, that is $E_{L_{II}}^{Yb} = 9976$ eV , the broadening due to resolution is small (2.74 eV for a 1 mm slit and Si (111) crystals).

Bibliography

1 *X-Ray Absorption*, D.C. Koningsberger, R. Prins (Eds.), Chemical Analysis, Vol. 92, Wiley, New York, 1988

2 *EXAFS Spectroscopy, Techniques and Applications*, B.K. Teo, D.C. Joy (Eds.), Plenum Press, New York, 1981

3 B.K. Teo, *EXAFS: Basic Principles and Data Analysis*, Inorganic Chemistry Concepts, Vol. 9, Springer, Berlin, 1986

4 P.A. Lee, P.H. Citrin, P. Eisenberger, B.M. Kincaid, Rev. Mod. Phys. **53**, 769 (1981)

5 T.M. Hayes, J.B. Boyce, Solid State Phys. **37**, 173 (1982)

6 E.A. Stern, Contemp. Phys. **19**, 289 (1978)

7 W.L. Schaich, Phys. Rev. B **29**, 6513 (1984)

8 A.G. McKale, S.K. Chan, B.W. Veal, A.P. Paulikas, G.S. Knapp, J. Phys. (Paris) Colloq. **47**, C8-55 (1986)

9 A.G. McKale, G.S. Knapp, S.K. Chan, Phys. Rev. B **33**, 841 (1986)

10 A.G. McKale, B.W. Veal, A.P. Paulikas, S.-K. Chan, G.S. Knapp, J. Am. Chem. Soc. **110**, 3763 (1988)

11 B.K. Teo, P.A. Lee, J. Am. Chem. Soc. **101**, 2815 (1979)

12 C.M. Varma, Rev. Mod. Phys. **48**, 219 (1976)

13 N.F. Mott, Phil. Mag. **30**, 403 (1974)

14 J.M.D. Coey, S.K. Ghatak, M. Avignon, F. Holtzberg, Phys. Rev. B **14**, 3744 (1976)

15 M.W. Elmiger, P. Wachter, J. Magn. Magn. Mat. **63 & 64**, 612 (1987)

16 Report of the *International Workshop on Standards and Criteria in X-Ray Absorption Spectroscopy*, Brookhaven, March 7-9, 1988; published in Physica B **158**, 701 (1989)

17 K.R. Bauchspieß, Diplomarbeit, Universität zu Köln, 1982

18 Yu.A. Babanov, V.V. Vasin, A.L. Ageev, N.V. Ershov, phys. stat. sol. (b) **105**, 747 (1981)

19 E.D. Crozier, Physica B **158**, 14 (1989)

20 J.J. Rehr, E.A. Stern, R.L. Martin, E.R. Davidson, Phys. Rev. B **17**, 560 (1978)

21 E.A. Stern, in *X-Ray Absorption*, D.C. Koningsberger, R. Prins (Eds.), Chemical Analysis, Vol. 92, Wiley, New York, 1988, Chap. 1

22 G. Bunker, Nucl. Instr. and Meth. **207**, 437 (1983)

23 E.D. Crozier, J.J. Rehr, R. Ingalls, in *X-Ray Absorption*, D.C. Koningsberger, R. Prins (Eds.), Chemical Analysis, Vol. 92, Wiley, New York, 1988, Chap. 9

24 L.E. Reichl, *A Modern Course in Statistical Physics*, University of Texas Press, Austin, TX, 1980

25 E. Sevillano, H. Meuth, J.J. Rehr, Phys. Rev. B **20**, 4908 (1979)

26 C.Y. Yang, M.A. Paesler, D.E. Sayers, J. Phys. (Paris) Colloq. **47**, C8-391 (1986)

27 I. Lindau, W.E. Spicer, J. Electron Spectrosc. Relat. Phenom. **3**, 409 (1974)

28 M.P. Seah, W.A. Dench, Surf. Interface Anal. **1** (1), 2 (1979)

29 J.J. Rehr (private communication)

30 M.A. Van Hove, W.H. Weinberg, C.-M. Chan, *Low-Energy Electron Diffraction*, Springer Series in Surface Sciences, Vol. 6, Springer, Heidelberg, 1986, Chap. 4

31 O. Keski-Rahkonen, M.O. Krause, Atomic Data and Nuclear Data Tables **14**, 139 (1974)

32 K.D. Sevier, *Low Energy Electron Spectrometry*, Wiley, New York, 1972, Chap. 6

33 W. Bambynek, B. Crasemann, R.W. Fink, H.-U. Freund, H. Mark, C.D. Swift, R.E. Price, P. Venugopala Rao, Rev. Mod. Phys. **44**, 716 (1972)

34 H.J. Leisi, J.H. Brunner, C.F. Perdrisat, P. Scherrer, Helv. Phys. Acta **34**, 161 (1961)

35 F. Calogero, *Variable Phase Approach to Potential Scattering*, Academic Press, New York, 1967

36 J.M. Clifton, R.A. Leacock, J. Comput. Phys. **38**, 327 (1980)

37 L.I. Schiff, *Quantum Mechanics*, 3rd edition, McGraw-Hill Kogakusha, Tokyo, 1968

38 K.N.R. Taylor, M.I. Darby, *Physics of Rare Earth Solids*, Chapman and Hall, London, 1972

39 J.C. Slater, Phys. Rev. **81**, 385 (1951)

40 F. Herman, S. Skillman, *Atomic Structure Calculations*, Prentice-Hall, Englewood Cliffs, N.J., 1963

41 A.W. Weiss, Phys. Rev. A **34**, 624 (1986)

42 G. Beni, P.A. Lee, P.M. Platzman, Phys. Rev. B **13**, 5170 (1976)

43 S.-H. Chou, J.J. Rehr, E.A. Stern, E.R. Davidson, Phys. Rev. B **35**, 2604 (1987)

44 J.W.D. Connolly, in *Semiempirical Methods of Electronic Structure Calculation*, Part A, G.A.. Segal (Ed.), Modern Theoretical Chemistry, Vol. 7, Plenum Press, New York, 1977

45 K. Schwarz, Phys. Rev. B **5**, 2466 (1972)

46 R. Latter, Phys. Rev. **99**, 510 (1955)

47 J.P. Desclaux, J. Phys. B **4**, 631 (1971)

48 C. Froese Fischer, Computer Phys. Commun. **1**, 151 (1969)

49 J.P. Desclaux, Computer Phys. Commun. **9**, 31 (1975)

50 I.P. Grant, B.J. McKenzie, P.H. Norrington, D.F. Mayers, N.C. Pyper, Computer Phys. Commun. **21**, 207 (1980)

51 C. Froese Fischer, *The Hartree-Fock Method for Atoms*, Wiley, New York, 1977

52 J.G. Norman, Molec. Phys. **31**, 1191 (1976)

53 L.F. Mattheiss, Phys. Rev. **133**, A1399 (1964)

54 T.L. Loucks, *Augmented Plane Wave Method*, Benjamin, New York, 1967

55 G.L. Hall, Am. J. Phys. **50**, 653 (1982)

56 G.L. Hall, D.O. Christy, Am. J. Phys. **34**, 526 (1966)

57 J.O. Hirschfelder, C.F. Curtiss, R.B. Bird, *Molecular Theory of Gases and Liquids*, Wiley, New York, 1954, p. 1037

58 T. Kihara, S. Koba, J. Phys. Soc. Jpn. **7**, 348 (1952)

59 M. Kitamura, S. Muramatsu, C. Sugiura, phys. stat. sol. (b) **142**, 191 (1987)

60 J.J. Rehr, R.C. Albers, C.R. Natoli, E.A. Stern, Phys. Rev. B **34**, 4350 (1986)

61 L.F. Mattheiss, J.H. Wood, A.C. Switendick, in *Energy Bands in Solids*, B. Alder, S. Fernbach, M. Rotenberg (Eds.), Methods in Computational Physics, Vol. 8, Academic Press, New York, 1968

62 P.P. Ewald, Ann. Physik **64**, 253 (1921)

63 J.C. Slater, *Insulators, Semiconductors, and Metals*, Quantum Theory of Molecules and Solids, Vol. 3, McGraw-Hill, New York, 1967

64 E. Francisco, V. Luaña, J.M. Recio, L. Pueyo, J. Chem. Educ. **65**, 6 (1988)

65 V.V. Dyakin, R.F. Egorov, V.P. Shirokovskii, phys. stat. sol. **36**, 447 (1969)

66 P. Lagarde, Phys. Rev. B **14**, 741 (1976)

67 D. Branson, Am. J. Phys. **47**, 1000 (1979)

68 M.E. Rose, *Relativistic Electron Theory*, Wiley, New York, 1961

69 W.H. Press, B.P. Flannery, S.A. Teukolsky, W.T. Vetterling, *Numerical Recipes*, Cambridge University Press, London, New York, 1986

70 B. Thomas, BYTE, April 1986, p. 191

71 C.F. Gerald, P.O. Wheatley, *Applied Numerical Analysis*, Addison-Wesley, Reading, 1984

72 J.E. Müller, W.L. Schaich, Phys. Rev. B **27**, 6489 (1983)

73 D. Norman, K.B. Garg, P.J. Durham, Solid State Commun. **56**, 895 (1985)

74 V. Fritzsche, P. Rennert, phys. stat. sol. (b) **142**, 15 (1987)

75 P. Rennert, Nguyen Van Hung, phys. stat. sol. (b) **148**, 49 (1988)

76 J.J. Barton, D.A. Shirley, Phys. Rev. A **32**, 1019 (1985)

77 J.J. Barton, D.A. Shirley, Phys. Rev. B **32**, 1892 (1985)

78 J.J. Barton, D.A. Shirley, Phys. Rev. B **32**, 1906 (1985)

79 E. Gillman, H.R. Fiebig, Comput. Phys. **2**, 62 (1988)

80 J.R. Taylor, *Scattering Theory*, Wiley, New York, 1972

81 R.C. Albers, A.K. McMahan, J.E. Müller, Phys. Rev. B **31**, 3435 (1985)

82 J.E. Müller, O. Jepsen, J.W. Wilkins, Solid State Commun. **42**, 365 (1982)

83 C.R. Natoli, in *EXAFS and Near Edge Structure*, A. Bianconi, L. Incoccia, S. Stipcich (Eds.), Chemical Physics, Vol. 27, Springer, Berlin, 1983, p. 43

84 F.W. Lytle, Ber. Bunsenges. Phys. Chem. **91**, 1251 (1987)

85 J.E. Müller, Thesis, Comell University, 1980

86 W. Jones, N.H. March, *Theoretical Solid State Physics*, Vol. 1, Dover, New York, 1985

87 I.A. Smirnov, phys. stat. sol. (a) **14**, 363 (1972)

88 L.L. Hirst, J. Phys. Chem. Solids **35**, 1285 (1974)

89 A. Jayaraman, P.D. Dernier, L.D. Longinotti, High Temp. High Press. **7**, 1 (1975)

90 A. Jayaraman, Comm. Sol. State Phys. **7**, 135 (1977)

91 R. Suryanarayanan, phys. stat. sol. (b) **85**, 9 (1978)

92 I.A. Smirnov, V.S. Oskotskii, Sov. Phys. Usp. **21**, 117 (1978)

93 D.I. Khomskii, Sov. Phys. Usp. **22**, 879 (1979)

94 A. Jayaraman, in *Handbook of the Physics and Chemistry of Rare Earths*, K.A. Gschneidner Jr., L. Eyring (Eds.), Vol. 2, North-Holland, Amsterdam, 1979, Chap. 20

95 J.M. Lawrence, P.S. Riseborough, R.D. Parks, Rep. Prog. Phys. **44**, 1 (1981)

96 J. Flouquet, P. Haen, C. Vettier, J. Magn. Magn. Mat. **29**, 159 (1982)

97 D.I. Khomskii, in *Quantum Theory of Solids*, I.M. Lifshits (Ed.), Mir, Moscow, 1982, Chap. 2

98 P. de V. du Plessis, S. Afr. J. Phys. **83**, 683 (1987)

99 B. Barbara, D. Gignoux, C. Vettier, *Lectures on Modern Magnetism*, Springer, Berlin, 1988, Chap. 13

100 E. Holland-Moritz, J. Magn. Magn. Mat. **38**, 253 (1983)

101 E. Holland-Moritz, M. Kasaya, Physica B **136**, 424 (1986)

102 M. Eibschütz, R.L. Cohen, E. Buehler, J.H. Wernick, Phys. Rev. B **6**, 18 (1972)

103 A. Iandelli, A. Palenzona, in *Handbook of the Physics and Chemistry of Rare Earths*, K.A. Gschneidner Jr., L. Eyring (Eds.), Vol. 2, North-Holland, Amsterdam, 1979, Chap. 13

104 S.V. Vlasov, O.V. Farberovich, Sov. Phys. Solid State **24**, 536 (1982)

105 S.D. Mahanti, T.A. Kaplan, M. Barma, Phys. Lett. **58** A, 43 (1976)

106 M. Iwamatsu, Phys. Lett. **81** A, 515 (1981)

107 C.J.M. Rooymans, Ber. Bunsenges. Phys. Chem. **70**, 1036 (1966)

108 A. Jayaraman, V. Narayanamurti, E. Bucher, R.G. Maines, Phys. Rev. Lett. **25**, 368 (1970)

109 A. Jayaraman, V. Narayanamurti, E. Bucher, R.G. Maines, Phys. Rev. Lett. **25**, 1430 (1970)

110 A. Jayaraman, A.K. Singh, A. Chatterjee, S. Usha Devi, Phys. Rev. B **9**, 2513 (1974)

111 M.B. Maple, D. Wohlleben, Phys. Rev. Lett. **27**, 511 (1971)

112 E. Bucher, V. Narayanamurti, A. Jayaraman, J. Appl. Phys. **42**, 1741 (1971)

113 B. Welber, A. Jayaraman, J. Appl. Phys. **50**, 462 (1979)

114 V.A. Sidorov, N.N. Stepanov, L.G. Khvostantsev, O.B. Tsiok, A.V. Golubkov, V.S. Oskotskii, I.A. Smirnov, Sov. Phys. Solid State **29**, 1509 (1987)

115 O.V. Farberovich, Sov. Phys. Solid State **22**, 393 (1980)

116 E. Kaldis, P. Wachter, Solid State Commun. **11**, 907 (1972)

117 K.G. Subhadra, D.B. Sirdeshmukh, Pramana **9**, 223 (1977)

118 E.E. Vainshtein, S.M. Blokhin, Yu.B. Paderno, Sov. Phys. Solid State **6**, 2318 (1965)

119 K.R. Bauchspiess, W. Boksch, E. Holland-Moritz, H. Launois, R. Pott, D. Wohlleben in *Valence Fluctuations in Solids*, L.M. Falicov, W. Hanke, M.B. Maple (Eds.), North-Holland, Amsterdam, 1981, p. 417

120 C.E.T. Gonçalves da Silva, L.M. Falicov, Phys. Rev. B **13**, 3948 (1976)

121 *Synchrotron Radiation Research*, H. Winick, S. Doniach (Eds.), Plenum Press, New York, 1980

122 P. Becker, P. Seyfried, H. Siegert, Z. Phys. B **48**, 17 (1982)

123 E.R. Cohen, B.N. Taylor, Rev. Mod. Phys. **59**, 1121 (1987) and
E.R. Cohen, B.N. Taylor, Physics Today, August 1987, p. BG11 and
E.R. Cohen, B.N. Taylor, J. Phys. Chem. Ref. Data **17**, 1795 (1988)

124 J.H. Beaumont, M. Hart, J. Phys. E **7**, 823 (1974)

125 R.W. James, *The Optical Principles of the Diffraction of X-Rays*, Ox Bow Press, Woodbridge, CT, 1982 (republication of the 1948 edition published by Bell and Hyman Ltd., England)

126 *International Tables for X-Ray Crystallography*, K. Lonsdale (Ed.), Vol. 3, Kynoch Press, Birmingham, England, 1962

127 U. Bonse, in *Synchrotron Radiation for X-Ray Crystallography*, International School of Crystallography, Erice, Italy, 1986

128 G. Materlik, V.O. Kostroun, Rev. Sci. Instrum. **51**, 86 (1980)

129 J.B. Roberto, B.W. Batterman, D.T. Keating, Phys. Rev. B **9**, 2590 (1974)

130 J. Goulon, M. Lemonnier, R. Cortes, A. Retournard, D. Raoux, Nucl. Instr. and Meth. **208**, 625 (1983)

131 D.C. Koningsberger, in *X-Ray Absorption*, D.C. Koningsberger, R. Prins (Eds.), Chemical Analysis, Vol. 92, Wiley, New York, 1988, Chap. 5

132 E.D. Crozier, N. Alberding, A.J. Seary, K.R. Bauchspiess, D. Jiang, R. Ingalls, B. Houser, SSRL Activity Report, 1985, p.55

133 K.R. Bauchspiess, E.D. Crozier, in *EXAFS and Near Edge Structure III*, K.O. Hodgson, B. Hedman, J.E. Penner-Hahn (Eds.), Proceedings in Physics, Vol. 2, Springer, Berlin, 1984, p. 514

134 Z.U. Rek, G.S. Brown, T. Troxel, in *EXAFS and Near Edge Structure III*, K.O. Hodgson, B. Hedman, J.E. Penner-Hahn (Eds.), Proceedings in Physics, Vol. 2, Springer, Berlin, 1984, p. 511

135 F. Bridges, Nucl. Instr. and Meth. A **257**, 447 (1987)

136 J.A. Bearden, Rev. Mod. Phys. **39**, 78 (1967)

137 K. Kohra, M. Ando, T. Matsushita, H. Hashizume, Nucl. Instr. and Meth. **152**, 161 (1978)

138 W.H. McMaster, N. Kerr Del Grande J. H. Mallett, J.H. Hubbell,
Compilation of X-Ray Cross Sections, Lawrence Radiation Laboratory,
Report No. UCRL–50174, Sec. 2, R–1, 1969 (unpublished)
Report available from National Technical Information Service, U.S. Department of Commerce,
5285 Port Royal Road, Springfield, VA 22161

139 R. Woldseth, *X-Ray Energy Spectrometry*, Kevex Corp., Burlingame, CA, 1973

140 J.A. Victoreen, J. Appl. Phys. **19**, 855 (1948)

141 M. Hikam, M.Sc. Thesis, Simon Fraser University, 1987

142 F. Sauli, CERN Report 77-09 (1977) and
F. Sauli, in: T. Ferbel, *Experimental Techniques in High Energy Physics*, Frontiers in Physics,
Vol. 64, Addison-Wesley, Reading, 1987

143 H.W. Fulbright, Hdb. Physik **45**, 1, (1958)

144 G.F. Knoll, *Radiation Detection and Measurement*, Wiley, New York, 1979

145 P. Rabe, G. Tolkiehn, A. Werner, Nucl. Instr. and Meth. **171**, 329 (1980)

146 M.E. Rose, M.M. Shapiro, Phys. Rev. **74**, 1853 (1948)

147 E.J. Burge, Nucl. Instr. and Meth. **227**, 115 (1984)

148 B.M. Kincaid, Thesis, Stanford University, 1975

149 J. Perel, J. Phys. E **3**, 268 (1970)

150 E.A. Stern, K. Kim, Phys. Rev. B **23**, 3781 (1981)

151 J. Goulon, C. Goulon-Ginet, R. Cortes, J.M. Dubois, J. Physique **43**, 539 (1982)

152 A.E. Sandström, Hdb. Physik **30**, 78, (1957)

153 S.N. Vaidya, G.C. Kennedy, J. Phys. Chem. Solids **32**, 951 (1971)

154 C.S. Menoni, I.L. Spain, in *High Pressure Measurement Techniques*, G.N. Peggs (Ed.),
Applied Science Publishers, London, New York, 1983

155 R. Ingalls, E.D. Crozier, J.E. Whitmore, A.J. Seary, J.M. Tranquada, J. Appl. Phys. **51**, 3158
(1980)

156 *American Institute of Physics Handbook*, D.E. Gray (Ed.), 3rd edition, McGraw-Hill, New York,
1972, Chap. 4

157 J.M. Tranquada, Thesis, University of Washington, 1983

158 J.C. Jamieson, in *Proceedings of the Fourth International Conference on High Pressure*,
J. Osugi (Ed.), The Physico-Chemical Society of Japan, Kyoto 1975, p.11

159 R.F. Cooper, B. Yates, J. Phys. C **4**, L113 (1971)

160 A.J. Kirkham, B. Yates, J. Phys. C **1**, 1162 (1968)

161 J.J. Fontanella, D.E. Schuele, J. Phys. Chem. Solids **31**, 647 (1970)

162 K.K. Srivastava, H.D. Merchant, J. Phys. Chem. Solids **34**, 2069 (1973)

163 D.O. Welch, G.J. Dienes, A. Paskin, J. Phys. Chem. Solids **39**, 589 (1978)

164 H.D. Merchant, K.K. Srivastava, H.D. Pandey, Crit. Rev. Solid State Sci. **3**, 451 (1973)

165 A. Migault, J. Physique **33**, 707 (1972)

166 F.F. Voronov, V.A. Goncharova, Soviet Phys. JETP **23**, 777 (1966)

167 P.W. Bridgman, *The Physics of High Pressure*, Dover, New York, 1970 (republication of the 1931 edition published by G. Bell and Sons, Ltd.)

168 S. Floreen, in *Metals Handbook*, 9th Edition, Vol. 1, T. Lyman (Ed.), American Society for Metals, Metals Park, Ohio 1980, p. 445

169 T.J. Senn, *Evaluation of the Hazard Associated with Fabricating Beryllium Copper Alloys*, Lawrence Livermore Laboratory, Report No. UCRL–52258, 1977 (unpublished) Report available from National Technical Information Service, U.S. Department of Commerce, 5285 Port Royal Road, Springfield, VA 22161

170 K. Syassen, W.B. Holzapfel, Europhys. Conf. Abstr. **1A** 75 (1975)

171 G. Huber, K. Syassen, W.B. Holzapfel, Phys. Rev. B **15**, 5123 (1977)

172 K.R. Bauchspiess, E.D. Crozier, R. Ingalls, J. Phys. (Paris) Colloq. **47**, C8-975 (1986)

173 S.A. Urry, P.J. Turner, *Solution of Problems in Strength of Materials and Mechanics of Solids*, 4th edition, Pitman, London, 1981

174 W.R.D. Manning, S. Labrow, *High Pressure Engineering*, The Chemical Rubber Co., Cleveland, Ohio, 1971

175 R. Grover, I.C. Getting, G.C. Kennedy, Phys. Rev. B **7**, 567 (1973)

176 J.W. Dally, W.F. Riley, *Experimental Stress Analysis*, 2nd edition, McGraw-Hill, New York, 1978

177 J.W. Cook, Jr., D.E. Sayers, J. Appl. Phys. **52**, 5024 (1981)

178 P.R. Bevington, *Data Reduction and Error Analysis for the Physical Sciences*, McGraw-Hill, New York, 1969

179 B. Lengeler, P. Eisenberger, Phys. Rev. B **21**, 4507 (1980)

180 E.O. Brigham, *The Fast Fourier Transform*, Prentice-Hall, Englewood Cliffs, N.J., 1974

181 F.J. Harris, Proceedings of the IEEE **66**, 51 (1978)

182 E.A. Stern, D.E. Sayers, F.W. Lytle, Phys. Rev. B **11**, 4836 (1975)

183 J. Freund (private communication)

184 D.W. Marquardt, J. Soc. Indust. Appl. Math. **11**, 431 (1963)

185 W.E. Deming, *Statistical Adjustment of Data*, Dover, New York, 1964

186 C.A. Martin, G. Monti, J. Comput. Phys. **75**, 244 (1988)

187 K.R. Bauchspieß, *Least-Squares Fitting of EXAFS Spectra using EXAFIT* (unpublished)

188 K.R. Bauchspiess, N. Alberding, E.D. Crozier, Phys. Rev. Lett. **60**, 468 (1988)

189 W.T. Eadie, D. Drijard, F.E. James, M. Roos, B. Sadoulet,
Statistical Methods in Experimental Physics, North-Holland, Amsterdam, 1971

190 G. Martens, P. Rabe, N. Schwentner, A. Werner, Phys. Rev. Lett. **39**, 1411 (1977)

191 T. Sasaki, T. Onda, R. Ito, N. Ogasawara, Jpn. J. Appl. Phys. **25**, Part I, 640 (1986)

192 S. Ainsworth, D.P. Woodruff, Solid State Commun. **56**, 461 (1985)

193 R.D. Parks, S. Raaen, M.L. denBoer, V. Murgai, T. Mihalisin, Phys. Rev. B **28**, 3556 (1983)

194 M. Croft, R. Neifeld, C.U. Segre, S. Raaen, R.D. Parks, Phys. Rev. B **30**, 4164 (1984)

195 G. Kaindl, G.K. Wertheim, G. Schmiester, E.V. Sampathkumaran, Phys. Rev. Lett. **58**, 606 (1987)

196 F. Le Normand, L. Hilaire, K. Kili, G. Krill, G. Maire, J. Phys. Chem. **92**, 2561 (1988)

197 F.K. Richtmyer, S.W. Barnes, E. Ramberg, Phys. Rev. **46**, 843 (1934)

198 G.K. Wertheim, M.A. Butler, K.W. West, D.N.E. Buchanan, Rev. Sci. Instrum. **45**, 1369 (1974)

199 A. Bianconi, A. Marcelli, I. Davoli, S. Stizza, M. Campagna, Solid State Commun. **49**, 409 (1984)

200 H. Dexpert, R.C. Karnatak, J.M. Esteva, J.P. Connerade, M. Gasgnier, P.E. Caro, L. Albert, Phys. Rev. B **36**, 1750 (1987)

201 B. Poumellec, J.F. Marucco, B. Touzelin, Phys. Rev. B **35**, 2284 (1987)

202 L. Vegard, Z. Phys. **5**, 17 (1921)

203 T. Penney, B. Barbara, T.S. Plaskett, H.E. King, Jr., S.J. LaPlaca, Solid State Commun. **44**, 1199 (1982)

204 D. Wohlleben, in *Moment Formation in Solids*, W.J.L. Buyers (Ed.), NATO ASI Series, Vol. B117, Plenum Press, New York, 1984, p. 171

205 P.A. Varotsos, K.D. Alexopoulos, *Thermodynamics of Point Defects and Their Relation with Bulk Properties*, Defects in Solids, Vol. 14, North-Holland, Amsterdam, 1986

206 J. Grammatikakis, C.A. Londos, J. Phys. Chem. Solids **49**, 1465 (1988)

207 A. Chatterjee, A.K. Singh, A. Jayaraman, Phys. Rev. B **6**, 2285 (1972)

208 K.R. Bauchspieß, E.D. Crozier, R. Ingalls, Physica B **158**, 492 (1989)

209 H.A.A. Sidek, G.A. Saunders, R.N. Hampton, R.C.J. Draper, B. Bridge, Phil. Mag. Letters **57**, 49 (1988)

210 J.E. Whitmore (private communication)

211 G. Krill, J.P. Kappler, J. Röhler, M.F. Ravet, J.M. Léger, F. Gautier in *Valence Instabilities*, P. Wachter, H. Boppart (Eds.), North-Holland, Amsterdam, 1982, p. 155

212 G. Krill, J.P. Kappler, M.F. Ravet, C. Godart, J.P. Sénateur, J. Magn. Magn. Mat. **47** & **48**, 190 (1985)

213 E. Beaurepaire, J.P. Kappler, D. Malterre, G. Krill, Europhys. Lett. **5**, 369 (1988)

214 N. Wetta, Thèse, Université Louis Pasteur, Strasbourg, 1987

215 R.M. Martin, J.B. Boyce, J.W. Allen, F. Holtzberg, Phys. Rev. Lett. **44**, 1275 (1980)

216 J.B. Boyce, R.M. Martin, J.W. Allen, F. Holtzberg in *Valence Fluctuations in Solids*, L.M. Falicov, W. Hanke, M.B. Maple (Eds.), North-Holland, Amsterdam, 1981, p. 427

217 G. Krill, J.P. Kappler, J. Röhler, in *EXAFS and Near Edge Structure*, A. Bianconi, L. Incoccia, S. Stipcich (Eds.), Chemical Physics, Vol. 27, Springer, Berlin, 1983, p. 190

218 H. Launois, M. Rawiso, E. Holland-Moritz, R. Pott, D. Wohlleben, Phys. Rev. Lett. **44**, 1271 (1980); see also erratum notice on p.1644

219 W. Kohn, T.K. Lee, Y.R. Lin-Liu, Phys. Rev. B **25**, 3557 (1982)

220 K. Baba, Y. Kuroda, Solid State Commun. **39**, 671 (1981)

221 Y. Kuroda, K.H. Bennemann, Phys. Rev. B **23**, 4114 (1981)

222 G. Wortmann, B. Perscheid, W. Krone, J. Phys. (Paris) Colloq. **47**, C8-979 (1986)

223 N. W. Ashcroft, N.D. Mermin, *Solid State Physics*, Holt, Rinehart and Winston, New York, 1976

224 J.C. Slater, *Introduction to Chemical Physics*, McGraw-Hill, New York, 1939

225 M.G. Broadhurst, F.I. Mopsik, J. Chem. Phys. **52**, 3634 (1970)

226 J.S. Dugdale, D.K.C. MacDonald, Phys. Rev. **89**, 832 (1953)